Index

United Kingdom Nirex Limited

Report no : S/98/003

Science Report

Nirex Safety Assessment Research Programme

A NATURAL ANALOGUE STUDY OF CEMENT-BUFFERED, HYPERALKALINE GROUNDWATERS AND THEIR INTERACTION WITH A REPOSITORY HOST ROCK

PHASE II

March 1998

NIREX

S/98/003

A NATURAL ANALOGUE STUDY OF CEMENT-BUFFERED, HYPERALKALINE GROUNDWATERS AND THEIR INTERACTION WITH A REPOSITORY HOST ROCK

PHASE II

Maqarin Natural Analogue Site Study Group

(Edited by C.M. Linklater)

July 1998

List of contributors

W.R. Alexander	GGWW, University of Berne, Berne, Switzerland
S. Börjesson	Chalmers Technical University, Gothenburg, Sweden
I. Casas	MBT, Barcelona, Spain[†]
M.R.Cave	Analytical Geochemistry Group, British Geological Survey, Keyworth, UK
A.V. Chambers	AEA Technology plc, Harwell, UK
S.R.N. Chenery	Analytical Geochemistry Group, British Geological Survey, Keyworth, UK
I.D. Clark	Department of Geology, University of Ottawa, Ottawa, Canada
J. Cook	Analytical Geochemistry Group, British Geological Survey, Keyworth, UK
P. Coombs	Fluid Processes Group, British Geological Survey, Keyworth, UK
P. Fritz	Umweltforschungszentrum Leipzig-Halle, Leipzig, Germany
S.J. Gardner	Fluid Processes Group, British Geological Survey, Keyworth, UK
A. Haworth	AEA Technology plc, Harwell, UK
C.R. Hughes	Department of Geology, University of Manchester, Manchester, UK
E.K. Hyslop	British Geological Survey, Murchison House, West Mains Road, Edinburgh, UK
S.D.J. Inglethorpe	Mineralogy and Petrology Group, British Geological Survey, Keyworth, UK
O. Karnland	Clay Technology AB, Ideon, Lund, Sweden
H.N. Khoury	University of Jordan, Amman, Jordan
C.M. Linklater	AEA Technology plc, Harwell, UK
A.B. MacKenzie	Scottish Universities Research and Reactor Centre, East Kilbride, UK
I.G. McKinley	Nagra, Wettingen, Switzerland
A.E. Milodowski	Mineralogy and Petrology Group, British Geological Survey, Keyworth, UK
J.M. Pearce	Mineralogy and Petrology Group, British Geological Survey, Keyworth, UK
S. Reeder	Analytical Geochemistry Group, British Geological Survey, Keyworth, UK
C.A. Rochelle	Fluid Processes Group, British Geological Survey, Keyworth, UK

[†] now at Quantisci, Parc Tecnològic del Vallés, 08920 Cerdanyola, Spain

E. Salameh	University of Jordan, Amman, Jordan
P. Sellin	SKB, Stockholm, Sweden
S. Short	ANSTO, Lucas Heights, New South Wales, Australia[‡]
B. Smith	Analytical Geochemistry Group, British Geological Survey, Keyworth, UK
N.S.Stone	AEA Technology plc, Harwell, UK
G.E. Strong	Mineralogy and Petrology Group, British Geological Survey, Keyworth, UK
C.J. Tweed	AEA Technology plc, Harwell, UK
J.M. West	Fluid Processes Group, British Geological Survey, Keyworth, UK
N. Wheal	Department of Geology, University of Manchester, Manchester, UK

[‡] now at Forbes Rigby PTY Ltd, Wollongong, Australia

Acknowledgements

The funding made available for this work by Nagra, Nirex and SKB is gratefully acknowledged by all participants.

Special mention should go to all those involved in collection of the field samples, particularly Hani Khoury and Elias Salameh (University of Jordan) and Tony Milodowski and Ewan Hylsop (BGS).

The isotope hydrogeology studies benefited greatly from the support of Ontario Hydro during the laser micro-sampling and recarbonation studies (Phase 1b). Hani Khoury, Tony Milodowski and BGS personnel are thanked for their assistance in the mineral phase isotope studies.

The authors would like to thank colleagues within their respective organisations for technical discussions during the course of the project and internal reviews of the report.

Susannah Reay is gratefully acknowledged for her editorial assistance, and her efforts with respect to document formatting, and organisation of figures and appendices.

ABSTRACT

This report is the final compiled report of work undertaken in the Jordan Natural Analogue Project (Phase II). It describes, in the main, a programme of field work and interpretation based on the Maqarin site in Northern Jordan, with additional data from sites in Central Jordan. The sites comprise metamorphosed zones with a mineralogy resembling 'cement' surrounded by clay biomicrite. At Maqarin, there is an active hyperalkaline groundwater system. The sites provide natural analogues of key processes that might occur within the 'alkaline disturbed zone' of a cementitious repository.

The main aim of Phase II was to investigate the interaction between hyperalkaline waters and unaltered clay biomicrite. The nature and sequences of secondary alteration products forming within fractures are described, along with evidence of wallrock alteration adjacent to fractures. Detailed geochemical analyses were carried out to determine the distribution of major and trace elements both within fracture infill, and in profiles within the fracture wallrock.

Groundwater samples were collected in order to improve on the extent and quality of data obtained during Phase I (reported in Nagra NTB 91-10). These data were used as input to geochemical modelling studies of trace element solubility and speciation, and also modelling of water-rock interaction using coupled chemistry/transport codes. Supporting studies of isotope hydrogeology provided information on the age of the system and a further study of microbiological activity at the site was undertaken.

The Maqarin project has provided much insight into the reaction of high pH water with carbonate rock in a system that has evolved over a geological timescale. This understanding can be used to guide the performance assessment of repository systems involving cementitious materials.

The main technical work reported here was carried out between April 1992 and March 1993. Phase II of the Maqarin project was funded jointly by Swiss Nationale Genossenschaft für die Lagerung radioaktiver Abfälle (NAGRA), United Kingdom Nirex Limited (Nirex), and the Swedish Svensk Kärnbränslehantering AB (SKB).

EXECUTIVE SUMMARY

Waste disposal concepts for intermediate-level radioactive wastes and some low-level wastes generally involve emplacement in an underground cementitious repository. Swelling clays, such as bentonite, may additionally be used as backfill material to further isolate the repository. The cementitious materials produce an alkaline porewater in the near field of such a repository and the solubility of radionuclides under these chemical conditions is generally very low. In the case of high-level waste disposal concepts, bentonite is the most commonly proposed material for part of the containment system, although some structural cement is often envisaged in the design.

Prior to the construction of such underground repositories, extensive investigations are carried out to determine the suitability of potential sites. These investigations include calculations of the post-closure performance of such a repository. The safety case for radioactive waste disposal will depend on models of repository performance covering many thousands or possibly millions of years. Many of the supporting data for these performance measurements are obtained from laboratory studies under simulated repository conditions. However, the timescale of these experiments is necessarily short. Laboratory measurements are therefore complemented by natural analogue studies - investigation of a natural system that has features or processes analogous to those expected in a radioactive waste repository. This enables study of a system that has evolved over geological timescales, and so provides confidence that laboratory measurements can be used to infer repository behaviour over much longer times.

One important issue to be considered in the assessment of a repository design incorporating cement or concrete is the impact of the 'alkaline disturbed zone'. Groundwater moving through cementitious materials in an underground repository is expected to acquire a high pH as a result of groundwater/cement interactions. This alkaline water will then interact with the geosphere around the repository altering the mineralogy and consequently the chemical and physical properties of the system. The key issues to be considered for the performance assessment of the repository are:

- the extent of the alkaline disturbed zone,
- the changes to the hydrogeological and radionuclide retardation properties of the rocks within this zone.

The information needed for consideration of these issues is obtained from a combination of laboratory investigations of alkaline water/rock interactions and field investigations of chemically similar systems.

This report is the final compiled report of work undertaken in the Jordan Natural Analogue Project (Phase II). It describes, in the main, a programme of field work and interpretation based on the Maqarin site in Northern Jordan (Figure 1), with additional data from sites in Central Jordan. These sites provide an unique field scale natural analogue of a cementitious radioactive waste repository. They comprise metamorphosed zones with a mineralogy resembling 'cement', in a host rock termed a Bituminous Marl, which is comprised mainly of clay biomicrite (clay-rich limestone) enriched in trace elements (e.g. U, Cr, Se, Sr, Ba, Pb, Cr, Ni). At Maqarin, there is an active groundwater system in the area; some groundwater interaction occurs within the metamorphic zones resulting in hyperalkaline waters which discharge at several locations. Figure 2 shows Piper trilinear plots for the major ion components of the Maqarin groundwaters. In Central Jordan, the metamorphism and

subsequent hydration phenomena are apparently much older than at Maqarin, and the hyperalkaline groundwater system is now extinct.

Phase 1 of the project (reported in Nagra NTB 91-10) was carried out during 1990-91 and focused on the chemistry within the cementitious zone. Particular emphasis was placed on the measurement of the aqueous concentrations of naturally-occurring trace elements and their locations within the solid phase, in order to build confidence in representations of chemistry in the near field of a cementitious repository.

The main aim of Phase II, carried out between 1992 and 1993, was to investigate the interaction between these high pH waters and the clay biomicrite downstream from the cementitious zone. This provides an analogue for the 'alkaline disturbed zone' expected in the host rock downstream from a cementitious repository. An understanding of the effect of a cementitious repository on the surrounding host rock, particularly the scale of the interaction and the nature of the reaction products, is an important contributor to the assessment of the performance of a cementitious repository.

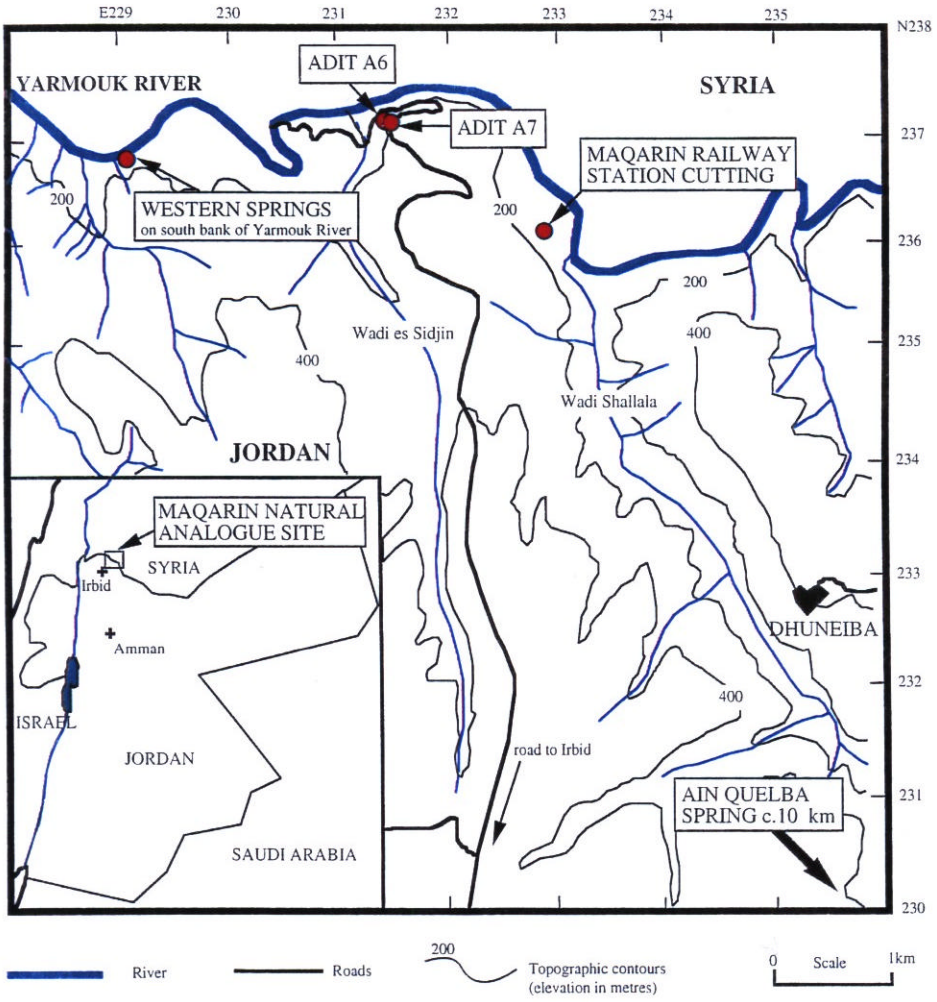

Figure 1 **Map of the Maqarin area, northern Jordan showing principal topographic features and the location of sampling sites**

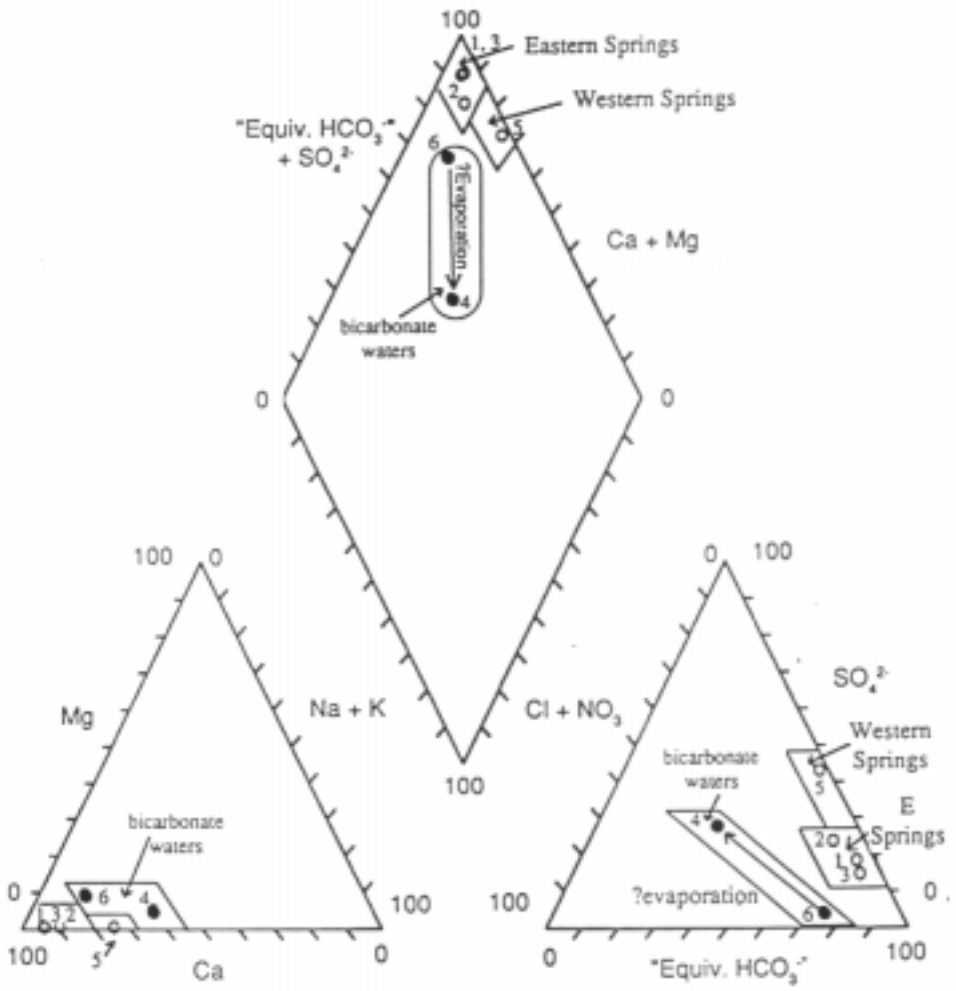

Figure 2 **Piper trilinear plot for the major ion components of the Maqarin groundwaters (as m equivalent %) showing principal variations and similarities of the different groundwater types. Note: the hyperalkaline groundwaters have been plotted with OH- recalculated as equivalent HCO3- to enable them to be compared to normal bicarbonate waters.**

1 - M1, 2 - M2, 3 - M3, 4 - M4, 5 - M5, 6 - M6.

The Phase II Jordan study involved:

- detailed mineralogical and chemical characterisation of samples of altered clay biomicrite.
- additional measurements of groundwater chemistry and associated speciation modelling. The main aim was to improve on the extent and quality of data obtained during Phase 1 of the project, particularly for those elements where the concentrations were close to the detection limits, and also to obtain some evidence of the speciation of key elements through the use of ion-exchange techniques.
- coupled chemistry/transport modelling to interpret the observations.
- a stable isotope study to provide information on the age of the system.
- a further study of microbiological activity at the site.

Most of the work has been focused on a fracture zone within a man-made horizontal adit excavated into the hillside, approximately 50m above the River Yarmouk. The adit has permitted access to altered rock from a fracture abutting the cementitious zone. This has permitted insight into the expected nature of the alkaline/rock interaction as a function of distance from a cementitious repository.

Results from the Phase II Maqarin study suggest that the most important alteration products are CSH(I) and CSH(II) hydrogels and related minerals such as tobermorite, tacharanite and jennite, and zeolites. In more calcareous environments it would appear that the dominant zeolite species will be similar to laumontite whereas in more silicate-dominated host rocks more siliceous zeolites such as mordenite sub-group will be more important. The alteration can be subdivided into 4 stages:

STAGE 1 'Aragonite Stage': Early fracture reactivation and initiation of hyperalkaline groundwater movement and precipitation of aragonite on fracture walls - possibly as a result of mixing of $Ca(OH)_2$-saturated groundwaters with background bicarbonate waters originally present in the clay biomicrite.

STAGE 2 'Ettringite-Thaumasite Stage': Precipitation of fracture-filling thaumasite (with minor ettringite in solid solution) and gypsum. Wallrock alteration was most probably initiated during this stage with the dissolution of clay minerals and calcite.

STAGE 3 'CSH Stage': Fracture reactivation, dissolution and replacement of earlier-formed thaumasite accompanied by the precipitation, initially, of CSH(I) (Al-substituted) or tobermorite then subsequently, CSH(II) (Al-substituted) or jennite. Major wallrock alteration occurred during this stage.

STAGE 4 'Zeolite Stage': Fracture reactivation, replacement of earlier CSH and thaumasite by fracture-sealing zeolites: initially high-Si zeolites of mordenite-dachiardite composition; then subsequently, zeolites progressively varying from 'epistilbite', to 'yugarawaralite' and finally, 'laumontite', accompanied by minor amounts of gypsum. This may reflect the progressive loss of silica from the system as hyperalkaline leaching continued. It would appear that zeolite alteration has affected the wallrock only very slightly.

The influence of zeolite alteration decreased rapidly away from the metamorphic zone; 'Stage 4' zeolite precipitation was not observed at distances greater than a few metres. Ettringite and thaumasite ('Stage 2') were precipitating in fractures at distances of at least 140m from the metamorphic zone.

The alteration stages described above are reflected in the observed mineral paragenesis within the fracture, and also in the profiles of alteration within the adjacent wallrock. Figure 3 shows Al, Si and Ca concentrations within the wallrock as a function of distance from the fracture. Significant alteration within the wallrock extends for only very small distances (μm to mm). This was possibly due to blocking of available porosity by secondary products, which would tend to inhibit matrix diffusion perpendicular to the fracture. At distances of greater than 20m from the metamorphic zone, no significant wallrock alteration was observed.

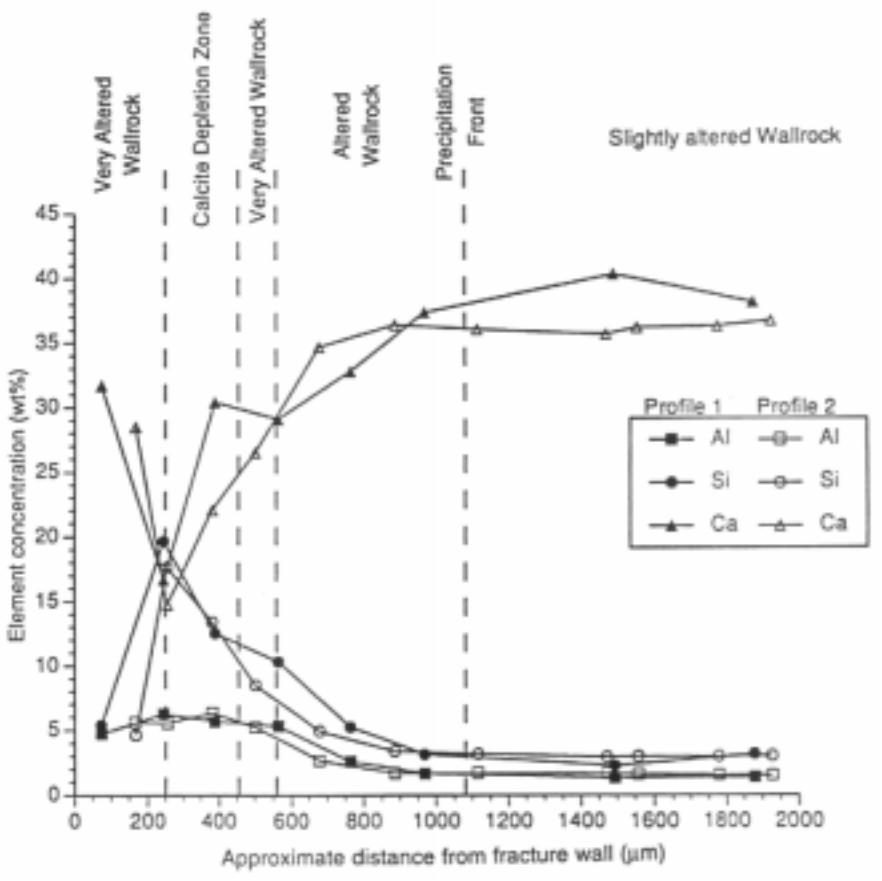

Figure 3 **Al, Si and Ca concentrations from electron probe microanalyses along two profiles through wallrock alteration sample A960.**

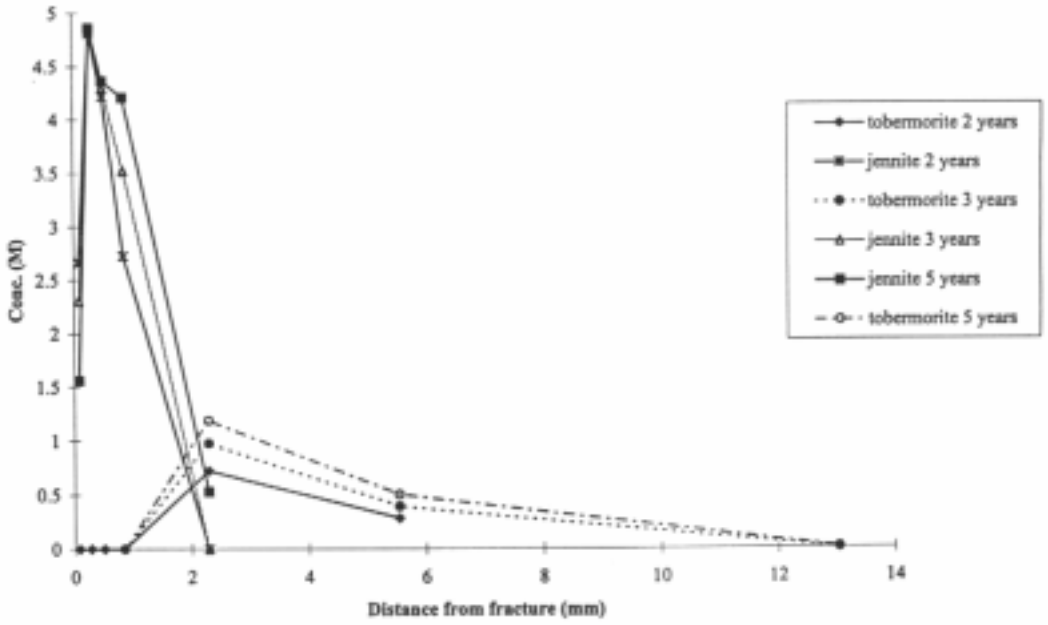

Figure 4 **Predicted precipitation of CSH phases as a function of distance from the fracture wall.**

Coupled chemistry/transport modelling of the alkali rock interaction was performed using the CHEQMATE and MARQUISS programs (implementing an equilibrium and kinetic modelling approach respectively). For both the equilibrium and kinetic approaches, modelling showed that, for diffusive transport into the host rock perpendicular to the fracture, the general trends in terms of the types of mineral alteration were in agreement with those observed. Predicted reaction distances were typically greater than those observed, i.e. several mm's (Figure 4). This may be due to limitations in the representations of chemical kinetics, due to insufficient data, or modification of the transport processes as reaction proceeds and porosity decreases. MARQUISS simulations of transport along the fracture predicted rapid migration of reaction fronts.

Table 1 Fracture minerals acting as sinks for various trace elements.

Mineral	Ba	Sr	Fe	Cr	Cu	Zn	Mn	Co	Pb	Th	U
Jennite											⊕
Zeolite ('wairakite')	⊕	⊕	⊕	⊕	⊕		⊕	⊕	(⊕)	?	⊕
Ettringite				⊕		⊕					
Thaumasite											
Calcite		(⊕)					⊕				
Aragonite		⊕									
Hydrated CSH	⊕	(⊕)				⊕	⊕		⊕		(⊕)
Brucite									(⊕)		⊕
Portlandite	⊕	⊕			(⊕)	⊕	⊕	⊕	(⊕)		(⊕)

indication in parenthesis ( ) shown to identify subordinate role as a sink for trace elements.

Table 1 shows which fracture minerals are observed to act as sinks for key trace elements. Zeolite, jennite, tobermorite or CSH take up significant amounts of U, Pb, Sr and Ba. It was observed, however, that the volumetrically more important alteration products, ettringite and thaumasite, incorporated considerably lower amounts of trace elements (except for Cr and Zn).

The conclusion of work on trace element solubility and speciation in the hyperalkaline groundwaters reinforces the conclusions of Phase I: in most cases, the observed solution concentrations for the elements of interest are several orders of magnitude less than would have been predicted assuming that the elemental concentrations were fixed by the simple stoichiometric oxides, hydroxides, carbonates and sulphates contained in the thermodynamic databases. There are two main limitations to the prediction of elemental solubilities by the method used here. First, the minerals included in the databases are pure end-members and therefore not representative of the minerals observed to form trace element sinks at Maqarin. Second, it is very difficult to test effectively how realistic is the predicted elemental speciation. Attempts to measure speciation in the groundwater samples were inconclusive.

The maximum age of hyperalkaline groundwaters at Maqarin has not yet been established. The lack of ^{36}Cl from nuclear weapons testing in these groundwaters supports evidence from ^{3}H that these waters are older than at least 40 years. There is also uncertainty as to the age of the metamorphic (combustion) event. ^{14}C concentrations in the secondary carbonates formed by recarbonation of portlandite and CSH-like phases suggest that some alteration may be less than a few hundred years old. However, $^{230}Th/U$ dating of secondary fracture minerals has suggested that the hyperalkaline groundwater fracture-flow system may have been operative for the order of 80 000 to 100 000 years These apparently conflicting estimates of age have been rationalised in terms of several episodes of water-rock reaction.

The microbial investigation has shown that a diverse population of alkaline tolerant microbes are found at all sites sampled at Maqarin. Tolerance was demonstrated up to pH 11 and appeared particularly associated with sulphate reducing bacteria. Only microbes that could exploit nutrient rich conditions were detected. This implies that a constant supply of nutrients and energy sources was present at all the sites. However, the actual activity of microbes in-situ was not determined and this remains an area of uncertainty.

The presence of a quantity of all nutrients in all environments, and the fact that no oligotrophic microbes were detected, suggests that the overall process of microbial growth is governed by energy constraints.

In summary, the Maqarin project has provided much insight into the reaction of high pH water with carbonate rock in a system that has evolved over a geological timescale. This understanding can be used to guide the performance assessment of repository systems involving cementitious materials.

The main technical work reported here was carried out between April 1992 and March 1993. Phase II of the Maqarin project was funded jointly by Swiss Nationale Genossenschaft für die Lagerung radioaktiver Abfälle (NAGRA), United Kingdom Nirex Limited (Nirex), and the Swedish Svensk Kärnbränslehantering AB (SKB).

CONTENTS

APPENDICES

1. INTRODUCTION

C.J. Tweed

Radioactive waste disposal concepts for intermediate-level waste (ILW) and some low-level wastes (LLW) generally involve emplacement in an underground cementitious repository; swelling clays, such as bentonite, may additionally be used as backfill material to further isolate the repository. The cementitious materials produce an alkaline porewater in the near field of such a repository and the solubility of radionuclides under these chemical conditions is generally very low. In the case of high-level waste disposal concepts, bentonite is the most commonly proposed material for part of the containment system, although some structural cement is often envisaged in the design.

Prior to the construction of such underground repositories, extensive investigations are carried out to determine the suitability of potential sites. These investigations include calculations of the post-closure performance of such a repository. The safety case for radioactive waste disposal will depend on models of repository performance covering many thousands or possibly millions of years. Much of the supporting data for these performance measurements are obtained from laboratory studies under simulated repository conditions. However, the timescale of these experiments is necessarily short. Laboratory measurements are therefore complemented by natural analogue studies - investigation of a natural system that has features or processes analogous to those expected in a radioactive waste repository. This enables study of a system that has evolved over geological timescales, and so provides confidence that laboratory measurements can be used to infer repository behaviour over much longer times.

One important issue to be considered in the assessment of a repository design incorporating cement or concrete is the impact of the 'alkaline disturbed zone'. Groundwater moving through cementitious materials in an underground repository is expected to acquire a high pH as a result of groundwater/cement interactions. This alkaline water will then interact with the geosphere around the repository altering the mineralogy and consequently the chemical and physical properties of the system. The key issues to be considered for the performance assessment of the repository are:

- the extent of the alkaline disturbed zone,
- the changes to the hydrogeological and radionuclide retardation properties of the rocks within this zone.

The information needed for consideration of these issues is obtained from a combination of laboratory investigations of alkaline water/rock interactions and field investigations of chemically similar systems.

This document is the final compiled report of work undertaken in the Jordan Natural Analogue Project (Phase II). It describes, in the main, a programme of field work and interpretation based on the Maqarin site in Northern Jordan, with additional data from sites in Central Jordan. These sites provide an unique field scale natural analogue to a cementitious radioactive waste repository. They comprise metamorphosed zones with a mineralogy resembling 'cement', in a host rock termed a Bituminous Marl, which is comprised mainly of clay biomicrite (clay-rich limestone) enriched in trace elements (e.g. U, Cr, Se, Sr, Ba, Pb, Cr, Ni). At Maqarin, there is an active groundwater system in the area; some groundwater interaction occurs within the metamorphic zones resulting in hyperalkaline waters which discharge at several locations. In Central Jordan, the metamorphism and subsequent hydration

phenomena are apparently much older than at Maqarin, and the hyperalkaline groundwater system is now extinct.

Phase 1 of the project was carried out during 1990-91 and focused on the chemistry within the cementitious zone. Particular emphasis was placed on the measurement of the aqueous concentrations of naturally-occurring trace elements and their locations within the solid phase, in order to build confidence in representations of chemistry in the near field of a cementitious repository.

The main aim of Phase II, carried out between 1992 and 1993, was to investigate the interaction between these high pH waters and the clay biomicrite downstream from the cementitious zone. This provides an analogue for the 'alkaline disturbed zone' expected in the host rock downstream from a cementitious repository. An understanding of the effect of a cementitious repository on the surrounding host rock, particularly the scale of the interaction and the nature of the reaction products, is an important contributor to the assessment of the performance of a cementitious repository. The study involved:

- detailed mineralogical and chemical characterisation of samples of altered clay biomicrite.
- additional measurements of groundwater chemistry and associated speciation modelling. The main aim was to improve on the extent and quality of data obtained during Phase 1 of the project, particularly for those elements where the concentrations were close to the detection limits, and also to obtain some evidence of the speciation of key elements through the use of ion-exchange techniques.
- coupled chemistry/transport modelling to interpret the observations.
- a stable isotope study to provide information on the age of the system.
- a further study of microbiological activity at the site.

Most of the work has been focused on a fracture zone within a man-made horizontal adit excavated into the hillside, approximately 50m above the River Yarmouk. The adit has permitted access to altered rock from a fracture abutting the cementitious zone. This has permitted insight into the expected nature of the alkaline/rock interaction as a function of distance from a cementitious repository.

The report has been arranged in chapters each dealing with specific aspects of the Jordan natural analogue study and contributed by the technical experts involved in that aspect of the project. References are given at the end of each chapter:

Chapter 2	Background
Chapter 3	Field work and sampling protocol
Chapters 4 and 5	Aqueous geochemistry and trace element speciation in Maqarin groundwaters
Chapters 6, 7 and 8	Mineralogy and petrography, uranium series elements and whole rock geochemistry, trace element distribution around fractures
Chapter 9	Study of mass transfer properties of Maqarin samples
Chapter 10	Study of isotope hydrogeology
Chapter 11	Study of microbiological activity at the site
Chapters 12 and 13	Geochemical modelling studies
Chapter 14	Conclusions

Full details of the analytical methodology are not given in the main text of the report but are included in the appendices.

The main technical work reported here was carried out between April 1992 and March 1993. Phase II of the Maqarin project was funded jointly by Swiss Nationale Genossenschaft für die Lagerung radioaktiver Abfälle (NAGRA), United Kingdom Nirex Limited (Nirex), and the Swedish Svensk Kärnbränslehantering AB (SKB).

2. BACKGROUND TO THE JORDAN NATURAL ANALOGUE PROJECT

A.E. Milodowski

2.1 Background to the Jordan Analogue Project

Nirex has investigated the suitability of the Borrowdale Volcanic Group (BVG) rocks at Sellafield as a potential host for an ILW/LLW repository. The BVG is composed largely of quartz, K-feldspar, albite, muscovite and chlorite with extensive carbonate (calcite and dolomite) fracture mineralisation. The Nirex disposal concept envisages the encapsulation of ILW, generally in cement-based grouts and the use of cementitious materials for backfilling and sealing the repository [1]. The Nirex repository concept has been designed to maximise radionuclide retention in the near field through the low solubility of most radionuclides of significance in hyperalkaline media allied to the large surface area afforded by the porous cementitious backfill.

Nagra is investigating the potential for L/ILW disposal in a marl host rock (Palfris Formation) at a site at Wellenberg. SKB has already a L/ILW facility (SFR) in operation, where cement-based structures, including large silos, are being used. Nagra and SKB are both currently considering the use of bentonite for backfilling and sealing shafts, vaults and exploratory boreholes in potential radioactive waste repositories for L/ILW, TRU and HLW [2]. Its high sorption characteristics and its swelling properties when saturated make bentonite particularly attractive for this purpose. The bentonite may be emplaced in conjunction with cement and concrete (used either as part of the engineered barrier system or within the construction of a repository). However, physical or mineralogical changes in the bentonite properties as a result of interaction with cement-buffered fluids could affect the performance of the seal.

Thus in the repository concepts outlined above, the near field will be dominated by cement-based materials. Cementitious materials will be used in the waste immobilisation matrices and backfill and in tunnel construction materials, grouts and seals [3, 4], and constitute by far the largest proportion of the material in the repository. Up to 1.5 million tonnes of cement are estimated to be utilised - approximately 87-90% by weight of the total repository materials - in the Swiss engineered barrier concept [5].

In such repositories, therefore, chemical conditions are expected to be highly alkaline, dominated by the chemistry of the cement porewaters for long periods of time. This alkalinity will result from ongoing hydration reactions of the cement phases with the groundwater. Models [6, 7, 8] suggest that initial hydration reactions of the cementitious materials with the groundwater will produce alkali hydroxide (KOH and NaOH) leachates, followed by an extended period (of the order of hundreds of thousands of years or more, depending on the quantity of cement and the groundwater flow rate) of high pH leachates (about pH 12.5) buffered by $Ca(OH)_2$ (portlandite) solubility and the dissociation of $Ca(OH)_2$ from calcium silicate hydrate ($CSH^{\dagger}$[9]) gels and other cement phases during progressive cement hydration. Geochemical modelling predicts that this hyperalkaline porewater will leach out of the near field and interact with the repository host rock [10, 11, 12, 13, 14]. This may significantly alter the original physical and geochemical properties of the host formation and therefore influence the retardation of radionuclides within this ‘disturbed zone’.

---

† - The standard cement chemistry shorthand is used in which C = CaO, S = SiO_2, H = H_2O, A = Al_2O_3 and F = Fe_2O_3

Comparisons of model predictions can be made with observations of alkali-aggregate reactivity in the construction industry [15, 16, 17, 18, 19, 20, 21, 22, 23, 24, 25, 26, 27]. Many of these studies have concentrated principally on the reaction of various polymorphs of silica with $Ca(OH)_2$ and the effect on the mechanical properties of the concrete. However, the mechanisms and kinetics of reactions have also been investigated. Reaction products identified include tobermorite, xonotlite, truscottite, gyrolite, foshagite and CSH gels. Van Aardt and Visser [21] have investigated the effect of $Ca(OH)_2$ attack on aluminosilicates including K-feldspar, labradorite, anorthite, sericite, kaolinite and greywacke rock. These authors found tetracalcium aluminium hydrates (C_4AH_n), alkali silicates, hydrogarnet and CSH phases as reaction products. Poole and Sotiropoulis [28] reported deleterious reactivity of dolomite in some concretes. Milodowski et al. [29] noted the dissolution of clinoptilolite (zeolite), quartz and opaline silica, and an unexplained 'hardening' of some Jurassic and Cretaceous mudrocks by cement pore fluids, in an experimental evaluation of the interaction of borehole cements with host rocks from the Harwell Research Site. Experimental studies into enhanced oil recovery by alkali-flooding [30, 31, 32, 33, 34], and on interactions between cement pore fluid and host rock in the repository disturbed zone [35] also indicate that alkali-rock reaction may significantly affect porosity and permeability through both mineral dissolution and the precipitation of secondary phases such as CSH and CASH (including tobermorite, jennite, hydrogarnet), zeolites, chlorite and $Mg(OH)_2$.

In the performance assessment of a potential radioactive waste repository, the precise retardation properties of both the near field and the potential alteration zone ('disturbed zone') in the far field must be carefully assessed. Experimental studies and observations of cement-aggregate systems, such as those discussed above, can help to elucidate the reaction mechanisms and/or provide useful thermodynamic or kinetic information for input into computer models. However, these studies are limited either because they do not adequately represent appropriate repository conditions or because short-term laboratory experiments (typically operating over a timescale of the order of a few months or less) cannot be assumed to be relevant to the time scales covered by a repository performance assessment (timescale of the order of thousands or even hundreds of thousands of years). Even investigations into alkali-aggregate reaction in 'old' concretes is of limited use since the history of the use of Portland cement is limited to the last 150 years, although the use of lime mortar may extend this to the order of 10^4 years [36]. In order to test models - and the applicability of laboratory-derived data - with respect to the long-term evolution of the repository environment, it is desirable to investigate appropriate field examples, i.e. 'natural analogues' [37, 38].

2.2 Natural Analogues of Cementitious Repository Systems

Appropriate natural analogues of a cementitious repository are very rare. Contemporary active highly alkaline (pH>10) groundwater systems similar to those anticipated within the near field and 'disturbed zones' of a repository have so far been identified principally from two restricted geological environments: from low-temperature serpentinisation of ophiolites and ultramafic rocks: e.g. California [39, 40], Oman [41, 42, 43], Cyprus [44], Yugoslavia [45] and New Caledonia [45, 46] and a unique site at Maqarin, northern Jordan, where hyperalkaline springs are found in association with spontaneous combustion-metamorphosed kerogenous marls and limestones [47, 48, 49].

The hyperalkaline groundwaters associated with the Oman ophiolite complex [50, 51, 52] and more recently, the unique portlandite-buffered groundwaters of the Maqarin area in northern Jordan [5], have been studied as natural analogues. These earlier natural analogue studies were applied specifically to examine microbial activity and the testing of thermodynamic

codes developed for predicting trace element speciation, solubility and solubility-controlling phases in repository safety assessment studies.

The unusual metamorphosed (calcined) calcareous rocks and their retrograde hydration alteration products found in the Maqarin area of northern Jordan represent particularly close analogues of a cementitious repository backfill. Furthermore, and in contrast to the earlier-studied Oman natural analogue [50, 51, 52], the Jordanian rocks are enriched in a number of trace elements analogous to elements relevant to radioactive waste inventories (e.g. U, Sr, Ba, Se, Mo, rare earth elements (REE), Co, Ni, Cu, Zn, Pb). In the Maqarin area the retrograde hydration is currently active and hyperalkaline springs and other groundwater discharges associated with this alteration present unique opportunities to (i) study the mobility of analogue trace elements in alkaline groundwater systems, (ii) to evaluate the long-term effects of cement hydration and stability of cement phases, (iii) investigate the interaction of an alkaline plume with the surrounding host rocks, and (iv) assess the geomicrobiology of hyperalkaline groundwater systems. Similar rocks also occur over large areas of central Jordan (Daba-Siwaqa area) and the Sweileh area, near Amman. However, these sites no longer have active hyperalkaline groundwater systems but do represent palaeo-systems part of which are analogous to that now seen at Maqarin.

Study of these natural analogue sites significantly extends our understanding of hyperalkaline groundwater-rock interaction processes, from the limited observations that can be made from relatively short-duration laboratory experiments to geological timescales required for repository performance assessment (i.e. 10^4-10^6 years).

2.3 References

[1] A. Atkinson and G.P. Marsh, *Engineered Barriers: Current Status*, Nirex Report, NSS/G102, 1988.

[2] R.P. Brenner and P. Jedelhauser, *Bohrlochversiegelung: Konzet Und Machbarkeitsnachweis*, NAGRA Technical Report, NTB 89-26, 1989.

[3] R.P. Brenner, G. Eppinger and K. Mettier, *Stollenversiegelung: Konzept Und Machbarkeitsnachweis*, NAGRA Technical Report, NTB 91-05, 1991.

[4] Svensk Kärnbränslehantering AB (SKB), *Treatment and Final Disposal of Nuclear Waste*, Programme for Research, Development, Demonstration and other measures, SKB RD&D Programme 1992

[5] W.R. Alexander (Ed), *A Natural Analogue Study of the Maqarin Hyperalkaline Groundwaters. I. Source Term Description and Thermodynamic Database Testing*, NAGRA Technical Report, NTB 91-10, 1992.

[6] A. Atkinson, *The Time-Dependence of pH within a Repository for Radioactive Waste Disposal*, UKAEA Technical Report, AERE-R11777, 1985.

[7] U.R. Berner, *Modelling Porewater Chemistry in Hydrated Portland Cement*, Scientific Basis for Nuclear Waste Management, **10**, 319-325, 1987

[8] A. Atkinson and R.M. Guppy, *Evolution of pH in a Radwaste Repository*, UKAEA Technical Report, AERE -R126961, 1988

[9] F.M. Lea, *The Chemistry of Cement and Concrete*. Edward Arnold, London, 3rd Edition, 1970

[10] F.T. Ewart, S.M. Sharland, P.W. Tasker, *The Chemistry of the Near-Field Environment*, Scientific Basis for Nuclear Waste Management, **IX**, 539-546, 1985.

[11] B.Fritz, B. Mad, Y. Tardy, *Geochemical Modelling of the Evolution of a Granite-Concrete-Water System around a Repository for Spent Nuclear Fuel,* Swedish Nuclear Fuel and Waste Management Company Technical Report, SKB 88-18, 1988

[12] A. Haworth, S.M. Sharland, P.W. Tasker and C.J. Tweed, *Evolution of the Groundwater Chemistry around a Nuclear Waste Repository,* Scientific Basis for Nuclear Waste Management, **XI**, 645-651,1988.

[13] R. Dayal and R. Klein, *CO_2/Grout Interactions and their Relevance to ^{14}C Attenuation in Cementitious Backfill Materials,* Radiochimica Acta, **44/45**, 263-270, 1988.

[14] I. Lunden and K. Andersson, *Modelling of the Mixing of Cement Pore Water and Groundwater using the PHREEQE Code,* Scientific Basis for Nuclear Waste Management, **12**, 949-956, 1989

[15] D.R. Moorehead and E.R. McCartney, *The Mechanism of the Quartz-Lime Solution Reaction at Temperatures up to 500•C,* Society of the Chemical Industry, 86-91, 1967.

[16] R. Kondo, *Kinetic Study on Hydrothermal Reaction between Lime and Silica,* Society of the Chemical Industry, 92-97, 1967.

[17] Z. Sauman, *Hydration Rate of Dicalcium Silicate in Mixes with Quartz under Hydrothermal Conditions,* Society of the Chemical Industry, 101-109, 1967.

[18] D.M. Roy and A.M. Johnson, *Investigations of Stabilities of Calcium Silicate Hydrates at Elevated Temperatures and Pressures,* Society of the Chemical Industry, 114-120, 1967.

[19] O. Henning and B. Gerstner, *Zur Infrarot Und Röntgenalytischen Charakterisierung Natürlicher Und Synthetischer Kalziumsilikahydrate,* Wissenschaftliche Zeitschrift der Hochschule für Architektur und Bauwesen Weimar, **19**, 287-293, 1972.

[20] O. Henning and B. Gerstner, *Untersuchungen Zur Wechselwirkung Zwischen Quartz Und Kalciumhydroxid Unter Hydrothermalen Bedinggungen,* Wissenschaftliche Zeitschrift der Hochschule für Architektur und Bauwesen Weimar, **19**, 53-58, 1972.

[21] J.H.P. van Aardt and S. Visser, *Calcium Hydroxide Attack on Feldspars and Clays: Possible Relevance to Cement Aggregate Reactions,* Cement and Concrete Research, **7**, 643-648, 1977.

[22] A.F. Baker and A.F. Poole, *Cement Hydrate Development at Opal-Cement Interfaces and Alkali-Silicate Reactivity,* Quarterly Journal of Engineering Geology, **13**, 249-254, 1980.

[23] P.G. Fookes, *An Introduction to the Influence of Natural Aggregates on the Performance and Durability of Concrete,* Quarterly Journal of Engineering Geology, **13**, 207-229, 1980.

[24] W.J. French, *Reactions between Aggregates and Cement Paste - An Interpretation of the Pessimum,* Quarterly Journal of Engineering Geology, **13**, 231-247, 1980

[25] J.E. Gillot, *Properties of Aggregates Affecting Concrete In North America,* Quarterly Journal of Engineering Geology, **13**, 289-303, 1980.

[26] L.S. Dent-Glasser and N. Kataoka, *The Chemistry of 'Alkali Aggregate' Reaction,* Cement and Concrete Research, **11**, 1-9, 1981.

[27] Building Research Establishment (BRE), *Alkali-Aggregate Reactions in Concrete,* Building Research Establishment Digest, 258, 1982.

[28] A.B. Poole and P. Sotiropoulis, *Reactions between Dolomitic Aggregate and Alkali Pore Fluids in Concrete,* Quarterly Journal of Engineering Geology, **13**, 281-287, 1980.

[29] A.E. Milodowski, I.A. George, A.J. Bloodworth and N.S. Robbins, *Reactivity of Ordinary Portland Cement (OPC) Grout and Various Lithologies from the Harwell Research Site,* British Geological Survey, Fluid Processes Research Group Report, FLPU 85-15, 1985.

[30] A.L. Bunge and C.J. Radke, *The Migration of Alkali Pulses in Reservoir Sands,* Society of Petroleum Engineers Journal, 988-1011, Dec. 1982.

[31] Z. Novosad and J. Novosad, *Determination of Alkali Losses Resulting from Hydrogen Ion Exchange in Alkaline Flooding,* Society of Petroleum Engineers Journal, 49-52, Feb. 1984.

[32] R.W. Lentz, W.D. Horst, J.O. Uppot, *The Permeability of Clay to Acidic and Caustic Permeants,* American Society for Testing and Materials, ASTM STP 874, 1985.

[33] S.M. Mohnet, J.H. Brae and W.L. Foley, *A Study of Mineral/Alkali Reactions.* Society of Petroleum Engineers, Reservoir Engineering, 653-667, Nov. 1987.

[34] P.J. Krumrine and J.S. Falcone, *Rock Dissolution and Consumption Phenomena in an Alkaline Recovery System,* Society of Petroleum Engineers, Reservoir Engineering, 62-68, Feb. 1988.

[35] D. Savage, K. Bateman, C. Hughes, A. Milodowski, J. Pearce, E. Rae and C Rochelle, *The Evalution of Chemical Mass Transfer in the Disturbed Zone of a Deep Geological Disposal Facility for Radioactive Wastes. I: Reaction of Silicates with Calcium Hydroxide Fluids,* Nirex Report, NSS/R244, 1997.

[36] W. Miller, W.R. Alexander, N. Chapman, I. McKinley and J. Smellie, Chapter 4 in *Natural Analogue Studies in the Geological Disposal of Radioactive Wastes,* (Nagra Technical Report NTB 93-03), Studies in Environmental Science 57, Elsevier, Amsterdam, 1994.

[37] N.A. Chapman, I.G. McKinley and J.A.T. Smellie, *The Potential of Natural Analogues in Assessing Systems for Deep Disposal of High Level Radioactive Waste,* NAGRA Technical Report, NTB 84-41, 1984.

[38] N.A. Chapman and I.G. McKinley, *The Geological Disposal of Nuclear Waste,* John Wiley and Sons, 1987.

[39] I. Barnes and J.R. O'Neil, *The Relationship between Fluids in Some Alpine-Type Ultramafics and Some Possible Modern Serpentinization, Western United States,* Geological Society of America, Bulletin, **80**, 1947-1960, 1969.

[40] I. Barnes, J.B. Rapp, J.R. O'Neil, R. A. Sheppard, and A.J. Gude, *Metamorphic Assemblages and the Direction of Flow of Metamorphic Fluids In Four Instances of Serpentinization,* Contributions to Mineralogy and Petrology, **35**, 263-276, 1972.

[41] C. Neal and G. Stanger, *Calcium and Magnesium Hydroxide Precipitation from Alkaline Groundwaters in Oman, and their Significance to the Process of Serpentinization,* Mineralogical Magazine, **48**, 237-241, 1984.

[42] C. Neal and G. Stanger, *Hydrogen Generation from Mantle Source Rocks in Oman,* Earth and Planetary Science Letters, **66**, 315-320, 1983.

[43] I.D. Clark and J-Ch. Fontes, *Paleoclimatic Reconstruction in Northern Oman Based on Carbonates from Hyperalkaline Groundwaters,* Quaternary Research, **33**, 320-336, 1990.

[44] T.M. Pantazis, *Thermal Mineral Waters of Cyprus,* Proceedings of the International Congress on Thermal Waters, Geothermal Energy and Volcanism, Mediterranean Area, Volume 2: Thermal Waters, 367-386, 1976.

[45] I. Barnes, J.R. O'Neil and J.J. Trescases, *Present Day Serpentization in New Caledonia, Oman and Yugoslavia,* Geochimica et Cosmochimica Acta, **42**, 144-145, 1978.

[46] J. Launay and J-Ch. Fontes, *Les Sources Thermales De Prony (Nouvelle Calédonie) Et Leurs Précipités Chimiques: Exemple De Formation De Brucite Primaire,* Géologie de la France, **1**, 83-100, 1985.

[47] M. Saines, P. Dickson and P. Lambert, *An Occurence of Calcium Hydroxide Groundwater in Jordan,* Groundwater, **18**, 503, 1980.

[48] I. Barnes, T.S. Presser, M. Saines, P. Dixon and A.F. Koster van Groos, *Geochemistry of Highly Basic Calcium Hydroxide Groundwater in Jordan,* Chemical Geology, **35**, 147-154, 1982.

[49] H.N. Khoury, E. Salameh and Q. Abdul-Jaber, *Characterisation of an Unusual Highly Alkaline Water from the Maqarin Area, Northern Jordan,* Journal of Hydrogeology, **81**, 79-91, 1985.

[50] A.H. Bath, N. Christofi, C. Neal, J.C. Philp, M.R. Cave, I.G. McKinley and U. Berner, *Trace Element and Microbiological Studies of Alkaline Groundwaters in Oman, Arabian Gulf: A Natural Analogue for Cement Pore-Waters,* British Geological Survey, Fluid Processes Research Group Report, FLPU 87-2/ NAGRA Technical Report, NTB 87-16, 1987.

[51] A.H. Bath, U. Berner, M. Cave, I.G. McKinley and C. Neal, *Testing Geochemical Models in a Hyperalkaline Environment,* Natural Analogues in Radioactive Waste Disposal, Proceedings of a Symposium organised by the Commision of the European Communities under the Programme on Radioactive Waste Management, 1987.

[52] I.G. McKinley, A.H. Bath, U. Berner, M. Cave and C. Neal, *Results of the Oman Analogue Study,* Radiochimica Acta, **44/45**, 311-316, 1988.

3. SITE DESCRIPTION AND FIELD SAMPLING PROGRAMME

A.E. Milodowski, E.K. Hyslop, H.N. Khoury and E. Salameh

3.1 Introduction

This chapter describes the location and local geological framework of the sampling sites examined during Phase II of the Jordan Natural Analogue Project. This enables the data obtained from groundwater and solid samples to be correlated, and places any interpretations into a geometrical context of the groundwater flow systems. The chapter also attempts to provide some of the boundary conditions required for subsequent geochemical modelling.

Two areas were studied:

(a) the Maqarin area in northern Jordan where active hyperalkaline springs, associated with retrograde hydration of thermally-metamorphosed bituminous limestones and argillaceous limestones, had been studied previously under Phase I of the Jordan Natural Analogue Project [1];

(b) the Daba-Swaqa area of central Jordan - where metamorphosed bituminous limestones (and their retrograde hydrated equivalents) similar to those found at Maqarin also occur, but are no longer associated with hyperalkaline groundwater phenomena.

Field work was undertaken between 16-28 May 1992 by A.E. Milodowski (BGS), E.K. Hyslop (BGS), H.N. Khoury (University of Jordan) and E. Salameh (University of Jordan), with logistic support provided by the University of Jordan. The Maqarin site lies on the Jordan-Syria border along the Yarmouk River, and is a highly restricted militarised zone with border posts maintained by the Jordanian Army. Access to the site required approval from the Jordanian military authorities and was restricted to a maximum period of 3 days within the border area. The Maqarin site was visited on 19, 20 and 21 May. During the site access periods, the maximum amount of time was spent collecting groundwater and rock samples, and measuring in situ parameters required for subsequent geochemical modelling exercises. As far as was possible, all sample preservations were carried out on-site within the time available. However, where large volume samples needed to be processed (e.g. for groundwater trace element speciation experiments), samples were treated as soon as possible in the geochemistry laboratories at the University of Jordan in Amman. Access restrictions did not apply to any of the central Jordan analogue sites visited.

Samples were also collected from Maqarin for a geomicrobiology study of the high pH groundwater system (Chapter 11). This involved sterile field sampling techniques and innoculations (in triplicate) of specific growth media for particular key microbial groups using the methodology adopted by Bath et al. [2] and used previously during the Phase I study [1]. Further details of the microbiological sampling are described in Chapter 11. Most innoculations were carried out in situ except for the samples taken from the Western Springs area, where insufficient on-site time was permitted by the Jordanian Army. For this site, large bulk samples of water were collected and processed for microbiology in Amman, within four hours of sampling. In addition to innoculations of specific growth media, a test using dip-slides (Millipore SPC tester) for aerobic heterotrophs was also performed. These were all innoculated in situ and subsequently were visually examined every 24 hours for evidence of microbial growth for a period of up to 7 days from time of sampling. Water samples for

epifluorescence microscopy, and samples of sediment/rock in contact with the groundwaters were sampled and stored in sterilised bottles or sealed sterile plastic bags, respectively.

All samples (with the exception of samples collected for trace element speciation analysis, which were shipped direct to ANSTO, Australia, from Jordan) were returned to the United Kingdom from where they were distributed to the various collaborating organisations for analysis.

3.2 The Maqarin Natural Analogue Site

3.2.1 Objectives of the Maqarin field programme

The objectives for the field sampling programme at the Maqarin site were as follows:

(i) Identify one or more discrete hyperalkaline groundwater flow systems where the interaction between the groundwater and background (unmetamorphosed) argillaceous bituminous limestone host rock (or other silicate-bearing rock types) could be fully examined. This rock-water interaction may then provide a suitable analogue system for the interaction between the hyperalkaline cement porewater plume and the host-rock disturbed-zone around a hypothetical radioactive waste repository. Following the observations from the pilot study by Milodowski et al. [3] and a brief reconnaissance visit by W.R. Alexander (University of Berne) and J.A. Smellie (Conterra) earlier in January 1992, it was felt that efforts should be focused on either the Jordan-Syria Unity Dam site investigation Adit A6, or the Maqarin railway station cutting (Eastern Springs site). These were both sampled previously during Phase I. The reconnaissance visit had identified possible fractures in bituminous argillaceous limestone or marl lithologies at both of these sites, which were actively conducting high pH groundwaters, and might furnish suitable systems with which to test coupled geochemical codes.

(ii) Sample groundwaters, background and altered lithologies associated with the system(s) identified in (i) above. If possible, groundwater samples representing water entering the system and after reaction with the host rock, and associated altered host-rock material, were to be collected. Geochemical data obtained from the groundwater samples would constrain the inflow and outflow parameters of the geochemical model system. Mineralogical and petrographic characterisation of the unaltered host rock would provide starting data for the geochemical modelling, whilst observations from the altered wallrock samples would be used to evaluate the model predictions.

(iii) Assess the groundwater flux through the system(s) sampled in (i) above, to provide estimates for flow-rate parameters to be used in the coupled code geochemical modelling.

(iv) Re-sample hyperalkaline groundwater discharge sites examined in the Phase I study with the aim of improving the geochemical (major and trace element) data obtained previously during Phase I. In addition, the higher pH groundwater discharges on the bank of the Yarmouk River (Western Springs site) were to be re-evaluated to determine whether they might represent, at least in part, an analogue of the early-stages of the evolution of a high pH plume within the repository disturbed zone (i.e. Na-K-Ca-OH groundwater system, rather than Ca-OH system).

(v) Sample ‘normal background’ bicarbonate groundwaters in order to characterise the probable background (‘upstream’) geochemical characteristics of groundwaters which are reacting with the thermally metamorphosed rocks to produce the hyperalkaline

groundwaters. Data on these groundwaters were not obtained previously during Phase I but would be needed to fully characterise the geochemistry of the Maqarin groundwater flow system.

(vi) Collect groundwaters and associated precipitates for microbiological analysis. This sampling programme was undertaken specifically on behalf of Nagra, for work being undertaken to test microbiological models.

(vii) Collect groundwater samples for the characterisation of organic species (for subsequent investigation by the University of Linköpping, Sweden).

(viii) Collect groundwater and solid samples for environmental and stable isotope analyses - i.e. ^{37}Cl, ^{3}H,$^{1}H/^{2}H$, $^{13}C/^{12}C$, $^{18}O/^{16}O$, $^{34}S/^{32}S$ (for subsequent investigation by the University of Ottawa, Canada), to try to constrain groundwater origins, reaction pathways and estimate residence time.

(ix) Collect and preserve groundwater samples to enable the characterisation of the in situ speciation of analogue trace elements using specially-prepared ion-exchange resin kits (for subsequent analysis by ANSTO, New South Wales, Australia).

(x) If possible, to collect samples of wood (or other cellulosic material) and steel which had been in contact with high pH groundwaters (e.g. old pit props from Adit A6, steel from old rails resting in hyperalkaline springs in the disused railway cutting near Maqarin station - Western Springs). These were to be collected specifically on behalf of AEA Technology Harwell. Additional samples of reacted bituminous limestone and marl were also collected for physical matrix diffusion properties characterisation by AEA Technology and for clay material characterisation by Clay Technology AB, Lund, Sweden).

3.2.2 Location and geological setting

(i) Site location and topography

The Maqarin Natural Analogue Site is situated about 16 km north of the city of Irbid and 25 km east of the River Jordan, on the southern bank of the Yarmouk River (Wadi Yarmouk) which forms the border between Syria and Jordan (Figure 3.1). The area is a region of high plateau deeply incised with recent V-shaped valleys of the Yarmouk River and its tributaries (Figure 3.1, Plate 1). The elevation of the region ranges from 30-400 m above sea-level. The site is also the location for the future Jordan-Syria Unity Dam Project on the Yarmouk River, which will have an intended storage capacity of more than 400M m^3. The location of the sampling sites is shown on Figure 3.1.

(ii) Background geology

Stratigraphy

The regional geology and hydrogeology of the Maqarin site is described in Alexander [1] and references therein, and only a brief account of the geology is presented here. The area is underlain by a marine sequence of Upper Cretaceous (Campanian-Maestrichtian-Danian) to Lower Tertiary (Lower Paleocene-Eocene) chalks, marly chalks, limestones, phosphatic limestones and cherts (Figure 3.2). Bituminous limestones and marls are common within this sequence, comprising up to 300 m of strata in the Bituminous Marl Formation (B3). The organic matter (bitumen and kerogen) content of these rocks ranges up to 20% and total S content may exceed 4.8% [4]. The Bituminous Marl Formation is the equivalent of the Muwaqqar Formation (B3) elsewhere, and overlies the Amman Formation (B2) - which does

not outcrop in the Maqarin area. In turn these rocks are overlain by limestones, chalks and cherty limestones of the Lower Palaeocene-Middle Eocene Rijam Formation (B4) and the Upper Eocene Wadi Shallala Formation (B5).

A thick sequence of up to 120 m of Quaternary alkali olivine flood basalts (intercalated with tuff, clay and gravel horizons) caps the plateau on both sides of the Yarmouk River, filling former river courses and forming wadi terraces (Plate 1). The Yarmouk River and associated streams have cut into these strata. Holocene wadi deposits, comprising alluvial fluviatile gravels, sands and silts, together with hill-slope (colluvium) deposits of clay with pebbles and boulders of chert, limestone and basalt, are found along the Yarmouk River and its tributaries. The main geological and structural elements of the area are shown in Figure 3.3.

Structure

The strata show very little deformation and are almost horizontal (Plate 1) or only gently dipping, although gentle flexures (probably related to the evolution of the regional Jordan Valley Rift system) affect the region. At Maqarin on the Jordanian side of the Yarmouk River, the Bituminous Marl Formation was uplifted to a higher elevation than at any other place in the Yarmouk Valley by a generally NE-SW trending anticline plunging to the north-east [5]. The orientation of this anticlinal structure changes significantly across the area (Figure 3.3). In the south of the area the axis trends approximately NNE-SSW, changing towards an ENE-WSW orientation on the Syrian side of the border as the structure plunges to the north-east. Close to the section intersected by Adit A6 and Adit A7, its orientation is virtually NE-SW.

A number of minor faults have been recorded in the dam site investigation adits at Maqarin [5, 6] associated with fault breccias. Two sets of joints with NW-SE and N-S trends [5, 6] have been identified, and these may be structurally related to the regional flexuring. The orientation of the NW-SE joints would appear to represent transverse tensional joints, whilst the N-S joints may represent one set (i.e. possibly sinistral S1) of shear-joints (S-type joints) formed in response to the NW-SE compressional movements that caused the NE-SW regional flexures.

Low-pressure/high-temperature metamorphic zones

The Maqarin hyperalkaline groundwaters are spatially associated with the occurrence of irregular and discontinuous lenses of unusual high-temperature, low-pressure metamorphic rocks (marbles) which occur within highly fractured zones in the Cretaceous to Tertiary sedimentary strata, mainly within the Bituminous Marl Formation [5, 6, 7]. Similar but larger areas of this type of marble also occur within marls and limestones at the same stratigraphic level in central Jordan [8, 9, 10, 11], and within the stratigraphically equivalent Hatrurim Formation (Mottled Zone) in Israel [12, 13, 14, 15, 16, 17, 18]. However, contemporary hyperalkaline groundwaters have only been reported from the Maqarin area.

The metamorphic assemblage in these rocks belongs to the sanidinite and pyroxene hornfels facies [19, 20] and is similar to that produced by contact metamorphism of limestones and marls by igneous intrusions. However, the metamorphic rocks (and therefore the metamorphism) show no relationship to the distribution of the Quaternary volcanic rocks in the area (in central Jordan and Israel, no igneous rocks even occur in the vicinity of the marbles). The formation of the marbles is therefore attributed to thermal metamorphism and calcination caused by in situ combustion of abundant organic matter originally present in these rocks. Tectonic fracturing probably allowed the ingress of oxygen into the organic-rich strata, thereby actuating combustion (possibly triggered by exothermic pyrite oxidation). Away from

the anticlinal crests, the strata are less fractured and the marbles pass laterally into normal non-metamorphosed bituminous marls and limestones.

The mineralogy and geochemistry of these metamorphic rocks and their retrograde hydration and alteration were studied in detail during the Phase I investigations [1] and are only briefly summarised here. Prograde thermal metamorphism produced a typical primary mineral assemblage of wollastonite, diopside, larnite, brownmillerite, spurrite, anorthite, ellestadite (a silicate-substituted apatite-like mineral), graphite, calcite, and apatite (carbonate, hydroxy and fluorapatite types). In the purer limestones, in the absence of quartz, simple calcination of the limestone took place to produce lime. Subsequent retrograde hydration and recarbonation products include among others: portlandite, ettringite, thaumasite, tobermorite(s), CSH gels, apophyllite, afwillite, calcite, gypsum and barite. Portlandite is present as a major rock-forming mineral in these altered rocks.

The high alkalinity of the $Ca(OH)_2$-saturated groundwater emanating from the metamorphic zones is related to the percolation of 'normal' bicarbonate groundwaters from the overlying non-metamorphic sedimentary strata (and probably in part from the underlying Amman Formation under artesian flow), through the metamorphic zones and its interaction with their primary metamorphic rocks and their retrograde alteration and re-carbonation mineral assemblages. Hyperalkaline groundwater discharges are associated with localised precipitation of calcite-aragonite (± ettringite) travertine deposits, stalactites and stalagmites, formed as a result of the rapid reaction of the high-pH waters with atmospheric carbon dioxide.

3.2.3 Adit A6 Site ('Eastern Groundwater Flow System')

(i) General location and geological features of sampling points

Adit A-6 was dug as an engineering test tunnel for the Jordan-Syria Unity Dam Project in 1979. It originates about 50 m above the river level and has been driven southwards (along N358°) for 450 m horizontally into the hillside (Figure 3.3). The adit is confined within the Bituminous Limestone Formation. Within the adit the strata are near-horizontal and the level essentially follows the same horizon for at least 180 m. The adit was the main focus for Phase II of the Jordan Natural Analogue study since it offered the potential to examine the effects of the interaction of hyperalkaline groundwater with unmetamorphosed marl host rock along a well-defined fracture flow-path: from the point where the groundwater enters fractures in the marl (as it leaves the metamorphic rocks) - the 'high pH inflow' - and at various points along flow paths up to c.140 m distant from the 'high pH inflow' (estimated by simple linear extrapolation along fractures in the marl).

The principal seepages of hyperalkaline groundwater into the adit occur in a wide, highly brecciated fracture zone intersected by the adit between 110-180 m from the entrance (Fracture Zone FZ4, Figure 3.4). Seeps within Fracture Zone FZ4 correspond to the sampling sites MQ-1 to MQ4 of the Phase I investigations [1]. Within FZ4 most groundwater influx occurs between 140-180 m but the abundance of fractures between 110-140 m completely sealed by secondary calcite, CSH minerals, ettringite and thaumasite indicates that the extent of this flowing fracture zone was originally much wider. FZ4 was resampled during Phase II, c.140 m from the adit entrance ('Groundwater Sampling Site M1', Figure 3.4). Two other major zones of inflow occur further back in the adit at c.210 m and c.300 m. However, these two zones are within highly unstable parts of the adit which has suffered extensive roof-falls and had partially collapsed, and they were therefore deemed unsafe for sampling. Major groundwater inflow zones all occur within the zone of high-temperature thermal

metamorphism intersected by the adit. The boundary between the metamorphosed and unmetamorphosed bituminous marl/limestone host rock is transitional occurring between 110-115 m.

It was evident from the distribution of small deposits of calcite-aragonite tufa on the walls of the adit that a number of minor seeps occur, or had occurred in the past, through fine (often hairline) fractures in the unmetamorphosed bituminous marl between the adit entrance and 110 m. The marl adjacent to many of these fractures displays some evidence of rock-water interaction. This is usually apparent as narrow zones (usually less than 3 mm but up to 5 mm wide) of bleaching or discoloration of the black or dark brown marl marginal to the fracture wall. Between 106-110 m the bituminous marl appears to be very extensively altered and very friable. Here the marl is cut by abundant closely-spaced (c.5-20 mm) fine (c.0.5-2 mm) anatomising networks of white veinlets containing cross-fibrous to fine powdery ettringite-thaumasite, and occasional veins of grey-white calcite. However, despite the extensive microfracturing, the fractures appear now to be completely sealed by secondary minerals and no evidence of active hyperalkaline groundwater seepage (i.e. tufa deposition) is apparent. Similar fracture alteration continues into the adjacent metamorphosed zone.

Three significant zones of fracturing were identified within the bituminous marl/limestone at c.25 m (Fracture Zone FZ1), 40-55 m (Fracture Zone FZ2) and c.60 m (Fracture Zone FZ3) from the adit entrance. All three zones display evidence of active hyperalkaline groundwater flow represented by minor tufa deposition on the adit walls from water dripping through the fractures. In all cases, water flows are very slow and only FZ2 produced enough water for adequate sampling ('Groundwater Sampling Site M2') sampled 45 m from the adit entrance.

In addition to collecting groundwater samples from M1 and M2, samples of marl containing representative fracture mineralisation were also collected along a traverse of the adit from the entrance to the metamorphic zone. Originally it was intended to take short cores using a portable electric Hilti coring tool supplied and shipped to Jordan by Nagra. Unfortunately, the drill proved inappropriate for drilling into the walls of the adit. Rock samples were therefore taken by carefully hammering and chiselling fracture material and wallrock exposed on the adit walls and roof, taking care to avoid causing any collapse of the roof in the more unstable areas of the adit. All solid samples were carefully wrapped in plastic 'cling-film' and sealed on site by coating the samples with melted paraffin wax (Shell Microwax®) in order to prevent the samples drying out, and to minimise alteration by reaction with atmospheric carbon dioxide.

Fracture orientations and apertures were also measured between the adit entrance and FZ4. Fracturing in the adit is dominated by a systematic set of NW-SE-trending major joints and veins (with minor cross-joints). Within a typical 1m E-W section of adit roof within FZ2 there are five major fractures (active water conduits) which vary in frequency from 5 cm to 40 cm apart, ranging in aperture from less than 0.5 to 5 mm. A typical 1m E-W section of adit roof within FZ4 contains 5-6 major fractures, ranging in aperture from <1 mm (hairline fractures) to 5-10 mm. The orientation of these features also varies systematically along the adit. Between the adit entrance and FZ3, the majority of the fractures have orientations parallel to N324° dipping north-easterly at 52°. However, further back into the adit the fractures progressively rotate towards a more north-westerly strike orientation, and by 110 m distant the fractures are parallel to N316° dipping north-easterly at 72°. This dominant fracture set is developed perpendicular to the axis of the regional anticlinal flexure and the variation in orientation of the fractures along the length of the adit reflects the variation in the

orientation of the anticlinal axis across the Maqarin area (see Figure 3.3). No evidence of fault displacement across fractures was identified in the marl section in Adit A6.

(ii) Sampling Site M1

This site is located 140 m from the adit entrance, within the principal zone of hyperalkaline groundwater corresponding to the highly brecciated metamorphosed zone (Fracture Zone FZ4). The Phase I investigations had shown no significant variation in the groundwater composition from a number of sites within FZ4 (sites MQ1-MQ4 [1]) and this zone was resampled at a single site - 'M1' - during Phase II in order to provide data representing the geochemistry of the hyperalkaline groundwater discharging from the metamorphic zone (i.e. analogous to the near-field cement porewaters of a repository).

At M1, water drips from a series of stalactite 'straws' developed from fractures in the west wall and in the roof of Adit A6 (Plate 2). The west wall is extensively covered by a dense coating, 10 to 30 cm, thick of white calcite 'flowstone' deposited from the groundwater seeps. The stalactite straws and flowstone deposits are mixed calcite and aragonite, formed by CO_2 diffusing from the adit atmosphere into the high pH $Ca(OH)_2$-saturated water. They remain saturated with groundwater by water surface tension effects [1]. Several drips were collectively sampled into a polythene sheet funnel (pegged onto the adit wall) with polypropylene tubing leading from the corner of the polythene bag to a large Nalgene® sample bottle on the adit floor. The flow at M1 was rapid and the collecting system was flushed by at least 3 volumes of the flowing groundwater before samples were finally collected. The pH, Eh, temperature and conductivity were measured in the water collected in the Nalgene® bottles after sufficient had collected for analysis. Sufficient water could be collected from M1 (i.e. 25-30 litres within one hour) for both the trace element speciation/preconcentration experiments, and microbiology sampling.

(iii) Sampling Site M2

Site 'M2' is 45m from the adit entrance within Fracture Zone FZ2 and is located within the unmetamorphosed Bituminous Marl Formation section. As at M1, tufaceous deposition occurs where the groundwater discharging from fractures comes into contact with CO_2 in the adit atmosphere, forming thin coatings of calcite-aragonite flowstone on the adit walls and very small, weak calcite-aragonite stalactite straws from the fractures in the roof of the adit. M2 corresponds to a single major fracture which appears to conduct the bulk of the hyperalkaline groundwater discharge within FZ2. This major fracture is a very regular linear feature 5-6 mm wide, and has been largely infilled with white to cream-coloured secondary minerals forming a complex symmetrical banded/crustiform-, locally colloform-textured (cf. [21, 22]) vein. Several closely spaced, parallel hairline fractures within a 1-2 cm wide zone either side of this fracture also produce very minor seepages.

Groundwater samples were collected by the technique used at M1. Polythene sheeting was pegged over the major dripping fracture in the adit roof to form a collecting 'funnel'. Polypropylene tubing was led from the apex of the polythene sheet funnel into a large Nalgene® sample bottle on the adit floor (Plate 3). Water was collected from a total fracture path length of 1.21m. Water collection was slow, and the system was left set up overnight, collecting water at a rate of 1 l in 24 hours. Additional water from M2 was collected from a conductive subsidiary fissure adjacent to the main fracture in the east wall of the adit (within 2 cm of the main fracture trace - sealed at this point). This fissure was 0.5 mm wide and water was collected from a 1.5 m section of the fissure at a rate of 0.3 l in 6 hours.

The groundwater seepage at this site was very slow, and so the diffusion of atmospheric CO_2 into the sample was minimised by maintaining a U-bend filled with water in the plastic tubing leading to a tight-fitting collecting bottle (thereby reducing the surface area accessible to the atmosphere). The pH, Eh, temperature and conductivity were measured in the water collected in the Nalgene® bottles after sufficient had collected for analysis. There was no difference in the pH of water collected immediately on collection and after 24 hours and this, together with the lack of any carbonate precipitate, suggested that little reaction with the atmosphere occurred during sampling. Insufficient water could be collected from M2 for either the trace element speciation/preconcentration experiments or microbiology sampling.

After groundwater collection was complete, samples of the fracture mineralisation and associated marl wallrock were collected from the groundwater sampling points. Samples of wallrock hosting fracture mineralisation were obtained intact.

(iv) Geometry and flow parameters of the fracture flow system

The geometry of the Adit A6 hydrogeological system is illustrated diagramatically in Figure 3.4. The groundwater flow in the adit is controlled by the distribution of fractures; seepage through the rock matrix was not evident. It was impossible to continuously observe the variation in alteration along any one specific fracture path because the orientation of the adit is at an angle to the regional fracture pattern. However, from a consideration of the measured orientations of the adit, the principal fractures and the metamorphic zone-unmetamorphosed marl contact, geometric estimates can be made of the fracture flow-path length from the high pH inflow at the metamorphic zone-marl contact to specific fracture sampling points (for mineralogy or groundwater) in Adit A6. Compilation of the observations from a number of fractures intersected by the length of the adit should enable a picture of the alteration pattern along individual fractures to be constructed.

Estimates of flow path length, groundwater flux and input groundwater and downstream groundwater required to define boundary conditions for geochemical modelling are described below. These estimates are based on a number of assumptions and the reliability and/or sources of error in these assumptions are also discussed. All orientations are measured clockwise from true north.

'Near-field' groundwater (M1)

The groundwater entering the fractures in the unmetamorphosed marl is assumed to be typical of groundwater equilibrated within the metamorphic zone at FZ4. No groundwater could be sampled at the precise junction between the metamorphic zone and the marl. FZ4 was sampled at several points during Phase I (MQ-1 to MQ4 inclusive [1]) and no significant variation in groundwater chemistry was noted. This indicates that the groundwater composition within FZ4 appears to be uniform and groundwater M1 (also sampled within this zone) is therefore considered to be representative of groundwater discharging from the metamorphic zone (i.e. near-field porewater analogue).

Downstream groundwater (M2)

M2 represents the only hyperalkaline groundwater discharge that could be sampled for analysis within the unmetamorphosed marl. Its composition therefore defines the downstream groundwater data that can be input into the geochemical models, or that can be used to validate downstream model predictions. M2 effectively discharges through a single, very uniform fracture for which the corresponding mineralogical, geochemical and porosity characteristics has been well-defined (Chapters 6, 7 and 8; sample A965).

Fracture flow-path length to discharge point M2

The flow path length of the marl-hosted fracture discharging at M2, from the high pH groundwater inflow, is estimated to be of the order of c.80 m.

Calculation of this parameter is based on the following assumptions:

(a) The fracture orientation of N324° measured in FZ2 is constant along its length.

This is an oversimplification of the system and fracture orientations are seen to rotate from N324° to N316° along the adit in a southerly direction between FZ2 and the contact zone at 110 m. Simple extrapolation of fractures from the adit walls along a N324° orientation will therefore underestimate the flow path lengths. A path length of 90 m is estimated from the contact zone to M2 if a N316° fracture orientation is considered. Therefore linear extrapolation of fracture orientations from Adit A6 may underestimate even simple linear flow path lengths by up to 12.5%.

(b) The E-W orientation of the boundary between the metamorphic zone observed at 110 m in Adit A6 is uniform and linear, and extends laterally to the east of the adit.

This is a major source of uncertainty in the geometry of the system. There is little information on the lateral continuity or morphology of the metamorphic zone either side of Adit A6. Surface geological mapping of the area (illustrated in Figure 3.3) indicates that metamorphosed rocks are still present for at least 200 m due west of the 110 m contact zone in Adit A6. However, because the actual contact zone is obscured at the surface by drift deposits (landslip material, soil cover and slopewash sediments) it is impossible at present to evaluate the reliability of the E-W extrapolation. The metamorphic zones are closely related to areas of intense fracturing and brecciation. Since the fractures are orientated in a NW-SE direction, the distribution of the metamorphic zones might also be expected to be influenced by this orientation. If this were the case, the metamorphic contact would be displaced further to the south than has been estimated in extrapolating fracture path lengths beyond the east wall of the adit. Consequently, the extrapolated path lengths of the fracture flow system should be regarded as minimum path lengths.

(c) The flow path is linear along a simple single planar fracture

This represents an oversimplification and considers that the fracture represents a simple planar sheet. It is evident within the adit that minor cross joints occur which may link closely-spaced adjacent major joints. This model also does not take into account the possibility of channelling of groundwater within the fissure porosity. Both of these factors would tend to increase the total length of the fracture flow path. Again therefore, the estimate of path length should be regarded as a minimum estimate.

Measurement of fracture and adit orientation

The adit and fracture orientations are both used in the calculation of fracture path lengths. Orientations were measured by sighting compass-clinometer and corrected to true north. The orientations were estimated to be within ±2°. Error in these measurements would produce an uncertainty of only c.2.5% in the estimate of fracture path lengths. This is insignificant in comparison to the other uncertainties (above) and can therefore be ignored.

Estimate of groundwater flow rate along the fracture at M2

Estimation of the flux of hyperalkaline groundwater through the main conductive fracture (Fracture 1) and for a subsidiary fracture (Fracture 2) discharging at M2 was made based on the groundwater flow-rate measured during sampling and from the known cross-sectional areas of the fractures. Both fractures gave similar flux estimates, after the effective porosity of any fracture infill was taken into account. The basis of the calculations are detailed below.

(a) **Fracture 1:**

- mineralised by jennite, aragonite, calcite, ettringite, thaumasite and chromian smectite
- fracture porosity (estimated by petrography, sample A965) = 17.1%
- sampled path length of fracture = 1210 mm
- mean fracture width = 5 mm
- water collected = 1000 ml/24 hrs

Flow rate $Q = 1.16\ 10^{-5}\ ls^{-1}$

Area of fracture sampled $A = 6.05\ 10^{-3}\ m^2$

Flux $QI = Q/A = 1.92\ 10^{-3}\ ls^{-1}m^{-2}$

(Flux through effective conductive area of fracture 1 = $1.12\ 10^{-2}\ ls^{-1}m^{-2}$*)*

(b) **Fracture 2:**

- unmineralised fissure
- sampled path length of fracture = 1500 mm
- mean fracture aperture = 0.5 mm
- water collected = 300 ml/6 hrs

Flow rate $Q = 1.39\ 10^{-5}\ ls^{-1}$

Conductive area of fracture sampled $A = 7.5\ 10^{-4}\ m^2$

Flux $QI = Q/A = 1.85\ 10^{-2}\ ls^{-1}m^{-2}$

Effect of Adit A6 on groundwater flow through fractures in the Bituminous Marl

In modelling the rock-water interaction along the fracture discharging at M2, it is necessary to use an appropriate estimate of the groundwater flux through the fracture. The flux determined above at the M2 discharge site represents flow following disturbance of the natural system by the construction of the adit. Therefore, it may not be valid to compare and evaluate model predictions using this estimate of the flux, with direct observation of the mineralogical and petrographic characteristics of the fracture alteration and mineralisation - most of which would appear to predate the adit. Therefore the effect that the adit has on the groundwater movement must also be taken into account.

The effect of the adit on the local hydrogeological flow pattern is considered qualitatively in Figure 3.5. In the undisturbed system, the flow lines are controlled by the natural head

distributions which in turn will be related to the topography, regional precipitation, evaporation and evapotranspiration, and by the distribution of permeability within the system. In a simple (isotropic) undisturbed system, equilibrium is reached in which the water table (or piezometric head surface) at depth closely follows the shape of the topographic surface. Groundwater flows towards the piezometric 'low points' which usually correspond to the topographic low points such as the valley bottoms (Figure 3.5a).

Construction of an adit creates an artificially low head. In this case (Figure 3.5b), the adit represents the point of lowest pressure in the system and, consequently, flow is now directed towards the adit, both from above, laterally and below. If water drainage from the adit is unimpeded (as is the case in Adit A6), the adit represents a highly conductive zone within which a low piezometric head is maintained. This increases the local hydraulic gradients in the region of the adit and consequently, the present groundwater flux through the adit region is greater than in the original undisturbed system.

This effect is considered in more detail in Figure 3.6. If the host rock around the adit is considered to be isotropic (again an oversimplification in a bedded sedimentary system, with an almost unidirectional fracture pattern), the flow of groundwater towards the adit will be radial. Given that the total volume of water draining from the adit remains constant, and because the volume of rock drained increases with radial distance from the adit, then the flux towards the adit must decrease with increasing distance from the adit. The flux can be expressed by Equation 1 (Figure 3.6). Extending this, the flux at any point along the fracture at a specific distance from the adit can be given by Equation 2 (Figure 3.6). It can be seen from this relationship, that the flux decreases as an inverse function of the radial distance from the adit. Applied to the fracture at M2, with an estimated path length of 80 m from the inflow to the point of discharge, it illustrates that the flux entering the fracture (assuming all other properties remaining constant) at the metamorphic zone contact may be two orders of magnitude lower than that measured at the M2 discharge point in the adit. In the undisturbed system, prior to the construction of Adit A6, the flux through the M2 fracture will probably have been even lower.

The flux value measured at M2 should, therefore, be regarded as an upper limit for modelling purposes. A more appropriate upper limit value should perhaps be at least two orders of magnitude lower (i.e. $< 2.4\ 10^{-5}\ ls^{-1}m^{-2}$) as given by Equation 2 (Figure 3.6).

3.2.4 Adit A7 Site

Adit A7 was also dug as an engineering test tunnel for the Jordan-Syria Unity Dam Project in 1979. It is located about 100 m to the east of, and at elevation about 75 m higher than Adit A6. It too has been driven southwards (parallel to Adit 6) for c.450-500 m horizontally into the hillside (Figure 3.3). Adit A7 is hosted within the chalks and chalky limestones of the Lower Palaeocene-Middle Eocene Rijam Formation (B4) which immediately overlies the Bituminous Limestone (B3) encountered in Adit A6. In many places the adit was in a very unstable condition - pit props had been completely removed and there was evidence of several recent major roof-falls. The air in the adit was generally poor and beyond about 300 m became foul such that the adit could not be explored safely beyond this point due to the lack of oxygen.

For the most part, the adit is dry and it has no hyperalkaline groundwater discharges. Droplets of water on the roof and walls of the adit are common, and appear to be caused by condensation of water vapour from the humid atmosphere in the adit. A small shallow pool of standing water associated with small seepages through fractures in the floor of the adit was

found at about 250 m from the adit entrance (Groundwater Sampling Site M4). This indicates that the groundwater table comes close to the floor of the adit at this point. This water was sampled directly by syringe, and pH and Eh were measured directly from the pool. This water represents an example of bicarbonate-type groundwater associated with the Lower Palaeocene-Middle Eocene Rijam Formation. However, given that M4 represents shallow standing water its composition may also be affected by evaporation effects or contamination (e.g. by wildlife living in the adit) to some extent. No other sites of groundwater discharge were evident in Adit 7.

3.2.5 Maqarin Railway Cutting ('Eastern Groundwater Flow System')

This site is located about 200 m north-west of the abandoned Maqarin railway station, about 1.5 km to the south-east of the entrance of Adit A6 and about 15-20 m above river level (Figure 3.1). Two railway cuttings into the bedrock of the hillside, with a total length of about 50 m, were created in the early 1900's during the construction of the now-disused railway from Damascus to Haifa. Hyperalkaline discharge occurs along both faces over a 4 m high face, creating a spectacular curtain of creamy-white and yellow flowstone with columns, stalactites and stalagmites (Plate 4). The bulk of the flowstone is composed of calcite and aragonite (±vaterite) but the tops of active stalagmites have irregular mammalated surfaces coated with colloform or 'fluffy' efflorescences of yellow-brown ettringite. The site had been sampled previously during Phase I, at several points along the cutting, and the groundwater geochemistry was shown to be uniform [1].

It had been thought during the brief Phase I examination of the railway cutting that the hyperalkaline groundwater discharged directly from the metamorphic zone at this site. However, closer examination during this study revealed that the bulk of the groundwater discharged through unmetamorphosed rocks along a distinct interface between highly fractured, massive, 0.3-1 m bedded, biomicritic limestone overlying less permeable shaley-laminated bituminous marl or limestone (Plates 4 and 5). The upper limestone was highly fractured by a close-spaced network of bedding-parallel and sub-orthogonal, sub-vertical fractures (Plate 5). Most of these fractures are fine hairline fissures and their surfaces are usually coated in white powdery secondary products. In many cases the adjacent wallrock displayed signs of bleaching or alteration. Samples of the fracture alteration were taken for petrographic analysis. As for Adit A6, rock samples were wrapped in 'cling-film' prior to being coated in paraffin wax to prevent them drying-out.

At this site it appears that, prior to the construction of the cutting, some groundwater discharge had probably occurred through wadi colluvial deposits. These were seen nearby and were heavily cemented by secondary carbonates and ettringite. The colluvial material includes boulders and pebbles of chert and basalt, in addition to limestone, marl and chalky rock fragments. Samples of this material were also taken for analysis. In addition to the collection of rock samples, small samples of steel pins and bolts from the torn-up sections of the old rail track, which had been lying in pools of hyperalkaline groundwater, were collected for Nagra and AEA Technology.

Groundwater sampling employed the same methodology used in Adit A6. Polythene sheeting was affixed beneath dripping stalactites to collect and funnel water into a number of collecting vessels (Plate 6) along a face of about 3 m. pH, Eh, conductivity and T were measured as soon as possible within the collected water (Plate 6). This site corresponds to 'Groundwater Sampling Site M3'. It was possible for sufficient water to be collected from M3 (i.e. 25-30 litres within a few hours) for both the trace element speciation/preconcentration experiments,

and microbiology sampling. In addition, samples were taken for isotopic analysis (^{37}Cl, $^{13}C/^{12}C$, $^{18}O/^{16}O$, D/H, $^{34}S/^{32}S$), as well as for bulk geochemical analysis. Flow-rate was estimated at about 2 l hr^{-1} from a total face area of c.300-500 cm^2.

3.2.6 Wadi Yarmouk Bank Seepage ('Western Springs Flow System')

On the Jordanian side of the Yarmouk River, about 2.5 km west of Adit A6, natural hyperalkaline springs discharge through colluvial deposits and river gravels at about 1 m above river level (Plate 7). This locality was sampled during Phase I corresponding to sites MQ-5 and MQ-6 [1], and was resampled during Phase II ('Groundwater Sampling Site M5'). These springs discharge along about 80-100 m of river bank forming extensive deposits of travertine. Hyperalkaline groundwater seeps from various points both at discrete flowing springs, usually associated with fissures (bedding-parallel) in the colluvium and as diffuse discharges through the colluvium. The groundwaters discharging from this site have a distinctive greenish-yellow colouration (Plate 7), shown previously by Alexander [1] to be due to the presence of significant levels of chromate ion in solution.

The colluvial deposits comprise a mixture of basalt, chert, limestone, chalk and marly chalk boulders (some in excess of 1 m diameter) in a matrix of basalt, chalk, limestone and quartz sand and gravel. Most of the basalt clasts appear fresh but surfaces exposed to hyperalkaline groundwater show signs of bleaching or discolouration up to 5 mm in from their surface. Within the seepage area, the colluvial deposits are well-cemented by secondary minerals precipitated from the groundwater (Plate 8). Surfaces of the deposits are usually encrusted with laminated carbonate and portlandite, and often stained with finely crystalline green chrome-rich ettringite, which precipitates from evaporating pools of standing hyperalkaline groundwater. However, as shown in Chapter 6, beneath the surface in contact with the atmosphere, zeolitic material is a major cement in addition to carbonates..

The site furnished ample water, and samples were taken for microbiology, organic characterisation, isotopic analysis (^{37}Cl, $^{13}C/^{12}C$, $^{18}O/^{16}O$, D/H, $^{34}S/^{32}S$) and trace element speciation, as well as for bulk geochemical analysis. Samples of colluvium in contact with the groundwater were also collected for mineralogical and petrological analysis. Petrological samples were wrapped in 'cling-film' and sealed in paraffin wax.

3.2.7 Ain Quelba Spring

Ain Quelba is situated within Wadi Shallala, about 15 km to the south-southeast of Maqarin. Here normal bicarbonate-type groundwater discharges as natural springs from fractures in the Chalky Limestone (B4) Formation that overlies the Bituminous Limestone and its metamorphic equivalents. The Ain Quelba Spring ('Groundwater Sampling Site M6') is typical of the regional groundwater from this upper aquifer. The spring is used as a local water supply and a concrete bunker has been built over it (Plate 9) in order to protect the spring discharge point from contamination by local livestock. Samples were taken from a mild steel outlet pipe that discharges groundwater from the bunker. Microbiological samples were not collected at the time of the main field visit. However, the spring was resampled by the University of Jordan for microbiology about 8 months later and the samples shipped to the UK for analysis.

3.2.8 Sampling protocol

(i) Field measurements

Geochemical parameters measured in the field at the sampling points include temperature, pH, Eh, conductivity and dissolved oxygen. The field measurements are summarised with other groundwater analyses in Chapter 4.

Two Orion portable meters (ORION RESEARCH Model SA250) and specific ion electrodes were used to measure temperature (±0.1 °C), pH (±0.01 pH unit) and Eh (±0.1 mV). pH and temperature were determined using a Ross combination glass electrode. Considerable BGS experience with this type of electrode with experimental high pH systems had demonstrated that this electrode was particularly reliable at high pH. The pH electrodes were calibrated with commercially-available buffer solutions at pH7 and 9.2, or at 9.2 and 12 depending on the pH range of the sample being measured. The pH12 buffer solution used in the field was subsequently determined to have a pH of 11.92 at 22°C when measured in the UK laboratories of the BGS.

Eh was measured with a standard Pt-Ag/AgCl electrode verified with Zobell's solution (standard solution Eh = 200-250 mV) and corrected (corrected Eh = uncorrected Eh +(244-T), where T is the temperature in degrees Celcius). As was the case in Phase I, the flow from the hyperalkaline seeps was too low to enable Eh to be measured within a sealed flow-through cell. At sites M4 and M5, Eh, pH, temperature and conductivity were measured by immersing the electrodes/probe directly in the discharging groundwater (M5), or in standing pools of water (M4), from which samples were taken for analysis. In the case of the Ain Quelba Spring, a sealed perspex flow-through cell was used to measure pH, Eh and temperature. During measurement, Eh readings typically drifted slowly downwards.

Conductivity was measured using a hand-held Bibby Conductivity SMC-1 conductivity probe. The conductivity probe was calibrated using a standard conductivity KCl solution.

It was originally intended to measure dissolved oxygen by a separate specific ion electrode with the Orion meters but the electrode was damaged in transit. An alternative method for determining dissolved oxygen was adopted, using commercially-available small portable colorimetric dissolved oxygen test kits (CHEMetrics CHEMets(R) kits: Model K-7512 and Model K-7501). These kits contained pre-prepared vials of colorimetric reagent, sealed under vacuum, into which a fixed volume of groundwater was taken up when the seal of the vial was broken. The colour developed was assessed visually by comparison with a set of vials of standard concentrations for a range of dissolved oxygen contents. The kits used were prepared for two ranges of dissolved oxygen (0-1 ppm; 1-12 ppm dissolved O_2), and measurements reported are considered to be accurate to within ±1 ppm.

Bicarbonate was determined only on sample M6 (Ain Quelba Spring) - normal bicarbonate-type groundwater - after collection of a large (1 l) sealed sample. Bicarbonate was determined by burette titration of 20 ml aliquots of groundwater with 0.0109N sulphuric acid, using Bromocresol Green indicator. Titrations were checked against 200ppm bicarbonate standard solutions pre-prepared at BGS.

(ii) Geochemical samples

Major and trace cations

30 ml samples for the analysis of major cations (Ca, Mg, Na, K), trace cations (Si, Ba, Sr, Mn, Fe, Al, Co, Ni, Cu, Zn, Cr, Mo, Cd, Pb, V, Li), NH_3, total S and Si were taken on-site, directly at the sampling point, by using a plastic syringe to minimise atmospheric contact, and filtered

'on-line' through 0.45 •m pore diameter Acrodisc nylon filter disks directly into Nalgene® bottles. The samples were preserved by acidification to 1% with respect to AristaR HNO_3. A blank sample (M7) using double-distilled water (supplied by BGS) and processed on-site in the same manner was also prepared.

Ultratrace cations

30 ml samples for ultratrace elements (U, Th, rare earth elements) for direct analysis by Inductively Coupled Plasma Mass Spectrometry (ICP-MS) were collected separately in addition to the major and trace cation samples. The samples were taken on-site by plastic syringe, filtered on-line through 0.45 •m Acrodisc nylon filter disks and stored in Nalgene® bottles after acidification to 1% with respect to AristaR HNO_3. A blank sample (M7) using double-distilled water (supplied by BGS) and processed on-site in the same manner was also prepared.

Similarly preserved larger (500 ml) samples were collected for later trace element preconcentration on ion exchange columns, to enable analytical detection limits to be improved.

Major and trace anions

60 ml samples for major and trace anions (Cl, SO_4, NO_3, NO_2 and Br), and for Total Organic Carbon (TOC) and Total Inorganic Carbon (TIC) were taken in a similar manner as for major and trace cations, except the samples remained unacidified. A blank sample (M7) using double-distilled water (supplied by BGS) and processed on-site in the same manner was also prepared

Reduced sulphur

30 ml samples for the determination of reduced sulphur were taken by plastic syringe directly at the sampling points. The samples were collected unfiltered and then preserved with the addition of NaOH (made up to 1% by weight NaOH). A blank sample (M7) using double-distilled water (supplied by BGS) and processed on-site in the same manner was also prepared.

Selenium and arsenic

30 ml samples for the determination of Se and As were taken and filtered as for major and trace cations but were preserved by acidification to 1% with respect to AristaR HCl. A blank sample (M7) using double-distilled water (supplied by BGS) and processed on-site in the same manner was also prepared.

Ferrous iron

Samples for the determination of ferrous iron were taken directly using a plastic syringe and filtered through 'on-line' 0.45 •m pore diameter Acrodisc nylon filters directly into Sterylin plastic tubes to which 1 ml of 1% 2,2-bipyridyl solution (HCl acidified) had been added. The volume was made up to 10 ml total with the sample. The 2,2-bipyridyl forms a stable red complex with ferrous iron in solution. A blank sample (M7) using double-distilled water (supplied by BGS) and processed on-site in the same manner was also prepared.

Microbiology sampling

Microbiological sampling is not described in detail here as this will be discussed in Chapter 11. As far as possible all sampling was carried out using sterile techniques as described previously in Alexander [1].

Trace element speciation samples

Samples for trace element speciation determination to be carried out by ANSTO were not processed on site because of the limited time available and the large volumes of water that required processing. Instead, large 25 l samples of groundwater were collected from sites M1, M3 and M5 in sealed polythene containers. These were returned to the University of Jordan in Amman where they were processed within 18 hours of collection. The samples were syringe-filtered through 0.45 •m pore diameter Acrodisc nylon filter disks to minimise contact with the atmosphere. The filtered groundwater was processed by adding directly to pre-prepared ion-exchange resin kits supplied by ANSTO, following prescribed instructions provided by ANSTO. The processed samples were then air-freighted direct to Australia from Jordan for subsequent analysis at ANSTO.

3.3 The Daba-Siwaqa Area, Central Jordan

3.3.1 Objectives of the field programme

The Daba-Siwaqa area of central Jordan hosts a large area of combustion-related thermally-metamorphosed marls and limestones similar to those encountered at Maqarin. As at Maqarin, these rocks have suffered retrograde hydration and alteration as a result of groundwater penetration after the thermal event [9]. There is evidence that a hyperalkaline groundwater system developed as a result of retrograde hydration of these rocks, resulting in the formation of significant and extensive travertine deposits [23]. However, the metamorphism and subsequent hydration phenomenon in this area of Jordan are apparently much older than at Maqarin, and the hyperalkaline groundwater system is now extinct.

The principal objectives for the field sampling programme in this area were:

(i) Evaluate the potential to examine the effects of palaeo-hyperalkaline groundwater interaction on unmetamorphosed marl. If this was possible then the sites in central Jordan might furnish analogue information on the later stages of evolution of hyperalkaline groundwater interaction in the near field and disturbed zone environments of a repository.

(ii) Collect samples of secondary CSH-type alteration products from both the retrograde hydrated metamorphic rocks and from altered unmetamorposed marls for investigation as analogues of cement hydration phases.

3.3.2 Location and geological setting

(i) Site location and general characteristics

The Daba-Siwaqa area is located between 30 and 50 km south of Amman and lies to the east of the Desert Highway which runs from Amman to Aqaba (Figure 3.7). The region varies in altitude from 680-918 m above sea level and possesses a semi-arid to desert climate with a very low winter rainfall (annual rainfall <100 mm). Streams are ephemeral and the area supports no significant vegetation. Much of the region is covered by a thin veneer of unconsolidated Pleistocene to Recent fluvial and lacustrine gravels, and Holocene to Recent alluvium and gravel (wadi deposits). High-temperature, low-pressure, combustion-metamorphosed marbles - the Daba Marble Zone - similar to rocks encountered at Maqarin, underlie some 375 km^2 of the Daba-Siwaqa area [8, 24]. The Daba Marble is worked locally for ornamental or decorative stone in a number of small, intermittently-worked quarries near El Hammam to the south-east of Daba (Figure 3.7).

(ii) Background geology

An account of the regional geological framework of the Daba-Siwaqa area is provided by Bender [24] and the origin of Daba-Marble and its associated retrograde alteration has been discussed by subsequent authors [7, 8, 10, 23].

The Daba Marble is stratigraphically, structurally, mineralogically and lithologically very similar to the 'Mottled Zone' in Israel and the West Bank of the Jordan [9, 10, 24] which has been described in detail by various authors [12, 13, 14, 15, 16, 17, 18]. The metamorphic zone is hosted within a carbonate-dominated, shallow marine sequence of Upper Cretaceous-Lower Tertiary bituminous/organic-rich rocks of the upper part of the Muwaqqar Chalk Marl Formation (Maestrichtian-Paleocene), and the lower part of the Um Rijam Chert Limestone Formation (Eocene) (Figure 3.8). These rocks are the stratigraphic equivalents of the kerogenous rocks hosting the metamorphic lenses seen in the Maqarin area.

The Daba Marble is characterised by a primary mineral assemblage typical of the sanidinite facies of high-temperature low-pressure thermal metamorphism. Over 48 metamorphic minerals have been recorded from this area [9, 10, 23]. The principal minerals include a prograde assemblage of spurrite (the most abundant rock-forming mineral, forming up to 80% of some marbles), calcite, wollastonite, diopside, grossular-andradite garnet, spinel, fluorapatite, graphite, ellestadite (silicoapatite group mineral - formally called wilkeite) and anthracite. This assemblage is more normally associated with the contact zones of igneous intrusions into limestones, but as at Maqarin however, the metamorphic rocks are not associated with any igneous activity and the formation of these marbles is attributed to the in situ combustion of the abundant organic matter contained within these rocks [9, 10, 12, 13, 16, 23]. The rocks are highly brecciated, and low-temperature mineralisation occurs along veins and in cavities, representing later, multistage retrograde alteration resulting from hydration, carbonation and sulphatisation processes. Major secondary minerals include calcite, portlandite, thaumasite, ettringite and tobermorite.

The distribution of the Daba Marble Zone is strongly fault-controlled. Structurally two dominating fault trends occur (Figure 3.7) with NW-SE and E-W orientations, with less important NS and NE-SW faults. The high degree of fracturing associated with the faulting facilitated combustion of the bituminous rocks by providing pathways for oxygen ingress. Three major fault zones of Miocene age [9, 24] affect the area forming a NNW-SSE striking depression within which the marbles are confined (Figure 3.7). This depression is sub-parallel to the Jordan Rift Valley - to which it is structurally related. The three major fault zones affecting the area are:

Siwaqa Fault Zone: Forming a long and narrow area of 50-800 m width extending westwards 40 km to the Jordan Rift Valley. It is a zone of intense disturbance and is affected by E-W striking faults, displaying up to 200 m vertical displacement.

Zarqa-Ma'in-Daba-Dhiban Fault Zone: Forming a zone of faults with WNW-ESE trends extending across the area in a westerly direction to the Zarqa-Ma'in hot spring area in the Jordan Rift Valley. This fault zone displays a vertical displacement of the order of 100 m.

Wadi El Hammam Fault Zone: Forming a zone of faults parallel to the Zarqa-Ma'in-Daba-Dhiban Fault Zone with a vertical displacement of 80 m.

Gentle folding is associated with the regional compression and local folding is associated with the faulting. The marble occurs as a stratified lenticular horizon and reaches a maximum thickness of about 10 m in the area of El Hammam.

Travertines (primarily chemical deposits of calcium carbonate) occur throughout much of the Daba Marble Zone. They form porous laminated precipitates containing abundant fossilised or calcite- and silica-replaced vegetation, much of which appears to be the stems and roots of reeds - indicating that the travertines formed during a considerably wetter climate than at present. Being more indurated and resistant to ablation and erosion than the surrounding soft chalks, marls and reactive marbles, they now cap the summits of hills and ridges in the area.

Clark et al. [23] have shown by stable isotope analysis that the calcite in the travertines is extremely depleted from equilibrium values for common CO_2 sources, with $\delta^{13}C$ values as low as -22‰ PDB[†] . Similar depletions are found in the modern travertines in the Maqarin area, and these authors concluded that the central Jordan travertines were similarly deposited from palaeo-hyperalkaline groundwater spring discharges by uptake of atmospheric CO_2. Clark et al. also attempted to date a travertine from Khan-ez-Zabib by a combination of thermoluminescence, electron spin resonance, ^{14}C and $^{230}Th/^{234}U$ radiometric techniques. These authors obtained mid-Pleistocene ages of between 700-900 ka (B.P.), and have further suggested that this age is probably also close to the timing of the actual metamorphic event. This contrasts with much older Late Miocene (13.6 ± 2 Ma) ages obtained by apatite fission-track annealing dating technique for the metamorphic event in the 'Mottled Zone' of Israel [25].

3.3.3 Sampling sites

Three sites were examined and sampled in the Daba-Siwaqa area. In two of these sites (Daba road cutting on the Desert Highway, and travertine-capped Khan-ez-Zabib Hills) palaeo-hyperalkaline discharges had formed major travertine deposits, and alteration of the host lithologies along fractures associated with these secondary deposits could be examined and sampled. A brief visit was made to small working quarries in the El Hammam area slightly further to the east to collect samples of the Daba Marble.

(i) Daba road cutting, Desert Highway.

An exposure of the metamorphosed (Daba Marble) and non-metamorphosed Muwaqqar Chalk Marl Formation capped by travertine was examined in the road cutting at the sides of the Amman-Aqaba Desert Highway, between about 1-3 km north of the village of Daba (Figure 3.7). This locality is close to the northern limit of the Daba Marble Zone and here the Muwaqqa Chalk Marl Formation appears to be only moderately to weakly metamorphosed, and passes gradationally northwards (over a distance 100-200 m laterally) into unmetamorphosed chalky marl or limestone. The rocks exposed at this locality do not appear to be particularly bituminous. For the most part the strata are virtually horizontal or only gently-dipping. However, small anticlinal flexures locally affect the rocks.

One such anticlinal flexure about 15-20 m in width was observed about 1 km north of Daba (Plate 10). The crest of the flexure was seen to be highly fractured with fine sub-vertical hairline fissures now filled with secondary calcite and CSH minerals (Plate 11). The rocks for 2 m either side of the crest of the fold are intensely reddened and 'spotted', densely crystalline and indurated by metamorphism, and contain no trace of original sedimentary bedding. However, laterally the marble passes rapidly into a zone of blocky-fractured porcellanous weakly-metamorphosed limestone with decreasing fracture intensity (6-8 m from the crest), and then into well-bedded and slightly-baked marly chalk or chalky limestone about 8-10 m

[†] PBD (Peedee Belemnite) is an internationally accepted reference standard used to report carbon isotopic ratios.

from the crest. The southern limb of the structure appears to be truncated by a poorly-exposed and highly fractured zone, possibly a fault. Northwards, the same bedding horizon can be traced into very friable, laminated to shaley chalky limestone which is apparently unmetamorphosed.

The road cutting is capped by up to 1 m of green-stained and partly silicified travertine. The travertine cap is best seen about 1 km north of Daba and is only locally present, much having been removed locally by erosion. Further north, it thins and dies out. The travertine is irregularly variable in structure, displaying laminated, massive, indurated, friable and locally vuggy forms. Cavities and fissures (0.1-5cm diameter) in the travertine are often coated or filled by a green earthy secondary mineral which has been shown elsewhere to be an unusual iron-free chrome-rich dioctahedral smectite - volkonskoite [23, 26]. These cavities are also commonly lined or filled by colourless to grey, fine, spherulitic or banded opaline silica or chalcedony. In some cases the silica is strongly green-coloured and includes earthy or finely disseminated volkonskoite. White secondary CSH minerals are also present in many of these fissures.

Subvertical fractures filled with secondary silica, calcite, volkonskoite or CSH minerals also penetrate the marble and adjacent unmetamorphosed rocks beneath the travertine. Fractures filled with secondary minerals were seen within the chalky marl/limestone host rock up to 3 km north of Daba. In most cases, the adjacent wallrock appeared to show some signs of alteration with green (?volkonskoite) staining, or partial silicification. Samples of fracture alteration and host-rock material were collected from the travertine deposit, marble and adjacent unmetamorphosed host rock. As the samples were dry at outcrop no special precautions were taken to seal the samples before analysis.

(ii) Khan-ez-Zabib Hills

The Khan-ez-Zabib Hills form a distinctive ridge (Plate 12) rising about 50 m above an otherwise featureless plain about 12 km south-east of Daba and 1-5 km east of the Desert Highway (Figure 3.7). Significant travertine deposits form resistant caps to the tops of these hills producing a distinctive flat-topped profile. The travertine exposed at the western-most end of this ridge was sampled and studied previously by Clark et al. [23]. During the present programme, travertines were examined both from the same site and also from exposures further to the east along the ridge.

At the western end of the ridge these deposits are several metres thick and are seen to rest directly on red spurritic marble and black graphitic marbles. These travertines display a variety of textures and include: travertine with fine horizontal lamination (<1 mm) of microcrystalline calcite; spongy-textured travertine with vertical tubular channels with ‘cross-structures’ which appear to be moldic channels and calcified replacements after roots and stems of plants (suggested by Clark et al. op. cit. to be the roots and stems of reeds); dense massive microcrystalline calcite interbanded (1-20 cm scale) with layers of porous friable chalky or earthy calcite. The travertines are locally silicified or have opaline silica filling or lining molds after plant roots and stems. In many cases, at outcrop the calcite walls of root cast channels can be lined by opaline or chalcedonic silica phases and filled by later earthy green calcareous clay (volkonskoite and fine calcite). The surfaces of the western outcrop of travertine are locally darkened by a fine black to brown polished surface veneer, probably representing ‘desert varnish’ seen on many rock outcrops in arid central Jordan.

The south-eastern end of the ridge displays a more complex situation, and a series of at least two discrete travertine horizons was identified during the Phase II field visit. A sharp NE-

SW-trending linear cross-cutting feature, which appears to be a fault, was seen in the shallow col which separates the south-eastern-most of the Khan-ez-Zabib summits from the main ridge. The fault-like structure is bounded on the eastern side by a prominent narrow seam (c.30-50 cm thick) of vivid dark green, tough, dense silicified rock (Plate 13) which has been undercut by erosion to form a small trench filled with drift and loose sediment. The upper half of this silicified 'seam' contains clear evidence of silica-replaced plant roots and stems, and moldic cavities in silica (after plant material) filled by earthy green clay (possibly volkonskoite). The fossilised root channels are vertically orientated in their growth positions. The lower part of the seam appears structureless or possibly sheared, brecciated, recrystallised and interbanded with seams of white silica, orientated parallel to the fault line. The rock contains very little carbonate and appears to be a travertine that has been largely replaced by silica phases.

To the east of the fault, the green silicified rock passes rapidly and laterally into soft, pale-green, earthy, fine-grained travertine. The green colouration of the travertine is spatially related to the fault, increasing significantly in intensity within 1 m of the fault. This suggests that the fault acted as a conduit for volkonskoite-mineralising solutions. A few tens of metres to the south-east, the green earthy travertine is overlain by a breccia or gravel densely cemented by white finely crystalline calcite and possible CSH minerals, and displaying imbricate clast fabric (Plate 14). This in turn is overlain, about 50 m further to the south-east, by a second horizon of discontinuously-preserved and irregularly interlaminated, earthy-green travertine and partly-silicified travertine with a soft, green volkonskoite-stained calcareous matrix. The uppermost part of this second travertine is silicified.

Finely crystalline, black and red marble is exposed locally to the west of the fault and indicates that the NE-SW fault has a downthrow to the south-east. The breccia separating the two travertine horizons comprises angular fragments of locally-derived metamorphosed chert, altered marble, chalky limestone and minor fragments of green volkonskoite-stained material derived from the underlying travertine deposit. Clasts in the breccia are orientated in an imbricate fabric dipping to the south or south-east, indicating derivation of material from north or north-west. The breccia is also fractured and veined by secondary carbonates, silica and volkonskoite, particularly where it is overlain by the upper travertine. The observations described above suggest that, as well as acting as a conduit and focus for hyperalkaline groundwater discharge, the fault was also periodically active during travertine formation, and probably presented a topographic feature (i.e. fault scarp) down which colluvial or scree deposits of locally-derived material were transported giving rise to the syntectonic intraformational breccia seen separating the two travertine horizons.

(iii) El Hamman quarries

A brief visit was made to a number of small working, or recently-worked quarries situated near to El Hammam to the east of the Khan-ez-Zabib ridge (Figure 3.7). Here fresh exposures of marble could be examined and sampled. The rocks were usually highly fractured and variously hued with secondary carbonates, CSH minerals and sulphates largely sealing fractures in the brecciated marble (Plate 15). The mineralogy of these rocks has been described in detail by Khoury and Nassir [10] and Nassir and Khoury [9]. Fresh blasting carried out at the time of the visit to one of the quarries exposed vein fillings and amygdales within the marble filled with soft moist plastic to gelatinous secondary CSH alteration products. Samples of this material were collected for future analysis.

3.4 References

[1] W.R. Alexander (Ed), *A Natural Analogue Study of the Maqarin Hyperalkaline Groundwaters. I. Source Term Description and Thermodynamic Database Testing,* NAGRA Technical Report, NTB 91-10, 1992.

[2] A.H. Bath, N. Christofi, C. Neal, J.C. Philp, M.R. Cave, I.G. McKinley and U. Berner, *Trace Element and Microbiological Studies of Alkaline Groundwaters in Oman, Arabian Gulf: a Natural Analogue For Cement Pore-Waters,* British Geological Survey, Fluid Processes Research Group Report, FLPU 87-2/ NAGRA Technical Report, NTB 87-16, 1987.

[3] A.E. Milodowski, J.M. Pearce, C.R. Hughes and H.N. Khoury, *A Preliminary Mineralogical Investigation of a Natural Analogue of a Cement-Buffered Hyperalkaline Groundwater Interaction With Marl, Maqarin, Northern Jordan,* NAGRA Unpublished Internal Report, 1992.

[4] A. Abed and B. Amireh, *Petrography and Geochemistry of Some Jordanian Oil Shales from North Jordan,* Journal of Petroleum Geology, **5**, 261-274, 1983.

[5] H.N. Khoury, E. Salameh and Q. Abdul-Jaber, *Characterisation of an Unusual Highly Alkaline Water from the Maqarin Area, Northern Jordan,* Journal of Hydrogeology, **81**, 79-91, 1985.

[6] H.N. Khoury, *The Origin of Highly Alkaline Waters from the Maqarin Area, North Jordan,* Dirasat, **12**, 125-131, 1985.

[7] H.N. Khoury and S. Nassir, *High Temperature Mineralisation in the Bituminous Limestone in Maqarin Area- North Jordan,* Neues Jahrbuch für Mineralogie Abhandlungen, **144**, 197-213, 1982.

[8] W. Heimbach and H. Rosch, *Die mottled zone in Zentral-Jordanien,* Geologisches Jahrbuch, B40, 3-17, 1980.

[9] S.G. Nassir and H.N. Khoury, *Geology, Mineralogy and Petrology of Daba Marble, Jordan,* Dirasat, **9**, 107-130, 1982.

[10] H.N. Khoury and S. Nassir, *A Discussion on the Origin of Daba-Siwaqa Marble,* Dirasat, **9**, 55-66, 1982.

[11] H.N. Khoury and E. Salameh, *The Origin of High Temperature Minerals from Sweileh Area, Jordan,* Dirasat, **13**, 261-269, 1986.

[12] Y.K. Bentor, S. Gross and I. Heller, *Some Unusual Minerals from the 'Mottled Zone' Complex, Israel,* American Mineralogist, **48**, 924-930, 1963.

[13] Y.K. Bentor, S. Gross and I. Heller, *High Temperature Minerals in Non-Metamorphosed Sediments,* Nature, **199**, 478, 1963.

[14] S. Gross, E. Mazor, S. Saas, I. Zak, *The 'Mottled Zone' Complex of Nahal Aylon (Central Israel),* Israel Journal of Earth Science, **16**, 84-96, 1967.

[15] Y.K. Bentor, S. Gross and Y. Kolodny, *New Evidence on the Origin of High Temperature Assemblage of the 'Mottled Zone', Israel,* Proceedings of the 24th International Geological Congress, Section 2, 265-275, 1972.

[16] Y. Kolodny and S. Gross, *Thermal Metamorphism By Combustion of Organic Matter; Isotopic and Petrological Evidence,* Journal of Geology, **82**, 489-506, 1974.

[17] S. Gross, *The Mineralogy of Hatrurium Formation, Israel,* Geological Survey of Israel Bulletin, **70**, 80, 1977

[18] Y. Kolodny, *Natural Cement Factory: A Geological Story,* Engineering Foundation Conference, 203-216, 1979.

[19] H.G.F. Winkler, *Petrogenesis of Metamorphic Rocks*, Springer-Verlag, 1976.
[20] A.H. Treiman and E.J. Essene, *Phase Equilibria in the System CaO-SiO_2-CO_2*, American Journal of Science, **283A**, 97-120, 1983.
[21] C.F. Park and R.A. McDiarmid, *Ore Deposits*, W.H. Freeman and Co.,1975.
[22] S.I. Tomkieff, *Dictionary of Petrology*, John Wiley and Sons Ltd, 1983.
[23] I.D. Clark, H.N. Khoury, E. Salameh, P. Fritz, Y. Gösku, A. Wieser, C. C ausse and J-Ch. Fontes, *Travertines in Central Jordan: Implications For Palaeohydrology and Dating*, Proceedings of the IAEA/UNESCO Symposium on Isotope Techniques in Water Resources Development, 1992.
[24] F. Bender, *Geologie von Jordanien-Beiträge zur regionalen Geologie der Erde*, Gebrüder Bornträger, 1968.
[25] Y. Kolodny, N. Barr and E. Sass, *Fission Track Age of the 'Mottled Zone Event' in Israel*, Earth and Planetary Science Letters, **11**, 269-272, 1971.
[26] H.N. Khoury, R.C. Mackenzie, J.D. Russell and J.M. Tait, *An Iron-Free Volkonskoite*, Clay Minerals, **19**, 43-57, 1984.

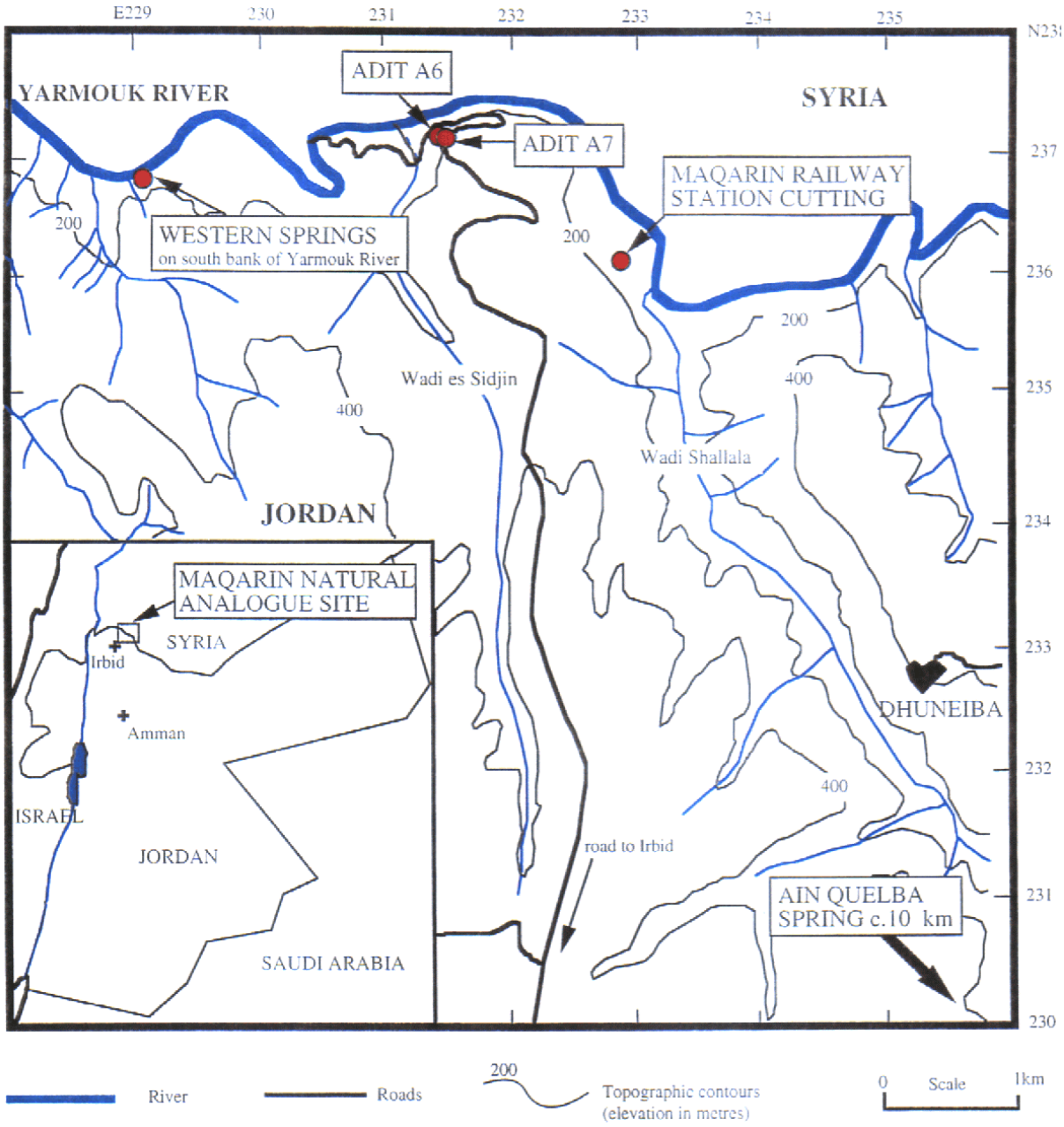

Figure 3.1 Map of the Maqarin area, northern Jordan showing principal topographic features and the location of sampling sites.

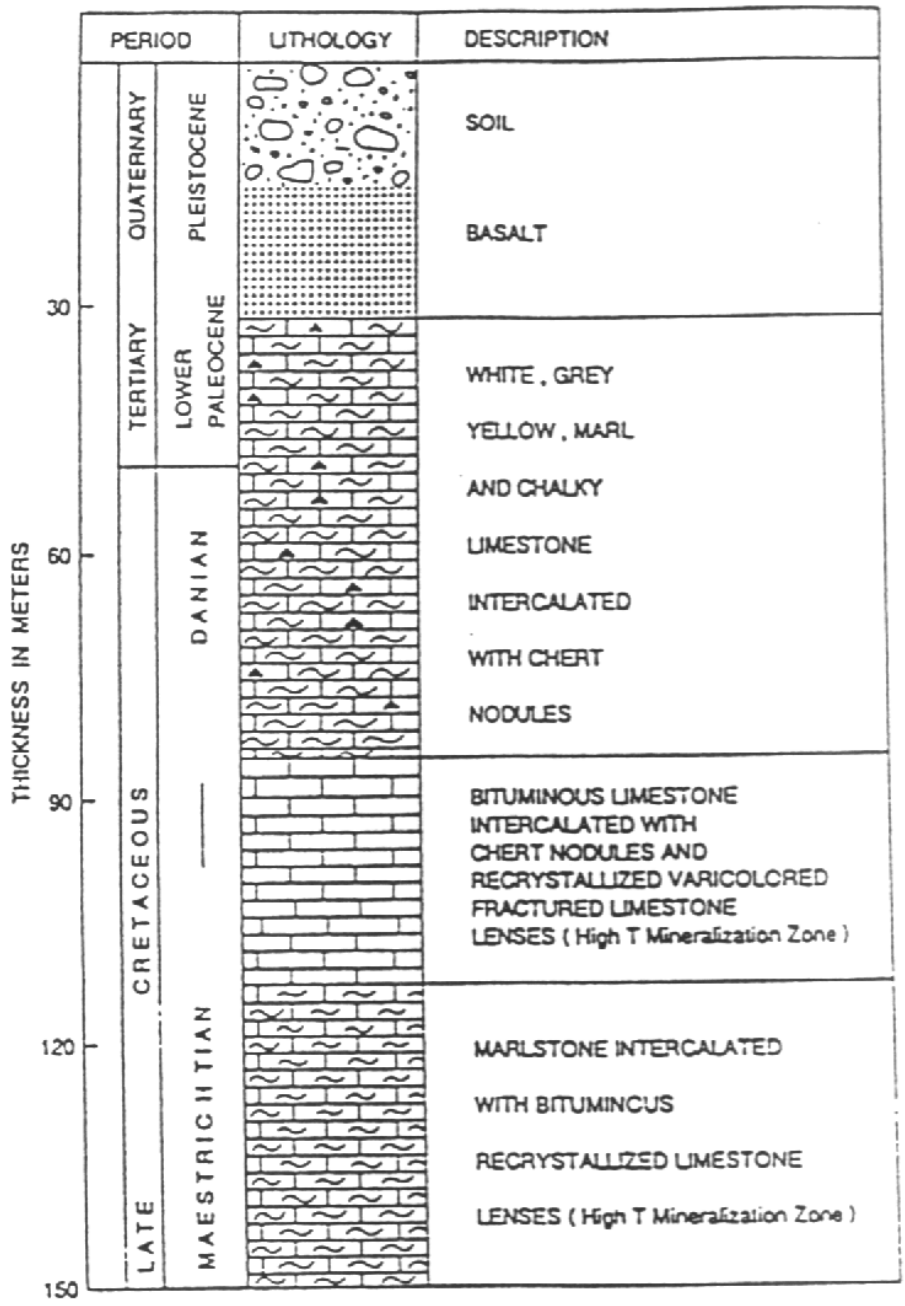

Figure 3.2 Lithostratigraphy of the Maqarin area (from [1]).

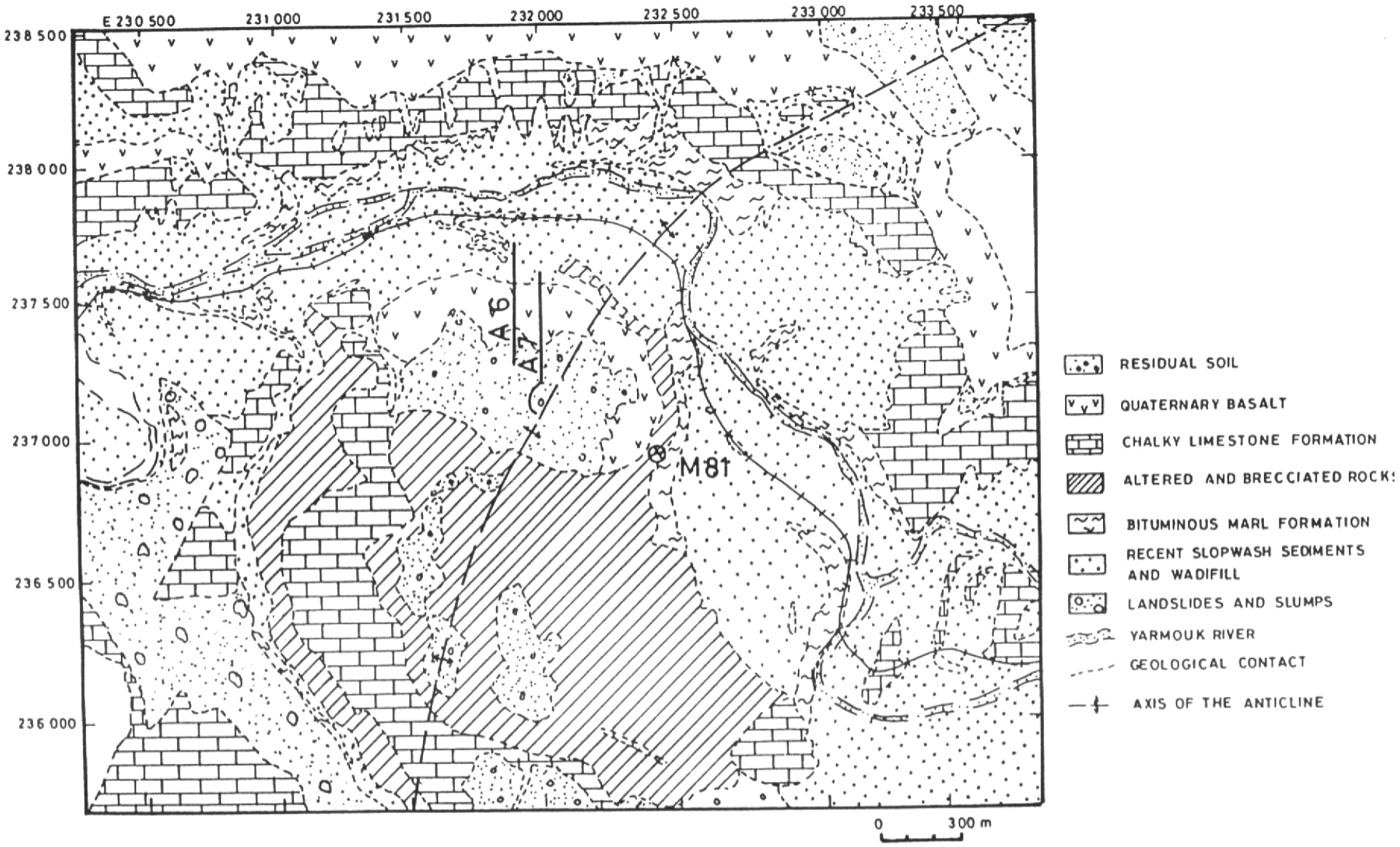

Figure 3.3 Geological map of the Maqarin area showing the principal features and distribution of the geological units

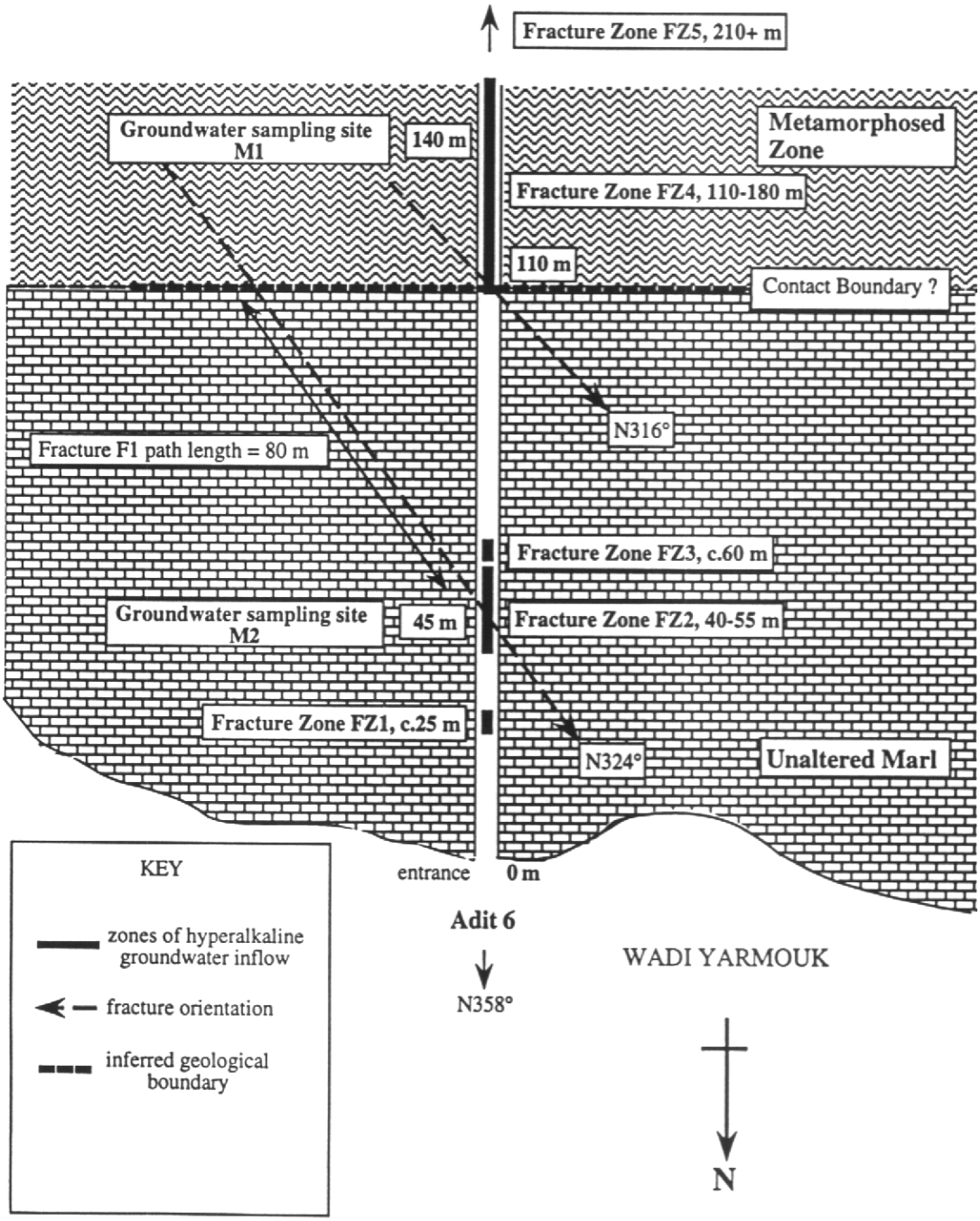

Figure 3.4 Plan diagram showing the local geology, and location and geometrical relationships of the principal hydrogeological features and sampling sites in Adit A6, Maqarin.

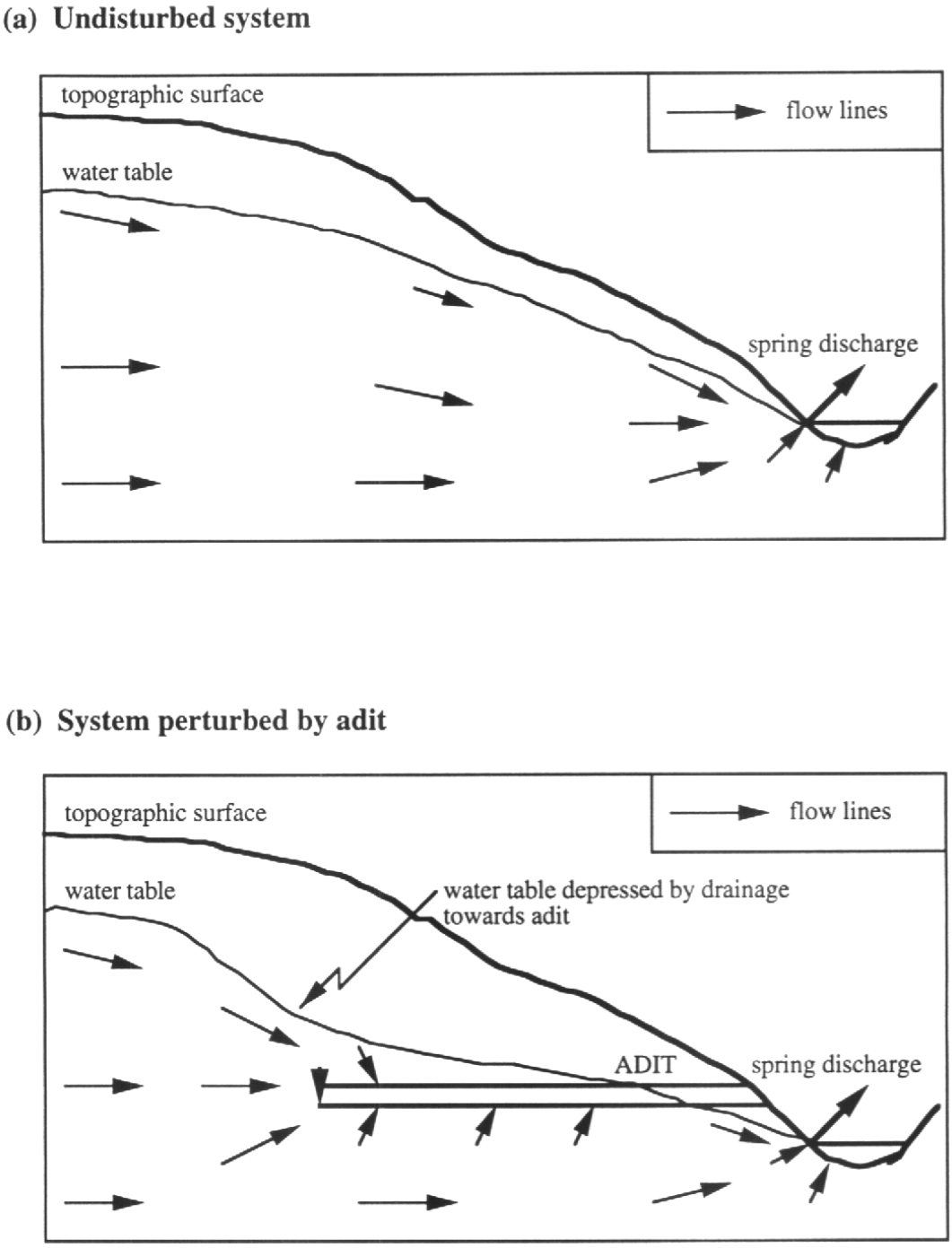

Figure 3.5 Schematic showing the effect of an adit into the hillside on the hydrogeological head distribution (water table) and flow paths: (a) undisturbed system with water table closely following the topographic surface and flow lines directed towards the piezometric low point (valley bottom); (b) system perturbed by the construction of an adit draining water to form a local piezometric low point, and causing locally increased flow towards the adit.

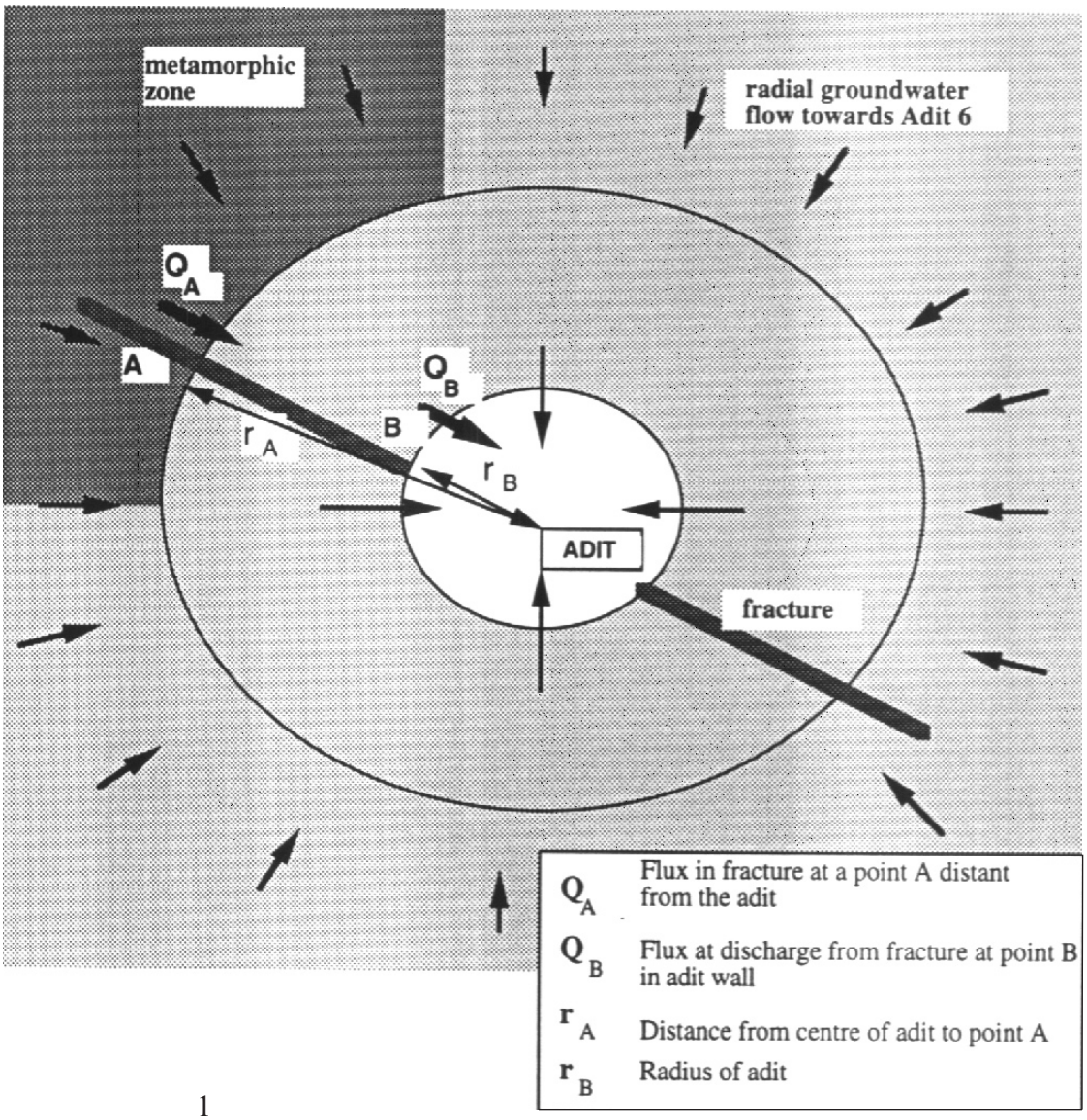

(1) $$Q \propto \frac{1}{2\pi r}$$

(2) $$\frac{Q_A}{Q_B} = \frac{r_B}{r_A} \longrightarrow Q_A = Q_B \frac{r_B}{r_A}$$

If the radius of Adit 6 at discharge point B (i.e. Site 'M2') is approximately 1m and the path length of the fracture extrapolated back to the metamorphic zone (i.e. Point A) is approximately 80m, then flux through fracture at point A (assuming fracture characteristics remain constant) is:

$$Q_A = Q_B \frac{1}{80+1} = 0.0123 \quad Q_B$$

Figure 3.6 Variation in groundwater flux along a fracture path, with distance from an adit wall, in a simple isotropic system with radial drainage towards the adit.

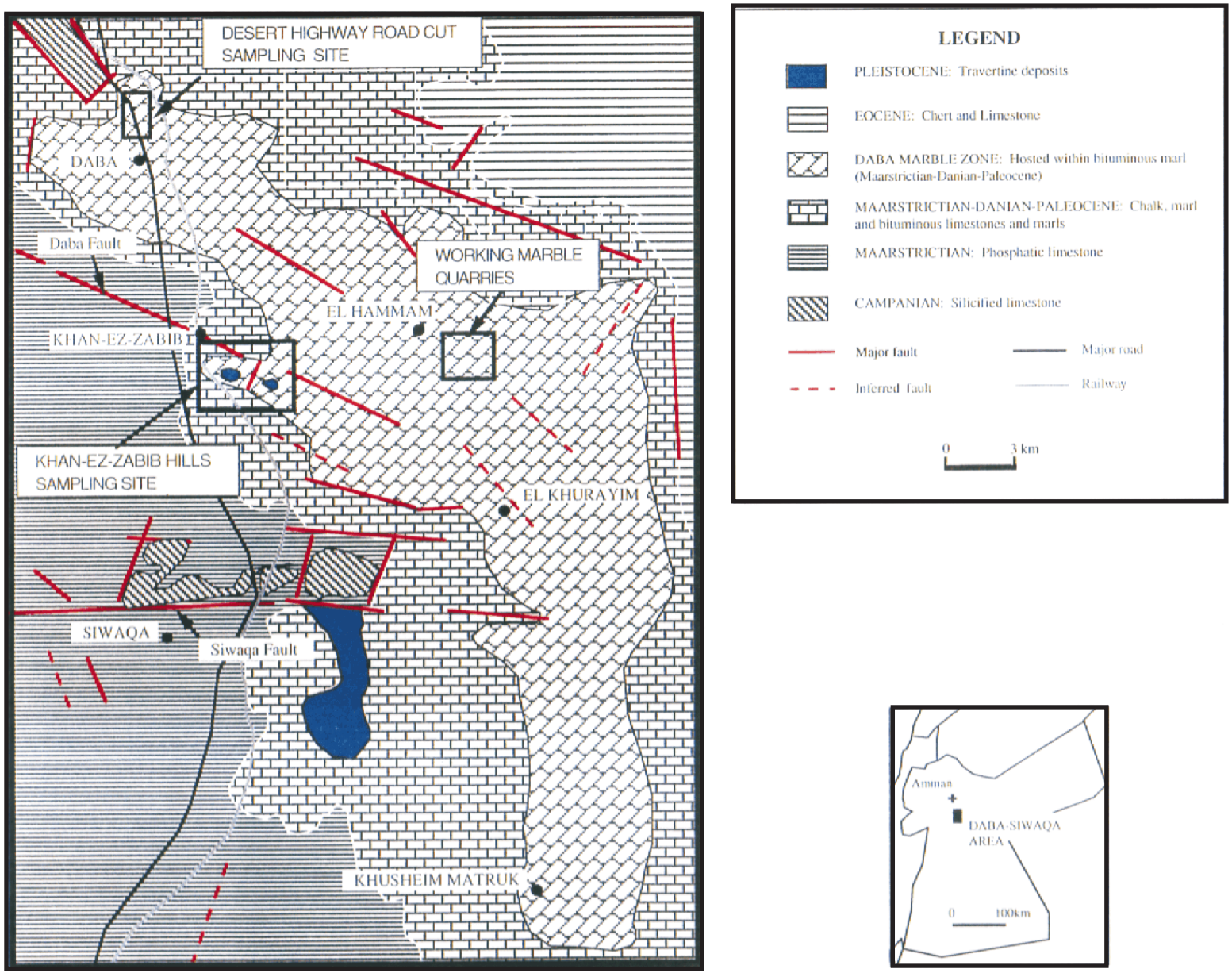

Figure 3.7 Simplified geological map of the Daba-Siwaqa area, Central Jordan (based on information from [9]) showing the principal features, lithological units and location of study sites.

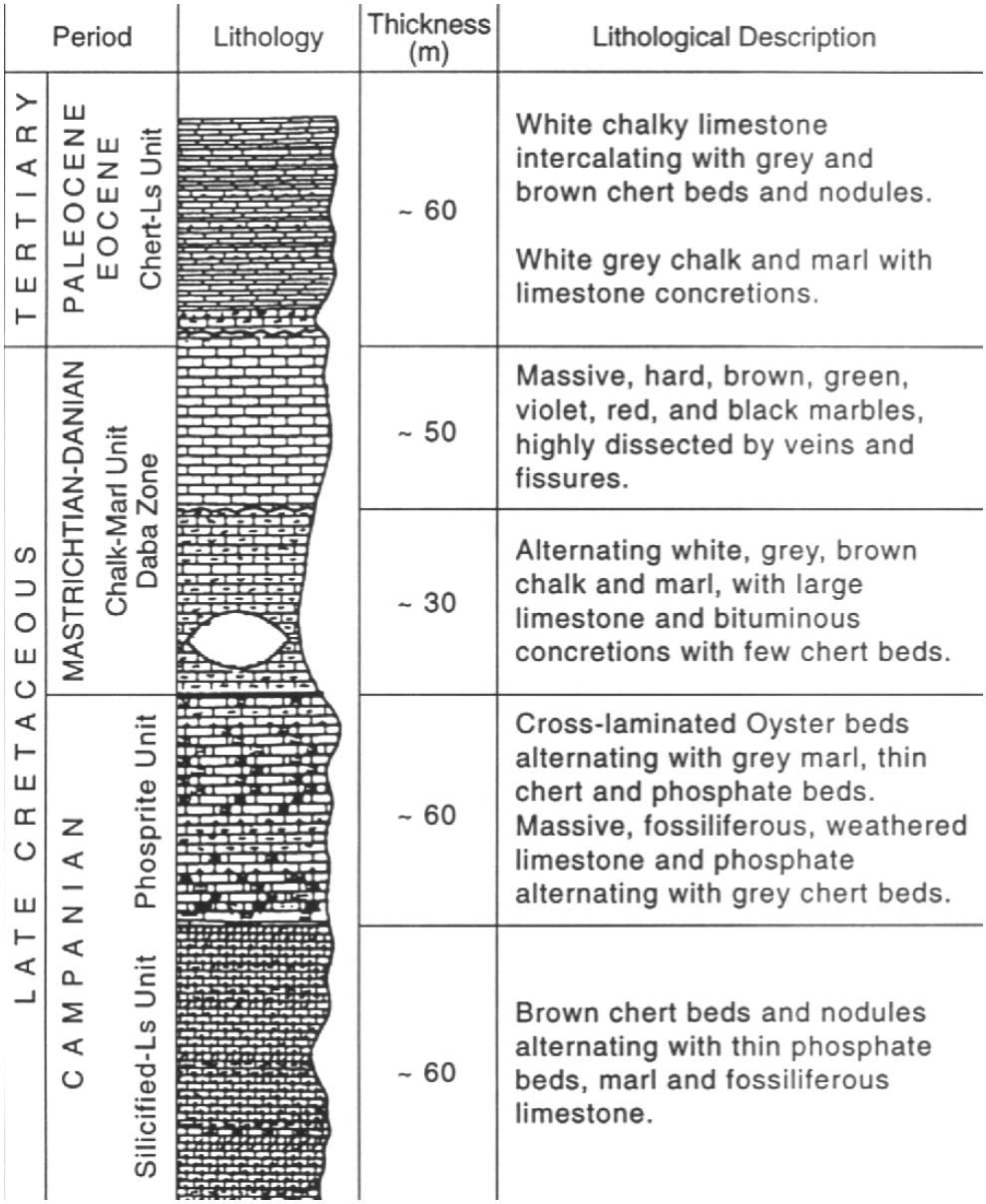

Figure 3.8 Lithostratigraphy of the Daba-Siwaqa area of central Jordan.

Plate 1 The Yarmouk Valley (looking northwards) illustrating the steeply-incised V-shaped valley carved into the near-horizontal Upper Cretaceous - Lower Tertiary chalks and limestones (C), overlain by Pleistocene flood basalts filling the palaeotopography of the pre-basalt surface (B).

Plate 2 Principal zone of hyperalkaline groundwater seepage in Adit A6 showing extensive deposition of calcite-aragonite tufa/travertine on the adit walls. Sampling Site M1.

Plate 3 Hyperalkaline discharge from a fracture in the unmetamorphosed Bituminous Marl in Adit A6 (Sampling Site M2) illustrating the sample collection technique using plastic sheet 'funnels' to collect drips discharging from a fracture in the adit roof.

Plate 4 Hyperalkaline discharge from unmetamorphosed Bituminous Marl in the disused Maqarin station railway cutting (Sampling Site M3). Extensive deposits of travertine are formed as $Ca(OH)_2$-saturated groundwater adsorbs atmospheric CO_2. Principal groundwater discharge occurs along the interface (X-X) between highly fractured blocky limestone overlying less-permeable laminated limestone.

Plate 5 Maqarin railway cutting - showing subvertical fracturing (F) in bituminous limestones and marls along which hyperalkaline groundwater seeps occur.

Plate 6 pH, Eh, T and conductivity are measured using portable Orion meter and specific ion electrodes. The electrodes are immersed directly in water accumulated from stalactite drips using plastic collecting sheets pinned to the face of the cutting. Maqarin railway cutting.

Plate 7 Hyperalkaline groundwater discharge from intergranular porosity and fractures in colluvium on the bank of the Yarmouk River (Maqarin 'Western Springs' - Sampling Site M5), and associated travertine deposits. The high pH water accumulates in pools in the surface of the zeolite-carbonate cemented colluvium and has a yellow-green colouration due to the high chromate ion concentration.

Plate 8 Colluvium and wadi gravels containing large boulders of basalt, limestone and cherts tightly cemented by zeolites and travertine (calcite, aragonite ± ettringite-thaumasite). Maqarin Western Springs (Sampling Site M5 - camera lens shown for scale).

Plate 9 The Ain Quelba Spring, Wadi Shallala, about 15 km SE of Maqarin (Sampling Site M6). This natural spring is used as a local water supply and discharges from fractures in the Lower Palaeocene-Middle Eocene Rijam Formation (B4) (Chalky Limestone Formation). Samples were collected directly from the mild steel discharge pipe leading from the concrete cover protecting the spring.

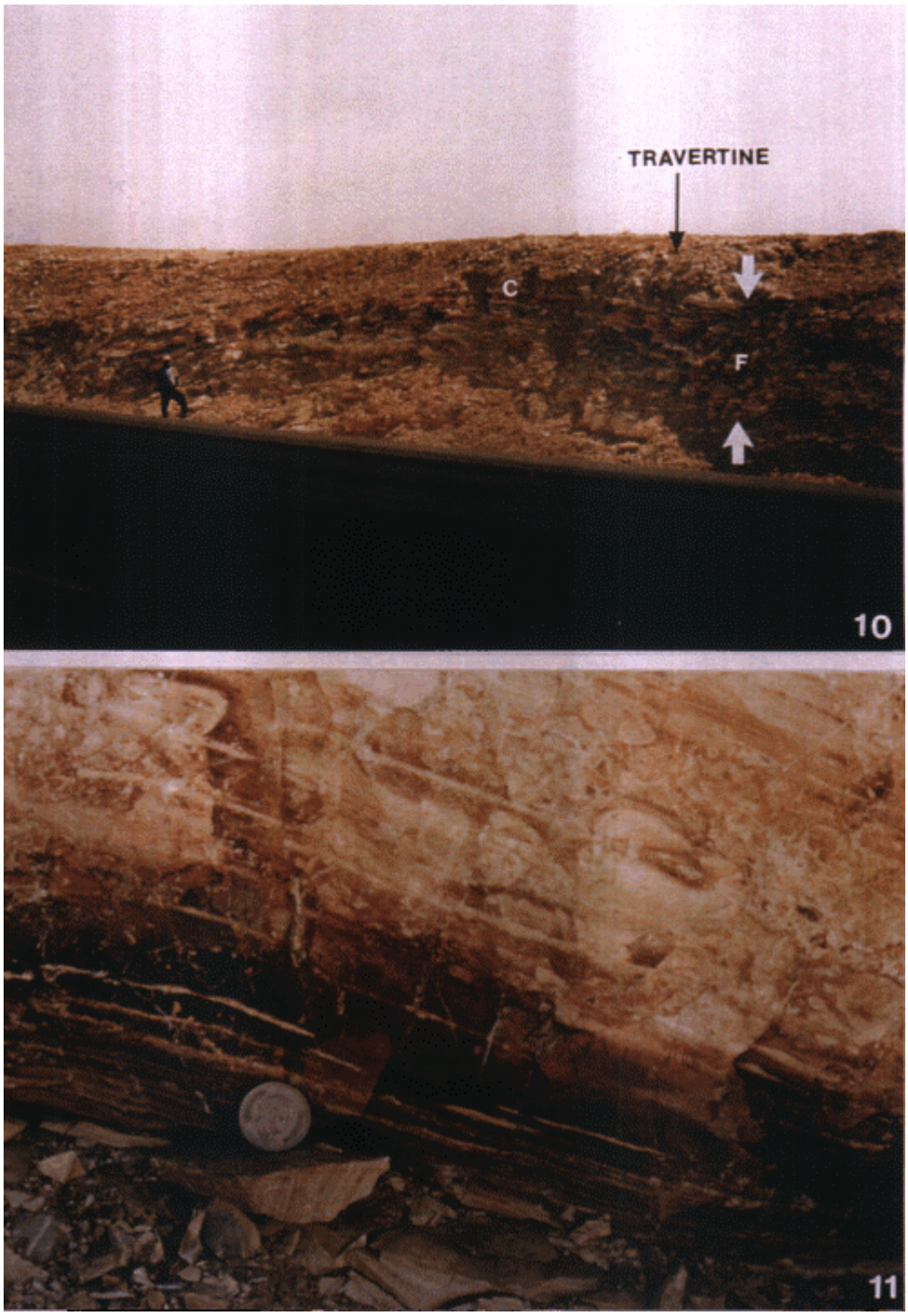

Plate 10 Road cutting (looking east) on the Desert Highway from Amman to Aqaba, about 1.5 km north of Daba, central Jordan. The cutting exposes a small anticlinal flexure which is intensely fractured and metamorphosed to red spurrite marble in the crestal region (C), becoming less metamorphosed towards the limbs of the fold. Travertine deposits form a thin laminated crust at the top of the cutting. The southern limb appears to be faulted out in a zone of fractures (F).

Plate 11 Fractured spurrite marble in the crest (C) of the anticlinal flexure exposed in the Daba road cutting.

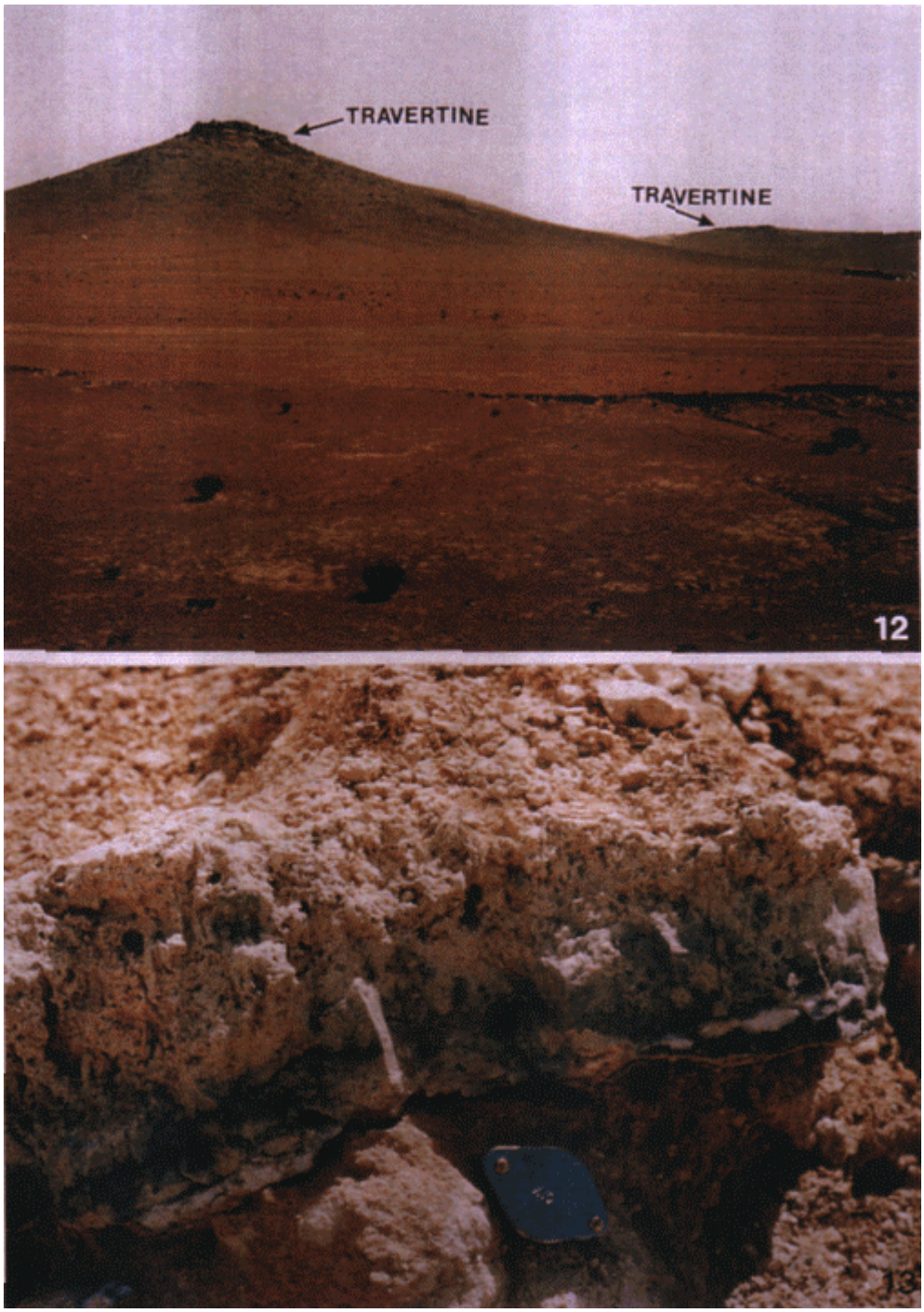

Plate 12 The Khan-es-Zabib Hills (looking east) viewed from the Desert Highway, south of Daba. The hills form a prominent ridge on the skyline with distinctive travertine caps. Central Jordan.

Plate 13 NE-SW fault exposed in the col separating the southeastern-most knoll from the main Khan-es-Zabib ridge. The fault exposes and juxtaposes highly silicified and green volkonskoite (chrome-smectite) impregnated travertine to the southeast against Daba Marble to the northwest.

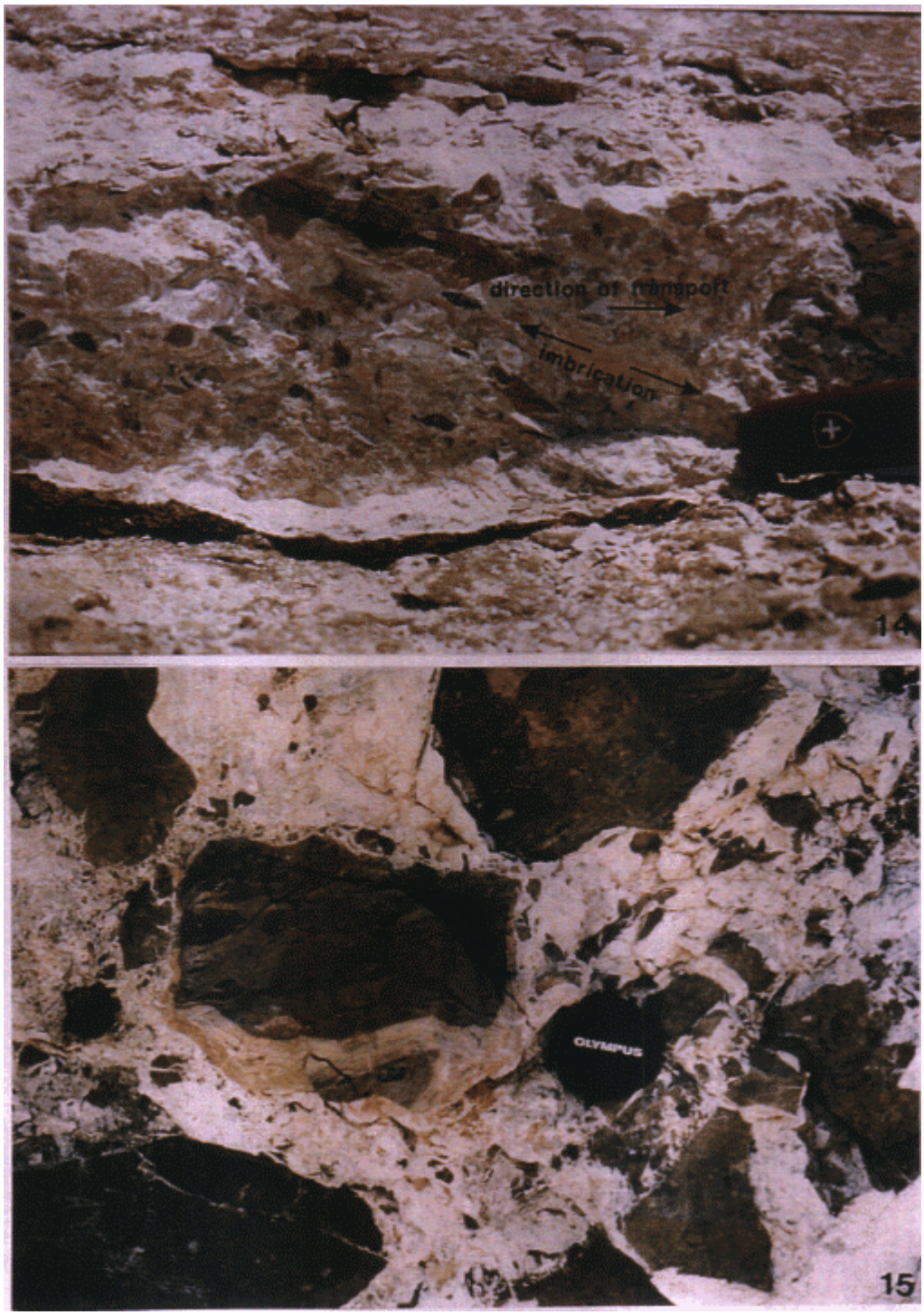

Plate 14 Travertine-cemented colluvium or wadi gravels showing an imbricate fabric of clasts. Khan-es-Zabib Hills (southeastern knoll).

Plate 15 Highly fractured/brecciated, variously coloured spurrite-apatite marble - Daba Marble - with secondary hydration products mineralising fractures. Daba Marble quarries, El Hamman, central Jordan.

4. AQUEOUS GEOCHEMISTRY AT MAQARIN

A.E. Milodowski, M.R. Cave, S. Reeder, B. Smith, S.R.N. Chenery and J.M. Cook

4.1 Introduction

This chapter describes the results of major, trace and ultratrace element analyses of groundwater samples collected during Phase II of the Jordan Natural Analogue Project. All groundwater analyses relate only to investigations at the Maqarin Natural Analogue Site since no relevant groundwater samples could be collected from the central Jordan sites.

Both the field observations and laboratory determinations are presented. The technical details and theoretical considerations of the analytical techniques used are discussed more fully in Appendix A, and are only briefly described here. All aqueous geochemistry determinations (other than field measurements) were undertaken at the Keyworth laboratories of the British Geological Survey (BGS).

4.2 Field Measurements

Temperature, Eh, pH, conductivity and dissolved oxygen were all determined in the field during sample collection. Bicarbonate was only determined, by titrimetric method, on the groundwater from the Ain Quelba Spring. The field sampling and analysis protocols are described in detail in Chapter 3. The results of the field measurements are summarised in Table 4.1.

As discussed in Chapter 3, the flow from the hyperalkaline seeps was generally too low to enable Eh to be measured out of contact with the atmosphere, within a sealed flow-through cell. Samples at sites M1, M2 and M3 were collected from drips before Eh and pH measurement. Measurements for samples M4 and M5 were made directly in accumulated pools or in the flowing stream issuing from the point of discharge. Only in the case of the Ain Quelba Spring, was a sealed perspex flow-through cell used to measure pH, Eh and temperature. During measurement, Eh readings typically drifted slowly downwards and results in Table 4.1 are reported only to the nearest 1 mV. Eh values for samples collected from drips (i.e. M1, M2, M3) in particular, should be regarded with caution because of the potential interaction with atmospheric O_2 that could have occurred during sampling and measurement.

4.3 Laboratory Measurements

4.3.1 General

Groundwater samples were flown to the U.K. and on receipt were stored at 4°C prior to analysis. The results of laboratory measurements for major solution components (pH, TOC, TIC, cations and anions) of the Maqarin groundwaters are summarised in Table 4.2. Table 4.2 also includes some of the field data (Eh, pH and T) for comparison and completeness. The trace element geochemistry data for the groundwaters are presented in Tables 4.3 and 4.4.

4.3.2 pH and total alkalinity

Laboratory measurements of pH and Total Alkalinity (presented in Table 4.2) were determined as soon as possible after delivery to the laboratory, with effort made to ensure minimal contact and reaction with the atmosphere. The methodology and protocol is detailed in Appendix A.

pH and Total Alkalinity were determined using a Radiometer VIT90 Titrator Controller module with an ABU93 autoburette and a SAM90 sample station. Sample pH was determined with Radiometer G2040B glass pH and K4040 calomel reference electrodes. The pH electrode was calibrated using pH7 and 9.2, or 7 and 13 buffers, depending on the sample pH. To check the accuracy of the field measurement, the pH buffer solution used in the field was measured against the laboratory pH 13 standard and gave a value of 12.92 at 22°C.

Theoretically, total alkalinity is a measure of the hydroxide, carbonate (x2) and bicarbonate contents, as well as any contributions from other anions that take part in hydrolysis, e.g. organic bases, silicates, borates, sulphides and phosphates. For these solutions, samples which were pH 12.0 have been characterised in terms of hydroxide and carbonate concentration. The concentration of bicarbonate in these solutions is assumed to be negligible (<5% [HCO_3^-] for the purposes of this calculation). For samples with pH <9.0 the concentration of hydroxide is assumed to be negligible (<10 mg/l [OH-]) and the results calculated as carbonate and bicarbonate concentration. Using these assumptions as the basis for the identification of end-points obtained during the titration, the concentrations are determined by direct calculation.

Because of the highly alkaline nature of some of the samples, contamination by adsorption of atmospheric CO_2 is a major potential problem. Every effort was made to fill the bottles to the brim in the field so that no air space existed on sampling, and that the samples were analysed quickly when returned to the laboratory. Nevertheless, some CO_2 adsorption will have occurred and the results for the hyperalkaline groundwater samples (M1, M2, M3, M5) must be regarded as maximum values.

4.3.3 Major cations and trace elements

Major cations (Ca, Mg, Na, K including Sr), and trace cations (Si, Ba, Mn, Fe, Al, Co, Ni, Cu, Zn, Cr, Zr, Mo, Cd, Pb, V, Li), total S and Si were determined directly by Inductively Coupled Plasma-Atomic Emission Spectroscopy (ICP-AES). The methodology and protocol are detailed in Appendix A. ICP-AES results are presented in Tables 4.2 and 4.3.

4.3.4 Major and trace anions

Major and trace anions (Cl, SO_4, NO_3, NO_2 and Br) were determined by ion chromatography. The methodology and protocol are detailed in Appendix A. Anion data are presented in Table 4.2

Most anions are stable in solution for an appreciable length of time and certainly with the delay between sampling and analysis during this project. Nitrate and nitrite will, however, be modified by microbial activity and for this reason ion chromatography analysis was carried out as soon as possible after receipt of the samples from Jordan. NO_2/NO_3 change very rapidly in normal groundwaters [1] and although the microbial activity in the Maqarin alkaline groundwaters is low, this factor must be considered in using the NO_2/NO_3 data for redox modelling. The highly alkaline nature of the samples

altered the column retention characteristics to shorter retention times compared to the standards. Consequently, the results for each sample had to be calculated manually as the integrator did not correctly identify each peak. This had no effect on the peak areas and hence did not affect the accuracy of the measurement.

4.3.5 Fluoride

Fluoride (F^-) was determined by ion-selective electrode using filtered unpreserved samples, and the results are presented in Table 4.2. An Orion Model 90/01 single junction reference electrode used in conjunction with an Orion Model 94/09 Fluoride electrode were used. Total Ionic Strength Adjustment Buffer was added to the samples at a ratio of 1:1. This functions to maintain sample pH between 5-5.5 and prevents interference from complexation of F^- by H^+ or OH^-, and also preferentially complexes interfering metal complexes (in particular, Fe and Al complexes).

4.3.6 Total organic and inorganic carbon

Total organic carbon (TOC) and total inorganic carbon (TIC) were determined on filtered unpreserved samples. The technique measures total carbon (inorganic carbon + organic carbon) and inorganic carbon in two separate stages. Inorganic (IC) carbon content represents the sum of the carbonate and bicarbonate present in solution. The methodology and protocol is detailed in Appendix A.

The method is essentially interference free as long as the IC or TOC is converted to CO_2 during the two different oxidation procedures, which is verified by external check standards. The error in the analysis of the organic carbon is slightly greater than that for the inorganic carbon as it is calculated by difference. The inorganic carbon values in the hyperalkaline groundwater samples (M1, M2, M3, M5) must be regarded as maximum values as small amounts of atmospheric carbon will probably have been adsorbed.

4.3.7 Reduced sulphur

Reduced sulphur was determined by hydride generation ICP-AES using the method described by Cave and Green [2]. The methodology and protocol are detailed in Appendix A.

Sulphide is stabilised under alkaline conditions but it is still likely that some loss will be incurred within a relatively short timescale. For this reason, reduced sulphur content is determined as soon as possible after collection of the samples. The reduced sulphur content is determined on an unfiltered sample (Chapter 3), as it is likely that degassing of the H_2S would occur on filtration. Particulate sulphide may therefore contribute to the reported total. The reported value may also include a contribution from any organic sulphur released from solution as gaseous organic sulphur species or sulphide gas on acidification.

4.3.8 Arsenic and selenium

As and Se were determined by hydride generation ICP-AES following the method published by Cave and Green [2]. Analyses were performed on samples preserved by acidification to 1% with respect to AristaR HCl (Chapter 3). The methodology and protocol are detailed in Appendix A. The results are presented in Table 4.3.

4.3.9 Reduced iron

Reduced iron (Fe^{2+}) was determined by colourimetric method using the chromogenic reagent 2,2-bipyridyl. The methodology and protocol are detailed in Appendix A.

Ferrous iron is rapidly oxidised in air to ferric iron, so the sampling methods used must ensure that air is excluded during sampling and filtration. For this reason, the samples were filtered out of contact with air by using plastic syringes with on-line Acrodisc nylon filter disks fitted to the ends of the syringes. The water was filtered directly into a sample tube into which 2,2-bipyridyl solution colourimetric reagent had been added previously, thereby ensuring that the reduced iron is stabilised immediately. The complex stabilises the ferrous iron in solution and deterioration is considered negligible over the timescale between collection and analysis.

The validity of the data can also be checked by comparing the results for the colourimetric method with the ICP-AES results for total Fe. The value for the reduced iron should never be higher than the total Fe (within the error of the analytical measurements).

4.3.10 Ammonium

Ammonium was determined colourimetrically using a flow-injection analysis method. Full details of the methodology and protocol is detailed in Appendix A.

The sample type and method of sampling are important in this determination. The amount of free ammonia present varies with pH. Above pH 12, the ammonium/ammonia equilibrium in solution is such that over 90% exists as free ammonia. For the samples with high pH (M1, M2, M3 and M5) there would, undoubtedly, have been losses of ammonia (i.e. during collection and filtration) during the sampling although they were acidified in the field. It is not possible to give accurate estimates of these losses and this should be taken into consideration when interpreting the data and the NH_4 values should be regarded as minimum values.

4.3.11 Orthophosphate

Orthophosphate was determined colourimetrically using a flow injection technique based on the method published by Osburn et al. [3]. The methodology and protocol are described in Appendix A.

4.3.12 Rare earth elements, thorium and uranium

The geochemical behaviour of U, Th and the rare earth elements (REE) is relevant to understanding the migration behaviour of waste-form radionuclides in the geosphere. U is itself a major component of radioactive waste, and Th and REE's have similar chemical properties to Pu^{4+} or trivalent actinides. Information on their behaviour in the Maqarin hyperalkaline groundwater system will therefore be valuable in understanding and predicting the behaviour of the actinides in the disturbed zone of a radioactive waste repository.

U, Th and REEs were determined in Maqarin groundwaters during the Phase I study but values were close to analytical detection limits for inductively coupled plasma-mass spectrometry (ICP-MS) (Alexander [4]). Ion-exchange resins were also used during this earlier study in an attempt to determine the trace element speciation in the groundwater. The particular methodology and ion exchange columns used met with only limited success, but the technique did indicate the potential to improve analytical detection limits by the use of ion exchange resins to preconcentrate these trace elements prior to ICP-MS analysis.

Since Phase I, BGS detection limits for REEs by ICP-MS have been improved by 1-2 orders of magnitude with the routine use of ion-exchange resins to extract and produce a tenfold preconcentration of the REEs. The ICP-MS method is described in Appendix A.

The results of direct ICP-MS determinations for U and Th, and ion-exchange preconcentration-ICP-MS for REE's are included in Table 4.3.

A preliminary attempt was also made to improve U and Th detection limits by using a different ion-exchange resin to specifically extract these elements and produce a similar tenfold preconcentration prior to ICP-MS. The approach is described in more detail in Appendix A. The technique gave vastly and sometimes unrealistic higher Th standard recoveries than expected, and % recovery for the two U standards was variable (556% and 52%) casting doubt on the methodology employed. However, the higher recovery value is believed to be the result of an error made in the preparation of this standard. A recovery factor of 52% for the sample standard (0.5 ppb U) appears to be more reasonable. The analysis results are presented in Table 4.4 and compared with results for U and Th obtained with ion-exchange preconcentration-ICP-MS by ANSTO. However, the BGS ion-exchange extraction technique for U and Th is still only in a developmental stage and the data should be treated cautiously. Marked inconsistencies indicate that considerable work needs to be undertaken on the assessment of recoveries before any validity can be placed on the results produced by this particular method. Nevertheless results, with the exception of M4 (high in TOC), are broadly similar to those obtained by dilution and direct ICP-MS analysis of the original samples. Sample M4 (determined by direct ICP-MS analysis to contain 12.1 ppm U) deposited a significant quantity of light brown material onto the column. It seems likely that this material was organic matter sorbed to the support phase of the resin through hydrophobic interaction. This brown colouration was not eluted from the column and any associated U or Th may have remained with it, explaining the low concentration of U in the eluate (<0.002 ppb).

The BGS results for U shown in Table 4.4 are consistently lower than the ANSTO values by a factor of approximately 2. Taking into account that the BGS recovery for U was probably only approximately 50%, the BGS and ANSTO determinations for U are therefore in close agreement. The BGS values can be used to estimate the U concentration in the samples for which no ANSTO data are available.

4.4 Variations in the Geochemistry of the Groundwaters

4.4.1 Comparison with Phase I data for hyperalkaline groundwaters

The unusual chemistry of the high pH seepages from the Maqarin area were described in detail during the Phase I investigations [4] and the results of the present Phase II study on sites M1 (equiv. MQ1-3, Phase I), M3 (equiv. MQ7-9, Phase I) and M5 (equiv. M5-6, Phase I) confirm the general characteristics recognised previously. However, there are some differences between the data from the two studies, and this may influence the choice of certain parameters (for use in geochemical modelling) between the respective data sets

(i) pH data

Phase II field and laboratory pH determinations were made by BGS using two different pH instruments and in general, the laboratory measurements are very slightly lower than the field values, which may be accounted for by some adsorption of CO_2 by samples prior to laboratory measurement, or differences in the range of buffers used to calibrate the two systems used. For sample M3 the opposite trend is the case. Nevertheless, the field and laboratory pH analyses are in very close agreement (<0.1 pH unit difference) and the variations observed are all within experimental variation. These data also compare very closely with the Phase I BGS laboratory determinations (observed differences c.0.1 pH unit). However, the Phase I field determinations are significantly lower (by up to 0.42 pH

unit) than both laboratory and Phase II field measurements and a number of factors may explain these differences:

(i) The field pH meter used during Phase I was an inexpensive and unsophisticated instrument, in contrast to the meters used for the BGS laboratory and Phase II field analyses.

(ii) The BGS pH electrodes used in both Phase I (laboratory) and Phase II were of a type which experience with experimental systems had shown were reliable and robust at high pH. This had not been demonstrated for the Phase I field electrode.

(iii) The BGS Phase II field and BGS laboratory instruments were calibrated against reliable pH buffers (pH 7 and 12, and 7 and 13 respectively). In contrast, the field measurements for Phase I were only reliably calibrated using standard buffers within the range pH 7 to 11. This may be a significant source of error in the Phase I field measurements because the electrode response may not have been linear outside this range. Although the meter was checked at higher pH with a saturated solution of $Ca(OH)_2$ (theoretically pH 12.51 at 25°C) and correction applied on the basis of this [4], this secondary standardisation must be regarded cautiously. BGS experience with preparing $Ca(OH)_2$ fluids for experimental studies [5] has shown that a significant time (several days at 25°C [6]) may be required before equilibrium pH is reached. Furthermore, the grade of the $Ca(OH)_2$ used to prepared the solution can have a significant effect on final pH (small amounts of NaOH or KOH impurities present in some grades will increase pH [6]). The $Ca(OH)_2$ solution used during Phase I was prepared only 24 hours before use in the field, and only from a general purpose grade $Ca(OH)_2$ available at the University of Jordan at the time.

Taking account of these factors, and the consistency between the BGS Phase I and II data, the BGS-measured pH data for both Phases I and II are considered to be reliable, and the Phase I field pH values should be regarded with caution. In contrast to the Phase I results, the more recent study indicates that the pH in the western natural hyperalkaline springs on the bank of the Yarmouk River (Site M5) - defined as the 'Western Springs' system during Phase I [4] - is slightly higher (pH 12.9) than the 'Eastern Springs' system [4] which includes the Adit A-6 (Site M1) and Maqarin railway cutting (Site M3) seepages (pH 12.7).

(ii) Major cations and anions

The same two geochemically distinct hyperalkaline groundwater regimes identified during Phase I (i.e. the 'Western Springs' and the 'Eastern Springs') can also be recognised in the new data (Tables 4.1 - 4.4). The 'Western Springs' are clearly differentiated by higher hydroxide alkalinity and are considerably more mineralised, particularly with respect to Ca, K, Na, NH_3, Sr, SO_4 and NO_3, than the 'Eastern Springs'. For the most part, Ca, Mg, Na, OH, Cl, NO_3 and SO_4 values (Table 4.2) are very similar to the Phase I data (Appendix A2, [4]). NH_3 was only determined for the Western Springs during Phase I but again it would appear that the Phase II results show little change. The Phase II data are similar, or very close to the range in Phase I data at each site, with the exception of Ca from the Maqarin railway cutting groundwater discharge (M3) which is about 29% higher in the more recent study.

The principal difference between the present study and the Phase I dataset is for K and to a lesser extent Sr. K values for Phase II are 30% lower for the principal seepage zone in

Adit A6 (M1) and 27% lower for the 'Western Springs' (M5), but higher by 12.5% in the M3 site - where the Ca content was also found to be higher. Sr shows a similar distribution of reduced concentrations in the Phase II data for M1 (33%) and M5 (23%) but little change (c.2.5% reduction compared to the average value, but within the range of Phase I values) for the M3 site. The Ca:Sr ratio for the waters has clearly changed between the two visits. Ca:Sr has increased significantly at all sites: at M1 by 57%; and at M1 and M5 by 32-33%.

Although no detailed long-term monitoring data of groundwaters from the site is available to assess the significance of these variations, there is evidence from the petrographic studies of associated fracture mineralisation that indicates that these variations are real. Phase I studies demonstrated that many of the major secondary minerals (particularly calcite and apophyllite) in the metamorphic zone (and in minor veins in the enclosing marl) in Adit A6 were strongly zoned, displaying well-defined oscillatory variations in Ca:Sr, or less commonly veins in the enclosing marls displayed alternating layers of calcite and minor strontianite (Appendix C, [4]). More recently, this oscillatory behaviour in the Ca:Sr ratios of secondary mineral precipitates was also found to be extremely pronounced in fissures associated with the seepages at M3 - in which aragonite and strontian aragonite are actively precipitating (Chapter 6). The mineral variations imply that the groundwaters must similarly vary periodically in Ca:Sr. The variation in K is not so readily explained from mineralogical observations at all the sites. However, secondary zeolite (dachiardite and mordenite) gel-like cements in the colluvium associated with the Western Springs do show a diffuse zonation in K:Ca (Chapter 6), suggesting that K:Ca also varies periodically in the fluid phase.

Although not discussed in any detail, diagrams presented by Khoury et al. [7] of major ion concentration distributions for Maqarin groundwaters monitored over a year do suggest that K in particular varies seasonally, whilst the other major ions (including Cl) show little variation (Sr data was not presented). Both Phase I and Phase II field sampling programmes were carried out in the same season (May 1990 and May 1992 respectively) but the weather conditions earlier in 1992 were anomalous - with very high snow fall and rainfall. Consequently, aquifer conditions (e.g. water table, flow-gradients) may have been influenced and the effects may have persisted up until the Phase II field visit. This may account for the differences between the Phase I and Phase II major ion data, although surprisingly, no significant changes were observed for conservative Cl - implying that meteoric dilution was not a factor.

(iii) Trace elements

Trace element data (Table 4.3) for the Maqarin groundwaters for Phase II represent an improvement on the earlier data set, particularly for the REEs for which detection limits are now at least 2 orders of magnitude better. Even so, REEs other than La remain below detection but the detection limits indicate an upper limit of concentration of 0.001 ppb for Ce-Yb in the hyperalkaline groundwaters. La is present at levels significantly above detection in all the hyperalkaline groundwaters but appears to be present at slightly more elevated levels in the Eastern Springs (0.17-0.25 ppb) in comparison to the Western Springs (0.13 ppb), although there are too few data to evaluate the statistical significance of these observations.

Table 4.3 also lists improved data for Si and Al, which were both below detection in the previous study. Si is still below detection in M1, but the detection limit indicates a revised concentration limit of 0.02 ppm for silica in groundwater in the metamorphic zone

(at least in Adit A6). Si values for the M3 (railway cutting) and M5 (Yarmouk River bank) hyperalkaline discharges are similar, and very low (0.07-0.09 ppm). Ferrous iron determinations were made for Phase II but, as shown in Table 4.3, both ferrous and total iron remain below detection (0.01 ppm) in all the hyperalkaline groundwaters.

B, Li, Ba, Zn, Cr and Mo are all broadly similar to Phase I data [4] with most elements showing the same pattern of relative enhancement in the Western Springs. Se is also enhanced in the Western Springs relative to the Eastern Springs, as shown in Phase I. Although, the BGS data for Se (Table 4.3) are very close to previous unverified BGS ICP-MS estimates made during Phase I (unreported), they are a factor of 2.2-3.5 lower than the Phase I results determined by hydride-generation ICP-MS at the Geological Survey of Canada [4], and a factor of 2-2.2 lower than the Phase II analyses by ICP-MS at ANSTO (M1 = 114±1 ppb; M3 = 206±3 ppb; M5 = 1315±21 ppb). The ANSTO data would appear to be independently validated by the earlier Phase I (GSC) data, implying that the BGS results for Se are anomalously low and their quantitative value should therefore be regarded with caution.

BGS determination for Zr, Mn, Co, Ni, Cu, As and Cd were all below detection limits as in the previous study.

4.4.2 Relationships between hyperalkaline groundwaters and local bicarbonate groundwaters

Two samples of local 'background' bicarbonate-type groundwater were analysed for comparison with the hyperalkaline groundwaters (M4 and M6). Both samples are derived from the upper (perched) aquifer in the Rijam Formation (B4) which immediately overlies the Bituminous Limestone (B3) which hosts the metamorphic zones (Chapter 3). Geochemical data for these groundwaters are also presented in Tables 4.1-4.4.

M4 represents water accumulated in a very small, shallow pool within Adit A7. The pool appeared to be fed by very slow seepages from fractures in the floor of the Adit. The pool was in open contact with the adit atmosphere and its geochemistry may have been affected by evaporation processes as well as contamination from a variety of sources, including biota living in the adit (e.g. bats, fungi, and possibly larger animals - such as hyenas or foxes). This probably accounts for the very high TOC (42.2 ppm) compared to the much lower TOC of M6 (4.38 ppm).

M6 represents water discharging from fractures in the Rijam Formation (B4) in a natural spring at Ain Quelba in Wadi Shallala, c.15 km to the south/south-east of Maqarin. The spring presents a major discharge and provides a water supply for the local community. It is considered to be a representative sampling site for groundwater within the upper aquifer [8] and is taken to represent the upstream (input) groundwater in the repository analogy.

The major ion chemistries of all the Maqarin groundwaters studied during Phase II are compared in Figure 4.1. This is a trilinear plot or 'Piper diagram' in which the relative proportions of the major ions (as ionic milliequivalents %) are represented. This type of diagram is often used to help discriminate different groundwater types or examine the evolution of groundwater systems. In order to plot both hyperalkaline groundwaters and normal bicarbonate-type waters on the same diagram, OH^- has been recalculated and plotted as equivalent HCO_3^-. A number of interesting features are evident from this type of representation.

The Eastern Springs - represented by M1, M2 and M3 - are very similar in their major element chemistry. They are characterised by high-Ca relative to low-K+Na, and negligible Mg, and high OH^- relative to low-moderate SO_4^{2-}, and low $Cl+NO_3^-$ chemistries. By comparison, the Western Springs - represented by M5 - has significantly higher K+Na relative to Ca, and higher SO_4^{2-} relative to OH^- in comparison to the Eastern Springs group (Figure 4.1).

Surprisingly within the Adit A6 samples, the 'downstream' groundwater discharging from fractures in the marl (M2) appears to have a relative ionic composition intermediate between typical Eastern Spring compositions (M1 and M3), and the Western Springs (M5). Furthermore, just as in M5, M2 also shows an enrichment in Se (which mirrors that of SO_4^{2-}), though not in Cr and Mo. This could be viewed as implying that the Western Springs represent more evolved hyperalkaline groundwaters - originally derived from an Eastern Springs-type composition. However, this is inconsistent with earlier interpretations [4] which regarded the Western Springs to be a less evolved geochemically 'younger' groundwater, and closer in composition to the earliest groundwater expected to discharge from the metamorphic zone during the initial stages of hydration. It is also inconsistent with the pH variations (Table 4.2) which show that M5 has the highest pH of all samples (pH 12.9), whereas pH is reduced downstream from M1 (pH 12.7) to M2 (pH 12.4).

M2 is interpreted as the product of hyperalkaline groundwater derived from M1 after reaction with marl along the fracture flow path. The observed increase in K+Na relative to Ca in M2 can be attributed to the leaching of these elements from clay minerals in the marl wallrock, and the precipitation of predominantly secondary Ca-minerals - ettringite, thaumasite, calcite, tobermorite, jennite - along the flow path (Chapter 6). The relative increase in SO_4^{2-} in M2, relative to OH^-, and the reduction in pH can also be explained by the precipitation of the same minerals which would remove proportionately greater OH^-, relative to SO_4^{2-}, from solution:

ettringite	$Ca_6Al_2(SO_4)_3(OH)_{12}.25H_2O$	$OH:SO_4 = 4:1$
thaumasite	$Ca_6Si_2(SO_4)_2(CO_3)_2(OH)_{12}.24H_2O$	$OH:SO_4 = 6:1$
tobermorite	$Ca_5Si_6O_{16}(OH)_2.2\text{-}8H_2O$	$OH:SO_4 = \infty$
jennite	$Ca_9H_2Si_6O_{18}(OH)_8.6H_2O$	$OH:SO_4 = \infty$

The increase in Se and TOC in M2 relative to M1 can be explained by leaching of organic matter, and by oxidative alteration of pyrite, and other diagenetic sulphide and selenide minerals present in the host marl (Chapter 6 and Alexander [4]). Alexander [4] also showed that Se was associated with the bituminous organic matter in the marl, and oxidative leaching of the organics could release Se to the groundwater.

The normal bicarbonate-type groundwater from Ain Quelba Spring (M6) shows very close correspondence in terms of relative proportions of Ca, Na, K, Cl to the hyperalkaline Eastern Springs (Figure 4.1). This demonstrates that it is quite possible for the hyperalkaline groundwaters in the Eastern Springs to be derived directly from groundwater in the upper aquifer overlying the bituminous marl and its associated metamorphic zones. The principal differences between the bicarbonate groundwater and Eastern Springs hyperalkaline seepages is the reduction in Mg and replacement of HCO_3^- by OH^- in the hyperalkaline system.

Mg^{2+} concentrations are very low at high pH due the low solubility of $Mg(OH)_2$. Experimental reaction of a simulated bicarbonate-type marl groundwater with cementitious materials showed that Mg was rapidly removed from solution as brucite and/or talc, associated with carbonation of the cement materials [9, 10]. This process would explain the observed differences between the bicarbonate-type M5 groundwater and M1 or M3. Milodowski et al. [11] recorded crystalline brucite filling fractures in the early stages of alteration of partially metamorphosed marls and marbles at the margins of the metamorphic zone near the M3 site. This is consistent with reaction with Mg-bearing bicarbonate groundwaters as they enter the metamorphic zone.

The difference between the Eastern Springs (M1/M3) and the Western Springs (M5) can be accounted for by a difference in the timescale or extent to which the metamorphic zone in these two areas has been subjected to invasion and leaching by percolating groundwaters. As in cement hydration, Na and K (usually present as soluble salts e.g. sulphates, carbonates or oxides, in calcined marls) and elements such as Se - shown to be present in highly reactive metamorphic minerals such as oldhamite (CaS) and Cu-K-Na-selenide which rapidly dissolve in water [4] - are leached as KOH- and NaOH-dominated fluids during the early stages of hydration. The higher concentration of these elements, coupled with the higher pH of the Western Springs, suggests that this system is geochemically less evolved than the Eastern Spring discharges. In the Eastern Springs area, the limited K, Na and SO_4 would appear to have been more extensively leached from the high pH 'source' in the metamorphic rocks. Consequently, they no longer make a significant contribution of K and Na to the chemistry of the groundwater percolating through these rocks. In this area, only $Ca(OH)_2 \pm$ CSH, ettringite and thaumasite (still present in abundance in the metamorphosed rocks in the eastern part of the Maqarin flow system) effectively buffer the groundwater chemistry, and as a result the groundwaters retain many of the geochemical characteristics of the primary 'upstream' bicarbonate groundwater entering the metamorphic zone.

The lower regional aquifer in the Amman Formation (B4) underlying the Bituminous Marl Formation and the metamorphic zone, is known to be under artesian conditions. It could therefore, potentially make a contribution to the hyperalkaline flow system. However, the elevation of the Eastern Spring sites is likely to reduce the influence of the lower aquifer on the flow system in these sites. It may, however, make some contribution to the groundwater chemistry in the lower level Western Spring discharges. Unfortunately, no groundwater samples could be obtained from the lower aquifer to evaluate this possibility.

The bicarbonate groundwater from the standing pool in Adit A7 (M4) appears to be anomalous in terms of both cation and anion ratios. It is enriched in K+Na and in SO_4^{2-} (and to a lesser extent Cl, F), and depleted in HCO_3^- relative to M6. To some extent this may be the effect of contamination (discussed earlier) but could also be due in part to surface evaporation, whilst Ca and Mg have remained effectively buffered by contact with calcite in the limestone floor of the pool.

4.5 References

[1] W.R. Alexander, Personal Communication.

[2] M.R. Cave and K.A. Green, *Feasibility Study of the Determination of Iodide, Tin, Arsenic, Selenium and Hydrogen Carbonate in Groundwaters by Inductively*

Coupled Plasma Atomic Emission Spectroscopy using a Membrane Gas-Liquid Separator, Journal of Analytical Spectroscopy, **4**, 223-225, 1989.

[3] Q.W. Osburn, D.E. Lemmel and R.L. Downey, *Automated Method for Ortho, Ortho plus Hydrolysable and Total Phosphate in Surface and Waste Waters,* Environmental Science and Technology, **8**, 363-366, 1974.

[4] W.R. Alexander (Ed), *A Natural Analogue Study of the Maqarin Hyperalkaline Groundwaters. I. Source Term Description and Thermodynamic Database Testing,* NAGRA Technical Report, NTB 91-10, 1992.

[5] D. Savage, K. Bateman, C. Hughes, A. Milodowski, J. Pearce, E. Rae and C Rochelle, *The Evalution of Chemical Mass Transfer in the Disturbed Zone of a Deep Geological Disposal Facility for Radioactive Wastes. I: Reaction of Silicates with Calcium Hydroxide Fluids,* Nirex Report, NSS/R244, 1997.

[6] C.A. Rochelle, Personal Communication, 1993.

[7] H.N. Khoury, E. Salameh and Q. Abdul-Jaber, *Characterisation of an Unusual Highly Alkaline Water from the Maqarin Area, Northern Jordan,* Journal of Hydrogeology, **81**, 79-91, 1985.

[8] E. Salameh, Personal Communication, 1992.

[9] J.M. West, M.A. Allen, M.A. Brightman, M.R. Cave, S.J. Kemp, S. Gardner, K. Green, K. Harmon, J.J.W. Higgo, S. Ince, A.E. Milodowski, P. Moody, J. M. Pearce, S. Reeder, C.A.M. Ross, E.J. Rowe and P. Sibley, *The Effect of Microbial Activity on the Near and Far Fields of a Swiss Type B Repository - A Study of Gross Effects on Structures, Geochemistry, Radionuclide Sorption. April 1988-March 1991 Final Report,* British Geological Survey Technical Report, WE/91/13C, 43p, 1991.

[10] J.M. West, M.A. Allen, M.A. Brightman, M.R. Cave, S.J. Kemp, S. Gardner, K. Green, K. Harmon, J.J.W. Higgo, S. Ince, A.E. Milodowski, P. Moody, J. M. Pearce, S. Reeder, C.A.M. Ross, E.J. Rowe and P. Sibley, *The Effect of Microbial Activity on the Near and Far Fields of a Swiss Type B Repository - A Study of Gross Effects on Structures, Geochemistry, Radionuclide Sorption. April 1988-March 1991 Final Report. Appendix - Summary Of Methods And Results,* British Geological Survey Technical Report, WE/91/14C, 169p, 1991.

[11] A.E. Milodowski, J.M. Pearce, C.R. Hughes and H.N. Khoury, *A Preliminary Mineralogical Investigation of a Natural Analogue of a Cement-Buffered Hyperalkaline Groundwater Interaction with Marl, Maqarin, Northern Jordan,* NAGRA Unpublished Internal Report, 1992.

Table 4.1 Summary of field measurements.

Sample	Date	Field T (°C)	Field pH	Field Eh (mV)	Conductivity (µS/cm)	diss. O_2 (mg/l)	HCO_3^- (mg/l)
M1	21/5/92	24.8	12.74	278	5930	4.0	n.d.
M2	21/5/92	20.7	12.42	179	4400	4.0	n.d
M3	21/5/92	23.2	12.66	150	7220	11.0	n.d.
M4	20/5/92	21.5	7.84	275	650	4.0	n.d.
M5	21/5/92	25.2	12.92	242	10210	12.0	n.d.
M6	21/5/92	23.7	7.22	321	503	5.0	209.8
M7 (Blank)	21/5/92	n.d.	n.d.	n.d.	n.d.	n.d	n.d

Notes:

(a) n.d. - not determined.
(b) M6 Eh, pH and T values measured using sealed perspex flow-through cell.
(c) M5 - Eh, pH and T measured in flowing 'spring' at point of discharge.
(d) M1, M2 and M3 - Eh, pH and T measured directly in drip collection funnel system.
(e) M4 - Eh, pH, and T measured directly in sampled pool accumulated on floor of Adit A7.
(f) Eh data corrected to standard hydrogen electrode.

Table 4.2 Major cation, anion, pH, Eh, temperature, TOC and TIC data for Maqarin groundwaters.

Sample:	**M1**	**M2**	**M3**	**M4**	**M5**	**M6**	**M7** (blank)
Field Temp. (°C)	24.8	20.7	23.2	21.5	25.2	23.7	n.d.
Field Eh (mV)	278	179	150	275	242	321	n.d.
Field pH	12.74	12.42	12.66	7.84	12.92	7.22	n.d.
Laboratory pH	12.67	12.47	12.76	7.44	12.83	7.77	5.36
Conductivity (µS/cm)	5930	4400	7220	650	10210	503	n.d.
Diss. O_2 (mg/l)	4	4	11	4	12	5	n.d.
Ca (mg/l)	674	427	804	78.2	1120	75.3	<0.5
Mg (mg/l)	0.01	0.01	0.01	4.10	0.01	5.43	0.01
Na (mg/l)	47.2	51.2	46.6	43.2	136	12.4	<0.20
K (mg/l)	9.88	14.6	19.8	12.1	526	3.60	<2.50
NH_4 (mg/l)	<0.10	0.20	0.13	0.39	6.05	<0.10	<0.10
Sr (mg/l)	5.37	5.76	10.4	1.12	13.7	0.27	<0.001
CO_3 (mg/l)	37	22	29	<5	37	<5	<5
HCO_3 (mg/l)	<5	<5	<5	129	<5	217	<5
OH (mg/l)	422	258	526	<5	670	<5	<5
Cl (mg/l)	52.4	67.9	72.3	67.0	46.6	20.9	<2.00
SO_4 (mg/l)	305	273	289	85.5	1580	9.82	<2.00
NO_3 (mg/l)	3.28	3.68	7.73	34.8	39.1	25.2	<0.10
Major cation total (meq/l)	36.1	24.1	42.9	6.47	75.6	4.84	<0.01
Major anion total (meq/l)	33.9	23.6	40.1	6.40	75.5	4.78	0.00
Balance %	3.04	1.02	3.39	0.54	0.06	0.70	-
TOC (mg/l)	3.20	4.58	1.35	42.2	6.38	4.38	1.04
TIC (mg/l)	4.83	3.99	5.51	23.0	5.97	43.0	<0.10

Note: n.d. - not determined.

Table 4.3 Trace element data for Maqarin groundwaters.

Sample:	M1	M2	M3	M4	M5	M6	M7 (blank)
Br (mg/l)	0.14	<0.10	0.27	<0.10	<0.10	<0.10	<0.10
NO_2 (mg/l)	<0.10	0.16	<0.10	0.20	1.02	<0.10	<0.10
HPO_4 (mg/l)	0.01	<0.01	0.02	0.04	0.12	0.01	<0.01
F (mg/l)	0.29	0.30	0.31	0.96	0.98	0.34	0.01
Reduced S (mg/l)	0.053	2.434	0.032	0.034	0.281	<0.020	<0.020
B (mg/l)	<0.05	<0.05	<0.05	0.10	0.07	<0.05	<0.05
Li (mg/l)	0.02	0.03	0.06	0.01	0.58	<0.01	<0.01
Ba (mg/l)	0.027	0.023	0.040	0.035	0.019	0.349	0.002
Si (mg/l)	<0.02	0.41	0.09	28.4	0.07	13.3	<0.02
Al (mg/l)	0.14	0.18	0.15	0.03	0.14	0.02	<0.02
V (mg/l)	<0.01	<0.01	<0.01	0.14	<0.01	<0.01	<0.01
Mn (mg/l)	<0.001	<0.001	<0.001	0.008	<0.001	<0.001	<0.001
Total Fe (mg/l)	<0.01	<0.01	<0.01	0.25	<0.01	<0.01	<0.01
Reduced Fe (mg/l)	<0.01	<0.01	<0.01	0.24	<0.01	<0.01	<0.01
Co (mg/l)	<0.02	<0.02	<0.02	<0.02	<0.02	<0.02	<0.02
Ni (mg/l)	<0.02	<0.02	<0.02	<0.02	<0.02	<0.02	<0.02
Cu (mg/l)	<0.005	<0.005	<0.005	0.007	<0.005	<0.005	<0.005
Zn (mg/l)	0.070	0.028	0.017	0.022	0.011	<0.005	<0.005
Cr (mg/l)	0.75	0.32	0.62	0.05	5.38	<0.01	<0.01
Mo (mg/l)	0.10	0.08	0.08	<0.02	0.20	<0.02	<0.02
Cd (mg/l)	<0.005	<0.005	<0.005	<0.005	<0.005	<0.005	<0.005
Pb (mg/l)	<0.10	<0.10	<0.10	<0.10	<0.10	<0.10	<0.10
Zr (mg/l)	<0.01	<0.01	<0.01	<0.01	<0.01	<0.01	<0.01
As (µg/l)	<0.50	<0.50	<0.50	3.20	<0.50	0.70	<0.50
Se (µg/l)	60.0	62.9	107	30.7	591	1.14	<0.50
La (µg/l)	0.17	0.14	0.25	0.07	0.13	0.01	<0.01
Ce (µg/l)	<0.01	<0.02	<0.01	0.09	<0.01	0.01	<0.01
Pr (µg/l)	<0.001	<0.001	<0.001	0.020	<0.001	<0.001	<0.001
Nd (µg/l)	<0.001	<0.001	<0.001	0.050	<0.001	<0.001	<0.001
Sm (µg/l)	<0.001	<0.001	<0.001	0.020	<0.001	0.110	<0.001
Eu (µg/l)	<0.001	<0.001	<0.001	<0.001	<0.001	0.080	<0.001
Tb (µg/l)	<0.001	<0.001	<0.001	<0.001	<0.001	<0.001	<0.001
Dy (µg/l)	<0.001	<0.001	<0.001	0.020	<0.001	<0.001	<0.001
Ho (µg/l)	<0.001	<0.001	<0.001	0.010	<0.001	<0.001	<0.001
Er (µg/l)	<0.001	<0.001	<0.001	0.020	<0.001	<0.001	<0.001
Tm (µg/l)	<0.001	<0.001	<0.001	<0.001	<0.001	<0.001	<0.001
Yb (µg/l)	<0.001	<0.001	<0.001	0.020	<0.001	<0.001	<0.001
Lu (µg/l)	<0.001	<0.001	<0.001	<0.001	<0.001	<0.001	<0.001
Th (µg/l)	<0.40	0.07	<0.03	<0.03	<0.03	<0.03	<0.03
U (µg/l)	<0.03	<0.03	<0.03	12.1	0.05	0.83	<0.03

Note: All results are reported in ppm (mg/l) except the REE, U, Th, As and Se, which are reported in ppb (µg/l).

Table 4.4 Summary of U and Th concentrations for Maqarin groundwaters determined by direct ICP-MS[1] and ion-exchange pre-concentration ICP-MS[1,2].

Sample:	M1	M2	M3	M4**	M5	M6	M7 (blank)
	detection limit (ppb)						
Measured Th (ppb) by direct ICP-MS BGS	<0.4	0.07	<0.03	<0.03	<0.03	<0.03	0.03
Measured U (ppb) by direct ICP-MS BGS	<0.03	<0.03	<0.03	12.1	0.05	0.83	<0.03
Measured Th (ppb) by ion-exchange-ICP-MS* BGS	0.0024	0.0014	<0.0006	<0.0008	<0.0006	<0.0012	<0.0006
Measured U (ppb) by ion-exchange-ICP-MS* BGS	0.0012	0.0014	0.0012	0.0017	0.0024	0.0012	0.0006
Measured Th (ppb) by ion-exchange-ICP-MS* ANSTO	0.002	n/a	0.000	n/a	0.009	n/a	n/a
Measured U (ppb) by ion-exchange-ICP-MS* ANSTO	0.002	n/a	0.016	n/a	0.037	n/a	n/a

Notes:

1 BGS data - note data for ion-exchange preconcentration-ICP-MS should be treated with caution as the technique is still developmental.

2 ANSTO data

* Based on 100% recovery of U and Th; actual recovery probably 50%, therefore values should be doubled.

** Results from sequential extraction experiments may be low due to sorption of organic U complex to resin.

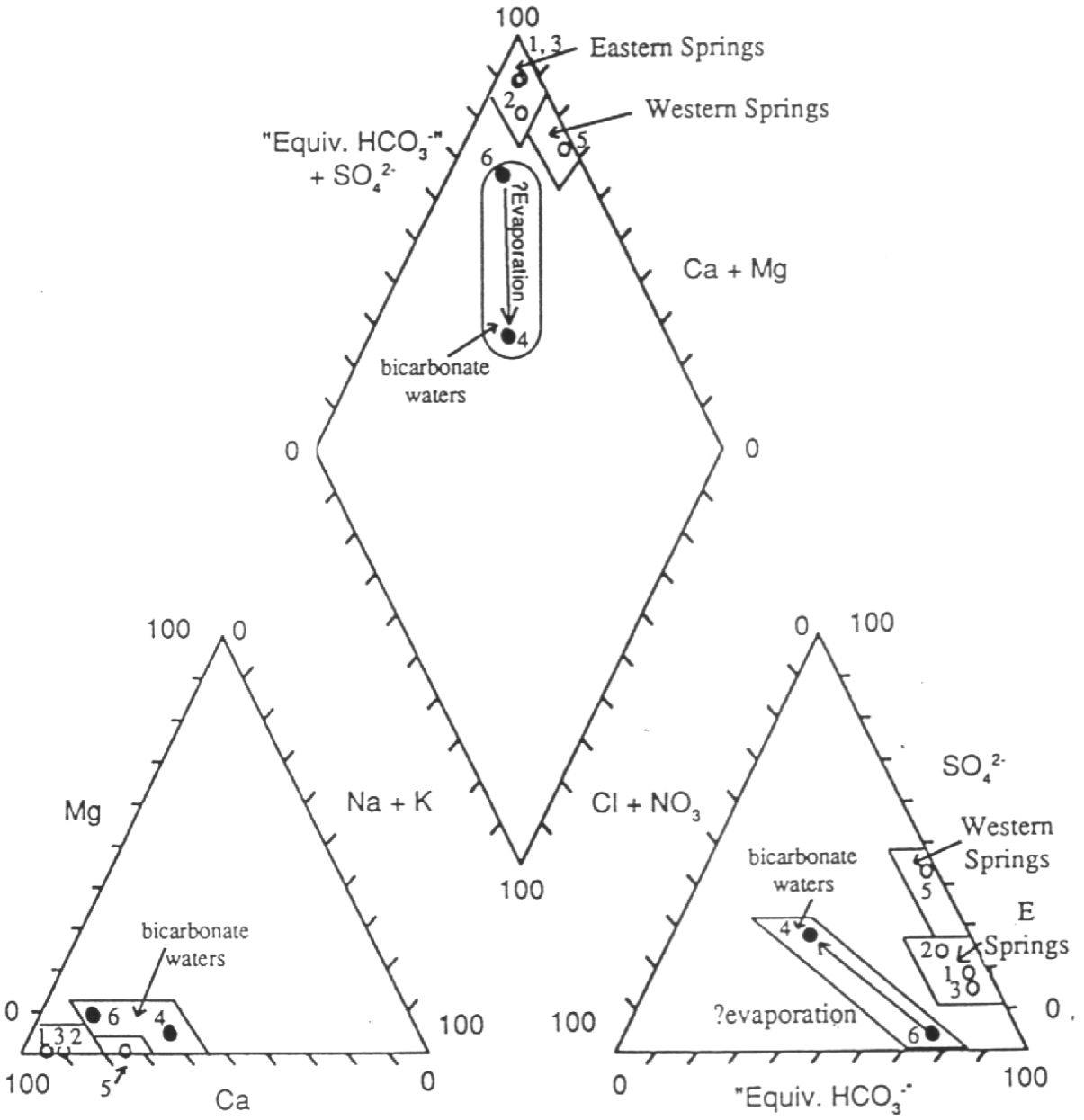

Figure 4.1 Piper trilinear plot for the major ion components of the Maqarin groundwater (as m equivalent %) showing the principal variations and similarities of the different groundwater types. Note: the hyperalkaline groundwaters have been plotted with OH^- recalculated as equivalent HCO_3^- to enable them to be compared to normal bicarbonate groundwaters.

1-M1, 2-M2, 3-M3, 4-M4, 5-M5, 6-M6.

5. ION EXCHANGE RESIN STUDIES OF SPECIATION IN MAQARIN GROUNDWATERS

S.A. Short

5.1 Introduction

A previous study attempted to use the principle of ion exchange to help validate speciation of trace elements in hyperalkaline Maqarin groundwater. That is, a cation exchanger was used to try to verify the significant presence of cationic species, an anion exchanger was used to try to verify the significant presence of anionic species and a non-polar substrate was used to try to verify the significant presence of hydrophobic species (such as might occur with 'humic' complexes or complexes with bitumen degradation products). The study employed small portable SEPAK columns which consisted of a silica substrate bonded with carboxymethyl groups (cation exchange), or with quaternary methyl amine groups (anion exchange) or with non polar straight-chain hydrocarbons (non-ionic or hydrophobic affinity). These cartridges had been used previously with some success in low ionic strength, moderate to neutral pH groundwaters at Poços de Caldas and Broubster natural analogues [1, 2]. The results of this earlier study (of Maqarin groundwaters) are thoroughly described in Alexander [3].

Unfortunately the results of the first study were disappointing and in most cases ambiguous. This was believed to have been due to alkaline dissolution of the silica substrate affecting speciation and/or site saturation and competition and/or kinetic effects due to use of a flow-through system.

For the present study an amended methodology was adopted in order to minimise or eliminate the limitations of the first study. Organic resins were used to avoid dissolution of the substrate and approximately one litre of filtered groundwater was equilibrated with an appropriate mass of exchange resin batch-wise in a sealed bottle.

5.2 Methods

Analytical grade ion exchange resins were obtained from Radiochemie Labor, University of Berne. Resins were dried for one week at 80°C and dispensed by mass into 1l or 500 ml HDPE bottles. These bottles had been pre-leached by soaking in 0.1 M high purity HNO_3 for at least one week. The following ion exchange resins were used.

Cation exchanger: Bio-Rad AG50W-X8, 100-200 mesh, 5.1 $meq.g^{-1}$ dry resin, Na^+-form.

Anion exchanger: Bio-Rad AG1-X8, 100-200 mesh, 3.2 $meq.g^{-1}$ dry resin, OH^--form.

These resins are based on a styrene divinylbenzene copolymer with 8% cross-linking and have large surface area. The cation exchange resin is a strong acid resin with sulphonate ($-SO_3^-$) groups and the anion resin is a strong base resin with quaternary ammonium ($-CH_2N^+(CH_3)_2$) groups [4]. The mass of resin dispensed was calculated to slightly exceed, in total exchange capacity, the total cation or anion equivalent respectively in one litre of water (8 and 16 grams for cation and anion resin respectively). The neutral resin used was of Bio-Rad Bio Beads SM 16, 20-50 mesh, composed of the same styrene divinylbenzene copolymer substrate as the exchange resins but with a much larger surface area and pore opening, and is similar to Rohm and Haas Amberlite XAD-8 commonly used to isolate humic material from water [5]. Experimentally, it has been used

successfully to confirm uranyl humate speciation predictions at pH 6 and 2 in (pH-adjusted) high calcium river water [6]. Mass dispensed (2.5 grams) was computed to give a surface area approximately normalised to that for the ion exchange resins.

The field sampling protocol is described in Chapter 3. Following receipt of the samples in Australia, the bottles were opened, acidified with high purity HNO_3 and stored for one week. A blank was made by placing one identical filter paper in acidified Milli-Q water. Separated resins were loaded (with filter paper) into pre-leached glass columns and leached with about 1 litre of 1 M HNO_3 (Milli-Q water) in an attempt to recover elements attached to the resins. Control of all acid additions and water volumes was made by weight. All solution were analysed with a VG Plasmaquad ICP-MS at the Centre for Advanced Analytical Chemistry (ANSTO Division of Coal and Energy Technology), Lucas Heights Research Laboratories by Mr Owen Farrell.

5.3 Results and Discussion

In Table 5.1 is shown a comparison of the data obtained on the water samples shipped to Lucas Heights (and acidified there) with data obtained by BGS. There are some interesting discrepancies which require consideration. Concentrations obtained for selenium at Lucas Heights (ANSTO) are a factor of ~2 greater than obtained by BGS. Similar discrepancies were recorded in the water exposed to resins so it is probable that there is a systematic measurement error in one of the laboratories. The other outstanding discrepancy is with lanthanum determinations where BGS find substantially higher concentrations than ANSTO.

The results of the batch resin exposure experiments are shown in Table 5.2 for those elements where reasonably meaningful results were obtained (Cr, Mo, Se, Co, Cu, Ni, Zn, Pb, and Mn). There was a negligible blank contribution from the paper filter used to separate resin and water in Amman. Significant amounts (relatively) of ultra-low trace elements (Sn, U, Th, La, Ce concentrations <0.3 ppb) leached from the resins, invalidating any attempt to obtain an approximate mass balance with that present in untreated water. Elution of the resins with 1M HNO_3 failed to elute more than about 50% of that known to be attached, thereby invalidating this part of the study. This was expected from a consideration of the ion exchange literature. It was not possible to elute elements from the resins with higher molarities of HNO_3 as the ICP-MS torch will not tolerate it. Elution with strong NaOH solutions is also not practicable due to the high solids loadings produced in the eluate, requiring dilution before ICP-MS analysis.

The results (of resin-water exposure) have produced some anomalous results regarding inference of major species polarity, especially for Co and Ni, which are totally at odds with the probable speciation [7, 8]. This is believed to be a consequence of using strong acid cation resins which, like soluble complexing agents, have functional (sulphonate) groups which are able to significantly disturb the aqueous speciation equilibria during the equilibration period. This also means that the results obtained with the strong base anion exchange resins which have quaternary ammonium functional groups are open to question but this is considered less likely by chemical analogue arguments.

In retrospect, it was a mistake to use strong acid cation exchanger and strong base anion exchange resins which are potentially able to disturb solution equilibria. Information about weak acid cation (e.g. Bio-Rad Bio-Rex 70) exchange resins indicated that such resins are chemically unstable above pH 10 [4] and it was this consideration (plus availability at short notice) which had ruled out their use for this study. It is noted that the

manufacturer recommends the use of 0.5 M NaOH for regeneration of these resins. Clearly some further discussion with resin manufacturers regarding pH stability, equilibration rates etc. would be desirable before repeating this work with weak acid and base resins. A weak base anion resin (Bio-Rad Bio-Rex 5) has been successfully used to bind actinide carbonate anions, including unstable Pu(IV) complexes [9].

5.4 Conclusions

Like the first study, this one has only been partly successful. Some conclusions can be made from this study which also provide much clearer guidelines for any further investigation. These are as follows:

(i) The batch equilibration method of exposure to ion exchangers is superior to the flow-through column or cartridge method because a greater period of time is available for equilibration and because it is easier to ensure precisely that an excess of available exchange sites is present. This largely eliminates kinetic and competitive effects. The results for Cr, Mo and Se show that nearly 100% uptake onto the exchanger is possible with this approach.

(ii) Exposure to strong acid cation exchangers (i.e. with sulphonate groups) disturbs the natural equilibrium between some trace metals (e.g. Co and Ni) and ligands like OH^- (and probably CO_3^{2-}). Less ambiguous studies may still be possible with weak acid cation exchangers with, for example, carboxymethyl or carboxylic functional groups (e.g. Bio-Rad Bio-Rex 70). Note that, in relation to (i) above that, weak acid cation exchangers are slower to equilibrate than strong acid exchangers.

(iii) Although exposure to strong base anion exchange resin may have interfered with coordinative equilibria in the groundwater this study suggests that Cr, Mo, Se and Mn occur overwhelmingly as anionic species. This might be absolutely confirmed by use of intermediate or weak base anion exchangers next time (e.g. Bio-Rad Bio-Rex 5, AG3- or AG4-X4).

(iv) There is no significant evidence of affinity for uncharged styrene divinylbenzene copolymer (almost invariably used as the substrate for purely organic resin-based ion exchangers) for Cr, Mo, Se, Co, Ni, and Mn showing an absence of association with hydrophobic organic molecules.

(v) There is significant evidence of affinity for uncharged styrene divinylbenzene copolymer by Cu, Zn and Pb. This suggests that these elements might be at least partly complexed by hydrophobic organic molecules. This effect is likely to be apparent no matter what type of organic cation or anion resins were used and must be accounted for in any future study with weaker ion exchangers. It should also be considered in interpretation of the results of speciation modelling.

(vi) Successful studies of trace elements that occur at the sub-ppb level (i.e. Sn, U, Th, REE's) would require the use of exchangers which are especially pure with respect to these elements. This may not be possible or will require quite elaborate procedures for resin decontamination.

(vii) Any future study should include monitoring of total dissolved organic carbon (DOC) in water before and after exposure to ion exchange resins as there seems some possibility of lower stability of weak acid and base resins at high pH compared to strong acid and base resins.

5.5 References

[1] B.P. Vickers, *The Use of Portable Speciation Equipment in Groundwater Studies at the Poços De Caldas Field Site (Brazil),* British Geological Survey Technical Report WI/89/9, 1989.

[2] B. Smith, M.E. Stuart, B.P. Vickers and D. Peachey, *The Characterisation of Organics from the Natural Analogue Site at Broubster, Caithness, Scotland,* British Geological Survey Technical Report WE/89/33, 1989.

[3] W.R. Alexander (Ed.), *A Natural Analogue Study of the Maqarin Hyperalkaline Groundwaters. I. Source Term Description and Thermodynamic Database Testing,* NAGRA Technical Report, NTB 91-10, 1992.

[4] Bio-Rad Laboratories, *Guide to Ion Exchange.* Cat. Number 140-9997. Richmond, California, 1989.

[5] Bio-Rad Laboratories, *Chromatography, Electrophoresis, Immunochemistry, Molecular Biology Catalogue.* Richmond, California, 1990.

[6] C. Lienert, *Saisonales Verhalten der Mobilitat von Uran im Zusammenhang mit den wichtigsten chemischen Komponenten im Fluss/Grundwasser Infiltrationssystem von Glattfelden (ZH).* PhD thesis, University of Berne, 1992.

[7] C.F. Baes and R.E. Mesmer, *The Hydrolysis of Cations* pp 242, 247, 1986.

[8] W.R. Alexander, R. Dayal, K. Eagleson, J. Eikenberg, E. Hamilton, C.M. Linklater, I.G. McKinley and C.J. Tweed, *A Natural Analogue of High Cement Pore Waters from the Maqarin Area of Northen Jordan. II: Results of Predictive Geochemical Calculations.* J. Geochem. Explor. **46**, 133-146, 1992.

[9] W. Faubel and S.A. Ali, *Decontamination of Carbonate Containing Process Streams in Nuclear Fuel Reprocessing by Ion Exchange Chromotography*, Nucl. Technol. **69(2)**, 178-185, 1985.

Table 5.1 Comparison of Trace Element Concentrations Measured at Lucas Heights and BGS.

	Site M1		Site M3		Site M5	
Element	**ANSTO**	**BGS**	**ANSTO**	**BGS**	**ANSTO**	**BGS**
Cr	810±13	750	707±8	620	6440±40	5380
Mo	113±6	100	97±1	80	252±5	200
Se	114±1	60	206±3	107	1315±21	591
Co	2.3±0.1	<20	2.8±0.1	<20	4.0±0.1	<20
Cu	6.5±0.7	<5	5.5±0.7	<5	10.3±2.1	<5
Ni	2.3±0.5	<20	4.0±0.4	<20	5.8±1.7	<20
Zn	69±1	70	25±1	17	17±1	11
Pb	0.7±0.1	<100	0.8±0.1	<100	0.7±0.1	<100
Mn	0.5±0.5	<1	0.9±0.1	<1	7.2±0.6	<1
Fe	0±7	<10	0±7	<10	11±11	<10
Sn	0.05±0.01	-	0.10±0.01	-	0.27±0.04	-
U	0.002±0.001	<0.03	0.016±0.001	<0.03	0.037±0.002	<0.05
Th	0.002±0.001	<0.40	0.000±0.001	<0.03	0.009±0.002	<0.03
La	0.011±0.007	0.17	0.010±0.003	0.25	0.021±0.002	0.13
Ce	0.001±0.001	<0.01	0.002±0.001	<0.01	0.016±0.001	<0.01

Notes: All concentrations in $\mu g.l^{-1}$ (ppb). ANSTO data for M1 mean of 2 samples; for M3 mean of 2 samples; for M5 mean of 3 samples.

Table 5.2 Observed Percentage Uptake of Major Trace Metals to Ion Exchange Resins.

	Chromium	**Molybdenum**	**Selenium**
Site M1	**(810±13 ppb)**	**(113**±6 ppb)	**(114**±1 ppb)
Uptake to neutral resin	0.2±1.9	-4.4±5.3	-0.8±0.9
Uptake to cation resin	6.8±1.9	2.7±5.3	0.8±0.9
Uptake to anion resin	99.3±2.3	96.5±10.5	97.4±1.2
Site M3	**(707±8 ppb)**	**(97±1 ppb)**	**(206±3 ppb)**
Uptake to neutral resin	-2.0±1.6	1.0±1.0	0.5±1.5
Uptake to cation resin	-1.1±1.6	-2.0±1.0	0.5±1.5
Uptake to anion resin	99.2±1.6	97.9±1.4	94.7±2.0
Site M5	**(6440±40 ppb)**	**(252±5 ppb)**	**(1315±21 ppb)**
Uptake to neutral resin	-0.9±1.2	1.6±2.0	0.5±1.6
Uptake to cation resin	0.6±1.2	-2.0±1.0	-0.3±1.6
Uptake to anion resin	95.9±0.9	97.9±1.4	89.3±2.1

	Cobalt	**Copper**	**Nickel**
Site M1	**(2.3±0.1 ppb)**	**(6.5±0.7 ppb)**	**(2.3±0.5 ppb)**
Uptake to neutral resin	-4±4	23±19	-26±31
Uptake to cation resin	79±6	23±19	100±37
Uptake to anion resin	-4±4	54±19	-91±37
Site M3	**(2.8±0.1 ppb)**	**(5.5±0.7 ppb)**	**(4.0±0.4 ppb)**
Uptake to neutral resin	4±4	9±22	30±15
Uptake to cation resin	73±4	-45±23	65±16
Uptake to anion resin	-4±4	27±22	-35±15
Site M5	**(4.0±0.1 ppb)**	**(10.3±2.1 ppb)**	**(5.8±1.7 ppb)**
Uptake to neutral resin	2±2	22±23	-7±31
Uptake to cation resin	81±3	-7±22	64±36
Uptake to anion resin	-5±5	32±23	33±32

	Zinc	**Lead**	**Manganese**
Site M1	**(69±1 ppb)**	**(0.7±0.1 ppb)**	**(0.5±0.5 ppb)**
Uptake to neutral resin	10±1	43±16	80±128
Uptake to cation resin	1±1	43±16	-100±141
Uptake to anion resin	61±2	57±16	-20±102
Site M3	**(25±1 ppb)**	**(0.8±0.1 ppb)**	**(0.9±0.1 ppb)**
Uptake to neutral resin	12±4	12±13	-30±117
Uptake to cation resin	-32±4	62±15	-11±112
Uptake to anion resin	56±15	38±13	-67±134
Site M5	**(17±1 ppb)**	**(0.7±0.1 ppb)**	**(7.2±0.6 ppb)**
Uptake to neutral resin	12±1	43±16	1±8
Uptake to cation resin	-65±7	71±16	35±9
Uptake to anion resin	41±6	0±14	83±11

6. MINERALOGY AND PETROLOGY

A.E. Milodowski, J.M. Pearce, E.K. Hyslop, C.R. Hughes, S.D.J. Inglethorpe, G.E. Strong, N. Wheal, A.B. Mckenzie, O. Karnland and H.N. Khoury.

6.1 Introduction

6.1.1 General

This chapter describes the detailed mineralogical and petrological characteristics of the alteration of non-metamorphic rocks (clay biomicrite limestones (‘marls’), basalt, chert) by rock-water interaction with high pH (pH c.12.5 to 12.9) groundwaters from the Maqarin and Daba-Siwaqa areas. It includes both data from Phase II of the Jordan Natural Analogue Project and data from the preliminary Nagra investigations of marl-hyperalkaline groundwater interaction [1]. The metamorphism, mineralogy, mineral chemistry and alteration of the high-temperature metamorphic zones hosted within, or closely associated with, these unmetamorphosed country rocks has been described in great detail in earlier accounts [1, 2, 3, 4, 5] and are therefore not discussed here.

The principal aim of this study was to investigate - as an analogue of the interaction of cement pore-fluids with repository host-rocks - the alteration of unmetamorphosed country rocks (mainly bituminous clay biomicrite limestone) which were affected by hyperalkaline (portlandite-saturated) groundwaters discharging from the metamorphic zones. The study was focused mainly on the Maqarin site in northern Jordan, where it was intended that mineralogical information (on primary host rock and alteration) should correspond to well-defined points along the flow-paths of the high pH fluids through the host rock. Where possible, samples were taken to correspond to the actual sites from which groundwaters were sampled in order that changes in the groundwater chemistry could be directly compared to mineralogical changes. Information on the mineralogy of the unaltered host rock would be used to establish one of the initial boundary parameters in subsequent geochemical modelling of the site. The alteration mineralogy and petrological changes, observed in relation to hyperalkaline water-rock interaction, would be compared to the model predictions as a form of validation of the geochemical codes and their thermodynamic databases.

Most effort has been expended on defining a well-constrained fracture-flow system in Adit A6 at Maqarin, where corresponding information on the geochemistry of inflowing (‘high pH input’) and outflowing (‘low pH outlet’) groundwaters could be obtained or extrapolated. However, whilst it is not possible to directly correlate observations on the alteration in the Western Springs area of Maqarin, with those in the Adit A6, they do provide a valuable insight into the early stages of the evolution of a high-pH groundwater system. Observations from the older, more evolved analogue sites in central Jordan (where hyperalkaline groundwater activity is now extinct), provide further insight into the later stages of the evolution of a high-pH plume around a radioactive waste repository.

The mineralogical and petrological observations presented here enhance the current understanding of the rock-water interaction processes that would affect a repository disturbed zone. Furthermore, these studies identify the most probable phases that will control the geochemistry of the repository disturbed zone and therefore, enable a more realistic definition of the minerals that should be included in predictive geochemical models to be compiled.

6.1.2 Analytical techniques

A comprehensive suite of mineralogical and petrological techniques was used in the characterisation of materials from Maqarin and central Jordan. This included qualitative and semi-quantitative mineralogical analysis using X-ray diffraction analysis (XRD) of bulk material and orientated clay-fraction separates, and thermal analysis - including thermogravimetric analysis (TG) and evolved gas analysis (EGA) - to quantify volatile-bearing species (e.g. carbonates, organic matter, sulphides, kaolinite). Petrographic and mineral compositional analyses were undertaken using: hand specimen observation; optical petrographic microscope examination of polished thin sections; backscattered scanning electron microscopy coupled with semi-quantitative energy-dispersive X-ray microanalysis (BSEM-EDXA) of polished thin sections; quantitative computerised petrographic image analysis of BSEM images (BSEM-IA); wavelength-dispersive (WD) and energy-dispersive (ED) electron microprobe analysis (EMPA); transmission electron microscopy (TEM); and analytical transmission electron microscopy (ATEM). Petrographic polished thin sections used in these analyses were prepared after impregnation of the material with a blue-dyed epoxy-resin to consolidate the material. The use of a blue dye in the resin enabled the presence of porosity within the sample to be more easily distinguished when examined optically. Grain size analysis and cation-exchange capacity (CEC) were also determined.

On the basis of these observations, selected material was submitted for natural decay series (uranium and thorium) analysis by alpha spectrometry in an attempt to place time constraints (by $^{230}Th/^{234}U$ age determination) on the rock-water interaction. Most analyses were carried out by the British Geological Survey (BGS) except ATEM and natural decay-series analysis which were undertaken by the University of Manchester and the Scottish Universities Research and Reactor Centre, East Kilbride (SURRC), respectively. The analytical methodology used is summarised in Appendix B. However, salient points regarding the usefulness of the BSEM-IA analyses are discussed below in more detail.

Attempts to quantify the mineralogy and porosity of host-rock and altered fracture wall-rock material by BSEM-IA were largely unsuccessful. In BSEM mode, the scanning electron microscope image obtained from a flat polished specimen is related to the composition, density and crystallinity of the material being examined (cf. Goldstein et al., [6]). BSEM image brightness is proportional to the average atomic number of the material and its density, thus allowing the distribution of different minerals or phases to be determined on the basis of their chemical composition. The technique has considerably finer spatial resolution than conventional optical petrographic techniques and is therefore particularly useful in the study of argillaceous and other fine-grained materials [7, 8, 9]. However, the problem encountered was that many of the alteration products in the rocks from Maqarin possess very similar chemistries and, in particular, could exhibit major solid-solution characteristics and zoning such that their chemical composition was not necessarily constant. Many of the secondary minerals also show variable states of hydration. Consequently, the backscatter coefficients for many of the phases were very similar and the resultant BSEM image contrast characteristics (grey-level range) could not be determined reliably for any given phase. Initially, BSEM grey-level limits were selected and digitised for four grey-levels that were believed to correspond to specific major 'phases' (calcite, ettringite-thaumasite, clay minerals, epoxy resin-filled porosity) in an attempt to measure their volumetric proportions by IA. However, more detailed BSEM-EDXA examination showed that variations in

composition and very-fine admixtures of phases produced the same grey-level within the image field. This image definition problem was further exacerbated by the grain size of most of the secondary alteration products in the wallrock matrix being extremely fine, with particle sizes close to the practical working resolution of the BSEM technique (c.0.2 - 0.5 •m).

Although trends in the BSEM-IA data vaguely corresponded to visual mineralogical variations, quantitative BSEM-IA calculations proved to be very inconsistent. This was demonstrated when comparing the IA data with reliable quantitative bulk mineralogical determinations by EGA or TG - even for major components such as calcite. Consequently, the present BSEM-IA determinations are considered to be erroneous and are not presented or discussed further. The computer BSEM-IA technique could however, have promise for future work if used in conjunction with digital EMPA X-ray microanalysis mapping, which would then provide a chemical control on the variations influencing the BSEM images.

Porosity was estimated by using ED-EMPA to analyse for Cl in the epoxy-resin impregnated pore spaces in thin sections. In this approach, the electron beam was defocused over c.50 •m diameter areas of the thin section rather than using a conventional focused electron beam. However, it must be noted that these analytical conditions are far from ideal for quantitative EMPA. The normal ZAF (atomic number, X-ray absorption and X-ray fluorescence) corrections do not really apply to situations in which element distribution, or phase components, are not uniformly-distributed within the analytical volume of the electron beam. Nevertheless, given the very fine-grained (sub-micron) and intimately-admixed minerals of the altered wallrock associated with the hyperalkaline fracture alteration, it was felt that defocused beam EMPA data might provide a reasonable 'first approximation' of the major element geochemistry of the rock matrix. The epoxy-resin used to impregnate the samples prior to sectioning is Cl-bearing (c.1.8% Cl) and therefore, the Cl content of a given area of section (given that these background rocks have a very low Cl-content - <700 ppm Cl [2] - below the limit of ED-EMPA detection) can be used to estimate the proportion of resin impregnation, and hence an estimate of porosity.

Following detailed characterisation of the materials, a representative suite of secondary minerals was selected and separated for stable isotopic analysis (O, C, H/D, and S isotopes). The results of these isotopic investigations are given in Chapter 10.

Over 50 rock and mineral samples were collected (some of which were retained at the University of Jordan). However, only a proportion of these could be analysed in the present study. A summary of the samples examined is given in Tables 6.1 and 6.2.

6.2 Maqarin

6.2.1 Unmetamorphosed background marl

(i) Petrography

Primary mineralogical and petrological characteristics

The unaltered organic-rich (kerogenous) marls, limestones and chalks encountered in the Maqarin area, in Adit A6 and the railway cutting are all bituminous clay-biomicrites [10, 11]. The rocks vary in colour from light grey to brown and black. Many of the darker ones have a distinctive 'tarry' hydrocarbon odour. With the exception of A967 (from the Maqarin railway cutting), which is dolomitic, all are calcitic.

The organic-rich clay-biomicrites comprise largely silt-grade to fine sand-grade fragmental calcareous (calcitic) microfossil detritus (10-200 •m) floating in a fine grained (<5 •m) matrix of comminuted foraminiferal tests, variably preserved coccolith plates and other calcareous microfossil detritus (Plates 16 and 17)). The matrix also contains finely-disseminated clay minerals. Most of the coarser microfossil detritus consists of foraminiferal tests but calcareous coccolith fragments, wheel-shaped spicules (possibly sponge or echinodermata spicules), and occasional pelloidal calcite grains and fragments of 'bivalves' are also present. For the most part, the individual clay minerals in the matrix could not be resolved by BSEM-EDXA, but occasionally fine silt-grade (<10 •m) detrital illite or degraded muscovite particles, and local concentrations of kaolinite can be recognised. Although the kaolinite is generally not well crystallised, some face-to-face stacks of pseudohexagonal books were observed by SEM. Traces of very fine (<1 •m) TiO_2 (probably anatase or rutile) and fine silt-grade albite are disseminated throughout the matrix. The matrix appears to be quite close-packed with only very fine (<0.5 •m) intergranular porosity (Plate 17). EPMA scan data for Cl from epoxy-resin impregnated thin sections indicates typical porosities of about 30%.

Diagenetic modification

Diagenetic modification of the rocks appears to be largely related to early (near-surface or shallow burial) diagenetic processes. Compaction and cementation has been minimal, and many of the more-intact foraminifera tests show very little evidence of compactional deformation (Plate 18). Cavities within foraminifera tests have been partly infilled with authigenic minerals including minor non-ferroan, non-manganoan calcite (Plate 18), amorphous, silica, pyrite (Plate 18), and possible minor 'glaucony'[1] (Plate 19). As well as occurring within test cavities pyrite also occurs disseminated throughout the matrix, usually as framboidal (spherical) aggregates of tiny (<1 •m) octahedral crystals (Plate 20). Framboidal pyrite locally replaces 'glaucony'. In the samples examined much of the pyrite and 'glaucony' has been oxidised and is now partially pseudomorphed by hematite or goethite (Plate 19). Coarser, well-crystallised euhedral pyrite also replaces earlier framboidal pyrite and 'glaucony'.

In addition to pyrite, other sulphides and sulphosalts are also present in trace amounts, these include framboidal sphalerite, galena, Ni-Se, Ag-Se, Ag-Cu-Ni-Fe-Zn-Cd-S-Se, and Fe-Cu-Zn-Ni-S, and Zn-Cu-Fe-Ni-Se minerals. These also, occur as framboids, commonly associated with framboidal pyrite (often concentrated around pyrite framboid margins - implying slightly later stage accumulation) within foraminiferal tests and are most probably complex sulphide and selenide sulphosalt minerals. Similar minerals, and also possible native selenium (probably replacing microbial mucilage or cell tissues), were found during a preliminary assessment of the unaltered host rocks during Phase I [2]. Barite is present as a trace authigenic mineral filling certain tests, and locally replacing the micritic matrix (Plate 21). Barite cements compactionally-deformed bioclastic detritus and therefore formed during burial diagenesis. Some foraminiferal tests have oil or hydrocarbon-filled cavities, often enclosing earlier-formed framboidal sulphide and selenide minerals.

---

[1] The term 'glaucony' as used here, is a general term applied to an Fe-rich micaceous clay mineral with characteristics similar to glauconite sensu-lato but with undefined chemistry, or with more than 10% smectite interlayers, or a green clay mineral. Glauconite sensu-stricto has well-defined compositional limits and is an Fe-rich, micaceous clay mineral [ideal formula - $(K,Na,Ca)_{1.2\text{-}2.0}(Fe^{3+},Al,Fe^{2+},Mg)_4(Si_{7\text{-}7.6}Al_{1\text{-}0.4}O_{20})(OH)_4.nH_2O)$] with less than 10% smectite interlayers [18].

Apatite or near-amorphous calcium phosphate (collophane) is a significant component in the bituminous clay biomicrite. It is mostly present as minute (<1 •m) crystallites disseminated throughout the groundmass of the rock. Some coarser calcareous microfossil fragments, pellets (faecal pellets) or possibly bone fragments are replaced by apatite or amorphous collophanic material. Apatite replacements appear to predate carbonate cements within which they are sometimes included.

Many of the foraminiferal tests display little evidence of recrystallisation and their radial-fibrous microcrystal fabrics are still preserved, even in tests which have suffered some compactional crushing and diagenetic mineralisation (Plate 21). However, tests which contain authigenic calcite infills (Plate 18) usually show some recrystallisation and loss of their original microfibrous fabric. Calcite is abundant as a cement within intact foraminiferal tests. During Phase I it had been tentatively suggested that two generations of calcite were present: an early microcrystalline overgrowth lining developed on calcite crystallites forming the test wall; and a later coarser euhedral void-filling calcite. However, in the present study only a single coarse euhedral void-filling calcite generation was recognised in the unaltered rock matrix (Plate 18). Calcite is a relatively late diagenetic mineral and includes earlier-formed authigenic sulphides, selenides, silica and 'glaucony'. Authigenic calcite can be seen within some compacted forams enclosing fragments of crushed test wall (Plate 22) demonstrating that calcite authigenesis occurred during or after the main burial phase experienced by these rocks. Alexander et al. [12] showed that the calcite forming this late diagenetic cement also mineralises fault breccias in the limestones.

Sample A967 is dolomitic and visual estimates from BSEM images give dolomite contents of approximately 20%. Dolomite contents calculated from estimates of whole rock Mg content (from broad area scan of polished sections using combined EMPA-laser ablation ICP-MS analyses, Chapter 8) indicate a slightly higher content of dolomite, up to 28%. BSEM-EDXA and EMPA show that the dolomite is non-ferroan; it occurs as subhedral to anhedral grains replacing and overprinting primary micritic carbonate matrix, and locally replacing microfossil detritus (Plate 23). In A967, dolomite also fills any remaining porosity within foraminiferal tests, enclosing earlier authigenic calcite (Plate 24).

Fine-grained red hematite, goethite and amorphous iron oxyhydroxides replace pyrite and 'glaucony'. These minerals often fill microfossil cavities or are present in hairline cracks and along bedding-plane partings. In some cases they are closely associated with gypsum and a previously unreported Se-rich analogue of gypsum.

Summary of diagenetic mineral paragenesis

The petrofabric relationships described above suggest that the diagenetic paragenesis of these rocks is relatively simple. It essentially comprises two major episodes: an early pre-compactional episode dominated by sulphide authigenesis (which includes minor 'glaucony' authigenesis); and a later carbonate-dominated episode which appears to post-date burial compaction (Figure 6.1).

Framboidal pyrite morphology and formation is usually associated with bacterial reduction during very early sediment diagenesis, within the zone of sulphide reduction in the top few centimetres of sediment [13]. Framboidal pyrite morphology is controlled by the formation of spheres of greigerite (Fe_3S_4) from an original mackinawite (FeS) precipitate [14, 15]. Framboidal pyrite recrystallises from greigerite by reaction with additional sulphur. Microbial mediation is not necessarily a prerequisite for this process,

which may also occur inorganically [13, 14, 15, 16, 17] but it does imply that authigenesis occurred at low-temperature (i.e. before significant burial). It seems likely that the other sulphosalts spatially associated with pyrite, which have also adopted a framboidal morphology, have a similar origin.

The restricted occurrence of 'glaucony' within foraminiferal test cavities is a common feature of glauconite authigenesis [18]. It requires a reducing environment to form and it would appear that suitable conditions were only achieved within micro-environments in foram chambers. It probably represents the earliest mineral, precipitated within anoxic micro-environments contained within organic-rich microfossil cavities, whilst the surrounding sediment porewater was still oxic. With continued accumulation of organic-rich sediment, and microbial sulphate reduction, the porewaters became sufficiently reducing to precipitate pyrite in the adjacent sediment as well as in the forams. Any ferrous iron would be mopped up by pyrite, thereby causing cessation of any further 'glaucony' formation. During the later stages of pyrite formation, the porewaters appeared to have become enriched in base metals (Zn, Pb, Cd, Cu, Ni, Ag) and Se - most probably liberated from the organic matter (see next section) during bacterial decomposition - and framboidal sulphosalts were precipitated incorporating these elements. Apatite precipitation is also likely to be very early diagenetic, associated with the microbial degradation of the organic matter and the liberation of phosphate. With increasing burial, earlier-formed pyrite appears to have recrystallised to coarser pyrite.

Later carbonate precipitation is associated with some degree of compaction, and indicates deeper burial conditions. The precipitation of these phases may relate to later-stage fermentation or thermal decarboxylation diagenesis of the organic matter, which occurs with increasing burial. Minor hydocarbon (liquid oil) migration appears to have accompanied this, or closely followed carbonate precipitation.

Secondary goethite, iron oxyhydroxides, gypsum and a previously-unreported Se-rich mineral similar to gypsum appear to be the last phases to have precipitated and are most probably related to oxidative weathering alteration of the pyritic bituminous clay-biomicrite.

(ii) Bulk mineralogy

Bulk mineralogical compositions of the unaltered bituminous limestones and clay-biomicrites from Adit A6 and the Maqarin railway cutting are summarised in Tables 6.3-6.6. XRD analyses show that the bulk of the Bituminous Marl Formation rocks in these sites are composed mainly of calcite with minor amounts of apatite (hydroxy-, fluor- and carbonate apatite) and kaolinite (Table 6.3; Figure 6.2). In the railway cutting some of the rocks from the upper blocky limestone (Plate 4, Chapter 3) are also very dolomitic (A967). Quantitative grain size analysis indicates that between 9-21% of the material has a particle size less than 2 •m. However, the clay mineral content is very low and kaolinite was the only clay mineral detectable by XRD, although traces of detrital illite or degraded muscovite were also identified from BSEM-EDXA petrographic studies of the same samples. This is consistent with the results of a more regional study of the Chalk Marl Formation (which includes the Bituminous Marl Formation - see Chapter 3) by Abed and Amireh [19]. These authors concluded that the clay mineralogy of these rocks consists almost entirely of kaolinite with traces of illite, and found no evidence of the smectite (montmorillonite) reported by Shahar and Wurtzberger [20] from equivalent strata in Israel.

Complementary EGA (and TG) analyses confirm the XRD results, indicating calcite contents between 57-89% by EGA and 73-88% by TG. It should be noted that CO_2 evolved during EGA from any dolomite present will not have been distinguished from calcite by these techniques and consequently it will be included as 'equivalent calcite'. EGA identified the presence of minor amounts of pyrite (0-3%) and organic material - containing between 1.1 - 8.1% equivalent organic carbon and 0.2 - 0.5% equivalent organic sulphur. Ammonia is also evolved in significant amounts, simultaneously with CO_2 and SO_2, from the organic matter during thermal analysis (Figure 6.3) indicating that the organic material is both sulphur- and nitrogen-bearing. This characteristic indicates that the type of organic material present is more typical of complex compounds such as amino-acids, amides, thio-organic aromatic compounds etc., rather than simple hydrocarbons such as alkanes, alkenes, alcohols, carboxylic acids [21]. Porphyrin compounds may also contain nitrogenous groups and potentially are able to account for the liberation of ammonia. Porphyrins would also be a potential source of many of the trace elements (e.g. Ni, V, Cr, Cu, Zn, Mo, Co) in these rocks [21], part of which are associated with the organic fraction [2]. There was no evidence from EGA for ammonium within clay minerals (ammonia evolution from clay minerals occurs at higher temperature than organic matter oxidation and is readily distinguished by EGA).

Petrographic studies suggest that the pyrite in the analysed samples has been partially oxidised to orange-red hematite or goethite. Most of the ferric oxide or oxyhydroxide minerals observed are secondary alteration products after pyrite, although some also replace authigenic 'glaucony'. This is probably the result of weathering oxidation (e.g. railway cutting samples A966 and A9647) or due to oxidation in air following the construction of Adit A6 (e.g. samples A961, A962, A963, A964, A965). The pyrite present in these rocks is very fine-grained framboidal and disseminated pyrite and as such is very susceptible to oxidation. It is likely that deeper into the marl, behind the exposed rock faces, the pyrite content is higher than indicated by the results here. Assuming that most of the Fe content of the rock (Appendix Table C3.1) represents former pyrite, then pyrite contents may originally have been as high as 5%.

Normative mineral compositions have been calculated from whole-rock geochemical data (Appendix Table C3.1) and are presented in Table 6.6 for the lowest and highest clay content (i.e. corresponding to the lowest and highest Al content) samples A961 and A962, respectively. These calculations are based on ideal end-member mineral stoichiometries (Table 6.6). The choice of minerals in the normative calculations was based on the results of XRD, EGA and petrographic observations. For the purpose of the normative calculations, the chemical components were assigned as follows:

(i) All Mg is assigned to dolomite and the equivalent Ca subtracted from total Ca.

(ii) All P is assigned to hydroxyapatite and the equivalent Ca subtracted from the residual Ca total after (i).

(iii) All residual Ca is assigned to calcite.

(iv) All K is assigned to illite (ideal muscovite) and the equivalent Al and Si subtracted from the respective total Al and Si.

(v) All Na is assigned to albite and the equivalent Al and Si subtracted from the residual Al and Si after (iv).

(vi) All residual Al is assigned to kaolinite and the equivalent Si subtracted from the residual Si after (v).

(vii) All residual Si after (vi) is assigned to silica (i.e. quartz, although it is most probably all present as amorphous silica or hydrous opal (i.e. $SiO_2.nH_2O$).

(viii) All S is assigned to pyrite and the equivalent Fe is subtracted from the total Fe.

(ix) All residual Fe after (viii) is assigned to ferric oxide (although it may be present as hematite or goethite, or amorphous iron oxyhydroxide).

Normative calculations are in close agreement with the XRD and thermal analysis results indicating whole rock compositions of 74-75% calcite, c.1% dolomite, 3-5% apatite, 0.7-1% albite, 1-2% illite or muscovite, 1.9-5.3% kaolinite, 0.5-1% pyrite, 0.5-2% ferric oxide, and 1.7-5.2% quartz, amorphous silica or opal. Some of the K ascribed to illite (muscovite) in the normative calculations will of course be accounted for by glauconite (or 'glaucony') which has been identified in these rocks as an authigenic mica mineral. These data are consistent with earlier analyses for the Chalk Marl Formation from the Maqarin area [19] which are summarised in Table 6.7. However, the more siliceous (up to 37% quartz) and clay-rich (up to 17% total clay) rocks described by Abed and Amireh [19] are not encountered in either Adit A6 or the Maqarin railway cutting sites.

The CEC of one unaltered sample of bituminous clay-biomicrite (A963) is around 38 meq/100 g.

6.2.2 Alteration by hyperalkaline groundwater interaction

(i) Adit A6

'High pH' upstream alteration zone

Evidence of interaction between unmetamorphosed bituminous biomicrite and hyperalkaline groundwater can be seen along the entire distance of the adit from the metamorphic zone (c. 110 m from adit entrance) to the adit entrance. Alteration is also evident within enclaves of biomicrite within the metamorphic zone (i.e. beyond 110 m from the adit entrance).

The most intense alteration occurs within about 2-3 m of the main metamorphic zone between 110-107 m from the adit entrance (represented by sample A960), and within the enclaves of marl in the metamorphic zone. Here the rocks are highly fractured and locally brecciated, with the development of abundant very close-spaced (typically 0.1-10 mm apart) fine fractures varying in thickness from 0.005-2 mm. Hyperalkaline groundwaters (and associated alteration) appear to have exploited earlier calcite vein mineralisation, utilising partings which have opened up between the calcite vein-fill and the host wallrock (Plate 25). Despite the considerable fracturing and alteration no seepages of alkaline water are now observed. These fractures are now largely sealed by secondary calcium silicate hydrate (CSH) minerals, ettringite-thaumasite, gypsum, calcite, aragonite and zeolitic vein minerals, which form a dense meshwork of anastomosing veins and veinlets.

Within this region, the biomicrite wallrock is severely altered - most evident in the change from its original dark-brown or black colour to a light-grey or chalky appearance. The degree of bleaching decreases sharply beyond about 3 m from the metamorphic zone but can still be seen immediately adjacent to fractures up to 20 m distant (e.g. A962). XRD

shows that the bulk mineralogy of these leached rocks is generally similar to that of their unaltered equivalents, except that kaolinite is absent and gypsum is usually present. In contrast, EGA (Figure 6.3) reveals a total loss of pyrite and organic matter (including nitrogenous - i.e. NH_3-evolving, and sulphurous - i.e. SO_2-evolving compounds). This is also evident in thin section where the opaque pyrite and opaque to orange-brown hydrocarbon and kerogenous organic matter are leached adjacent to fractures (Plate 26). Mobilised organic matter is observed to be re-concentrated at the interface between fresh rock (or relicts of unaltered rock) and the bleached rock (Plate 26), coinciding with zones of enhanced uranium (see Chapter 7).

Most wallrock alteration takes place within 0.5-4 mm of the principal fractures (Plates 25 and 28). Within this narrow alteration zone the fine-grained matrix calcite, kaolinite, silica, and traces of illite (detrital muscovite) and albite are dissolved, and pyrite, trace sulphide minerals and 'glaucony' are oxidised. The resultant altered rock comprises corroded relicts of coarser calcite particles (foram tests, shell fragments etc.) floating in a secondary assemblage of intimately intergrown fine-grained gypsum, micro-fibrous ettringite-like mineral (or ettringite-thaumasite solid-solution), gibbsite, amorphous sodium-calcium-aluminosilicate hydrate gel (CASH) and very minor amounts of an amorphous magnesium silicate hydrate gel. Secondary goethite replaces pyrite and 'glaucony'. Much of the altered matrix material is too fine and intimately mixed to resolve under BSEM and consequently, only a tentative identification of the mineralogy of the alteration assemblage is possible. The wallrock porosity is significantly enhanced for up to 1 mm from the larger fractures. In sample A960, virtually all the fine-grained matrix calcite has been removed within a thin alteration band developed between 0.25-0.45 mm from the fracture wall (Plate 26). In this zone the wallrock has been virtually completely replaced by fine-grained secondary minerals (except for relicts of coarser shell fragments). This highly altered zone has significantly enhanced porosity and petrographic observations suggest that it may have developed by alteration along an anastomosing network of hairline fractures sub-parallel to the main fracture (Plate 28).

Phosphatised shell detritus displays some alteration to very fine or near-amorphous or gel-like hydrous calcium phosphate - indicating that apatite is dissolved and reprecipitated as collophane-like material, at least on a local scale. Discrete ettringite, gibbsite, gypsum and CASH gel often infill cavities within relict foram tests in the altered wallrock. Gibbsite appears to be most extensively developed immediately adjacent to the fracture wall. At the interface between highly leached wallrock and largely unaltered wallrock, a narrow zone is developed within which fine-grained calcite (or possibly aragonite) is precipitated as a matrix cement, reducing the porosity (Plate 25). Organic matter is also concentrated along the same front (Plate 26). However, carbonate cementation occurs along a broader and more diffuse front, and several sub-parallel bands or 'fronts' of carbonate cementation may be developed ahead of the zone of organic concentration (Plate 25). Similar, but less well-developed wallrock alteration was described by Milodowski et al. [1] from the Maqarin railway cutting area.

ATEM analysis of typical altered wallrock (sample A960) close to the fracture surface showed that most of the secondary products were extremely fine grained, microfibrous CASH phases. CASH compositions determined by ATEM are illustrated, and compared to other theoretical calcsilicate and calcium aluminosilicate minerals, in Figure 6.4. Individual crystallites were difficult to resolve, even by TEM, but many analyses fall within a restricted compositional field (A, Figure 6.4). A single ATEM analysis lies close to the zeolite field (B, Figure 6.4) but displaced towards the bulk of the CASH analyses.

Zeolites with mordenite-dachiardite and wairakite compositions are present as major fracture-filling phases in this sample (see below). This single zeolitic analysis (B, Figure 6.4) could represent a composite analysis representing dachiarditic zeolite with a minor amount of the more abundant CASH alteration product (A, Figure 6.4). The remaining analyses in Figure 6.4 are best explained as falling on a mixing line between CASH field B and calcite and/or gypsum (field C, Figure 6.4) - both of which are known from XRD to be present in fine admixture in the altered wallrock.

The bulk of the secondary CASH products (B, Figure 6.4) are very similar (although slightly less calcic) to reaction products from experimental reaction of albite or microcline with $Ca(OH)_2$ or mixed Ca-Na-K-OH alkaline fluids [22, 23]. Assuming that Al substitutes for Si, and Na and K substitute for Ca in the mineral structure, the bulk of the CASH has an equivalent 'Ca:Si' of 0.83-1.33. This lies within the compositional range (0.83-1.5) expected for tobermorite-structured CSH(I) gels [24], rather than the jennite-structured CSH(II) type gels [24, 25, 26]. The fibrous morphology of this phase is consistent with chain-structured phases such as tobermorite, xonotlite, rosenhanite, suolinite or CSH(I). ATEM analyses also indicate that these wallrock alteration products incorporate up to 2.5 weight % S (as SO_4) within the structure. Ideally, these minerals should not contain aluminium. However, previous experimental and natural analogue studies [23, 27] have all shown that these near-amorphous CSH alteration products can incorporate significant amounts of aluminium. Milodowski et al. [1] had earlier demonstrated that even well-crystallised jennite and tobermorite from the Maqarin site are aluminous, with a similar level of Al substitution to that seen in the CASH in this study.

No ATEM analyses could be obtained from the minor amounts of magnesium silicate gel identified by BSEM. By analogy with earlier studies of material from Maqarin railway cutting [1], this is probably a poorly crystalline talc-like alteration product. ATEM analyses also suggest that minor thaumasite rather than ettringite is present in the wallrock.

The fracture mineralisation of the 'high pH' end of the system is also complex. Early calcite-cemented vein-filling breccia in fractures near the metamorphic zone (Plate 25, sample A960) have parted from the wallrock, and the exposed surfaces are seen to have been subsequently mineralised by hyperalkaline groundwater reaction products. Initial mineralisation was by needles of calcium carbonate - probably aragonite (Plate 27). The remaining fissure porosity has been infilled by a complex mixture of gypsum, ettringite-thaumasite, amorphous CSH gel (jennite to tobermorite in composition), and very hydrous, fibrous to gel-like minerals of zeolitic compositions (Plates 29 and 30). BSEM shows that following initial calcium carbonate precipitation, the main fractures and associated minor fractures were mineralised by thaumasite (with some ettringite solid-solution component) and gypsum. Subsequently, fracture reactivation disrupted these early mineralisation fabrics and brecciated thaumasite fragments were then partially coated and replaced by a fibrous tobermorite-like CSH phase. This in turn became progressively cemented and overprinted by a more calcic jennite-like CSH phase. In the final stages of hyperalkaline activity the vein fillings were again brecciated by late fracture movement, and a fibrous to prismatic zeolite was precipitated as a major fracture infill. This partially replaces earlier CSH minerals and thaumasite (Plate 29). Zeolite mineralisation was also accompanied by minor amounts of gypsum.

XRD evidence indicates the possible presence of wairakite together with thaumasite and gypsum (Figure 6.5) within this late-stage fracture mineralisation. However, the XRD data is not definitive (sample A960) due to co-interference from thaumasite and gypsum.

EMPA data (Figure 6.6) for fracture infills from A960 indicates that the late zeolite mineralisation is more complex. EMPA and BSEM-EDXA show that two possible zeolites are present:

(i) a blocky high-Si zeolite intermediate in composition to Ca-mordenite ($(Ca,Na_2,K_2)Al_2Si_{10}O_{24}.7H_2O$) and dachiardite ($(Ca,Na,K)_3Al_4Si_{18}O_{45}.14H_2O$) - a related mordenite subgroup zeolite and;

(ii) a more calcic fibrous zeolite with a composition varying from epistilbite ($CaAl_2Si_6O_{16}.5H_2O$), through yugawaralite, to wairakite ($CaAl_2Si_4O_{12}.2H_2O$), leonhardite ($CaAl_2Si_4O_{12}.3.5H_2O$), or laumontite ($CaAl_2Si_4O_{12}.4H_2O$) (Figure 6.6).

BSEM indicates that the blocky mordenite-dachiardite precipitated earliest and has been largely resorbed or replaced by the later fibrous calcic zeolites. It should however be noted that the later more calcic zeolite is unstable under the BSEM and EMPA electron beam irradiation. Its low backscatter coefficient (producing the duller BSEM image in Plate 30) suggests that it is more hydrous than the earlier mordenite-dachiardite-like mineral it replaces. This is inconsistent with the composition of wairakite which contains much less structural water and a higher Ca content. The identification of wairakite by XRD (above) is therefore, possibly slightly misleading - the natural zeolite is probably a more hydrous 'relative' - i.e. laumontite or leonhardite - rather than wairakite.

Laumontite, leonhardite and wairakite have identical proportions of Ca:Si:Al, and laumontite can be relatively easily dehydrated to give leonhardite or wairakite (e.g. by sample grinding for XRD or under the electron beam during EMPA). Wairakite is normally only found in relatively high-temperature hydrothermal or geothermal systems, whereas in low-temperature systems (i.e. below c.250°C) the more hydrous laumontite (or its partially dehydrated equivalent leonhardite [28]) is the stable phase [27], and would therefore be the phase most likely to be expected within the low-temperature regime associated with the Maqarin hyperalkaline groundwater system.

Quantitative mineralogical data for the fine-scale (sub-millimetre) wallrock alteration bands adjacent to a major fracture in sample A960 are given in Table 6.8 and shown in Figure 6.7. These data are normative mineralogical calculations based on EMPA of broad areas of the fine-grained clay-grade matrix using a defocused electron beam. Although the analytical conditions are not ideal for EMPA and the data do not take into account the effect on the whole-rock chemistry of coarse grains (mainly calcite), the approach used does enable some estimate to be made of the gross geochemistry within the fine-scale alteration. Broad-beam EMPA analyses of unaltered rock compare reasonably well with conventional whole-rock XRF data. Normative calculations have been made on the basis of the following assumptions:

(i) All Mg is incorporated within ideal talc.

(ii) All P is incorporated within ideal hydroxy-apatite.

(iii) All S is incorporated within ideal gypsum.

(iv) All Fe is incorporated within ideal goethite.

(v) All Si not accounted for by (i) is incorporated within CSH gel with a molar ratio of Ca:Al:Si = 23:5:22 (typical of CSH represented in Field A, Figure 6.6).

(vi) All excess Al not accounted for by (v) is incorporated within ideal gibbsite.

(vii) All excess Ca not accounted for by (ii), (iii) and (v) is incorporated within ideal calcite.

(viii) The deficit of the total of all minerals from 100% is taken to represent the structural OH + H_2O within the CSH (this cannot be determined directly from EMPA data), and is added to the CSH component.

(ix) Where calculations actually gave negative values for calcite in highly altered zones, the calcite content is considered to be zero and the error in the normative calculation is adsorbed within the CSH content value since this is likely to be quite variable in composition in any case.

(x) All Cl is assumed to be derived from the epoxy-resin used to impregnate the samples for thin section preparation and on this basis is used to calculate the porosity.

Normative calculations (Figure 6.7, Table 6.8) confirm the BSEM observations showing that most alteration has occurred within 1 mm of the fracture wall. Matrix calcite is virtually completely removed between 0.25-0.40 mm from the main fracture wall, which corresponds to the zone of major secondary mineral formation - which is symmetrically distributed either side of the fractures (Plate 28). The depletion in calcite is mirrored by an increase in secondary CASH which may comprise more than 80% of the most altered wallrock zone. Minor gibbsite and gypsum also increase in significance with increasing degree alteration. The minor amount of magnesium-silicate hydrate gel (calculated as talc) shows very little variation, although it is enhanced slightly within the more altered rock, probably by residual concentration of immobile Mg. Apatite similarly shows little evidence of leaching or concentration, and this would suggest that the alteration of apatite identified petrographically results only in very local mobilisation and reprecipitation of phosphates. Porosity initially decreases from typical background levels of c.30% to c.20-22% as alteration increases. This reduction in porosity corresponds principally to cementation of the matrix by secondary remobilised calcite and organic matter (± CASH) along the reaction fronts described earlier. However, in the highly altered rock within about 0.1-0.2 mm either side of the open hairline fracture, porosity dramatically increases to over 70%, due largely to the loss of major calcite.

CEC determinations on clay biomicrite within this alteration zone (samples A970 (highly altered) and A971 (moderately altered to slightly altered) - from unmetamorphosed enclaves within the metamorphic zone) show increased CEC (56 meq/100g and 46 meq/100g respectively) compared to the background fresh clay biomicrite (A963 - 38 meq/100g). However, since there is no significant smectite in the unaltered clay biomicrite, and since even 100% kaolinite (the main clay mineral present in minor amounts in the clay biomicrites) would be unlikely to give a CEC of more than 12 meq/100g, clay minerals cannot be responsible for the CEC of 38 meq/100g in the unaltered rock. The high CEC of the fresh clay biomicrite may possibly be due to organic matter, or may be erroneous due to dissolution effects of fine-grained carbonate or gypsum during CEC determination. Determination of CEC using ammonium acetate

exchange is known to give false CEC values with fine carbonate and gypsum bearing rocks [29]. The increased CEC in the altered rocks may be related to the neoformation of minerals with high CEC's e.g. zeolites or CSH/CASH gels.

The paragenesis of the fracture mineralisation associated with hyperalkaline alteration of bituminous clay biomicrite at the 'high pH inflow' end of Adit A6 is summarised in Figure 6.8. The alteration can be subdivided into 4 stages:

STAGE 1 'Aragonite Stage': early fracture reactivation and initiation of hyperalkaline groundwater movement and precipitation of aragonite on fracture walls - possibly as a result of mixing of $Ca(OH)_2$-saturated groundwaters with background bicarbonate waters originally present in the clay biomicrite.

STAGE 2 'Ettringite-Thaumasite Stage': precipitation of fracture-filling thaumasite (with minor ettringite in solid solution) and gypsum. Wallrock alteration was most probably initiated during this stage with the dissolution of clay minerals and calcite.

STAGE 3 'CSH Stage': fracture reactivation, dissolution and replacement of earlier-formed thaumasite accompanied by the precipitation, initially, of CSH(I) (Al-substituted) or tobermorite then subsequently, CSH(II) (Al-substituted) or jennite. Major wallrock alteration occurred during this stage.

STAGE 4 'Zeolite Stage': Fracture reactivation, replacement of earlier CSH and thaumasite by fracture-sealing zeolites: initially high-Si zeolites of mordenite-dachiardite composition; then subsequently, zeolites progressively varying from 'epistilbite', to 'yugawaralite' and finally, 'laumontite', accompanied by minor amounts of gypsum. This may reflect the progressive loss of silica from the system as hyperalkaline leaching continued. It would appear that zeolite alteration has affected the wallrock only very slightly.

Intermediate alteration zone

The influence of zeolite alteration decreases rapidly away from the metamorphic zone. Possible fracture-filling zeolite of heulandite composition (ideally $(Ca,Na_2)Al_2Si_7O_{18}.6H_2O$) was tentatively-identified in sample A963 (60 m from adit entrance), from SEM studies at Clay Technology AB. A single ATEM analysis was obtained for a very fine grained secondary phase with a composition very close to laumontite or leonhardite (or wairakite) but this is statistically unreliable and the presence of zeolites could not be confirmed by XRD or other petrographic observations by BGS (which identified only the presence of gypsum, ettringite, thaumasite and calcite). Beyond this distance no further evidence of zeolitic alteration has been found. In contrast, veins dominated by creamy white to pale pinkish-brown, dense, 'wax-like' or 'putty-like' fillings of tobermorite (± minor amounts of calcite) are well-developed between about 85-100 m from the adit entrance (e.g. A962). These veins may reach up to

1 cm in thickness. XRD shows that the tobermorite is crystalline giving well-defined XRD patterns for the 11Å tetrahydrate tobermorite ($Ca_5Si_6O_{16}(OH)_2.4H_2O$). A small XRD peak at about 7-7.5 °2 (CoK radiation) tentatively suggests that the 14Å octahydrate tobermorite ($Ca_5Si_6O_{16}(OH)_2.8H_2O$) may also be present. Most of these fractures are tightly sealed and only a few fractures of this type show any evidence of present-day active hyperalkaline seepage - manifested by traces of groundwater 'weeping' at the interface between the tobermorite vein fill and the fracture wall.

BSEM shows that these veins are inhomogeneous, texturally quite complex and the result of a series of alteration 'events'. The tobermorite veins have an antitaxial 'cross-fibre' texture characteristic of a 'crack-seal' mechanism of vein growth [30], rather than simple fissure infilling (Plates 31 and 32). Often the veins carry inclusions of host wallrock and the tobermorite fibres are curved away from the perpendicular at the vein margins. This indicates progressive 'crack-seal' growth of the vein from the vein centre outwards, with lateral (transverse) movement of the fracture during vein growth.

The veins also display alteration along longitudinal and transverse hairline cracks, and along the interface between vein and wallrock (Plates 31, 32 and 33). Under BSEM this is evident in a decrease in grey-level (i.e. decrease in backscatter coefficient due to decreasing density of average atomic mass). Within the bulk of the vein, a denser fibrous CSH mineral is seen to be partially altered and replaced by interstitial CSH material which is nearly optically isotropic, and appears slightly darker (mid-grey) on BSEM images (Plate 33). Towards the vein margins, or adjacent to cracks, the interstitial CSH phase is altered to amorphous or isotropic CSH material which appears dark on BSEM images (Plates 31, 32 and 33). The original fibrous CSH phase appears more resistant to this later alteration than the interstitial CSH and persists as partially replaced relicts within the more altered regions of the vein (Plate 33).

Qualitative BSEM-EDXA and quantitative EMPA shows little difference in Ca:Si:Al ratio between the original (brighter) fibrous mineral and the intermediate interstitial (mid-grey) CSH (Plate 33). EMPA analyses (Figure 6.10) of these two phases correspond very closely to tobermorite with significant Al substitution (Al:Si = 1:10 - 1:6). The difference in image brightness between these two phases represents differences in hydration state, and they therefore correspond to the 11Å octahydrate and 14Å tetrahydrate forms of tobermorite identified by XRD. This indicates that tobermorite originally precipitated as fibrous 11Å tobermorite but then became partially hydrated and replaced by 14Å tobermorite. The later alteration along cracks and vein margins is significantly lower in Ca and EMPA data (Figure 6.10) indicate that it corresponds to a progressive range in compositions from aluminous tobermorite to aluminous okenite (ideally $CaSi_2O_5.2H_2O$) or nekoite (ideally $Ca_3Si_6O_{12}(OH)_4.H_2O$), with progressive alteration. The low Ca:Si CSH alteration appears to be a syntaxial and isovolumetric replacement of the precursor tobermorite. This would suggest that the late CSH phase has a similar structure to tobermorite - okenite and tobermorite both have chain-structures and typically display fibrous morphologies [24, 31]. Other phases such as gyrolite, truscottite and reyerite which fall within, or close to the Ca:Si(±Al) compositional range displayed by the late CSH have sheet-like structures, typically producing platey crystals [24, 31, 32] and are unlikely to be represented by this alteration.

The late CSH alteration is also associated with the precipitation of calcium carbonate (probably calcite) or possibly portlandite within the hairline fractures associated with the late CSH alteration (Plate 34). This is most probably related to the dissociation (and subsequent carbonation) of $Ca(OH)_2$ from the tobermorite during alteration. In this

respect, the alteration closely mirrors the progressive hydration and ageing of CSH(I) hydrogels in Portland-type cement paste [33, 34, 24] and a similar style of alteration was described in CSH mantles developed around partially-hydrated larnite nodules within contact-metamorphosed chalks from Northern Ireland [27]. Tobermorite-structured CSH(I) hydrogels are normally considered to have Ca:Si ratios within the range 0.8-1.7 [24, 35]. The natural CSH alteration of aluminous tobermorite from Maqarin would appear to extend this possible range to significantly lower Ca:Si values (i.e. Ca:Si+Al = 0.5).

Again, as discussed earlier, these natural CSH minerals incorporate significant levels of aluminium, in excess to that in hitherto-recorded natural aluminous tobermorite-structured minerals such as tacharanite ($Ca_{12}Al_2Si_{18}O_{15}(OH)_2.3H_2O$) [36]. This implies that significant solid-solution of Al for Si can occur in natural-system CSH phases. Figure 6.10 shows a slight increase in Al:Si with progressive alteration and hydration of the tobermorite. Extrapolated, this trend suggests that with increasing alteration the reaction products may eventually move towards mordenite-like and dachiardite-like compositions in the 'zeolite field'. This would be consistent with the alteration paragenesis described earlier from the high pH 'upstream' alteration zone (sample A960), where dachiardite-mordenite-like zeolite is seen to replace earlier-formed CSH phases.

The wallrock adjacent to these veins shows only minor alteration compared to that seen further 'upstream'. Minor leaching of primary calcite and the formation of traces of ultrafine secondary CSH, ettringite-thaumasite and gibbsitic alteration in the wallrock is generally restricted to within a few millimetres of the fractures, and often only within 100-200 •m of the fracture wall (Plate 32). XRD shows that kaolinite is still present in the wallrock and therefore, its dissolution is very limited. The wallrock porosity is reduced immediately adjacent to tobermorite veins by calcite precipitation within a diffuse zone typically less than 200 •m wide. This is similar to the cementation observed in the 'upstream' zone (sample A960) except that the zone of matrix cementation has not moved far into the host rock.

Alteration at groundwater discharge site M2 and further 'downstream' in Adit A6

The active hyperalkaline groundwater discharge site M2 (Chapter 3) is characterised by a zone of well-developed fractures between 40-55 m from the adit entrance. The principal flow is derived from a single large fracture largely mineralised by porous, laminated and colloform (micro-botryoidal) secondary ettringite, thaumasite and jennite representatively sampled in sample A965 (Plate 35). A number of very small seeps of alkaline groundwater occur between M2 and the adit entrance and are associated with hairline fractures. Many of these fractures are sealed or partly sealed by fine fibrous gypsum, and/or ettringite, and/or thaumasite (e.g. sample A6.9, Alexander, [2]).

In general, the wallrock associated with all these fractures shows very little evidence of significant alteration. Some alteration is noted along the margins of hairline and major fractures in sample A965 (site M2). However, the alteration zone is restricted to within only 0-1mm of fracture walls, varying irregularly along the length of the fracture. XRD and BSEM petrography show that the clay biomicrite wallrock matrix still contains fine-grained calcite, minor amounts of apatite or collophane, kaolinite and traces of detrital illite or fine grained muscovite. EGA and optical petrographic observations indicate that there is also little change in the organic content of the rock adjacent to the fractures. XRD indicated the presence of traces of possible jennite and ettringite in the wallrock up to 30 mm distant from the fracture wall in sample A965. This is probably

due to the incorporation of hairline vein-filling secondary minerals (see below) within samples of wallrock analysed by XRD. The alteration generally is very similar to that seen adjacent to tobermorite veins upstream (see above), except that calcite cementation of the matrix marginal to the veins is not evident.

At M2 the mineralisation and vein structure is very complex (e.g. sample A965). Hairline fractures (< 0.6 mm wide) run subparallel to the principal fracture (Plate 35) forming an anastomosing network in the matrix. These are invariably monominerallic and largely sealed by cross-fibre thaumasite or thaumasite-ettringite. These hairline fractures are typical of the fracture mineralisation observed further downstream towards the adit entrance. The principal fracture is about 5-6 mm wide and filled by a complex banded assemblage of interlaminated fibrous ettringite and thaumasite, colloform to spherulitic jennite (Plate 36), with minor amounts of fine-grained microgranular calcite, fibrous aragonite and thin honeycomb-textured laminae of Cr-Mg-Al-Ca-rich clay tentatively identified as a 'smectitic' clay (Plate 37). The smectite was identified by BSEM-EDXA but not confirmed by ATEM or XRD analyses. An XRD trace of the vein infilling is illustrated in Figure 6.11 and shows that jennite, ettringite, thaumasite and calcite make up the bulk of the vein fill. XRD also shows that the jennite is well-crystallised.

No ATEM data are available for jennite from A965 but EMPA revealed that it is close to ideal jennite in composition (average molar Ca:Si = 1.48), with only very little Al substitution for Si (average molar Al:Si = 0.01). This is surprising given the significant aluminium contents in crystalline tobermorite and amorphous CSH phases elsewhere in Adit A6 in this study. Milodowski et al. [1] recorded small amounts of Al substitution in jennite from the Maqarin railway cutting, although, it was shown that the vein margin jennite tended towards 'ideal' jennite, whereas the later-formed vein-centre jennite was lower in Ca, and incorporated a small amount of Al in solid-solution - trending towards the CSH (I) and tobermorite compositions described here from Adit A6 (towards the metamorphic / 'high-pH' zone). In contrast, ATEM data (Field A, Figure 6.12) for the nearby poorly crystalline secondary CSH alteration in sample A964 (40m from the adit entrance) display a range of compositions from aluminous jennite or aluminous CSH(II) to aluminous CSH(I) or aluminous tobermorite compositions (with up to 10 mole % substitution of Si by Al). At the less calcic end of the range, the composition of CSH in A964 trends towards that of the tobermorite A962. The compositional variations shown by secondary CSH minerals at the M2 site tends to suggest that well-crystallised jennite is less able to incorporate aluminium than either crystalline tobermorite and poorly-crystalline CSH(I) gels, or poorly-crystalline jennite-structured CSH(II) gels.

Many paragenetic episodes or bands of mineralisation can be seen in A965, progressively infilling the fractures from the fracture walls. This is illustrated in Figure 6.13 and summarised below:

STAGE 1 'Carbonate Stage': early fracture reactivation and initiation of hyperalkaline groundwater movement and precipitation of fibrous aragonite and then fine scalenohedral calcite coatings on fracture walls - possibly as a result of mixing of $Ca(OH)_2$-saturated groundwaters with the original bicarbonate porewaters in the clay biomicrite.

STAGE 2 'Ettringite-Thaumasite Stage': precipitation of radial-fibrous fracture-filling ettringite, followed by encrustation and partial replacement of ettringite by spherulitic to fine radiating masses of thaumasite. The

thaumasite was succeeded by further ettringite precipitation which, in turn, was coated with a very thin film of Mg,Cr-rich smectitic clay (associated with coprecipitation of Cr-rich ettringite (Plate 36)), prior to precipitation of further fibrous ettringite.

STAGE 3 'CSH Stage': dominated by precipitation of spherulitic and colloform fracture coatings of dense fibrous jennite resting on underlying ettringite and thaumasite (Plates 37 and 38). The jennite extensively replaces and overprints the preceding thaumasite and ettringite. STAGE 2 and STAGE 3 are transitional (Figure 6.13) with alternations between ettringite-thaumasite (± minor smectite and calcite) precipitation (locally replacing the preceding jennite) and jennite precipitation (with replacement of ettringite and thaumasite), before jennite finally dominated the mineral precipitation at M2 (sample A965). Jennite is the last mineral precipitated at M2 and appears to be the major phase presently in contact with water discharging at M2.

STAGES 1-3 at M2 correlate very closely to STAGES 1-3 seen in the 'High pH' upstream alteration zone. However, mineralisation and alteration at M2 is less advanced and does not show the later development of zeolites (STAGE 4) seen at the 'high pH' inflow end of the system. Within the M2 region, the relationship between crystalline jennite (seen in A965) and aluminous tobermorite-like CSH(I) (seen upstream of M2) is unclear since neither phase is seen juxtaposed in the same sample. However, the range in composition of the poorly-crystalline CSH(I) (which varies between tobermorite/CSH(I) and CSH(II); Figure 6.12) and the fact the poorly-crystalline CSH(I) and CSH(II) gels in the 'upstream' part of the system (sample A960) occur in close proximity to each other, suggests that jennite at M2 is paragenetically equivalent to the CSH gels formed adjacent to the metamorphic zone.

Summary of secondary mineral distribution in Adit A6

A summary of the overall lateral distribution of the fracture-hosted secondary alteration phases related to the interaction of hyperalkaline groundwater with bituminous clay biomicrite in Adit A6 is presented in Figure 6.14. The distribution is expressed in terms of distance along fracture flow-paths, from the point of intersection of the fracture with Adit A6 extrapolated along fracture-strike to the metamorphic zone (i.e. the point at which high pH groundwater enters the clay biomicrite fracture system). Data from the Phase I Jordan Analogue Study [2] have also been included to complete the picture of the mineral distribution.

With the exception of Stage I carbonate (calcite or aragonite) mineralisation (cf. Figures 6.8 and 6.13), there is a systematic variation in fracture mineralogy with distance from the metamorphic zone ('high pH' groundwater inflow), with the paragenetically earliest minerals having greater lateral extent than each proceeding mineral. Stage I calcite and aragonite fracture coatings are evident to c.82m along the fracture flow-paths, but absent beyond c.120m. Sulphate-dominated (gypsum-ettringite-thaumasite) Stage 2 mineralisation occurs along the entire fracture path-length studied (i.e. extending >130 m from the 'high pH inflow'). CSH-dominated Stage 3 mineralisation is considerably less extensive than Stage 2 but has influenced alteration of the bituminous clay biomicrite for up to c.87 m distance from the high pH source. The late-stage zeolite-dominated

(mordenite-dachiardite-'wairakite/laumontite') Stage 4 alteration is mainly restricted to within 2-3m of the 'cement zone', although very tentative identification of zeolites (?heulandite and/or ?'wairakite/laumontite') within sample A963 may indicate some minor zeolitic alteration locally extending as far as c.62m from the 'high pH source'.

The variation in mineral distribution probably reflects the progressive evolution of the groundwater as it interacts with the host rock along the flow path. Progressive changes with time at any given point will reflect the evolution of the inflowing hyperalkaline groundwater as it leaches the 'cement' source (metamorphic zone). Irrespective of the position along the flow-path, early ettringite and/or thaumasite mineralisation fills and effectively seals all minor hairline fractures (<0.5 mm aperture), preventing or severely-limiting any penetration and alteration by subsequent CSH- or zeolite-mineralising fluids. CSH and zeolite mineralisation are restricted to the major fracture zones and to fractures >0.5 mm in aperture, or to fractures which have been reactivated and have subsequently dilated along the interface between wallrock and earlier vein-filling mineralisation. Only in these situations are the more evolved fluids able to react with earlier minerals and replace them with CSH minerals and subsequently, zeolite minerals.

(ii) Uranium disequilibrium studies and alteration timescale in Adit A6

Vein mineralisation and associated adjacent wallrock from samples A960, A962 and A965 were analysed for natural decay series (uranium and thorium) radionuclides. The materials were carefully hand-separated after detailed mineralogical characterisation and determination of their uranium distribution characteristics. The results for ^{238}U, ^{234}U, ^{230}Th, ^{226}Ra, ^{232}Th, $^{234}U/^{238}U$, $^{230}Th/^{234}U$ and $^{226}Ra/^{230}Th$ are presented in Table 6.9.

A very useful method for presentation of natural decay series results for rock analysis is by cross-plotting radionuclide activity ratios. In the present work the approach of Thiel et al. [37] is adopted; this uses a cross-plot of the $^{234}U/^{238}U$ activity ratio (representing the state of secular equilibrium or disequilibrium between the daughter nuclide ^{234}U with respect to its parent ^{238}U) against the $^{230}Th/^{234}U$ activity ratio (representing the state of secular equilibrium or disequilibrium between the daughter nuclide ^{230}Th with respect to its parent ^{234}U). This is illustrated in Figure 6.15. With the assumption of initial secular equilibrium conditions which have subsequently been perturbed by rock-water interaction, plots of this type can be used to identify samples which have been affected by uranium deposition or removal processes. Thiel et al. [37] show that for this type of activity cross-plot there is a region in the upper part of the diagram, with disequilibrium compositions defined by $^{234}U/^{238}U$ in excess of unity and above a line intersecting the $^{234}U/^{238}U$ axis at c.0.3 (which represents the locus or envelope of all disequilibrium decay curves), which can be explained by overall U accumulation (from either a single event or the result of a complex series of multiple events). Similarly, there is an equivalent region in the lower part of the diagram, defined by $^{234}U/^{238}U$ less than unity and below the locus of all disequilibrium decay curves, which can be explained by overall leaching of uranium (from either a single process or the result of a complex series of multiple processes). There are also two areas which are forbidden for any single-process of U redistribution. Extension of this approach to include the possibility of continuous or sudden (relative to the ^{230}Th half-life) discontinuous processes can, as discussed by Scott et al. [38], be used to identify those areas of the diagram which can be reached by operation of various processes. All activity ratios falling within these 'forbidden regions' unambiguously result from complex U mobilisation.

The pre-metamorphic (diagenetic) vein calcite (A960CD1), zeolitic alteration and associated altered wallrock (A960CD2), tobermorite vein filling (A962CD1) and jennite-ettringite vein-filling (A965CD1) all fall within the field of uranium deposition (Figure 6.15). These samples all have $^{234}U/^{238}U$ activity ratios greater than 1 and $^{230}Th/^{234}U$ activity ratios less than 1, indicating deposition of uranium from groundwater within the last 10^6 years. The accumulation of uranium in these samples is consistent with detailed uranium fission-track registration petrography (Chapter 7) which shows that jennite and tobermorite - in samples A965 and A962 respectively, and the zeolitic alteration in A960 have incorporated uranium. Furthermore, enhanced levels of uranium are observed in the altered wallrock close to the veins associated with remobilisation of organic matter, and its concentration along narrow alteration fronts at the interface with the unaltered rock have enhanced uranium concentrations relative to the background rocks (see Section 6.2.2 and Chapter 7). Figure 6.15 suggests that the degree of disequilibrium increases progressively downstream of the metamorphic zone, from A960 through A962 to A965.

In contrast, the fission-track registration petrography of the altered wallrock adjacent to tobermorite veins in A962 reveals that uranium has been leached from the host-rock. This leaching appears to be related to the early ettringite mineralisation. The leaching of uranium from wallrock in sample A962 is reflected in the uranium disequilibrium data (subsamples A962CD2 and A962CD3, Figure 6.15). These samples have $^{230}Th/^{234}U$ activity ratios greater than unity, indicative of ^{234}U loss to groundwater. The $^{234}U/^{238}U$ activity ratios are slightly less than unity, also consistent with recent, relatively rapid loss of ^{234}U, since there has not been time for the re-development of isotopic equilibrium by 'ingrowth' loss of ^{234}U. Figure 6.15 shows that these wallrock samples fall within the overall field of uranium removal.

Further downstream, in sample A965, fission-track registration and petrographic observation indicate minimal alteration of the host-rock, or mobilisation of uranium, adjacent to jennite-ettringite-thaumasite veins at site M2. The uranium disequilibrium data are consistent with these observations, showing that, within error, the wallrock of A965 (subsample A965CD2) is undisturbed by rock-water interaction with respect to the uranium-series isotopic system.

An attempt to constrain the timescale of the hyperalkaline alteration system was made by dating the vein and alteration minerals using the $^{230}Th/U$ method [39]. Fission-track registration and BSEM petrography indicated no wallrock or detrital U-bearing components in the vein materials in A960CD1, A962CD1 or A965CD1. Consequently, ages have been calculated by assuming zero initial ^{230}Th (i.e. no detrital Th) in these samples, and that the ^{230}Th now present has grown-in by decay of ^{234}U coprecipitated and incorporated within these vein minerals from groundwater at the time of mineralisation. On the basis of this assumption dates can be assigned to A962CD1 - 90 000 years; and A965CD1 - 80 000 years (also shown in Figure 6.15). However, a puzzling aspect about the U/Th systematics is that the $^{230}Th/^{232}Th$ activity ratio for these samples is low and similar to that in the adjacent wallrocks - signifying detrital Th despite petrographic evidence to the contrary. Possibly some of the Th in the fracture minerals has been mobilised the short distance from the adjacent wallrock, or along the fractures with the organic material (which has been mobile), perhaps as a colloid or chelate. The assumption of zero initial ^{230}Th must be erroneous and without correcting for this, the true ages of mineralisation must be younger.

Although the $^{234}U/^{238}U$ activity ratio in the early calcite vein (A960CD1) is greater than unity, the $^{230}Th/^{234}U$ activity ratio is so close to unity that it would not be possible to date its deposition other than to say that it occurred over 500 000 years ago. An age of 160 000 years, obtained from zeolite-CSH-ettringite-rich wallrock alteration in A960CD2 is affected by the incorporation of host rock contamination (contributing a 'detrital' component of ^{230}Th). Therefore the assumption of zero initial ^{230}Th in this subsample will be erroneous and the age is an overestimate of the true age of alteration and mineralisation.

In summary, the uranium-series disequilibrium data suggest that the initial faulting and fracturing of the Maqarin rocks (which was accompanied by calcite vein mineralisation, represented by A960CD1 - predating the hyperalkaline alteration and probably related to diagenetic fluid mineralisation) occurred over 500 000 years ago. However, despite the possibility that the ages are overestimated, the dates obtained for the tobermorite (A962CD1) and jennite-ettringite-thaumasite (A965CD1) vein minerals - 90 000 and 80 000 years - are remarkably close and may indicate that the hyperalkaline groundwater activity started of the order of 10 000 - 100 000 years ago (given also that the date for A965CD1 from the M2 site may be 'over-young' due to minor influence of presently-active jennite precipitation). These ages also constrain the combustion-metamorphism - which must be older, but possibly less than 10^6 years ago (given that the early calcite vein mineralisation in A960CD1 is probably younger than 10^6 years).

The ages for the Maqarin hyperalkaline mineralisation are consistent with late-Pleistocene to Holocene ages (123 000-19 000 years) obtained by $^{230}Th/U$-dating of carnotite-mineralised faults in Israel associated with the regional Mid-Miocene to Holocene development of the Dead Sea transform [40] - which represent the most recent displacements, locally affecting near-surface soil horizons in the Dead Sea area of Israel [40]. It is likely that the Yarmouk Valley and Maqarin area, which is structurally-related to the formation of the Jordan Valley-Dead Sea Rift was similarly affected by late-Pleistocene to Holocene faulting.

(iii) Maqarin Station railway cutting.

The mineralogy of the fracture alteration hosted by the bituminous clay biomicrite seen in the railway cutting is generally very similar to that seen in Adit A6. However, the degree of wallrock alteration and extent of fracture mineralisation is much reduced by comparison. Many fractures are apparently unmineralised or have only very fine dust-like coatings of white or creamy-white secondary precipitates of calcite, aragonite, thaumasite or ettringite. Most fractures show relatively simple mineralisation usually dominated by either ettringite (e.g. samples A966, M93) or calcite ± aragonite (e.g. sample A967). Some larger fractures, however, do contain more complex mineralisation with tacharanite-like CSH-ettringite, jennite-ettringite-thaumasite-calcite (sample M81, M93) or zeolitic/CSH gel - ettringite/thaumasite-aragonite-calcite (sample M91) as described earlier by Milodowski et al. [1].

The ettringite veins are basically very simple microcracks in the clay biomicrite, usually developed as sub-vertical orthogonal micro-joints or as partings along bedding laminae. In most cases they are less than 0.5 mm wide. The ettringite occurs as colloform radiating masses of fibre-crystals coating fracture walls, or as cross-fibre vein fillings of fine needle-like crystals growing perpendicular to the fracture wall indicative of a progressive crack-seal mechanism vein mineral growth. The wallrock adjacent to the ettringite veins shows similar leaching and enhanced porosity similar to that seen in Adit A6. The depth

of the wallrock alteration zone is very narrow, generally of the order of 0.3-2 mm. The interface between the altered wallrock and the 'fresh' clay biomicrite is usually sharp and delineated by a thin zone (typically 20-40 •m thick) of calcite-cemented matrix, effectively sealing the matrix porosity along this 'alteration front'. TEM observation of the wallrock shows direct alteration of detrital illite and kaolinite to secondary ettringite or CASH phases. The clay minerals are seen to exfoliate parallel to the basal cleavage with secondary CASH or ettringite forming between the exfoliated cleavage sheets. However, no well-defined ATEM data of wallrock alteration products could be obtained and most ATEM analyses appear to be very fine, unresolved admixtures of ettringite, calcite and other secondary alteration products.

ATEM and EMPA show that most ettringite is Si-substituted, implying a significant solid-solution with thaumasite (e.g. Figures 6.16 and 6.18). There appears to be no systematic distribution or paragenetic relationship between the occurrence of ettringite and thaumasite, although in some cases (e.g. M93) the vein margin material appears to be closer to ettringite. Individual fractures show considerable variation in mineral composition (see Milodowski et al. [1]) and a complete spectrum between ettringite and thaumasite (even within the same fracture) is present within the railway cutting. EMPA results also show that ettringite and thaumasite are deficient in S [1] compared to the ideal mineral stoichiometries (e.g. Figure 6.17). This does not appear to be due to admixture with unresolved CSH minerals but most probably reflects substitution of silicate or sulphate by carbonate (which cannot be measured by EMPA or ATEM). Alternatively, this may reflect some complex solid-solution between ettringite and other CSH or CASH phases. [24] suggests that there is considerable potential for such solid-solutions within the CASH system.

The ettringite-thaumasite fracture alteration appears to be one of the earliest alteration products. Sub-vertical ettringite-thaumasite veins are sometimes re-utilised by subsequent CSH-type (CSH gels, jennite) mineralisation and bedding-parallel ettringite-thaumasite-filled joints are cross-cut by CSH-type and jennite (M81) or an aluminous CSH/CASH phase with a composition similar to but significantly more aluminous than tacharanite (Figure 6.16). Unfortunately no XRD data could be obtained to confirm the precise mineralogical identity of this phase. Tacharanite is structurally similar to tobermorite and CSH(I) gels but contains significant Al [36]. Both 'tacharanite' and jennite are seen to replace earlier-formed ettringite and thaumasite. The morphology and textures exhibited by jennite and 'tacharanite' veins are identical to those seen in jennite in sample A965 from Adit 6. The paragenetic relationships between ettringite-thaumasite and CSH phases are consistent with observations from Adit A6.

Fracture mineralisation in a major joint up to 5 mm wide (sample M91), mineralised dominantly by ettringite-thaumasite, also contains small 'globular to spherulitic masses' of amorphous CASH gel (containing minor amounts of Na and K in addition to Ca). These gel masses are chemically-zoned and have earlier 'zeolitic cores' with a molar Ca(±0.5Na+0.5K):Al:Si ratio close to laumontite and outer 'rims' intermediate in composition between 'zeolite' and tacharanite-like CSH (Figure 6.19). The relationship of the CASH gel with other vein minerals in the sample (ettringite, thaumasite, possibly fine-grained aragonite) is complex. The margins of the CASH gel globules are replaced by fine grained acicular calcium carbonate which also fills late dilatant hairline partings at the vein margins. The acicular habit of this late carbonate alteration suggests that it is aragonite.

Milodowski et al. [1] had suggested that the zeolite gel represented relicts of vein mineralisation that was subsequently enclosed in ettringite-thaumasite. However, re-examination of both the samples and earlier data suggests that the picture is not so clear. The precise petrographic relationships between the gel and the ettringite is obscured by secondary carbonate replacement. Although the gel occurs near the vein margin, which would normally tend to suggest early formation in simple vein systems, it is not necessarily the case of the cross-fibre type ettringite veins. Cross-fibre veins grow by a progressive crack-seal mechanism and do not demonstrate normal 'vein-stratigraphy' relationships. Instead, the youngest part of such veins is often at the vein margins since the fibre-crystals may grow from the median line of the vein outwards as the crack widens [30]. Thus, in this case the vein margin minerals may actually be the youngest phases. This would be consistent with the observation of late calcium carbonate alteration in dilatant cracks along the vein margin and which is also seen replacing the 'zeolitic gel'. Furthermore, the vein-marginal distribution of 'zeolite' gel possibly associated with late dilatant fracture re-activation is directly comparable to that seen in Adit A6 (sample A960). The laumontite-like zeolite composition is also very similar to the late-stage zeolite alteration seen in Adit A6. As a result, the earlier paragenesis defined by Milodowski et al. [1] for fracture alteration in the railway cutting has been reconsidered and is now believed to be identical to that defined for the 'High-pH inflow zone' seen in Adit A6.

Interestingly, the greatest degree of wallrock alteration is also seen in sample M91. In this respect it also closely resembles that seen in sample A960, close to the metamorphic zone in Adit A6. In M91, wallrock alteration is seen to a depth of 1-2 mm. Both micritic calcite and calcareous microfossil debris have been leached to leave a highly microporous residual matrix comprising finely admixed ettringite-thaumasite and/or amorphous CSH gel, Mg-rich material (possibly brucite - $Mg(OH)_2$) and Mg-Si-rich material (possibly talc - $Mg_3[Si_4O_{10}][OH]_2$), or sepiolite - $Mg_4[Si_6O_{15}][OH]_2.6H_2O$). This is accompanied by a significant increase in porosity. The alteration is similar to that seen in fractures in the nearby exposures of marble, in which brucite and hydrotalcite ($Mg_6Al_2CO_3[OH]_{16}.4H_2O$) have been confirmed by XRD, together with the tentative identification of talc or sepiolite. As in other samples a fine 'calcite cementation front' (non-porous) is present at the interface between altered rock and fresh rock.

Most hyperalkaline seepage in the railway cutting occurs along very fine, closely-spaced sub-orthogonal networks of sub-vertical and bedding-parallel hairline fractures, most of which are less than 1mm wide. These tend to be mineralised largely by calcite and minor amounts of aragonite. They represent the youngest fracture mineralisation, cross-cutting earlier sealed veins. Calcite and aragonite were probably precipitated in these fractures by interaction of atmospheric CO_2 with the $Ca(OH)_2$-saturated groundwater in the fractures close to the face of the railway cutting. This late carbonation process is probably responsible for the calcium carbonate mineralisation seen along the reactivated margins of earlier ettringite-CSH and ettringite- 'zeolite' veins (e.g. M91).

Wallrock adjacent to these fractures often shows no evidence of leaching although one sample (A967) from a horizon of dolomitic clay biomicrite displayed wallrock leaching to a depth of between 2-7 mm into the host rock. In this sample, authigenic dolomite and ankerite/ferroan dolomite, rather than primary calcite detritus is preferentially dissolved leaving a Mg-rich or Mg-Al-Si-Ca-rich residual matrix (the precise composition is unknown). Unlike other examples of wallrock alteration, this dolomitic rock showed no evidence of a 'calcite precipitation front' at the interface between altered and fresh rock

(Plate 42). Instead, the transition between leached and unaltered wallrock generally appears to be gradational over 1-2 mm.

The fabric of the calcite infill associated with this young fracture alteration is texturally very complex. The fracture infills comprise finely laminated and microporous crusts (Plate 39) dominated by calcite but with minor amounts of patchy radial-fibrous masses of Sr-rich aragonite locally nucleated on the surfaces of some calcite laminae. The laminated crusts are locally irregular and distorted, appearing to have 'spalled' from the underlying substrate through periodic drying-out and shrinkage, and expansive growth of further calcite crystals within the porosity of the crust (Plate 39). In many respects, the textures closely resemble those seen in calcrete or caliche soil profiles formed in arid or semi-arid environments. It suggests that the mineral growth occurred near-surface under very limited or no confining stress. This is consistent with the proposal that these veins have formed at or near the surface of the rock face by interaction of the hyperalkaline groundwater with atmospheric CO_2.

Detailed BSEM-EDXA petrography reveals that these vein carbonate laminae are also complexly chemically-zoned (Plate 40). The cores of each calcite crystal in the base of each lamina comprise essentially pure calcite but progressively grade along their growth axis to become very enriched (several percent) in Sr. It is often within these Sr-rich laminae that strontian aragonite and/or calciostrontianite are present as minor constituents. Closer examination reveals locally finer-scale Sr-rich/Sr-poor zonation within individual major growth zones. This oscillatory zoning reflects periodic changes in Sr:Ca ratio in the groundwater. This may possibly be related to periodic dilution of the hyperalkaline groundwater discharges near to the outcrop surface by fresh meteoric water during periods of high rainfall. During hot-dry periods, evaporation of groundwater from fractures close to the surface of the railway cutting may concentrate Sr during calcite precipitation with the residual fluid progressively becoming Sr-rich and eventually stabilising the precipitation of Sr-aragonite and strontianite. During high rainfall, the porewaters in fractures near to the surface of the railway cutting would be diluted and tend to precipitate low-Sr calcite as a result.

The rainfall in the Maqarin area is largely seasonal, with most rainfall /snowfall occurring between December-March. In the fracture examined in sample A967 between 70-80 major 'coupled-zones' of Sr-poor/Sr-rich calcite are present. If these are assumed to represent 'seasonal' variations in groundwater chemistry, then it implies that the fracture in A967 has been active over a period of 70-80 years. If it is further assumed that hyperalkaline activity in this fracture was continuous over this period, then dilation of the fracture occurred about 70-80 years ago - similar to the age of the construction of the railway cutting (c.1905). Consequently, it seems likely that this fracture opened up as a result of the actual railway construction or associated minor subsequent stress-relief. If these tentative conclusions are correct, then the observations imply that dolomite alteration and dissolution in hyperalkaline groundwater occurs relatively rapidly. In contrast, the dissolution of calcite by hyperalkaline groundwater is much slower. Comparison with Adit 6 observations, suggests that a similar degree of wallrock alteration in the calcitic rocks of Adit 6 has only occurred after 10^4-10^5 years of hyperalkaline groundwater-rock interaction.

(iv) Western Springs

A very limited petrographic study was made of the effects of the interaction of the hyperalkaline groundwaters with the colluvium through which they discharge in the Western Springs area.

Primary mineralogy and petrography

The wadi colluvium contains abundant large boulders and clasts of basalt, clay biomicrite limestone and cherts, within a poorly-sorted sand-grade matrix of comminuted basalt fragments, quartz and minor amounts of limestone fragments. The clay biomicrite and limestone detritus is derived locally and is similar to the in-situ material described from Adit A6 and the Maqarin Station railway cutting. The basalt is relatively fresh, comprising major calcic plagioclase (very fine laths (<50 •m) and small phenocrysts 100-200 •m grain size), large equant euhedral phenocrysts of olivine (up to 500 •m diameter) and subhedral magnetite (<100 •m) in an ophitic groundmass of titanaugite pyroxene. The olivine phenocrysts are largely intermediate Mg-Fe rich olivine with a fine marginal zone of fayalite (Fe-rich olivine). Titanomagnetite crystals are compositionally-zoned with hercynite-chromite cores and titanomagnetite rims.

High-pH alteration

Within the Western Springs groundwater discharge area the colluvium is well-cemented by precipitates from the hyperalkaline groundwater. The surfaces of the colluvium across which the groundwater flows are coated with creamy-white laminated crusts composed largely of calcite (Plates 7 and 8). Small amounts of a yellow fibrous mineral (probably Cr-ettringite) form effluorescences on these crusts.

Beneath the immediate travertine-coated surface the mineralogy of the colluvium is completely different. The rims of basalt clasts are oxidised and replaced by a thin hydration layer of goethitic iron oxyhydroxide (Plate 41). Immediately beneath this iron oxyhydroxide the basalt clasts show minor dissolution of plagioclase, olivine and clinopyroxene (titanoaugite) with the secondary porosity partly filled by amorphous iron oxyhydroxide and an undefined amorphous Ca-K-Al-Fe±Mg-silicate gel-like alteration product. The iron oxyhydroxide alteration layer on the clasts is also encrusted by a Ca-K-Na-Al-silicate hydrogel (Plate 43) with 4-5 wt % K and 1-2 wt % Na. Better crystallised radiating fine needle-like masses of Ca-K-Na-Al-silicate mineral has formed from the surface of the Ca-K-Na-Al-silicate hydrogel as a third alteration layer (Plate 43). This later material typically has very low first-order birefringence and low relief in thin section. The third layer has a very similar composition to the underlying Ca-K-Na-Al-silicate hydrogel but appears to be much less hydrated. This fibrous mineral also occurs as pore-filling spherulitic aggregates in the interstitial matrix of the colluvium. The Ca-K-Na-Al-silicate hydrogel and associated crystalline Ca-K-Na-Al-silicate appear to form between 15-30% of the intergranular matrix, filling porosity or replacing primary matrix basalt and silicate grains. Against open porosity, calcium carbonate (?aragonite or calcite) replaces or encrusts the Ca-K-Na-Al-silicate hydrogel and crystalline Ca-K-Na-Al-silicate (Plate 42).

XRD analysis of the matrix of the altered colluvial breccias indicates that it comprises largely calcite and a zeolite tentatively identified as belonging to the mordenite sub-group. Compositional fields (determined by EMPA) of the Ca-K-Na-Al-silicate hydrogel and fibrous silicate alteration are shown in Figure 6.20. The earlier amorphous gel covers a range of compositions between calcic mordenite $(Ca,Na_2,K_2)(Al_2Si_{10})(O_{24}.7H_2O)$ and calcic dachiardite $(Ca,Na_2,K_2)5(Al_{10}Si_{38})(O_{96}.25H_2O)$. The later more crystalline fibrous

Ca-K-Na-Al-silicate is similar in composition but with a narrower range, falling intermediate between calcic dachiardite and calcic mordenite. Dachiardite is also a member of the mordenite sub-group of zeolites. Thus the EMPA data is consistent with the tentative identification of a mordenite sub-group zeolite by XRD.

In contrast to the Eastern Springs area (Adit A6, Maqarin Station railway cutting), no evidence was found of CSH gels, jennite or tobermorite alteration products in the altered colluvium material. In the Western Springs area, the predominant alteration appears to be mordenite-group zeolite, whilst zeolitic alteration of clay biomicrite in the Eastern Springs is volumetrically very small compared to ettringite and CSH-type (tobermorite, jennite, tacharanite, CSH(I), CSH(II)) alteration products. This possibly reflects the difference in lithology between the colluvium and the clay biomicrites. The basalt in the colluvium supplies significant K and Na and Al, whereas the clay biomicrites are typically low in K, Na and Al by comparison. Despite the major difference between the host lithologies of the Eastern Springs and the Western Springs, similar types of zeolitic alteration are recorded from both areas. The late-stage zeolitic alteration observed in sample A960 from near to the metamorphic zone in Adit A6 comprises an early zeolite with similar characteristics to that from the Western Springs but is superseded in the Adit A6 system by later laumontite or wairakite-like zeolite compositions (not evident in the Western Springs area).

6.3 Central Jordan

6.3.1 General

No active groundwaters are now associated with the combustion-metamorphosed Daba Marble Zone of central Jordan. However, there is evidence that hyperalkaline groundwater activity was once extensive in this area with the development of major deposits of travertine over a wide area. Beneath the travertine deposits the underlying chalks and marls show evidence of fracture alteration by hyperalkaline rock-water interaction. A major feature of this is the precipitation of significant amounts of opaline or amorphous silica gel associated with a locally abundant green fine-grained chrome-rich clay mineral identified previously as volkonskoite [41] - a low-Fe chromium-smectite. It would appear that hydration and alteration of the marls and associated marbles in central Jordan may be significantly more evolved than the currently-active system observed at Maqarin.

6.3.2 Unmetamorphosed background marls

The Muwaqqar Chalk Marl Formation (which hosts the Daba Marble Zone) in central Jordan is very similar in mineralogy to the Bituminous Marl Formation in Maqarin. These rocks comprise clay biomicrites and non-argillaceous biomicritic limestones (terminology of Folk [10] and Pettijohn [11]) and chalks. Most samples were essentially chalky-white in appearance.

Three samples of unmetamorphosed Muwaqqar Chalk Marl Formation rocks (A980, A981 and A982) were examined from the Daba road cutting (localities described in Chapter 3). As at Maqarin, the biomicrite and clay biomicrite comprises largely silt-grade to fine sand-grade fragments of calcareous (calcite) microfossils (100-300 •m) with a matrix of fine-grained calcitic coccolithic and comminuted microfossil material. Much of the microfossil component appears to be foraminifera tests. These are commonly preserved intact and are dominated by large ‘globulose’ forms. Often, the shell-walls of the fossil detritus have been replaced by fine-grained authigenic apatite or micro-

colloform or framboidal collophane (amorphous calcium phosphate). Fine-grained collophanic or apatitic calcium phosphate is also disseminated through the matrix. Some collophanic material appears to be fossil fish scales. Although the porosity of the rocks are high, most porosity is ultra-fine with pore sizes typically less than 1 •m. Locally concretionary chert nodules ('flints') are developed within the limestones. Discrete fragments of organic matter were identified in one sample (A980).

Bulk XRD also shows that these rocks are composed predominantly of calcite and apatite, with minor amounts of quartz. Additional XRD of orientated clay-fractions carried out by Clay Technology AB also identified smectite and illite in small amounts.

6.3.3 Alteration by hyperalkaline groundwater interaction

Numerous sub-vertical hairline fractures cut the biomicrites in the Daba road cutting. The intensity of fracturing and degree of alteration appears to increase towards the onset of the metamorphic zone. Many of these fractures contain amorphous colloform silica (probably opal) as coatings on the fracture wall. The wallrock alteration associated with these fractures appears to be less well-defined than at Maqarin. Much of the wallrock shows recrystallisation of the micrite, but it is not clear from limited study whether this has been caused by hyperalkaline wallrock alteration or is diagenetic in origin. Closer towards the metamorphic zone (sample A982) the whole rock appears to have suffered severe alteration and at this point and has become very friable. In thin section, sample A982 is cut by fine hairline fractures which have been mineralised by a low-birefringent secondary Ca-Al-silicate mineral. This alteration product also penetrates into the adjacent matrix of the rock.

ATEM analyses were attempted in order to define the composition of the secondary alteration in samples A981 and A982. Unfortunately most analyses could not be interpreted clearly and appeared to represent unresolved admixtures of phases. However, the results suggested that most analyses fell on a mixing-line trend between calcite and yugawaralite or laumontite when plotted on Ca:Si:Al ternary compositional plots. This implies that the alteration product is probably a calcic zeolite similar to yugawaralite or laumontite.

The type of zeolitic alteration observed in central Jordan is similar to, but more extensively-developed than, the late zeolitic alteration observed in Adit A6 and the Maqarin Station railway cutting. This would appear to indicate that the same alteration processes have affected both areas and that zeolite is quite likely to be formed as a late-stage alteration product of hyperalkaline rock-water interaction.

6.3.4 Travertine deposits

Although two travertine horizons were recognised in the field, separated by a thin sequence of breccias (containing fragments of the earlier travertine), both travertines show very similar mineralogical characteristics. They are composed largely of calcite and opaline silica.

The fossilised relicts of plant material are abundant. The cellular structure of the original stems or roots is well-preserved (Plate 44). Calcite is micritic or microsparry and fills between plant stems and also infills cellular cavities within the fossil plant stems. Most organic matter appears to have been removed or replaced by silica. Opaline silica replaces the original organic cellular walls of the plant stems or roots (Plate 44). Silica or microcrystalline quartz has also overprinted and partially (locally completely) replaced

the fine calcite matrix groundmass (Plate 44). Where silica lines cavities in the travertine it has a colloform or botryoidal texture (Plate 45). BSEM reveals that this colloform silica or opal is very finely banded although no difference in composition can be identified. A chrome-rich very-fine grained clay-like mineral (intimately admixed with micritic calcite), probably volkonskoite (cf. Khoury et al. [41]) - although this could not by confirmed by XRD in this study - occurs disseminated throughout the fine calcite matrix or entrapped within spherulitic silica in silicified regions. This clay mineral also contains significant amounts of Zn and Cu (detected by EDXA). Calcite and 'volkonskoite' mineralisation appears to predate silicification. Microcrystalline apatite is present in minor amounts and replaces original plant cell wall material, again probably pre-dating silicification. Minor amounts of late pore-lining or pore-filling gypsum and ettringite, and traces of barite (lower travertine) or hashemite - the Cr analogue of barite (upper travertine) - also occur within cavities.

Two samples of silicified travertine shown by fission-track registration (Chapter 7) to be enriched in U (hosted within the secondary opaline silica) were submitted for natural (uranium/thorium) decay series analysis. The data are presented in Table 6.10 and plotted using $^{234}U/^{238}U$ vs. $^{230}Th/^{238}U$ activity diagram in Figure 6.21 (modified after Thiel et al. [37] and Scott et al. [38]).

The lower travertine (A974) has a $^{234}U/^{238}U$ activity ratio slightly greater than unity indicating relatively recent deposition of U from groundwater (Figure 6.21). However, the $^{230}Th/^{234}U$ activity ratio is so close to unity that it would not be possible to date the deposition other than to say that it was greater than 500 000 years ago. The deposition of U is consistent with fission-track registration observations which clearly show major uranium concentration within the travertine, particularly by incorporation in opaline silica adjacent to open pores. This suggests that uranium uptake post-dates the deposition of silica.

The upper travertine (A976) shows different uranium-series disequilibrium characteristics. The $^{230}Th/^{234}U$ activity ratio is significantly greater than unity indicating relatively-recent U leaching since the system has not re-equilibrated with respect to ^{230}Th. The $^{234}U/^{238}U$ activity ratio is 1 within error - consistent with recent but relatively rapid loss of uranium (although this has to be equilibrium loss of ^{234}U and ^{238}U.

The loss of uranium from the upper travertine may account for the lower total U content in A976 compared to A974, as shown by both fission-track registration petrography and alpha-spectrometry. Fission-track petrography (Chapter 7) suggests that the main difference in U distribution between the two travertines is in the U content of the opaline silica lining open porosity. In the lower travertine (A974) pore-lining opaline silica contains up to 160 ppm U at void edges, whereas in the upper travertine (A976) pore-lining opaline silica only contains up to 75 ppm U. In contrast, the U distribution elsewhere within the bulk of the travertine is similar for both samples or only very slightly lower in the upper travertine.

A possible explanation for the dissimilar uranium-series disequilibrium characteristics of the two travertines is that uranium has been leached from the upper travertine by downward-percolating groundwater and re-deposited within the underlying travertine. This downward movement would tend to suggest that the late-stage remobilisation of U was not caused by hyperalkaline groundwater circulation but is rather the result of meteoric precipitation and weathering. However, it seems very unlikely that the loss of U from the upper travertine is the result of contemporary weathering. Both travertines are

presently exposed adjacent to each other and would be expected to suffer leaching and loss of U to the same extent since they are mineralogically and petrographically very similar. Therefore, the difference in U disequilibrium behaviour between the two travertines may have been inherited from a more humid period prior to uplift and the development of the present erosion surface at Khan-ez-Zabib. If this is the case then the present erosion surface is probably less than 500 000 years old.

6.4 Summary and Conclusions

6.4.1 Maqarin

The pattern of fracture mineralisation and wallrock alteration associated with the interaction of hyperalkaline groundwater with clay biomicrite is complex. It is evident that close to the metamorphic zone (representing the high pH inflow zone) the sedimentary rocks show significant evidence of reaction with the marl. The alteration is mainly developed as narrow zones (1-2 mm) with enhanced porosity along the fracture margins. The secondary alteration products are dominated by brucite, hydrotalcite, CSH hydrogels, ettringite-thaumasite and poorly crystalline Mg-rich silicate (possibly akin to sepiolite or talc-like alteration products). Close to the metamorphic zone (0-3 m) in Adit A6, calcite is precipitated at the interface between relatively fresh rock and highly leached and altered rock. This significantly reduces matrix porosity along this interface and may inhibit lateral matrix-diffusion processes. Similar effects are seen adjacent to major fractures in the Maqarin Station railway cutting. By analogy with mineralogical alteration in Adit A6 this implies that discharge at this site is close to the metamorphic zone (indeed, the metamorphic rocks crop-out nearby).

Down-flow from the high-pH groundwater source, wallrock alteration of the clay biomicrite is significantly reduced. Beyond about 20 m downstream there is little evidence of wallrock alteration and no significant calcite cementation occurs in the matrix. By analogy with the repository disturbed zone, this implies that whilst rock matrix diffusion may be reduced by cementation of fracture wallrock porosity close to the high pH source, this effect will be less significant down-stream of the high pH source.

The more dolomitic rocks appear to show considerably more wallrock alteration than more common calcite-dominated rocks. Dolomite appears to be much more readily-dissolved than calcite. In very late fractures in the Maqarin railway cutting leaching and dissolution of dolomite in the host-rock has affected the fracture wallrock to depths of the order of 7 mm. These late fractures most probably relate to the construction of the rail cutting (c. 1905) giving an indication that alteration has occurred over a relatively-short timescale. By contrast, ^{230}Th/U dating of secondary minerals in Adit A6 suggests that a similar scale of alteration, in calcite-dominated rocks, is only just achieved over a timescale of c.100 000 years.

Observations of the fracture mineralogy and petrography indicate that the fractures tend to become sealed with time by secondary precipitates. The most important secondary minerals are ettringite, thaumasite, CSH hydrogels (CSH(I) and CSH(II) -types), and CSH hydrogel-related minerals such as tobermorite, jennite and tacharanite. As an analogue, this would tend to suggest that fractures in the repository disturbed zone will also tend to become sealed by secondary minerals.

CSH hydrogels, tobermorite and tacharanite appear to be capable of incorporating significant amounts of Al. This property may inhibit zeolite formation and may provide one of the reasons to explain the difference between some model predictions - which

predict that zeolite should be the major alteration product within the repository disturbed zone - and the field analogue system at Maqarin. However, zeolite formation is observed within the fracture mineralisation in the clay biomicrites but appears to be confined to within a few metres of the high pH source. In contrast, jennite typically has a very low Al content.

Zeolite formation is complex. Early-precipitated zeolite and amorphous zeolitic-gels appear to be similar in composition to high-Si zeolites such as mordenite or dachiardite. However, with increasing reaction, they become considerably more calcic and similar in composition to wairakite, laumontite and leonhardite. The identification of wairakite in Maqarin material is probably artifactual in part - it seems more likely that at the low-P/T conditions pertaining to this alteration, laumontite or leonhardite (which readily dehydrate to wairakite) represent the actual in-situ zeolitic alteration.

Ettringite and thaumasite are the most widespread fracture minerals precipitating in fractures at distances of at least 140 m downstream of the high-pH inflow. Ettringite and thaumasite also represent the earliest major high-pH fluid fracture mineralisation, preceded only by minor aragonite or calcite precipitates on fracture surfaces (believed to result from the initial interaction of the $Ca(OH)_2$-saturated groundwater with background bicarbonate groundwaters in the matrix porosity of the clay biomicrites. Paragenetically, these are superseded by CSH minerals such as tobermorite, CSH(I), CSH(II), and jennite. Jennite is possibly slightly later in paragenesis than the other CSH minerals. In the clay biomicrite, close to the high-pH source, zeolites occur late in the fracture mineral paragenesis replacing earlier-formed CSH minerals, ettringite and thaumasite.

Hyperalkaline springs in the Western Springs area discharge through a completely different lithology. Here the groundwater reacts with a significant amount of basalt present within the Quaternary wadi colluvium (boulder breccias). In this locality, CSH minerals were not observed to form as alteration products of the marl. Instead, the major alteration product is a Ca-K-Na zeolite and amorphous zeolitic gel precursor with compositions intermediate to mordenite and dachiardite. These form the major cement to the colluvial deposit locally forming up to 30% of the intergranular matrix.

Results from the Maqarin study suggest that the most important alteration products of the alkali/rock interaction are CSH(I) and CSH(II) hydrogels and related minerals such as tobermorite, tacharanite and jennite, and zeolites. In more calcareous environments it would appear that the dominant zeolite species will be similar to laumontite whereas in more silicate-dominated host rocks more siliceous zeolites such as mordenite sub-group zeolites will be more important.

The implications from $^{230}Th/U$ dating on the age and evolution of the Maqarin system merit further consideration. The diagenetic calcite vein dated by the ^{230}Th ingrowth method at between 500ka and 2Ma, provides a maximum age for the metamorphism which produced the cement zone mineral assemblage. Tobermorite vein filling and jennite-ettringite vein filling produced ages of 90ka and 80ka respectively and a zeolite altered rock matrix an age of 160Ka. The zeolitic sample is almost certainly contaminated with detrital ^{230}Th, producing an overestimate of the age and questions remain on the tobermorite and jennite ages. Although fission-track registration and BSEM petrography strongly suggest that no wallrock was present nor was there any detrital U-bearing components in the vein materials, the samples certainly contain ^{232}Th. This was possibly introduced as colloidal Th, incorporated from the groundwater by the cement phases during formation. If this were the case, it might also be expected that at least some of the

^{230}Th present in the veins was also originally present in the groundwater supplied so indicating that the calculated ^{230}Th ingrowth ages are a maximum. It is not, however, possible to correct these maximum ages for a potential Th colloidal input as it is impossible to assess any previous (or, indeed, current) ^{230}Th/^{232}Th ratios for the colloids. Also, no meaningful correction can be applied to the zeolitic rock matrix age as no natural decay series data exist for undisturbed, unaltered Bituminous Marl.

In Chapter 10, a ^{14}C age of less than 650a is quoted for recarbonated cement zone material from Adit A-6. This age does not necessarily contradict the ^{230}Th ingrowth ages. It simply confirms a scenario of repeated re-activation of fractures and consequent multi-phase fracture infill. Indeed, the persistence of secondary fracture materials of differing ages suggests that, once sealed, the secondary fracture-filling mineralogy in the hyperalkaline disturbed zone can remain stable for safety assessment relevant timescales - with the implication that radionuclides associated with these secondary phases also can be isolated from the evolving groundwaters. No data exist for the porous media flow Western Springs system although the petrological data cited above suggest that the system has remained open throughout its lifetime, implying that any age calculated must be a reflection of a complex multi-phase reaction.

6.4.2 Central Jordan

Only a very limited study was made of the palaeo-hyperalkaline alteration from the Daba area of central Jordan. The alteration probably represents a more advanced stage than is currently seen in the Maqarin area. Within the limited material examined, calcic zeolite is again seen as a potentially important fracture alteration mineral in clay biomicrite, confirming the Maqarin observations.

During late stages of hyperalkaline activity, amorphous or opaline silica and smectitic clay would appear to be important secondary minerals. Observations from the major travertine deposits in the area suggest that smectite is precipitated prior to silica. Silica mineralisation would appear to represent the last 'dying-gasp' of the hyperalkaline system. Perhaps one of the most important implications of the late silica precipitation is the demonstration that the late amorphous silica precipitates from central Jordan were capable of incorporating significant amounts of U (up to 160 ppm). By analogy with the repository disturbed zone, smectite and silica might be expected to form as alteration products in the late-stage evolution of the hyperalkaline plume.

6.5 References

[1] A.E. Milodowski, J.M. Pearce, C.R. Hughes and H.N. Khoury, *A Preliminary Mineralogical Investigation of a Natural Analogue of a Cement-Buffered Hyperalkaline Groundwater Interaction with Marl, Maqarin, Northern Jordan,* NAGRA Unpublished Internal Report, 1992.

[2] W.R. Alexander, *A Natural Analogue Study of the Maqarin Hyperalkaline Groundwaters. I. Source Term Description and Thermodynamic Database Testing,* NAGRA Technical Report, NTB 91-10, 1992.

[3] H.N. Khoury and S. Nassir, *High Temperature Mineralisation in the Bituminous Limestone in Maqarin Area- North Jordan,* Neues Jahrbuch für Mineralogie Abhandlungen, **144**, 197-213, 1982.

[4] S.G. Nassir and H.N. Khoury, *Geology, Mineralogy and Petrology of Daba Marble, Jordan,* Dirasat, **9**, 107-130, 1982.

[5] H.N. Khoury and E. Salameh, *The Origin of High Temperature Minerals from Sweileh Area, Jordan,* Dirasat, **13**, 261-269, 1986.

[6] J.I. Goldstein, D.E. Newbury, P. Echlin, D.C. Joy, C. Fiori and E. Lifshin, *Scanning Electron Microscopy and X-Ray Microanalysis: A Text for Biologists, Materials Scientists And Geologists,* Plenum Press, 1981.

[7] D.H. Krinsley, K. Pye and A.T. Kearsley, *Application of Backscattered Electron Microcopy in Shale Petrology,* Geological Magazine, **120**, 109-118, 1983.

[8] J.M. Huggett, *An SEM Study of Phyllosilicates in a Westphalian Coal Measures Sandstone using Backscattered Electron Imaging and Wavelength-Dispersive Spectral Analysis,* Sedimentary Geology, **40**, 233-247, 1984.

[9] K. Pye and D.H. Krinsley, *Petrographic Examination of Sedimentary Rocks in the SEM using Backscattered Electron Detectors,* Journal of Sedimentary Petrology, **54**, 877-888, 1984.

[10] R.L. Folk, *Practical Petrographic Classification of Limestones,* Bulletin of the American Association of Petroleum Geologists, **43**, 1-38, 1959.

[11] F.J. Pettijohn, *Sedimentary Rocks,* Harper and Row, Third Edition, 1975.

[12] W.R. Alexander, A.B. Mackensie, R.D. Scott and I.G. McKinley, *Natural Analogue Studies in Crystalline Rock: The Influence of Water-Bearing Fractures on Radionuclide Immobilisation in a Granite Rock Repository,* NAGRA Technical Report, NTB 87-08, 1989.

[13] J.D. Hudson, *Pyrite in Ammonite-Bearing Shales from the Jurassic of England and Germany,* Sedimentology, **29**, 209-213, 1982.

[14] R.E. Sweeney and I.R. Kaplan, *Pyrite Formation: Laboratory Synthesis and Marine Sediments,* Economic Geology, **68**, 618-634, 1973.

[15] D.T. Rickard, *Kinetics and Mechanism of Pyrite Formation at Low Temperatures,* American Journal of Science, **274**, 636-652, 1975.

[16] D.T. Rickard, *The Origin of Framboids,* Lithos, **3**, 269-293, 1970.

[17] R.T. Greer, *Evaluation of Pyrite Particle Size, Shape and Distribution Factors,* Energy Sources, **4**, 23-51, 1978.

[18] S.G. McRae, *Glauconite,* Earth Science Reviews, **8**, 397-440, 1972.

[19] A. Abed and B. Amireh, *Petrography and Geochemistry of Some Jordanian Oil Shales from North Jordan,* Journal of Petroleum Geology, **5**, 261-274, 1983.

[20] Y. Shahar and U. Wurtzberger, *A New Oil Shale Deposit in the Northern Negev,* Proceedings of the 7th World Petroleum Congress, **3**, 719-728, 1967.

[21] G.C. Speers and E.V. Whitehead, *Chapter27: Crude Petroleum,* Springer Verlag, pp638-675, 1969.

[22] D. Savage, C. Hughes, A. Milodowski, K. Bateman, J. Pearce, E. Rae and C. Rochelle, *The Evolution of Chemical Mass Transfer in the Disturbed Zone of a Deep Geological Disposal Facility for Radioactive Wastes, I Reaction of Silicates with Calcium Hydroxide Fluids,* Nirex Report, NSS/R244, 1997.

[23] D. Savage, K. Bateman, P.Hill, C. Hughes, A. Milodowski, J. Pearce and C. Rochelle, *The Evolution of Chemical Mass Transfer in the Disturbed Zone of a Deep Geological Disposal Facility for Radioactive Wastes, II Reaction of Silicates with Na-K-Ca Hydroxide Fluids,* Nirex Report, NSS/R283, 1997.

[24] F.M. Lea, *The Chemistry of Cement and Concrete,* Edward Arnold, Third Edition, 1970.

[25] J.A. Gard and H.F.W. Taylor, *Calcium Silicate Hydrate(II),* Cement and Concrete Research, **6**, 667-678, 1976.

[26] H.F.W. Taylor, *Proposed Structure for Calium Silicate Hydrate Gel*, Journal of the American Ceramic Society, **69**, 464-467, 1986.

[27] A.E. Milodowski, P.H.A. Nancarrow and B. Spiro, *A Mineralogical and Stable Isotope Study of Natural Analogues of Ordinary Portland Cement (OPC) and CaO-SiO_2-H_2O (CSH) Compounds*, Nirex Report, NSS/R240, 1989.

[28] W.A. Deer, R.A. Howie and J. Zussman, *Rock Forming Minerals, Volume 4: Framework Silicates*, Longman Group Ltd, 1963.

[29] D.J. Morgan, Personal Communication.

[30] A.J. Barker, *Introduction to Metamorphic Textures and Microstructures*, Blackie, 1990.

[31] L. Heller and H.F.W. Taylor, *Crystallographic Data for the Calcium Silicates*, Her Majesty's Stationary Office (HMSO), 1956.

[32] O. Henning, *Cements: The Hydrated Silicates and Aluminates*, In *The Infrared Spectra of Minerals*, Mineralogical Society, 1974.

[33] A. Atkinson, *The Time-Dependence of pH within a Repository for Radioactive Waste Disposal*, UKAEA Technical Report, AERE-R11777, 1985.

[34] A. Atkinson and R.M. Guppy, *Evolution of pH in a Radwaste Repository*, UKAEA Technical Report, AERE-R126961, 1988.

[35] A. Atkinson, J.A. Hearne and C.F. Knights, *Aqueous Chemistry and Thermodynamic Modelling of CaO-SiO_2-H_2O Gels*, UKAEA Technical Report, AERE-R12548, 1987.

[36] G. Cliff, J.A. Gard, G.W. Lorimer and H.F.W. Taylor, *Tacharanite*, Mineralogical Magazine, **40**, 113-126,1975.

[37] K. Thiel, R. Vorwerk, R. Saager and H.D. Stupp, *^{235}U Fission Tracks and ^{238}U Series Disequilibria as a Means to Study Recent Mobilisation of Uranium in Archaean Pyritic Conglomerates*, Earth and Planetary Science Letters, **65**, 249-262, 1983.

[38] R.D. Scott, A.B. Mackenzie and W.R. Alexander, *The Interpretation of Natural Decay Series Disequilibrium in Non-Ideal Systems: An Example from Poços De Caldos, Brazil*, Journal of Geochemical Exploration, **46**, 323-343, 1992.

[39] M. Ivanovich, A.G. Latham and T.L. Ku, *Uranium Series Disequilibrium Applications in Geochronology*, In *Uranium Series Disequilibrium: Applications to Environmental Problems*, Oxford University Press, 1982.

[40] Y. Eyal, A. Kaufman and M. Bar-Matthews, *Use of $^{230}Th/U$ Ages of Striated Carnotites for Dating Fault Displacements*, Geology, **20**, 829-832, 1992.

[41] H.N. Khoury, R.C. Mackenzie, J.D. Russell and J.M. Tait, *An Iron-Free Volkonskoite*, Clay Minerals, **19**, 43-57, 1984.

Table 6.1 Summary list of samples examined from Maqarin area.

BGS sample code	Field sample code	Sample location / sample description
[Note: all Adit A6 samples locations defined by distance (in parentheses) from adit entrance]		
A960	AEM2/MQN2a	Adit A6 - 2.5m north of metamorphic zone (c.108m) - unmetamorphosed soft, plastic grey leached marl/micritic limestone containing fractures with intense alkali interaction. Containing calcite + CSH minerals + ettringite.
A961	AEM7/MQN10	Adit A6 - (7m) - fresh, dark, massive unmetamorphosed bituminous marl/micritic limestone with no obvious fracturing or signs of alteration/interaction with high pH groundwaters.
A962	AEM3/MQN3	Adit A6 - (99m) - dark-black, massive unmetamorphosed bituminous marl/micritic limestone with fractures tightly sealed by buff-pink, dense, brittle putty-like fine-grained CSH mineral (tobermorite) typical of several veins seen between c.100-85m. Fracture surfaces show slight staining by alkaline interaction but are not associated with active groundwater seeps.
sample left in Jordan	MQN4	Adit A6 - (70m) dark bituminous marl/micritic limestone with fine fractures filled by fibrous-powdery ettringite or thaumasite. No active groundwater seeps.
A963	AEM4/MQN5	Adit A6 - (60m) dark bituminous marl/micritic limestone with wet fracture surfaces coated with calcite and gypsum. Alkaline interaction apparent on external surfaces.
sample left in Jordan	MQN6	Adit A6 - (55m) dark bituminous marl/micritic limestone with fracture mineralisation similar to A965.
A964	AEM5/MQN8	Adit A6 - (40m) dark bituminous marl/micritic limestone in area of hyperalkaline discharge. Contains a few sub-vertical fractures filled by ettringite and thaumasite and associated with intense bleaching of rock parallel to fractures and horizontal bedding laminae.

BGS sample code	Field sample code	Sample location / sample description
A965	AEM10/MQN23	Adit A6 - (45m) dark bituminous marl/micritic limestone with major fracture actively conducting main flow of hyperalkaline groundwater. Wallrock alteration is apparent from bleaching, and fracture is largely sealed by complex laminated to colloform fill of ettringite, thaumasite, jennite and calcite. Corresponds exactly to groundwater sampling site M2.
A966	AEM15/MQN20	Maqarin railway cutting - mid-grey unmetamorphosed blocky marl/micritic limestone with numerous subvertical joints and hairline fractures actively conducting hyperalkaline groundwater. From zone of main active seepage and travertine deposition. Surfaces coated with ettringite, calcite or aragonite. Corresponds to groundwater sampling site M3.
A967	AEM17/MQN/22	Maqarin railway cutting - as A966, showing alteration on fracture surfaces but not associated with active groundwater seeps.
A968	AEM18/MQN24	Western Springs - fragments of wadi deposit/colluvial material containing pebbles of basalt, marl, limestone chert tightly cemented by zeolitic matrix and encrusted in travertine carbonates. Corresponds to seepages at groundwater sampling site M5.
A969	AEM14/MQN19	Maqarin railway cutting - fragments of colluvium/wadi gravels 30m north-west of cutting and groundwater sampling site M3. Appears to be site of hyperalkaline seepage through colluvium and is cemented by travertine deposits. Contains fragments of basalt, chert and micritic limestone.
A970	AEM8b/MQN11b	Adit A6 - (c.224m) Unmetamorphosed micritic limestone, with fractures filled by calcite and ettringite in zone active hyperalkaline groundwater discharge. Adit area very unstable.
A971	AEM8c/MQN11c	Adit A6 - (c.224m) Soft or highly altered micritic limestone.
n/a	M81	Maqarin railway cutting. Weakly metamorphosed micritic limestone with fractures showing wallrock alteration and products of interaction with hyperalkaline groundwater

BGS sample code	Field sample code	Sample location / sample description
		(from Milodowski et al., [1]).
n/a	M91	Maqarin railway cutting. Unmetamorphosed bituminous micritic limestone containing fine hairline fractures with evidence of hyperalkaline groundwater interaction. From zone of active hyperalkaline groundwater seepage (from Milodowski et al., [1]).
n/a	M93	Maqarin railway cutting. Unmetamorphosed laminated bituminous micritic limestone containing fine hairline fractures with evidence of hyperalkaline groundwater interaction. From zone of active hyperalkaline groundwater seepage (from Milodowski et al., [1]).
n/a	A6.7	Adit A6 (c.0m) Unmetamorphosed bituminous clay biomicrite with fine hairline fractures mineralised by ettringite or thaumasite (from Alexander et al., [2]).
n/a	A6.9	Adit A6 (c.106m) Unmetamorphosed bituminous clay biomicrite with fine hairline fractures mineralised by ettringite or thaumasite (from Alexander et al., [2]).

Table 6.2 Summary list of samples examined from Daba-Siwaqa area.

BGS sample code	Field sample code	Sample location / sample description
A972	AEM23/CJ6	Daba road cutting - red recrystallised calcite-apatite marble with secondary aragonite-filled veins.
A973	AEM24/CJ7	Daba road cutting - grey brecciated flint with alteration along fracture surfaces and secondary silica, calcite, possibly CSH and chrome smectite clay coatings in fractures.
A974	AEM26/CJ13	Khan-es-Zabib - green earthy travertine with secondary microspherulitic silica (opaline). Adjacent to fault on downthrown side, and lies beneath travertine-cemented colluvial or wadi breccia. Contains opaline silica-lined moulds after plant stems and roots and secondary green chrome smectite clay - 'Lower Travertine'.
A975	AEM28/CJ15	Khan-es-Zabib - calcite-ettringite-CSH-opal-cemented colluvial or wadi breccia overlying lower travertine (A974), and containing fragments of green volkonskoite-stained travertine - 'Intertravertine Breccia'.
A976	AEM29/CJ17	Khan-es-Zabib - silicified and chrome smectite-impregnated travertine containing well-preserved plant root and stem moulds lined by microspherulitic opaline silica. 'Upper Travertine'.
A977	AEM30/CJ18	Khan-es-Zabib - Chert nodules from travertine-cemented colluvial breccia showing intense alteration zones around clast edges.
A978	AEM31/CJ20	Daba Marble quarries, El Hammam - apatite marble.
A980	AEM34/CJ24	Daba road cutting - unmetamorphosed soft chalky marl micritic and phosphatic limestone.
A981	AEM35/CJ25	Daba road cutting - lateral equivalent of A980 but fractured with possible alteration by palaeohyperalkaline fluids associated with local travertine mineralisation.
A982	AEM36/CJ36	Daba road cutting - lateral equivalent of A980, unmetamorphosed marl/micritic limestone showing severe alteration by palaeohyperalkaline fluids associated with local travertine formation.

Table 6.3 XRD analysis of unaltered bituminous clay biomicrites, Adit A6, Maqarin.

BGS sample code	Bulk mineralogy	<2•m Mineralogy
A961	calcite, apatite	apatite, kaolinite
A962	calcite, apatite, possible kaolinite	apatite, kaolinite
A963	calcite, apatite, possible kaolinite	apatite, kaolinite, gypsum
A965	calcite, apatite, possible ettringite	apatite
A966	calcite, apatite, quartz, ettringite, possible kaolinite	not determined
A967	calcite, dolomite/ankerite	not determined

Table 6.4 EGA results from unaltered bituminous clay-biomicrites, Adit A6, Maqarin.

BGS sample code	Calcite* (%)	Organic carbon (%)	Organic sulphur (%)	Ammonia evolution	Pyrite (%)	Other
A961	71 (88)	6.0	0.4	evolved	0.4	
A962	63 (73)	1.1	not detected	not detected	not detected	
A963	62 (88)	8.1	0.5	evolved	1.0	
A965	57 (80)	4.9	0.2	evolved	not detected	
A966	65 (73)	4.3	0.2	evolved	3.0	
A967	89**	1.3	not detected	trace	?trace	

* Figures in parentheses indicate calcite content determined by thermogravimetry.

** Dolomite/ankerite also identified by XRD and by petrography but has been calculated from EGA as equivalent calcite.

Table 6.5 Acid insoluble residue contents (including < 2 •m fraction) of clay-biomicrites after carbonate removal by buffered acetic acid/Na-acetate leach.

BGS sample code	Acid soluble portion (mass %)	Acid insoluble residue (mass %)	<2 •m fraction (mass %)
A961	80	20	12
A962	not determined	not determined	not determined
A963	68	32	21
A965	84	16	9
A966	not determined	not determined	not determined
A967	not determined	not determined	not determined

Table 6.6 Normative mineralogical composition for unaltered bituminous clay-biomicrite samples A961 and A962 calculated from whole rock geochemical analysis, assuming ideal mineral formulae.

Mineral	A961 (%)	A962 (%)
Calcite [$CaCO_3$]	74.4	74.8
Dolomite [$CaMg(CO_3)_2$]	1.1	1.1
Apatite [$Ca_5(OH)(PO_4)_3$]	3.5	4.6
Albite [$NaAlSi_3O_8$]	1.0	0.7
Illite [$KAl_2(AlSi_3O_{10})(OH)_2$]	1.1	2.1
Kaolinite [$Al_4(Si_4O_{10})(OH)_8$]	1.9	5.3
Pyrite [FeS_2]	0.9	0.5
Ferric Oxide [Fe_2O_3]	0.6	1.8
Silica/quartz/opal [SiO_2]	1.7	5.2
TOTAL	86.0	96.1

Table 6.7 Summary of the average and range of mineralogical compositions for the Chalk Marl Formation from the Maqarin region (data from [19]).

Mineral	Mean (%)	Range (%)
Total carbonates	68.8	41-88
Calcite	67.9	40-88
Dolomite	1.3	0-12
Apatite	5.1	2.5-9.44
Albite	not determined	not determined
Illite	not determined	not determined
Kaolinite	not determined	not determined
Total clay	5.0	0-17
Pyrite	2.0	1.2-4.1
Ferric oxide	not determined	not determined
Quartz	7.0	0-37
Organic matter	14.8	0.12-40

Notes:
(i) Calcite was determined from CO_2 analysis after accounting for dolomite.
(ii) Dolomite calculated from Mg content when its presence was identified by XRD.
(iii) Apatite calculated as ideal francolite variety by from P content.
(iv) Total clays calculated on the basis of Total Clay = 100-(carbonate+quartz+organic matter).
(v) Pyrite calculated from S content.
(vi) Quartz was determined by quantitative XRD.

Table 6.8 Normative mineralogical composition for altered bituminous clay-biomicrite matrix in sample A960, calculated from broad defocused beam EMPA analyses.

Distance from fracture (mm)	**1.30**	**1.15**	**0.93**	**0.69**	**0.50**	**0.38**	**0.26**	**0.17**
Calcite [$CaCO_3$]	69.2	67.1	64.2	58.6	27.9	0.0	0.0	41.0
Apatite [$Ca_5(OH)(PO_4)_3$]	10.3	11.4	14.7	8.6	6.1	13.1	8.2	13.9
Gypsum [$CaSO_4.2H_2O$]	1.6	1.3	1.2	1.2	3.6	3.9	2.1	2.0
'CASH' [Ca:Si:Al = 23:22:5]	14.5	15.7	15.3	26.2	52.6	70.5	84.0	29.5
Talc [$Mg_3Si_4O_{10}(OH)_2$]	1.2	1.0	1.3	1.1	1.4	2.3	1.9	2.3
Goethite [FeO(OH)]	1.1	1.1	0.9	0.8	0.7	2.3	0.5	0.8
Gibbsite $Al(OH)_3$	2.1	2.4	2.4	3.5	7.7	7.9	3.3	10.5
Porosity	29.4	24.3	21.0	22.0	37.6	70.7	43.1	50.3

Table 6.9 Uranium, thorium and radium radiometric isotope determinations for fracture mineralisation and altered wallrock in bituminous clay biomicrites from Adit A6.

(a) RADIONUCLIDE CONCENTRATIONS (Bq/kg)

Sample	Description	^{238}U	^{234}U	^{230}Th	^{226}Ra	^{232}Th
A960CD1	Pre-hyperalkaline ground- water interaction calcite vein fill (diagenetic).	26.1±0.8	30.9±0.9	29.0±1.4	25±3	3.4±0.4
A960CD2	Zeolitic alteration-and ettringite-thaumasite-CSH wallrock alteration.	381±10	520±12	410±10	429±20	23.8±1.4
A962CD1	Pure tobermorite vein-fill (monominerallic).	78±2	144±3	82±3	699±50	10.5±0.7
A962CD2	Wallrock 3cm distant from tobermorite vein contains minor ettringite-filled cracks.	254±4	242±4	290±8	196±10	39.9±2.1
A962CD3	Wallrock immediately adjacent to tobermorite vein (0-1cm).	280±4	268±4	287±6	240±17	12.2±0.8
A965CD1	Jennite vein-fill with minor ettringite-thaumasite.	280±5	570±9	303±8	207±14	18.1±1.1
A965CD2	Wallrock adjacent to jennite vein fill. Contains ettringite veinlets.	146±3	149±3	148±3	150±10	8.7±0.5

(b) ACTIVITY RATIOS

Sample	$^{234}U/^{238}U$	$^{230}Th/^{234}U$	$^{226}Ra/^{230}Th$
A960CD1	1.18±0.05	0.94±0.05	0.86±0.11
A960CD2	1.36±0.05	0.79±0.03	1.04±0.05
A962CD1	1.84±0.06	0.57±0.02	8.5±0.7
A962CD2	0.95±0.02	1.20±0.04	0.67±0.04
A962CD3	0.95±0.02	1.07±0.03	0.84±0.06
A965CD1	2.04±0.05	0.53±0.02	0.68±0.05
A965CD2	1.02±0.03	0.99±0.03	1.01±0.07

Table 6.10 Uranium, thorium and radium radiometric isotope determinations for silicified travertine from central Jordan (Khan-ez-Zabib hills). Values determined on 'whole-rock' samples dominated by opaline silica.

(a) RADIONUCLIDE CONCENTRATIONS (Bq/kg)

Sample	Description	^{238}U	^{234}U	^{230}Th	^{226}Ra	^{232}Th
A974CD1	Partly-silicified travertine with secondary opaline silica, fine secondary micro- crystalline earthy calcite admixed with green volkonskoite clay. Lower Travertine horizon.	844±14	886±13	848±20	727±36	5.0±0.3
A976CD1	Highly silicified travertine almost entirely replaced by opaline silica and containing relicts of microcrystalline calcite and minor volkonskoite. Upper Travertine horizon.	264±5	270±5	303±8	258±15	22.1±1.5

(b) ACTIVITY RATIOS

Sample	$^{234}U/^{238}U$	$^{230}Th/^{234}U$	$^{226}Ra/^{230}Th$
A974CD1	1.05±0.02	0.96±0.03	0.86±0.05
A976CD1	0.98±0.02	1.15±0.04	0.85±0.05

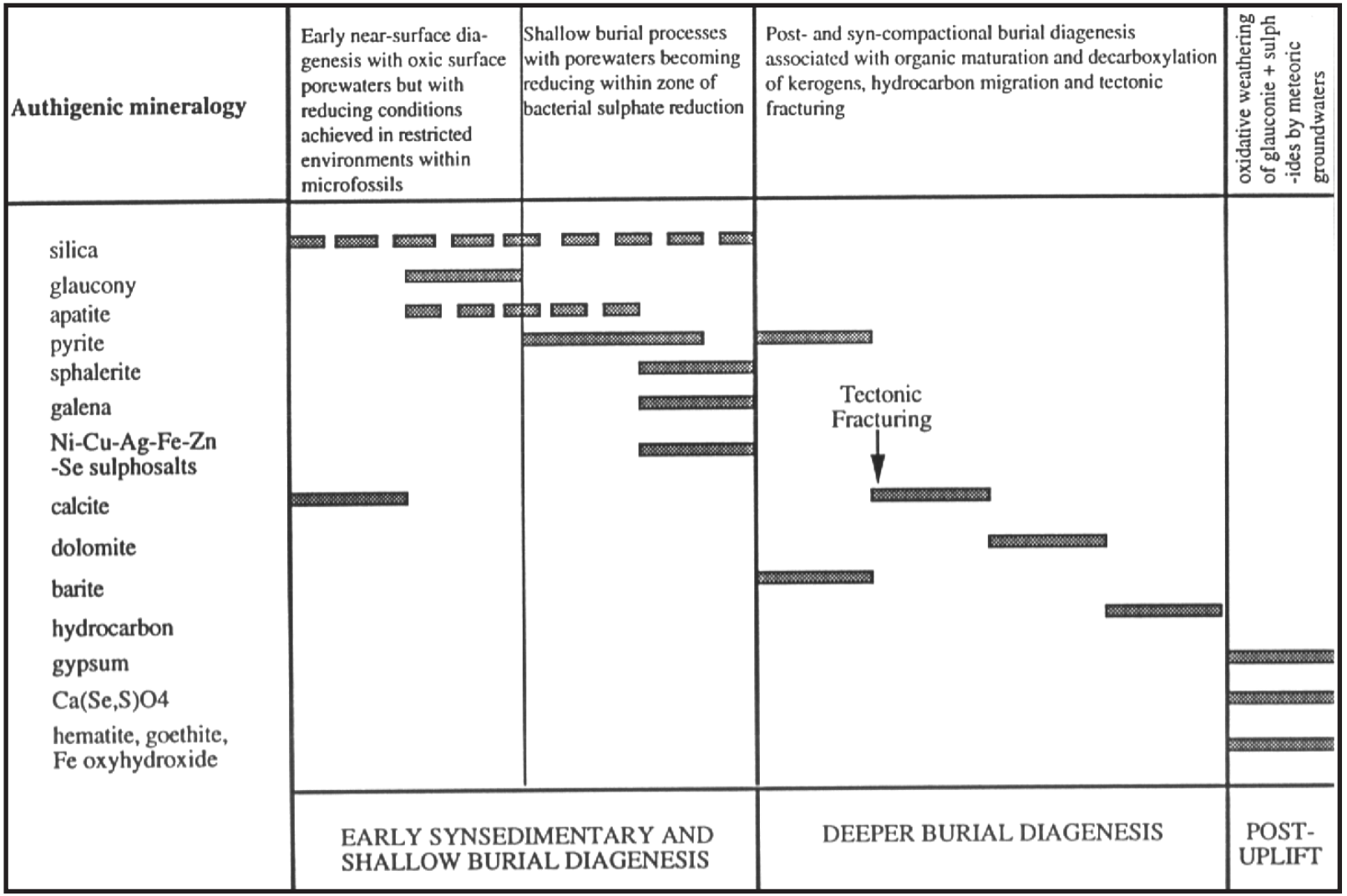

Figure 6.1 Summary of the diagenetic modification of the Bituminous Marl Formation, Maqarin, northern Jordan

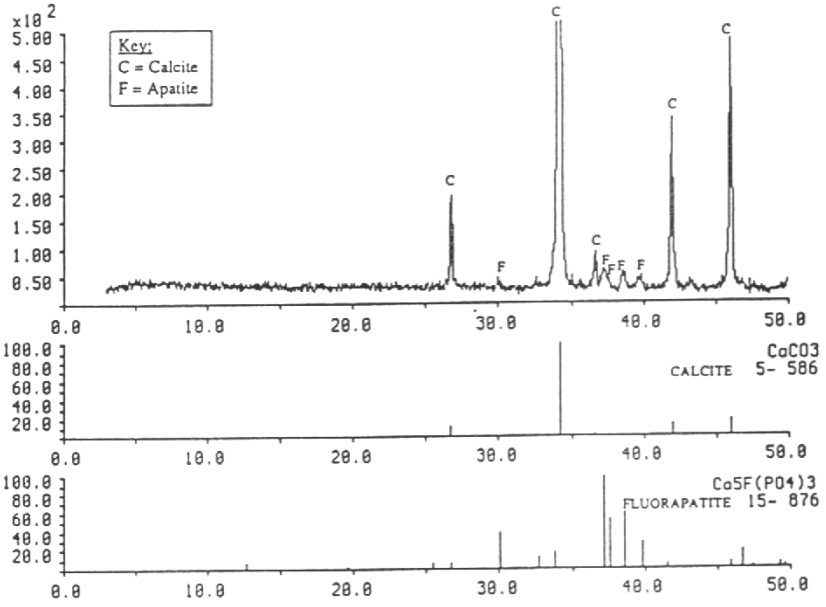

Whole-rock X-ray diffraction analysis: Sample A961.

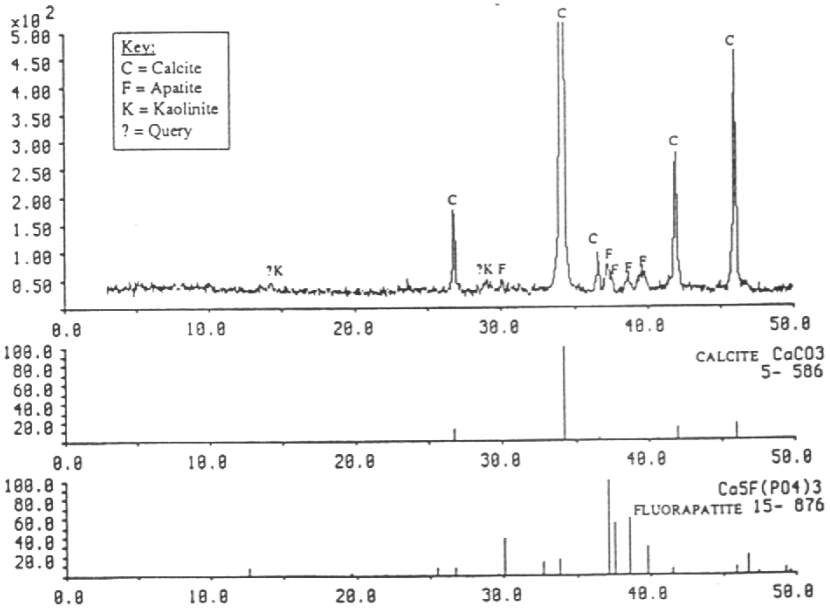

Whole-rock X-ray diffraction analysis: Sample A962.

Figure 6.2 Whole-rock X-ray diffraction traces for typical unaltered bituminous clay-biomicrites from the Maqarin site. JCPDS reference patterns for calcite and fluorapatite are shown for comparison.

C = calcite, F = fluorapatite, K = kaolinite. Horizontal axis - diffraction angle (2θ), vertical axis - intensity (counts per second).

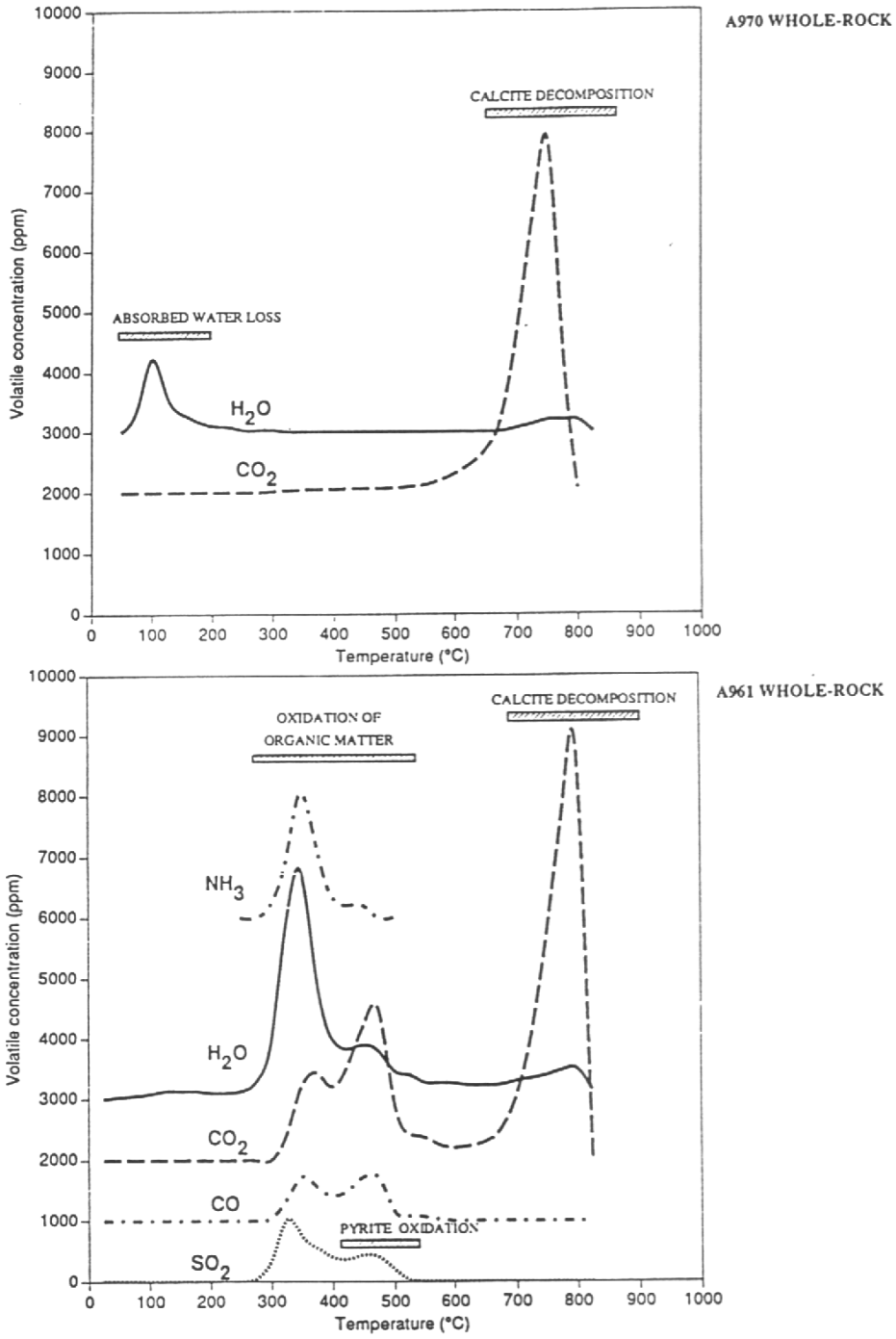

Figure 6.3 EGA evolution profiles for H_2O, CO_2, CO, SO_2 and NH_3 for altered (hyperalkaline groundwater-leached) clay-biomicrite A970 (top) and unaltered bituminous clay-biomicrite A961 (bottom). EGA analyses using 100 mg sample size heated at 20°C/minute in a 2:1 N_2/O_2 carrier gas flowing at 300 ml/minute. Note: SO_2 response is exagerated by a factor of 10, and NH_3 response is exagerated by a factor of 100.

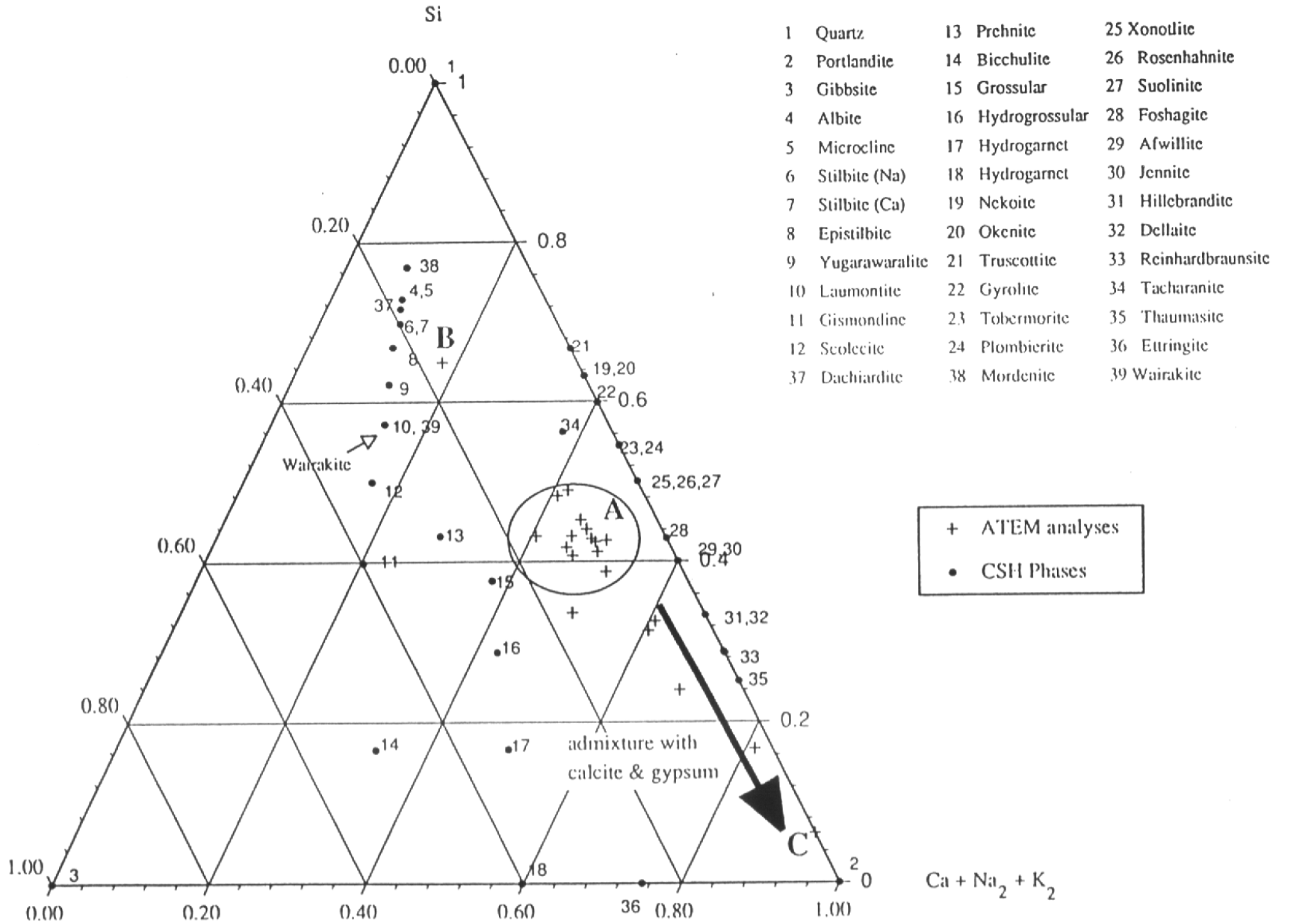

Figure 6.4 **Ternary ($Ca+Na_2+K_2$)-Al-Si (molar ratio) compositional plot of CASH phases in altered wallrock in Sample A960 (determined By ATEM)**

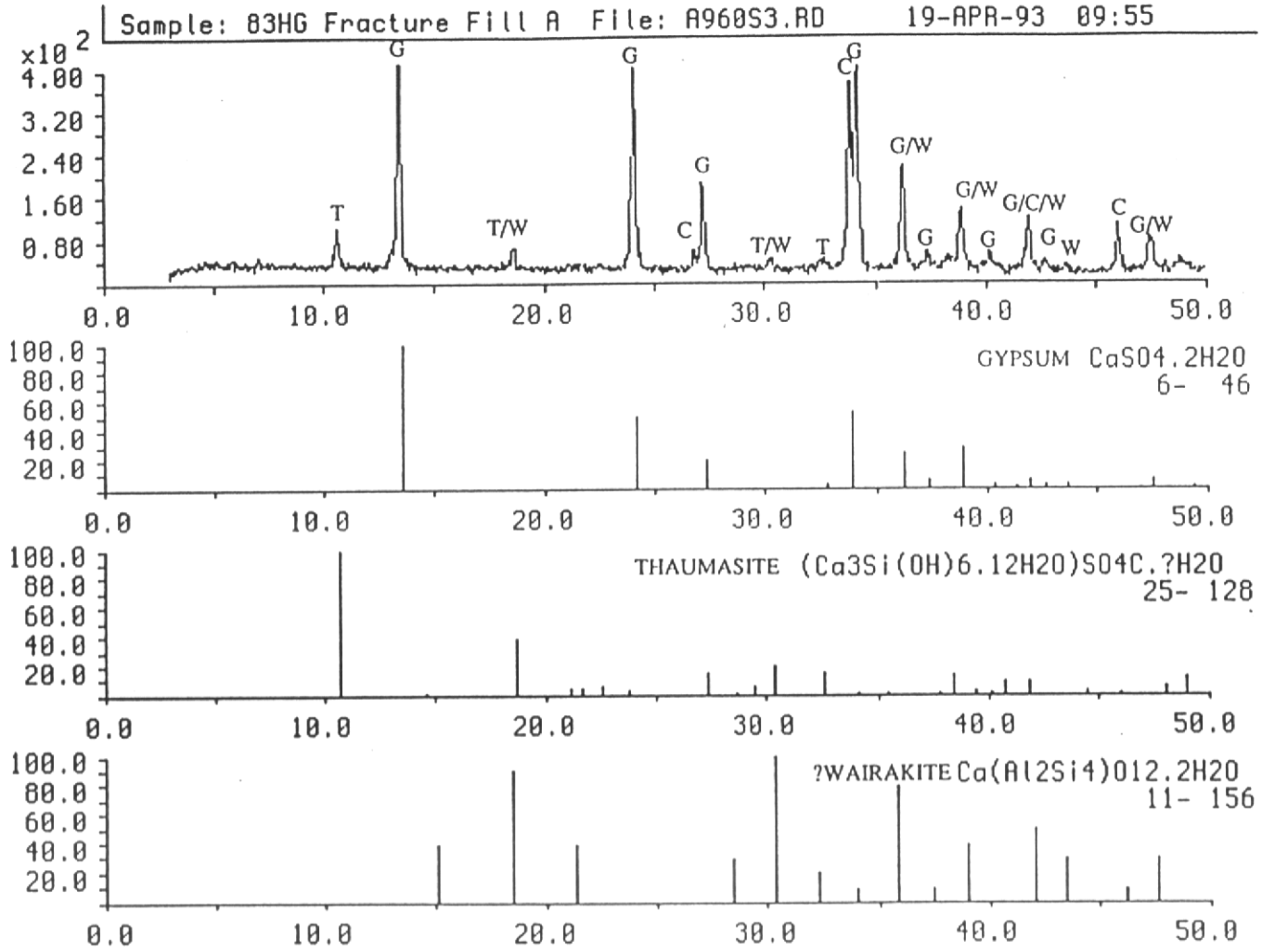

Figure 6.5 XRD pattern for late fissure-filling fracture mineralisation (developed between early calcite breccia and host wallrock) in Sample A960. JWDS reference patterns for gypsum, thaumasite and wairakite are shown for comparison.
G = gypsum, T = thaumasite, W = wairakite.
Horizontal axis -diffraction angle (2), vertical axis -intensity (counts per second).

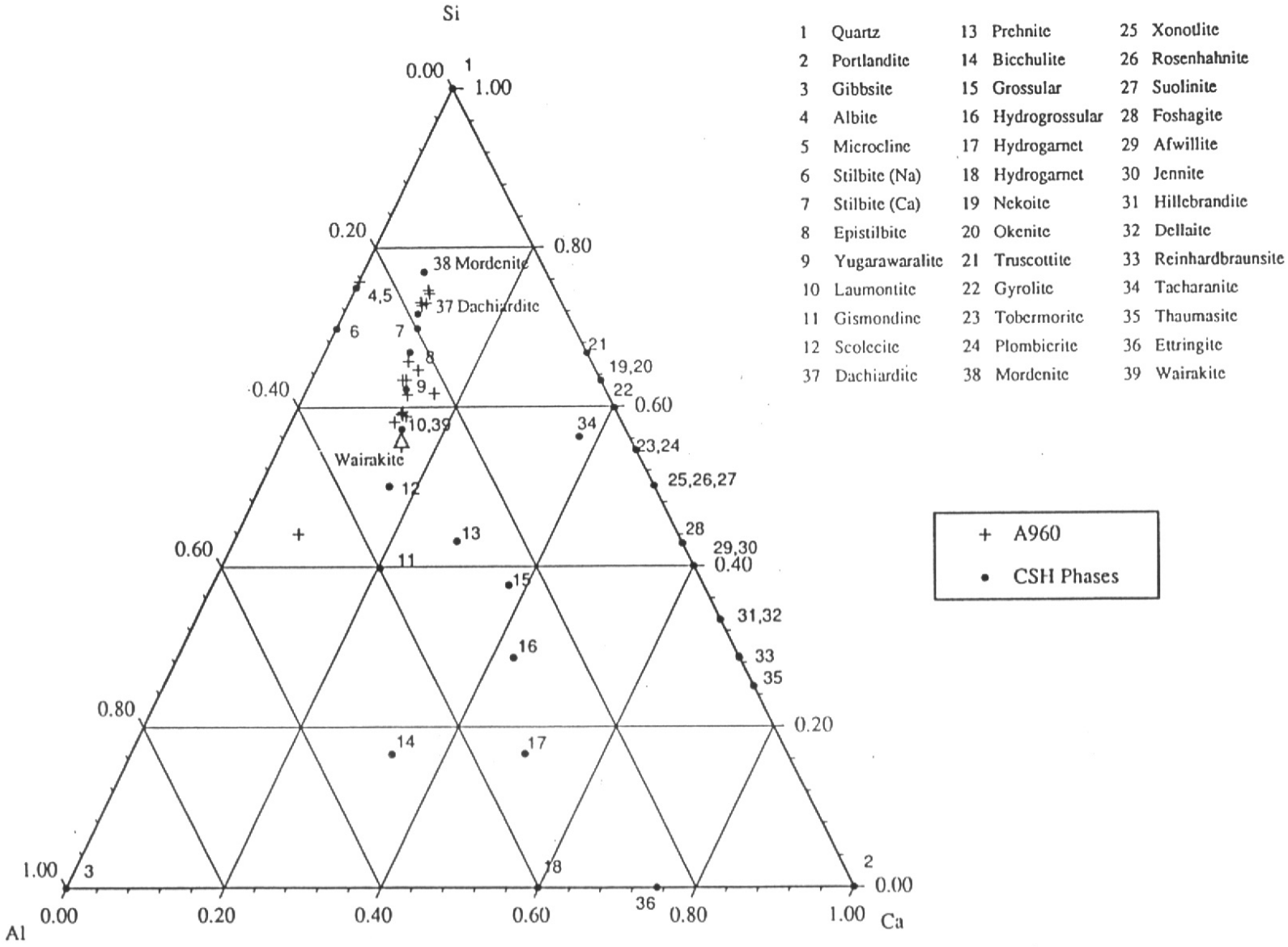

Figure 6.6 Ternary ($Ca+Na_2+K_2$)-Al-Si (molar ratio) compositional plot of zeolitic phases in fracture mineralisation in Sample A960 (determined by EMPA).

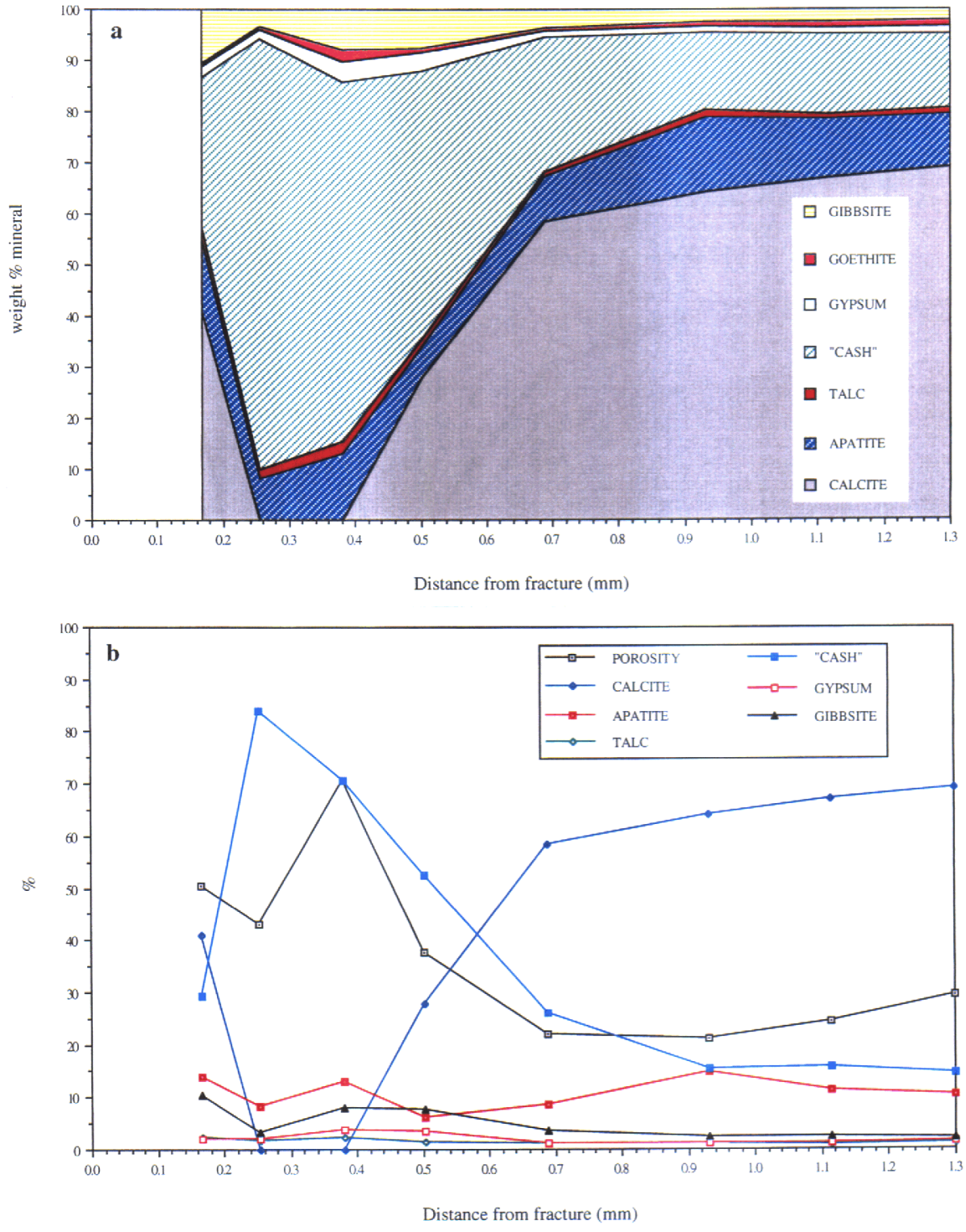

Figure 6.7 Variation in normative mineralogy of altered wallrock as a function of distance from fracture wall, sample A960, Adit A6: (a) relative mineral proportions; (b) variation in mineral contents and porosity.

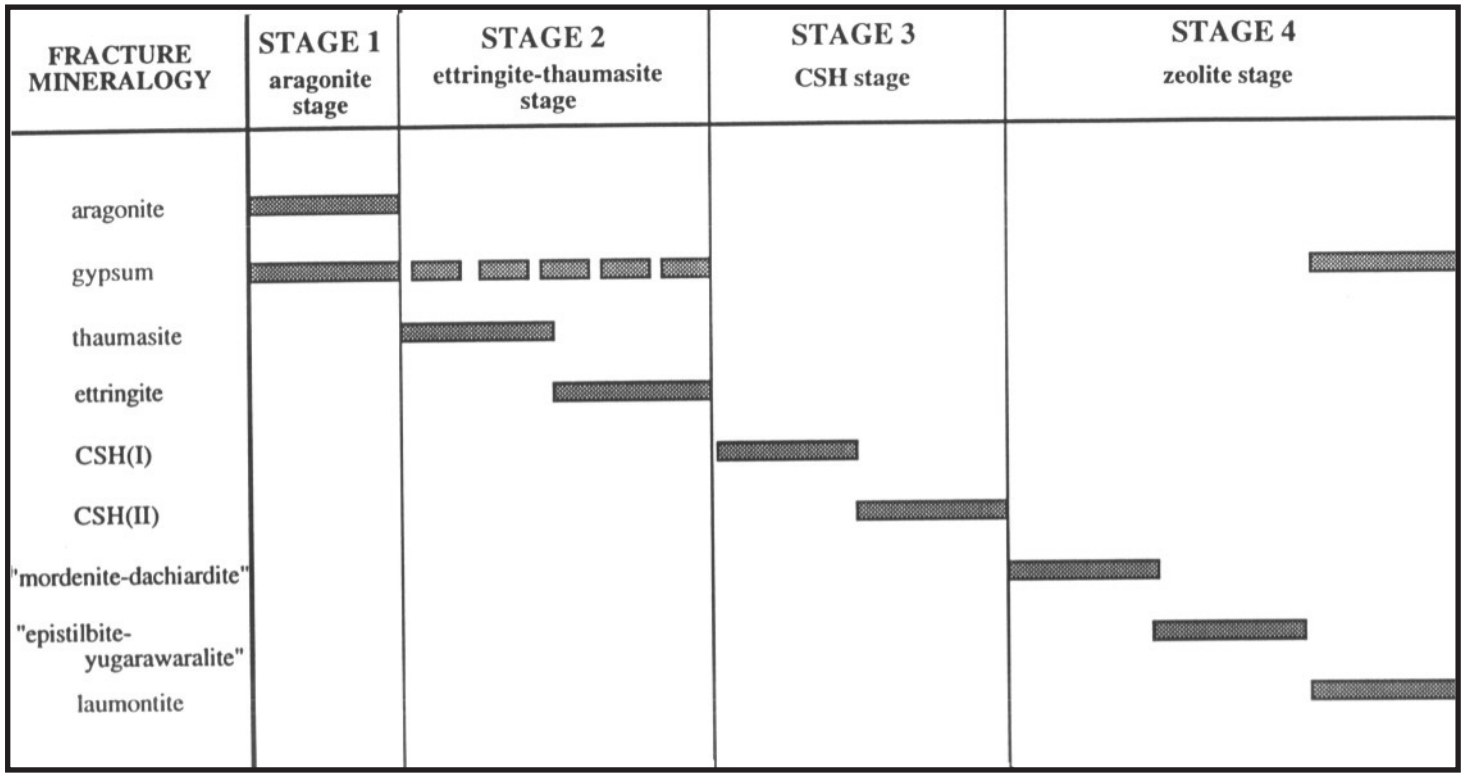

Figure 6.8 Summary mineral paragenesis from the 'high pH upstream zone' of the hyperalkaline interaction with kerogenous clay biomicrites in Adit A6.

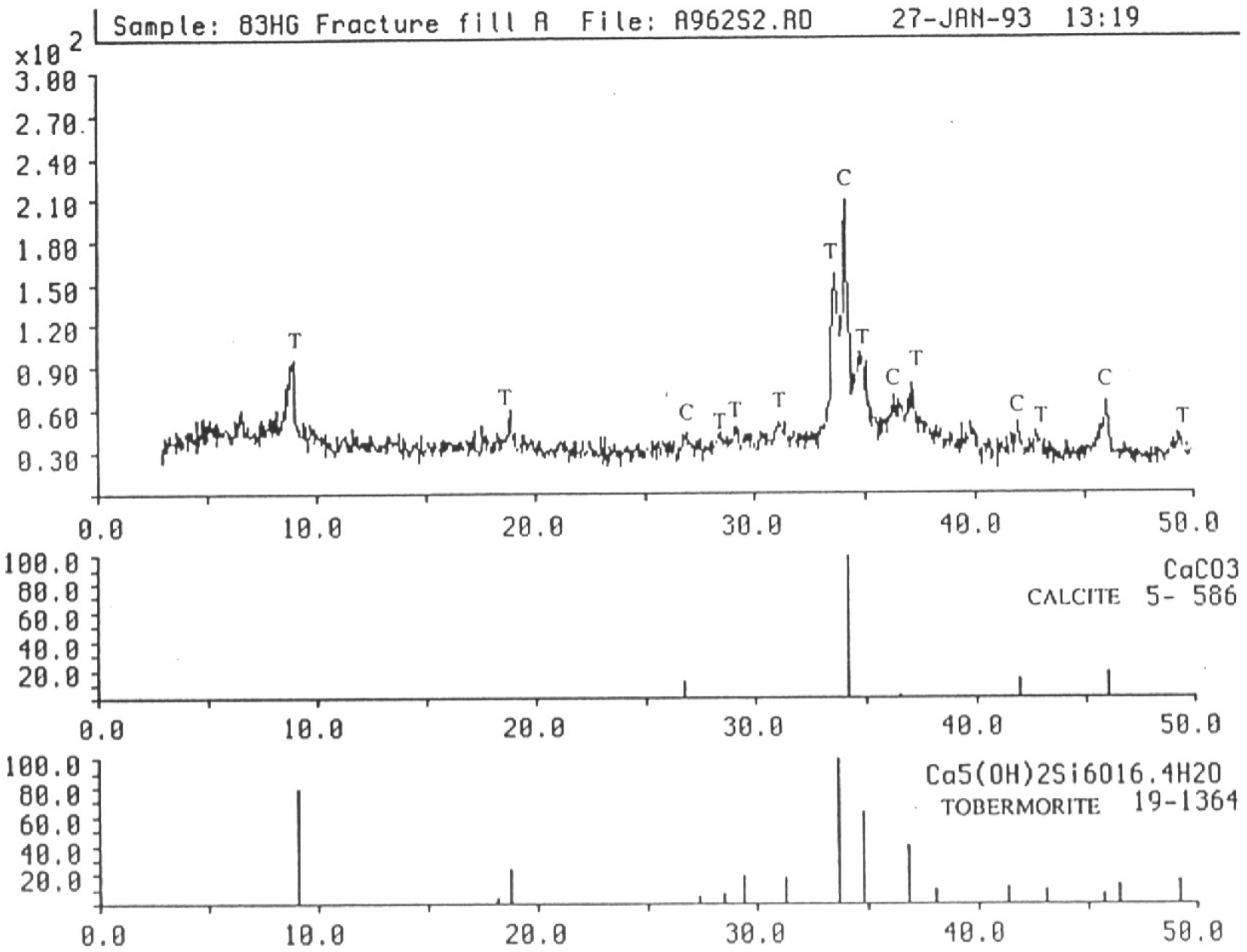

Figure 6.9 XRD pattern for fracture-filling tobermorite (with minor calcite) in Sample A962. JCPDS reference patterns for calcite and 11Å tobermorite are shown for comparison.
C = calcite, T = tobermorite.
Horizontal axis -diffraction angle (2), vertical axis - intensity (counts per second).

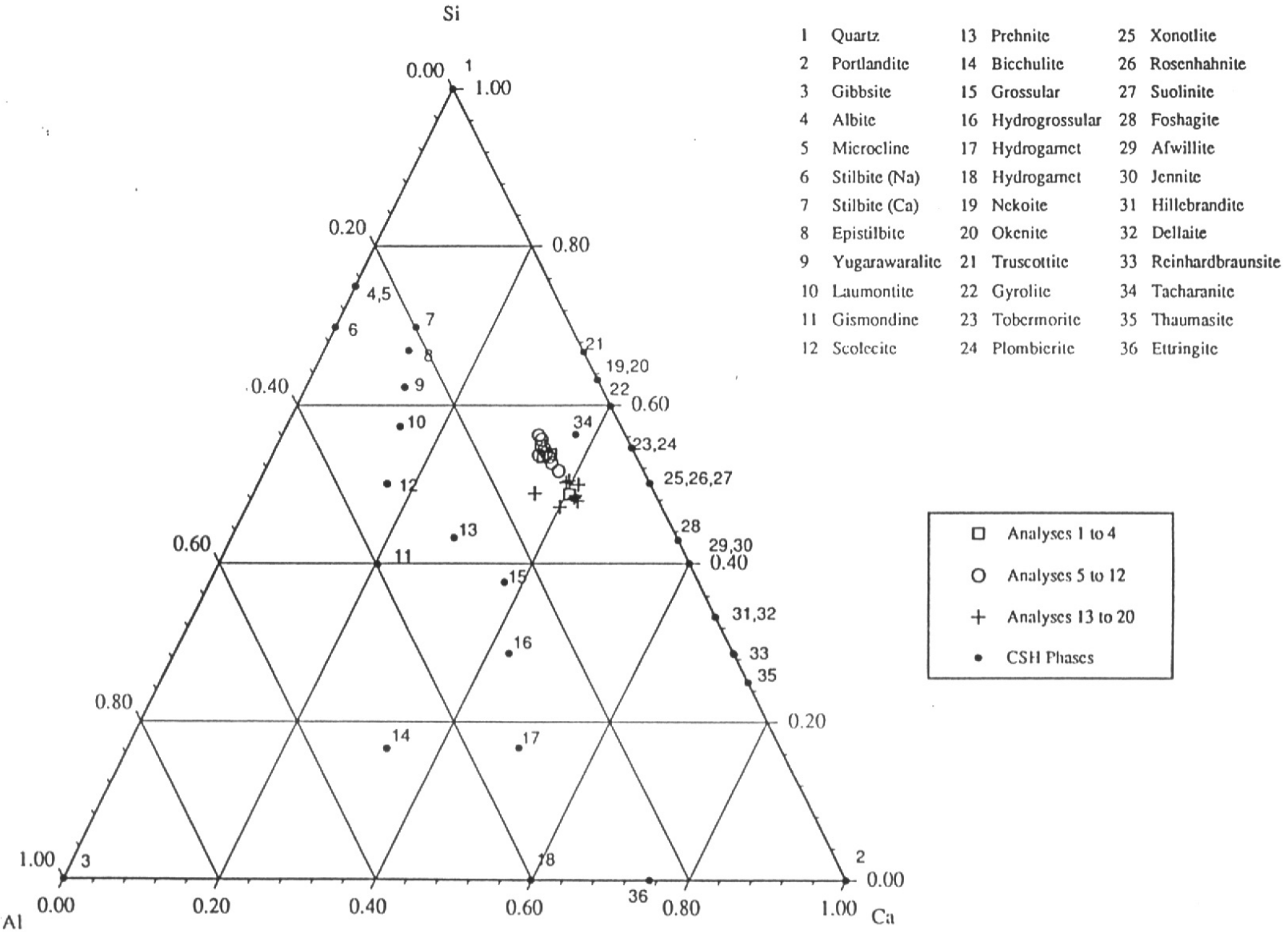

Figure 6. 10 Ternary Ca-Al-Si (molar ratio) compositional plot of tobermorite and other secondary CSH phases in fracture mineralisation in Sample A962 (determined by EPMA). Analyses 1-4 and 13-20 are fibrous primary and hydrated tobermorite, analyses 5-12 are late alteration of tobermorite veins.

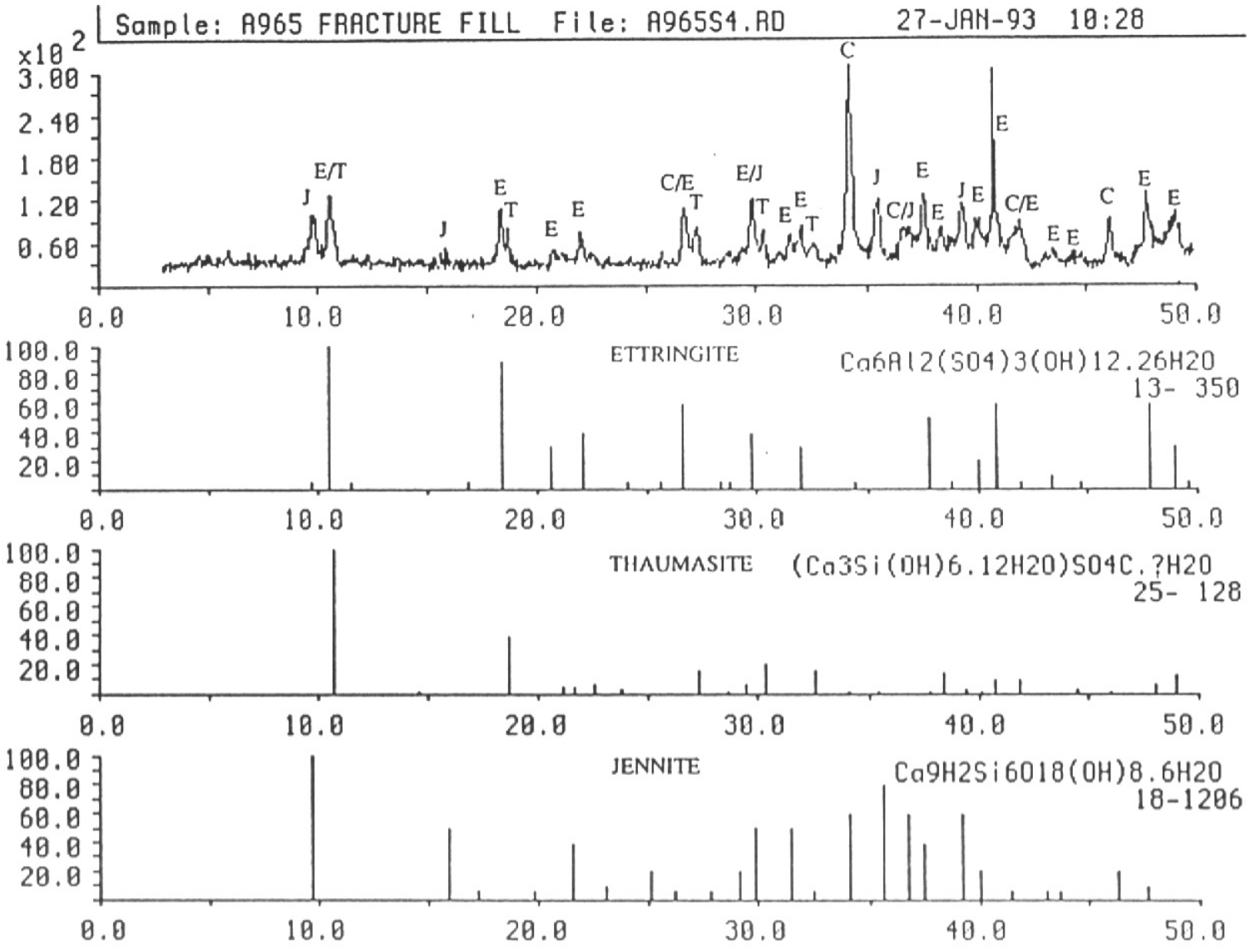

Figure 6.11 XRD pattern for fracture mineralisation in Sample A965. JMS reference patterns for ettringite, thaumasite and jennite are shown for comparison.
C = calcite, E = ettringite, J = jennite.
Horizontal axis -diffraction angle (2), vertical axis -intensity (counts per second).

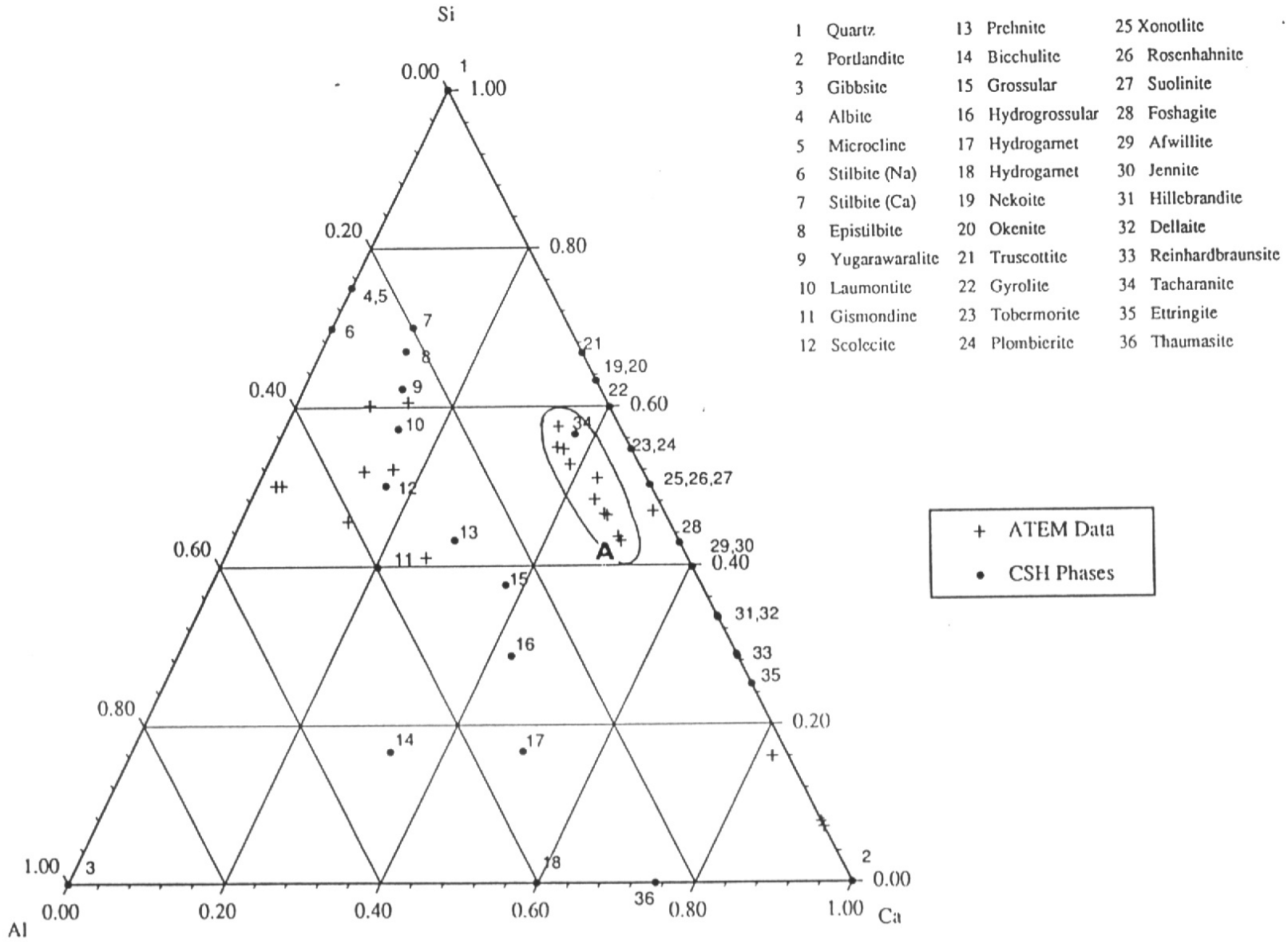

Figure 6.12 Ternary Ca-Al-Si (molar ratio) compositional plot of secondary CSH phases in fracture mineralisation in Sample A964 (determined by ATEM). Field A represents data from vein-filling CSH probably related to aluminous tobermorite or CSH(I) minerals. Other data show considerable scatter and probably represent poorly-constrained mixed analyses with other phases.

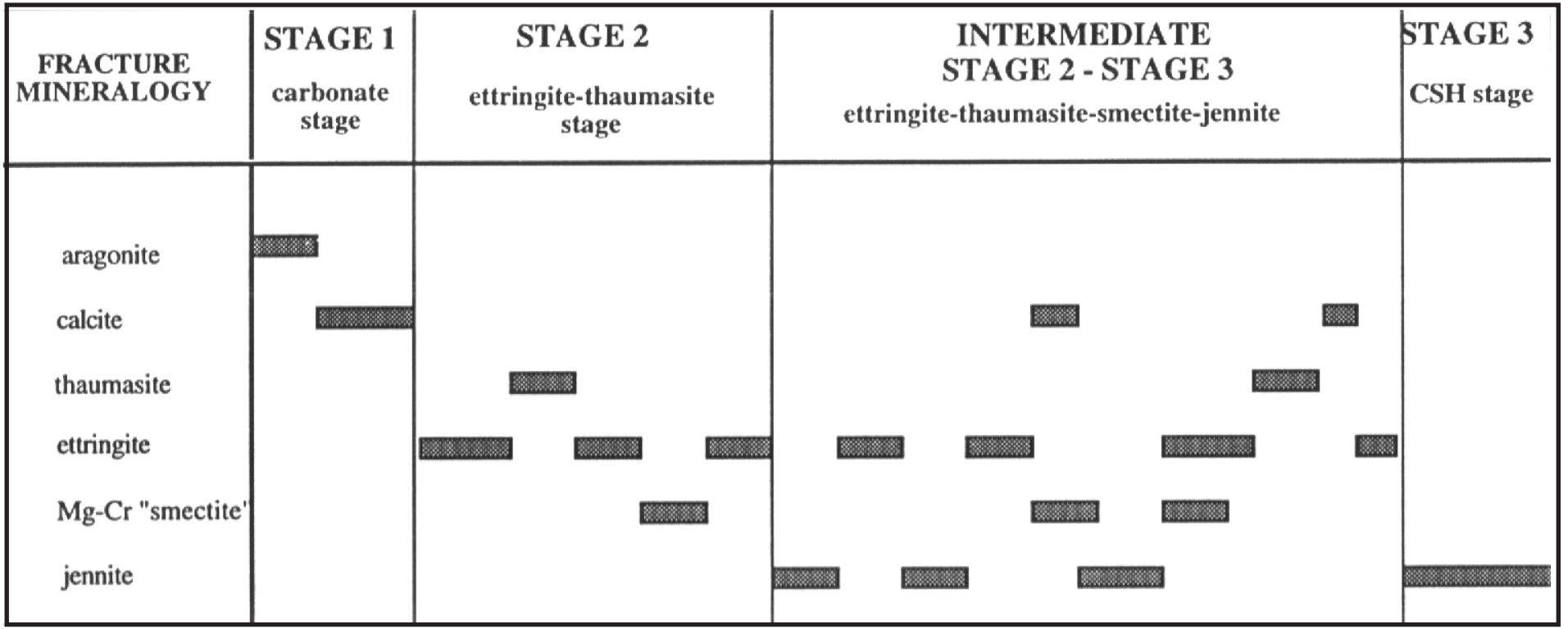

Figure 6.13 Summary mineral paragenesis from the 'low pH' downstream M2 Site of hyperalkaline interaction with bituminous clay biomicrites in Adit A6.

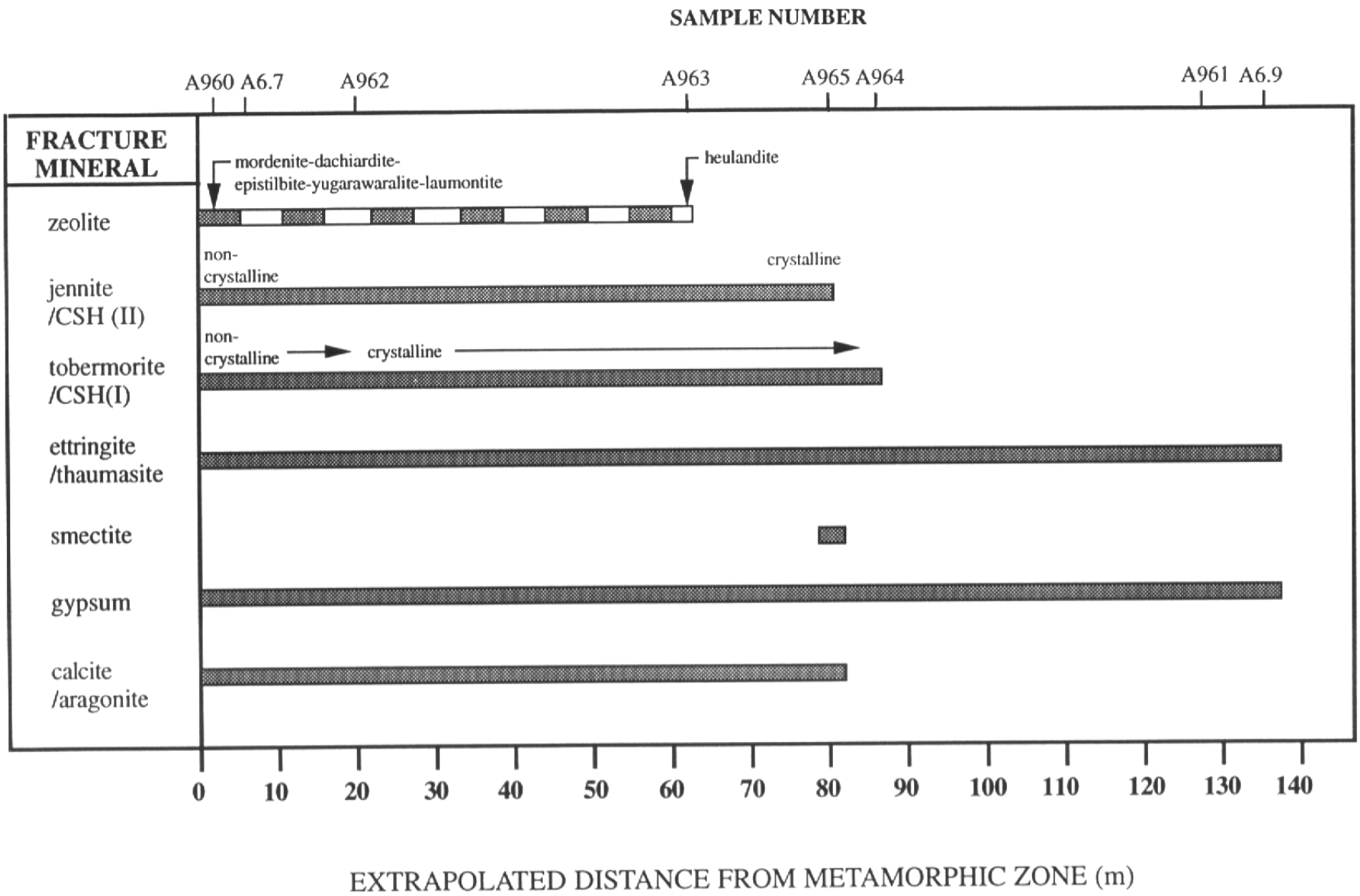

Figure 6.14 Summary of the lateral distribution of fracture-hosted secondary minerals related to hyperalkaline groundwater -bituminous clay biomicrite interaction in Adit A6. Distribution is expressed terms of distance from the metamorphic zone -clay biomicrite contact extrapolated along fracture strike (in metres).

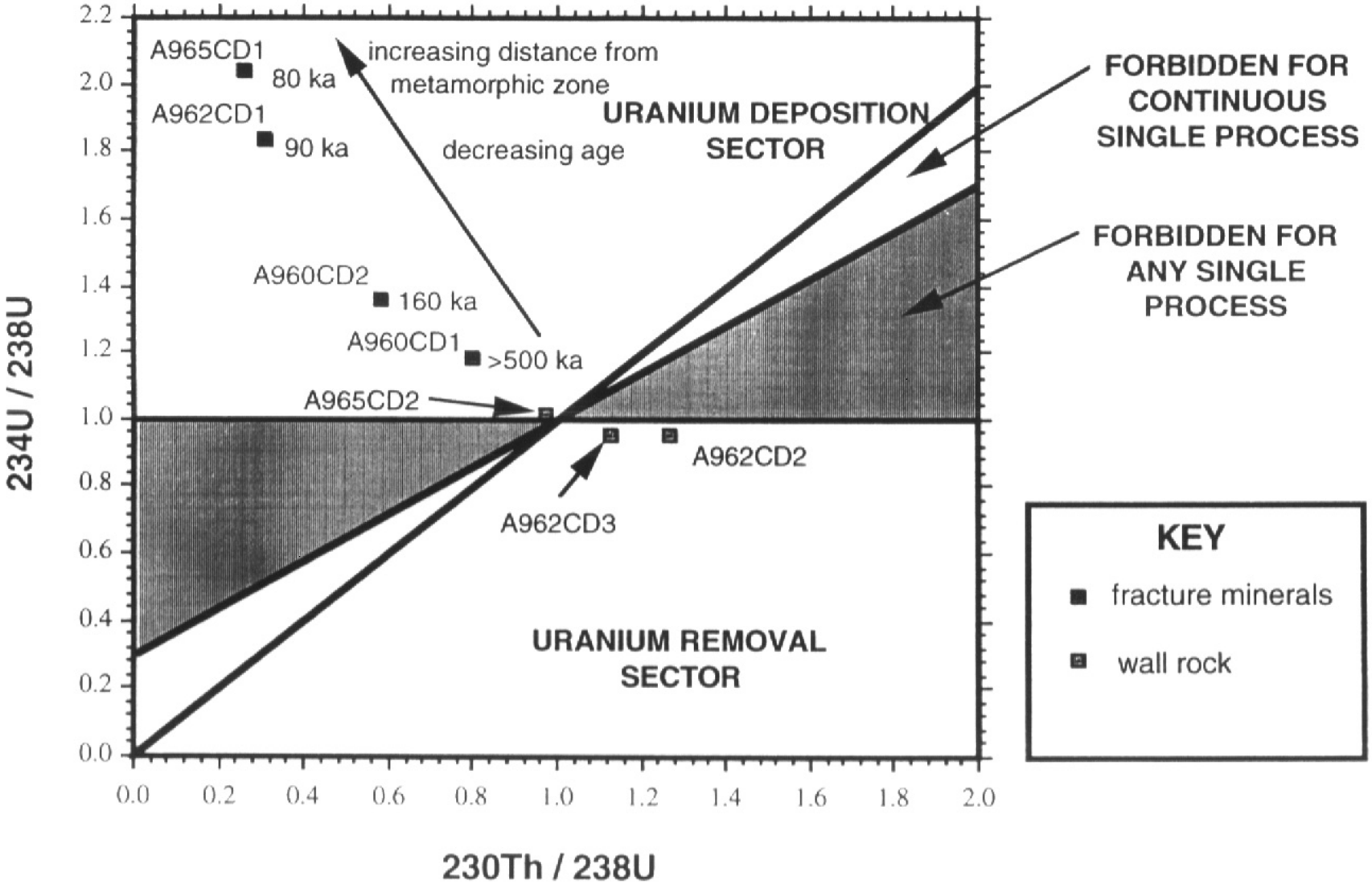

Figure 6.15 Cross-plot of $^{234}U/^{238}U$ and $^{230}Th/^{234}U$ activity rations for samples from Adit A6, based on [36] and [37]. Plot includes errors. Also shown are ages calculated from the ingrowth of ^{230}Th, based on [38].

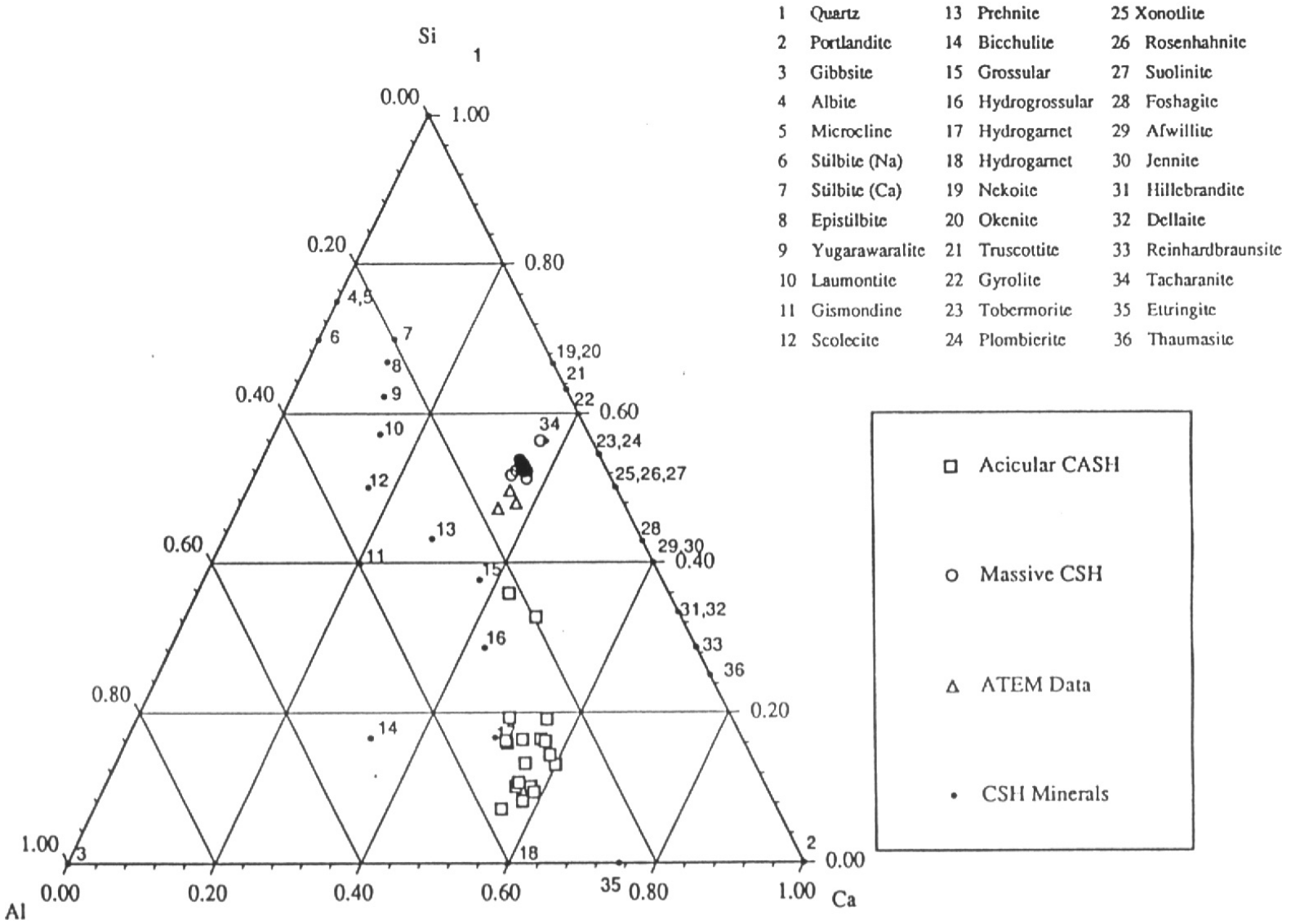

Figure 6.16 Ternary Ca-Al-Si (molar ratio) compositional plot of ettringite, thaumasite ('acicular CASH') and other secondary CSH ('massive CSH') phases in fracture mineralisation in Sample M93 (determined by EMPA and ATEM). Maqarin Station railway cutting (data from [1]).

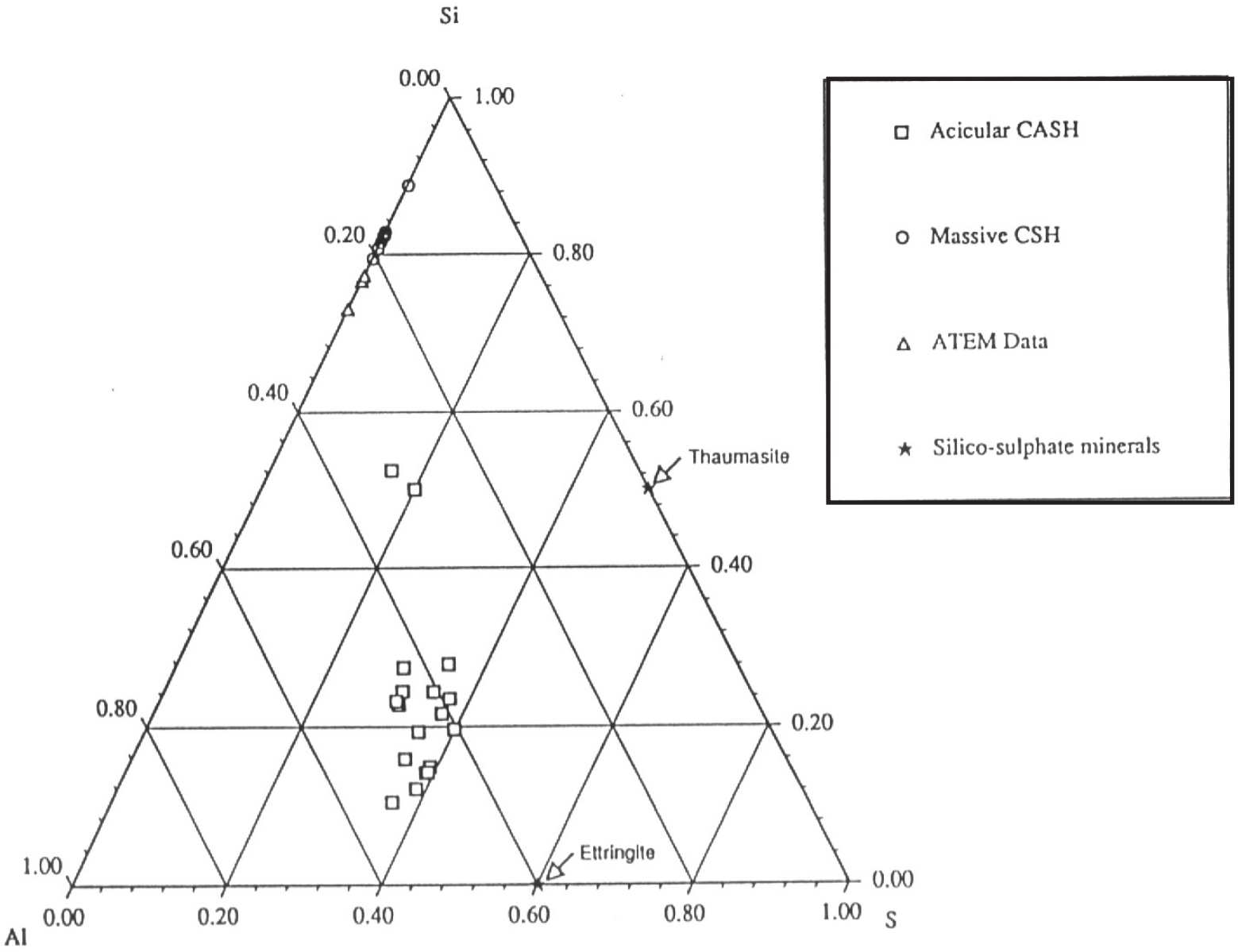

Figure 6.17 Ternary Si-Al-S (molar ratio) compositional plot of ettringite, thaumasite ('acicular CASH') and other secondary CSH ('massive CSH') phases in fracture mineralisation in Sample M93 (determined by EWA and ATEM). Maqarin Station railway cutting (data from [1]).

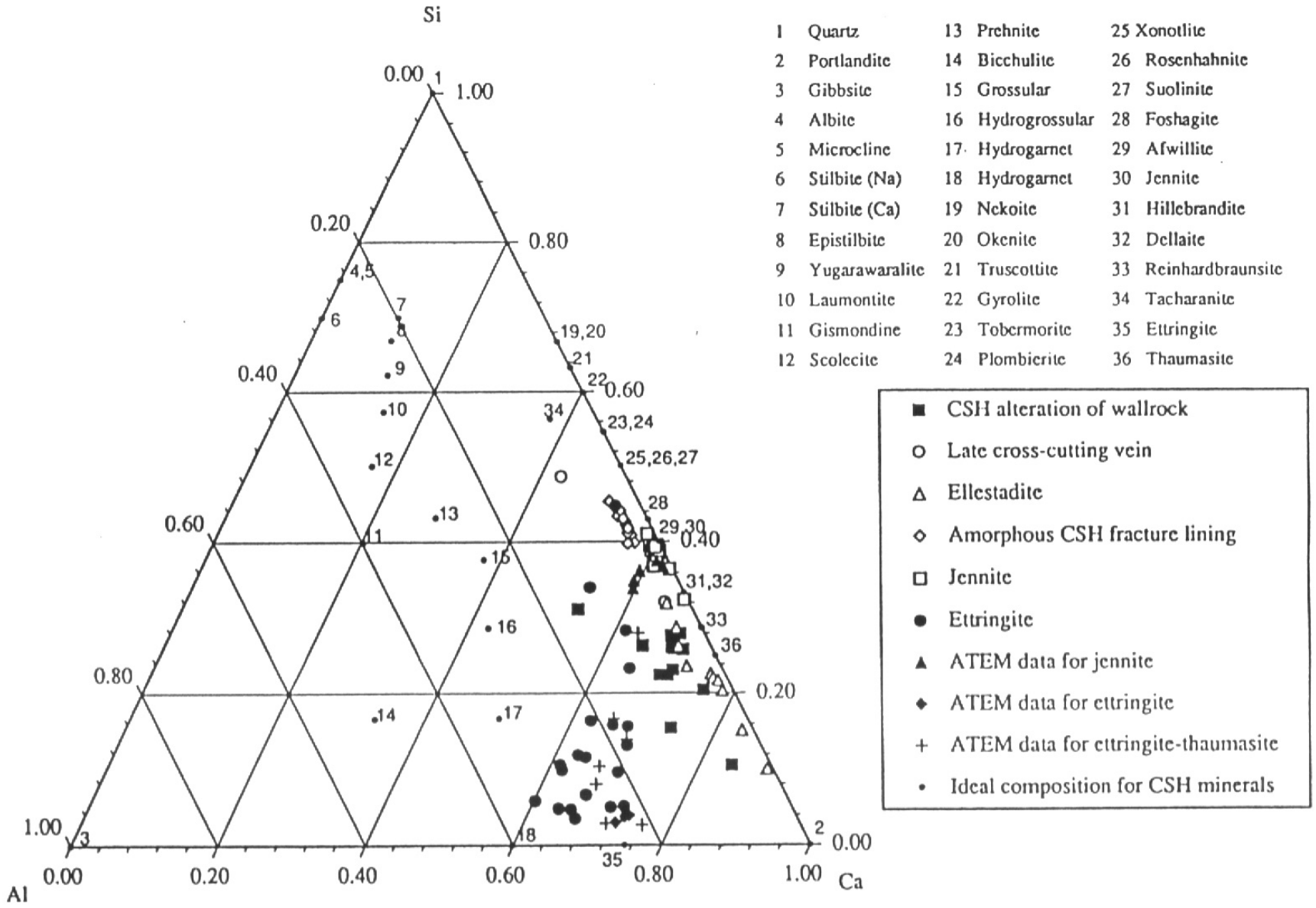

Figure 6.18 Ternary Ca-Al-Si (molar ratio) compositional plot of ettringite, thaumasite and other secondary CSH phases in fracture mineralisation in Sample M81 (determined by EMPA and ATEM). Maqarin Station railway cutting (data from [1]).

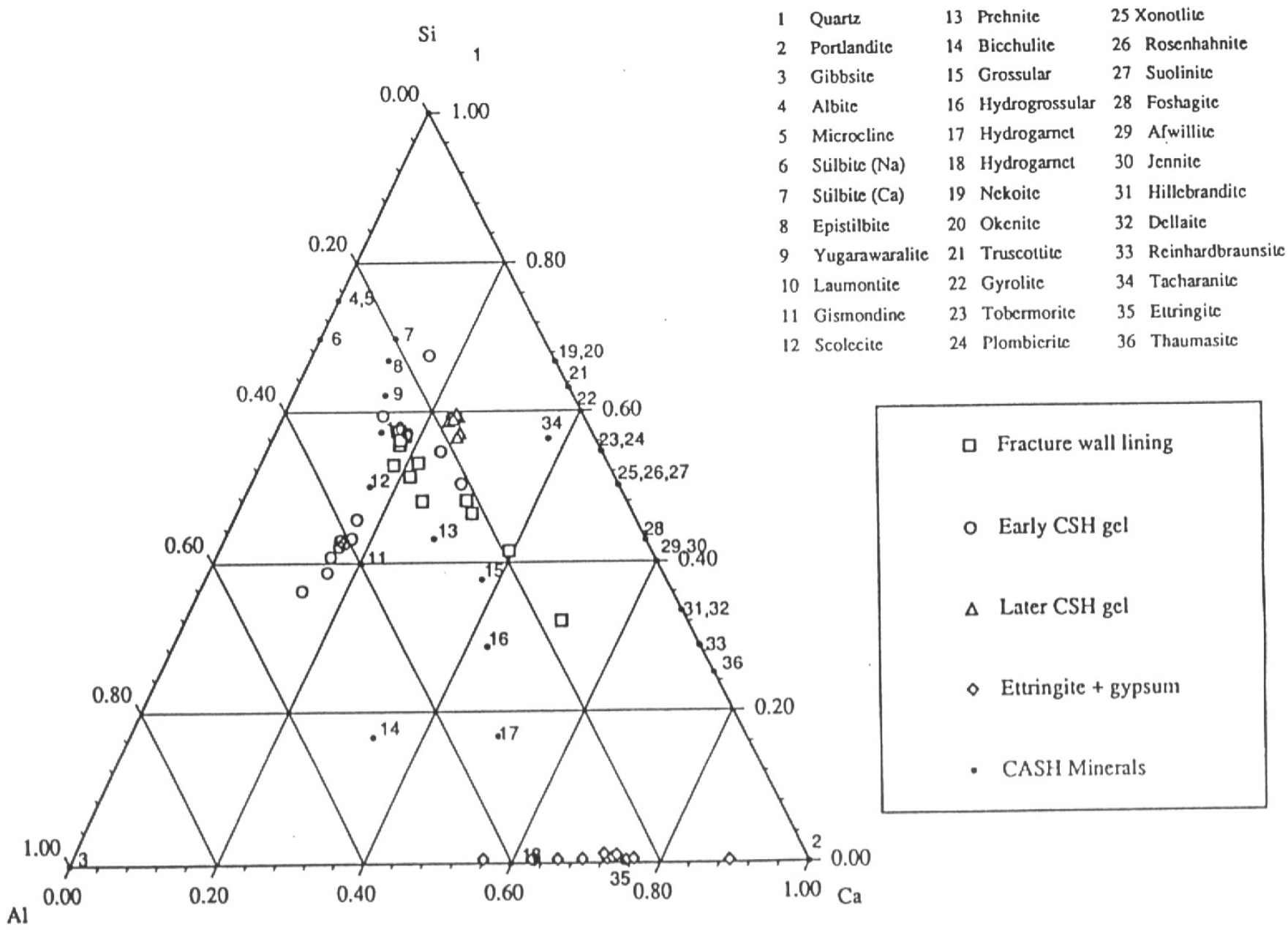

Figure 6.19 Ternary Ca-Al-Si (molar ratio) compositional plot of ettringite, thaumasite, CASH and CSH phases in fracture mineralisation in Sample M91 (determined by EMPA and ATEM). Maqarin Station railway cutting (data from [1]).

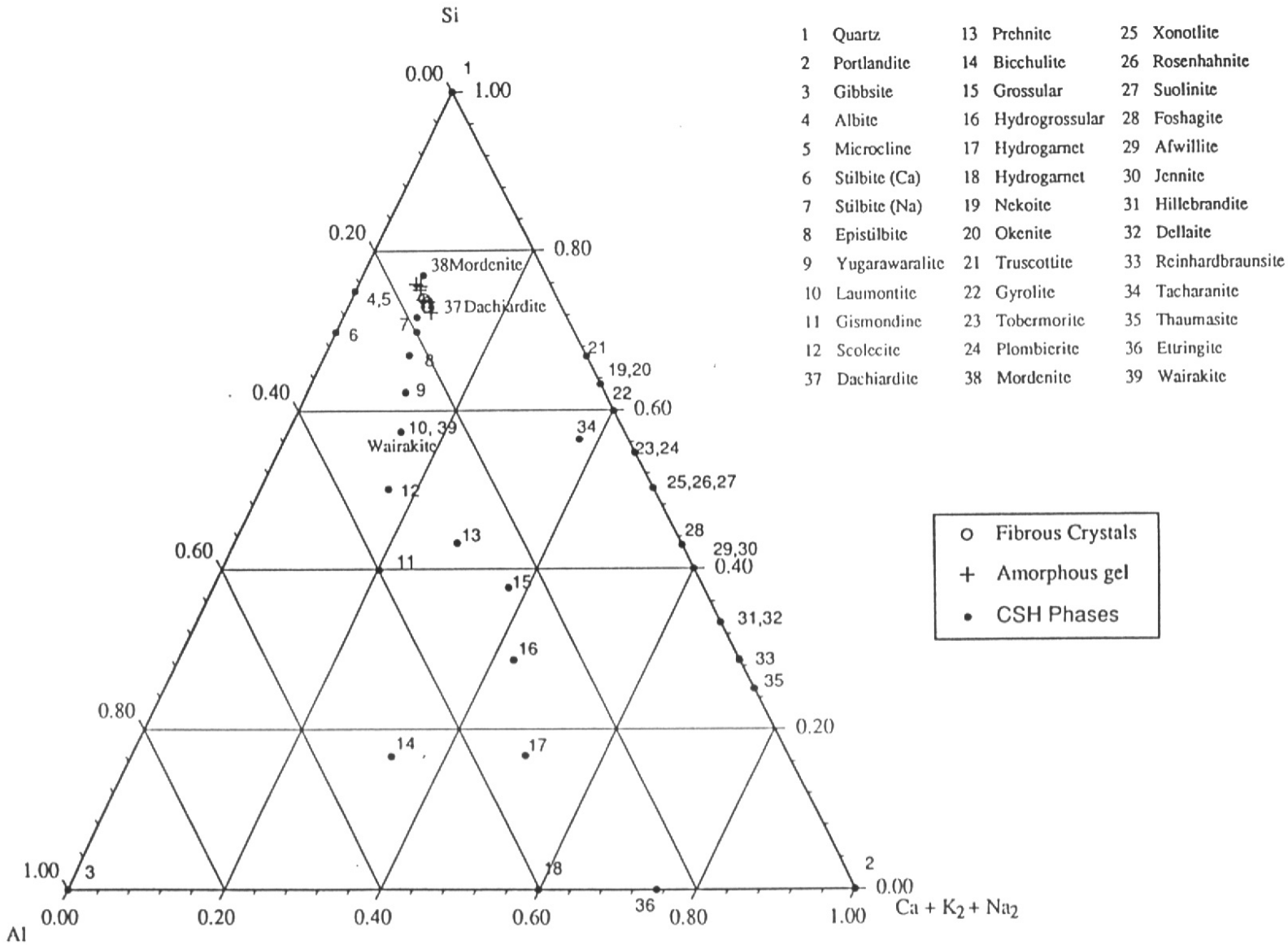

Figure 6.20 Ternary (Ca+Na2+K2)-Al-Si (molar ratio) compositional plot of secondary Ca-Na-K-Al-Si alteration products in colluvium matrix from the Western Springs (Sample A968). Analyses by EMPA.

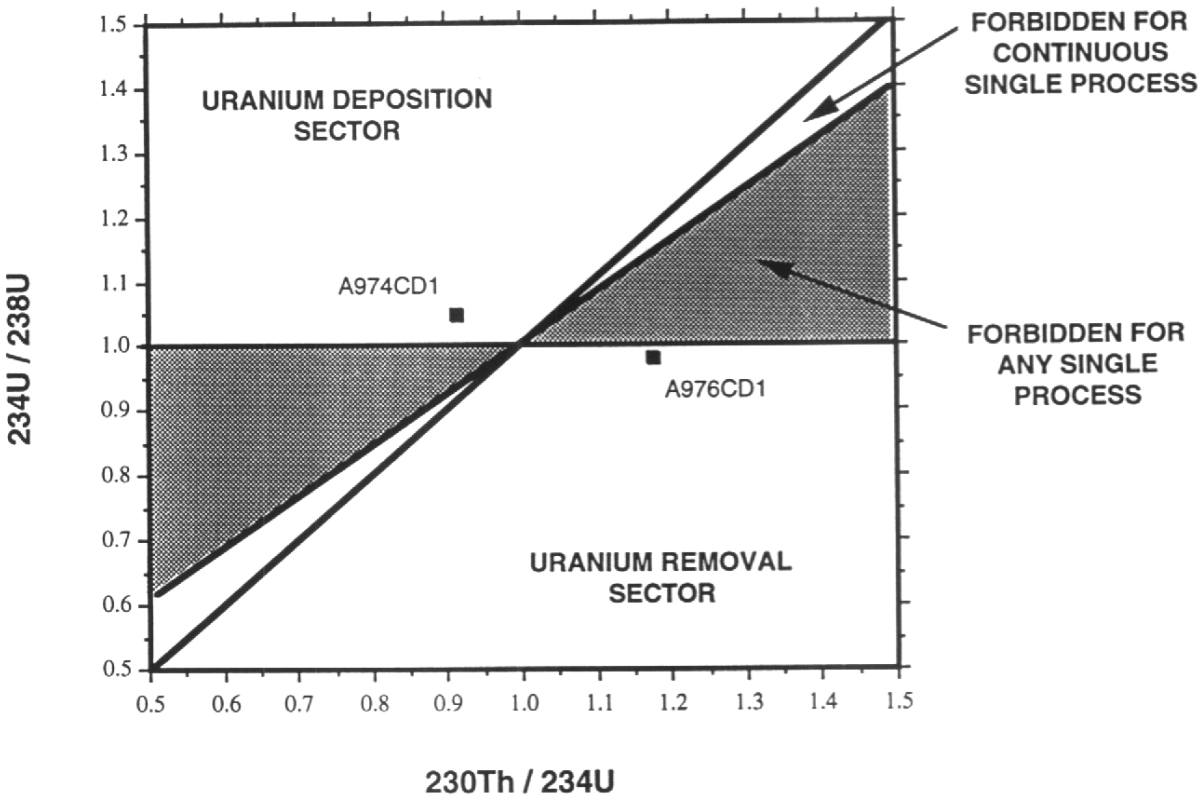

Figure 6.21 Cross-plot of $^{234}U/^{238}U$ and $^{230}Th/^{234}U$ activity rations for travertime Samples from Khan-es-Zabib (based on [36] and [37]).
Plot includes errors

Plate 16 BSEM photomicrograph of clay biomicrite showing foraminifera disseminated in a matrix of finely-comminuted clay- and silt-grade bioclastic (calcitic) detritus (bright) admixed with very fine interstitial clay and organic matter (dark grey). Porosity in the rock is dark. Sample A962, Adit A6, Maqarin.

Plate 17 BSEM photomicrograph showing detail of the matrix fabric of a typical clay biomicrite. It shows silt-grade shell fragments, spicules and other bioclastic (calcite) detritus (bright) in clay-grade matrix of very fine calcite (bright) with disseminated silica and kaolinite (dull). The matrix is close-packed with only very fine (generally $<<1\mu m$) pores (shown by dark areas). Sample A965, Adit A6, Maqarin.

Plate 18 BSEM photomicrograph showing chambered foraminiferal test containing authigenic framboidal pyrite (bright) enclosed in relatively coarsely crystalline euhedral calcite cement (grey) which partially fills some chambers (open porosity shown by dark areas). Sample A962, Adit A6, Maqarin.

Plate 19 BSEM photomicrograph showing calcitic microfossil test (grey) in clay biomicrite, filled by 'fibrous' altered authigenic 'glaucony'. Sample A962, Adit A6, Maqarin.

Plate 20 BSEM photomicrograph of clay biomicrite matrix showing framboidal (spherical) aggregates of fine-grained ($<1\mu m$) pyrite crystals (bright). Sample A962, Adit A6, Maqarin.

Plate 21 BSEM photomicrograph showing authigenic barite cement (bright) confined within compacted and fractured microfossil test in clay biomicrite. The barite is cementing, replacing and overprinting the fine-grained interstitial matrix. Sample A962, Adit A6, Maqarin.

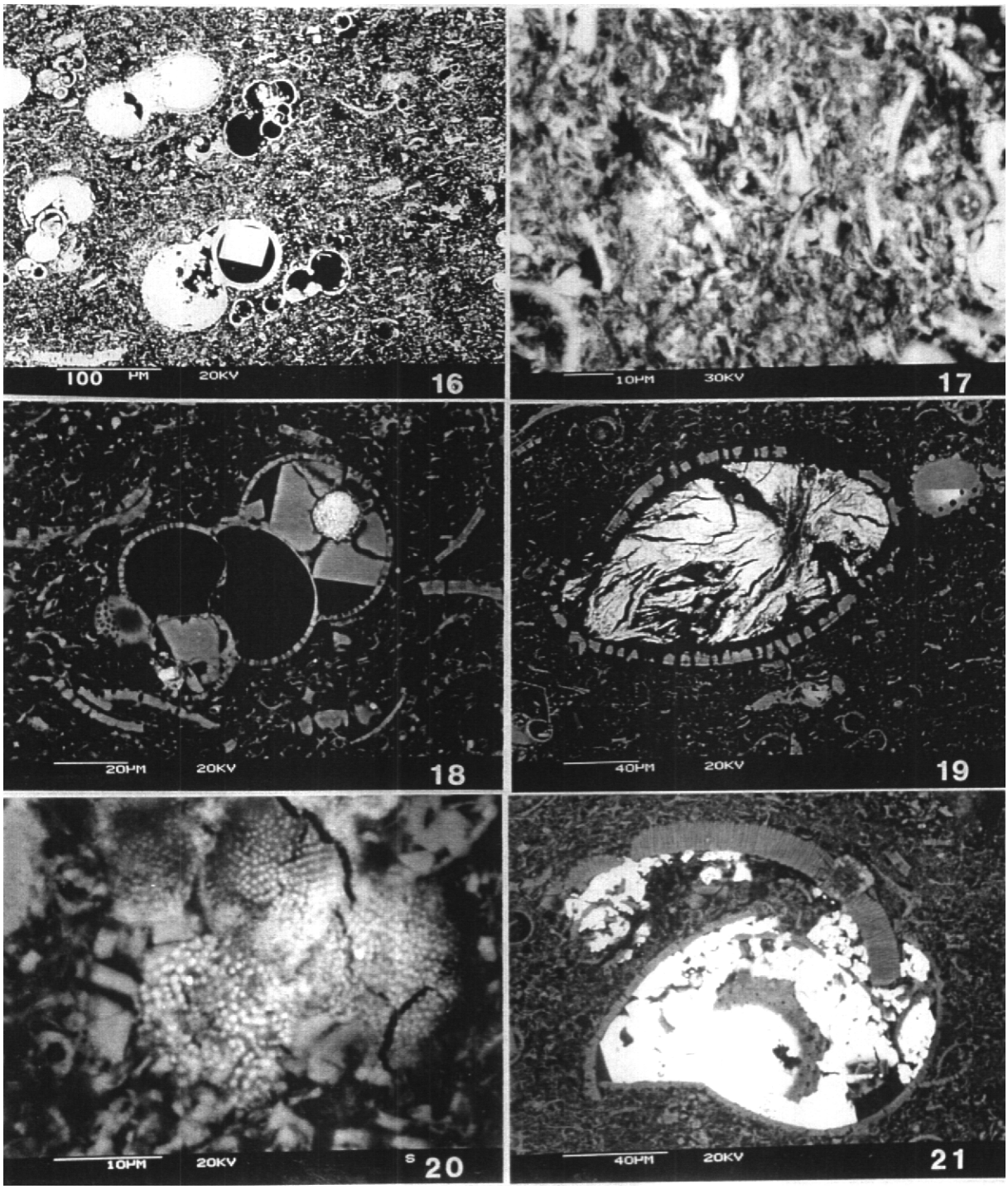
100 μM 20KV
16
10μM 30KV
17
20μM 20KV
18
40μM 20KV
19
10μM 20KV
S 20
40μM 20KV
21

Plate 22 BSEM photomicrograph of clay biomicrite containing compactionally-crushed and fractured foraminiferal tests. The internal cavities in the tests have been infilled by subhedral-euhedral calcite cement (grey) after compaction. Sample A962, Adit A6, Maqarin.

Plate 23 BSEM photomicrograph of partially-dolomitised clay biomicrite limestone. Shows small sub-rhombic non-ferroan dolomite crystals (d) overprinting and partially replacing the fine-grained calcite matrix (bright). The micritic matrix has been recrystallised and coarsened slightly, and has lost some of its primary texture. Sample A967, Maqarin railway cutting.

Plate 24 BSEM photomicrograph of dolomitic clay biomicrite limestone showing foraminiferal test with chambers filled by calcite cement (light grey) and later non-ferroan dolomite cement (dark grey). Rock matrix is highly dolomitised (dark grey). Sample A967, Maqarin railway cutting.

Plate 25 BSEM photomicrograph of altered clay biomicrite. Shows early calcite-cemented microbreccia vein (bright). The vein has subsequently parted from wallrock biomicrite allowing alteration by hyperalkaline groundwater to penetrate along the calcite vein-wallrock interface. Leaching of the fine-grained calcite in the matrix of the wallrock and the production of secondary CSH, CASH, ettringite, thaumasite and gypsum has occurred to a depth of up to 1mm either side of the calcite vein breccia. The altered wallrock is seen as dark bands parallel to the central vein fill. Sample A960, Adit A6, Maqarin.

Plate 26 Photomicrograph (transmitted, plane-polarised light) showing thin colourless microfibrous ettringite veinlet cutting organic-rich clay biomicrite. The unaltered host rock is stained orange-brown in colour due to disseminated fine-grained organic matter. Leaching of the rock adjacent to the ettringite vein has 'bleached' the rock of the organic matter, which is now concentrated as a thin, diffuse, dark-opaque band along the interface between altered (greenish) and unaltered (brown) host rock. Sample A960, Adit A6, Maqarin (width of field = 0.6mm).

Plate 27 BSEM photomicrograph of alteration along the interface between early calcite vein breccia and host clay biomicrite. Early needles of aragonite (a) line the surface of the vein calcite; later fibrous zeolite (z) and fragmented CSH (cs) partially fill the fissure between the wallrock and the early calcite vein fill. Sample A960, Adit A6, Maqarin.

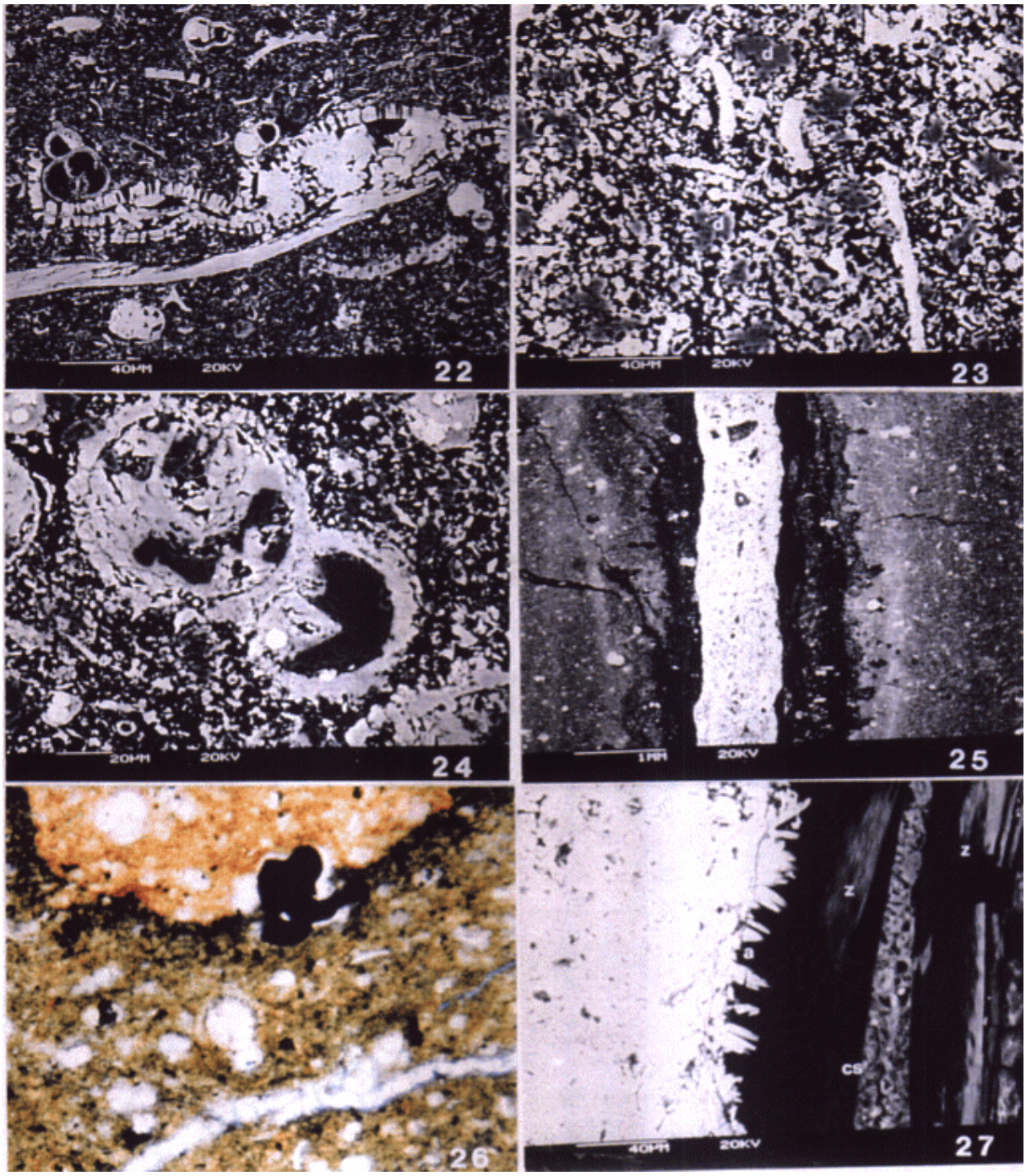
40µm 20KV
22
d
d
40µm 20KV
23
20µm 20KV
24
1mm 20KV
25
26
z
z
a
cs
40µm 20KV
27

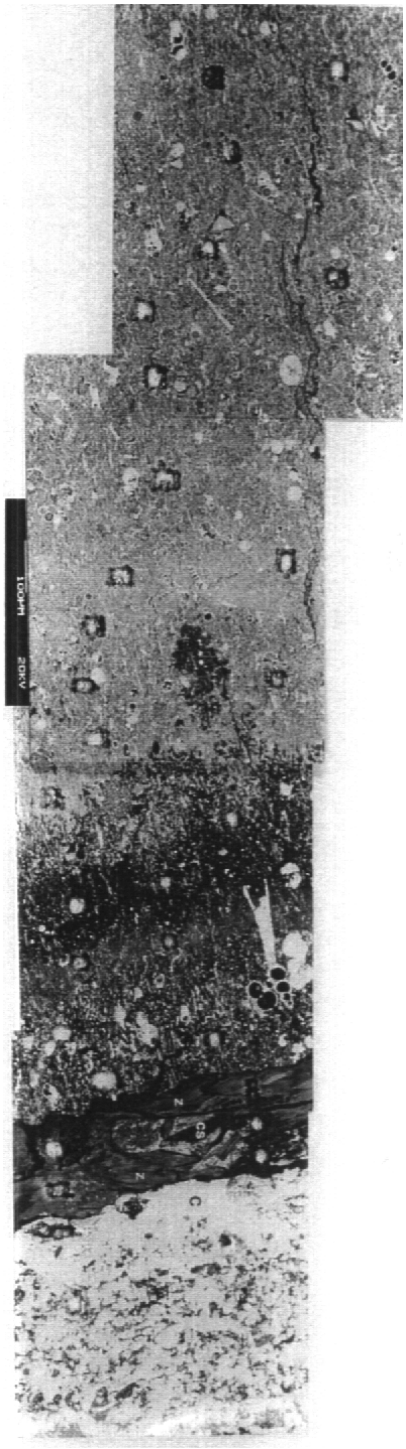

Plate 28 BSEM photomicrograph photomosaic montage of calcite-ettringite fracture mineralisation and associated wallrock alteration in kerogenous clay biomicritic limestone (chalk). Shows early central calcite vein microbreccia (c), marginal fissure mineralised by zeolite (z) and intergrown CSH(I) and CSH(II) (cs). The calcite-leached altered wallrock zone (dark zone) can be seen to grade into less altered/fresh wallrock away from the fracture wall. Note dark 'rectangular areas' are LAMP-ICP-MS laser ablation pits. Sample A960, Adit A6, Maqarin.

Plate 29 BSEM photomicrograph showing a complex alteration assemblage developed along the interface between an early calcite vein breccia (c) and wallrock altered by hyperalkaline groundwater (w). The photograph shows fibrous zeolite (z) cementing between fragments of intergrown CSH(I) and CSH(II) (cs), and in the lower part of the photograph, zeolite has replaced the CSH minerals. Sample A960, Adit A6, Maqarin

Plate 30 BSEM photomicrograph showing a complex alteration assemblage developed along the interface between an early calcite vein breccia (c) and wallrock altered by hyperalkaline groundwater (w). The photograph shows fibrous zeolite (z) resting on corroded gypsum (g). Sample A960, Adit A6, Maqarin.

Plate 31 BSEM photomicrograph showing a fracture in kerogenous clay biomicrite filled by cross-fibrous tobermorite (t). The margins of the tobermorite are dark due to later hydration alteration which has produced a more hydrous, amorphous CSH product (cs). This late CSH alteration also replaces the early CSH/tobermorite along a network of microcracks in the main vein fill. Sample A962, Adit A6, Maqarin.

Plate 32 BSEM photomicrograph showing detail of the margin of a tobermorite vein cutting kerogenous clay biomicrite. The tobermorite (t) forms a cross-fibre vein filling. BSEM shows that the tobermorite comprises a brighter fibrous component with slightly duller interstitial material. Along the margins of the vein the tobermorite has been altered to amorphous CSH (cs). The brighter, denser tobermorite is more resistant to hydration than the interstitial component and persists as relicts in the amorphous hydration product. Secondary calcite has 'cemented' the adjacent wallrock for up to 0.5mm from the vein (bright margin). Sample A962, Adit A6, Maqarin.

Plate 33 BSEM detail of altered tobermorite in Plate 32. Photograph shows fibrous texture of tobermorite with bright tobermorite fibres and duller, more hydrous or less calcic interstitial tobermorite. This has been replaced by dark hydrous and amorphous CSH towards the vein margin. Note that the fibrous brighter tobermorite is more persistent within the altered zone of the vein.

Plate 34 BSEM photomicrograph of tobermorite vein margin showing penetration of late calcite along fine hairline cracks in the tobermorite vein infilling. Sample A962, Adit A6, Maqarin.


C
Z
CS
Z
W
100PM
20KV
29

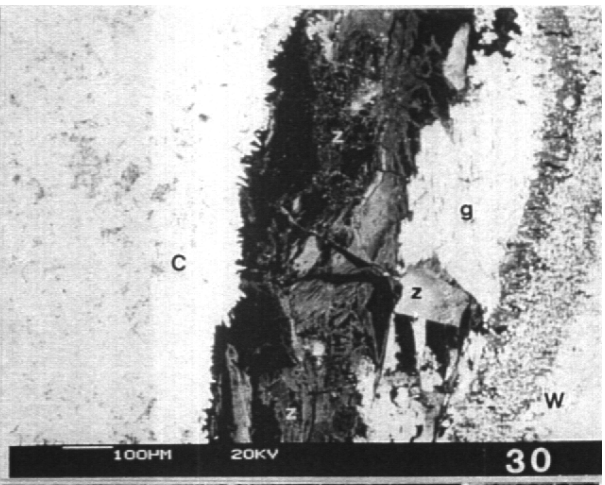
Z
g
C
Z
Z
W
100PM
20KV
30

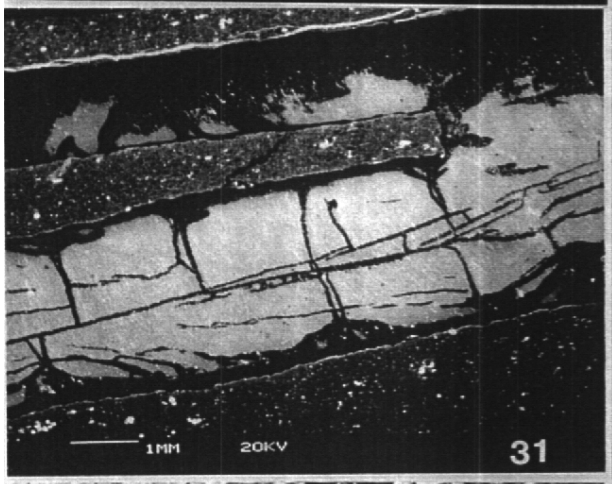
1MM
20KV
31

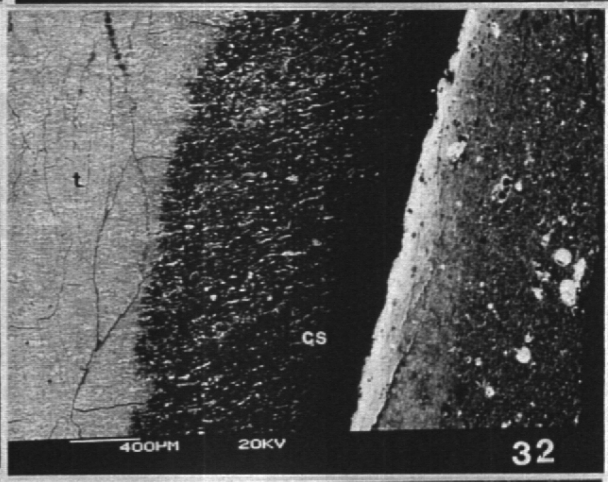
t
CS
400PM
20KV
32

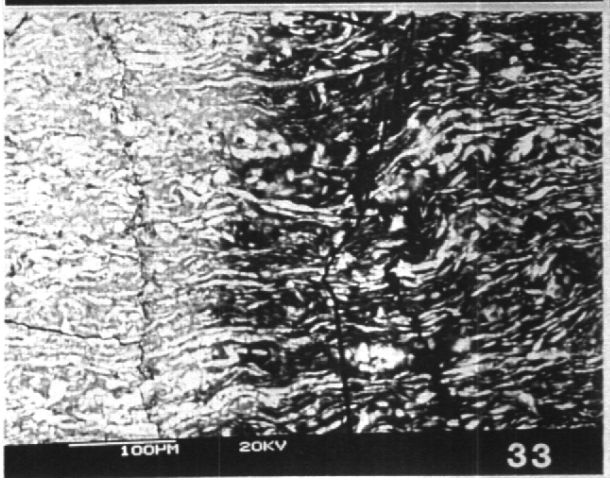
100PM
20KV
33

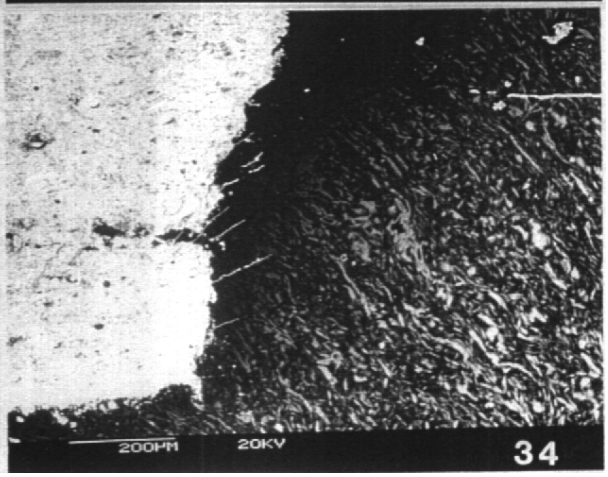
200PM
20KV
34

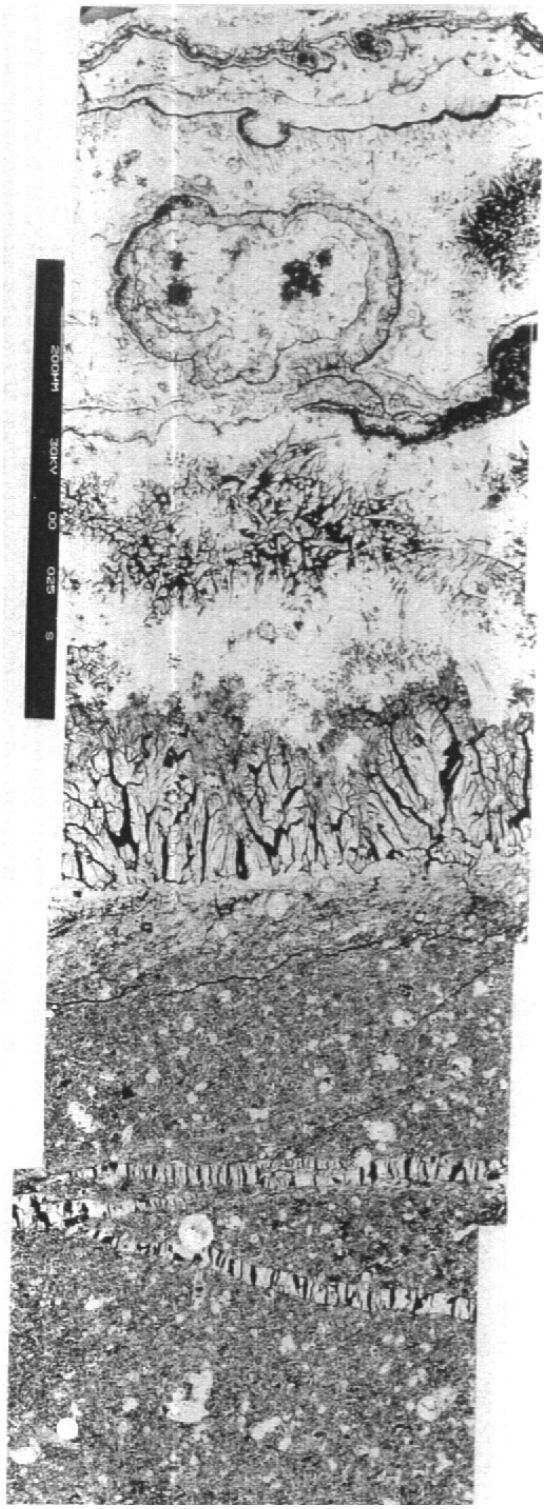

Plate 35 BSEM photomicrograph photomosaic montage of a fracture in kerogenous clay biomicritic limestone (chalk) with complex mineralisation by alternating bands of dense colloform jennite (bright) and porous fibrous ettringite and/or thaumasite. The wallrock margin shows slight alteration (brighter) due to impregnation with ettringite-thaumasite. Fine hairline veinlets of fibrous ettringite are seen within the wallrock and run parallel to the main vein. Sample A965, Adit A6, Maqarin.

Plate 36 BSEM photomicrograph showing complex interbanding of jennite and ettringite-thaumasite growth in a vein. Image shows colloform and radial fibrous jennite (bright) and fibrous ettringite (dull grey) with shrinkage cracks due to dehydration. Sample A965, Adit A6, Maqarin.

Plate 37 BSEM photomicrograph showing 'honeycomb-textured' Mg-Cr-Al-Ca-rich clay mineral coating a layer of fibrous ettringite-thaumasite with complex jennite-ettringite-thaumasite vein filling. Sample A965, Adit A6, Maqarin.

Plate 38 BSEM photomicrograph showing intergrowth of Cr-Mg-rich clay (cl) with colloform jennite (j) and ettringite (et). Note ettringite is partially replaced by jennite. Sample A962, Adit A6, Maqarin.

Plate 39 BSEM photomicrograph showing texture of the finely-laminated and microporous calcite crusts filling fractures in kerogenous, dolomitic clay biomicrite. The crusts display needle-like texture in any given growth band, with needles orientated perpendicular to the fracture walls or band walls. Bands show growth zoning due to variations in calcite composition: bright bands are Sr-rich, duller bands are pure calcite. Sample A967, Maqarin railway cutting.

Plate 40 BSEM photomicrograph showing detail of calcite crystal growth-zoning within laminated fracture lining crust depicted in Plate 39. Zoning comprises complex alternations of Sr-rich and pure calcite.

Plate 41 BSEM photomicrograph of a thin section through the edge of an altering basalt clast reacting with hyperalkaline groundwater. The surface of the clast is encrusted and replaced by a gelatinous Fe oxyhydroxide alteration product (f). Laths of plagioclase (mid-grey) within the clast, and interstitial clinopyroxene (bright) show corrosion and dissolution at the edge of the clast. A thin layer of zeolitic Ca-Na-K-Al-silicate gel (z) rests on the Fe oxyhydroxide surface and permeates the matrix of the conglomerate. Sample A968, Western Springs, Maqarin.

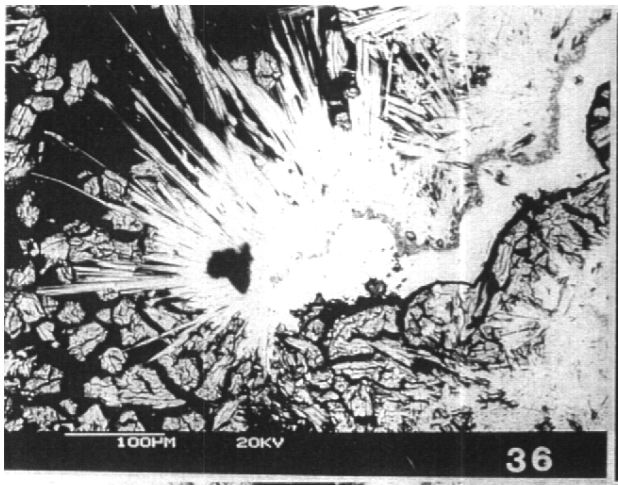
100PM 20KV
36

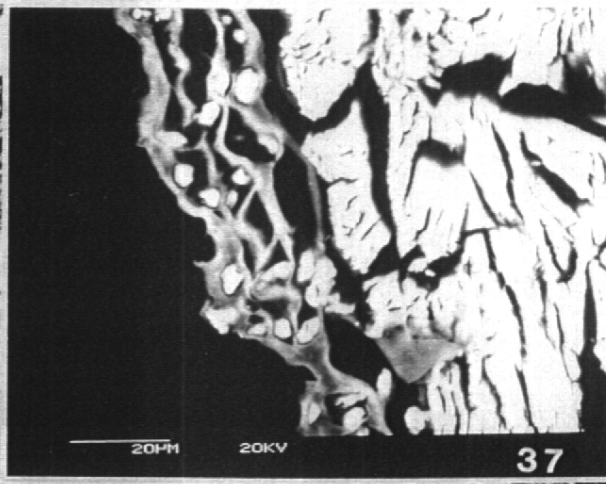
20PM 20KV
37

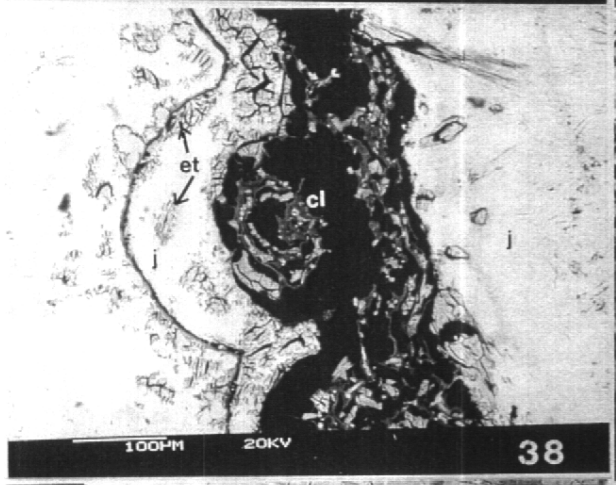
et
cl
j
j
100PM 20KV
38

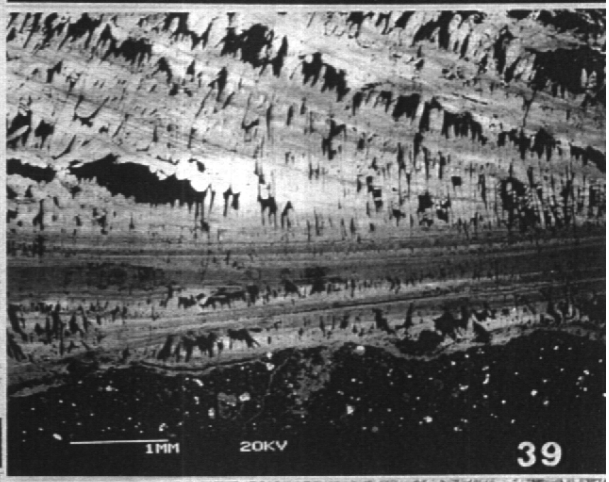
1MM 20KV
39

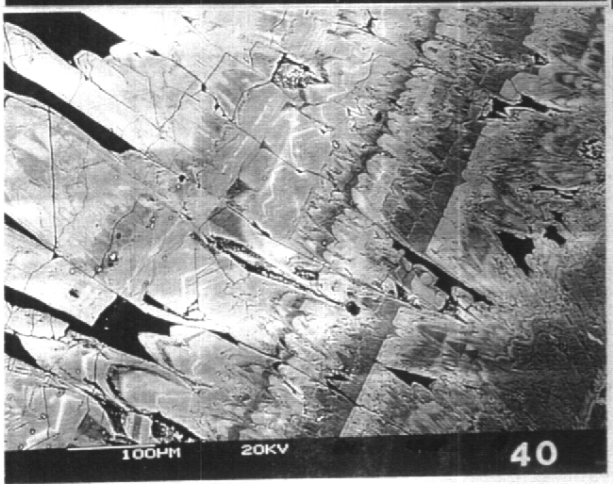
100PM 20KV
40


z
z
f
f
200PM 20KV
41

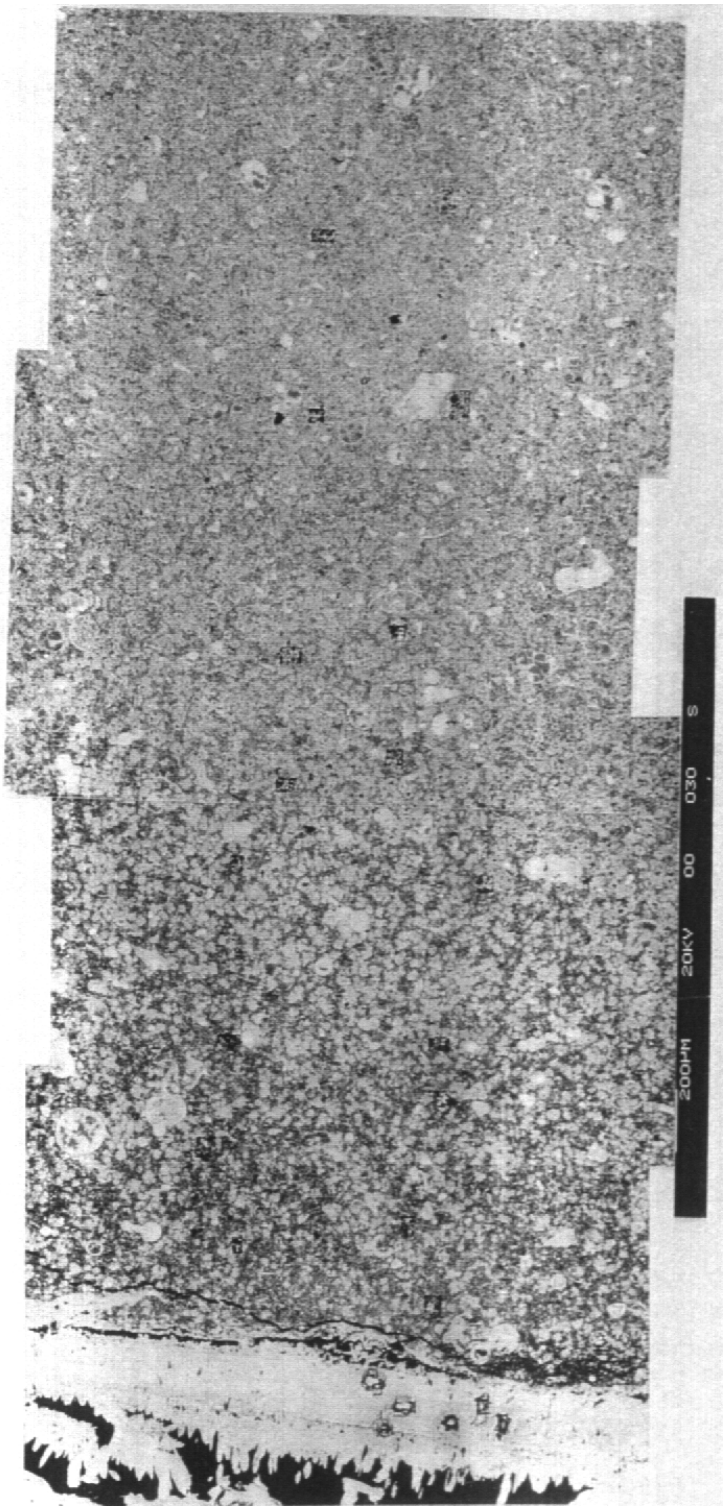

Plate 42 BSEM photomicrograph mosaic showing aragonite-calcite vein cutting dolomitic kerogenous clay biomicrite. Th host rock shows diffuse alteration for up to 2.5mm away from the vein margin. Note: square laser ablation pits are visible in the section. Sample A967, Maqarin railway cutting.

Plate 43 BSEM photomicrograph of the altered rim of a basalt clast that has reacted with hyperalkaline groundwater. The clast surface is coated with gelatinous, zeolitic Ca-Na-K-Al silicate hydrogel (z1). A later fibrous, zeolitic precipitate is nucleating on the earlier gel (z2). Calcite or aragonite (bright) cements between the fibrous zeolite where the zeolite is exposed in open intergranular porosity. Sample A968, Western Springs, Maqarin.

Plate 44 BSEM photomicrograph of thin section of silicified travertine, showing a section through the cellular fabric of silica-replaced plant stem or root. The stem/root cavities have been mineralised by calcite (bright) and the cell walls of the plant material replaced by later opaline silica. The opaline silica (grey) largely replaces the original fine-grained calcite matrix (bright) of the rock. Sample A976, Khan-es-Zabib, central Jordan.

Plate 45 BSEM photomicrograph showing the finely-laminated colloform-spherulitic texture of the opaline silica. The opal has precipitated on top of euhedral calcite (bright) and lines open cavities in the travertine deposits. Sample A974, Khan-es-Zabib, central Jordan.

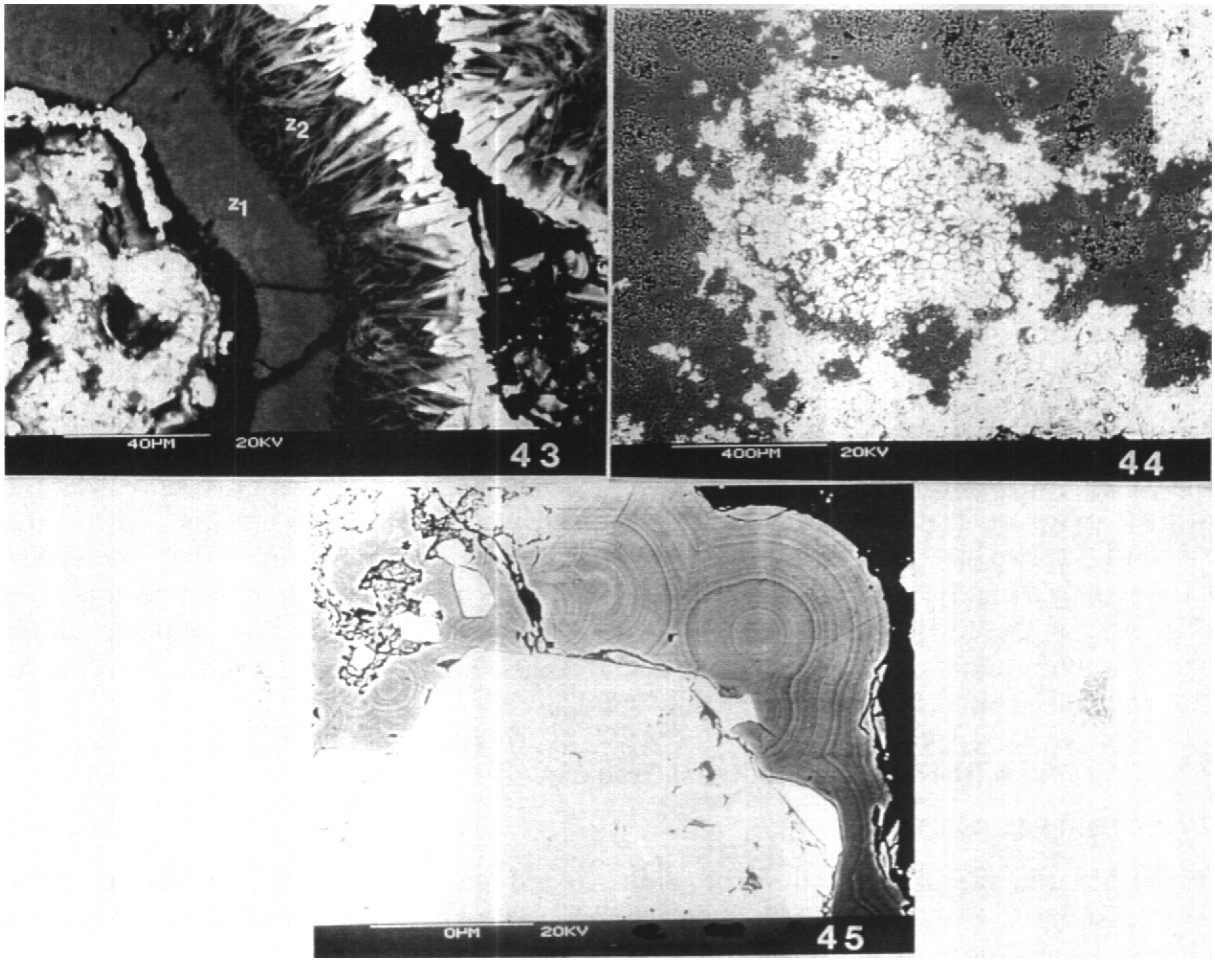

7. URANIUM DISTRIBUTION AND WHOLE ROCK GEOCHEMISTRY

E.K. Hyslop

7.1 Introduction

U distribution studies were performed on solid samples from both the Maqarin area and Central Jordan, collected during the Jordan Analogue Phase II field visit in May 1992. The distribution of U was determined by fission track analysis of polished thin sections from selected samples.

U contents of specific mineralogical components were determined by track counting using optical microscopy in comparison with U-doped glass standards irradiated alongside the samples. Identification of host phases was performed using backscattered scanning electron microscopy in conjunction with an energy-dispersive X-ray microanalyser. The fission track technique is particularly sensitive to low levels of U, <50 ppm.

This chapter presents the U distribution studies and bulk rock geochemical data, first for samples from Maqarin and then Central Jordan. The behaviour of U and other elements is discussed separately for the two areas, and then a comparison is drawn between the two hyperalkaline systems. Appendix C1 gives details of the techniques employed in the fission track analysis, and the full petrological and U distribution descriptions are given in Appendix C2. Bulk rock geochemical data are listed in Appendix C3.

Whole rock geochemical analyses for Na, Mg, Al, S, P, K, Ca, Ti, V, Cr, Mn, Fe, Co, Ni, Cu, Zn, Sr, Cd, Ba, Se, As, P and total S were routinely determined by inductively-coupled plasma - atomic emission spectroscopy (ICP-AES) - using a Fisons/ARL 3580 ICP-AES - after dissolution by HF/perchloric acid attack, followed by reduction of the solution and redissolution in HNO_3. Y, REE's, Th and U were determined by inductively-coupled plasma - mass spectrometry (ICP-MS) on the same solutions after further dilution. ICP-MS was carried out using a VG Plasmaquad2+ instrument (cf. Appendix A11) with appropriate standards. SiO_2 was determined spectrometrically (following a separate fusion) using the method based on that described by Jeffrey and Hutchinson [1]. Very high SiO_2 values obtained for two of the silicified travertine samples were checked by X-ray fluorescence (XRF) analysis and found to be reliable. Note that S has been determined as total S by ICP-AES: in altered rocks it is likely to be present as sulphate rather than sulphide and this may therefore influence some analytical totals (Appendix C3). Loss on ignition/drying was also determined up to 110°, at 450° and at 1050°C.

7.2 Uranium Distribution Studies at Maqarin

7.2.1 Samples

At the Maqarin site, five samples from Adit A6 and one from the Maqarin Station railway were examined. All samples are unmetamorphosed marl (impure organic-rich limestone) affected to varying degrees by fracturing and interaction with hyperalkaline fluids. Of the Adit 6 samples, two are highly fractured marls from close to the metamorphic zone, two from zones of discrete fracturing c.50 m from the metamorphic zone (FZ2 and FZ3 - within water sampling point M2), and a relatively unfractured sample from the adit entrance c.100 m from the metamorphic zone. The sample from the railway cutting is highly fractured and has undergone interaction with hyperalkaline groundwaters.

7.2.2 Uranium distribution in Adit 6

The five samples from Adit 6 represent a sequence from highly altered marl close to the metamorphic zone to relatively unaltered marl unaffected by fracturing and alkaline fluid interaction.

Sample A960 (MQN2) is highly veined and altered marl collected 2.5 m from the metamorphic zone. The fractures are surrounded by calcified alteration zones several tens of millimetres wide, over which the distribution of U has been affected. Dispersed U in the relatively unaltered marl matrix away from the fractures is typically present at levels of c.16 ppm U, with concentrations of c.40-50 ppm in phosphatic (collophane) fossil debris. U in the calcified alteration zone is more uniformly distributed at levels of c.23 ppm U. BSEM indicates the presence of fine grained apatite in this altered material, with which the U is probably associated. Close to the vein, primary collophanic material has undergone dissolution (Plate 46), which may have released U to be redistributed into the neoformed apatite in the altered wallrock. Secondary concentrations of U are associated with specific mineral phases formed at vein edges and on the wallrock margins (Plate 47). CSH-gels contain 100-150 ppm U (also Cr, Ni, Zn, V and Fe detectable by BSEM-EDXA) and Ca-zeolite contains 25-30 ppm U.

Two profiles of U levels in marl matrix obtained by fission track counting in sample A960 are shown in Figure 7.1. The profiles represent traverses from the fracture edges inwards through the porous and highly altered wallrock, into less altered host marl. Although there is a significant range in the U content of the altered wallrock, U concentrations are generally enhanced in the porous zone immediately adjacent to the fracture surface (range of U concentration = 30-55 ppm), and within parts of the calcified alteration zone (range of U concentration = 20-70 ppm), compared to the variability in the background unaltered marl (range of U concentration = 15-30 ppm).

Sample A962 (MQN3) was collected 11 m from the metamorphic zone. It has also undergone intense matrix alteration associated with series of microfractures, and shows similar features to A960. U is dispersed throughout the matrix of relatively unaltered marl at levels of c.14 ppm U, whilst in the calcified alteration zones it reaches slightly higher levels of c.16 ppm U. BSEM also indicates concentration of Cr, Ni, Zn, Cu, Se and Fe in the vein wallrock. U is present in a hydrous Ca-Si-Al phase in the vein margins at levels of up to 11 ppm U.

Samples A963 and A965 are from fracture zones in the adit approximately 50 metres from the metamorphic zone. They contain abundant narrow veins but do not display such well developed wallrock alteration as samples A960 and A962.

Sample A963 (MQN4) was collected 50 m from metamorphic zone at fracture site FZ3. It contains narrow alteration zones generally <1 mm wide. In the less altered matrix dispersed U is present at levels of c.13 ppm U. Altered wallrock adjacent to veins has undergone slight depletion (11-13 ppm U). Low levels of U are present in vein minerals (<7 ppm U).

Sample A965 (MQN23) is from 65 m from the metamorphic zone (Fracture site FZ2, water sample site M2). It contains a network of veins containing calcite, Cr and Zn-bearing clay, ettringite, thaumasite and jennite. U is present in fibrous jennite in void fills in the central parts of veins at levels of 10-15 ppm U (Plate 48). U is not present in any other vein phases. Dispersed U in the marl matrix is present at levels of c.10 ppm. No difference in U levels is detected in the altered vein wallrock.

Sample A961 (MQN10) was collected 103 m from metamorphic zone (c.7 m inside adit entrance) and represents a relatively unaltered ‘background’ marl. It contains no visible alkali

alteration or veining. U is dispersed throughout the matrix at levels of 12-16 ppm U with no evidence of remobilisation.

7.2.3 Uranium mobility in the Adit 6 marls

Data from the U distribution study in Adit 6 using fission track analyses are summarised in Figure 7.2. There appears to be little significant variation in the whole rock U content along the adit, from the metamorphic zone ('cement zone'), through the metamorphic zone - marl interface, and throughout the host marl. The measurements along the adit are essentially along the same stratigraphic horizon, and any variations observed probably just represent background 'scatter'.

In contrast, bulk rock analyses (ICP-AES and ICP-MS) appear to show an enhanced U level close to the metamorphic zone (Figure 7.3). 32 ppm U was measured in sample A960, close to the metamorphic zone, compared to 12 ppm measured in the altered rocks at the M2 site and a value of 16 ppm for the unaltered 'background' marl sample taken from over a hundred metres from the metamorphic zone. However, unlike fission track analyses which refer only to dispersed U in the marl matrix, whole rock ICP-MS data may include U concentrations in for example, collophanic debris. The high value measured in the case of sample A960 is almost certainly due to the high U concentrations associated with phosphatic (collophane) fossil debris in this sample (Section 7.2.2, Appendix C2).

The data do not therefore suggest large-scale mobilisation of U around the metamorphic zone. There is however, evidence that small-scale mobilisation has occurred within the wallrock adjacent to individual fractures and veins. The fission track results indicate that in sample A960, U distribution has been affected over a distance of several tens of millimetres from the vein. Uranium mobilisation in the marl appears to be the result of redistribution of finely dispersed U associated with fine grained organic matter in the marl matrix, and breakdown of collophanic detrital material containing higher concentrations of U. In the altered vein wallrock U is redistributed and associated with fine grained secondary Ca-phosphate in the altered rock matrix.

7.2.4 Geochemistry of samples from Adit 6

Figure 7.3 shows the variation of Ni, Zn, Cr, Cu and U in bulk rock samples along Adit 6. Compared to the unaltered background sample from the adit entrance (A961), all of these elements (except Cu) show enhanced levels in samples adjacent to the metamorphic zone. The reasons for the apparent enhancement in U close to the metamorphic zone have been discussed in the previous section. Full geochemical data are presented in Appendix C3, which shows that most other elements show a random variation along the adit profile (representing initial lithological compositional variation). This would appear to rule out the possibility of the decreasing element abundances outlined above resulting from initial sedimentological variation between the samples. The enhancement in those elements in marl from close to the metamorphic zone is therefore considered genuine. It is notable that the rare earth elements also show a pattern of decreasing abundance related to distance from the metamorphic zone.

Samples A965 and A966 were each split into 3 fractions prior to bulk rock geochemical analysis (Appendix C3). Fraction (i) represents the most highly altered wallrock 0-5 mm from vein margins, (ii) is altered wallrock from >5 mm from the vein, and the bulk sample (denoted on the table by the sample code only) represents the least altered or host material. The elements plotted on Figure 7.2, when considered for sample A965, show inconsistent changes between the 3 fractions. Ni and Cu are strongly depleted in both the altered wallrock

fractions, whilst Cr is enhanced. Data for U and Zn are equivocal. The sample from the railcut (A966) shows enhancement of Ni and Cu in the wallrock fraction - the opposite of A965 - and depletion of Zn. It would therefore appear that elements have behaved differently in different parts of the system at Maqarin, consistent with the behaviour of U in Adit 6.

Two samples were analysed from beyond the metamorphic zone at 224 metres in Adit 6 (A970 and A971). They have similar compositions to the other marl samples from the adit, though with slightly higher levels of Cr and Cu. The rail cut sample (A966) is also similar in composition to the Adit 6 samples, and is within the range of the element variation shown in Figure 7.2.

7.2.5 Element mobility in the Adit 6 fracture system

Bulk rock geochemical analysis of samples from the metamorphic zone in Adit 6 (data from Jordan Phase 1 study) indicates that the compositions of the metamorphic rocks are similar to the unmetamorphosed marls investigated in this study. Ca and Si concentrations are enhanced in the metamorphic zone primarily as a result of decarbonation (loss of CO_2) of the marl and the formation of metamorphic calcsilicate minerals. Bulk rock analysis confirms observations from fission track analysis, indicating little, if any, significant variation in bulk U content from the metamorphic zone and along the host marl section. However, fission-track registration observations show enhanced tracks, indicating significant enhancement of uranium, along the margins of fractures mineralised by CSH phases near the contact with the metamorphic zone. Further down-gradient in the marl (c. 50 m from the metamorphic zone) reduction in fission-track density in the wallrock immediately adjacent to fractures mineralised by high pH phases indicates that some uranium has been mobilised. In these fractures, fission track analysis reveals that uranium has been taken up by secondary jennite mineralisation. In contrast, ettringite-thaumasite mineralisation, present in some veins, contains negligible uranium. This is confirmed by microanalyses of secondary CSH minerals, thaumasite and ettringite reported in Chapter 8.

Bulk rock analyses (Figure 7.3) may suggest that some enrichment of Cr, Ni and Zn in the metamorphic zone, compared to the down-gradient marl. However, there are too few data to realistically evaluate systematic variation in trace elements along the Adit 6 profile.

The petrographic and geochemical evidence indicates no major (bulk) transport of uranium in hyperalkaline groundwater discharging from the metamorphic zone, and flowing through fractures in the marl. However detailed fission track registration and petrographic analysis does demonstrate that uranium is remobilised locally from primary matrix organic matter into secondary CSH minerals, and consequently, is redistributed at least on a minor scale within the wallrock, close to the fracture.

7.2.6 Railway cutting locality

One sample of fracture alteration was examined from the railway cutting locality (A966; MQN20). It is an unmetamorphosed marl (similar to the Adit 6 samples) which is highly veined and altered as a result of hyperalkaline water interaction. Dispersed U throughout the matrix averages c.13 ppm, and small concentrations of 30-50 ppm U are present in detrital collophane. Altered wallrock around veins is slightly depleted in U with levels of 9-10 ppm. No U is present in vein minerals (mainly ettringite and thaumasite). Chemical analyses of bulk rock samples from the railway cutting locality show values of 13-15 ppm U, similar to levels in the marls from Adit 6.

The evidence from the railway cutting supports that from Adit 6. The sample has relatively low U, consistent with alteration a short distance (perhaps several tens of metres) from a metamorphic zone. The vein wallrocks show slight U depletion and the vein minerals have little or no U content, similar to the samples from the c.50 m zone in Adit 6.

7.3 Uranium Distribution Studies in Central Jordan

7.3.1 Samples

Samples were collected from two localities in Central Jordan, the Daba roadcut and the Khan-ez-Zabib mountain. These localities have similar lithologies to those at Maqarin, but show evidence of having undergone fracturing and interaction with hyperalkaline fluids in the geological past. The Central Jordan localities may provide an indication of the later stage processes of hyperalkaline interaction and the ageing behaviour of such products.

7.3.2 Khan-ez-Zabib locality

The four samples from Khan-ez-Zabib represent a sequence of ancient Pleistocene Wadi deposits, formed under similar conditions to those presently occurring at Maqarin, dated at 700-900 ka BP [2]. These interbedded breccias and travertines contain evidence of several generations of carbonate cementation, and opaline silica precipitation. The rocks are commonly green in colour and enriched in Cr.

7.3.3 Uranium distribution at Khan-ez-Zabib

Sample A974 is a siliceous travertine composed of mixed granular carbonate and clays with variable amounts of U up to c.30 ppm U. The clays contain Cr, Zn, Cu, Fe and Mg detectable by BSEM-EDXA. Later carbonate has developed as coarser grained calcite which has negligible U content. Opaline silica is a major phase forming finely laminated coatings and botryoidal void infills. It contains significant levels of U, typically 40-60 ppm, though up to 160 ppm at void edges (Plate 49). Fossilised plant material is also present, replaced by carbonate, silica, clays and phosphate. It is enriched in U with typically 100-130 ppm U (Plate 50).

The travertine is overlain by a breccia (A975) containing clasts of chert, marl, marble and earlier Cr-rich deposits. Clasts of marl have altered margins with depletion of U from 6-9 ppm U in the centres to 1-3 ppm U in the margins. The breccia is cemented by granular carbonate containing negligible U, and opaline silica containing 7-15 ppm U. Fragments of collophane in the clasts contain levels of 50-100 ppm U but appear to be degraded and partially replaced by the silica.

Sample A976 is a further travertine deposit overlying the breccia. It consists of brown granular carbonate, much of which has replaced plant root material prior to cementation by opaline silica. The carbonate contains patchy U of up to c.40 ppm U. Silica is present as linings on open voids where it generally contains 25-50 ppm U, though up to 75 ppm U in places. Late ettringite and Cr-rich barite are present.

Sample A977 is a breccia containing clasts of chert with highly altered margins. The less altered central parts of chert clasts contain up to 5 ppm U, whilst the outer 2-3 mm has a calcified fringe containing 5-6 ppm U. The immediate margins of the chert contain higher concentrations of 9-12 ppm U, and 16-18 ppm where in contact with open voids. The carbonate matrix of the breccia contains low U (5-6 ppm U), and fossilised cellular plant material contains 50-100 ppm U.

7.3.4 Discussion of Khan-ez-Zabib

The Khan-ez-Zabib deposits have formed as a result of precipitation from ancient hyperalkaline groundwaters interacting with wadi-type deposits. They are dominated by several generations of carbonate precipitation and opaline silica infilling voids. Interaction of the alkali fluids with clasts of marl has resulted in substantial depletion of U from clast margins, which may represent leaching of U from sedimentary phosphatic hosts (collophane fossil debris). Chert clasts show the opposite effect with enhancement of U at margins, in a broad calcified fringe up to 3mm wide, containing up to 20 ppm U compared to a normal content of c.5 ppm U. Higher U concentrations occur adjacent to open voids.

Hydrated silica precipitates contain the most significant concentrations of U, commonly 20-80 ppm U and up to 160 ppm U. U levels in silica are particularly enhanced adjacent to open voids. Matrix carbonate has lower and more variable U contents, and levels of up to 40 ppm U are present in patches commonly associated with inclusions of fine grained clays (commonly metal bearing) and phosphate. Late barite and ettringite, despite containing other trace metals do not contain significant U.

7.3.5 Daba roadcut locality

Four samples from the Daba roadcutting were chosen to represent the transition from unmetamorphosed marls to fractured, veined and altered marls affected by high pH fluids, and finally to a metamorphosed marl also affected by alkali fluids. As with the Khan ez Zabib samples, these rocks have undergone alteration and metamorphism in the geological past and as such represent an ancient analogue for the processes presently occurring at Maqarin.

The samples are:

A980 Chalky marl, unmetamorphosed with little alkali interaction

A981 Unmetamorphosed marl containing veins from interaction with alkali fluids.

A982 Unmetamorphosed chalky marl, highly veined and affected by alkali fluids.

A972 Fractured veined highly altered metamorphosed rock from anticline crest.

Samples A980, A981 and A982 are lateral equivalents from the same bedding plane, sampled over a distance of c.15 metres, and thus provide a similar profile to the samples examined in Adit 6 at Maqarin.

7.3.6 Uranium distribution at Daba

Sample A980 is a chalky marl containing rare calcite veins. The marl matrix contains low levels of <3 ppm U, with small patches containing typically 20-40 ppm U (though up to 70 ppm U) related to collophanic replacement of microfossils. Large voids are filled by relatively coarse grained clear calcite with negligible U.

Sample A981 contains common veins forming a fracture network, with altered wallrock showing calcification. The calcified wallrock in the PTS is impervious to resin, unlike both the vein-filling phase and the less altered marl. The fractures themselves are open and porous. The relatively unaltered marl matrix contains c.1.5 ppm U, with patches of phosphatic fossil material containing 20-40 ppm U. Altered wallrock contains slightly enhanced levels of c.2.5 ppm U. Vein fillings have negligible U.

Sample A982 contains vuggy open veins. The rock matrix contains <3 ppm U, though patchy fossil material replaced by collophane has 20-45 ppm U. Altered wallrock adjacent to veins has enhanced levels of 3-4 ppm U. The main vein fill contains no U, though granular linings along wallrock and void margins have 10-20 ppm U. The U appears to be associated with a fine mixture of hydrous Ca-Al-Si zeolite with Fe-Cr clay.

The highly altered sample A972 is highly veined. The rock matrix contains low U values (<1 ppm), but small patchy fossil material has 30-50 ppm U (Plate 51). The major vein filling (?ettringite) has <1 ppm U. U levels in the vein wallrock appear to be unaffected.

7.3.7 Discussion of Daba samples

The samples examined from Daba represent a single chalky marl lithology with low levels of dispersed U in the matrix of <3 ppm U, and common microfossil debris containing several tens of ppm U, related to phosphatic material and possible hydrocarbon. Vein fillings are largely calcite and ettringite, both of which have negligible U. Some vein margins and open voids are lined by a mixture of zeolite and metal-bearing clay that contains 10-30 ppm U.

As the lithology has become increasingly fractured and affected by alkali fluids, alteration zones in vein wallrock become wider and are calcified (also less porous than the original marl host rock). This altered wallrock contains slightly enhanced levels of U compared to the surrounding less altered host rock. U is generally absent from the vein phases, but is present in a zeolite-clay mixture at vein margins.

7.3.8 Bulk rock geochemistry of the central Jordan samples

Chemical data are presented in Appendix C3. The samples from Daba are generally similar to the marls at Maqarin, though slightly richer in Ca reflecting their more chalky nature. Lower LOI (at 450°C) and S may reflect different organic carbon components. The Daba rocks also have lower Se, As and REE abundances.

The travertine from Khan ez Zabib (sample A976) has a distinctly different composition from the marls, with significantly lower Al, P, Ti, Fe, Ni, Cu, Sr and REE. It has higher Cr, Si and U than the marls.

7.4 Comparison of Samples from the Central Jordan and Maqarin Localities

The Daba sequence of increasing fracturing and alteration in an impure marl is analogous to the sequence of samples examined from Adit 6. The ancient wadi deposits at Khan ez Zabib appear to be the products of hyperalkaline groundwater discharges similar to the present day hyperalkaline seepages occurring at the Western Springs locality at Maqarin.

The samples from Central Jordan show some similarities to those from Maqarin. Fractured marls at Daba have undergone a similar enhancement of U in calcified wallrock, and the presence of U in zeolite and clay at vein margins is very similar to the altered rocks from close to the metamorphic zone in Adit 6. Alteration of marl clasts in breccias from Khan-ez-Zabib show a similar concentration of U in calcified wallrock to those observed in Adit 6.

The presence of relatively high levels of U in opaline silica has not been recorded at Maqarin, and it may represent an important stage in an evolved hyperalkaline groundwater system. This aspect would appear to merit further study.

7.5 References

[1] P.G. Jeffery and D. Hutchinson, *Chemical Methods of Rock Analysis,* Pergamon series in Analytical Chemistry, Volume 4, 3rd edition, Pergamon Press, Oxford, 1981.

[2] I.D. Clark, H.N. Khoury, E. Salameh, P. Fritz, Y. Gösku, A. Wieser, C. Causse and J-Ch. Fontes, *Travertines in Central Jordan: Implications for Palaeohydrology and Dating,* Proceedings of the IAEA/UNESCO Symposium on Isotope Techniques in Water Resources Development, 1992.

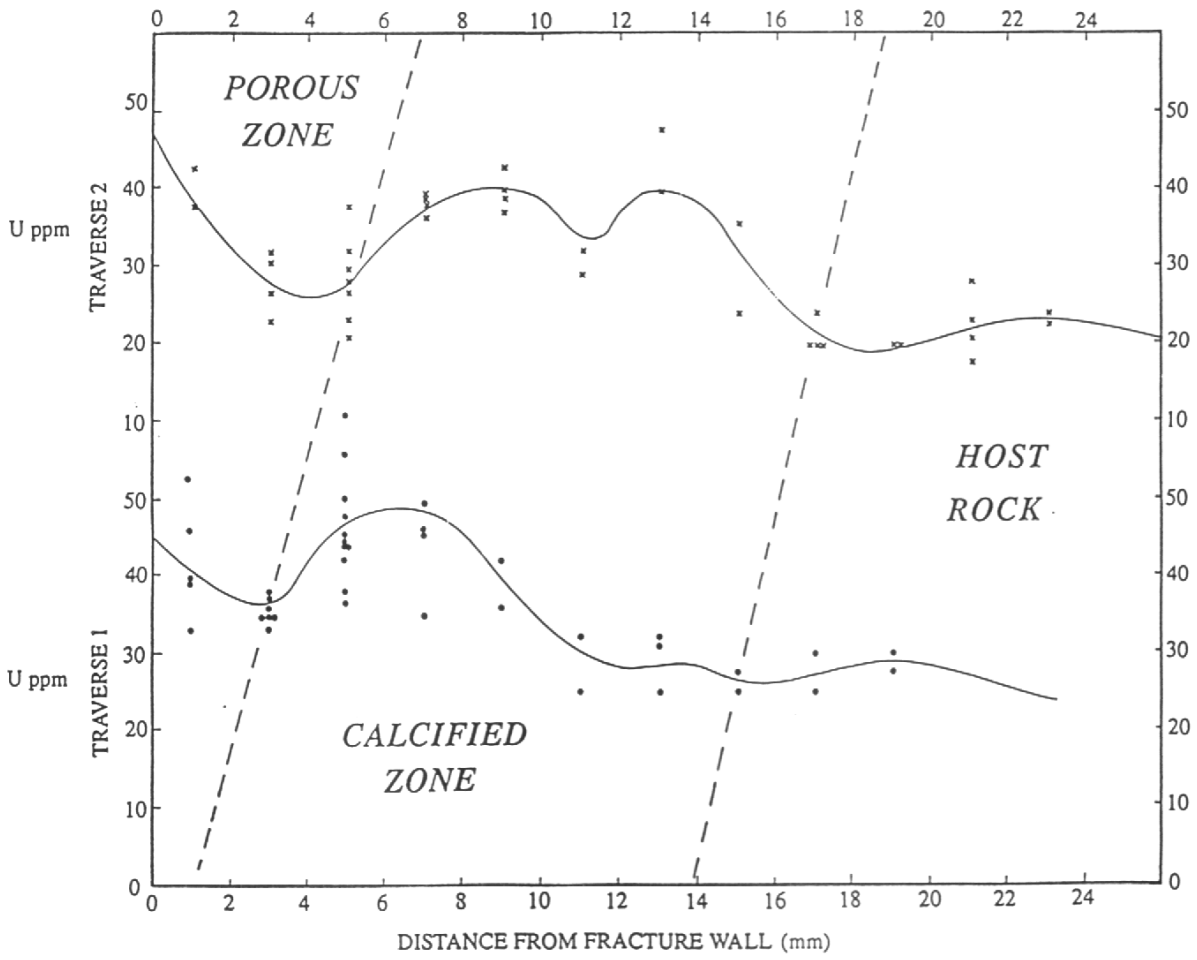

Figure 7.1 U concentration profiles along two traverses across altered wallrock in Maqarin sample A960 (bituminous marl near edge of metamorphic contact zone in Adit A6). Both traverses start from the vein edge (left hand side of figure) outwards through the porous wallrock and calcified zones into the marl host rock (right hand side of figure). U data are in ppm and were obtained from track counting. Note enhancement of U in calcified zone (concentrated towards the vein side), and increase in porous zone at immediate fracture edge.

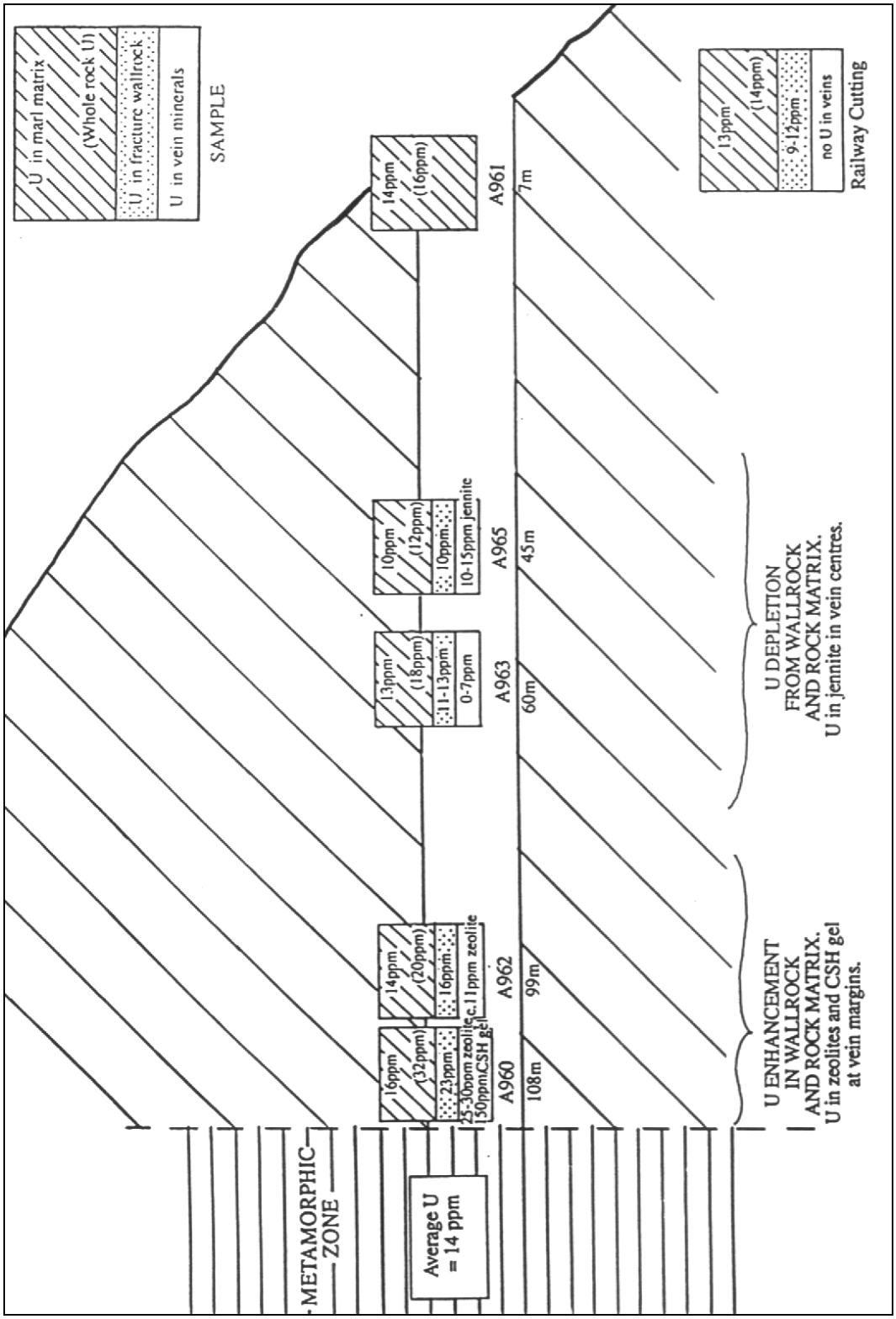

Figure 7.2 Diagrammatic section through Adit A6 at Maqarin showing U data (in ppm) for sample examined in this study. Each sample is represented by a box showing the various components (a key is shown in the top right hand corner). The sample from the railway cutting (A966) is shown for comparison, bottom right.

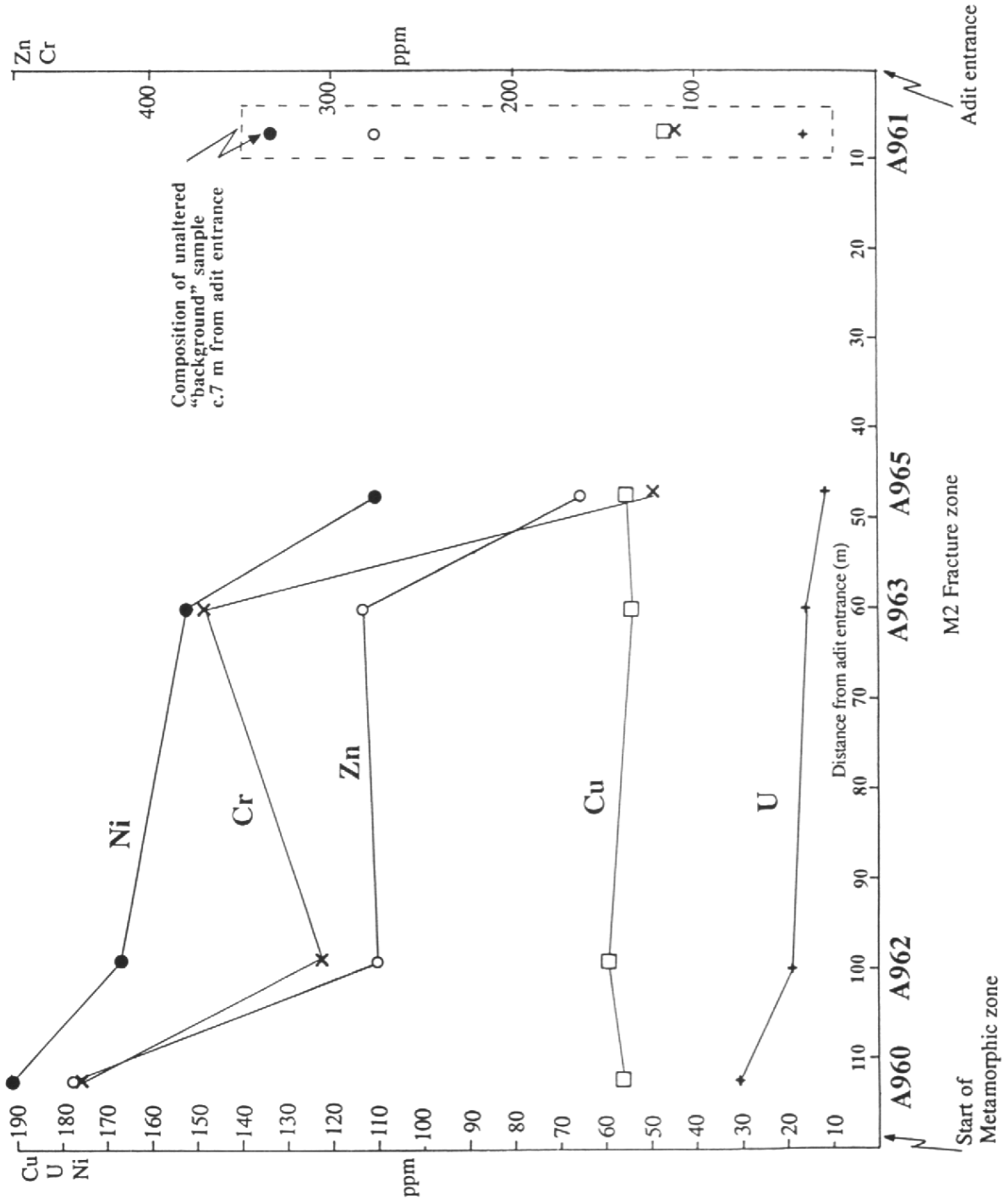

Figure 7.3 Chemical profiles across Adit A6 for U, Ni, Cu, Zn and Cr from analysis of bulk rock samples (determined by ICP-AES and ICP-MS). Note the separate scales for U, Ni and Cu (left side) and Zn and Cr (right side).

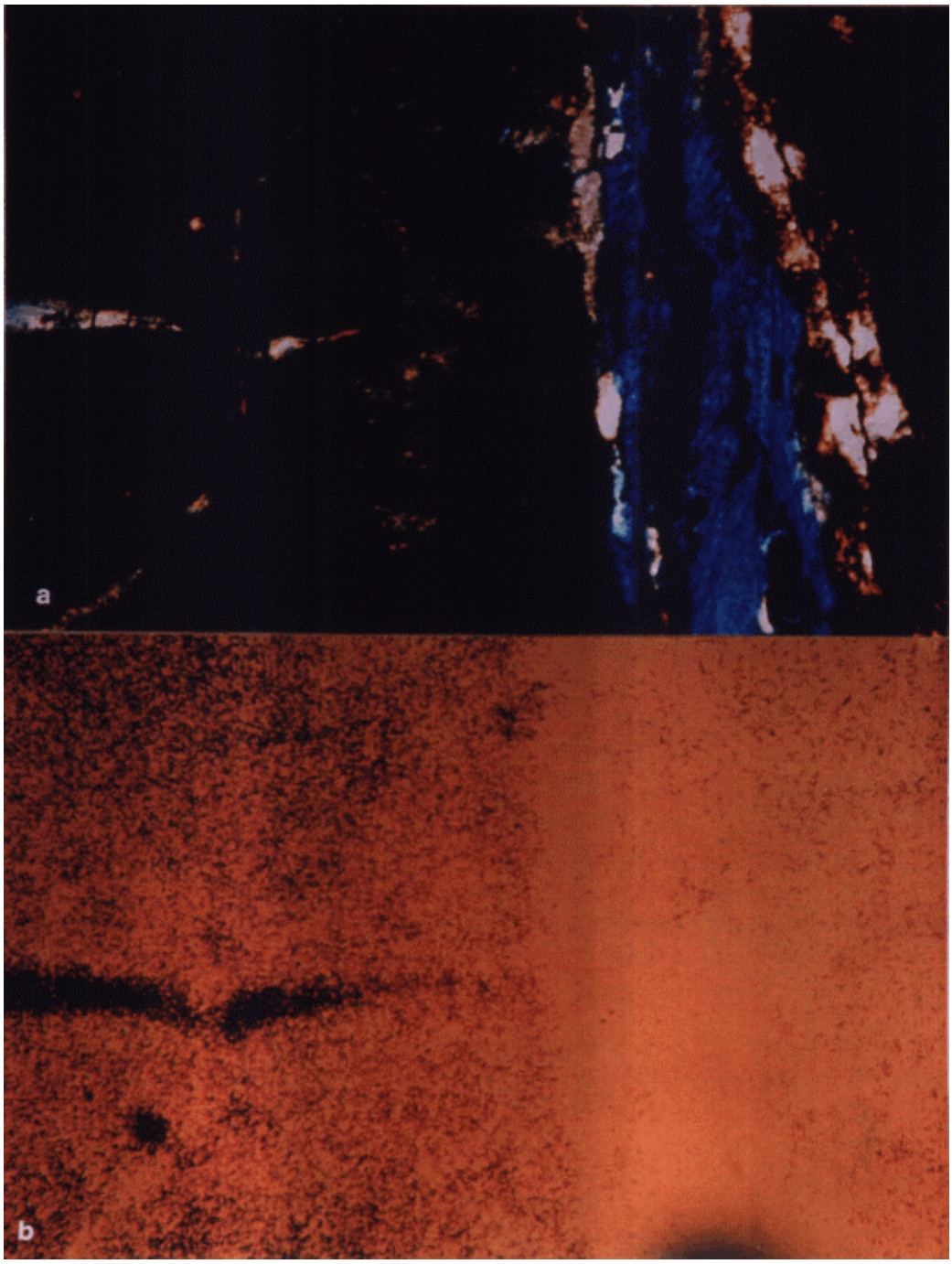

Plate 46a Edge of a fracture in Sample A960 from adjacent to the metamorphic zone in Adit A6, Maqarin. The central part of the fracture is open (blue-coloured resin). The dull central part of the photograph is a complex mix of calcite, ettringite, thaumasite and gypsum. The marl matrix (left-hand side) is highly altered and semi-opaque. An elongate phosphatic fossil fragment (clear band centre-left) is present in the altered wallrock.

Plate 46b Fission track print of Plate 46a showing moderate uniform density of tracks in altered wallrock (equivalent to c.30ppm U) and higher concentration in fossil fragment (50-150ppm U). The phosphate becomes degraded towards the fracture and the U content is reduced. The vein material has a low U content associated with fine-grained apatite.

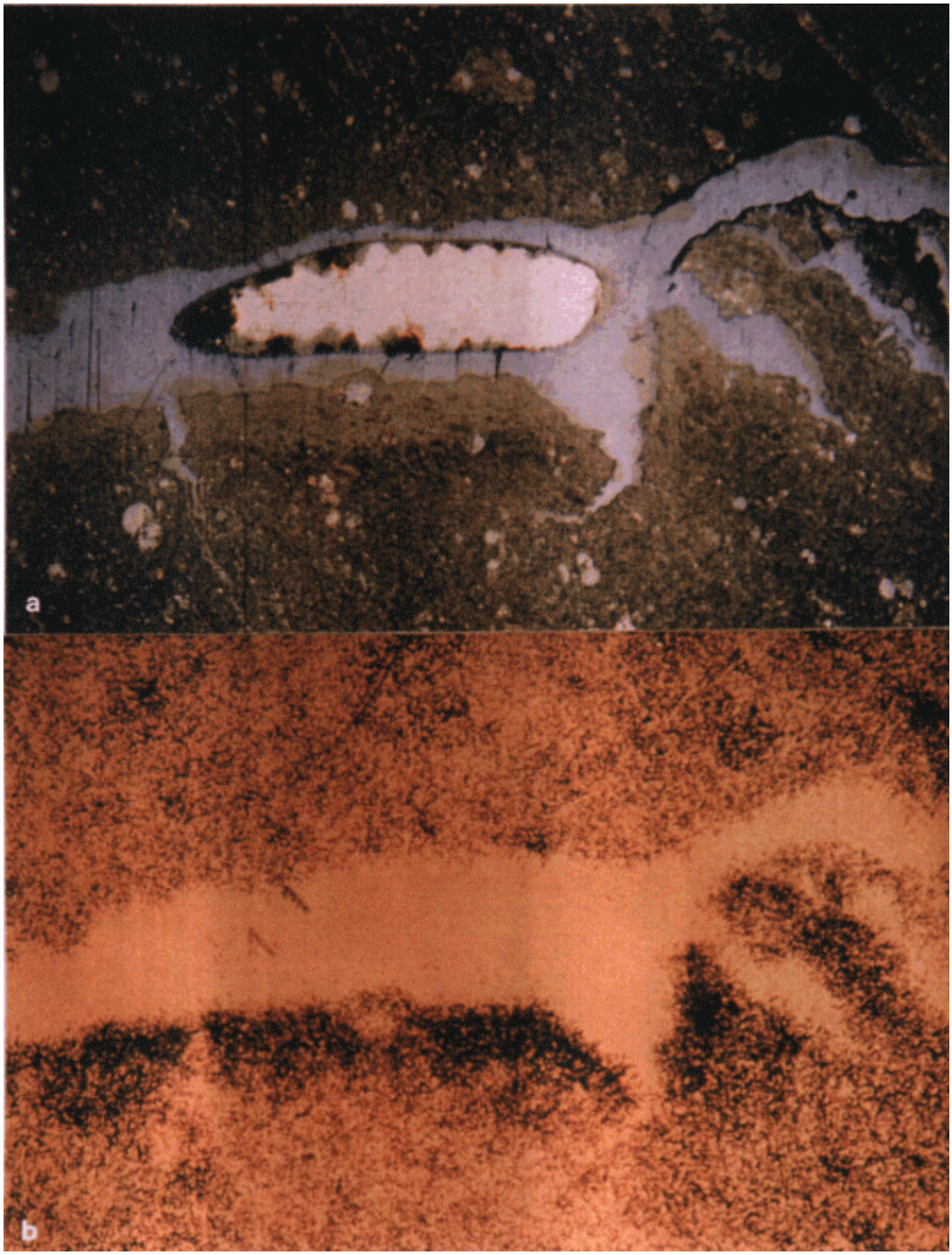

Plate 47a Sample A960 from adjacent to the metamorphic zone in Adit A6, Maqarin, showing an open fracture in altered porous marl wallrock. The open fracture is defined by blue dye resin (light area the centre is a hole in the thin section). The fracture margin has a CSH gel deposit (light yellow-grey). Mixed reflected and transmitted light. Field of view 1.8mm across.

Plate 47b Fission track print of Plate 47a showing U concentrations (at levels of c.150ppmU) in CSH gel along the fracture walls. The altered marl wallrock contains a uniform U concentration of c.25ppm U.

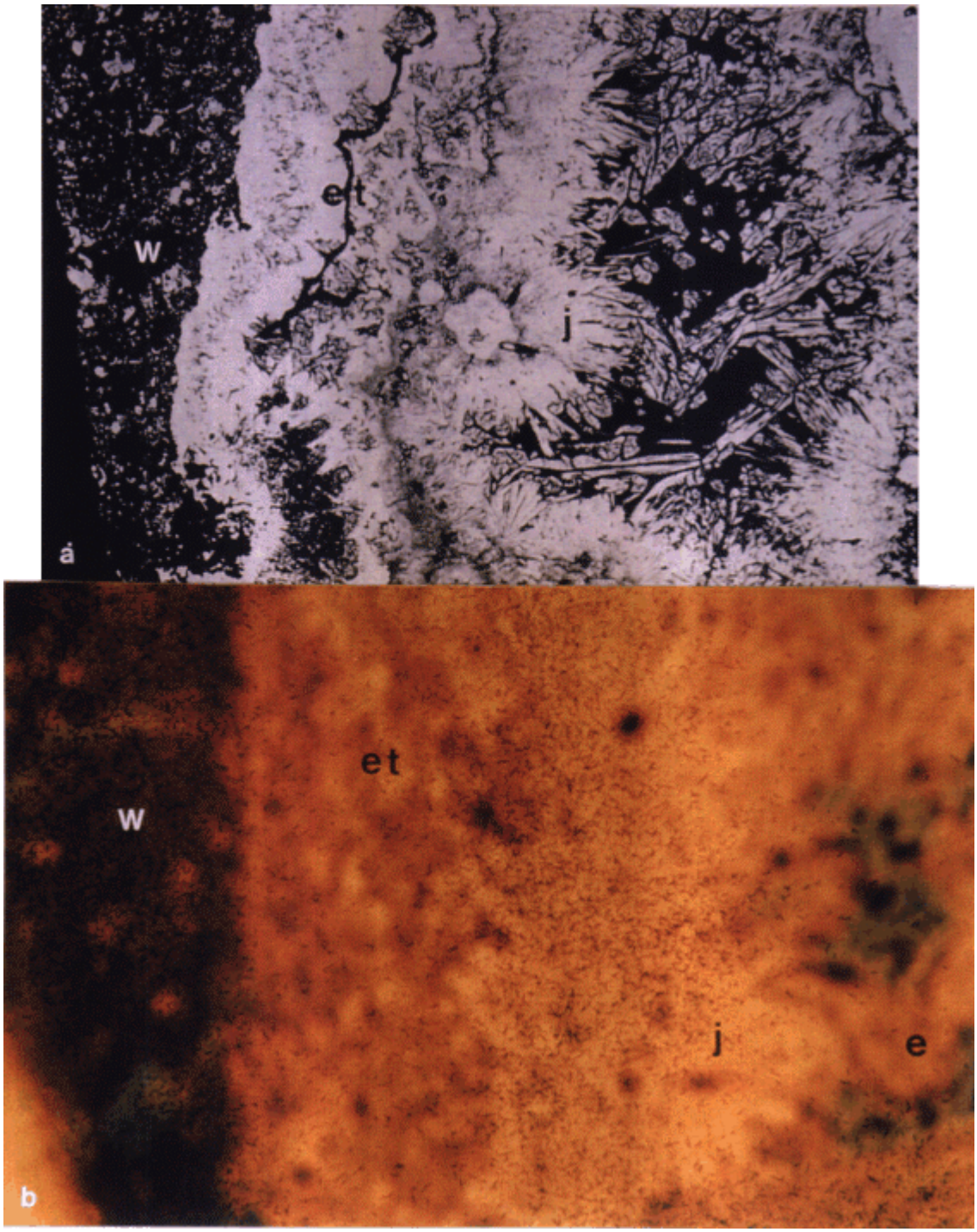

Plate 48a BSEM photomicrograph showing the edge of a vein in Sample A965 from the c.50m fracture zone in Adit A6, Maqarin. The vein has a complex fill with early calcite-clay mixture coating the wallrock (w), itself coated by ettringite-thaumasite (et). Open vugs in the vein centre are lined by radial fibrous jennite (j) with a later filling of tabular-shaped ettringite (e). Field of view 20mm across.

Plate 48b Fission track print overlay of Plate 48a showing the presence of fission tracks exclusively in jennite (equivalent to 10-15ppm U). No (or very low) U is present in other vein phases. The altered marl wallrock contains c.10ppm U.

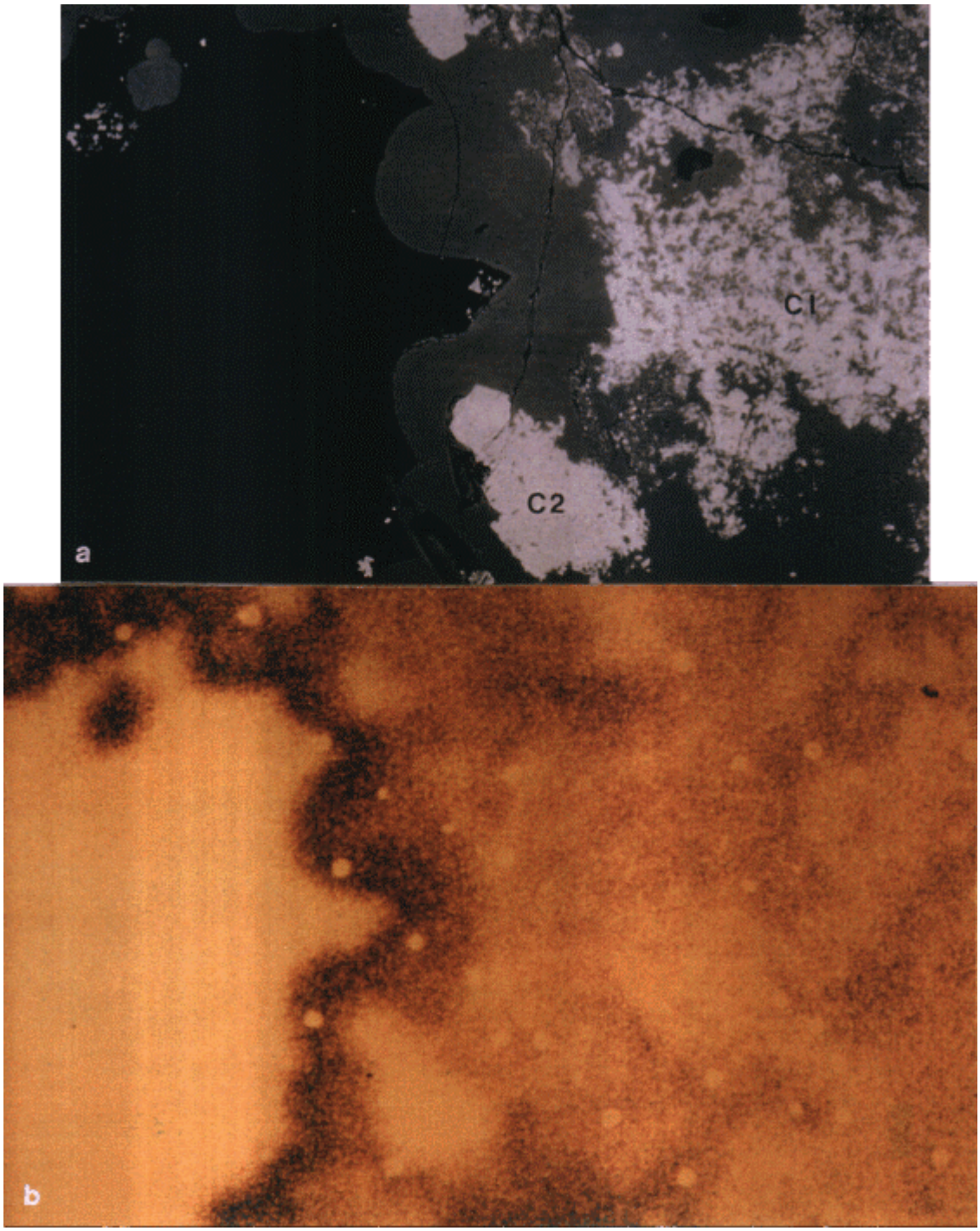

Plate 49a BSEM photomicrograph showing the edge of an open void in a travertine deposit from Khan-es-Zabib in central Jordan (Sample A974). Two generations of carbonate are present, an early mixture with clay (C1-centre right) and later coarser-grained, more pure calcite (C2-bottom centre). Opaline silica (dull grey) forms extensive finely-laminated coatings and botryoidal masses around void margins. Field of view 2.2mm across.

Plate 49b Fission track print of Plate 49a showing presence of high levels of U in the opaline silica, with the highest concentrations at vug edges (concentrations range from 60-80ppm U, with up to 150ppm U at edges). Early carbonate-clay mixture has variable U of up to c.60ppm U, whilst later calcite contains negligible U.

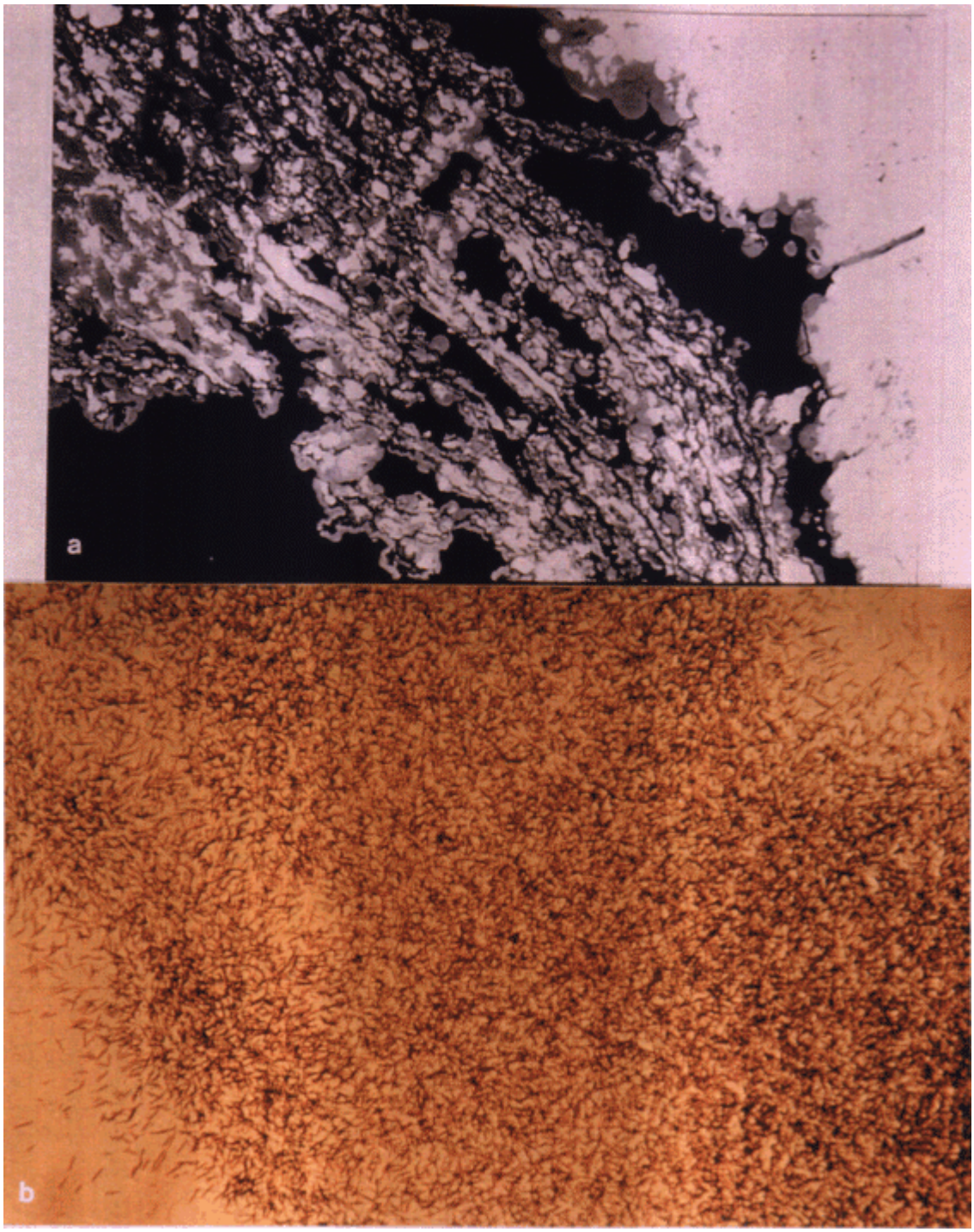

Plate 50a BSEM photomicrograph of part of a fossilised plant root in a travertine deposit (Sample A974). The organic materials has been replaced by a mixture of carbonate and phosphate, partly preserving the original fibrous texture. Thin coatings of later silica (dark grey) are present in the root material and on the carbonate travertine matrix (light material, left-hand side). Field of view 1mm across.

Plate 50b Fission track print of Plate 50a showing a concentration of U in the fossil material (50-150ppm U associated with phosphate) and in the silica coatings within the plant fragment and coating the carbonate matrix (60-80ppm U).

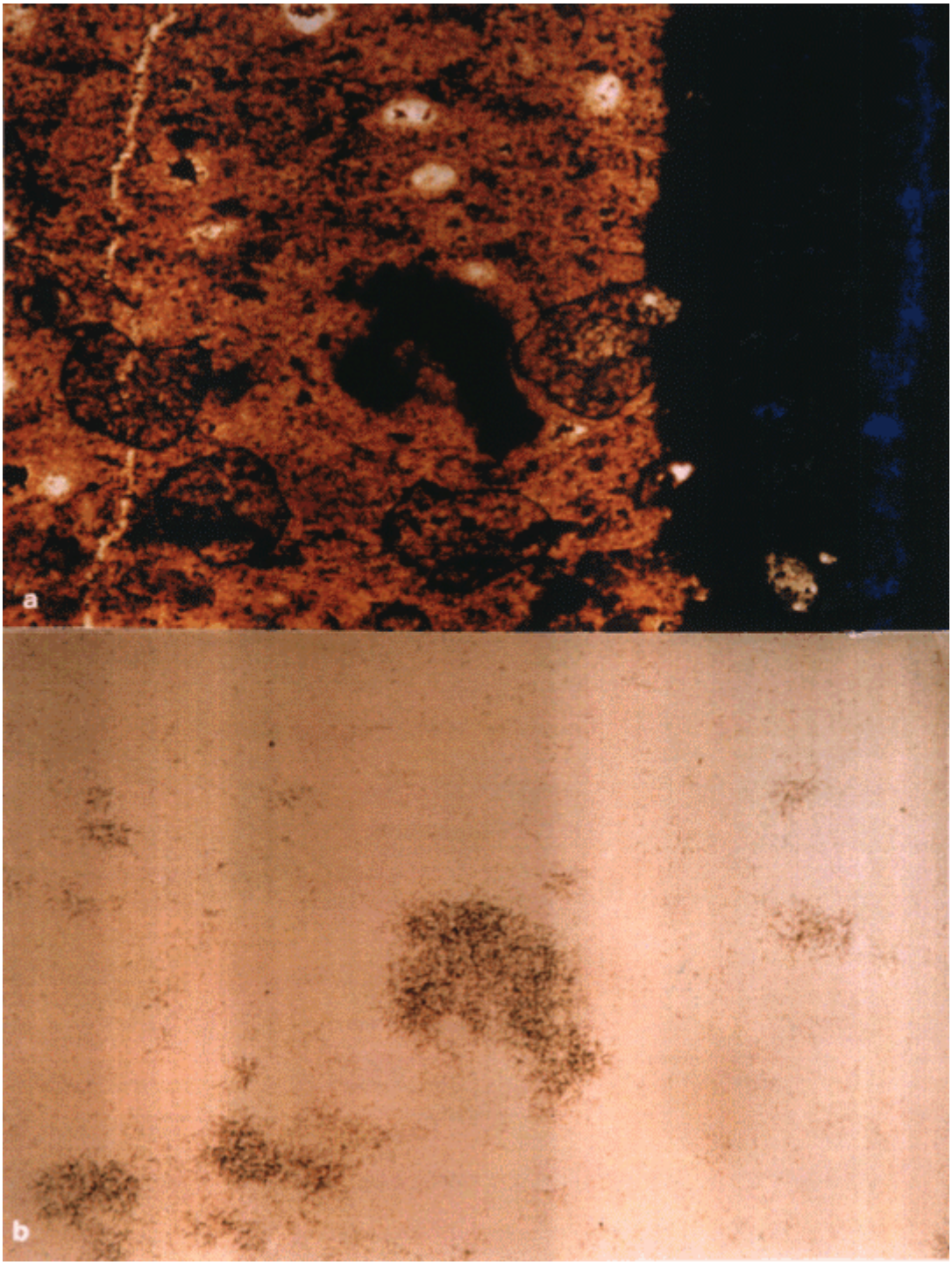

Plate 51a Sample A972 from the Daba roadcut showing the edge of an ettringite-filled fracture. The altered marl wallrock is semi-opaque. Plane-polarised, transmitted light. Field of view 1.8mm across.

Plate 51b Fission track print of Plate 51a showing primary U distribution in the marl with low levels of a few ppm U dispersed throughout the matrix, and higher concentration of 30-60ppm U in the collophanic microfossil material. Levels of U appear to be slightly reduced in the most altered wallrock.

8. TRACE ELEMENT DISTRIBUTION IN FRACTURE ALTERATION

J.M. Pearce, S.R.N. Chenery and A.E. Milodowski

8.1 Introduction

8.1.1 Analysis of fine-scale sub-millimetre alteration zones

Alteration of bituminous clay-biomicrites by hyperalkaline groundwaters in the Maqarin Natural Analogue Site characteristically produces very fine-scale sub-millimetre wallrock alteration zones (described in detail in Chapter 6 and Chapter 7). Alteration on such a fine scale presents major sampling problems for conventional whole-rock chemical analysis if it is intended to examine the distribution and mobility of trace elements within these alteration zones. For this reason it was decided to try to use the recently-developed laser-ablation microprobe inductively-coupled plasma mass spectrometry (LAMP-ICP-MS) technique to determine the variation in trace element distribution within the very fine-grained matrix of the narrow wallrock alteration zones. The advantage of this technique is that it has good spatial resolution (able to analyse areas down to 5μm diameter) coupled with very high sensitivity for many elements (to sub-ppm level depending on ablation volume and analysis conditions). The aim was to try to use a Nd:YAG laser microprobe to ablate relatively large areas of sample (c. 50 to 100 μm^2) to provide an indication of the distribution and mobilisation of trace elements on a fine scale within the wallrock, away from fracture surfaces.

The LAMP-ICP-MS produces data in the form of elemental ratios (Appendix B). Determination of element concentrations requires that one of the determinands is known absolutely. In order to provide this information, similar areas adjacent to LAMP-ICP-MS ablation areas were analysed by wavelength-dispersive electron microprobe analysis (EMPA) using a 40μm diameter defocused electron beam. The intention of the 'broad-beam' EMPA was to provide an 'average' major element composition of the rock matrix within the narrow alteration zones. It must be noted that these analytical conditions are far from ideal for quantitative EMPA. The normal ZAF (atomic number, X-ray absorption and X-ray fluorescence) corrections do not really apply to situations in which element distribution, or phase components, are not uniformly-distributed within the analytical volume of the electron beam. However, given the very fine-grained (sub-micron) and intimately-admixed mineralogy of the altered wallrock associated with the hyperalkaline fracture alteration, it was felt that defocused beam EMPA data might provide a reasonable 'first approximation' of the major elements composition of the rock matrix, which could be used to provide some degree of calibration for the LAMP-ICP-MS data from the same zones. For this purpose, EMPA data for Ca were used to normalise the LAMP-ICP-MS data.

Comparison of 'broad-beam' EMPA-normalised LAMP-ICP-MS data for rock matrix away from the alteration zones with whole-rock analyses determined by conventional whole-rock dissolution methods show reasonable agreement. Therefore, the assumptions made above do enable some useful semi-quantitative observations on trace element distributions to be made. However, it was found that LAMP-ICP-MS data for Si and Al, and Ba (because of its presence in discrete non-uniformly distributed barite) appear to be subject to significant error and are probably unreliable (Appendix B8)

Details of the EMPA and LAMP-ICP-MS operating conditions are given in Appendix B8.1. The concentrations of major elements (Si, Al, Fe, Ca, Mg, S, P) and Cl were determined by EMPA at each analysis point. The counting times for each element varied according to its approximate relative concentration. Cl was determined as a measure of porosity at each analysis point since the resin used to impregnate the samples during thin section preparation contains 1.81 wt.% Cl (determined by EPMA). Hence by simple calculation, and assuming all Cl detected is due to the presence of the resin only, the porosity can be estimated. The porosity accounts for a significant proportion of the analysis volume - up to 70% in some cases. A correction for this porosity was then applied to both major and trace elements concentrations in order to determine their equivalent weight percent/ppm concentration in whole-rock.

The concentrations of Mg, Mn, Fe, Co, Cu, Zn, Sr, Ba, Pb, Th, and U were measured by LAMP-ICP-MS. The position of each analysis point was noted on a BSEM photomosaic map of the thin section.

Three samples, A960, A965 and A967, were selected for analysis by LAMP-ICP-MS to determine the variation in trace element distribution within the altered wallrock zones adjacent to major fractures displaying hyperalkaline groundwater interaction. Sample A960 represents rock-water interaction at the 'high pH inflow' end, and sample A965 the downstream 'low pH' M2 discharge point, of the fracture-flow system studied in Adit A6 (Chapter 6). Sample A967 represents a currently-active fracture from the Maqarin Station railway cutting site. In each sample, a representative area of fracture mineralisation and wallrock alteration was identified for detailed analysis. Two profiles of analysis points were made in each sample, extending from the fracture wall into the host wallrock. It was initially thought that the profiles extended into unaltered wallrock but evidence presented below suggests that this was not the case for A960.

8.1.2 Trace element analysis of secondary minerals

The trace element composition of the major secondary alteration minerals were also determined by LAMP-ICP-MS analysis and EMPA. Sample inhomogeneity did not affect these analyses since single mineral phases were analysed by EMPA rather than mineral mixtures. Secondary minerals sampled during the Phase II programme, together with well-developed examples of other secondary hyperalkaline alteration vein minerals previously examined by Milodowski et al. [1] were analysed by LAMP-ICP-MS.

8.2 Geochemical Variation in Altered Fracture Wallrock

8.2.1 Geochemical variations associated with wallrock alteration in Sample A960

(i) Major elements

Duplicate analysis profiles were produced from the fracture margin to about 2000 μm into the wallrock (Table 8.1). The variations in major elements, determined by EPMA, compare very well between the two profiles. The alteration zone across which the micro-geochemical traverses were determined is shown in Plate 28 (see Chapter 6). As discussed in Chapter 5, the wallrock alteration extends beyond the limit of the sample with most readily-observed alteration in thin section occurring within 1 mm of the fracture surface. This is delineated by a diffuse 'precipitation front' of calcite cement. The most intense wallrock alteration occurs, not at the actual interface with the fracture but between about 250- 550 μm and is distinguished by a zone of extensive calcite dissolution ('Calcite Depletion Zone'), and major alteration and replacement of the rock by secondary alteration phases which include major ettringite and/or thaumasite,

amorphous CASH- and/or CSH-type compounds and gypsum. This major zone of alteration appears to be associated with a zone of hairline micro-fractures sub-parallel to the main fracture.

Ca concentrations within the very altered wallrock close to the fracture wall are c.30 wt.% (Figure 8.1). At about 200 μm from the fracture wall Ca decreases to c.15 wt.%. This corresponds to the zone of major dissolution of calcite and its replacement by secondary CSH, CASH, thaumasite and ettringite (Chapter 6). The Ca concentrations increase with increasing distance from the fracture wall - into the less-altered rock - reaching a maximum of c.40 wt.% at 1500 μm.

Si concentrations are depleted at the fracture margin (c.5 wt.%). This reflects the leaching of diagenetic silica, detrital illite and kaolinite by high pH fluids. Si increases to a maximum of 18 to 20 wt.% at 200 μm from the fracture wall (Figure 8.1) and correlates with the extensive development of secondary CSH, CASH, gypsum and thaumasite minerals. Thereafter, Si concentrations decreases steadily between 200 and 800 μm to a background level of c.4 wt.% as alteration decreases away from the main fracture. Al closely follows Si but is not so enriched within the calcite dissolution zone (Figure 8.1). This probably reflects the fact that CSH and thaumasite, rather than CASH, ettringite or zeolitic alteration products dominate the major wallrock alteration and calcite depletion zone (Chapter 6).

S concentrations remain generally low throughout the profile, with a slight enhancement between 200 μm and 550 μm corresponding to the zone of major calcite depletion (Figure 8.2). The enhancement of S is principally related to the formation of secondary sulphur-bearing minerals such as ettringite, thaumasite and gypsum within the altered wallrock. Cl concentrations (representing epoxy-resin-impregnated porosity) increase dramatically at approximately 400 μm from the fracture wall. This reflects major calcite dissolution and secondary porosity formation (up to 70% porosity - see Figure 5.7, Chapter 6). Further into the host rock, Cl decreases rapidly to c.0.5 wt.% (equivalent to 25-35% porosity) beyond 900 μm (Figure 8.2).

(ii) Trace elements

The duplicate alteration profiles generally correspond well for any given trace element. However, when the concentrations are close to or below the LAMP-ICP-MS detection limit the profiles tend to correlate poorly and the trace element variation (reflected in the departure/scatter) is probably erroneous.

Mg, Fe and Mn have relatively low concentrations in these bituminous clay biomicrites and for convenience are grouped with the trace elements. Mg concentrations are c.2600 ppm at the fracture margin but increase sharply to 4500-6400 ppm within the first 200μm of the wallrock (Figure 8.3). Thereafter, Mg decreases to 2000-2500 ppm beyond about 800 μm. The enhancement of Mg near the fracture wall between 0-800 μm is interpreted to represent residual concentration as a result of the leaching of other more mobile components (principally Ca). Petrographic observations (Chapter 6, [1]) suggest that Mg is incorporated in secondary Mg-rich minerals such as brucite, talc, or hydrotalcite within these narrow alteration zones.

Cu is generally enhanced within the altered wallrock (150-300 ppm) decreasing gradually to <60 ppm in less altered ‘background’ rock at the end of the profile studied (1950 μm). However, Cu appears to be particularly enriched (up to c.540 ppm) within the zone of

major alteration between about 300-600 μm from the main fracture wall, where CSH-gypsum-thaumasite are the principle phases present.

Cr varies between 900 and 2050 ppm with enhancement up to 3000 ppm at 400 μm (Figure 8.3) in the calcite dissolution zone. Here Cr is most probably incorporated within sulphate minerals as chromate (substituting for sulphate) in secondary sulphate-bearing minerals such as gypsum, ettringite and thaumasite - which are the major alteration products in this zone.

The two profiles for Mn (Figure 8.5) are not as consistent as for other transition metals such as Cr and Cu but show a similar trend. Figure 8.5 suggests that like Cr, Mn is enhanced (above background levels of about 30-50 ppm) within the major calcite dissolution zone. Jouravskite ($Ca_3Mn[CO_3][SO_4][OH]_6.12H_2O$) -the manganese analogue of ettringite and thaumasite - has been recorded from Adit A7 at Maqarin as an alteration product of the marble (Milodowski et al., [1]). It therefore seems likely that Mn is also incorporated in solid-solution within ettringite or thaumasite within the highly altered wallrock zone seen in sample A960.

The distribution of Zn is generally similar to Cu, Mn and Cr. It is enhanced within the highly-altered calcite depletion zone where Zn reaches c.550 ppm, compared to background levels of around 150-250 ppm either side. Pb is also slightly enhanced towards the more altered zone and fracture wall. The agreements between the duplicate alteration profiles for Zn and Pb are not as good as for many other elements.

Co concentrations throughout the sample are very close to the detection limit (~ 5 ppm) and consequently no reliable observations of the variation in its distribution could be determined.

LAMP-ICP-MS data suggest that U concentrations (Figure 8.6) are generally between 70-100 ppm but increase significantly (up to c.150 ppm) within the highly-altered calcite depletion zone at c.350 μm from the fracture wall. The background U levels are 3-4 times higher than levels determined by fission-track registration analysis (FTR) from the same section (see Chapter 7). Similarly, Appendix Table B1 suggests that LAMP-ICP-MS analyses are overestimating U in comparison to conventional whole-rock analysis techniques. FTR (and earlier studies in Alexander et al., [2]) has indicated that at least part of the U is associated with organic matter in the unaltered clay biomicrite. The organic matter will be preferentially ablated under the laser, and this would account for the overestimate of U by LAMP-ICP-MS. Nevertheless, LAMP-ICP-MS profiles indicate some U enhancement within the highly-altered zone about 350 μm from the main fracture wall. This was not detected by FTR. However, this zone is highly-porous, and this would have effectively 'diluted' the FTR track counts for U. In contrast, the porosity was taken into account when correcting the LAMP-ICP-MS data. The high levels of U recorded by LAMP-ICP-MS within the very altered CSH-rich calcite-depleted zone are not inconsistent with the levels of U recorded by FTR in CSH and zeolitic materials in the fracture infill (up to 150 ppm U in fracture-lining CSH). Th concentrations are close to the detection limit (~1 ppm) and hence no conclusions can be made with regard to Th distribution in the alteration profile.

Sr and Ba are enhanced within the highly altered zone between 200-600 μm from the fracture wall. These elements are most probably incorporated within secondary sulphate minerals. To some extent they may reflect residual concentration effects due to excessive

leaching of more mobile Ca. Sr and Ba are less mobile/less soluble than Ca in the presence of high sulphate concentrations

8.2.2 Geochemical variations associated with wallrock alteration in sample A965

(i) Major elements

Petrographic analysis of fracture material from Adit A6 shows that the width of the wallrock alteration zone in the clay biomicrites decreases significantly, downstream of the high pH groundwater source in the metamorphic zone. At the 'low pH' discharge site at M2 in Adit A6, the width of the wallrock alteration zone (Sample A965) appears to be very much reduced compared to that shown by sample A960 (see Chapter 6). The alteration observed in thin section is confined to within 400 μm of the main fracture wall although the degree of alteration is variable. Several sub-parallel veinlets of ettringite also cut the host rock beyond this distance (Plate 35, Chapter 6) and each may also be associated with narrow leached zones. In A965, no distinct calcite precipitation front was observed at the interface between fresh and altered wallrock. At this point any marginal alteration appears to be largely minor ettringite and jennite, and the original major calcite and trace amounts of kaolinite, illite, apatite or collophane are still present. Fewer LAMP-ICP-MS/EMPA analyses were made of the wallrock traverse of this sample and are presented Table 8.2. Geochemical variations are less-defined but some general observations can made and are described below.

Al, Si and S (Figures 8.8-8.9) are generally enhanced within the narrow alteration zone. This corresponds to the precipitation of ettringite and jennite within the microporosity of the wallrock immediately adjacent to the fracture (Plate 35, Chapter 6). Ca displays an apparent slight increase at c.100 μm but this is probably due to local inhomogeneity in the distribution of primary calcite bioclastic detritus, rather than the result of alteration. Cl (reflecting epoxy-resin impregnation) shows little variation across the alteration profile (Table 8.2) indicating very little change in porosity in the wallrock although, it may be reduced immediately adjacent to the fracture surface (0-100μm) due to major ettringite mineralisation. Major ettringite cementation and replacement of the wallrock occurs within 0-100 μm of the fracture surface and is reflected in the significantly enhanced Al and S contents, and the effective dilution of Si over this interval (Figures 8.8 and 8.9).

(ii) Trace elements

No realistic systematic variation in Mg, Fe and Co can be detected across the alteration zone except that these elements may be reduced immediately adjacent to the fracture (0-100 μm) due to replacement of the wallrock by ettringite (Plate 35, Chapter 6).

Cr, Cu and Zn (Table 8.2 and Figure 8.10) all show some enhancement within the alteration close to the fracture wall (0-100 μm), and appear to be concentrated within the ettringite alteration (Cu up to c.190 ppm; Cr up to c.820 ppm; Zn up to 1800 ppm). Cr is probably present as chromate, substituting for sulphate in the ettringite. Zn and Cu do not quite follow Cr and are reduced to background levels immediately adjacent to the fracture but the reason for this is not clear. Pb and Th are at detection limits (c.1 ppm) and therefore no realistic observations on their variation could be made.

Sr may show some enhancement (>4000 ppm) immediately adjacent to the fracture wall, which may be due to the precipitation of aragonite (Chapter 6). However over most of the profile it varies non-systematically between c.850-1600 ppm and this could easily reflect inhomogeneities in the inclusion of fossil fragments in LAMP-ICP-MS and EMPA analyses (some shell fragments and foraminiferal tests may be Sr-rich in contrast to the

finer calcitic coccolithic components forming the bulk of the rock matrix). Ba concentration is low throughout the altered wallrock with no apparent variation across the altered zone.

In contrast to A960, LAMP-ICP-MS data suggest that U is leached from the wallrock within 500 μm of the fracture in A965 (Figure 8.11). This is not supported by FTR analyses (Chapter 7) which shows no evidence for uranium mobilisation in the wallrock. The most probable explanation of the difference between FTR and LAMP-ICP-MS observations, is that U (associated with organic matter in the bulk of the wallrock) will preferentially volatilise and ablate under the laser, and thus, LAMP-ICP-MS records 'artificially' enhanced U levels from the unaltered wallrock. Petrographic observations reveal that organic matter is leached from wallrock immediately adjacent to the fracture. FTR results imply that any U which was associated with the organic matter has not migrated. Because U is no longer associated with organic matter (see earlier discussion in Section 8.2.1), the U levels (c.7-9 ppm U) determined by LAMP-ICP-MS within this narrow alteration zone are closer to the FTR analyses (c.10 ppm).

8.2.3 Geochemical variations associated with wallrock alteration in sample A967

(i) Major elements

Sample A967 represents a calcite-aragonite-mineralised fracture actively conducting hyperalkaline groundwater in the Maqarin Station railway cutting. The altered wallrock across which LAMP-ICP-MS micro-geochemical traverses were made is illustrated in Plate 5.27 (Chapter 6) and details of the LAMP-ICP-MS analyses are presented in Table 8.3.

Ca shows little or no variation across the alteration zone, and is generally present at c.30 wt.% throughout the profile (Figure 8.12). In contrast, Mg concentrations increase linearly with increasing distance from the fracture wall (Figure 8.13). Mg concentrations are <2.0 wt.% adjacent to the fracture margin but increase to >2.5 wt.% at c.3500 μm distant. Petrographic analysis (Chapter 6) shows that the sample is dolomitic. Dolomite is preferentially dissolved in the wallrock adjacent to fractures, whereas calcite appears to show relatively little alteration. However, the very fine-grained secondary matrix alteration products associated with the alteration zone are poorly-resolved amorphous Mg-rich aluminosilicates and very hydrous CSH- or CASH-type phases. Mg is highly immobile under high-pH conditions and elsewhere at Maqarin this results in the formation of Mg-rich residual secondary minerals such as brucite, talc or hydrotalcite. Nevertheless, micro-geochemical profiles of A967 show that either Mg has been leached from the narrow alteration zone or alternatively, has been diluted by formation of other secondary minerals (ettringite, thaumasite, CSH or CASH). There are some indications of a slight enhancement of Si in this zone which would be consistent with the introduction of Si. Al shows very little variation - i.e. no extensive ettringite replacement to account for the depletion in Mg (Table 8.3).

Cl concentrations follow an exponential trend decreasing with increasing distance from the fracture wall (Figure 8.14) indicating enhanced porosity within the altered wallrock. P concentrations are consistent across the alteration zone and this implies that although primary apatite or collophane may be altered there is no mobilisation of phosphate.

(ii) Trace elements

Sr shows little significant systematic variation across the alteration zone. Apart from two extreme values, concentrations are between 100 and 1500 ppm. In contrast, Ba may be

slightly enhanced close to the fracture wall (70-100 ppm compared to background levels of 40-70 ppm).

Fe, Zn and Pb all show slight enhancement close to the fracture wall (Table 8.1). Cu, Co, Cr, Mn, Th and U show no significant variations across the altered wallrock.

8.2.4 Trace elements in fracture minerals

Average compositions of secondary fracture-filling minerals from Maqarin are presented in Table 8.4. Full details of individual sample analyses are given in Appendix Table B3. These data are based on analysis of samples collected as part of the Phase II programme and on re-analysis of earlier Phase I programme samples and samples described by Milodowski et al. [1] by LAMP-ICP-MS. The principle alteration minerals analysed include: jennite, wairakite, ettringite, thaumasite, calcite, aragonite, CSH gel, brucite and portlandite. Significant differences in trace element uptake by these secondary minerals are apparent from these data. It should be noted here that 'wairakite' is used broadly to cover the 'zeolitic' alteration in general seen in Adit A6 (described in detail in Chapter 6). 'Wairakite' may in fact be laumontite (or leonhardite), but will also include mordenite-dachiardite-type zeolites which are present but not distinguished by LAMP-ICP-MS analyses. All recalculation of LAMP-ICP-MS data for zeolitic alteration has assumed an ideal 'wairakite' composition. This was necessary because the complex intergrowth of the different zeolites that was observed (Chapter 6) could not be resolved on the scale of the LAMP-ICP-MS analysis points.

Sr is concentrated in wairakite, portlandite and aragonite (1800-4400 ppm). Slightly lower but still significant concentrations of Sr (900-1100 ppm) are incorporated within CSH gels and calcite. These levels are 5-10 times higher than levels found in the other secondary minerals (typically <200 ppm), although ettringite may incorporate on average about 450 ppm Sr. Ba is similarly concentrated in wairakite, CSH and portlandite. Aragonite incorporates proportionately less Ba than Sr, but its Ba content is typically higher than calcite. The difference in uptake of Ba and Sr by calcite and aragonite is consistent with the difference in structure between the two minerals. Ba and Sr can form carbonate minerals (witherite and strontianite, respectively), both of which are orthorhombic and isostructural with aragonite (in contrast, calcite has a trigonal crystal structure which cannot so readily accommodate large Sr and Ba ions). Brucite, jennite, thaumasite and ettringite are typically low in Ba.

Mg is obviously incorporated in brucite, but wairakite, aragonite, CSH, portlandite and calcite can all incorporate significant amounts of Mg (2000-5600 ppm). Ettringite can also incorporate significant Mg. In contrast jennite and thaumasite are low-Mg minerals. Mn and Fe are similarly concentrated in wairakite, CSH, portlandite, brucite, calcite and aragonite (although aragonite contains lower levels than calcite). Jennite, ettringite and thaumasite display about an order of magnitude lower concentration of Fe and Mn.

Cu shows greatest concentration in wairakite/laumontite (c.550 ppm), with lower levels in portlandite (c.130 ppm) and calcite (c.73 ppm). Other secondary minerals typically contain less than 20 ppm Cu. Co is similarly hosted largely within wairakite and portlandite. Pb shows the greatest enrichment within CSH (c.2400 ppm) with much lower levels in brucite (c.430 ppm), portlandite and wairakite (c.50-80 ppm). Jennite, ettringite and thaumasite are typically very low (1-10 ppm) in Pb. Wairakite, ettringite and calcite appear to incorporate Cr to a greater extent than other minerals.

Th is close to detection limits in most minerals at levels between 0-2 ppm, although ettringite and thaumasite consistently appear to contain <1ppm Th. Wairakite (c.51 ppm

U), jennite (c.19 ppm U), brucite (26 ppm U) and portlandite (15 ppm U) are the principle hosts for uranium. Wairakite exhibits the greatest level of uranium incorporation. CSH and calcite also host moderate levels of U (8-10 ppm) in the samples examined by LAMP-ICP-MS. Minerals such as ettringite, thaumasite and aragonite typically have very low U (<3 ppm). This is consistent with uranium FTR studies (Chapter 6) which show that secondary zeolites (sample A960 from Maqarin and also A982 from central Jordan) contain 10-30 ppm U and CSH gels, jennite and tobermorite contain 6-15 ppm U. FTR analysis also indicated that locally CSH gels might contain up to 100-150 ppm U where uranium had been mobilised from particularly uraniferous primary sources. In contrast, ettringite, thaumasite, aragonite and gypsum contained little or no uranium (typically <<7 ppm U).

8.3 Summary Discussion and Conclusions

As shown in Chapter 6, the fracture mineralisation and wallrock alteration associated with the hyperalkaline alteration of bituminous clay biomicrites at Maqarin is very complex. Most of the veins have complex polycyclic and polymineralic mineralisation. In many cases, the veins are now sealed and the groundwater associated with their formation is no longer seen, nor can it be sampled, in contact with the actual minerals. The only exception is at the M2 sampling site in Adit A6 (at which groundwater was sampled flowing from jennite-ettringite-thaumasite-calcite-mineralised veins) and from the Maqarin Station railway cutting (where a number of slow seeps were sampled from fractures, some of which display calcite-aragonite-ettringite dominated mineralisation). Consequently, since the trace element composition of the groundwaters sampled and analysed cannot be unequivocally correlated with the groundwater responsible for the actual fracture mineralisation, no direct quantitative comparison can be made of the groundwater trace element composition with that of the minerals, with respect to the relative partition coefficients. However a number of qualitative conclusions with regard to the more important analogue elements (U, Ba, Sr, Pb) can be drawn from the observations. A summary of the principle mineralogical sinks for various trace elements is presented in Table 8.5.

At Maqarin, zeolite appears to be a major sink for most elements. From an analogue point of view, it is the most important mineral with respect to the concentration of U, incorporating significantly more U than any other alteration product. Jennite, brucite, portlandite and CSH are also important sinks for U. These account for the concentration of U and other trace elements within altered wallrock adjacent to fractures (in particular in sample A960). Jennite and CSH minerals are volumetrically considerably more significant than zeolite or other U-enriched minerals within the clay biomicrite fracture system at Maqarin (except within 2-3 m of the metamorphic zone). Consequently, these phases will be the most important minerals involved in the ‘fixation’ of uranium. Brucite also incorporates significant U but occurs largely within fractures in the metamorphic zone rather than in the non-metamorphosed country rocks. However, secondary very fine brucite formed by residual concentration within the leached wallrock may well be involved in fixation of U in the rock matrix.

Zeolite, CSH and jennite are the principle ‘sinks’ for Ba, Sr and Pb within the clay biomicrite fracture system, although zeolite is only significant adjacent to the metamorphic zone. Portlandite is potentially a major sink for Sr, Ba, and Pb but again occurs largely within the metamorphic rocks and is volumetrically insignificant in the clay biomicrite fracture system. Calcite and aragonite also concentrate Sr and Ba but these minerals are generally volumetrically insignificant (e.g. in Adit A6 fractures) except

where the groundwaters interact with atmospheric carbon dioxide (e.g. fracture alteration in the Maqarin Station railway cutting). Ba is a particularly good analogue for Ra and this study would suggest that by analogy, CSH and jennite are likely to be the most important phases for Ra fixation at Maqarin.

In contrast, ettringite and thaumasite appear to incorporate considerably lower amounts of trace elements except for Cr and Zn. In particular, thaumasite and ettringite display very low contents for U and Pb, and also considerably lower Sr and Ba than zeolite, CSH and jennite. However, ettringite and thaumasite are volumetrically major alteration products within the clay biomicrite fracture system. Beyond, about 80-90m downstream of the metamorphic zone, ettringite and thaumasite are the principle alteration products (Chapter 6).

Experimental studies have shown that significant uptake of U can occur by ion-exchange/sorption on zeolites (e.g. Na-chabazite, Na-pollucite and analcime) and CSH gels [3, 4]. In contrast, Sr shows a relatively low uptake by ion-exchange or sorption on these minerals [3, 5, 6]. This implies that the high levels of Sr and Ba present in zeolite, and Sr, Ba and Pb in CSH and jennite, are incorporated by co-precipitation with Ca in solid-solutions in these minerals, rather than by ion-exchange or sorption processes. Ba-zeolites are known to occur elsewhere in nature (e.g. harmotome). In the case of Maqarin phases, it is not known whether U uptake is controlled by surface-sorption, ion-exchange or co-precipitation mechanisms.

It is surprising that ettringite and thaumasite from Maqarin have such low Sr and Ba contents compared to the secondary zeolite and CSH minerals. Barret et al. [7] considered that ettringite would be an important sink for Sr in cement systems. By analogy, Ba and Ra would be expected to behave similarly to Sr. The same process would be expected to apply to thaumasite since it is isostructural with ettringite.

The Maqarin natural analogue study has shown that ettringite-thaumasite and CSH-tobermorite-jennite-zeolites alternate in precipitation - probably due to fluctuations in concentrations of sulphate and silica in the groundwater (for reasons as yet undetermined). These minerals frequently replace each other - as for example, in Adit A6 veins (Figure 6.13 summarises the mineral paragenesis observed at this location). This study demonstrates that zeolite, jennite, tobermorite or CSH take-up significant contents of U, Pb, Sr and Ba. However, when they are replaced by ettringite or thaumasite their trace elements contents were not retained, and a large proportion must have been re-released to the groundwater. Other published work [8] also indicates that ettringite and thaumasite are likely to be the principle alteration products of interaction with sulphate-bearing groundwaters. Therefore, if migrating radionuclides had been incorporated in secondary CSH minerals and zeolites in the disturbed zone, they could potentially be re-released to the groundwater as a result of their alteration to ettringite or thaumasite.

8.4 References

[1] A.E. Milodowski, J.M. Pearce, C.R. Hughes and H.N. Khoury, *A Preliminary Mineralogical Investigation of a Natural Analogue of a Cement-Buffered Hyperalkaline Groundwater Interaction with Marl, Maqarin, Northern Jordan,* NAGRA Unpublished Internal Report, 1992.

[2] W.R. Alexander, *A Natural Analogue Study of the Maqarin Hyperalkaline Groundwaters. I. Source Term Description and Thermodynamic Database Testing,* NAGRA Technical Report, NTB 91-10, 1992.

[3] G. Berger, *Distribution of Trace Elements between Clays and Zeolites and Aqueous Solutions similar to Sea Water*, Applied Geochemistry, Supplementary Issue **1**, 193-203, 1992.

[4] A. Perruchot, F. Delbove, J.M. Paulus and J.P. Adloff, *Behaviour of Uranyl and Neptunyl Cations during Ion Exchange between Silicate Gels* $pSiO_2$-(A,B)-nH_2O *and Aqueous Solutions* (A^{2+},B^{2+}) (A^{2+} = UO_2^{2+}, NpO_2^{2+}; B^{2+} = Mg^{2+}, Ca^{2+}, Ni^{2+}): *An Experimental Study*, Applied Geochemistry, Supplimentary. Issue **1**, 95-107, 1992.

[5] J.M. Lameille, G. Goutiere, J.C. Petit and M. Regourd, *Retention of Cobalt, Cesium and Strontium in the Hydrates of* C_3S, C_3A *and Gypsum*, Journal of the American Ceramic Society, **70(8)**, 604-614, 1987.

[6] S.L. Hoyle and M.W. Grutzeck, *Incorporation of Cesium into Hydrating Calcium Aluminosilicates*, Journal of the American Ceramic Society, **29**, 209-213, 1989.

[7] P. Barret, D. Bertrandie, J.M. Casabonne-Massonave and D. Damidot, *Short Term Processes of Radionuclide Immobilization in Cement: A Chemical Approach*, Applied Geochemistry, Supplementary Issue **1**, 109-124, 1992.

[8] F.M. Lea, *The Chemistry of Cement and Concrete*, Edward Arnold, Third Edition, 1970.

Table 8.1 EPMA and LAMP-ICP-MS data for sample A960 alteration profile.

		EPMA analyses (wt.%)							LA-ICP-MS analyses (ppm)											
	Distance																			
Point	(µm)	Mg	Al	Si	P	S	Cl	Ca	Mg	Al	Fe	Mn	Cr	Cu	Co	Zn	Pb	Sr	Ba	Th	U
Profile 1																					
A960/7	7	0.2	.7	.	1.9	0.	1.8	32	67	.	0.	7	20 2	28		197	12	1082	99	2	7
A960/8	2	0.2	6.3	20	2	0.	1.2	17	2 2	.	0.	16	82	121		83	9	1 62	223		32
A960/9	389	0.3	.6	13	6.6	0.8		30	06	6.	1.2	99	31	36	1	3 2	20	1773	3 2	3	1 0
A960/10	6	0.2	.3	10	3	0.6	1	29	3686	7.7	0.	0	187	383	10	2	13	2083	397	2	99
A960/11	76	0.1	2.6	.3	1.6	0.3	0.6	33	2131	3	0.	1	936	198		23	10	1 02	22	2	82
A960/12	968	0.1	1.7	3.1	1.6	0.2	0.	37	2 0	2	1.	7	1178	230		2 1	1	1 19	1 1	3	101
A960/13	1 9	0.1	1.3	2.3	1.3	0.2	0.6	0	2210	1.	0.		976	136	3	22	13	1 73	81	3	88
A960/1	1879	0.1	1.	3.1	1.7	0.3	0.7	38	2 6	1.	0.	2	8	62		200	10	1 1	1 9	1	62
Profile 2																					
A960/19	23								267		0.		1 1	171	2	183	1	112	86	2	7
A960/20	168	0.2	.6	.7	2.6	0.	1.8	28	63 6	3.	0.	6	163	201		2 1	2	1209	111	2	91
A960/21	2	0.1	.6	18	1.	0.	1.	1	372	10	0.3	2	16 3	197		112	1	1986	33	3	76
A960/22	381	0.2	6.3	13	2.	0.7	.	22	7	7.7	1.	61	3019	3 2	7	70	17	1 71	2 9		130
A960/23	02	0.1	.2	8.	1.1	0.7	1.1	26	2 63	6.	0.	30	12 0	29	6	179	13	203	31	3	86
A960/2	606								18 9		0.	39	9 0	236	6	336	9	1 66	39		80
A960/2	678	0.1	2.7	.9	1.6	0.2	0.	3	2169	.8	0.		887	172		2 3	9	1 89	2 9	1	83
A960/26	770								2 90		0.	0	868	169	3	199	10	128	166	3	98
A960/27	88	0.2	1.7	3.	2.7	0.2	0.	36	2	2.1	0.6	6	961	186		210	11	1 7	138	1	8
A960/28	979								2101		0.6	38	891	197		196	13	13	116	2	103
A960/29	111	0.1	1.7	3.2	2.1	0.3	0.6	36	20 8	1.7	0.7	1	978	222		19	13	12 1	83	1	79
A960/30	13								2 0		0.8		1018	193	7	217	17	12 6	6	2	91
A960/31	1 72	0.1	1.7	2.9	1.	0.3	0.7	36	211	0.8	0.8	9	989	131		236	12	1213	68	2	82
A960/32	1 7	0.1	1.6	3	1.9	0.3	0.8	36	2319	0.8	0.7	7	936	96	3	20	8	12 3	62	2	89
A960/33	1779	0.1	1.	3	2	0.3	0.8	36	2366	1.	0.7	6	909	70	6	18	10	1223	80	2	76
A960/3	1928	0.1	1.	3	2.3	0.3	0.8	37	2 20	1.6	0.6	8	1030	9		203	7	1299	106	1	8

Table 8.2 EPMA and LAMP-ICP-MS data for sample A965 alteration profile.

EPMA analyses (wt.%)										
Distance (µm)	Si	P	Cr	Al	Ca	Mg	Fe	S	Cl	Sr
0	0.	0.2	0	2.3	28	0	0.2	.7	0.2	0
31										
36	0.	0.	0	1.7	28.	0.2	0	3.	0.3	0
76	0.	0.	0	1.	26.8	0	0.2	3.1	0.	0
107										
116	0.6	2.6	0	0.9	22.	0.2	0	2.3	0.6	0.2
12										
16	0.6	1.3	0	2.1	26.	0.2	0	.	0.	0.2
227	0.6	.1	0	0.9	2 .1	0.3	0.2	2.2	0.6	0
276	0.	0.	0	0.	26	0.3	0	1.	0.	0
28										
293										
36	1.2	0.6	0	0.1	22.3	0.2	0	1.2	0.	0
62	2.1	0.8	0	0.3	23.	0.3	0	1.2	0.	0.2
98	2.2	0.7	0	0.3	22.6	0.	0.	1.2	0.	0
87	1.6	0.3	0	0.3	2 .2	0.3	0.3	1	0.	0
6 9	1	0.2	0	0.2	2 .	0.2	0.	0.9	0.	0.2
702	0.9	0.3	0	0.2	2	0.1	0.2	0.8	0.	0
720										
7 6	1	0.	0	0.3	21.8	0.3	0.6	1.7	0.	0

LA-ICP-MS analyses (ppm)													
Mg	Al	Cr	Mn	Fe	Co	Cu	Zn	Sr	Ba	Pb	Th	U
2	267 6			831		107	78	136	17			
2267	3 199	82	18	8	31	188	1822	109	11	18		7
603	28216	270	2	3 60	19	66	03	1063	2			8
3790	39 89	66	17	30	30	9	6	861	19			7
2877	93	3 3	31	2 22	30	9	13	1 8	31	2	0	9
273	9096	366	32	26 9	21	82	306	1 11	29	2	0	9
101	27 7	17	30	98	22	12	78	137	1 9		1	18
3339	1896	32	1	7662	13	120	3 7	1 9	3	3	0	18

Table 8.3 EPMA and LAMP-ICP-MS data for sample A967 alteration profile.

		EPMA analyses (wt.%)								LA-ICP-MS analyses (ppm)												
	Distance																					
Point	(μm)	Mg	Al	Si	P	S	Cl	Ca	Fe	Mg	Al	Cr	Mn	Fe	Co	Cu	Zn	Sr	Ba	Pb	Th	U
Profile 1																						
A967/10	172	1.7	1.2	2.1	0.6	0.3	0.2	33.6	0.	1.68	0.70	117	111	6 13	2	30	68	1363	7	12	2	11
A967/11	62	2.	1.6	3	1.2	0.	0.2	30.	1.3	1.90	0.93	109	80	078	2	36	7	12 0	1	3	1	9
A967/12	936	1.8	1.	2.	0.7	0.3	0.1	32.2	0.	2.0	1.01	109	1 1	81	6	3	7	1 22	69		1	10
A967/13	1 0	2	1.8	2.9	0.7	0.3	0.1	31.7	0.	2.1	1.18	129	10	3802	1	3	3	1 03	8	3	2	10
A967/1	18 6	1.6	1	0.9	0.	0.2	0	3 .	1.1	1.73	0.63	139	187	3376	2	26	9	11 9	6	6	1	
A967/1	2160	3.3	1.9	3.6	0.	0.6	0	29.	0.3	2.	0.77	127	16	1	3	37	0	1196	69	12	2	13
A967/16	29	2.6	1.2	1.6	1.2	0.2	0	33	0.	2.73	0.7	1 2	1 8	2 18	3	20	1	13	2		1	
A967/17	3 8	2.6	1.7	2.9	0.9	0.3	0	31.	0.3	2.	0.8	97	102	2878	2	2	16	1363	0		1	7
Profile 2																						
A967/26	120	3.1	2.2	2.1	0.7	0.	0.	29.3	1.1	1.91	0.9	98	386	8120	6	1	12	1188	9	10	2	8
A967/2	0	1.9	1.2	2.1	2	0.3	0.2	32.7	0.8	2.07	1.01	112	79	96	2	37	102	1396	8		1	9
A967/2	796	1.9	1.	2.	0.9	0.3	0.1	31.3	1.2	1.9	0.9	123	93	3782	3		6	1		2	2	10
A967/23	1016	2.	1.8	3.1	0.7	0.	0.1	2 .1	.2	1.63	0.81	98	91	329		26	2	1000	32	3	2	9
A967/22	1 6	1.1	0.9	0.8	0.	0.1	0	38.1	0.	2.2	1.29	1 7	1	766	2	39	6	1 96			1	9
A967/21	1876	2.7	1.9	3.2	0.8	0.3	0.1	31.3	0.	2.18	0.9	118	129	2788	3	2		1238	6	3	1	8
A967/20	2236	1.9	1.2	0.9	0.	0.2	0	3 .7	0.	2. 3	0.	139	17	22	1	19	23	1092	3	6	1	
A967/19	302	2.3	1.1	1.6	0.6	0.2	0	33.8	0.3	2.22	0.70	1	1 7	3 98	2	30	30	129		7	1	
A967/18	3 2	2.2	1.7	2.	0.8	0.3	0	32.3	0.	3.17	1.02	12	168	011	1		20	1370	6	6	2	8

Table 8.4 Average major (EPMA) and trace (LAMP-ICP-MS) element data for Fracture-filling alteration minerals from Maqarin

	Jennite		Wairakite		Ettringite		Thaumasite		Calcite		Aragonite		Hydrated CSH		Brucite		Portlandite	
EPMA Data																		
		s.d		s.d		s.d		s.d		s.d		s.d		s.d		s.d		s.d
Mg	0.0	0.02	0	0	0.0	0.11	0.02	0.01	0.1	0	0.6	0	0.01	0	2. 1	0	0	0
Al	0.12	0.1	1.19	0	2.79	1.8	1.86	0. 8	0.79	0	0.26	0	0.06	0	0	0	0	0
Si	16.22	0.28	0.1	0	0.	0.	2.9	0.83	0.3	0	0.3	0	.13	0	0	0	0	0
Ca	3 .3	0. 8	18.97	0	20.7	2.3	21.1	1. 2	39.82	0	0.18	0	0.	0	0	0	.09	0
Fe	0.01	0.03	0	0	0.02	0.03	0.01	0.01	0.03	0	0.16	0	0.02	0	0	0	0	0
P	0.38	0.02	0.02	0	0.12	0.12	0.2	0.02	0.18	0	0.19	0	0.06	0	0	0	0	0
S	0.12	0.11	10.22	0	8.63	1.81	.07	0.06	0.0	0	0.09	0	0.12	0	0	0	0	0
Cl	0.0	0.02	0.73	0	0. 2	0.2	0. 2	0.06	0.02	0	0.02	0	0.0	0	0	0	0	0
LA-ICP-MS Data																		
Mg	2 3	131	6 0	380	982	1097	67	20	2038	1233	018	8301	3032	2 2	n.d.	n.d.	227	1 12
Cr	191	138	872	10	739	2126	112	1 2	39	336	3	27	8	38	126	81	131	
Mn	9	2	6	39	6			3	6	29	16	1	37	1	23	n.d.	n.d.	n.d.
Fe	3	27	6820	69 6	7	79	26	91	2 33	2767	21 7	2971	3 00	2386	221	2980	03	6327
Co	1	1	21	22	1	1	0	0		1	7	10	n.d.	n.d.	9	n.d.	19	n.d.
Cu	12		2	37	8		10	2	73	39	17	13	19	1	17	1	130	66
n	2 0	3	207	102	327	802	99	130	9	8	36	36	300	2 3			368	2 7
Sr	16	10	23 2	1 2	9	261	181	33	9 1	306	1836	1 9	1103	308	32	11	20	1029
Ba	8		799	90	10	7	3	1	0	28	76	8	20	87	17		371	91
Pb	2	1	1	29	7	6	1	1	18	7	21	23	2 07	83	28	3	80	36
h	1	1	2	0	0.39	0.3	0	0	1	1	1	0	1	0	n.d.	n.d.	1	n.d.
	19		1		3	3	1	1	10	6	1	n.d.	8	2	26	n.d.	1	11

Table 8.5 Fracture minerals acting as sinks for various trace elements.

Mineral	Ba	Sr	Fe	Cr	Cu	Zn	Mn	Co	Pb	Th	U
Jennite											⊕
Zeolite (‘wairakite’)	⊕	⊕	⊕	⊕	⊕		⊕	⊕	(⊕)	?	⊕
Ettringite				⊕		⊕					
Thaumasite											
Calcite		(⊕)					⊕				
Aragonite		⊕									
Hydrated CSH	⊕	(⊕)				⊕	⊕		⊕		(⊕)
Brucite									(⊕)		⊕
Portlandite	⊕	⊕			(⊕)	⊕	⊕	⊕	(⊕)		(⊕)

indication in parenthesis ( ) shown to identify subordinate role as a sink for trace elements.

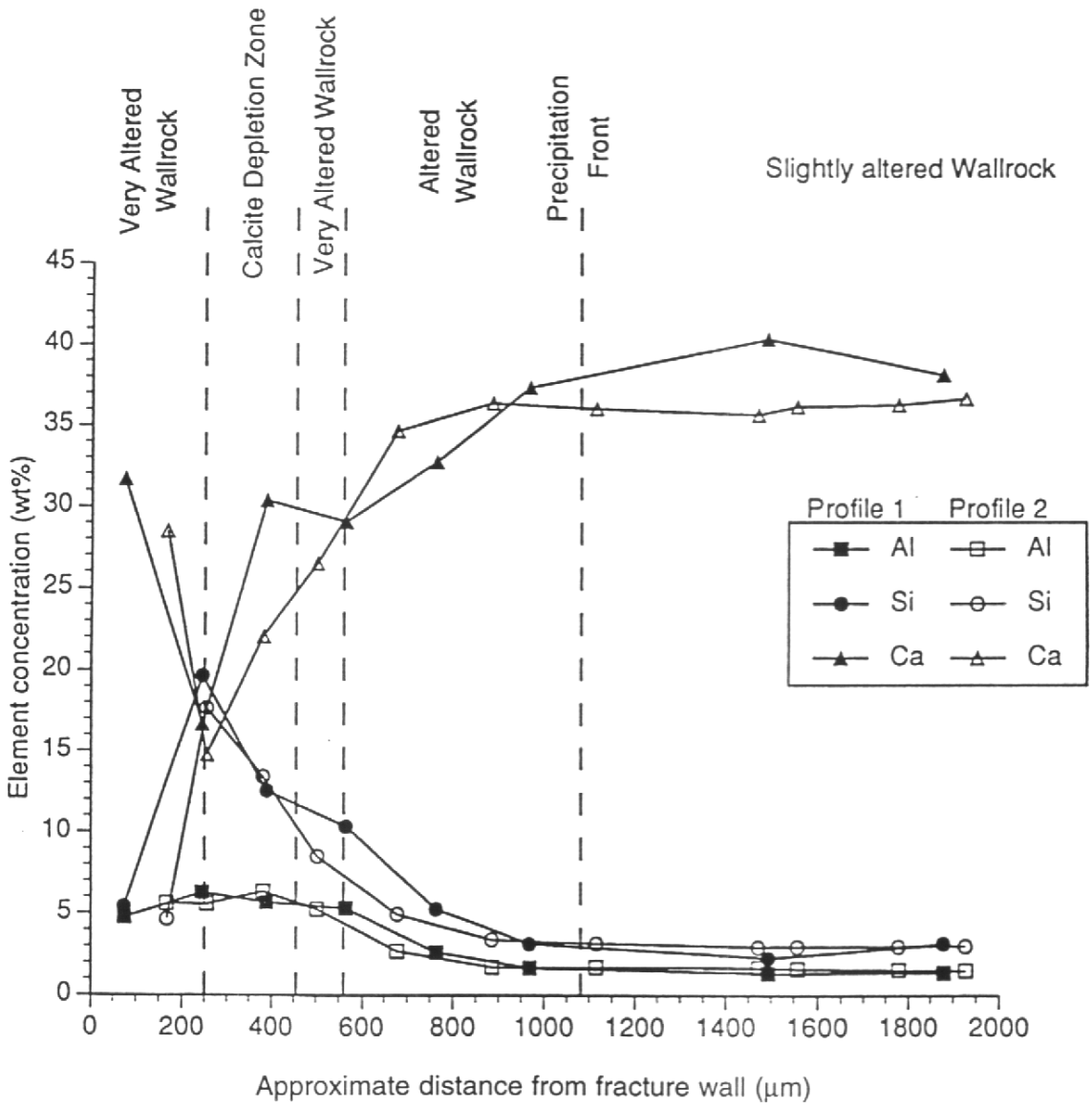

Figure 8.1 Al, Si and Ca concentrations from EMPA along two profiles through wallrock alteration in sample A960.

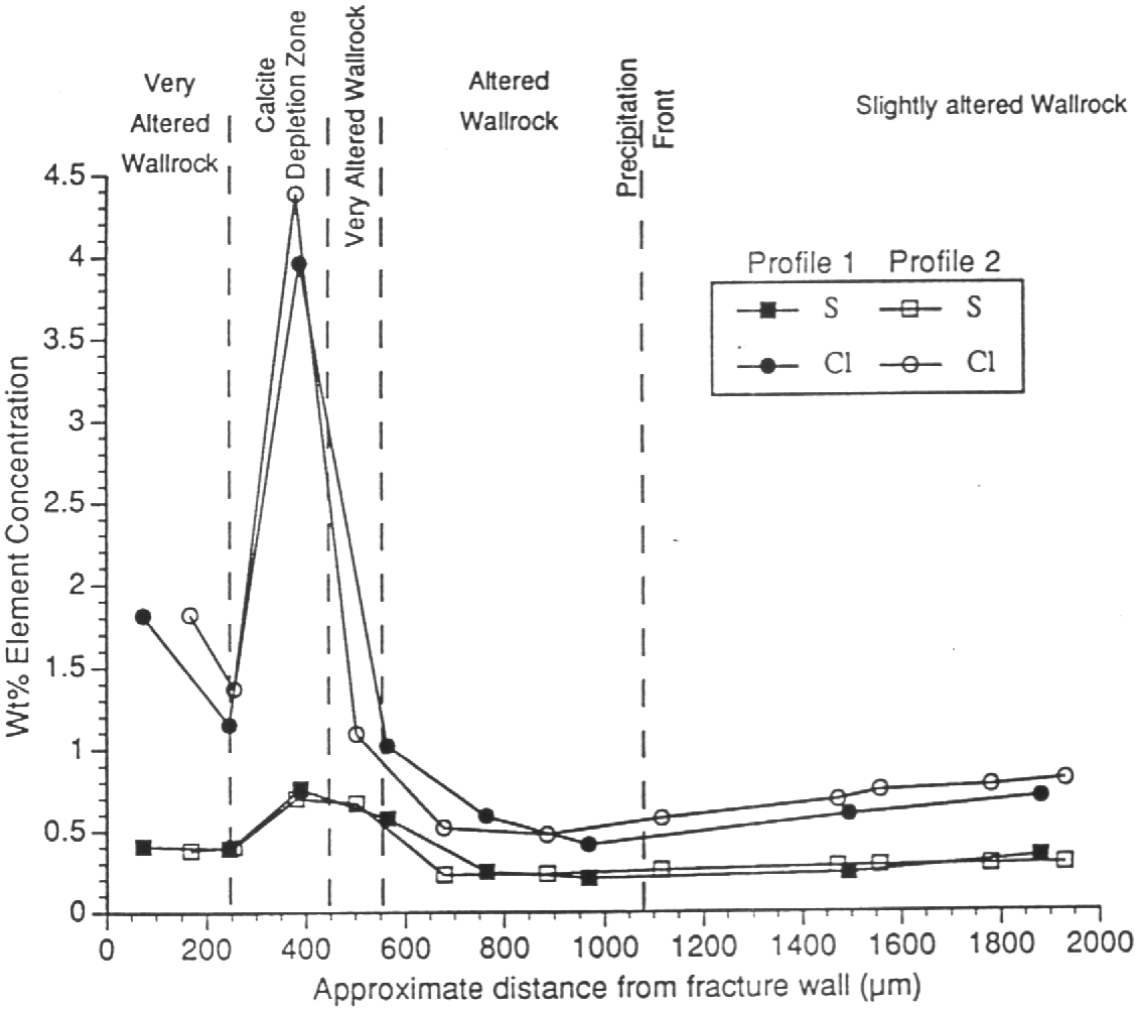

Figure 8.2 S and Cl concentrations from EMPA along two profiles through wallrock alteration in sample A960.

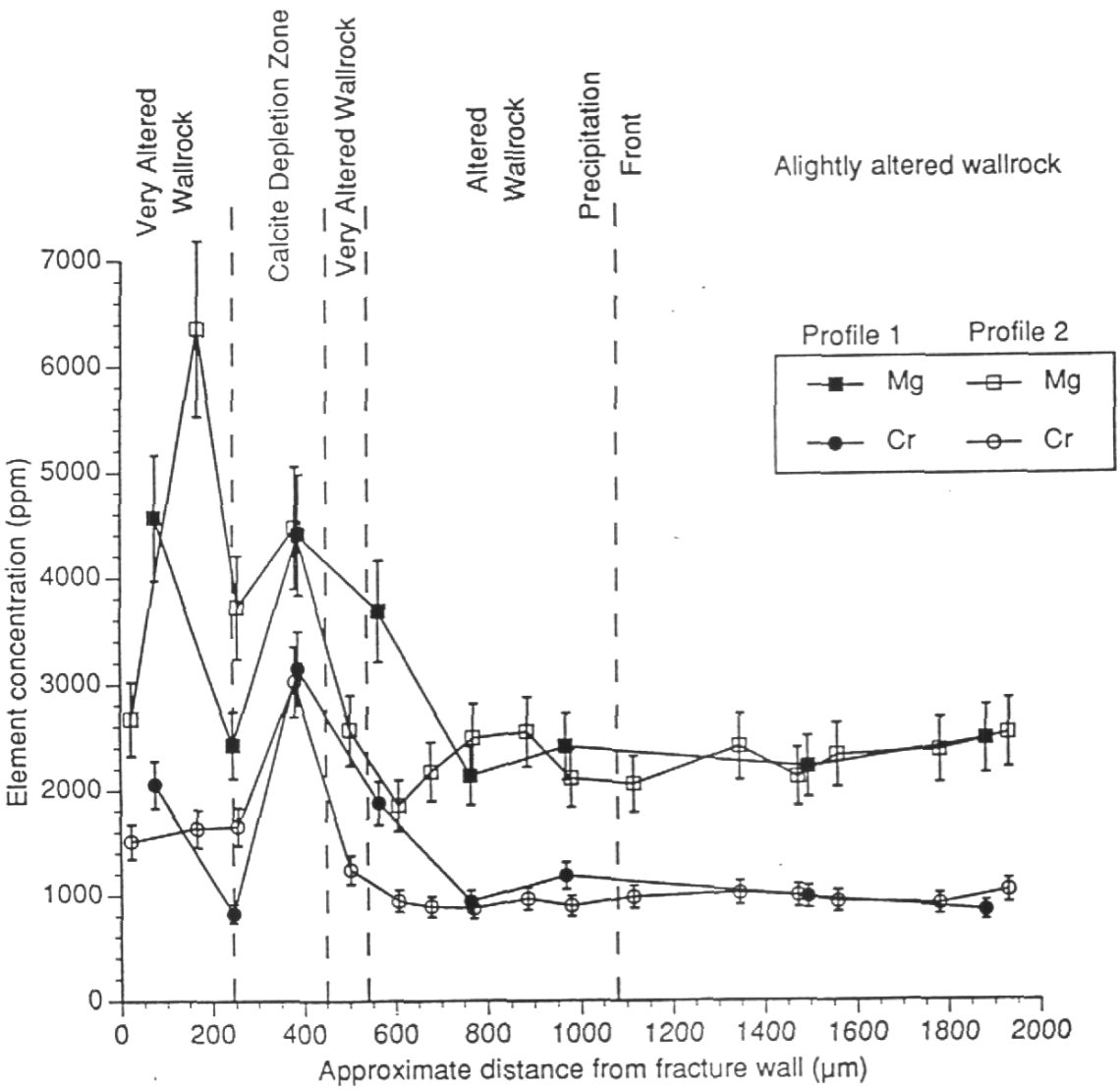

Figure 8.3 Mg and Sr concentrations from LAMP-ICP-MS analyses along two profiles through wallrock alteration in sample A960.

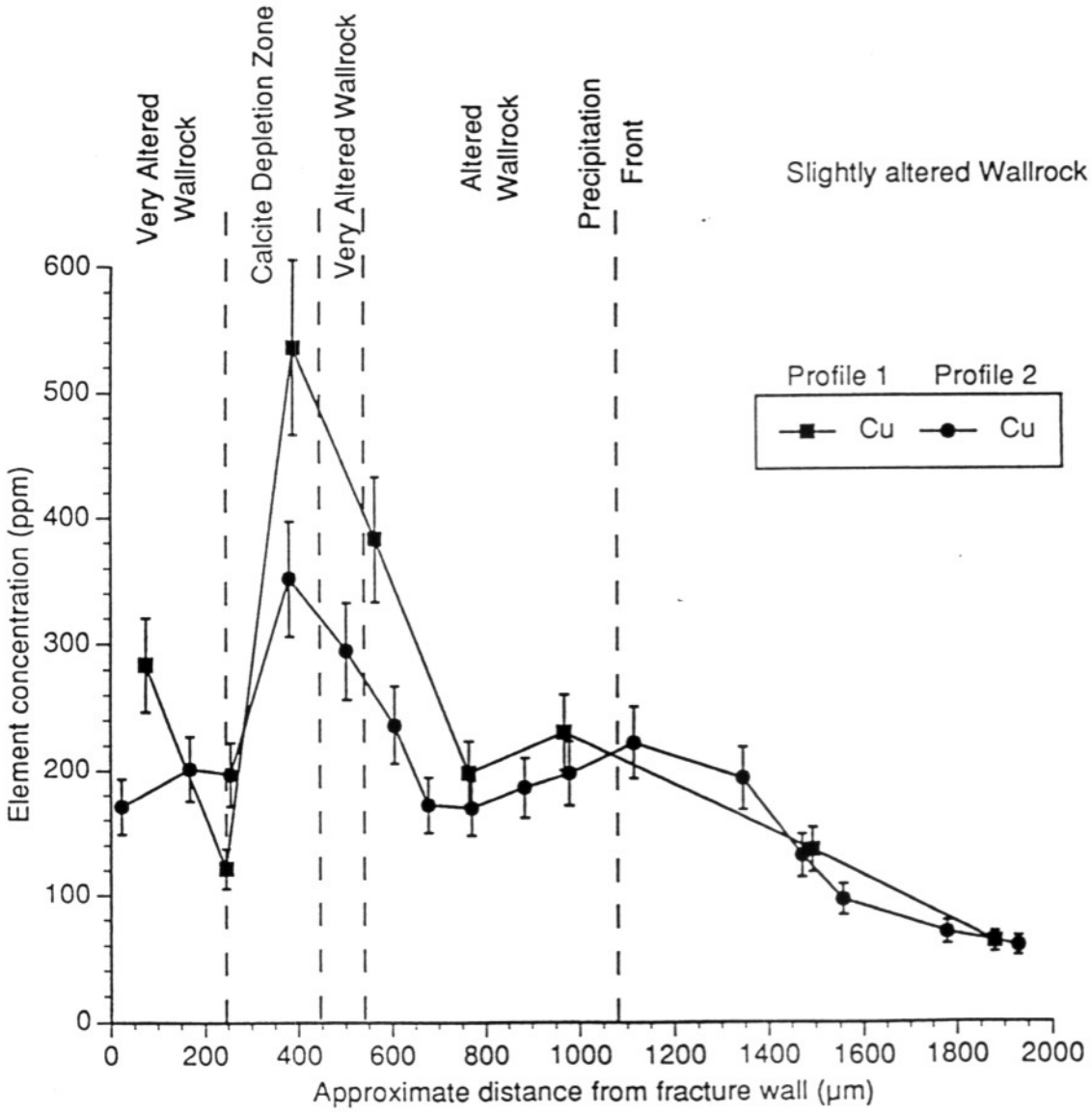

Figure 8.4 Cu concentrations from LAMP-ICP-MS analyses along two profiles through wallrock alteration in sample A960.

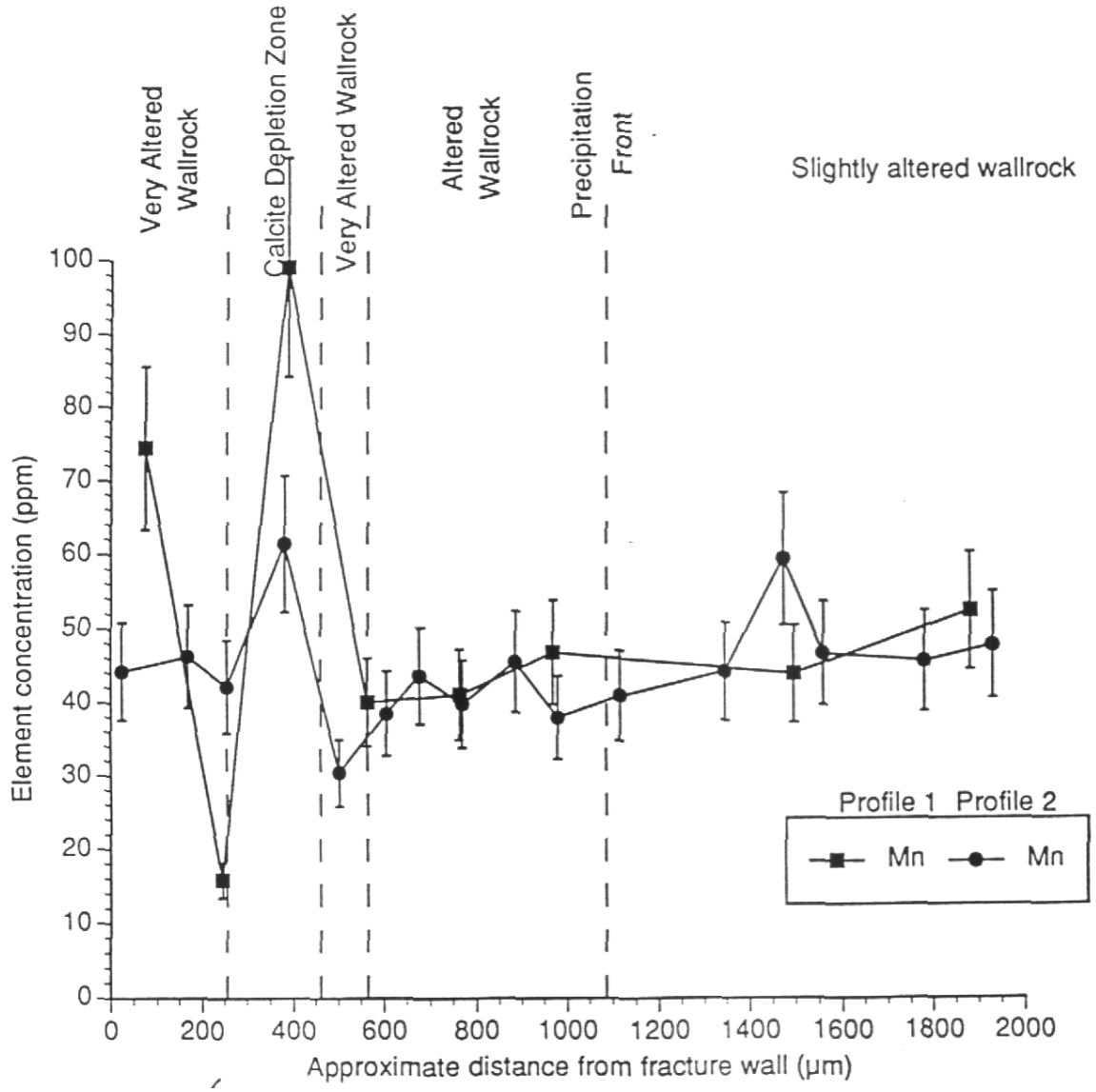

Figure 8.5 Mn concentrations from LAMP-ICP-MS analyses along two profiles through wallrock alteration in sample A960.

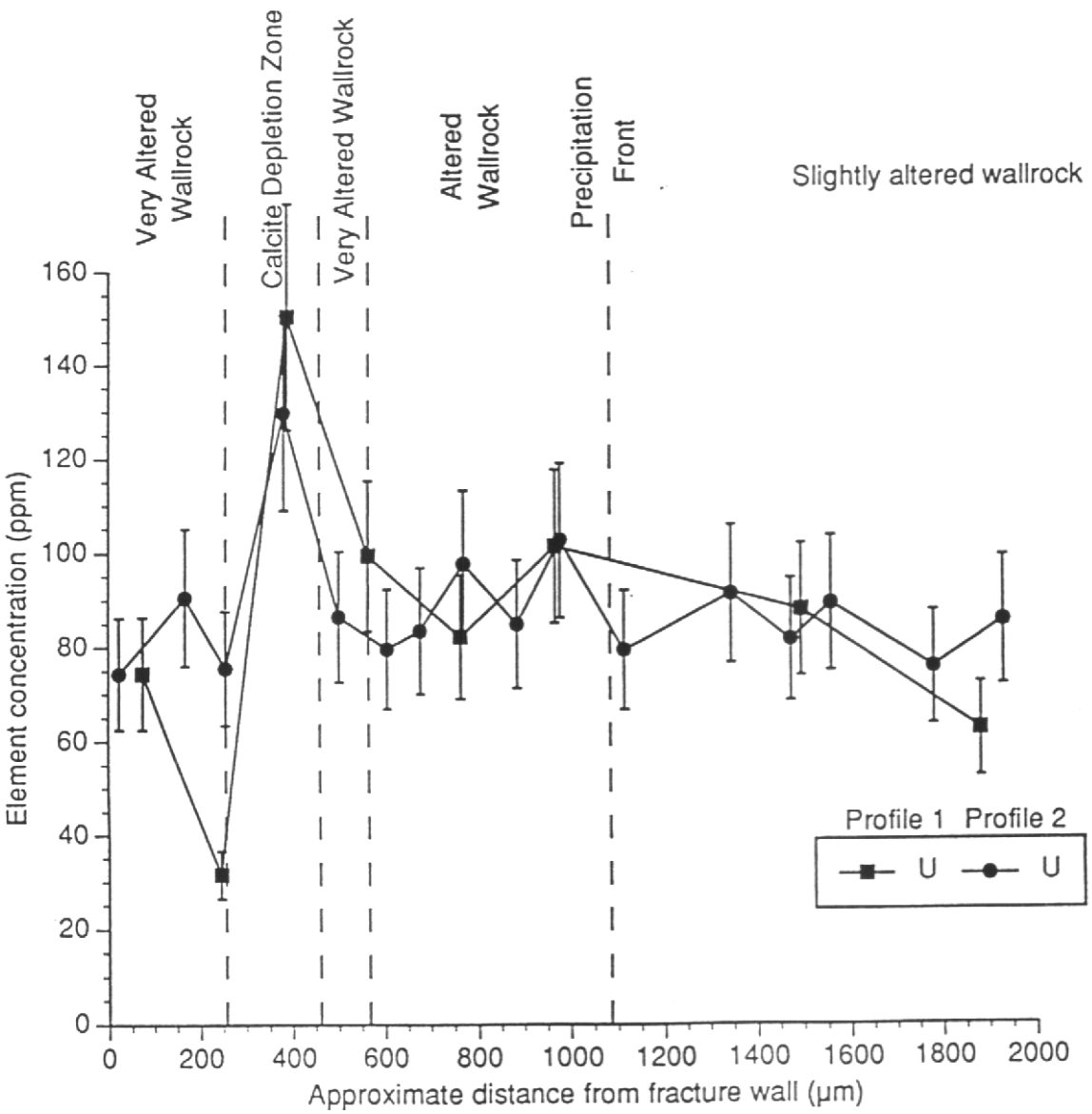

Figure 8.6 U concentrations from LAMP-ICP-MS analyses along two profiles through wallrock alteration in sample A960.

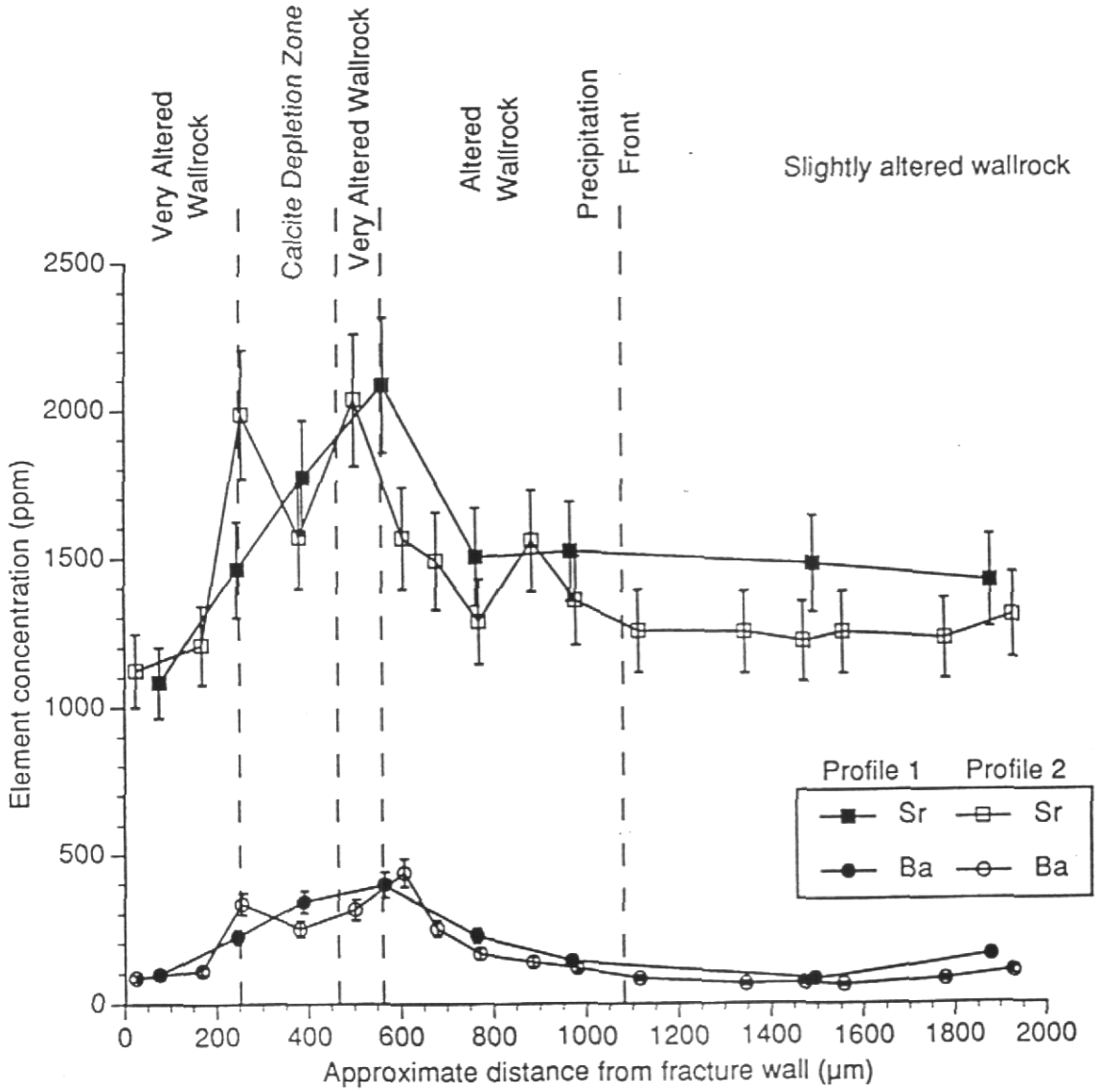

Figure 8.7 Sr and Ba concentrations from LAMP-ICP-MS analyses along two profiles through wallrock alteration in sample A960.

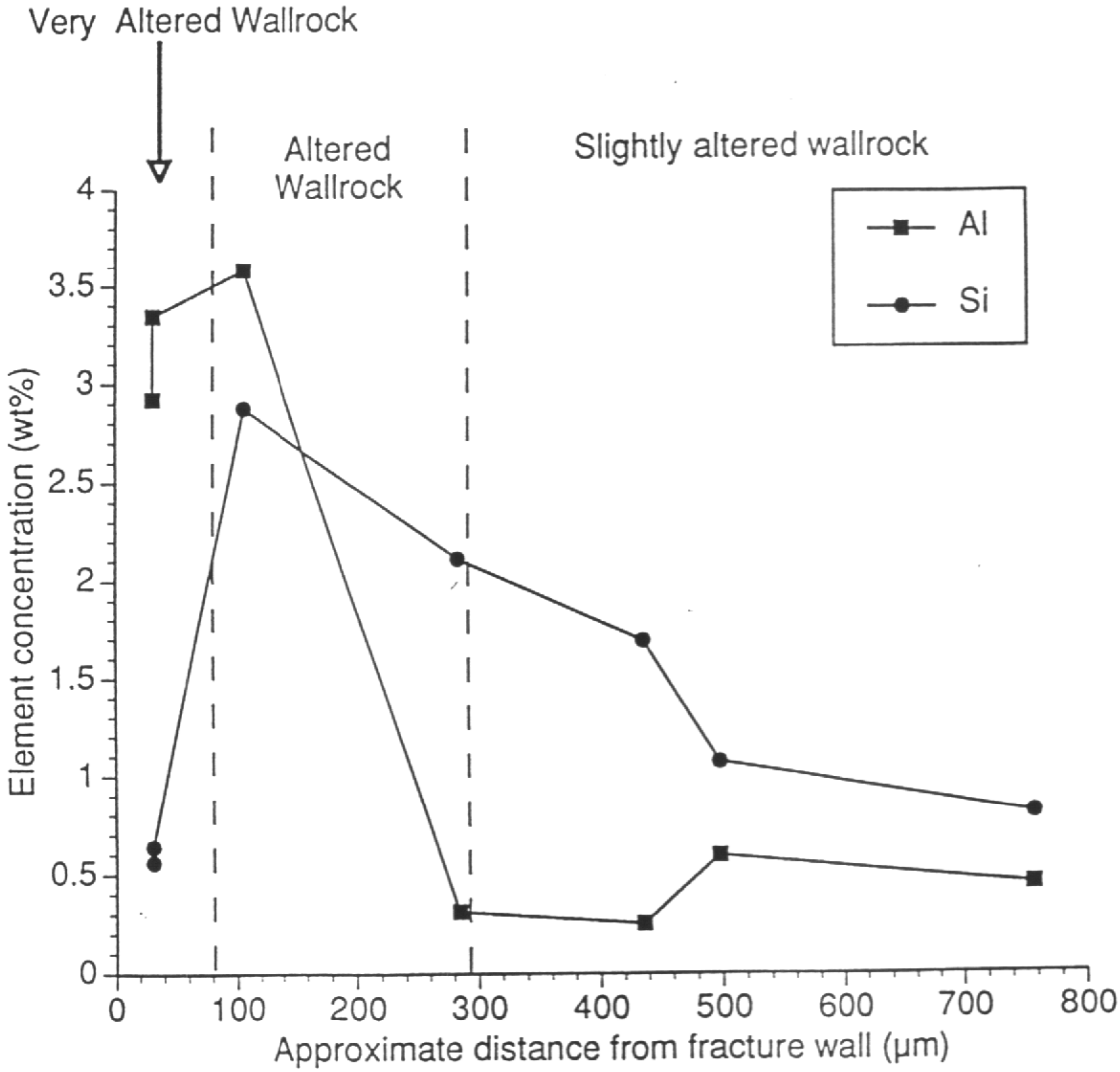

Figure 8.8 Al and Si concentrations from EMPA along two profiles through wallrock alteration in sample A965.

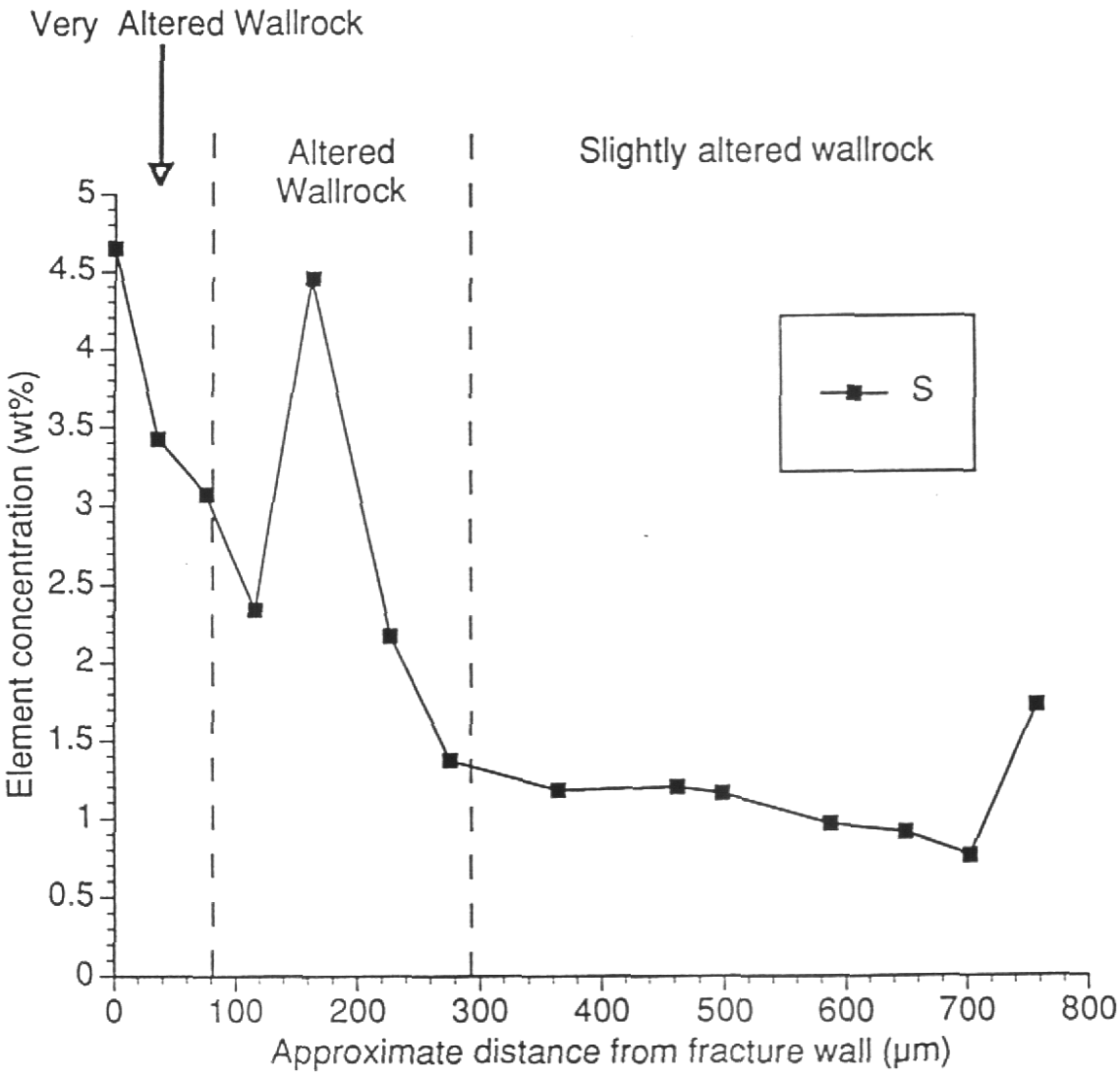

Figure 8.9 S concentrations from EMPA along two profiles through wallrock alteration in sample A965.

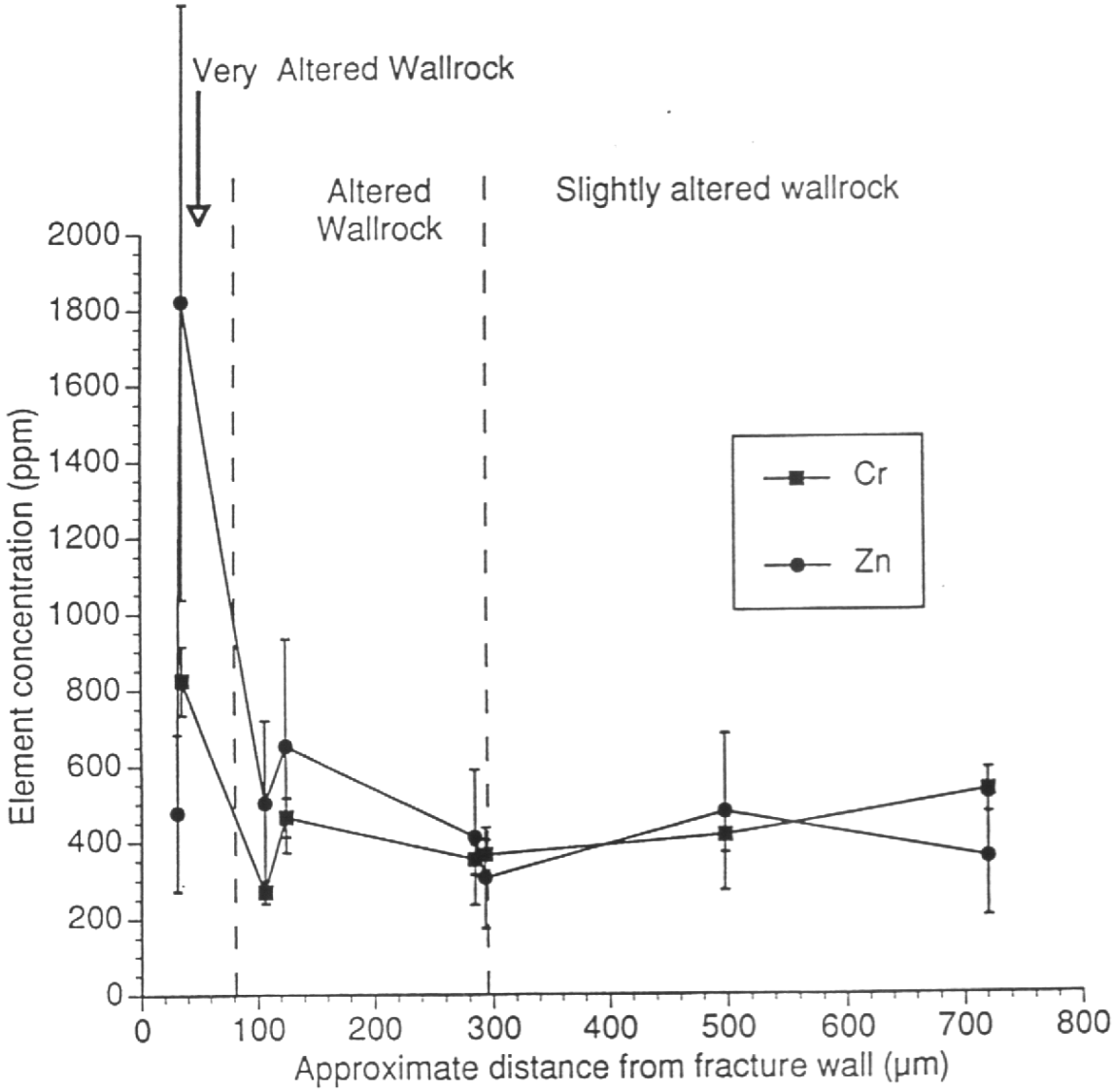

Figure 8.10 Cr and Zn concentrations from LAMP-ICP-MS analyses along two profiles through wallrock alteration in sample A965.

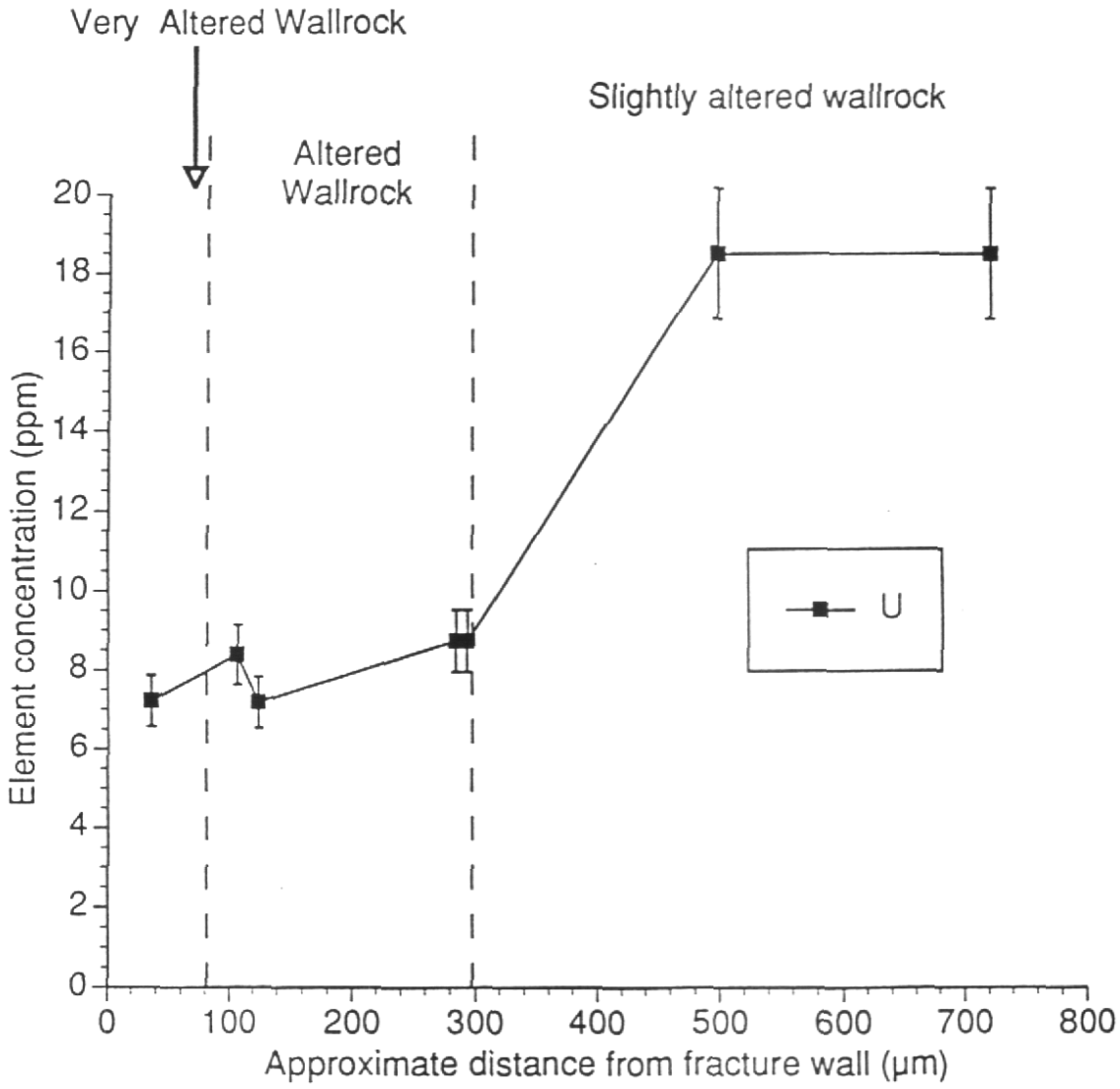

Figure 8.11 U concentrations from LAMP-ICP-MS analyses along two profiles through wallrock alteration in sample A965.

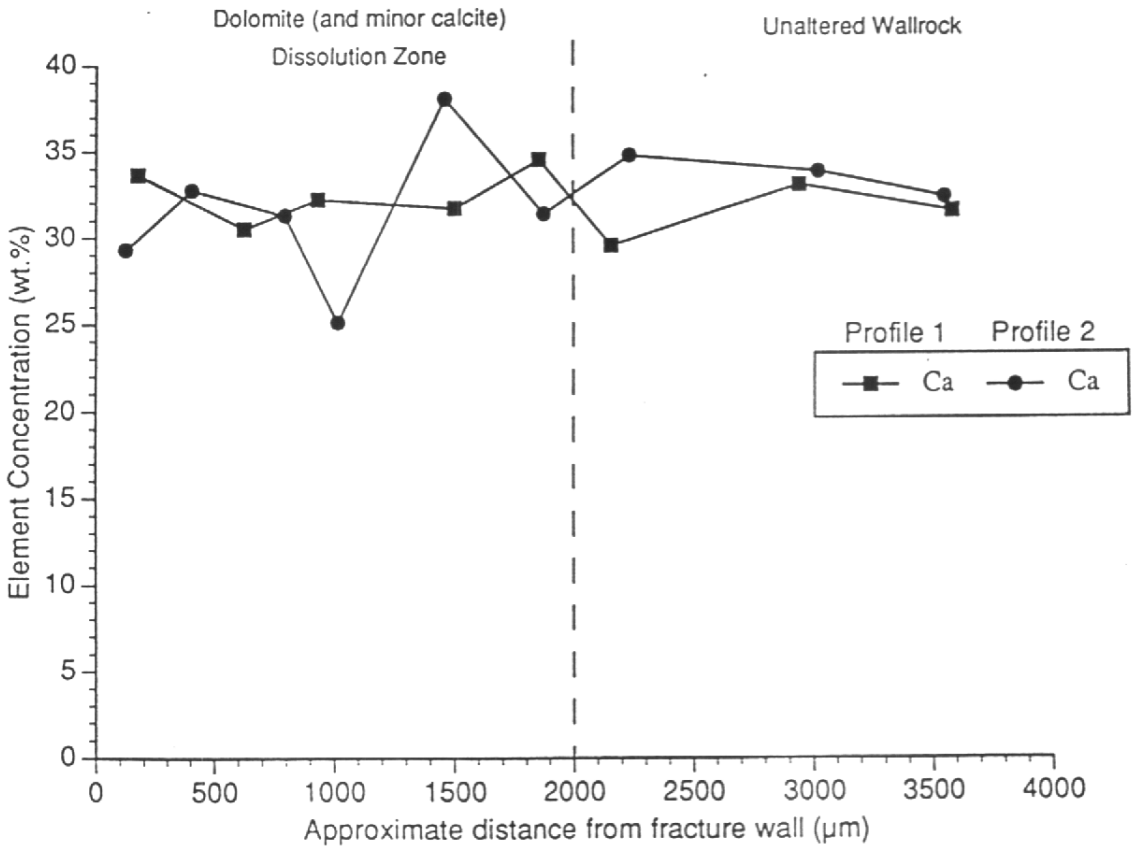

Figure 8.12 Ca concentrations from EMPA along two profiles through wallrock alteration in sample A967.

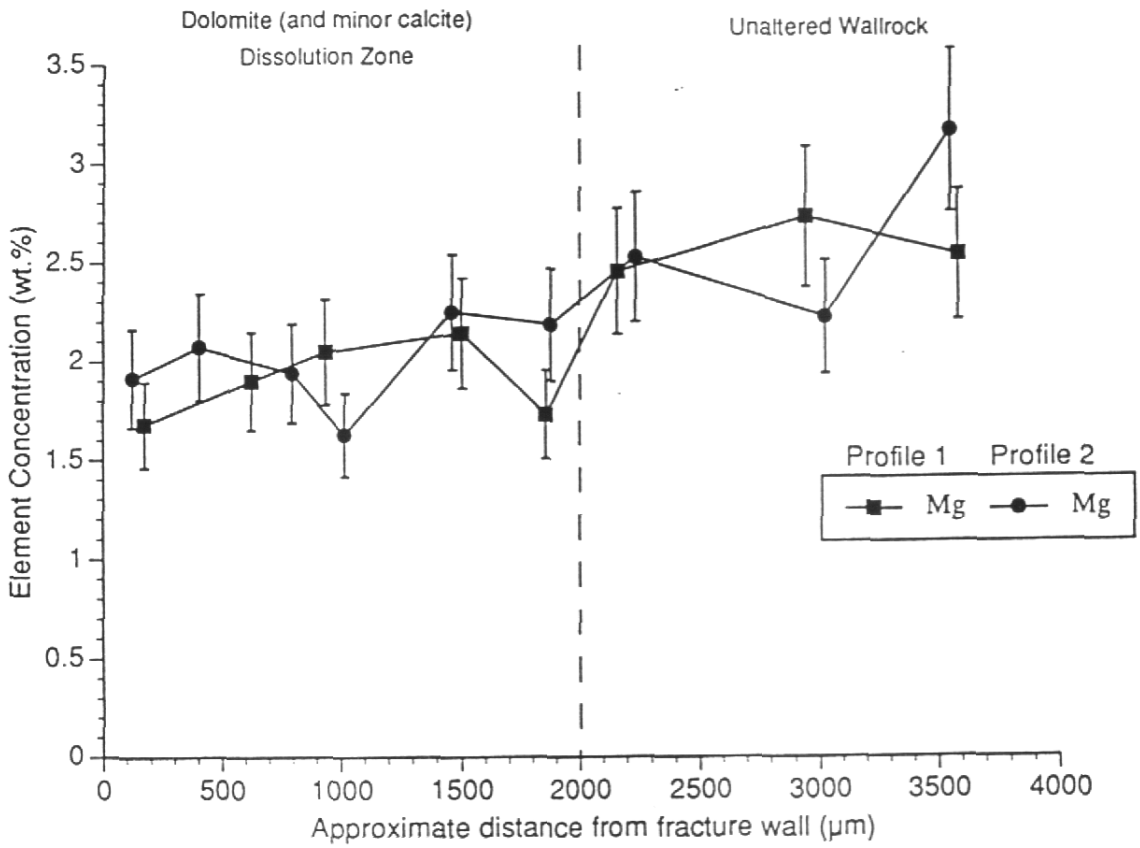

Figure 8.13 Mg concentrations from LAMP-ICP-MS analyses along two profiles through wallrock alteration in sample A967.

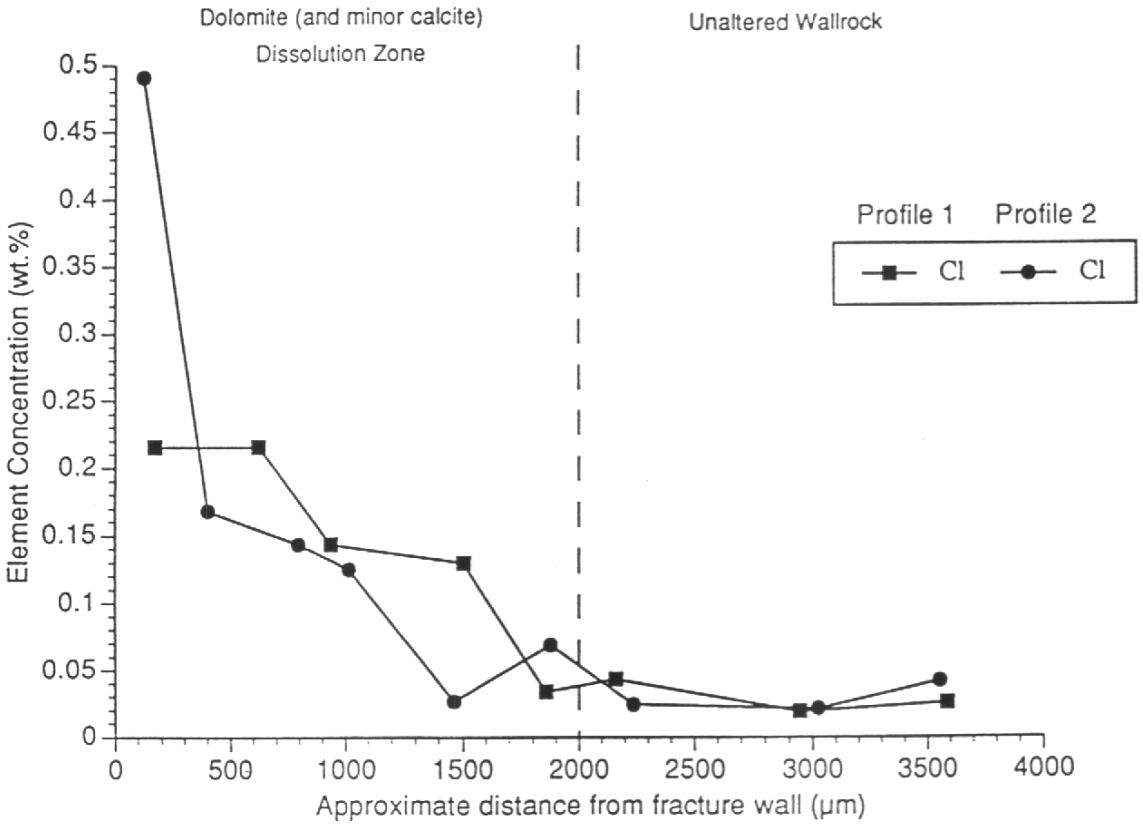

Figure 8.14 Cl concentrations from EMPA along two profiles through wallrock alteration in sample A967.

9. MASS TRANSFER PROPERTIES OF ROCK SAMPLES CONTAINING ALKALINE FRACTURES TAKEN FROM THE MAQARIN SITE

N.S. Stone

9.1 Introduction

The aim of this small programme of work was to measure the diffusivity of samples of altered carbonate rock as a function of distance from a water-conducting fracture. The diffusivity profile will give an indication of the effect of alkali/rock interaction on the transport properties of the material and also provide data for input into the coupled chemistry modelling described in Chapter 13.

9.2 Experimental Details

9.2.1 Methodology

Measurements of diffusion coefficients were undertaken using the through-diffusion technique. In through-diffusion experiments, a sample of rock is sandwiched between two reservoirs. Figure 9.1 shows a diagram of the experimental apparatus. A tracer is added to one of the reservoirs, and diffuses from the high-concentration reservoir through the rock and into the other reservoir (measurement cell). The tracer concentration in the measurement cell is monitored until its rate of rise becomes substantially constant. The increase in concentration in the measurement cell can be plotted to give a breakthrough curve. The asymptotic tangent to this curve is then used to determine the intrinsic diffusion coefficient, D_i value. In this study, tritiated water (HTO) was used as the tracer.

The porosity of the samples was measured by carrying out in- and out-diffusion experiments. For in-diffusion experiments, samples are placed in contact with a known volume of active tracer solution. The tracer diffuses into the sample and the corresponding drop in solution concentration is monitored. Out-diffusion experiments are exactly opposite to in-diffusion experiments; an active sample is placed in contact with a known volume of inactive solution. The tracer diffuses out of the sample and the increase in concentration in the solution is monitored. Using these techniques, porosity can be calculated by means of mass-balance calculations.

9.2.2 Sample preparation

Two samples were studied:

Sample AEM10 Marl with two faces comprising mineralised fracture planes. Between the two fractures are layers of altered and unaltered marl.

Sample AEM7 Unaltered marl. This sample was studied to provide estimates of diffusion properties of the marl prior to alkaline alteration.

Both samples were taken from Adit A6. Further information regarding the samples is given in Table 6.1 (Chapter 6).

The samples were subcored and sliced. In the case of AEM10, the core was perpendicular to one of the fracture faces and slices were taken as a function of distance from the fracture. Subsample AEM10/1 was discarded because it largely comprised the calcite fracture infill.

9.2.3 General

The work was was performed in a low oxygen positive pressure box (containing 0.1% oxygen).

Two groundwaters were used for the experimental programme:

- M2 - a hyperalkaline groundwater from the Adit A6 site.
- M6 - a typical, near-neutral bicarbonate-type groundwater from the area.

Detailed descriptions of the chemistry of these samples are given in Chapter 4. The compositions of the groundwaters prepared for use in this study are given in Tables 9.1 and 9.2.

All sub-samples from AEM10 (with the exception of AEM 10/1) were immersed in a 50:50 solution of M2 groundwater and UHP water and placed under a vacuum of 100 mbar to remove air from the sample. A 50:50 mixture was used to prevent any mineral precipitation from the fluid during the vacuum process (evaporation of solution can occur during evacuation, leading to concentration and possible precipitation of certain components). Samples of AEM 7 were de-aired in a similar manner, this time using M6 simulated groundwater.

Samples AEM 10/2, 3, 4 and 5, and sample AEM 7/3 were sealed into the central part of a perspex through-diffusion cell using Araldite MY753 oxy-resin. The cells were assembled as shown in Figure 9.1. The reservoir cell was filled with simulated groundwater (M2 for AEM 10 samples, and M6 for AEM 7 samples) containing 5000 Bq ml^{-1} tritiated water. The measurement cell was filled with inactive groundwater. The cell was designed so that there was no hydraulic gradient across the sample.

Samples were withdrawn from the measurement cell at regular intervals and the tracer concentration determined using a 'Beckman' liquid scintillation counter. An equal volume of simulated groundwater was added to the measurement cell following sampling in order to maintain a constant volume. Every third sampling interval, the pH and temperature of solutions was noted, and the activity of the reservoir solution checked.

At the end of the experiment (approximately 800 hours), the rock samples were removed from the cell and placed into a known volume of simulated groundwater in order to carry out an out-diffusion experiment. The tritium concentration in the groundwater was monitored with time. When a constant concentration of tritium was achieved, the porosity of the rock was estimated by means of a mass balance calculation.

In addition to the above out-diffusion experiments, the remaining samples of AEM 7 (AEM 7/1, 4) and AEM 10 (AEM/6, 7, 8) were used to run independent in/out-diffusion experiments. The samples were placed in a known volume the appropriate groundwater containing the tracer HTO at a concentration of 5000 Bq ml^{-1}. The drop in tracer concentration was monitored with time. Once a steady concentration was established, the samples removed and placed into a fresh container with 10 ml of inactive simulated groundwater. The increase in tracer concentration was monitored with time. Porosity was calculated from these data by means of a mass-balance calculation.

9.2.4 Analysis of through-diffusion data

Analyses of data from the through-diffusion experiments were undertaken using an in-house computer program, which implemented a mathematical solution to the data obtained from the experiment at long times. This is when conditions of steady-state

diffusion have been reached. This solution, which is based on a porous medium, 'single-porosity' approach, was outlined by Lever [1]. This approach treats all the porosity in the rock sample as accessible and assumes that local access to the porosity occurs rapidly.

Experimental data and known variables (e.g. sample length etc.) are fed into the computer program and then interpreted interactively using a graphics screen. The program automatically corrects data for sample removal from the measurement cell thus taking into account dilution effects.

The user first identifies the experimental data where conditions of steady-state diffusion have been established. The software then processes the data to obtain a least-squares linear fit to determine experimental parameters. As a typical through-diffusion curve can be split into two regions, transient and steady-state (linear), the initial analysis phase concentrates on the linear option of the dataset.

The program calculates and then outputs values, on-screen, for the intrinsic diffusion coefficient (D_i) and the rock capacity factor (α) for the tracer being used in the experiment. Definitions for D_i and α can be found in [1] and [2]. The α value for a conservative tracer is equivalent to the porosity accessible to the tracer.

After analysing the linear portion of the dataset, the user can then model the experimental data using the values of D_i and α obtained during the first phase. The program uses these values and other known variables to calculate concentration data over a fixed time-frame entered by the user. The curve generated by the program covers both the transient and steady-state regions of the experiment. The user can then compare the experimental data with the theoretical curve based on a 'single-porosity' model. The mathematical solution for this curve has been derived by Lever [1]. The equation is as follows:

$$C_m = \frac{ALC_o}{V^2}\left[\frac{D_i t}{L^2} - \frac{\alpha}{6} - \frac{2\alpha}{\pi^2}\sum_{n=1}^{\infty}\frac{(-1)^n}{n^2}\exp\left\{-\frac{D_i n^2 \pi^2 t}{L^2 \alpha}\right\}\right]$$

where V is the volume of solution in the measurement cell

C_m is the concentration of tracer in the measurement cell

C_o is the concentration of tracer in the high-concentration reservoir

A is the cross-sectional area of the rock sample

L is the thickness of the rock sample

t is the duration of the experiment

Values of D_i and α can then be refined interactively to allow D_i and α to be recalculated until a good match to the experimental data is achieved.

9.3 Results

The results are shown in Tables 9.3 and 9.4. Diffusion coefficients in the range $3.7\ 10^{-12}\ m^2s^{-1}$ to $3.05\ 10^{-11}\ m^2s^{-1}$ were determined from the five through-diffusion experiments. The highest coefficient was obtained from the unaltered marl (AEM 7/3). Three of the measurements taken from samples of AEM 10 (potentially altered wall-rock adjacent to a fracture) give diffusion coefficients lying quite close to the value measured

for the unaltered marl (within a factor of two or three). The lowest diffusion coefficient was measured in the case of AEM 10/4, a sample lying 21.5mm from the fracture. The lowest porosity value was also measured in the case of this sample.

Because the samples used in this study were only a few millimetres thick, errors associated with the measured alpha values are large. The porosity values given in Tables 9.3 and 9.4 are therefore calculated using data from in- and out-diffusion experiments. Porosity measurements were made on a total of 11 samples. Porosity values of approximately 30% were measured in the case of the unaltered marl. This is consistent with estimates based on petrographic techniques (Chapter 6).

At distances of greater than 29mm from the fracture in AEM 10, the calculated porosity values correspond to those of unaltered marl, ~30%. However, at lesser distance from the fracture deviations from this porosity are observed; porosities of 24%, ~11% and 38% were measured at distances of 6.8mm, 14-21.5mm and 29mm respectively. It is possible that the reductions in porosity close to the fracture correspond to regions where precipitation of secondary alteration minerals has occurred. Such precipitation might result in blocking of porespace. However, the mineralogical observations described in Chapter 6 suggest that wall-rock alteration occurs on a very small scale (μm-mm). It is not therefore clear what causes the variation in porosity observed in the present study.

9.4 Conclusions

The main conclusions from this study are as follows:

- The data give an estimate of diffusivity to an accuracy of around an order of magnitude. It is recommended that a values of 3 $10^{-11}m^2s^{-1}$ be used as input to the coupled chemistry/transport modelling (Chapter 13).
- Estimates of porosity for samples of unaltered marl were consistent with those determined using petrographic techniqes, ~30%. Porosities for AEM 10 samples range from 11% to 40%. The values deviating most from that of unaltered marl were found in the subsamples taken from within 30mm of the fracture.
- The samples used in the study were several millimetres thick. This precludes their use in determining changes in the physical properties of the rocks within the zone of alteration around a fracture at Maqarin, as such zones were found to extend distances of only microns to millimetres from the fracture (Chapter 6).

9.5 References

[1] D.A. Lever, *Some Notes on Experiments Measuring Diffusion of Sorbed Nuclides through Porous Media*, UKAEA Report, AERE-R.12321, 1986.

[2] P.J. Bourke, D. Gilling, N.L. Jefferies, D.A. Lever and T.R. Lineham, *Laboratory Experiments of Mass Transfer in the London Clay*, Nirex Report, NSS/R135, 1988.

Table 9.1 Groundwater M2. Artificial groundwater made up into 5 litres of UHP water.

Chemical	Amount (g)	Added as
Calcium Hydroxide.	2.85	$Ca(OH)_2$
Calcium Sulphate.	2.41	$Ca(SO_4)_2.2H_2O$
Calcium Carbonate.	0.148	$CaCO_3$
Sodium Carbonate	0.154	Na_2CO_3
Potassium Chloride	0.124	KCl
Sodium Chloride	0.510	NaCl

pH of groundwater M2 = 12.20.

Table 9.2 Groundwater M6. Composition of artificial groundwater made up into 5 litres of UHP water.

Chemical	Amount (g)	Added as:
Calcium Carbonate	0.95	$CaCO_3$
Sodium Chloride	0.1468	NaCl
Calcium Sulphate	0.071	$CaSO_4.2H_2O$
Magnesium Nitrate	0.21	$Mg(NO_3)_2$
Potassium Chloride	$5.9\ 10^{-3}$	KCl

pH of groundwater = 9.80 adjusted to pH 7.57 by the addition of 0.1 M HCl.

Table 9.3 Summary of experimental results for sample AEM10

Sample	Sample thickness (mm)	Distance from fracture (mm)	D_i(HTO) (m^2s^{-1})	Alpha	Porosity (%)
AEM10/1	2	0	-	-	-
AEM10/2	3.80	6.8	$2.32\ 10^{-11}$	1.1	24.0
AEM10/3	4.40	14.2	$1.42\ 10^{-11}$	N/C	11.99
AEM10/4	4.30	21.5	$3.70\ 10^{-12}$	0.24	11.20
AEM10/5	4.50	29	$8.69\ 10^{-12}$	0.16	37.72
AEM10/6	4.72	36.7	-	-	31.1 ± 4.4*
AEM10/7	4.30	45	-	-	33.1 ± 4.7*
AEM10/8	1	58	-	-	31.7 ± 10.8*

* An error limit is given because the samples were offcut and it was hard to calculate the volume of the samples.

Table 9.4 Summary of experimental results for sample AEM 7

Sample	Length (cm)	D_i(HTO) (m^2s^{-1})	Alpha	Porosity (%)
AEM7/3	0.452	$3.05\ 10^{-11}$	N/C	28.94
AEM7/1	0.460	-	-	30.58
AEM7/4	0.470	-	-	28.9 ± 4.2*

* An error limit is given because the samples were offcut and it was hard to calculate the volume of the samples.

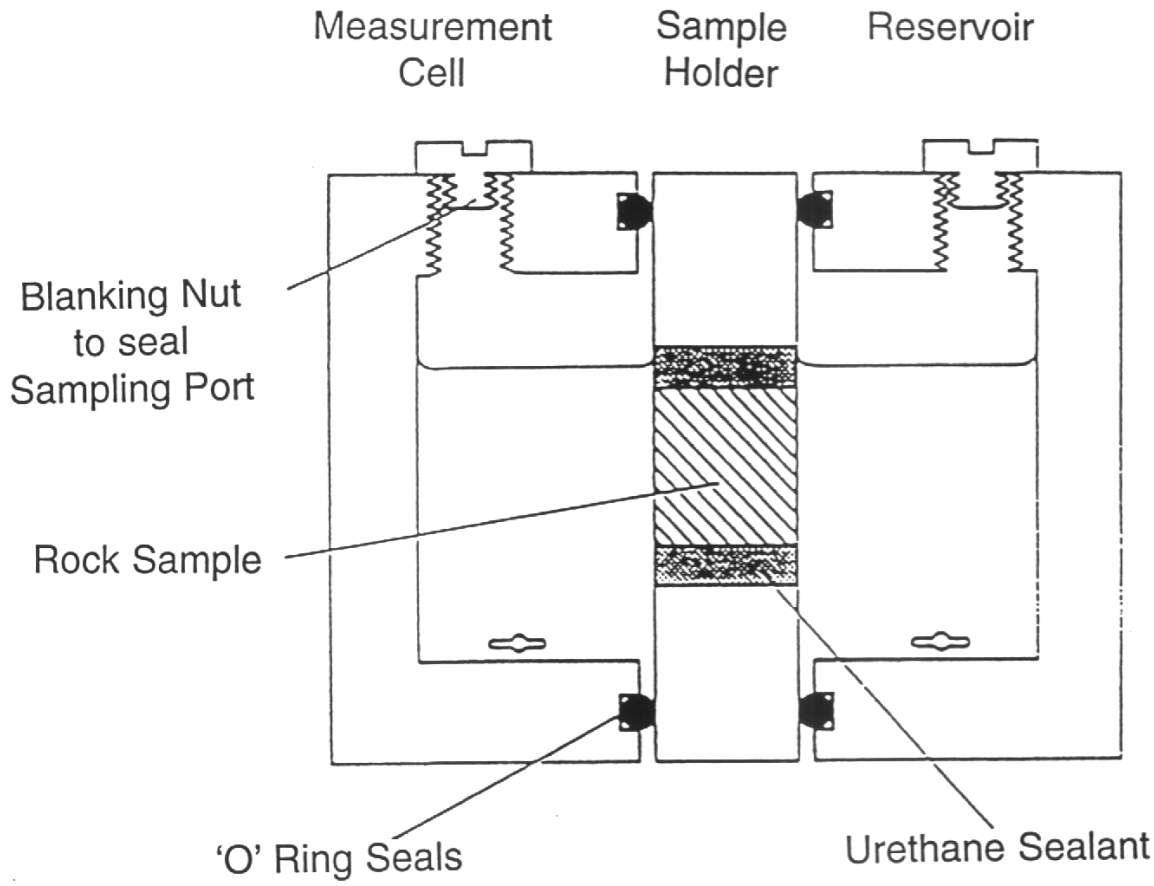

Figure 9.1 Schematic diagram of a through-diffusion cell. The rock sample is sealed into the central part of the cell and the reservoir and measurement cell are filled with simulated groundwater. The tracer is added to the reservoir and its breakthrough into the measurement cell is monitored with time.

10. ISOTOPE HYDROGEOLOGY OF THE MAQARIN HYPERALKALINE GROUNDWATERS

I.D. Clark and P. Fritz

10.1 Introduction and Objectives

The principal interest in isotope hydrogeology at the Maqarin natural analogue study site is to elucidate the origin of the hyperalkaline groundwaters, to evaluate controls on their aqueous chemistry and the nature of rock-water interaction, and to estimate their age and possibly the age of the metamorphic events. It is felt that this information is important in assessing their relevance as an analogue to the early and later stage movement of groundwater through a cementitious repository. In addition to these aspects, it was felt that the stable isotope contents of calcites as well as of mineral hydration waters and hydroxide phases would shed some light on the sequence of metamorphic reactions.

10.2 Sampling and Analysis

Samples were collected for environmental isotope and geochemical analysis during the field campaign of June, 1992, described in Chapter 3. Stable isotope ratios in water samples were measured in the Stable Isotope Laboratory, University of Ottawa by standard methods involving measurement of CO_2 gas equilibrated with water samples at 25°C (for ^{18}O) and measurement of hydrogen gas evolved by the reduction of water by reaction on zinc at 430°C. Tritium concentrations were measured by the Institute for Hydrology/GSF by counting on propane synthesised from water.

Water samples for dissolved sulphate analysis were filtered to 0.45μm and collected in 500ml bottles. No cadmium acetate was added as earlier studies have shown these waters to be sulphide-free. Dissolved sulphate was precipitated as $BaSO_4$ from solution with $BaCl_2 \cdot 2H_2O$. This was mixed with copper oxide and converted to SO_2 for mass spectrometric analysis of ^{34}S by high temperature reaction (University of Ottawa), and to CO_2 for analysis of ^{18}O by high temperature reaction with graphite (University of Waterloo).

Dissolved chloride was stripped from 11 samples and converted to AgCl targets for ^{36}Cl analysis according to routine methods. Analyses were performed on the Atomic Energy of Canada Ltd. particle accelerator facility at Chalk River, Ontario. All isotope data for water and dissolved constituents are given in Tables 10.1 and 10.2.

Mineralogical samples were analysed for the ^{2}H content of hydration waters and hydroxide. Analyses were carried out by drying powdered samples under vacuum at 25°C, then dehydrating at 200°C for 10 minutes. Water vapour was trapped with liquid nitrogen and non-condensable gases removed prior to freezing onto zinc metal in glass break-seals before reaction and analysis. Deuterium was analysed on H_2 produced by heating the breakseals to 430°C according to standard methods.

10.3 Age of Groundwaters

Tritium

As discussed in the Phase I report [1], Maqarin Eastern Spring groundwaters are tritium free, indicating mean residence times of at least several decades. One of the two Western Spring samples was also tritium free and the other had a measured value of 3 TU. This

suggests that these springs may have a component of modern recharge. Repeat sampling was undertaken in Phase II (Table 10.1). This third ^{3}H analysis from the Western Springs is tritium-free, indicating that these groundwaters are dominated by recharge water older than at least 40 years. Phase II samples from Adit A-6 and the Railway Cutting are very close to the 1σ detection limit, confirming that the mean residence time of these groundwaters is at least 40 years.

Recent investigations at the Western Springs area show that these hyperalkaline groundwaters discharge from the contact between the bedrock and overburden. In this setting, minor amounts of tritium can be attributed to contamination by overburden groundwaters.

Carbon-14

The dissolved inorganic carbon content (DIC) of the hyperalkaline groundwaters is maintained at less than 2 mg l^{-1} by the high pH and high Ca^{2+} content. This low level, and the rapid uptake of atmospheric CO_2, greatly increase the risk of ^{14}C contamination during sampling. Further, the series of alteration reactions involving metamorphic CO_2 and secondary carbonate minerals complicate the origin of DIC, and has precluded $^{14}C_{DIC}$ dating of the groundwater.

Chlorine-36

Three Phase II samples were submitted to AECL Chalk River for ^{36}Cl activity measurement (Adit A6 - M1, Railway Cutting - M3 and Western Springs - M5). These data are given in Table 10.2. Chlorine-36 in groundwaters originates from a variety of sources, which can be used to provide hydrogeological information:

(i) Natural atmospheric production of ^{36}Cl occurs due to solar activation of atmospheric argon. It is then incorporated into groundwaters during recharge. Decay from input concentrations can be used to estimate subsurface mean residence times. However, the long half-life of ^{36}Cl (300,000 years) makes this suitable only for very old groundwaters.

(ii) During the era of thermonuclear bomb testing, the high neutron fluxes generated caused an activation of marine Cl^- and atmospheric Ar, generating a fallout peak several orders of magnitude greater than natural levels. The occurrence of high ^{36}Cl (>5000 10^5 atoms l^{-1}) would indicate, like tritium, that the groundwaters are young.

(iii) In situ production in aquifers with high concentrations of radioactive elements (U, Th, K) is a third mechanism for ^{36}Cl production. Ingrowth towards secular equilibrium can then be used to estimate subsurface residence times. However, this mechanism is generally important for groundwaters with long residence times in crystalline rocks, and carbonate rocks such as found at Maqarin are not an important source for ^{36}Cl.

(iv) In arid regions, ^{36}Cl will accumulate in the recharge environment due to evaporation and epigenic production by cosmic radiation, largely on Cl-salts at the surface. Elevated levels of ^{36}Cl are then an indication of water loss prior to recharge due to evaporative concentration and long surface residence times for salts. Natural atmospheric production is a function of latitude, with fallout in the Maqarin region in the order of 14 atoms $m^{-2}\cdot s^{-1}$. Given an average of 350 mm of rainfall annually at Maqarin, this would provide a concentration in rainfall of about 12.6 10^5 atoms l^{-1}. Little is known about ^{36}Cl production at the ground

surface, although indications are that this could be similar to or greater than atmospheric fallout [2].

From the geochemical studies in Phase I [1], it was determined that the source of chloride in the hyperalkaline groundwaters was external, likely originating as marine aerosols. There were no significant contributions of Cl^- from the alteration zones. The $^{36}Cl/Cl$ ratio should then preserve recharge conditions. From Table 10.2, the ^{36}Cl contents of the hyperalkaline groundwaters are over ten times higher than the calculated concentration in fallout from natural atmospheric production. However, they are much lower than the range anticipated if 'bomb' ^{36}Cl were present. The measured levels suggest significant evaporative concentration and/or surface leaching in the recharge area prior to infiltration. The following points can be made:

(i) An input concentration in rainfall in the recharge area can be calculated from the average fallout rate of ^{36}Cl for this latitude (14 atoms$\cdot m^{-2}\cdot s^{-1}$[3]) and the average annual rainfall for Maqarin (350 mm). The concentration of ^{36}Cl in rainfall is then 12.6 10^5 atoms l^{-1}. If surface production is as high as 2 to 4 times atmospheric production, infiltrating groundwaters (prior to any evaporative loss) would have well below 100 10^5 atoms l^{-1}.

(ii) The ^{36}Cl concentrations are elevated above this level in all three samples. This strongly suggests that evapotranspirative concentration in the recharge environment occurs. Stable isotope enrichment in the Eastern system groundwaters show an evaporative trend, which supports this interpretation.

(iii) The lack of bomb ^{36}Cl indicates that the chloride in these waters (and hence the waters themselves) have entered the system prior to the era of weapons testing (1947 to 1969). This is consistent with the tritium levels which are less than detection for all but one sample.

10.4 Stable Isotopes in Hyperalkaline Groundwaters

Stable isotope data may provide some insights into the origin of and processes affecting these highly alkaline waters. The stable isotope composition of rainfall has been monitored at Irbid, 20 km south of the study area and used to define a local meteoric water line (LMWL) [4]. From Figure 10.1, both the Eastern and Western groundwaters are isotopically enriched with respect to the LMWL, which may be an evaporative enrichment due to low infiltration rates. This is supported by the single value for neutral pH groundwaters at Maqarin (Figure 10.1), and is consistent with the elevated concentrations of ^{36}Cl discussed above.

Comparison of the isotopic signature of the hyperalkaline springs with the mean composition of artesian groundwaters from the regional B2 aquifer shows that these waters do not contribute recharge to the hyperalkaline groundwaters. Upward leakage of regional groundwaters from this underlying aquifer at Maqarin is unlikely.

Western groundwaters show a small but consistent ^2H enrichment over the Eastern groundwaters, which may be a result of mineral hydration reactions.

Deviation of shallow non-thermal groundwaters from the local meteoric water line can occur due to recharge or subsurface processes:

(i) Evaporation of groundwaters during recharge will impart a positive enrichment for both ^{18}O and ^2H along a line with slope of about 3 to 5 (Figure 10.2). Modest evaporation is evident in the single non-alkaline groundwater sampled in the

Maqarin area, although it falls within the range observed for local rain on Figure 10.1.

(ii) Hydration of silicate and sulphate minerals (anhydrite to gypsum), if the mineral to residual water ratio is large, will selectively enrich the residual water in ^{2}H and deplete it in ^{18}O (e.g. †[5] $\varepsilon^{18}O_{water\text{-}gyp} \approx 4‰$; $\varepsilon^{2}H_{water\text{-}gyp} \approx -20‰$) (Figure 10.2). For gypsum, the residual water during hydration evolves isotopically along a trend line above the meteoric water line, ideally along a line with slope of about -5. For other hydration reactions, a principal feature is deuterium enrichment, which may be the case for the Maqarin hyperalkaline groundwaters. Fractionation factors for hydration of CSH phases in cements have not been established.

(iii) In highly alkaline groundwaters, strong H_2O-hydroxide fractionation during hydration reactions may impart isotopic enrichments on H_2O. The fractionation between water and OH^- is in the order of 40‰. The fractionation for deuterium is considerably greater (up to 1400‰), and so in hydroxide precipitating systems, the residual water should show progressive enrichment, particularly in ^{2}H. A $\delta^{18}O$ enrichment of 1 to 2‰ in water during hydration of cement (pH >10) has been noted [6].

During mineral hydration under conditions of low water/rock ratio, the mineral hydration waters will be depleted, and the first pore volume of groundwater moving through the reaction zone will have a reciprocal enrichment. If the selective enrichment for ^{2}H observed for the Western Springs in Figure 10.1 is attributed to mineral hydration, then mineral hydration waters should have low $\delta^{2}H$ values. This would be consistent with the higher pH and degree of mineralisation in the Western groundwater (Figure 10.3, and Chapter 4). As discussed below, $\delta^{2}H$ values for mineral hydration waters are indeed depleted, suggesting that the ^{2}H enrichment in the Western hyperalkaline groundwaters may be in part due to mineral hydration. If so, they would be close to the first porewaters discharging from the alteration zone.

10.5 Isotopes in Mineral Phases from the Metamorphic Zone

Environmental isotopes in carbonate phases (^{13}C and ^{18}O) and in the hydration waters of alteration minerals in brecciated zones in Adit A-6 have been examined. In Phase Ib, a laser microsampling study was undertaken to look at the carbonate phases. The results of this study will be briefly discussed here as a basis for the current work analysing ^{2}H contents in hydration waters. The ^{2}H composition of hydration waters for early and later stage mineral phases (Table 10.3) from the reaction zones at Maqarin were examined to:

(i) evaluate their possible use in establishing reaction sequences, and

(ii) to establish whether the effects of extensive hydration reactions on the residual fluid would be apparent in the hyperalkaline groundwaters. This could establish whether the Western groundwaters represented the first pore volume passing through the alteration zone.

---

† - The fractionation factor, α, between two substances A and B is defined as: $\alpha_{A\text{-}B} = R_A/R_B$, where R is the ratio of heavy to light isotope in the relevant substance. Often, α, is very close to unity, and is common to discuss fractionation in terms of 'permil (‰) fractionations', or $10^3 \ln\alpha$. For example, if $\alpha = 1.0036$, then the permil fractionation would be 3.6. In the literature, different ways of expressing the fractionation factor are used. In the text above, it is defined as ε. This quantity is defined as $\varepsilon = (\alpha\text{-}1)10^3$ and is approximately equal to $10^3 \ln\alpha$.

Carbonate Phases - $\delta^{13}C$ and $\delta^{18}O$

Mineralogical evidence and stable isotope information acquired through Nd-YAG laser micro-sampling and standard isotope analysis methods suggest that calcination with subsequent recarbonation has been extensive. The results are illustrated in Figure 10.4. Partially calcined 'marble' shows ^{13}C and ^{18}O depletions characteristic of high-temperature metamorphic carbonates. Early secondary carbonates are highly depleted in ^{13}C and ^{18}O, documenting recarbonation in an elevated temperature environment under non-saturated conditions with the participation of organic C from combusted bitumen. Later stage carbonates were precipitated in a lower temperature environment.

The following model outlines the probable sequence of reactions from initial high temperature calcination of the bituminous marls, to the subsequent retrograde alteration by a CO_2-rich atmosphere under non-saturated conditions during cooling (Figure 10.5).

High temperatures generated in the reaction zones led to decarbonation and a prograde metamorphic assemblage dominated by isotopically depleted carbonate minerals including spurrite and recrystallised calcite ($\delta^{13}C \approx -14‰$), plus metamorphic silicates, complex anhydrous sulphosilicates, sulphides and oxides. Retrograde alteration of this high temperature assemblage began in the initial phase probably with water vapour which hydrated oxide phases and led to the formation of calcium hydroxide and the various calcium-silica-hydrate phases. Under the non-saturated conditions prevailing in these reaction zones, strong temperature gradients promoted the circulation of an atmosphere rich in CO_2 from combusted bitumen and calcination of the marls. The high accessibility of CO_2 to reaction sites resulted in extensive carbonation of hydroxide and CSH phases. However, as carbonation proceeded, temperatures in the alteration zones were dropping, permeability for the circulating atmosphere was becoming restricted by accumulation of reaction water and recirculating local meteoric waters. This reduction in permeability as carbonation proceeds has been documented by Reardon et al. [7] in laboratory columns.

Under conditions of complete saturation recarbonation ended and secondary alteration in these zones evolved to hydroxide and sulphate dissolution reactions. These reactions characterise the hyperalkaline groundwaters observed discharging today from the metamorphic zones at Maqarin.

Radiocarbon measurements were carried out on selected sub-samples to assess the participation of atmospheric CO_2 dioxide in the recarbonation process. Most interesting is a value of 92.4 pmC for the matrix in one sample (M39P, [8]) composed of portlandite, with ingrown calcite and ettringite. This value is close to modern atmospheric values, and the sample can have formed no earlier than 650 a. Clearly, a modern process of recarbonation occurs in some zones. Contributions of ^{14}C-free CO_2 during recarbonation result in lower ^{14}C-activities, as is the case for other samples within the recarbonation zone (e.g. A6.3P - ^{14}C = 4.82 pmC; A6.6P, ^{14}C = 19.68 pmC). The high ^{14}C activity of M39P cannot be attributed to recarbonation after sampling because the ^{13}C ($\delta^{13}C$ = -15.7‰) is close to that of soil CO_2 in arid regions, and not atmospheric CO_2 ($\delta^{13}C$ = -7‰).

Mineral Hydration Waters - $\delta^{2}H$

Samples were supplied by the British Geological Survey and sample numbers correspond to those used in mineralogical studies (Table 10.3). Duplicate analyses were undertaken

on all samples. Differences between these duplicates reflect sample inhomogeneities. In most cases, repeat analyses are close.

While the samples analysed here were collected from the metamorphic zone which hosts the eastern hyperalkaline groundwaters, it is unlikely that they were precipitated from the specific hyperalkaline groundwaters analysed in this program. These values are considered to be representative hydration products of the hyperalkaline waters. Additional analyses are required to determine a representative standard error on these analyses.

These data show that for most samples, hydration waters of secondary minerals are in general strongly depleted with respect to the current hyperalkaline groundwaters, and can account for the δ^2H enrichment observed in the hyperalkaline waters. No information exists in the literature for the fractionation of ^2H between thaumasite and water or ettringite and water. Further, it should be noted that both minerals contain hydroxide which likely fractionates differently than hydration waters. However, the representation of hydrogen in hydration waters exceeds that of hydrogen in hydroxide by a factor of 4 to 6.5. Nonetheless, in these minerals ^2H fractionation is likely to be similar to that in other hydrated minerals such as gypsum. Hydrogen in gypsum is depleted in ^2H by about 20‰.

The degree of enrichment imparted on the hyperalkaline groundwaters by mineral hydration will be a function of both the fractionation factor (-20‰ in the case of gypsum) and the volume ratio between the hydrating mineral and the water. In the case of Maqarin it is too early to establish this ratio in a quantitative fashion. No mineral samples from the Western groundwaters, for which the larger isotopic enrichment was observed, have yet been collected. Nonetheless, the following points can be made:

(i) Most mineral hydration waters are depleted in ^2H with respect to the hyperalkaline groundwaters, indicating that a reciprocal enrichment of the waters has taken place.

(ii) The mean δ^2H value for mineral hydration waters is -57.5‰, while the mean δ^2H for the Western hyperalkaline groundwaters is -18.4‰. However, the standard deviation for the hydration waters is 62.2‰ indicating a high degree of heterogeneity. This is likely linked to the rates and timing of hydration by the hydrating fluids. Progressive hydration of minerals with a single aliquot of water will result in the progressive enrichment of the water, and of the hydration waters for minerals subsequently hydrated.

(iii) The very slight enrichment of the Western hyperalkaline groundwaters over the Eastern waters and local, neutral pH groundwaters (Figure 10.1) suggests that these porewaters represent a much larger reservoir that the hydration waters in the alteration zones. For larger porewater/hydration water ratios, the δ^2H value for the hyperalkaline porewaters would be significantly more enriched.

(iv) Using a simple Rayleigh distillation of local groundwaters with an initial δ^2H=-25‰ and an average for ^2H in mineral hydration waters of δ^2H=-58‰ ($\varepsilon^2H_{water\_mineral}$ = -33‰) shows that a loss of about 20% of pore water in the reaction zone during hydration would enrich the residual pore water to δ^2H=-18‰.

10.6 Origin of Dissolved Sulphate

Dissolved sulphate in the hyperalkaline groundwaters is intimately linked with the metamorphic event and subsequent retrograde alteration. The Western Springs have sulphate contents exceeding 1500 mg/l, while in the Eastern Springs SO_4^{2-} levels are only

about 250 mg/l. Both aqueous sulphate and sulphate minerals from the alteration zones have likely originated from the combustion of organic sulphur in bitumen and from the oxidation of diagenetic pyrite. Both are present, although evolved gas analyses (Chapter 6, Table 5.4) show organic sulphur to be more stoichiometrically more important. The $\delta^{34}S$ values for dissolved sulphate from the hyperalkaline groundwaters (Figure 10.6) fall into the narrow -5 to 0‰ range for Mesozoic petroleum and bitumen. Data for Mesozoic petroleum and bitumen were taken from Krouse [9]. The enriched ^{18}O values are typical for sulphate which has formed through the oxidation of reduced sulphur with the participation of atmospheric oxygen.

Thus, SO_4^{2-} and sulphate minerals likely originated from oxidation of organic sulphur and pyrite during combustion. The exact reactions which took place are difficult to establish, although a series of intermediary sulphur species, including SO_2, sulphite [SO_3^{2-}] and thiosulphate [$S_2O_3^{2-}$], are likely to have formed. Subsequent oxidation would then have occurred under aqueous conditions with the participation of H_2O to produce the range of values observed.

10.7 Summary

The maximum age of hyperalkaline groundwaters at Maqarin has not yet been established. The lack of ^{36}Cl from atmospheric nuclear weapons testing in these groundwaters supports evidence from ^{3}H that these waters are older than at least 40 years.

The age of the combustion event has not yet been determined at Maqarin. However, ^{14}C concentrations in the secondary carbonates formed by recarbonation of portlandite and CSH-like phases suggest that some alteration may be less than a few hundred years old. $^{230}Th/U$ dating of secondary hyperalkaline vein mineralisation has suggested that the hyperalkaline groundwater fracture-flow system may have been operative for very much longer times (Chapter 6). It is thought that the system has undergone more than one period of reaction, leading to the apparently conflicting estimates of age.

Retrograde alteration and recarbonation in the metamorphic zone has apparently taken place under non-saturated conditions, with a solution characterised by elevated concentrations of dissolved carbonate originating as CO_2 from combusted bitumen, high dissolved sulphate, and an elevated temperature. Following saturation of the metamorphic zone, groundwaters have evolved towards low P_{CO2} values and high pH values, representing a change from alteration/precipitation reactions to dissolution of secondary phases.

Stable isotope contents ($\delta^{18}O/\delta^{2}H$) of the hyperalkaline groundwaters show that recharge is by infiltration of local meteoric waters. No contribution from regional artesian groundwaters from the underlying B2 aquifer is observed. Stable isotope values together with chlorine-36 data indicate that evaporation may have occurred during recharge.

The higher salinity Western groundwaters show a ^{2}H enrichment over the lower salinity Eastern groundwaters, which may be attributed to fractionation during the hydration of secondary minerals. Values of $\delta^{2}H$ for mineral hydration waters are depleted on average by 30‰ from the hyperalkaline waters. Thus, mineral hydration in the alteration zone has likely imparted a secondary ^{2}H enrichment on the hydrating fluids. These stable isotope data support geochemical evidence that the Western groundwaters represent the first pore volume discharging from the alteration zone. The Eastern groundwaters do not show this same ^{2}H enrichment, and probably represent subsequent pore volumes. As no measurements of $\delta^{18}O$ in hydration waters have yet been carried out, an effect of ^{18}O

enrichment in the porewaters cannot yet be assessed. This supports the hypothesis that these two systems represent early and later stage discharge from the alteration zones.

Additional analyses of $\delta^{18}O$ and $\delta^{34}S$ in sulphate support earlier data that SO_4^{2-} in the hyperalkaline groundwaters originates by oxidation of organic sulphur, with contributions from pyrite, during combustion.

Future work should examine alteration minerals from the Western alteration zone, for which hydration and recarbonation is considered to be at an earlier stage. Additional isotopic work should aim at analysing the ^{18}O composition of mineral hydration waters to further elucidate the isotopic nature of the alteration fluid and the possible timing of the alteration reactions.

10.8 References

[1] W.R. Alexander, *A Natural Analogue Study of the Maqarin Hyperalkaline Groundwaters. I. Source Term Description and Thermodynamic Database Testing*, NAGRA Technical Report, NTB 91-10, 1992.

[2] G. Milton, AECL, Personal Communication.

[3] J.A. Andrews and J-Ch. Fontes, *The Importance of In Situ Production of Certain Radionuclides in Hydrology and Geochemistry (^{36}Cl and ^{14}C).* Proceedings, International Symposium on the Use of Isotope Techniques in Water Resource Development. Int. Atomic Energy Agency, March 11-15, 1991, Vienna, 1992.

[4] W. Bajjali, *Isotopic and Hydrochemical Characteristics of Precipitation in Jordan.* Unpublished M.Sc. Thesis, University of Jordan, Amman, Jordan, 99 pp, 1990.

[5] J.W. Valley, H.P.Taylor Jr and J.R. O'Neil (Editors), *Stable Isotopes in High Temperature Geological Processes*, Reviews in Mineralogy **16**, p652, Min. Soc. America, 1986.

[6] R.A. Dakin, R.N. Farvolden, J.A. Cherry and P. Fritz, *Origin of Dissolved Solids in Groundwaters of Mayne Island, British Columbia, Canada.* Journal of Hydrology, **63**, 233-270, 1983.

[7] E.J. Reardon, B.R. James and J. Abouchar, *High Pressure Carbonation of Cementitious Grout.* Cement and Concrete Res. **19**, 385-399, 1989.

[8] I.D. Clark, P. Fritz, H.K. Seidlitz, P. Trimborn, A.E. Milodowski, J.M. Pearce and K.N. Khoury, *Recarbonation of Metamorphosed Marls in Jordan.* Applied Geochemistry, **8**, 473-481, 1993.

[9] H.R. Krouse, *Sulphur Isotopes in our Environment.* in: Handbook of Environmental Isotope Geochemistry, Volume 1, The Terrestrial Environment (Eds. A.P. Fritz and J-Ch. Fontes), Elsevier, 1980.

Table 10.1 Stable isotope data for Maqarin groundwaters

Sample ID	**M1**	**M2**	**M3**	**M4**	**M5**	**M6**
Locality	Adit A-6	Adit A-6	Rail Cut	Adit A-7	Western Seeps	
Field Data						
Temperature	24.8	24.8	23.2	21.5	25.2	23.7
pH	12.74	12.42	12.66	7.84	12.92	7.22
Isotopes						
$\delta^{18}O$ (‰ SMOW)	-4.2	-4.2	-4.0	-2.8	-4.0	-4.5
$\delta^{2}H$ (‰ SMOW)	-26	-22	-20	-10	-18	-21
^{3}H TU (± 1σ)	1.4 ± 1.2	0.9 ± 1.2	1.5 ± 1.2	4.1 ± 1.2	0.7 ± 1.2 0.1 ± 1.2	3.9 ± 1.2
SO_4 - ^{34}S (‰CDT)	0.5	0.0	-1.1	na	-2.2	9.6
SO_4 - ^{18}O (‰SMOW)	12.40	11.39	9.75	na	8.19	na

na - not analysed (insufficient sample)

Table 10.2 ^{36}Cl contents of Maqarin hyperalkaline groundwaters

Sample	**Location**	**Cl (ppm)**	**$^{36}Cl/Cl$ (E-15)**	**$^{36}Cl/l$ (E+05)**
M1	Adit A6	52.4	14.6 ± 2	129
M3	Rail Cut	72.3	44.2 ± 6	540
M5	Western	46.3	25.1 ± 4	197

Table 10.3 ^{2}H contents of hydration water from retrograde alteration minerals

Sample	**Dominant Mineral**	**Secondary Minerals**	**Sequence**	**$\delta^{2}H$ ‰**	
					repeat
A 960 CB1	thaum.	zeolite, gypsum, calcite	early, immediately following decarbonation	-38	-31
A 960 CB2	thaum.	zeolite	veinlet in unaltered host, near A 960 CB1	-44	
A 962 CB1	tob.	v. minor calcite	late stage hydration	+92	+78
A 962 CB3a	tob.	none	late stage hydration	-126	-80
A 962 CB3b	tob.	none	late stage hydration	-75	
A 965 CB1a	jenn.	ett., thaum.	intermediate	-36	-37
A 965 CB1b	jenn.	ett., thaum.	intermediate	-26	
A 965 CB2	ett.	none	early stage	-41	-56
M 39 P	ett.	port.	early stage	-90	-100
A 6.3 Pa	ett.	thaum.	late stage	-80	-86
A 6.3 Pb	ett.	thaum.	late stage	-162	

tob. = tobermorite $Ca_5Si_6O_{16}(OH)_2 \cdot 2\text{-}8H_2O$
ett. = ettringite $Ca_6(Al(OH)_6)_2(SO_4)_3 \cdot 26H_2O$
thaum. = thaumasite $Ca_6(Si(OH)_4)_2SO_4(CO_3)_2 \cdot 26H_2O$
jenn. = jennite $Ca_9H_2(Si_6O_{18})_2(OH)_8 \cdot 6H_2O$
port. = portlandite $Ca(OH)_2$

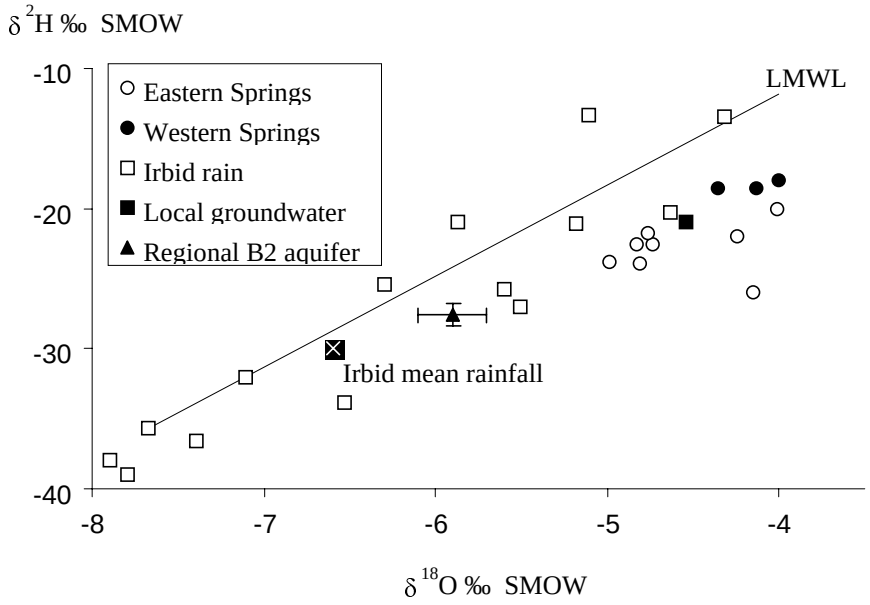

Figure 10.1 The stable isotope composition of precipitation and groundwaters from Maqarin. The local meteoric water line is defined as $\delta^2H=6.5\delta^{18}O+14$ from precipitation at Irbid [4].

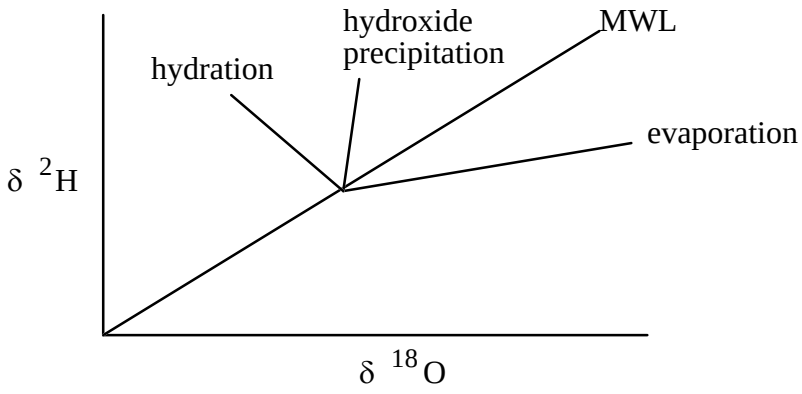

Figure 10.2 Evolution of the isotopic composition of groundwaters due to various recharge and subsurface processes. MWL is the meteoric water line defined by local rainfall.

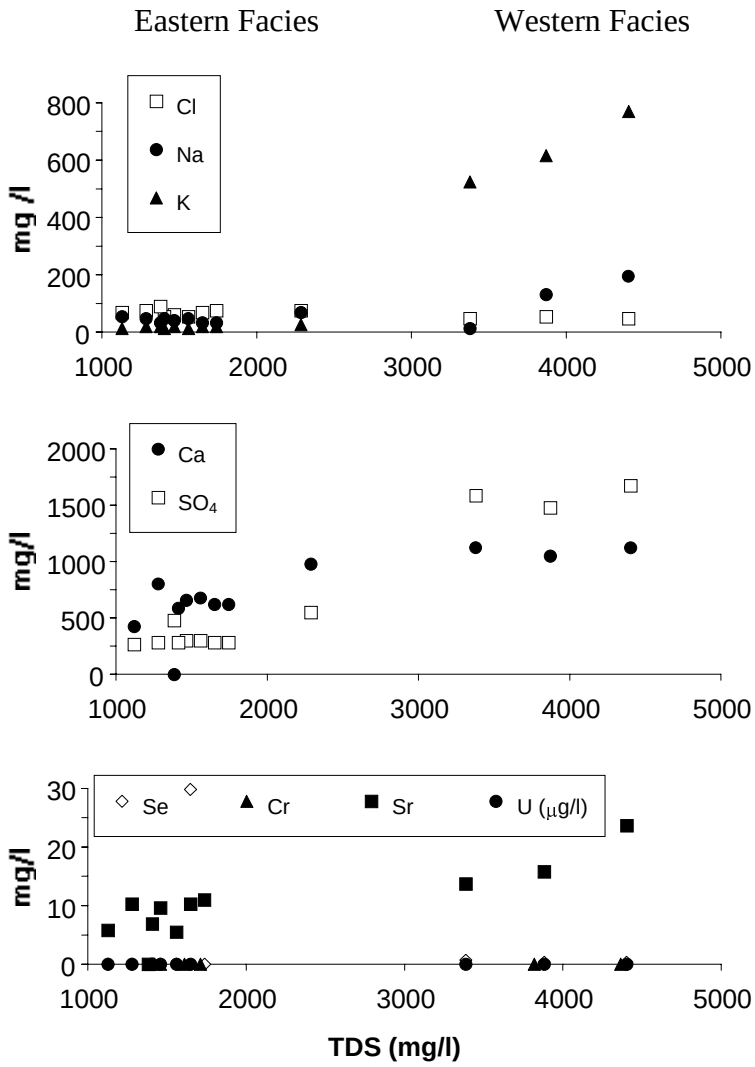

Figure 10.3 Correlation of major and minor species with total dissolved solids. Differences between eastern and western facies geochemistry reflect early and later stage dissolution of secondary minerals.

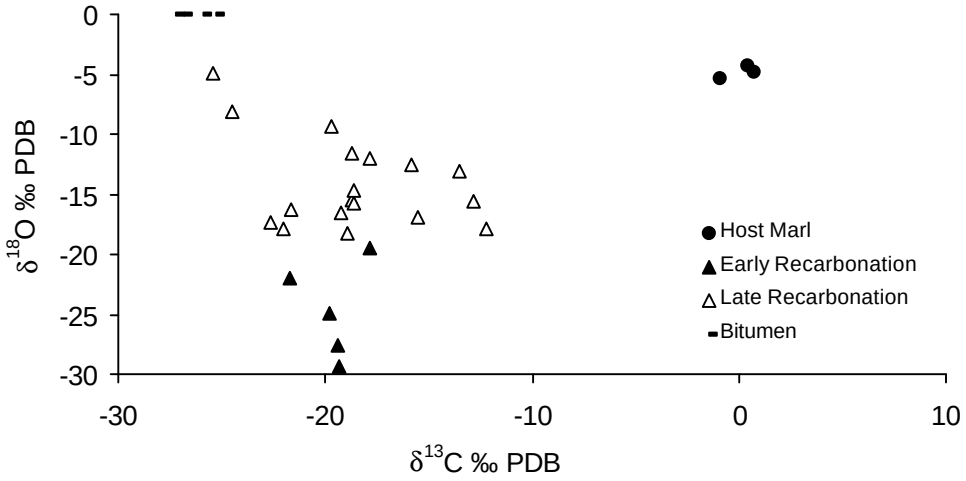

Figure 10.4 Stable isotope contents for carbonate sampled by laser microprobe. Low $\delta^{18}O$ contents of the early recarbonation phases indicates a higher temperature of formation in comparison with the ^{18}O enriched carbonates of the later carbonates.

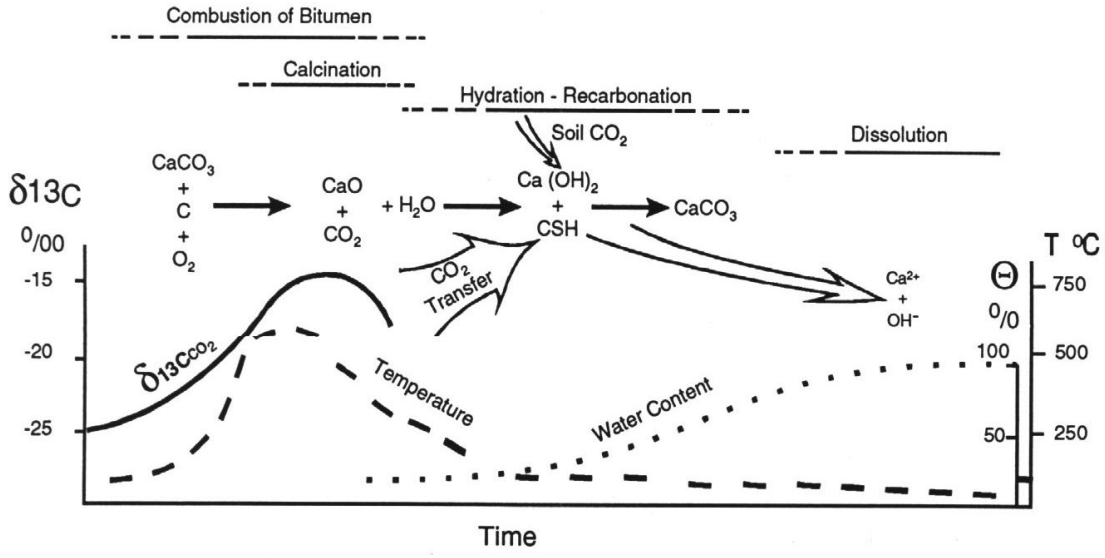

Figure 10.5 Conceptual model showing sequence of thermal metamorphic and retrograde alteration reactions with changes in temperature and humidity in the reaction zone.

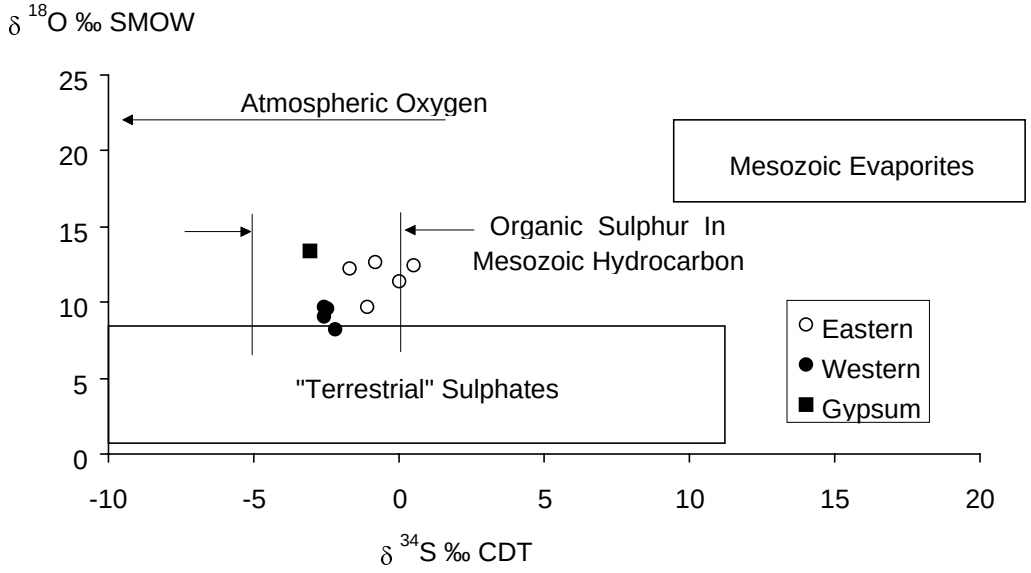

Figure 10.6 $\delta^{34}S$ vs $\delta^{18}O$ for dissolved sulphate sampled from hyperalkaline groundwaters, and for gypsum sampled from the secondary alteration zone. Field for Mesozoic bitumen and evaporites from [9].

11. NATURAL ANALOGUE FOR GEOCHEMISTRY AND MICROBIOLOGY OF CEMENT POREWATERS AND CEMENT POREWATER HOST ROCK/NEAR FIELD INTERACTIONS

P. Coombs, S.J. Gardner, C.A. Rochelle and J.M. West

11.1 Introduction

Laboratory studies have shown that microbes, particularly sulphate reducing bacteria, can grow in hyperalkaline conditions containing repository structural materials. As microbes are important catalysts in many geochemical processes (thereby gaining necessary energy and nutrients), it is important to investigate their significance within a hyperalkaline repository environment. The Maqarin site is a natural analogue of such an environment; the indigenous microbial population could therefore provide an indication of what microbial activity might be expected in the cement-influenced environment of a repository. Maqarin Phase I revealed that sulphate reducing bacteria were present [1]. The aims of the current study were:

- to isolate microbial species, determine their distribution, pH tolerance and morphology,
- to develop isolation and culturing techniques for hyperalkaline conditions,
- to review existing site geochemical information in order to determine which material is of significance in terms of biological growth requirements,
- to review potential foodstuffs for microbial use,
- to test microbiological models developed to predict the influence of microbial activity in a repository near-field and seek to describe the evolution of microbial communities and their impact on the near-field geochemistry and material stability.

These aims were achieved by studying samples from numerous locations at and around Maqarin. Field enrichments were carried out routinely on the samples, and for selected samples, additional laboratory investigations were carried out. The distribution of microbes between solid and liquid was investigated using epifluorescence microscopy and scanning electron microscopy. The results of the field and laboratory investigations are described in Sections 11.2 to 11.6. Sections 11.7 and 11.8 describe the results of the reviews, and discuss the potential uses of microbiological modelling at the site.

11.2 Sampling and Field Work

11.2.1 Sampling protocols

Liquid and solid samples were collected for microbial analysis from four sites (M1, M2, M3 and M5) in May 1992. Further samples were taken from M6 in February 1993. Details of the sites are given in Table 11.1. These sites can be viewed in the context of a repository environment with sites corresponding to upstream of a repository, the repository near field, and downstream of a repository. Table 11.2 categorises the sites in this manner.

Enrichments were carried out in the field using methods described in Bath et al [2] for the following groups of micro-organisms:

Heterotrophic bacteria

Oligotrophic bacteria

Sulphur oxidisers (Obligate and Facultative)

Sulphate reducing bacteria (SRBs)

Algae

Fungi

The compositions of media used to enrich the different groups of microbes are listed in Appendix E.

For on-site inoculation of liquid samples, each medium was prepared at 10 times concentrate and dispensed in 3ml amounts (except where stated) into acid-washed, sterile screw-top McCartney® bottles (30ml capacity). The lids contained a rubber septum to enable the injection of liquid samples. The media were to be reconstituted to normal concentration in the field by filling the bottles to capacity with the water samples. The final pH of the media would therefore be determined by the natural alkalinity of the water samples on inoculation. Media were prepared at normal strength for the enrichment of solid samples and dispensed into acid-washed, sterile Universals (28ml capacity). The media were sterilised by autoclaving at 15 psig, 121°C for 20 mins. Table 11.3 shows a summary of sample codes used to label the bottles and the contents therein.

Solid samples of approximately 4g were added to the appropriate Universal which were filled to capacity with normal strength media. The samples were added using a spatula to limit the amount of possible contamination. Unpreserved samples, 500-600g, were also collected at each site and placed in sterile Whirlpak® bags which were then sealed. Water samples were collected from each site using sterile 50ml syringes and injected via the rubber septum into the appropriate McCartney® vessel, approximately 25-27ml per bottle. Unpreserved water samples (500-1000ml) were also collected from each site in tightly sealed sterile Nalgene® bottles. All samples were then shipped to BGS, Keyworth for further analysis.

Millipore total count samplers were used at sites M1, M2, M3 and M5 as an on-site test for aerobic heterotrophs. This involved inoculating a sterilised grid impregnated with growth media with a sample of water. This was done by removing the sterile paddle, filling the sampler case to the indicated level (18ml) and reinserting the paddle. The sampler was then placed, side down, on a flat surface to allow the membrane to become uniformly wetted (1-2 mins) after which time the excess water was poured away and the paddle replaced firmly in the case to form an air tight seal. The sampler was then incubated grid side down for a 48 hour period and observations noted (Table 11.4). Further counts were made on receipt of the samplers at Keyworth.

11.2.2 Treatment of samples on arrival at BGS

The enrichment samples from sites M1, M2, M3 and M5 were received at Keyworth on 28 May 1992 and placed in cold storage at 4°C. On 1 June 1992 the samples were removed from the cold store and their condition observed. The enrichments containing Postgates B medium and solid material, sample tubes 5B, had blackening precipitates

indicating the presence of sulphate reducing bacteria (SRB). The enrichments were returned to the cold store until required for laboratory experiments.

The samples and enrichments from site M6 arrived at Keyworth on 24 February 1993 and their condition on arrival at Keyworth was noted. The unpreserved solid samples in Whirlpak® bags contained numerous live nematode worms and smelt strongly of hydrogen sulphide. These samples were perceived to be a potential health hazard and were disposed of by autoclaving. The enrichments containing solid material had dead nematodes present as well as varying amounts of fibrous plant material. The enrichments containing solid samples in Postgates B medium had blackening precipitates.

The pH of the water samples was checked by analytical chemists at Keyworth on receipt of the samples and again prior to the microbial laboratory work (Table 11.5).

11.3 Isolation of Microbial Species

11.3.1 Heterotroph enumeration

Sample tubes 1A or 1B, from sites M1 to M5, were used to inoculate plates of CPS medium (Appendix E1) using spread plate technique. Volumes of 100 μl of the field enrichment and 1:10 and 1:100 dilutions, made up with sterile distilled water were used to inoculate triplicate plates of sterile media which were then incubated at 25°C in aerobic and anaerobic atmospheres. The plates were examined for bacterial growths over a 2 to 9 day period and the number of colony forming units (CFU) noted (Figures 11.1 and 11.2).

11.3.2 Oligotroph enumeration

The procedure carried out in 11.3.1 was repeated with sample tubes 2A and 2B inoculating plates containing low nutrient, 1% CPS media. No visible growths resulted.

11.3.3 Detection of sulphur oxidisers

The sample tubes with the enrichments for sulphur oxidisers (3A and 3B, 4A and 4B) were monitored for a pH change over a 21 day period. No pH changes were detected.

11.3.4 Detection and isolation of sulphate reducing bacteria (SRB)

The presence of lactate utilising bacteria had been indicated by the diagnostic blackening of the enrichments containing the solid samples (5B) on their return from Jordan. The enrichments from sites M1 to M6 were inoculated, using spread plate technique, in triplicate onto plates of Postgates E media (Appendix E4.2). The inoculants were prepared at field enrichment strength, 1:10 and 1:100 dilutions using sterile distilled water and inoculated in 100μl volumes using a sterile pipette onto the plates of media. These were incubated in the dark at 25°C in an anaerobic chamber (Don Whitley Scientific) and monitored for bacterial growth. Isolation of SRB onto Postgates E proved difficult, although a number of anaerobic colonies were observed, notably from the solid sample from site M3 (Figure 11.3). However, none had the characteristic black colour associated with SRB.

11.3.5 Detection of algae

Enrichments 6A and 6B from sites M1-M6 were left in natural light in the laboratory and checked for any blue/green coloration occurring over a 14 day period. None was

observed. The sample 6B from site M6 containing solid material did however show a green tinge after 12 days indicating some algal presence.

11.3.6 Detection of fungi

Unpreserved water samples were inoculated onto plates of Sabourauds' Dextrose Agar (Appendix E6) and incubated at 30°C in an aerobic atmosphere for 48 hours. Samples from sites M1, M3 and M5 produced extensive fungal growth.

11.3.7 Summary

Heterotrophic bacteria were determined in all samples with sites M2 and M5 containing the largest numbers (up to 8 10^4 CFU ml^{-1}). Attempts to grow oligotrophs (those heterotrophs able to grow in low nutrient conditions) in both aerobic and anaerobic conditions were unsuccessful indicating that the heterotroph population is not adapted to these conditions. Organic carbon must therefore be constantly available and in high concentrations. Detection of sulphur cycle organisms only demonstrated the presence of sulphate reducing bacteria which could not be isolated satisfactorily on solid media. Sites M1 and M3 proved to be the most active. Algae were detected only in the solid material from site M6. Enrichments for fungi from M1, M3 and M5 produced extensive growth.

Looking at these results in terms of the repository analogue (Table 11.2), microbes are found in all locations including those analogous to the downstream of the repository (M2, M3 and M5). Interestingly, the lowest numbers of heterotrophs are found in the repository near-field analogue site itself (M1) with numbers up to 5 10^3 CFU ml^{-1}. Downstream analogue numbers tend to be higher in both solids and liquids than even those in the unaltered material (M6) except for M3 where low numbers are found in solid material. Possibly microbes are being introduced into the system from the surface in certain areas although this cannot be established beyond doubt in this study. The sites all contain heterotroph populations which will not tolerate oligotrophic conditions. Hence Maqarin is not a nutrient poor environment. The microbial population is diverse with sulphate reducing bacteria detected at all sites particularly in solid material. Algae were detected in M6 only (analogue of unaltered material) but this is not surprising as it is a surface site. Fungi were demonstrated in M1 (repository near-field analogue site) and also in downstream analogue sites. Fungi require large amounts of organic material and this again suggests that Maqarin sites are not nutrient poor.

Thus the sites show diverse microbial populations which appear to be unaffected by alkaline pH. The environment does not appear to be oligotrophic.

11.4 pH Tolerance of Heterotrophs and Sulphate Reducing Bacteria

11.4.1 Introduction

The pH tolerance of populations from the enrichments for heterotrophs and for sulphate reducing bacteria for sites M1 to M6 was ascertained using inoculation onto media of different pH values. These experiments were designed to ascertain the range of pH tolerance for both heterotrophs in general and, more specifically, SRB.

11.4.2 Methodology

CPS medium for heterotrophs was made up as described in Appendix E1 and pH adjusted using NaOH to 7, 9 and 11 prior to autoclaving. CPS broth was also prepared as

described in Appendix E1 but without the addition of agar. The pH was adjusted using NaOH to 4, 5, 6, 7, 9 and 11 and aliquots of 15 mls were dispensed into glass universals and labelled with the relevant pH, prior to autoclave sterilisation. Problems were encountered with pH adjustment with both solid and broth tests. Measurements of pH showed a drop had occurred after autoclaving. Table 11.6 shows pH changes in broths after autoclaving. In addition, it proved impossible to raise the pH above 11. The media appeared to have a buffering capacity which could not be overcome by the addition of NaOH.

Attempts to prepare similar plates and broths using Postgates B media (Appendix E4.1) failed because of the precipitation of the reducing agent, thioglycollic acid, when pH was altered.

Samples from solid enrichments for heterotrophs from all sites were inoculated onto CPS plates. Dilutions were prepared using sterile distilled water to achieve 1:10 and 1:100 dilutions. Triplicate 0.1ml inoculations of the neat and diluted samples were prepared, using the spread plate technique, for incubation in an aerobic and anaerobic environment at 25°C. Plates were assessed for growth at regular intervals and observations of colony characteristics and number of colony forming units (CFUs) noted after 3, 6, 9 and 14 days.

In addition, liquid enrichments for heterotrophs and SRB from sites M1 to M5 were inoculated into CPS broth of pH 4, 5, 6, 7, 9 and 11 and incubated for a period of 48 hours. Growth was assessed by examining and scoring the turbidity of the media. M6 samples did not form part of this study as samples were received after its completion.

11.4.3 Results

The results for pH tolerance assessment of samples from the heterotrophic solid enrichments from each site are given in Figure 11.4. The results show the microbial populations to be greatest at site M1 and M2, with the numbers being significantly higher than for sites M3 and M5. Populations at M6 are at levels between these two groups. The pH yielding the highest number of bacteria in both M1 and M2 is pH 9, where the micro-organisms appear to favour an anearobic environment. Most microbes were adapted to anaerobic, pH 7 conditions in M6 which is not surprising as this was the collection pH. Growth at pH 11 was observed in samples from sites M1, M2 and, surprisingly, from M6 with numbers being significantly less in M1 than in M2. Again the anaerobic population predominates in M2 pH 11 samples.

Assessments of pH tolerance were carried out for liquid samples from both heterotroph and SRB enrichments (using CPS broths of pH 4, 5, 6, 7, 9 and 11 for sites M1 to M5). The results are shown in Table 11.7. No growth was observed in broth cultures inoculated with samples from heterotrophic enrichments from any of the sites. Growth was observed for SRB enrichment samples from sites M1 and M2. The pH tolerance of the M1 samples ranged from pH 5 to pH 11 with pH 6 and pH 11 broth cultures showing the most growth as shown by the higher turbidity of the media. The pH tolerance of M2 samples ranged from pH 7 to pH 11, where an increase in turbidity was observed with increasing alkalinity of the media.

M6 samples did not form part of this study as samples were received after this study was completed

These results show that tolerance to alkaline pH was present in heterotrophs in unaltered materials (M6) and also in the repository near-field environment analogue (M1).

However, tolerances varied in downstream analogue samples with M2 showing tolerances similar to M1. These tolerances appear to be related to sulphate reducing bacteria only as shown by the broth enrichments (Table 11.2). Thus tolerance is demonstrated to pH 11 and exists in all sites sampled although to a lesser extent in downstream samples.

11.5 Activity of Sulphate Reducing Bacteria (SRB)

11.5.1 Introduction

The detection of SRB in this environment has potential significance in relation to sulphur cycling, particularly as pyrite is present in the unaltered rock. Although SRB were detected in samples, this does not, in itself, indicate exactly the state of activity nor where the activity is focused (in the solid or liquid phase). Thus their significance in sulphur cycling is uncertain. A simple experiment was performed to measure sulphate changes in closed systems containing liquid and solid material from two sites.

11.5.2 Methodology

Core material from sites M1 (repository near-field analogue) and M3 (downstream analogue) were selected. Previous studies had shown that core from these sites had produced a rapid, positive indication of the presence of SRB when inoculated into Postgates B medium. It was felt, therefore, that these samples would be most likely to contain active SRB. The experiment was performed in March 1993 so freshly sampled water from site M6 was used as the liquid phase as this was felt to be more likely to contain active SRB than waters sampled in the previous year.

A suite of sterile Universals was prepared in the anaerobic chamber (Table 11.8).

A 5 ml volume of supernatant was removed with a sterile syringe from each Universal after the contents had settled. Each sample for analysis was then filtered through a 0.2 μm Acrodisc (Gelman) into a sterile bijou and stored in the laboratory freezer until chemical analysis. These samples represent time 0 (T0) in the study. This procedure was repeated at weekly intervals and at the end of four weeks (T4) a selected number of the samples were sent for analysis to determine their level of sulphate.

11.5.3 Results and discussion

The results obtained showed no significant change in sulphate levels over a four week period (Table 11.9). This suggests that in this type of closed system, sulphate reduction is not possible without a supply of nutrients being available to stimulate the activity of the sulphate reducing bacteria. This is not surprising as this environment is not oligotrophic. A dynamic system is required for the process to occur as enrichment does stimulate sulphate reducers to develop. Further experiments with the addition of enrichments would be needed to confirm this view. Other samples taken remain unanalysed.

11.6 The Distribution of Microbes on Solid and Liquid Phases

11.6.1 Introduction

Detection of heterotrophs and SRB indicated that microbes were present in both the liquid and solid phases. Information on the exact distribution is useful for microbial modelling purposes. Two direct methods were used to obtain information:

epifluorescence microscopy and scanning electron microscopy. Results can then be compared.

11.6.2 Distribution using epifluorescence microscopy

Microbial numbers can be obtained by staining cells with acridine orange which enables them to be easily counted using a fluorescent microscope. Acridine orange stains the nucleic acids with DNA staining green and RNA staining red-orange. Solid and liquid samples from sites M1 (repository near-field analogue site) and M3 (downstream analogue site) were chosen to be studied as these had proved to be the most microbiologically active. These analyses were performed in March 1993. The method used follows that of Jass and Lappin-Scott [3] and can be summarised:

Preparation of reagents

(i) A cacodylate buffer solution was prepared by dissolving 8 g of cacodylic acid in 500 mls of distilled water and filter sterilising through a 0.45 μm Acrodisc. A 0.5% solution of gluteraldehyde fixative was prepared by diluting a 25% gluteraldehyde solution in the cacodylate buffer (1:50 dilution).

(ii) A potassium phosphate buffer solution was prepared by combining 42 mls of potassium phosphate dibasic solution (4.35 g K_2HPO_4 dissolved in 500 ml distilled water) with 8 mls of potassium phosphate monobasic solution (3.40 g KH_2PO_4 in 500 ml distilled water). The pH was adjusted to 7.5 with the monobasic solution, 5 mg of acridine orange stain added and the solution was then filter sterilised through a 0.45 μm filter (Gelman).

(iii) The membrane filters used were 25 mm 0.2 μm Nucleopore membranes which had been stained by soaking them in a solution of Irgalan black (2 g Irgalan black in 1 litre 2% acetic acid) for 24 hours and then air dried on filter paper. (The staining with Irgalan black enhances the contrast between the bacteria and the background when counting)

N.B. All solutions were filtered through a 0.45 μm filter (Gelman) prior to use.

Preparation of samples

Whirlpak® bags containing solid material from sites M1 and M3 were removed from the cold store and 10 g removed from each using a sterile spatula. Each solid sample was placed in a sterile Universal into which 10 mls of filter sterilised distilled water was added. The tubes were shaken and allowed to settle three times after which the supernatant was removed using a sterile pipette into a bijou. This formed the neat sample for epifluorescence studies of solid material. Groundwater was also taken from the cold store and dispensed into sterile Universals for the study of the liquid samples.

Staining procedure

A membrane was pre-wetted with a few drops of fixative and carefully placed with forceps onto the bottom of the filter apparatus avoiding wrinkling or the trapping of air bubbles. The chimney was sterilised by flaming in methanol and clamped in place. The vacuum pump (15 KPa) was switched on for a few seconds to secure the filter and 5 ml of sample (1 ml of bacterial sample in 10 ml gluteraldehyde fixative) pipetted into the

funnel. The vacuum was applied until all the sample had been drawn through the filter and 1 ml of acridine orange stain carefully pipetted into the funnel. After 2 minutes the vacuum was drawn and 1.5 ml isopropyl alcohol added to de-stain the sample slightly. The vacuum was left running for a few seconds to dry the filter which was then transferred with forceps onto filter paper to dry for a further 20 minutes. The stained membrane was then transferred to a clean, glass slide, a drop of immersion oil placed on top and covered with a glass cover slip.

Counting membranes

The membranes were counted using a Zeiss microscope with a 100 magnification power lens and oil immersion. For each sample three sets of counts were performed, for each 20 fields of view were randomly counted and the total numbers of bacteria for liquid and solid samples calculated. Results are given in Table 11.10.

11.6.3 Distribution using scanning electron microscopy (SEM)

The distribution of microbes using SEM was only investigated for site M1 (repository near-field analogue site). Both liquid and solid samples were assessed using a modified version of the method described by Jass and Lappin-Scott (1992). In brief, slurries of solid material were prepared with 0.1 M cacodylate buffer pH 7.4 and filtered through 0.2 μm Nucleopore filters to obtain a fine even layer of sample on the filter surface. 15 ml of the water sample from M1 was also filtered. Samples were then fixed in 3-5% gluteraldehyde in cacodylate buffer for 2 hours at room temperature, surface washed to remove residual gluteraldehyde and dehydrated with an ethanol/distilled water series increasing from 30% ethanol to 100% ethanol. Samples were allowed to air dry prior to mounting on aluminium stubs with colloidal carbon conducting cement (Leit-C). Once mounted, samples were coated with approximately 25 nm carbon in an evaporation coater (Edwards 306A carbon evaporation coater) and examined under the SEM.

M1 core preparation revealed the presence of clusters of rod shaped bacteria (0.5μm x 4.5-5μm) which were adhering to the solid material. No organisms were detected in M1 groundwater possibly because of the age of the sample. Photomicrographs showing the microbial clusters from M1 solid preparations are given in Plate 52.

11.6.4 Discussion

From epifluoresence microscopy total count investigations it appears that more microbes are present in the solid core material than are present in the water samples. In site M3 (downstream from the repository analogue) the solid to liquid microbe ratio appears to be 3:1 whilst at site M1 (repository near-field site analogue) this solid to liquid ratio increases to 20:1. The ratio is likely to be much higher as the method for extracting microbes from the solid material is likely to leave many attached to the surfaces and thus undetected in the examined extract. SEM studies of site M1 solid material revealed rod-shaped microbes adhering to surfaces confirming the findings from the epifluorescence microscopy. Samples prepared from the groundwater only did not reveal micro-organisms. Solid/liquid ratios were not determined for the SEM because of difficulties in calculating surface areas.

11.7 Review Of Site Geochemical Information And Potential Foodstuffs For Microbial Use

11.7.1 The Maqarin site

The 'bituminous marls' in north western Jordan have been the focus of several studies [4, 5, 6, 7] due to their potential for hydrocarbon resources, unusual mineralogy and the presence of hyperalkaline groundwaters. The rocks at Maqarin are organic-rich (kerogenous) marls and limestones. The geology of the site is summarised in Chapter 3. The sequence of unaltered rocks, prograde alteration and retrograde alteration assemblages is shown in Table 11.11.

The stratigraphically equivalent unmetamorphosed Hatrurim Formation [8] in north eastern Israel contains up to 26% organic matter [9] and shows similar mineralogy to that at Maqarin. Interestingly, Gross [9] has reported native sulphur in some samples, with this author attributing its presence to reduction of gypsum, possibly under the action of sulphate reducing bacteria.

As detailed in Table 11.2 several potential environments can be considered where microbes could be found:-

A Unaltered organic-rich marls and fluids [M4 and M6].

B Rocks having undergone retrograde metamorphism and hydration with highly alkaline fluids (equivalent to repository near-field conditions) [M1].

C Unaltered organic-rich marls with highly alkaline fluids(equivalent to the migration of a hyper-alkaline plume) [M2, M3 and M5].

11.7.2 Requirements for microbial growth

Microbes must use their environments for all the substances they need for the synthesis of cell materials and for energy generation [10]. Noy et al [11] and Grogan and McKinley [12] have used nutrient and energy supplies to constrain microbial growth in a radioactive waste repository. These previous studies and that of Stroes-Gascoyne [13] highlight the importance of carbon, nitrogen, phosphorus and sulphur as nutrients required for microbial growth. Indeed, Noy et al [11] and Grogan and McKinley [12] have used the formula $C_{160}N_{30}P_2S$ to express the relative ratios of these elements within a typical microbe. Consequently, more C-rich nutrients are required compared to those which are S-rich. The three studies above have also assumed that the supply of energy for microbial growth comes from redox reactions (e.g. oxidation of pyrite or hydrocarbons).

11.7.2.1 Energy requirements

Microbial energy requirements for Maqarin are likely to be derived from redox reactions [11, 12]. Previous work at Maqarin (for the hyperalkaline waters) had shown the presence of sulphate reducing bacteria only [14]. The present study concentrates on sulphate reducing bacteria although aerobes have been shown to be present. Indeed, SO_4^{2-} can be a very important oxidising agent for microbes in this environment and has parallels with observations from the Israeli sites [9] where native sulphur has been found, presumably as a product of bacterial reduction.

Examination of the detailed solid phase descriptions [7] suggest that the reducing agents at Maqarin would be hydrocarbons or pyrite depending on which environment (A-C) was considered (although Milodowski [15] notes the trace presence of reduced S/Se

compounds in the anhydrous regions of environment B). Table 11.11 shows the existence of pyrite in the unaltered rocks and not in those having undergone prograde alteration. As a consequence, pyrite could only be a reactant in environments A and C. Hydrocarbons could be present as either the original solid kerogenous material or dissolved in groundwater. The solid hydrocarbons may be important in environments A and C, though could have been destroyed in environment B as a result of thermal metamorphism. However, hydrocarbons dissolved in local groundwater could be found in all three environments. The form of such hydrocarbons is more problematic. As the energy produced by reaction will vary depending on which specific organic compound is reacted, it is necessary to know exactly which types of compounds exist, and their concentrations, in order that predictive computer models can be applied. Total organic carbon (TOC) measurements were made for water samples from Maqarin (Chapter 4). However, no detailed breakdown of the organics present has been conducted. As a consequence of this lack of data, a brief literature review of the types of organics in hydrocarbons was conducted.

Organics in hydrocarbons

The 15-20% organic content of the rocks probably provides the main source of nutrient carbon and the major source of reducing agents for redox reactions. No data could be found that has rigorous analyses for the types of organics present, though, as mentioned previously, they probably form a very heterogeneous group. However, Milodowski [15] notes that it is probably immature kerogen that may have just entered the oil window during maximum diagenesis. The high sulphur content [7], together with the high nitrogen content, would suggest a high proportion of aromatic hydrocarbons in the solid phase.

The lack of currently available data on the types of organic compounds present means that similarities will have to be drawn from other geological environments.

Relatively 'young' hydrocarbons such as those found in areas currently undergoing active high temperature hydrothermal alteration [16, 17] show a predominance of n-alkanes, especially in the C_{10}-C_{40} range, with a homologous series in between, and having a modal composition lying around C_{25}. Kvenvolden et al [16] looked at samples from the Gorda Ridge and noted that of the extractable organics:-

2%	aliphatic hydrocarbons (n-alkanes)
44%	aromatic hydrocarbons
54%	non hydrocarbons

The authors noted that no sulphur-containing aromatics were found.

Tissot and Welte [18] looked at a range of hydrocarbons from relatively young, light crude oils to more evolved bitumens. The compositions of these are given in Tables 11.12 - 11.14. Generally there are more n-alkanes in crude oils than bitumen, and more aromatics in bitumens than crude oils. They also note that n-alkanes with odd numbers of carbon atoms tend to predominate over those with even numbers as they derive from cuticular waxes of continental higher plants. Continental contributions tend to define the higher n-alkane fingerprint (say in the region C_{25}-C_{33}), whereas the lower n-alkane fingerprint (say in the region C_{15}-C_{17}) may represent heritage from algal material. Table 11.14 also shows average elemental compositions of typical resins and asphaltines.

Average values of ratios are given below:

Saturated HCs:aromatics	2.8	2.7	1.8
Alkanes: saturated HCs	0.49	0.48	0.47

Tissot and Welte [18] note that in crude oils oxygen is commonly found in carboxylic acid groups or ketones:-

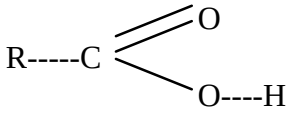

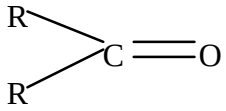

where:-R = an aliphatic organic group, and nitrogen tends to be found in ring structures:-

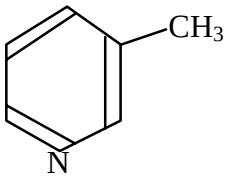

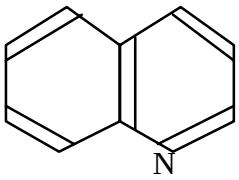

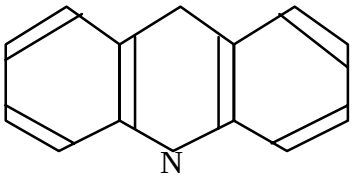

In more evolved hydrocarbons they found that in resins and asphaltines above 700 molecular weight there is a high probability of one or more atoms of O, N or S. Of these elements:-

- N is usually found in quinoline groups.
- O is usually found in ether bonds.
- S is usually found in benzothiophene groups (a), but also sometimes in thioalkane (b) and thioether (c) groups.

(a)

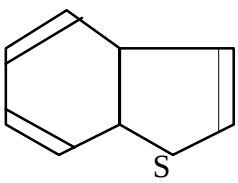

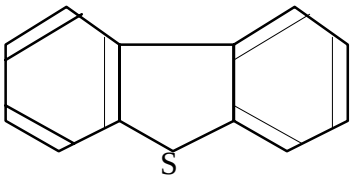

(b)

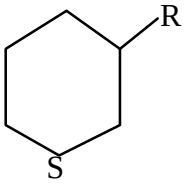

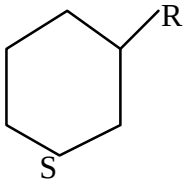

(c)

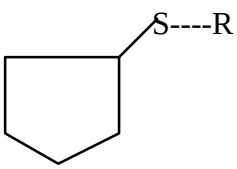

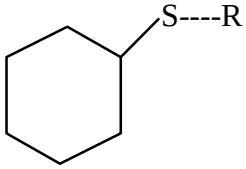

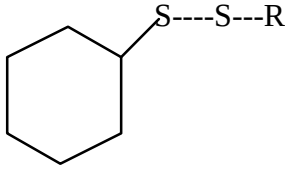

Many of the larger molecules mentioned above would be insoluble in water, and unless in colloidal form, would tend to be limited to the solid phase in environments A and C. As

small molecules tend to be more soluble in water than larger, more complex ones, they may be found in all three environments. Indeed, molecules that are already dissolved would be more readily available for use in microbes (i.e. the microbe would not have to expend energy in solubilising them first). Thermodynamic data for the smaller members of some common hydrocarbon groups are given in Shock and Helgeson [19] and have been included in the database of EQ3/6 [20, 21]. Such molecules may thus be more appropriate than the larger ones in modelling the microbial processes occurring at Maqarin.

Effects of biodegradation on hydrocarbons

Previous studies of hydrocarbon/microbe reactions have concentrated upon the oil/water contact of deeply buried oil reservoirs [22, 23, 24]. They have shown that microbial action preferentially removes the lighter hydrocarbons from crude oils, and as a consequence increases the proportions of those remaining within the oil (i.e. the oil gets heavier with biodegradation). This process is only rapid when oxygen is available, such as by ingress of meteoric water into an aquifer containing oil reservoirs and general order of decreasing reactivity can be assigned for the hydrocarbon groups (Table 11.15). For any particular group the smaller molecules tend to be destroyed first as these are more easily metabolised by microbes. Anaerobic bacterial reactions are also possible providing sources of aerobic synthesised metabolites are available, but are very much slower [23].

Miiller et al [24] notes that biodegradation of crude oil has the following effect:-

Increases S from 0.6 wt % to 1.6 wt %

Increases metals from 47 ppm to 293 ppm

Decreases saturates (such as n-alkanes) from 55 wt % to 20 wt %

Increases polars (such as organic acids) from 21 wt % to 41 wt %

Increases asphaltines (the heavier hydrocarbons) from 2 wt % to 21 wt %.

11.7.2.2 Nutrient requirements

Previous studies [11, 12, 13] have determined the most important nutrients for growth are C, N, P and S. In an average microbe these exist in the relative ratio of 160:30:2:1. Each of these nutrients will be considered separately from the fluid chemistry data available (Chapter 4). Solubility calculations were carried out using EQ3/6 version 7.0 (previously 3245.1090) [20, 21].

Carbon

For all three environments carbon for incorporation into the microbes is available in both its reduced form (as dissolved organic hydrocarbons) and its oxidised form (as HCO_3^- or CO_3^{2-}). There are no data presently available on the concentrations or types of molecules in organic form, however some distinctions can be made between environments.

Environ. A (M4 + M6) HCO_3^- averages 173 mg l^{-1}, CO_3^{2-} is below detection (due to speciation effects at near neutral pH).

Solubility calculations show these two fluids to be approximately saturated with respect to calcite, and thus the inorganic carbon is probably buffered by the abundance of this mineral in the rocks.

TOC averages 23.5 mg l^{-1}. As stated previously, this probably represents a heterogeneous group of compounds, as yet uncharacterised. The abundance of carbon as organic compounds probably precludes this element from being a growth-limiting factor. Oxidation of dissolved organics to HCO_3^- would seem a major source of redox energy. However, the lack of a detailed breakdown of the organics present prevents the calculation of the accurate potential redox energy available for incorporation into a predictive model for microbe growth.

Environ. B (M1) CO_3^{2-} averages 37 mg l^{-1}, HCO_3^- is below detection (due to speciation effects at high pH).

Solubility calculations show this fluid to be undersaturated with respect to calcite and would concur with the observation of calcite dissolution adjacent to high pH water-bearing fractures.

TOC averages 3.2 mg l^{-1}. Similar problems exist as for environment A, though the lower concentrations of TOC (by nearly an order or magnitude) would limit the maximum potential energy for microbe growth and available nutrient carbon.

Environ. C (M2, 3 + 5) CO_3^{2-} averages 23 mg l^{-1}, HCO_3^- is below detection (due to speciation effects at high pH).

Solubility calculations show these fluids to be undersaturated with respect to calcite and would concur with the observation of calcite dissolution adjacent to high pH water-bearing fractures.

TOC averages 4.1 mg l^{-1}. Similar problems exist as for environment A, though the lower concentrations of TOC (by nearly an order or magnitude) would limit the maximum potential energy for microbe growth and available nutrient carbon.

Therefore, it would appear that environment A has the potential (based on the nutrient carbon data available) for supporting 6 to 7 times the microbe population of environments B and C.

Nitrogen

As previously mentioned, the kerogenous material at Maqarin has a high nitrogen content so that it would not appear to be a microbe growth-limiting element.

Environ. A (M4 + M6) NO_3^- averages 30 mg l^{-1}, NO_2^- and NH_4^+ are present as traces only.

As the minimal nutrient-nitrogen requirements are ~5 times less than nutrient-carbon, then nitrogen would not appear to be a growth-limiting factor.

Environ. B (M1) NO_3^- averages 3.3 mg l^{-1}.

As for TOC, nutrient-nitrogen is about an order of magnitude lower in environment B than in environment A. However, nitrogen would again not appear to be a growth-limiting factor.

Environ. C (M2, 3 + 5) Average concs. are; NO_3^- 16.8 mg l^{-1}, NO_2^- 0.4 mg l^{-1} and NH_4^+ 2.1 mg l^{-1}.

The amount of nutrient-nitrogen far exceeds the TOC available in this environment, so nitrogen is not a growth-limiting factor.

Therefore, it appears that nitrogen is in excess in all environments and so would not be growth-limiting.

Phosphorus

In general all phosphate concentrations in solution are low even though in the solid phase it is abundant, P_2O_5 can make up to 7.5% by weight of the rock. The low concentrations in solution could lead to it being an important growth-limiting element.

Environ. A (M4 + M6) HPO_4^{2-} is ~0.04 mg l^{-1}.

Solubility calculations show M4 to be oversaturated with respect to at least one member of the apatite group. Although apatite is present in the rock, equilibration can not be confirmed as apatite reaction kinetics are generally slow, and phosphorus could be being released from the kerogenous material. Even though phosphorus is needed in small quantities in the microbe structure, concentrations are less than 1/80 of the TOC, so that phosphorus would appear to be a growth-limiting factor.

Environ. B (M1) HPO_4^{2-} concentration is 0.01 mg l^{-1}.

Solubility calculations show M1 to be oversaturated with respect to two members of the apatite group. Although apatite is present in the rock, equilibration can not be confirmed as apatite reaction kinetics are generally slow, and phosphorus could be leaching from nearby unaltered rocks.

The very low concentrations of HPO_4^{2-} would make phosphorus a growth-limiting factor.

Environ. C (M2, 3 + 5) HPO_4^{2-} averages 0.05 mg l^{-1}.

Solubility calculations show M3 and M5 to be oversaturated with respect to two members of the apatite group (the concentration in M2 was below the detection limit). Although apatite is present in the rock, equilibration cannot be confirmed as apatite reaction kinetics are generally slow, and phosphorus could be leaching from nearby unaltered rocks. Concentrations of HPO_4^{2-} are very low (just less than 1/80 that of TOC) and thus makes phosphorus just a growth-limiting factor.

Thus, the low concentrations of phosphorus throughout all three environments make it the growth-limiting nutrient.

Sulphur

Sulphur requirements for the assumed microbe composition are the lowest of all the nutrients. Consequently, the high concentrations of SO_4^{2-} in all environments ensure that sulphur is not growth-limiting. The high concentrations would make it useful as an important oxidising agent in redox reactions supplying energy for microbial growth. The sulphur could have originated from pyrite or organic compounds within the hydrocarbons. Indeed, Milodowski et al [7] note that up to 5% of the organic fraction of the unaltered Maqarin samples (rocks in environment A, and away from fractures in environment C) is sulphur.

Environ. A (M4 + M6) SO_4^{2-} averages 48 mg l^{-1}.

Solubility calculations show slight undersaturation with respect to gypsum, but approximate saturation with respect to barite. Such concentrations suggest oxidative release of sulphur from either organics or pyrite.

Environ. B (M1) SO_4^{2-} concentration is 305 mg l^{-1}.

Concentrations have increased markedly from environment A possibly as a result of thermal release from organics and pyrite.

Solubility calculations show slight oversaturation with respect to ettringite, saturation with respect to barite and slight undersaturation with respect to gypsum and celestite ($SrSO_4$). Previous modelling studies of trace elements [25] involved some initial modelling of major elements [26] which showed gypsum to be approximately saturated. However, the database used (HATCHES v.3) did not contain ettringite. Interestingly, ettringite and an isostructural mineral, thaumasite, are observed as major secondary phases at Maqarin (Table 11.11).

Environ. C (M2, 3 + 5) SO_4^{2-} concentrations average 280 mg l^{-1} for M2 and M3, but 1580 mg l^{-1} for M5.

M2 and M3 would appear to represent decreasing SO_4^{2-} from environment B due to mineral precipitation. The concentrations in M5 seem unusually high, though may represent S release from unaltered rock by interaction with the high pH fluid.

Concentrations have increased markedly from environment A possibly as a result of thermal release from organics and pyrite in environment B.

Solubility calculations show (for M2 and M3) saturation/slight oversaturation with respect to ettringite and barite, and slight undersaturation with respect to gypsum and celestite ($SrSO_4$). M5 is similar, but ettringite is oversaturated and gypsum saturated. Again this would concur with mineralogical observations of barite, ettringite/thaumasite and gypsum precipitates (Table 11.11).

Therefore, the high concentrations of SO_4^{2-} in all three environments ensure that sulphur is not a nutrient-limiting element. It is also a good potential oxidant for the microbe redox energy sources.

11.8 Use of microbiological models at Maqarin

The microbiological model MGSE requires data on nutrient and energy inventories available for microbial usage from both solid and liquid phases. However, there are potential problems that could be encountered in modelling the complex microbial processes at Maqarin. Fluid fluxes from fractures at Maqarin were measured and the results discussed in Chapter 3. A flux of $<2.4\ 10^{-5}$ $ls^{-1}m^{-2}$ is recommended for modelling studies. This recommended value is quite low. For the preliminary calculations described here, a higher flux of $2\ 10^{-4}$ $ls^{-1}m^{-2}$ ($6\ m^3m^{-2}y^{-1}$) was used to maximise the potential for microbial growth. These fluid fluxes plus measured concentrations in solution give a first approximation of input rates although there is a lack of compositional data for dissolved organics relevant to this study. However, some simplifications relevant to microbial modelling can be made:-

(a) SO_4^{2-} is the main oxidising agent used to provide energy from redox reactions for sulphate reducing bacteria. It appears in relatively high concentrations in solution

and a wide variety of sulphate minerals are present. Thus it is probably not 'nutrient-limiting'. Input rates could be determined from measured fluid flux.

(b) Dissolved organics are the most likely reducing agents for the redox reactions. However, there is a lack of data concerning types or concentrations. Small molecules are probably involved in most reactions as these dissolve readily in water. Data are also available that could be readily incorporated into present models [19, 20, 21]. Some thermodynamic data for other molecules are available [27, 28, 29, 30, 31]. However, these are usually not in the correct form for immediate incorporation into the databases of presently available models [11, 12] and would require significant manipulation. Input rates based on fluid flux could be used. The above problems would benefit from further studies of both fluid and solid samples from Maqarin.

(c) Phosphorus, as phosphate, could be derived from apatite dissolution or from the kerogenous phase. Input rates based on fluid flux could be used together with previous studies [32, 33, 34], which have investigated dissolution kinetics of apatite over a range of pH. This element appears to be the growth-limiting element at Maqarin (Section 11.7.2.2). P has also been found to be the limiting nutrient in other studies [14].

(d) Nitrogen, like carbon, probably derives from the organic phases present. input rates based on fluid flux and measured concentrations of NO_3^- and NH_4^- could be used although there are no data on N occurrence as amines or amino acids. Although NO_3^- could serve as an oxidising agent in redox reactions it appears that sulphate reducing bacteria dominate, and as a consequence, N may only be important as a nutrient.

Thus for initial modelling of potential microbial growth, fluid fluxes and nutrient/redox component concentrations could be used once the nature of the hydrocarbon phases are known. Reactions involving the above elements could then be assimilated in a similar fashion to those in previous studies [11, 14]. More detailed modelling could use mineral solubility-limiting concentrations, or concentrations limited by nutrient/redox component input rates from the solid phases which would be much harder to determine. Although literature dissolution rates for apatite [32, 33, 34] and gypsum [35, 36, 37] are available, data for the other important phases are not. Data for release rates from the solid kerogenous phase are similarly absent. In order for meaningful modelling to be undertaken, data would also be needed for the surface areas of these phases, and water/rock ratios. These data are difficult to obtain.

11.9 Conclusions

This study has shown that a diverse population of alkaline tolerant microbes are found at all sites sampled at Maqarin. Looking at the results in terms of a repository analogue, microbes were found in all locations including those analogous of downstream of the repository areas. The distribution of individual microbial species can be summarised as follows:

- The lowest numbers of heterotrophs are found in M1 (Environment B - Repository near-field) with numbers not exceeding 5 10^3 $CFUml^{-1}$. Downstream analogue numbers in both solids and liquids tend to be higher those in the unaltered material. The heterotroph populations would not tolerate oligotrophic conditions.

- No sulphur oxidisers were found, but sulphate-reducing bacteria were detected at all sites, particularly in solid material.
- Algae were detected in M6 only (Environment A - Repository upstream analogue) but this is not surprising as it is a surface site.
- Fungi were demonstrated in M1 (Environment B - Repository near-field analogue) and also in downstream analogue sites. Fungi require large amounts of organic material and this suggests that Maqarin sites are nutrient-rich.

The Maqarin microbial populations were only capable of exploiting nutrient-rich conditions. This implies that a steady supply of nutrients and energy was present at all sites. However, the actual activity of microbes in-situ was not determined and this remains an area of uncertainty.

Tolerance was demonstrated up to pH 11 and appeared particularly associated with sulphate reducing bacteria.

As a measure of the activity of sulphate-reducing bacteria, solid material was examined for sulphate disappearance. No significant change in sulphate levels was observed, suggesting that in this type of closed system sulphate reduction is not possible. Sulphate reduction is stimulated in an enriched, dynamic system. Further experiments with the addition of enrichments would be needed to confirm this view.

Investigations using epifluorescence microscopy and scanning electron microscopy suggested that the more microbes were present assoicated with the solid phase than the ligid phase.

A review of the available information from Maqarin has highlighted some of the shortcomings of the available data for input to modelling of microbial reactions. For example, data for the dissolution rates of certain key minerals are required. The importance of SO_4^{2-} and dissolved organics as the redox components responsible for microbial growth is of particular significance in the overall environment at Maqarin. The review has also highlighted the complex nature of the possible available organic species and shown which ones may provide most energy and thus likely to be utilised by microbes. Sources of thermodynamic data have been noted that could be useful in modelling, but further data from the Maqarin site would be useful in constraining the actual reactions to be used in such modelling.

The presence of a quantity of all nutrients in all environments, and the fact that no oligotrophic microbes were detected, suggests that the overall process of microbial growth is governed by energy constraints. Until a detailed breakdown of the organic phases present is produced, an accurate calculation of the potential for microbe growth is not possible. However, it should be possible to place an upper limit on the degree of reaction by consideration of an organic compound that will produce maximum energy when reacted and thus the maximum amount of microbes can be calculated. The generic microbial model MGSE (Microbe Growth in Subsurface Environments) [11] was used for these preliminary calculations. Sulphate reduction to sulphur was considered and all the total organic carbon (TOC) assumed to be the <HCOO> functional group (highest energy producing organic group in the MGSE database). Using the average data given in Chapter 4 (apart from environment C where only M2 and M3 were used for SO_4^{2-}) the theoretical maximum microbe production rates were as follows:-

Environment A (Unaltered material analogue)

3.1 grammes of microbes per year [nutrient (P) limiting]

= 2.1 10^{15} microbes for a flow rate of 6 m^3 m^{-2} y^{-1}

= 3.4 10^8 microbes ml^{-1}

Actual observed microbes = 6.0 10^4 CFU ml^{-1}

(plate counts - heterotrophs on CPS medium) at M6

Environment B (Repository near-field analogue)

1.2 grammes of microbes per year [nutrient (P) limiting]

= 0.8 10^{15} microbes for a flow rate of 6 m^3 m^{-2} y^{-1}

= 1.3 10^8 microbes ml^{-1}

Actual observed microbes= 5.0 10^4 CFU ml^{-1}

(plate counts - heterotrophs on Postgates B medium) at M1

Environment C (Downstream of repository analogue)

2.6 grammes of microbes per year [energy limiting]

= 1.7 10^{15} microbes for a flow rate of 6 m^3 m^{-2} y^{-1}

= 2.9 10^8 microbes ml^{-1}

Actual observed microbes = 6.0 10^4 CFU ml^{-1}

(plate counts - heterotrophs on Postgates B medium) at M3

Where:- a single microbe = $1.5x10^{-15}$ g wet weight.

all calculated quantities microbes are assumed to go into the liquid phase.

CFU = Colony forming Unit

Therefore, it would appear that environment A (the unaltered area analogue) has the greatest potential for microbial growth. This is not surprising as this is the surface environment. In Environments A and B the limit on maximum microbe growth is defined by the amount of nutrients (i.e. P) available. The calculated values were consistently greater than those observed. However, the difference in calculated and observed numbers is not surprising given the many assumptions made. Plate counts also tend to underestimate microbial numbers.

11.10 References

[1] W.R. Alexander (Ed.) *A Natural Analogue Study of the Maqarin Hyperalkaline Groundwaters. I. Source Term Description and Thermodynamic Database Testing,* Nagra Technical Report, NTB 91-10, 1992.

[2] A.H. Bath, N. Christofi, C. Neal, J.C. Philp, M.R. Cave, I.G. McKinley and U. Berner. *Trace Element and Microbial Studies of Alkaline Groundwaters in Oman, Arabian Gulf: A Natural Analogue for Cement Pore-Waters.* British Geological Survey, Fluid Processes Group Technical Report FLPU 87-2, 1987.

[3] J. Jass and H.M. Lappin-Scott. *Practical Course on Biofilm Formation using the Modified Robbins Device.* Biofilm Technologies Research Group, University of Exeter, 1992.

[4] A.M. Abed and B.S. Amireh. *Petrography and Geochemistry of some Jordanian Oil Shales from North Jordan.* Journal of Petroleum Geology, **5/3**, 261-274, 1983.

[5] I.D. Clark, H.N. Khoury, E. Salameh, P. Fritz, H.K. Seidlitz and A.E. Milodowski. *Origin of the Maqarin, Jordan Hyperalkaline Groundwaters: Isotopic and Geochemical Evidence for In Situ Combustion, Calcination and Recarbonation of Bituminous Marls.* Proceedings of the 7th International Symposium on Water-Rock Interaction - WRI-7 (Ed. Y.K. Kharaka and A.S. Maest), 1485-1489, 1992.

[6] H.N. Khoury and A.E. Milodowski. *High Temperature Metamorphism and Low Temperature Retrograde Alteration of Spontaneously Combusted Marls: The Maqarin Cement Analogue, Jordan.* Proceedings of the 7th International Symposium on Water-Rock Interaction - WRI-7 (Kharaka, Y.K. and Maest, A.S. eds.), 1515-1518, 1992.

[7] A.E. Milodowski, J.M. Pearce, C.R. Hughes and H.N. Khoury. *A Preliminary Mineralogical Investigation of a Natural Analogue of Cement-Buffered Hyperalkaline Groundwater Interaction with Marl, Maqarin, Northern Jordan.* NAGRA Unpublished Internal Report, 1992.

[8] Y. Kolodny and S. Gross. *Thermal Metamorphism by Combustion of Organic Matter: Isotopic and Petrological Evidence.* Journal of Geology, **82**, 489-506, 1974.

[9] S. Gross. *The Mineralogy of the Hatrium Formation, Israel.* Geological Survey of Israel Bulletin, **70**, 80p., 1977

[10] R.Y. Stanier, E.A. Adelberg and J.L. Ingrahan. *General Microbiology.* MacMillan Press, UK, 1977.

[11] D.J. Noy, C.A. Rochelle and J.M. West. *Computer Modelling of Microbial Processes using MGSE - Recharge in the Coppermills Borehole, Walthamstow.* British Geological Survey, Fluid Processes Group Technical Report, WE/92/16, 1992.

[12] H.A. Grogan and I.G. McKinley. *An Approach to Microbial Modelling: Application to the Near Field of a Swiss Low/Intermediate-Level Waste Repository.* Nagra Technical Report, NTB 89-06, 1990.

[13] S. Stroes-Gascoyne. *The Potential for Microbial Life in a Canadian High-Level Nuclear Fuel Waste Disposal Vault: A Nutrient and Energy Source Analysis.* Atomic Energy of Canada Limited Report, AECL-9574, 1989.

[14] J.M. West, S. Gardner, D. Noy, C.A. Rochelle and P. Coombs. *Artificial Recharge in the London Basin: Biogeochemical Studies.* British Geological Survey, Fluid Processes Group Technical Report, WE/92/2R, 1992a.

[15] A.E. Milodowski. Personal communication, 1993.

[16] K.A. Kvenvolden, J.B. Rapp, F.D. Hostettler, J.L. Morton, J.D. King and G.E. Claypool. *Petroleum Associated with Polymetallic Sulphide in Sediment from Gorda Ridge.* Science, **234**, 1231-234, 1986.

[17] B.R.T. Simoneit. *Petroleum Generation, an Easy and Widespread Process in Hydrothermal Systems: An Overview.* Applied Geochemistry, **5**, 3-16, 1990.

[18] B.P. Tissot and D.H. Welte. *Petroleum Formation and Occurrence. A New Approach to Oil and Gas Exploration.* 538 p. Springer-Verlag, Berlin, 1978.

[19] E.L. Shock and H.C. Helgeson. *Calculation of the Thermodynamic and Transport of Aqueous Species at High Pressures and Temperatures: Standard Molal Properties of Organic Species.* Geochimica et Cosmochimica Acta, **54**, 915-945, 1990.

[20] T.J. Wolery. *EQ3NR, A Computer Program for Geochemical Aqueous Speciation-Solubility Calculations: Theoretical Manual, User's Guide, and Related Documentation (Version 7.0).* Lawrence Livermore National Laboratory report, UCRL-MA-110662 PT III, 1992.

[21] T.J. Wolery and S.A. Daveler. *EQ6, A Computer Program for Reaction Path Modelling of Aqueous Geochemical Systems: Theoretical Manual, User's Guide, and Related Documentation (Version 7.0).* Lawrence Livermore National Laboratory report, UCRL-MA-110662 PT IV, 1992.

[22] A. Hollerbach. *Influence of Biodegradation on the Chemical Composition of Heavy Oil and Bitumen.* In 'Exploration For Heavy Crude Oil And Natural Bitumen'. American Association of Petroleum Geologists, Studies in Geology (Ed. R.F. Meyer), **25**, 243-247, 1987.

[23] T.R. Jack. *Microbial Aspects of Heavy Oil.* In 'Exploration For Heavy Crude Oil And Natural Bitumen'. American Association of Petroleum Geologists, Studies in Geology (Ed. R.F. Meyer), **25**, 249-255, 1987.

[24] D.E. Miiller, A.G. Holba and W.B. Hughes. *Effects of Biodegradation of Crude Oils.* In 'Exploration for Heavy Crude Oil and Natural Bitumen'. American Association of Petroleum Geologists, Studies in Geology (Ed. R.F. Meyer), **25**, 233-241, 1987.

[25] W.R. Alexander, R. Dayal, K. Eagleson, J. Eikenberg, E. Hamilton, C.M. Linklater, I.G. McKinley and C.J. Tweed. *A Natural Analogue of High pH Cement Porewaters from the Maqarin Area of Northern Jordan II: Results of Predictive Geochemical Calculations.* Journal of Geochemical Exploration, **46**, 133-146, 1992.

[26] C.M. Linklater, Personal Communication.

[27] P.W. Atkins. *Physical Chemistry.* Oxford University Press, 1983.

[28] G.H. Aylward and T.J.V. Findlay. *SI Chemical Data.* John Wiley and Sons, 1974.

[29] D.D. Wagman, W.H. Evans, V.B. Parker, I. Halow, S.M. Bailey and R.H. Schumm. *Selected Values of Chemical Thermodynamic Properties.* NBS Technical Note 270-3, 1968.

[30] D.D. Wagman, W.H. Evans, V.B. Parker, R.H. Schumm, I. Halow, S.M. Bailey, K.L. Churney and R.L. Nuttall. *The NBS Tables of Chemical Thermodynamic Properties, Selected Values for Inorganic and C1 and C2 Organic Substances in SI Units.* Journal of Physical and Chemical Reference Data, **11**, 2-83 - 2-110, 1982.

[31] R.C. Weast, M.J. Astle and W.H. Beyer. *CRC Handbook of Chemistry and Physics, 67th Edition.* CRC Press, Florida, 1987.

[32] A.B. Hull and J.R. Hull. *Geometric Modelling of Dissolution Kinetics: Application to Apatite.* Water Resources Research, **23/4**, 707-714, 1987.

[33] G.H. Nancollas, Z. Amjad and P. Koutsoukos. *Calcium Phosphates-Speciation, Solubility, and Kinetic Considerations.* In 'Chemical Modelling in Aqueous Systems' (Ed. E.A. Jenne), American Chemical Society, 475-497, 1979.

[34] E. Nickel. *Experimental Dissolution of Light and Heavy Minerals in Comparison with Weathering and Intrastratal Solution.* Contributions to Sedimentology, **1**, 1-68, 1973.

[35] A.F.M. Barton and N.M. Wilde. *Dissolution Rates of Polycrystalline Samples of Gypsum and Orthorhombic Forms of Calcium Sulphate by a Rotating Disc Method.* Transactions of the Faraday Society, **67**, 3590-3597, 1971.

[36] J. Cristoffersen and M.R. Cristoffersen. *The Kinetics of Dissolution of Calcium Sulphate Dihydrate in Water*. Journal of Crystal Growth, **35**, 79-88, 1976.

[37] S. Liu and G.H. Nancollas. *The Kinetics of Dissolution of Calcium Sulphate Dihydrate.* Journal of Inorganic and Nuclear Chemistry, **33**, 2311-2316, 1971.

Table 11.1 Description of sample sites

Code	Description
M1	Hyperalkaline groundwater discharge site through major fracture zone in metamorphic rocks in Adit A6. Rocks and water sampled.
M2	Hyperalkaline groundwater discharge site through fractures in unmetamorphosed marl country rocks approximately 45 m from the entrance to Adit A6. Rocks and water sampled.
M3	Groundwater discharge site in marl fractured country rocks in railway cutting on eastern area of site. Rocks and water sampled.
M5	Hyperalkaline groundwater discharge site in wadi colluvium exposed in southern bank of Yarmouk river. Rocks and water sampled.
M6	Ain Queibeh Spring, natural spring in chalky limestone in small valley bottom. Rocks and water sampled.

Table 11.2 Repository environments and their analogue sample site at Maqarin

Environment code	Repository environment	Site code
A	Unaltered host rock	M4 and M6 (N.B. M4 not sampled for upstream of repository microbiology)
B	Repository near field	M1
C	Host rock with hyper-alkaline plume downstream of repository	M2, M3 and M5

Table 11.3 Summary of sample bottles prepared for field work

Enrichment target group	Label	Field sample media	Contents	Volume
Heterotrophs	1A	Liquid	CPS (x10 conc.)	3mls
	1B	Solid	CPS	28mls
Oligotrophs	2A	Liquid	CPS (10% conc.)	3mls
	2B	Solid	CPS (1% conc.)	28mls
Sulphur oxidisers	3A	Liquid	media 3* (x10 conc.)	3mls
(Obligate)	3B	Solid	media 3*	28mls
Sulphur oxidisers	4A	Liquid	media 4* (x10 conc.)	3mls
(Facultative)	4B	Solid	media 4*	28mls
Sulphate reducers	5A	Liquid	Postgates B (x10 conc.)	3mls
	5B	Solid	Postgates B	28mls
Algae	6A	Liquid	Chu no.10 (x10 conc.)	3mls
	6B	Solid	Chu no.10	28mls
For epifluorescence	7A	Liquid	Gluteraldehyde (20%)	3mls
microscopy	7B	Solid	Gluteraldehyde (2%)	28mls
Unpreserved	8A	Liquid	Sample only	

All media compositions contained in Appendix E

N.B. All samples were prepared in triplicate for each sampling site.

Table 11.4 Millipore dip stick sampling (see Table 11.2 for explanation of Environment code)

Environment code	Sample no.	Exam. date	No. colonies/ml
B	M1 - 1	28.05.92	1
		01.06.92	4
	M1 - 2	28.05.92	0
		01.06.92	0
C	M2 - 1	28.05.92	1
		01.06.92	1
	M2 - 2	28.05.92	1
		01.06.92	1
C	M3 - 1	28.05.92	0
		01.06.92	0
	M3 - 2	28.05.92	0
		01.06.92	0
C	M5 - 1	28.05.92	0
		01.06.92	0
	M5 - 2	28.05.92	0
		01.06.92	0
A	M6	None performed	

Table 11.5 pH analysis of water samples (see Table 11.2 for explanation of Environment code)

Environment code	Sample site	pH (AGG analysis)	pH (micro. lab)
B	M1	12.67	10.91
C	M2	12.47	11.25
C	M3	12.76	11.36
C	M5	12.83	11.25
A	M6	7.60*	7.70**

AGG = Analytical Geochemistry Group result 10 July 1992
Micro. lab. = Microbiology Laboratory 1 October 1992
* Field measurement 16 February 1993
** Laboratory measurement 24 February 1993

Table 11.6 The effect of sterilisation on the pH of CPS broth

Before Sterilisation	After Sterilisation
4	4.15
5	5.18
6	6.07
7	7.09
9	9.10
11	10.45

Table 11.7 Observations in growth for samples from liquid enrichments in CPS pH broths after 48 hours incubation.

Heterotrophic enrichment			*SRB enrichment*		
Sample Code	**CPS broth pH**	**Growth (+/-)**	**Sample Code**	**CPS broth pH**	**Growth(+/-)**
M1	4	-	M1	4	-
	5	-		5	+
	6	-		6	+++
	7	-		7	++
	9	-		9	++
	11	-		11	+++
M2	4	-	M2	4	-
	5	-		5	-
	6	-		6	-
	7	-		7	++
	9	-		9	+++
	11	-		11	++++
M3	4	-	M3	4	-
	5	-		5	-
	6	-		6	-
	7	-		7	-
	9	-		9	-
	11	-		11	-
M5	4	-	M5	4	-
	5	-		5	-
	6	-		6	-
	7	-		7	-
	9	-		9	-
	11	-		11	-

Key + indicates growth, - indicates no growth.
M1 samples - Repository near-field analogue,
M2, M3, M5 samples - Downstream analogue

Table 11.8 Summary of sample bottles used in SRB activity experiment

Sample code	Contents
M1	25 mls M6 sterile water + 5 g M1 core
M3	25 mls M6 sterile water + 5 g M3 core
M6	25 mls M6 water

Table 11.9 Results of SO_4 analysis

Sample	Time (weeks)	SO_4 conc. (mg/l)
M1	0	302.50
M1	4	306.87
M3	0	288.49
M3	4	284.58
M6	0	15.94
M6	4	12.11

Table 11.10 Distribution of microbes on solid and liquid phases using epifluorescence microscopy

Site	Groundwater sample (No. microbes per ml)	Solid sample (No. microbes per ml)
M1	$1.7\ 10^4$ (s.e. $2.66\ 10^3$)	$3.43\ 10^5$ (s.e. $1.56\ 10^4$)
M3	$5.97\ 10^4$ (s.e. $1.95\ 10^4$)	$1.92\ 10^5$ (s.e. $33.93\ 10^3$)

s.e. = standard error

Table 11.11 Summary of the major rock constituents at Maqarin (based on [7])

Original organic-rich rock (Environment A)	Prograde alteration (high temps.) (Environment B)	Retrograde alteration (hydration) (Environments B/C)
15-20% organics	main minerals	main minerals
<5% sulphur	- wollastonite	- ettringite
main minerals	- diopside	- thaumasite
calcite	- larnite	- tobermorite
quartz	- brownmillerite	- CSH gels
dolomite	- spurrite	- apophyllite
apatite	- anorthite	- afwillite
pyrite	- ellestadite	- calcite
clay minerals	- graphite	- gypsum
	calcite	- barite
	apatite	- brucite
		zeolites

Table 11.12 Gross composition of crude oils expressed as weight percent of the fraction boiling above 210°C (data from [18])

	Normal producable crude oils	All crude oils including tars	Disseminated bitumen
Saturated hydrocarbons	57.2	53.3	29.2
Aromatic hydrocarbons	28.6	28.2	19.7
Resins and asphalt	14.2	18.5	51.1
Aromatic S (% of aromatic fraction)	2.07	-	1.85

Table 11.13 Average composition of hydrocarbons expressed as weight percent (data from [18])

	Normal producable crude oils	All crude oils including tars	Disseminated bitumen
n- + iso-alkanes	33.3	31.7	27.7
Cycloalkanes	31.9	32.1	29.3
Aromatics	34.5	36.2	43.0

Table 11.14 Average composition of resins and asphaltenes expressed as weight percent (data from [18])

		C	H	O	S	N	O+S+N
Crude oils	Resins	84.0	9.2	0	0	0	6.9
	Asphaltenes	85.0	8.1	2.4	0	0	7.3
Source rock bitumen	Resins	78.0	9.2	7.2	2.8	0.9	10.9
	Asphaltenes	74.4	7.5	7.6	3.0	1.7	12.3

Table 11.15 Relative reactivity, in decreasing order, of some organic species present in natural hydrocarbons (from [22, 23, 24]).

n-alkanes isoprenoid alkanes cyclic alkanes light aromatics light thiophenes	most reactive group, completely removed by microbial reactions, are generally small molecules.
steranes diasteranes triaromatic steranes	
naphthenes heavy, or highly branched aromatics and thiophenes	least reactive group, are generally large molecules.

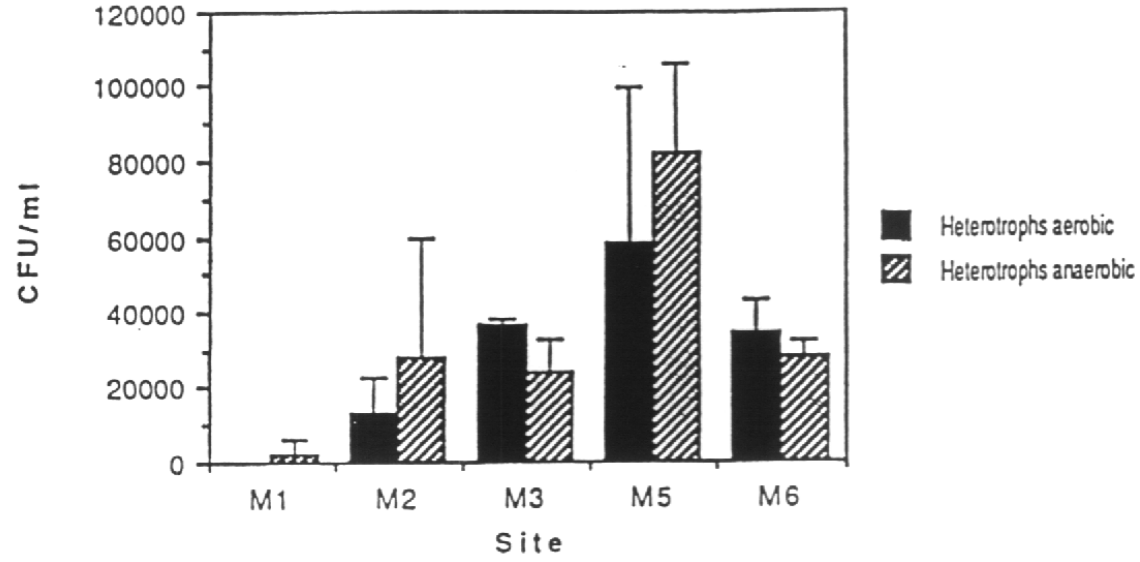

Figure 11.1 Enumeration of heterotrophs in liquid samples

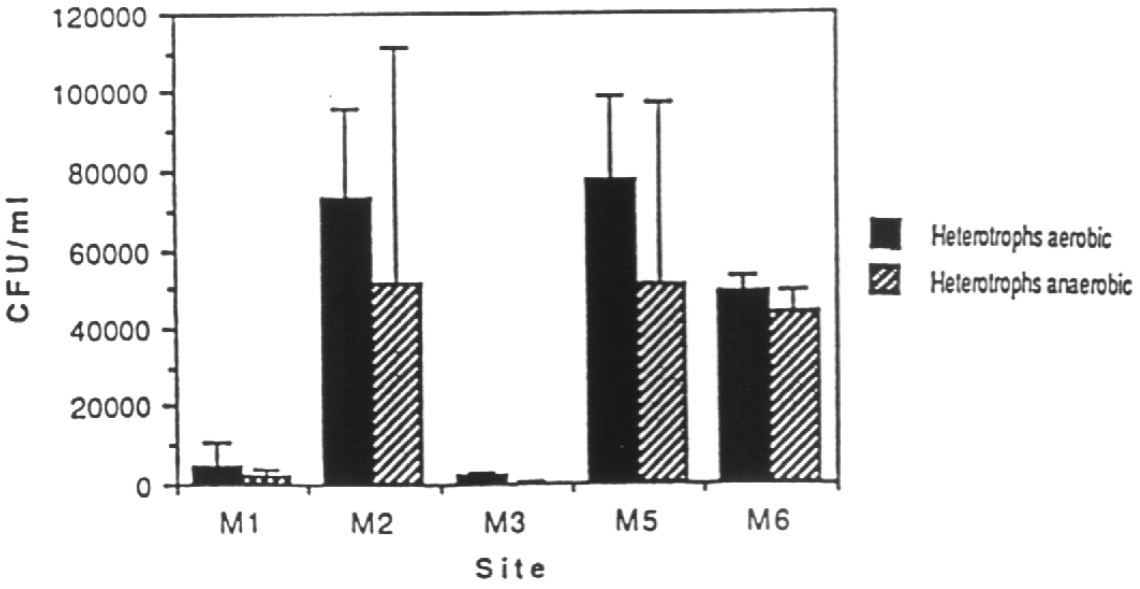

Figure 11.2 Enumeration of heterotrophs in solid samples

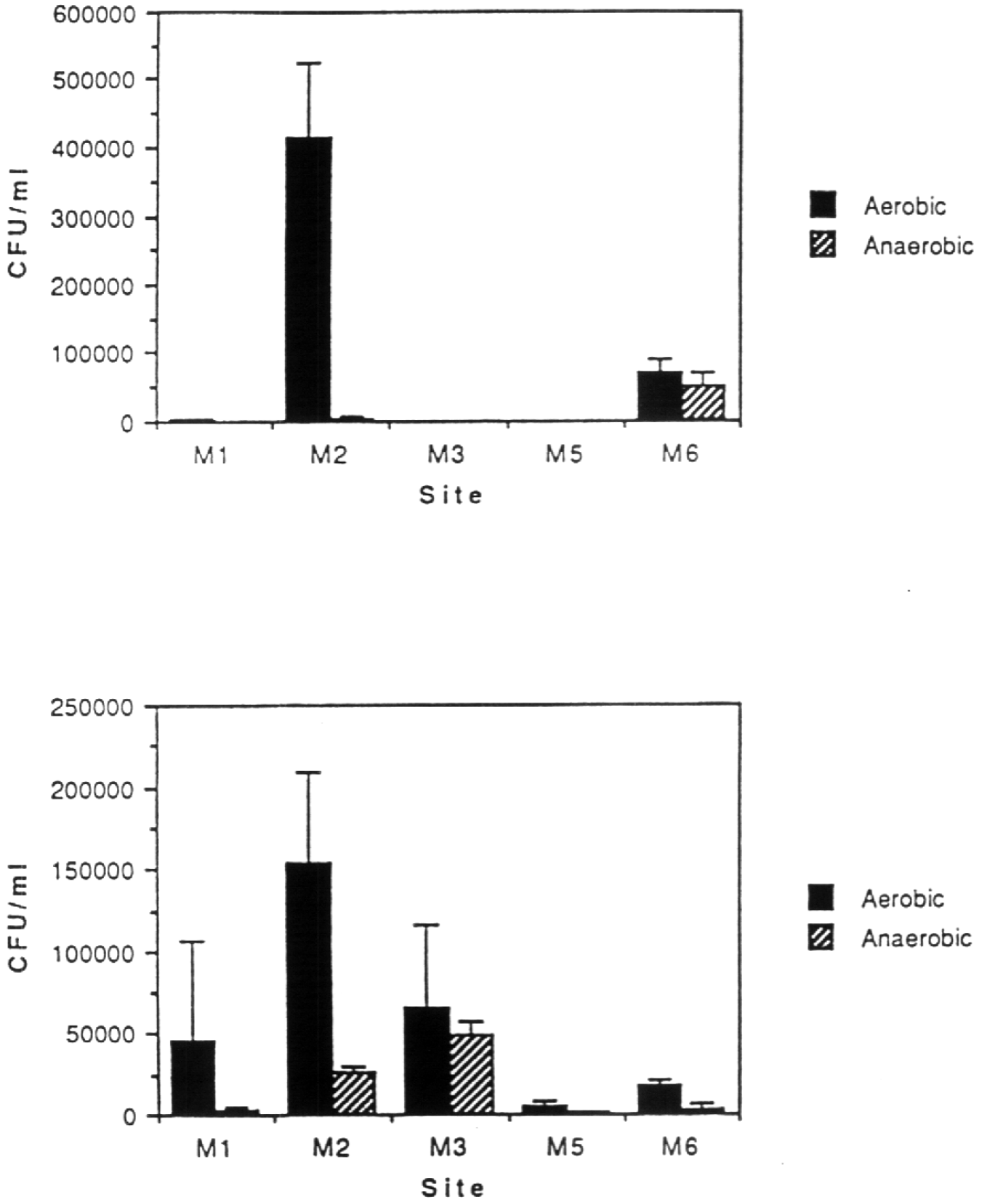

Figure 11.3 Bacterial enumeration of a) liquid and b) solid samples on Postgates E plates

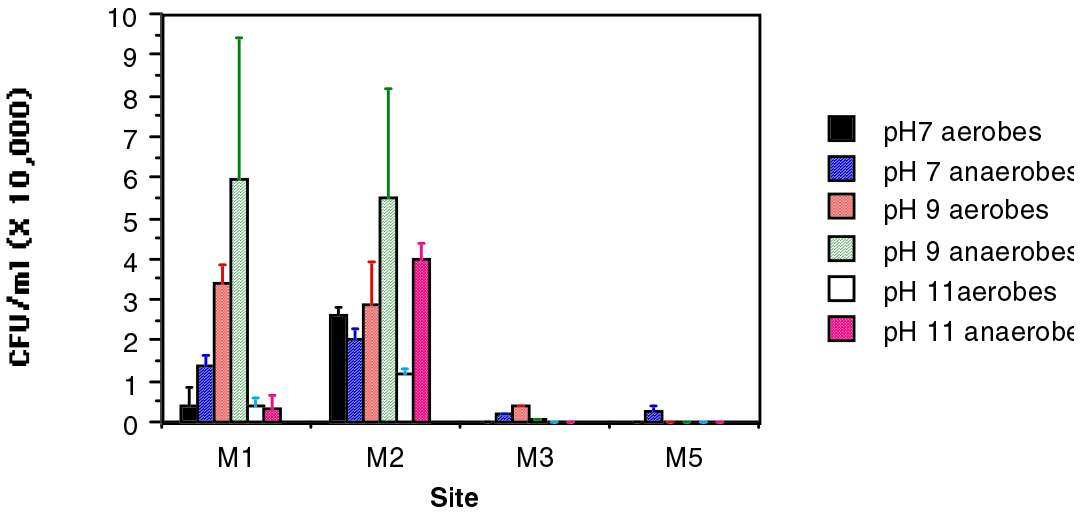

Figure 11.4 Results of microbial enumeration for samples from solid enrichments when grown on CPS plates of different pH. Results are mean of triplicate plate counts.

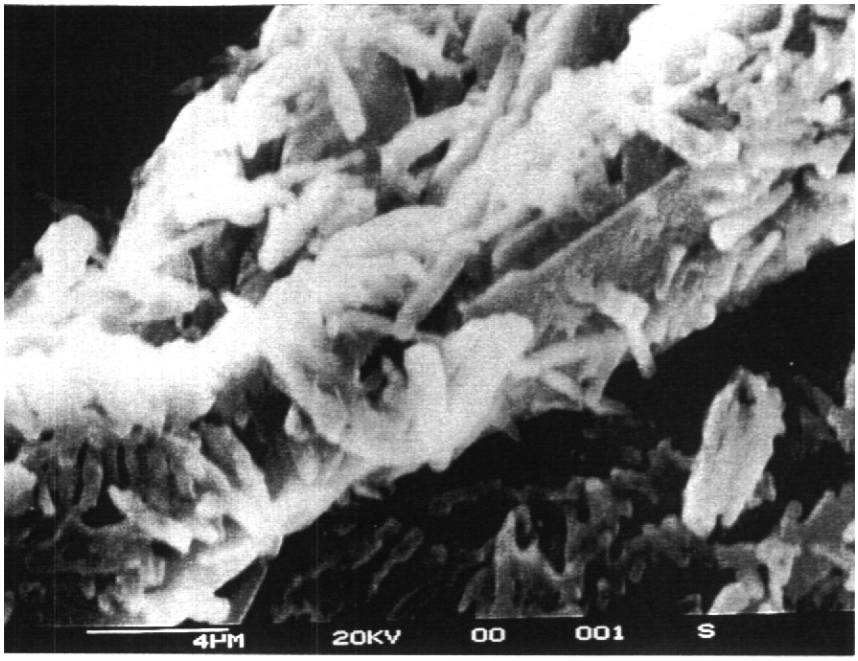

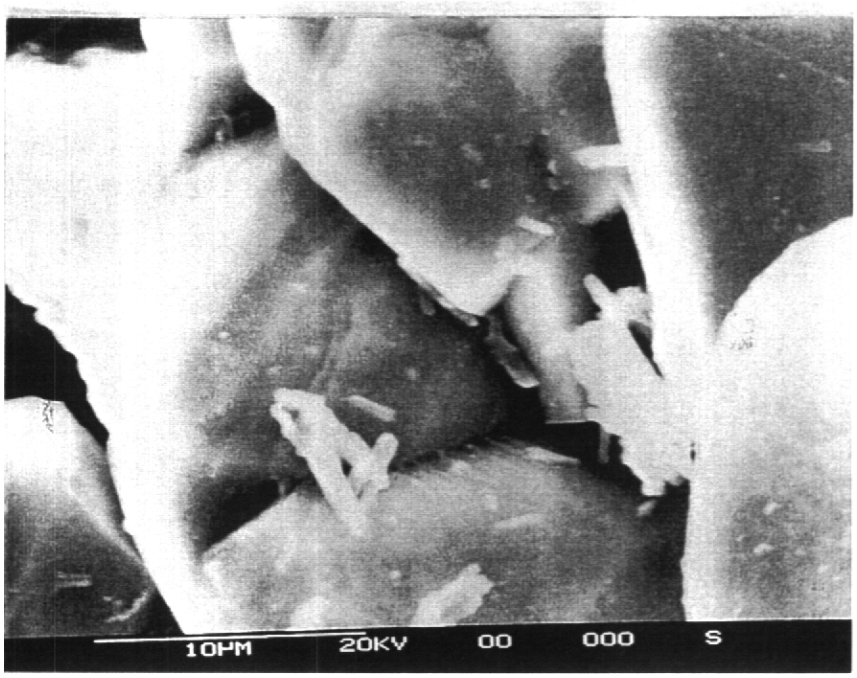

Plate 52 Scanning electron photomicrograph showing clusters of rod shaped bacteria detected in solid material from site M1.
a) bar, 4 μm
b) bar, 10 μm.

12. TESTING THE LIMITS OF APPLICABILITY OF THERMODYNAMIC DATABASES

W.R. Alexander, I.G. McKinley, C.M. Linklater, C.J. Tweed, I. Casas, S. Börjesson and P. Sellin.

12.1 Introduction

An important constraint on the rate of release of many radionuclides present in radioactive waste (radwaste) is set by their expected very low solubility[†] under the chemical conditions of the repository. For performance assessment of a repository for radioactive waste, geochemical codes may be employed to provide a quantitative definition of the solubility of the radionuclides of interest. An accurate description of the behaviour of the radionuclides is dependent on the thermodynamic databases (TDBs) utilised by the codes. These TDBs are normally compiled from data produced under controlled laboratory experiments (see the review of experimental techniques in [1]) or, where no appropriate experimental data exist, have been estimated by one of several possible methods, e.g. [2].

In compiling any such TDBs, care must be taken to ensure that the source data are critically evaluated to avoid inclusion of discrepant data (e.g. using an unproven or inappropriate experimental technique) or wrong data (e.g. conversion or transcription errors) which may introduce an error or bias into any calculations employing the TDB. Several strategies for critical evaluation of raw data are proposed by Nordstrom and Munoz [1], these and others are described in numerous recent TDB compilations [e.g. 3, 4].

To date, adequate thermodynamic data are available for many major elements considered in hydrogeochemistry. However, in the context of radioactive waste disposal, thermodynamic data are limited for many radioelements and further critical evaluation is useful (and, in some national programmes, mandatory) to provide confidence that the TDBs employed are applicable to the range of environments of interest. For example, laboratory-produced thermodynamic data for uranium minerals [4] have been produced under idealised conditions and usually apply only to pure phases. It would be appropriate to consider whether or not such data are applicable to the (complex) natural environment.

TDB testing has gradually developed in the radwaste community by iterative improvement through a series of studies. Laboratory experiments can be relatively well defined, but the phases that form over a laboratory timescale often vary from those expected over longer timescales or observed in natural systems, as a consequence of the very slow rate of equilibration of reactions involving the precipitation of solid phases. TDB testing is therefore often focused on field databases, either measurements of concentrations in natural waters or specific natural analogue studies, as these represent systems which have reacted for much longer periods and, in many respects, may be comparable to the system expected in the near- and far-fields of a repository.

[†] Solubility may be defined as the maximum equilibrium concentration, in a solution of defined chemistry, which can be reached by a specific element (this definition refers to concentrations in true solution and does not consider colloids). The definition of solubility limits for performance assessment is a procedure which involves integration of field, laboratory and theoretical information.

Although TDB's have been tested extensively in the case of major element geochemistry for many years, trace element geochemistry, particularly that of the actinides, has been less widely studied. The first natural system test of TDBs relevant to radioactive waste disposal was carried out within the Oman natural analogue study [5, 6, 7] and was carried on through the Poços de Caldas project [8, 9, 10] to the current study in Maqarin [11, 12, 13, 14, 15]. Within these studies, particular focus was given to controls on the solubility of trace elements.

The basic methodology adopted is explained below, and some comments made on the limitations of the procedure and, thus, on the applicability of the so tested databases.

12.2 Methods

12.2.1 Test procedure

The aims are twofold: first to assess the applicability of the thermodynamic databases employed at the high pH conditions anticipated within a cementitious repository and, second, to evaluate how well modelling groups (drawn from both performance assessment and geochemical backgrounds) can 'predict' radionuclide solubilities by comparing their predictions for a range of trace elements in a relevant natural system to direct observations. Agreement between prediction and observation provides some degree of 'validation' of the databases for use under high pH conditions [16]. Briefly, the method involves:

(i) Defining a groundwater major element chemistry: in this case three groundwater chemistries, based on measured data, were specified (Table 12.1) for the five modelling groups (Table 12.2). The modellers were allowed to comment on the appropriateness of the data (e.g. with respect to charge balance, degree of saturation with respect to major minerals, etc.) but were required to carry out further evaluations without correction of, for example, charge imbalance.

(ii) Blind prediction, based on an arbitrary trace element aqueous concentration[†] of 1 μgl^{-1}, of elemental speciation and degree of saturation of potential solubility controlling solids for U, Th, Ra, Se, Ni, Sn and Pb using two thermodynamic codes and five different databases (Table 12.2). In this phase of a database test, no data suppression (e.g. ignoring mineral phases unlikely to form in the particular groundwater system under consideration) is permitted as this will introduce a bias to the procedure. (This approach is valid because the major complexant, OH^-, is present at concentrations very much higher than the radioelement).

(iii) Comparison of results to determine major database discrepancies. This procedure is a simple intercomparison between the databases used (a type of verification) which can identify major inconsistencies in the databases.

(iv) Provision of measured concentrations of the seven trace elements of interest to the modelling groups (Table 12.3).

(v) Second phase of blind prediction of elemental speciation, solubility and appropriate solubility controlling solids.

[†] This particular procedure has been employed so that all speciation calculations are carried out at the same concentration. The alternative approach - calculating speciation for a concentration corresponding to 'saturation' - can make comparison between databases very difficult if the resulting concentrations vary significantly between the modelling groups.

(vi) Final comparison with highly detailed analytical data on the site mineralogy and approximate groundwater speciation (separation of anionic, cationic and non-ionic, or neutral, components). Interpretation of anomalies between the code predictions and the analytical data provide an idea of the applicability of the databases to a cementitious repository environment and may additionally indicate areas for database improvement.

12.2.2 Simplifications and potential problems

There are clearly simplifications in such a database testing procedure as practised here. The database tests carried out here are not exhaustive. The intention is to produce databases which are as accurate as possible and to understand any limitations in the predictions. In some countries the predictions from these databases are used directly as input to performance assessment and in this case, it is important that results are either accurate, or err on the side of safety by over-predicting releases of radionuclides from a repository.

Specific simplifications include:

(i) The blind prediction modelling exercise assumes that the concentration in the groundwater of any given trace element is controlled only by equilibration with the most stable phase present in the associated rock/water system. Theoretically, this phase could be part of either the primary or secondary mineral assemblage. In the case of control by a primary mineral, it is thus assumed that saturation of the contacting water can be achieved before the mineral has dissolved completely. This may not be true, in which case the trace element would be 'source-term limited' and the solution concentration would be controlled by the volume of the phase present in the primary mineral assemblage, and not equilibrium with the solution. It should be borne in mind that another possible control in natural systems might be the rate of leaching from the adjacent rock.

(ii) No equilibration with the identified solubility-limiting phase was carried out. For a low solubility trace element, the approach used here is sufficiently accurate and simplifies comparison of calculated speciation. For a highly soluble trace element, this procedure is less appropriate as saturation with this element may significantly influence groundwater chemistry. However, for most trace elements of interest to a performance assessment, this approach is probably justified as they are unlikely to be present (in either a repository or a natural analogue site) at concentrations high enough to perturb the water chemistry to any great extent.

(iii) All databases tested here (and the majority of databases in present use) assume solubility control by pure mineral phases whereas, in reality, co-precipitation or solid solution will be the most likely control for trace elements. Indeed, the detailed mineralogical data produced to date in this study [11, 17, 18] and those given in Chapter 6, show this to be the case in the Maqarin system. However, as it seems unlikely that relevant thermodynamic databases including co-precipitation and solid solution will be available for the foreseeable future, it is necessary to understand any differences between prediction and observation using existing databases and measurement. Similar comments may be passed on the influence of colloids and organics on the model results.

(iv) No charge balancing was carried out during the calculations. This is intended to simplify intercomparison of results as differing methods of charge balancing would require back calculation to non-balanced conditions to assess whether differences in results between the databases were simply an artefact of the

balancing procedure. In most groundwaters, the difference is not great anyway, but in highly mineralised systems, such as the Maqarin groundwaters, scoping calculations should be carried out to check that any charge imbalance does not skew the results. This has been done here and shown to produce differences of less than 1% in the calculated solubility.

12.3 Results and Discussion

12.3.1 Introduction

In previous database tests (such as at Oman and Poços de Caldas [7, 8, 9]), different databases have been tested at the same time so allowing intercomparison of the results. This has been useful in highlighting errors in some of the databases. When no reason for divergent results can be found, then more fundamental problems may exist in a database - problems that may have gone undetected in routine tests. The HATCHES (2.0) database of the Chalmers University group is the forerunner of the HATCHES (3.0) of MBT which is itself the forerunner of the latest HATCHES release, version 5.0 used by the AEA Technology group. A significant proportion of the data for solid phases in the HATCHES database were taken from an EQ3/6 database similar to that used by SKB and therefore the four databases share much common material (as will be seen in the results). The Nagra database NTB9118 is slightly different in that it represents a new collection of data, but clearly some of the sources are the same due to the fact that HATCHES (3.0) was also used as a source for this compilation.

Another, more traditional, way to carry out the TDB intercomparison would be to simply go through printouts of each TDB and do a species by species, line by line comparison [3]. However, this method does not enable the significance of discrepancies to be assessed.

The results are presented and discussed on an element by element basis, with a comparison of the first stage calculations (based on assumed concentrations of 1 μgl^{-1} for all the trace elements of interest) with those of the second stage, using the measured trace element concentrations (Table 12.3). Note that the in situ speciation technique (Chapter 5) was only successful when the trace element concentration was reasonably high, and thus comparative data exist only for Se, Ni and Pb.

12.3.2 Uranium

The U results are detailed in Tables 12.4a-f. All groups predict the presence of only anionic species but this cannot be checked as the U concentrations were below the detection limit of the field speciation technique (Chapter 5). Otherwise, there are no great differences between the HATCHES-based predictions, with $UO_2(OH)_4^{2-}$ dominating the predicted speciation. MBT note the presence of an additional anionic species, $UO_2(OH)_3^-$. This discrepancy arises because MBT have substituted the uranium database from HATCHES (3.0) with that compiled by the NEA [19]. Interestingly, the Nagra database indicates a preponderance of the same species in the two waters examined, reflecting the MINEQL/PSI (see [11] for comments) basis of the U data in this database. $UO_2(OH)_3^-$ is omitted from the HATCHES databases as calculations with this species predict a higher $UO_2(OH)_2$ solubility than is experimentally observed at high pH [20]. HATCHES (5.0) additionally indicates the presence of the neutral species $UO_2(OH)_2$, although this all but disappears on introduction of the field U concentrations (Tables 12.4.b,d and f).

In the solid phase predictions, all the HATCHES databases (Version 2.0 to 5.0) report $CaUO_4$ as the solubility limiting phase, and underpredict solubility. This was also observed in the Maqarin Phase I study [11]. An amorphous Ca-U oxide or carbonate is indeed present as part of the metamorphic mineral assemblage [11]. However, the data in HATCHES refer to a highly crystalline refractory phase and so are not directly applicable to this natural system. Indeed, the phase does not appear in the Nagra results as it has been omitted from the new database on the basis that it rarely appears in low temperature systems in nature. If the $CaUO_4$ phase is suppressed and the U oxides or hydroxides are chosen instead (as argued by Lemire [21]), then all the databases overpredict U solubility.

U solid phase chemistry is extremely complex in the Maqarin system as is clear from references [11, 17] and Chapter 6. The databases are adequate from the viewpoint of data input to a performance assessment in that they would predict more U release from a repository than would occur in reality[†], as long as U oxides and hydroxides rather than $CaUO_4$ are selected as solubility-limiting phases. It is worth investigating further thermodynamic data for less crystalline Ca-U oxide phases, as inclusion of data for such phases might provide more realistic estimates of U behaviour, particularly in cement-bearing systems.

12.3.3 Thorium

The five databases show good agreement in the case of Th (Tables 12.5a-f) with all predicting the aqueous speciation to be dominated by $Th(OH)_4$. In the Maqarin Phase I study, no analytical data were available for Th and so an assumed value of 0.1 μgl^{-1} was employed, leading to an apparent oversaturation of Th in the system [11]. Here, the analytical results show Th concentrations to lie below those previously assumed (0.002-0.009 μgl^{-1}) so allowing a more realistic test of the databases. However, of the five databases tested, all still predict oversaturation of at least one Th solid. The most complete database, HATCHES (5.0), predicts oversaturation only for crystalline ThO_2, other less crystalline phases are undersaturated. To date, no discrete Th phase has been identified in the Maqarin system so it is difficult to say that the more soluble non-crystalline Th phases represented in the databases are more realistic in this instance. Indeed, it seems possible that Th is source term limited in this system [11] and hence the possibility of further evaluation of the Th databases here is limited.

12.3.4 Radium

The new Nagra database does not yet contain an evaluated Ra dataset and so only the behaviour of the HATCHES databases can be assessed here. Not surprisingly, they all produce similar predictions of Ra solubility, with slightly different predicted speciation. The SKB group of databases are limited in that they contain only Ra^{2+}, $RaOH^+$ and $RaSO_4^o$ as the aqueous species and $RaCO_3$ and $RaSO_4$ as the solid phases. HATCHES (5.0) contains additional data [22, 23] with a modified constant for $RaSO_4^o$, extra aqueous species ($RaCO_3^o$ and $RaCl^+$) and additional solids (Ra and $RaCl_2.2H_2O$) as well as modified constants for the previously considered solids [11].

The predicted speciation is dominated by Ra^{2+}, although in calculations using HATCHES (5.0) significant $RaSO_4$ is also predicted, particularly for the M5 water (Tables 12.6a-f). The high levels of SO_4^{2-} in M5 (Table 12.1) account for the predicted increased role of

[†] The mineralogical data (Chapter 6) indicate that U is not source term limited at Maqarin, but if this were the case elsewhere, then the above results would not necessarily need to be taken as over predictions.

$RaSO_4(aq)$ in this instance. In comparison with the other TDBs, Ra is predicted to be more soluble in the calculations using HATCHES (5.0). This is due to the presence of a larger number of aqueous species in these calculations.

Pure Ra solids are extremely rare in nature. Ra is normally found in a mixed solid, where it has been involved in coprecipitation or solid solution with other alkaline earths. In the Maqarin system, the likely sources/sinks of Ra are thus gypsum and barite. The HATCHES databases would probably over-predict the solubility of Ra due to the inclusion of only pure end-member minerals.

Where the databases are likely to be used in a low SO_4^{2-} groundwater, it would be appropriate to further test the Ra data as other mechanisms of Ra uptake (e.g. exchange on clays) may occur.

12.3.5 Selenium

There are few quality Se data available in the literature so the strong dependence of all five databases on the Wagman et al [24] and Baeyens and McKinley [25] databases means there are few significant differences in the predicted speciation (Table 12.7a-f). SeO_4^{2-} dominates at the high Eh (generally more than +250mV) observed in the Maqarin waters, although a minor amount of SeO_3^{2-} is predicted to appear as the Eh drops to +150mV in water M3. The HATCHES databases predict almost identical saturation indices for a range of Ca-selenates and selenites. The only Se phase represented within NTB9118 is native selenium, and a very high solubility is calculated (the exact numerical values are meaningless in this context: saturation indices less than -10 or so simply represent extremely high solubility).

The prediction that speciation is dominated by anions is consistent with observation; ion exchange measurements suggest 90-97% of Se is anionic (Chapter 5). Mineralogical data [11] indicate the presence of both Ca-selenate and elemental Se in the Maqarin rocks (see also comments in [11]), but it is clear that the decision to include only elemental Se in the NTB9118 database because it is the 'only Se solid exerting significant control on the Se concentration of natural waters' [3] results in large over-predictions of solubility for oxic to sub-oxic systems such as Maqarin. A further test of the Se databases in a strongly reducing hyperalkaline environment would be worthwhile to test more rigorously the applicability of the NTB9118 database.

The likely connection between the behaviour of Se and S in this system [11] would suggest that Se is incorporated into S minerals before saturation of any pure Se phase is attained. Mixed Se-S minerals have certainly been identified at Maqarin [11].

McKinley et al. [7] have suggested that the type of approach used here to test databases may be invalid for Se due to the expected kinetic constraints on redox equilibria in the Se system. This may well be the case, but, as long as the results of the test are not over interpreted, it is suggested that further examination of new Se databases may be useful to identify major omissions.

12.3.6 Nickel

The nickel predictions (Tables 12.8a-f) appear more complicated than the predictions for the preceding elements as the HATCHES database for nickel evolved significantly between versions 2.0 and 5.0. The databases of CU[†], MBT and Nagra predict similar

[†] Note that HATCHES 2.0 contains no $Ni(OH)_4^{2-}$ and so this has been added at some time to the CU database.

speciation, with a predominance of $Ni(OH)_3^-$ and lesser amounts of $Ni(OH)_4^{2-}$ (and $Ni(OH)_2^o$ in the case of CU). HATCHES (5.0) predicts mainly $Ni(OH)_4^{2-}$, whereas the SKB database also includes substantial amounts of $Ni(OH)_3^-$.

The nickel database in HATCHES is based on the data from Baes and Mesmer [26], modified in the light of experimental measurements of Pilkington and Stone [27]. The modifications have been made in three stages:

- Initial modelling interpreted the Pilkington and Stone data without the $Ni(OH)_4^{2-}$ species (HATCHES v2.0, v3.0). Baes and Mesmer [26] provide a formation constant but this is an estimate based on the values for $Ni(OH)_2^o$ and $Ni(OH)_3^-$.
- The $Ni(OH)_4^{2-}$ species was included in HATCHES v5.0 as the Phase I TDB testing [11] had postulated that this species could be important at high pH.
- Further modelling of the Pilkington and Stone data was carried out including $Ni(OH)_4^{2-}$ and lead to further modifications, included in later releases of the HATCHES database.

It interesting to note that there is still a discrepancy between the predictions of the HATCHES databases (based on the Baes and Mesmer dataset) and the Nagra database which is based on the dataset of Baeyens and McKinley [25].

Interestingly, the in situ speciation data (Chapter 5) suggest a predominantly cationic form for the nickel in this system. However, as noted by Short (Chapter 5), these results are likely to be an artefact due to the use of 'strong acid cation resins which, like soluble complexing agents, have functional (sulphonate) groups which are able to significantly disturb the aqueous speciation equilibria during the (resin/groundwater) equilibration period'.

All five databases predict the most likely solubility controlling phase to be $Ni(OH)_2$, with NiO (bunsenite) slightly less saturated again. Note that NiO was included by Baeyens and McKinley [25] due to the rather uncertain solubility of $Ni(OH)_2$ in Baes and Mesmer [26].

Both AEA and MBT (using HATCHES (3.0) and HATCHES (5.0) respectively) include $NiFe_2O_4$ (the Ni-spinel trevorite) in their results for completeness. Fe spinels are present within the metamorphic rock assemblage at Maqarin [11]. It was therefore of interest to include some related phases in the calculations. Generally, it is assumed that spinels do not form in low temperature systems (and trevorite is, in any case, rare [28]) and that these phases would have limited relevance for performance assessment modelling. Modellers have therefore been recommended to suppress spinel in the databases (cf. also the results of the Poços de Caldas TDB tests in [9]). However, some recent studies have suggested that some spinels can form at low temperature, e.g. magnetite forming as a steel corrosion product under anoxic conditions [29]. It may be worth reassessing the potential of these phases to limit trace element solubility in repository environments.

A similar example is that of $NiSiO_3$ which Nagra has included in the results for the M5 water (Tables 12.8e, f) for illustration. Inclusion of such a phase in performance assessment calculations would lead to underprediction of nickel solubility. However, there is uncertainty regarding the environments in which such a phase would occur[†] and

[†] It is not clear if this phase even exists: the data [25] are based on estimates.

predictions based on its stability should be disregarded in performance assessment calculations.

12.3.7 Tin

The main difference in the predicted Sn speciation between groups (Table 12.9) is whether or not the database contains data for Sn(IV) hydrolysis products. Under hyperalkaline conditions, an increase in the solubility of cassiterite (SnO_2) has been shown to coincide with the appearance of $Sn(OH)_5^-$ in solution [30]. Sn(IV) hydrolysis products have also been shown to be significant at temperatures above 100°C [31]. The HATCHES (5.0) Sn database includes Sn(IV) hydrolysis products and has been tested directly against other experimental work carried out within the Nirex programme [32] and found to correctly predict Sn solubility over a range of pH conditions [11]. All of this would appear to support the inclusion of the Sn(IV) hydrolysis products and suggests that the predictions produced by the HATCHES (2.0) database are not applicable to this system (the very high saturation indices values reported by CU have no real physical meaning, simply that the database predicts extremely low solubility for cassiterite in this system).

The SKB database predicts that the $Sn(OH)_4^o$ species dominates the Sn aqueous speciation, producing a Sn solubility somewhat less than that predicted by AEA, MBT and Nagra. Comparison of the EQ3/6 and NTB9118 databases reveals that only 50% of all Sn species quoted are common to both databases, indicative of their different origins (the EQ3/6 data owe more to Sn ore geochemistry while NTB9118 leans heavily on HATCHES with its strong basis in radioactive waste research). What is common to all databases examined here is that various forms of cassiterite are predicted to be the solubility controlling phase.

Detailed re-examination of the Maqarin rock (following these predictions) has found no indication of a discrete Sn phase [33]. Cassiterite is normally found associated with hydrothermal mineralisation and igneous activity, rather than low temperature systems, and is thus arguably not relevant to a performance assessment database. Pearson et al. [3] have already suggested further work to expand Sn databases but this must take into account more relevant (i.e. low temperature) Sn phases to be of use.

12.3.8 Lead

The three HATCHES databases are very similar in their predictions for Pb speciation (100% $Pb(OH)_3^-$) and solubility controlling phases ($Pb(OH)_2$) with the CU results being slightly less conservative (Table 12.10a-f). The SKB database, however, predicts a completely different speciation (100% $PbCO_3$) and a related solubility controlling phase. The EQ3/6 database does not, however, include the Pb-hydroxides.

Overall, the prediction of high Pb solubility in these waters is compatible with the work of Baes and Mesmer [26] and Bayliss et al. [32] for hyperalkaline environments. Indeed, the predicted solubilities would be even higher were the $Pb(OH)_6^{2-}$ species, identified by Baes and Mesmer [26] and Brookings [34] to be present at high pH, included in the databases.

In situ speciation data for Pb is equivocal, with cationic, anionic and neutral species all measured (Chapter 5). The data for water M5, favours the EQ3/6 database prediction as no anionic Pb was measured, but the overall scatter in the data is such that no firm result should be evinced on the basis of the in situ speciation data. Mineralogical data indicate

that Pb is associated with a primary CuK-selenide phase plus sphalerite, pyrite and ferrites [11]. Discrete PbO, $Pb(OH)_2$ and $PbCO_3$ were not recorded.

12.4 Conclusions

The main conclusion of the database tests carried out here is effectively the same as that reached in Maqarin Phase I [11]: in most cases, the observed solution concentrations for the elements of interest are several orders of magnitude less than would have been predicted assuming that the elemental concentrations were fixed by the simple stoichiometric oxides, hydroxides, carbonates and sulphates contained in the thermodynamic databases.

There are two main limitations to the prediction of elemental solubilities by the method used here. First, the minerals included in the databases are pure end-members and are rarely observed in nature (nor are likely to be present in a repository system). Second, it is very difficult to test effectively how realistic is the predicted elemental speciation. For the case of the solids, the inclusion of more realistic phases, such as solid solutions, in the databases is likely to decrease solubilities. For the case of solution species, an error in predicted speciation could result in either overprediction or underprediction of solubility. If, for example, a particular database predicts the presence of x species and, in reality, only x-1 species exist, then it is likely that (all other things being equal) the database will predict solubility which is greater than in reality. Potential problems arise when an important species is missing from the database as this would lead to underprediction. As the evidence for the existence of many of the trace element species is little more than circumstantial, this could have a significant impact on the code predictions. This could be particularly important in assessing data for sorption databases where it is necessary to have a good idea of the speciation of any given element

In the case of U, inclusion of $CaUO_4$ resulted in underprediction of U concentrations in solution. A Ca-U oxide was identified within the mineral assemblages present in the metamorphic zone. It is thought that the inaccuracy of the predictions is related to the crystallinity of the phase included in the databases; if data were found for a less crystalline form, more realistic predictions could be achieved. In all databases, if the $CaUO_4$ phase is suppressed and the U oxides or hydroxides are chosen instead then the databases would overpredict U solubility.

The results for Th should not be over-interpreted as it possible that Th is source-term limited in this system and it would therefore be inappropriate to evaluate further the Th databases here. There are also problems in assessing the applicability of Se databases by tests such as carried out here because of the expected kinetic constraints on redox equilibria in the Se system.

The Ra and Pb results are a good illustration of the point that it is possible to expend too much effort in better defining the solid phase controls on solubility. The results of predictions based on pure end members are similar and overestimate the observed solubility. As such, these predictions are acceptable from a performance assessment point of view. Further work on Ra solid-solutions may be necessary only to increase the accuracy of predictions. More effort might be expended on examining the proposed additional species [26, 34]. In addition, for repository scenarios involving a low SO_4^{2-} hyperalkaline system it may be worth testing the Ra databases to assess the impact of mechanisms other than uptake by SO_4^{2-} minerals on the Ra solubility.

There are still discrepancies between tin data from different sources. EQ3/6-based databases do not include the anionic tin(IV) species present in HATCHES. Tin is a

potentially significant contributor to risk in some repository scenarios. In these cases, further work on the database may be appropriate. The first priority would be to bring together and evaluate both current data sets and concurrently search for any other relevant (i.e. low temperature) Sn thermodynamic data. Otherwise, it is recommended that the HATCHES based databases be employed in preference to the EQ3/6 database as they give the higher predicted solubility and have been tested under high pH conditions.

In the case of Ni, the laboratory data from the Nirex programme suggest that $Ni(OH)_4^{2-}$ should be omitted from the TDB. Questions still remain about the log K value for $Ni(OH)_3^-$ and this has a significant impact on the predicted speciation and may also affect predicted Ni sorption. Again, in the cases where Ni is identified as a potentially significant contributor to risk, further work may be required.

In conclusion, the databases tested here have been shown to overestimate solubilities, but there remain doubts that some of the data included in the TDB's are geochemically realistic. For this reason, it is necessary to have a sufficient understanding of the mineralogical characteristics of the system being modelled (natural or repository) such that predictions of the databases can be set in a geochemically consistent context. Only then can the predictions be considered fully acceptable for use in a repository performance assessment.

12.5 References

[1] D.K. Nordstrom and J.L. Munoz, *Geochemical Thermodynamics.* Blackwell Scientific, Oxford, UK, 1986.

[2] P.L. Brown and H. Wanner, *Predicted Formation Constants using the Unified Theory of Metal Ion Complexation.* NEA- OECD Report, NEA, Paris, France, 1989.

[3] F.J. Pearson, U. Berner and W. Hummel, *Nagra Thermochemical Database II. Supplemental Data*. Nagra Technical Report, NTB 91-18, 1992.

[4] I. Grenthe, R.J. Lemire, A.B. Muller, C. Nguyen-Trung and H. Wanner, *Chemical Thermodynamics of Uranium.* NEA-OECD Report NEA-TDB, NEA, Paris, France, 655pp, 1993.

[5] A.H. Bath, N. Christofi, et al., *Trace Element and Microbiological Studies of Alkaline Groundwaters in Oman, Arabian Gulf: A Natural Analogue for Cement Pore Waters.* Nagra Technical Report, NTB 87-16, 1987a.

[6] I.G. McKinley, U. Berner and H. Wanner, *Predictions of Radionuclide Chemistry in a Highly Alkaline Environment*. in Chemie Und Migrationsverhalten Der Aktinide Und Spalprodukte In Naturlichen Aquatischen Systemen. PTB-SE-14, 77-89, 1987.

[7] I.G. McKinley, A.H. Bath, U. Berner, M. Cave and C. Neal, *Results of the Oman Analogue Study.* Radiochim Acta **44/45**, 311-316, 1988.

[8] J. Bruno,J.E. Cross, J. Eikenberg, I.G. McKinley, D. Read, A. Sandino and P. Sellin, *Testing of Geochemical Models in the Poços De Caldos Analogue Study.* Nagra Technical Report, NTB 90-29, 1991.

[9] J. Bruno, J.E. Cross, J. Eikenberg, I.G. McKinley, D. Read, A. Sandino and P. Sellin, *Testing Models of Trace Element Geochemistry At Poços De Caldos.* J.Geochem. Explor. **46**, 451-470, 1992.

[10] N.A. Chapman, I.G. McKinley, E.P. France, E. Shea and J.A.T. Smellie, *The Poços De Caldos Project: An Introduction and Summary of its Implications for Radioactive Waste Disposal.* J.Geochem. Explor. **45**, 1-24, 1992.

[11] W.R. Alexander (Ed.) *A Natural Analogue Study of the Maqarin Hyperalkaline Groundwaters. I. Source Term Description and Thermodynamic Database Testing,* Nagra Technical Report, NTB 91-10, 1992.

[12] C.M. Linklater, Y. Albinsson, W.R. Alexander, I. Casas, I.G. McKinley and P. Sellin, *A Natural Analogue of High pH Cement Pore Waters from the Maqarin Area of Northern Jordan: Comparison of Predicted and Observed Trace Element Chemistry of Uranium And Selenium.* J.Contam. Hydrol. **21**, 59-69, 1996.

[13] W.R. Alexander, R. Dayal, K. Eagleson, J. Eikenberg, E. Hamilton, C.M. Linklater, I.G. McKinley and C.J. Tweed, *A Natural Analogue of High pH Pore Waters from the Maqarin Area of Northern Jordan II: Results of Predictive Geochemical Calculations.* J. Geochem. Explor. **46**, 133-146, 1992.

[14] C.J. Tweed and A.E. Milodowski, *An Overview of the Maqarin Natural Analogue Project - A Natural Analogue Study of a Hyperalkaline Cement Groundwater System* in H.von Maravic and J.A.T.Smellie (eds.), 5th NAWG Workshop, Toledo, Spain, 5-9 October, 1992, CEC EUR 15176 EN, Brussels, Belgium, 1994.

[15] S.M. Pate, I.G. McKinley and W.R. Alexander, *Use of Natural Analogue Test Cases to Evaluate a New Performance Assessment TDB. Appendix 1* in H.von Maravic and J.A.T.Smellie (Eds), Proc. Int. Workshop on Natural Analogues, Toledo, Spain, October, 1992. CEC EUR 15176, Brussels, Belgium, 1994.

[16] C.P. Jackson, D.A. Lever and P.J. Sumner, *Validation of Transport Models for use in Performance Assessments: A View Illustrated for Intraval Test Case 1b,* Nirex Report, NSS/R259, 1991.

[17] A.E. Milodowski, J.M. Pearce, C.R. Hughes and H.N. Khoury, *A Preliminary Mineralogical Investigation of a Natural Analogue of Cement-Buffered Hyperalkaline Groundwater Interaction With Marl, Maqarin, Northern Jordan.* Nagra Unpublished Internal Report, 1992a.

[18] A.E. Milodowski (Ed.), *A Natural Analogue Study of the Maqarin Hyperalkaline Groundwaters: A Draft Report on Hyperalkaline Groundwater/Rock Interaction.* Nagra Unpublished Internal Report, 1994.

[19] I. Grenthe, J. Fuger, R.J.M. Konings, R.J. Lemire, A.B. Muller, C.N-T. Cregu and H. Wanner, *Chemical Thermodynamics of Uranium*, Vol. 1, eds. H. Wanner and I. Forest, Nuclear Energy Agency, OECD, Elsevier 1992.

[20] G.M.N. Baston, M. Brownsword, J.E. Cross, J. Hobley, A.D. Moreton, J.L. Smith-Briggs and H.P. Thomason, *The Solubility of Uranium in Cementitious Near-Field Conditions.* Nirex Report NSS/R222, 1993.

[21] R.J. Lemire, *Effects of Ionic Strength Groundwaters on Calculated Equilibrium Concentrations in the Uranium-Water System.* AECL-9549, Atomic Energy of Canada Ltd, Pinawa, Canada, 1988.

[22] L.V. Benson and L.S. Teague, *A Tabulation of Thermodynamic Data for Chemical Reactions Involving 58 Elements Common to Radioactive Waste Package Systems.* Lawrence Berkeley Report LBL-11448, California, USA, 1980.

[23] D. Langmuir and A.C. Riese, *The Thermodynamic Properties of Radium.* Geochim. Cosmochim. Acta **49**, 1593-1601, 1985.

[24] D.D. Wagman, W.H. Evans, V.B. Parker, R.H. Schumm, I Halow, S.M. Bailey, K.L. Churney and R.L. Nuttal, *The NBS Tables of Chemical Thermodynamic Properties: Selected Values for Inorganic and C1 and C2 Organic Substances in SI Units.* J. Phys. Chem. Ref. Data, **11** (Suppl. No. 2), 392 pp, 1982.

[25] B. Baeyens and I.G. McKinley, *A PHREEQE Database for Pd, Ni and Se.* Nagra Technical Report NTB 88-28, 1989.
[26] C.F. Baes and R.E. Mesmer, *The Hydrolysis of Cations.* Jonn Wiley and Sons, New York, USA, 1976.
[27] N.J. Pilkington and N.S. Stone. *The Solubility and Sorption of Ni and Nb under High pH Conditions.* Nirex Report NSS/R186, 1990.
[28] W.A. Deer, R.A. Howie and J. Zussman, J. *An Introduction to the Rock-Forming Minerals.* Longman, London, UK, 1966.
[29] C.C. Naish, P.H. Balkwill, T.M. O'Brien, K.J. Taylor and G.P. Marsh. *The Anaerobic Corrosion of Carbon Steel in Concrete*, Nirex Report NSS/R273, 1990.
[30] V.L. Barsukov and A.P. Klintsova, *Solubility of Cassiterite in Water and Aqueous NaOH at 25°C.* Geochem. Int., 849-852, 1970.
[31] G.E. Kuril'chikova and V.L. Barsukov, *Stability of Hydroxystannate Complexes and Experimental Crystallisation of Cassiterite Under Hydrothermal Conditions.* Geochem. Int., 31-37, 1970.
[32] S. Bayliss, F.T. Ewart, R.M. Howse, S.A. Lane, N.J. Pilkington, J.L Smith-Briggs and S.J. Williams, *The Solubility and Sorption of Ra and Sn in a Cementitious Near-Field Environment.* Sci. Basis Nucl. Waste Manag. XII, 879-888, 1989.
[33] A.E. Milodowski, Personal Communication, 1994.
[34] D.G. Brookings, *Eh-pH Diagrams for Geochemistry.* Springer-Verlag, Berlin, Germany, 1988.

Table 12.1 Chemistry of the three waters used in the test cases: M1, M3 (Eastern Springs) and M5 (Western Springs).

Sample	M1	M3	M5
Temperature (Celsius)	24.8	23.2	25.2
pH (field)	12.74	12.66	12.92
pH (lab.)	12.67	12.76	12.83
Eh (field) mV	+278	+150	+242
Major Elements (mgl^{-1})			
Ca	674	804	1120
Na	47.2	46.6	136
K	9.88	19.8	526
Cl	52.4	72.3	46.6
SO_4	305	289	1580
NO_3	3.28	7.73	39.1
Trace Elements (mgl^{-1})			
Mg	0.01	0.01	0.01
NH_4	<0.10	0.13	6.05
NO_2	<0.10	<0.10	1.02
Fe (total)	<0.01	<0.01	<0.01
Al	0.14	0.15	0.14
Si	<0.02	0.09	0.07

The analytical value for the TIC produced significant oversaturation in calcite (saturation index = +2) so it was decided to input TIC at 0.5 mgl^{-1}, bringing calcite below saturation. The reason for the high analytical value is unclear but may reflect sorption of atmospheric CO_2 during sampling (Chapter 4).

Table 12.2 Details of the codes and associated databases used by the five groups.

Model Group	Code	Database
AEA (WEG)	HARPHRQ[1,2]	HATCHES (5.0)[6]
Chalmers Univ. (CU)	PHREEQE[3]	HATCHES (2.0)[6]
MBT (Barcelona)	PHREEQE[3]	HATCHES (3.0)[6] and SKBU[7]
Nagra	RIPP2s[4]	NTB9118[8,9]
SKB	EQ3NR (version 324R110)[5]	SKB (in-house database)[10]

1 Brown, P.L., Haworth, A., Sharland, S.M. and Tweed, C.J. (1990) HARPHRQ: a geochemical speciation programme based on PHREEQE. Nirex Report NSS/R188.

2 Haworth, A., Heath, T.G. and Tweed, C.J. (1995) HARPHRQ: a computer programme for geochemical modelling. Nirex Report NSS/R380.

3 Parkhurst, D.L., Thorstenson, D.C and Plummer, L.N. (1980) PHREEQE - a computer programme for geochemical calculations. USGS Wat. Res. Invest. 80-96, 210p (revised and reprinted Aug 1990).

4 Pate, S.M., Yusef, R. and Hamilton E. (1992) RIPP2s, a user`s manual. Nagra Internal Report NIB 90-48, Nagra, Wettingen, Switzerland.

5 LLNL, (1987) EQ3NR, version 3245R136, Lawrence Livermore National Laboratory, University of California, USA.

6 Nirex (1996) HATCHES versions 2.0, 3.0 and 5.0 as released to the NEA, Paris, in November 1989, 1990 and 1992 respectively. See also, Cross, J.E. and Ewart, F.T. (1991) HATCHES - a thermodynamic database management system. Radiochim. Acta 52/53, 421-422.

7 Puigdomènech, I. and Bruno, J. (1988) Modelling uraniom solubilities in aqueous solutions: validation of a thermodynamic data base for the EQ3/6 geochemical codes. SKB Technical Report TR 88-21, SKB, Stockholm, Sweden.

8 Pearson, F.J. and Berner, U. (1991) Nagra thermochemical database I. Core data. Nagra Technical Report NTB 91-17, Nagra, Wettingen.

9 Pearson, F.J., Berner, U and Hummel, W. (1992) Nagra thermochemical database II. Supplemental data. Nagra Technical Report NTB 91-18, Nagra, Wettingen.

10 SKB, (1993) SKB in-house thermodynamic database (revised version of LLNL database stage 47, SKB, Stockholm, Sweden.

Table 12.3 Concentrations (units of μgl^{-1} unless stated) of the seven trace elements of interest

Element	Analyst	M1	M3	M5
U(ngl^{-1})	ANSTO	2±1	16±1	37±2
Th(ngl^{-1})	ANSTO	2±1	*6±1	9±1
Ra	**	0.01	0.01	0.01
Se	ANSTO	114±1	206±3	1315±21
Ni	ANSTO	2.3±0.5	4.0±0.4	5.8±1.7
Sn (ngl^{-1})	ANSTO	50±10	100±10	270±40
Pb	ANSTO	0.7±0.1	0.8±0.1	0.7±0.1

AEA and MBT both used this data set (Table 5.1, Chapter 5) while Nagra, CU and SKB all used BGS data from Table 4.3, Chapter 4. The differences in concentration are small, but Nagra re-ran the calculations using these data as a check. No significant differences were observed in the calculated solubility controlling phases or in the speciation and so the predictions for SKB and CU were corrected by hand.

* - In Table 5.1, a value of zero is given for Th concentration. As this value was considered unusually low, an estimated value was used in the calculations. The estimated value is intermediate between those of the M1 and M5 waters.

** - No measurements for radium were made during Maqarin Phase II. The values given in Table 12.3 are calculated based on measurements carried out during Phase I, which showed that Ra was typically below detection (0.01 μgl^{-1}).

Table 12.4a Predicted U solution speciation and selected solid phase saturation indices for an assumed concentration of 1μgl^{-1}

Uranium M1 pH=12.74, pe=4.7

	AEA[1]	CU[2]	MBT	NAGRA	SKB
Aqueous species (%)					
$UO_2(OH)_4^{2-}$	79	100	94	14	100
$UO_2(OH)_3^-$			6	86	
$UO_2(OH)_2$	16				
Solubility control (saturation index†)					
$CaUO_4$	9.35	5.86	5.54		5.84
Schoepite			-8.04		
$UO_3.2H_2O$	-3.44			-6.9	
$Na_2U_2O_7$	-2.45				
$UO_2(OH)_2$	-3.56				

1 AEA used the lab. pH (12.67).
2 CU charge balanced with pH, giving pH=12.27.

Table 12.4b Calculated U solution speciation and selected solid phase saturation indices for observed U concentration of 2 ngl^{-1}

Uranium M1 pH=12.74, pe=4.7

	AEA[1]	CU[2]	MBT	NAGRA	SKB
Aqueous species(%)					
$UO_2(OH)_4^{2-}$	99.5	100	94	14	100
$UO_2(OH)_3^-$			6	86	
$UO_2(OH)_2$	0.5				
Solubility control (saturation index)					
$CaUO_4$	6.65	3.111	2.90		3.11
Schoepite			-10.74		
$UO_3.2H_2O$	-6.14			-9.6	
$Na_2U_2O_7$	-7.85				
$UO_2(OH)_2$	-6.26				

1 AEA used the lab. pH (12.67).
2 CU used a 'calculated pH' of 12.39.

† The saturation index is defined as the log (activity product of the ions in solution:solubility product). Positive values of saturation index indicate that the solution is predicted to be oversaturated with respect to a particular mineral phase and precipitation would be expected. Negative values indicate that a solution in equilibrium with a given solid would show a higher concentrations of its ions than is measured.

Table 12.4c Predicted U solution speciation and selected solid phase saturation indices for an assumed concentration of 1μgl^{-1}

Uranium M3 pH=12.66, pe=2.54

	AEA[1]	CU[2]	MBT	NAGRA	SKB
Aqueous species(%)					
$UO_2(OH)_4^{2-}$	85	100	87		100
$UO_2(OH)_3^-$			13		
$UO_2(OH)_2$	11				
Solubility control (saturation index)					
$CaUO_4$	9.63	5.89	5.72		5.97
Schoepite			-7.77		-7.75
$UO_3.2H_2O$	-2.45				
$Na_2U_2O_7$	-3.56				
$UO_2(OH)_2$	-3.44				

1 AEA used the lab. pH (12.76)
2 CU charge balanced with pH, giving pH=12.43.

Table 12.4d Calculated U solution speciation and selected solid phase saturation indices for an observed U concentration of 16 ngl^{-1}

Uranium M3 pH=12.66, pe=2.54

	AEA[1]	CU[2]	MBT	NAGRA	SKB
Aqueous species(%)					
$UO_2(OH)_4^{2-}$	100	100	87		100
$UO_2(OH)_3^-$			13		
$UO_2(OH)_2$					
Solubility control (saturation index)					
$CaUO_4$	7.57	4.36	3.93		4.45
Schoepite			-9.56		-9.27
$UO_3.2H_2O$	-6.29				
$Na_2U_2O_7$	-5.55				
$UO_2(OH)_2$	-5.43				

1 AEA used the lab. pH (12.76).
2 CU used a ‘calculated pH’ of 12.49.

Table 12.4e Predicted U solution speciation and selected solid phase saturation indices for an assumed concentration of 1μgl^{-1}

Uranium M5 pH=12.92, pe=4.1

	AEA[1]	CU[2]	MBT	NAGRA	SKB
Aqueous species(%)					
$UO_2(OH)_4^{2-}$	90	100	97		100
$UO_2(OH)_3^-$			3	78	
$UO_2(OH)_2$	7				
$UO_2(OH)_5^{2-}$				22	
Solubility control (saturation index)					
$CaUO_4$	9.32	5.84	5.56		5.75
Schoepite			-8.51		-8.49
$UO_3.2H_2O$	-3.84			-7.1	
$Na_2U_2O_7$	-2.06				
$UO_2(OH)_2$	-3.96				

1 AEA used the lab. pH (12.83)
2 CU charge balanced with pH, giving pH=12.42.

Table 12.4f Calculated U solution speciation and selected solid phase saturation indices for an observed U concentration of 37ngl^{-1}

Uranium M5 pH=12.92, pe=4.1

	AEA[1]	CU[2]	MBT	NAGRA	SKB
Aqueous species(%)					
$UO_2(OH)_4^{2-}$	100	100	97		100
$UO_2(OH)_3^-$			3	78	
$UO_2(OH)_2$					
$UO_2(OH)_5^{2-}$				22	
Solubility control (saturation index)					
$CaUO_4$	7.90	4.48	4.14		4.44
Schoepite			-9.94		-9.80
$UO_3.2H_2O$	-5.27			-8.5	
$Na_2U_2O_7$	-4.93				
$UO_2(OH)_2$	-5.39				

1 AEA used the lab. pH (12.83).
2 CU used a ‘calculated pH’ of 12.60.

Table 12.5a Predicted Th solution speciation and selected solid phase saturation indices for an assumed concentration of 1μgl^{-1}

Thorium M1 pH=12.74, pe=4.7

	AEA[1]	CU[2]	MBT	NAGRA	SKB
Aqueous species(%)					
$Th(OH)_4$	100	100	100	100	100
Solubility control (saturation index)					
$Th(OH)_4$ (c)	-1.86			-6.3	
$Th(OH)_4$	-3.76				
ThO_2 (c)	5.74		5.7		
ThO_2	-0.06	1.24	1.2	1.2	1.25

1 AEA used the lab. pH (12.67).
2 CU charge balanced with pH, giving pH=12.27.

Table 12.5b Calculated Th solution speciation and selected solid phase saturation indices for an observed Th concentration of 2ngl^{-1}

Thorium M1 pH=12.74, pe=4.7

	AEA[1]	CU[2]	MBT	NAGRA	SKB
Aqueous species(%)					
$Th(OH)_4$	100	100	100	100	100
Solubility control (saturation index)					
$Th(OH)_4$ (c)	-4.56			-8.9	
$Th(OH)_4$	-6.46				
ThO_2 (c)	3.04		3.0		
ThO_2	-2.76	-1.44	-1.5	-1.4	-1.46

1 AEA used the lab. pH (12.67).
2 CU used a ‘calculated pH’ of 12.39.

Table 12.5c Predicted Th solution speciation and selected solid phase saturation indices for an assumed concentration of 1μgl^{-1}

Thorium M3 pH=12.66, pe=2.54

	AEA[1]	CU[2]	MBT	NAGRA	SKB
Aqueous species(%)					
$Th(OH)_4$	100	100	100		100
Solubility control (saturation index)					
$Th(OH)_4$ (c)	-1.86				
$Th(OH)_4$	-3.76	-3.76			
ThO_2 (c)	5.74		5.7		
ThO_2	-0.06	1.24	1.2		1.24

1 AEA used the lab. pH (12.76).
2 CU charge balanced with pH, giving pH=12.43.

Table 12.5d Calculated Th solution speciation and selected solid phase saturation indices for an observed Th concentration of 6ngl^{-1}

Thorium M3 pH=12.66, pe=2.54

	AEA[1]	CU[2]	MBT	NAGRA	SKB
Aqueous species(%)					
$Th(OH)_4$	100	100	100		100
Solubility control (saturation index)					
$Th(OH)_4$ (c)	-4.56				
$Th(OH)_4$	-6.46				
ThO_2 (c)	3.04		3.6		
ThO_2	-2.76	-0.33	0.95		-0.33

1 AEA used the lab. pH (12.76).
2 CU used a ‘calculated pH’ of 12.49.

Table 12.5e Predicted Th solution speciation and selected solid phase saturation indices for an assumed concentration of 1μgl^{-1}

Thorium M5 pH=12.92, pe=4.1

	AEA[1]	CU[2]	MBT	NAGRA	SKB
Aqueous species(%)					
$Th(OH)_4$	100	100	100	100	100
Solubility control (saturation index)					
$Th(OH)_4$ (c)	-1.85			-6.3	
$Th(OH)_4$	-3.75	-3.76			
ThO_2 (c)	5.75		5.76		
ThO_2	-0.05	1.24	1.19	1.3	1.24

1 AEA used the lab. pH (12.83).
2 CU charge balanced with pH, giving pH=12.42.

Table 12.5f Calculated Th solution speciation and selected solid phase saturation indices for an observed Th concentration of 9ngl^{-1}

Thorium M5 pH=12.92, pe=4.1

	AEA[1]	CU[2]	MBT	NAGRA	SKB
Aqueous species(%)					
$Th(OH)_4$	100	100	100	100	100
Solubility control (saturation index)					
$Th(OH)_4$ (c)	-3.90			-8.3	
$Th(OH)_4$	-5.80				
ThO_2 (c)	3.70		3.65		
ThO_2	-2.10	-0.78	-0.86	-0.8	-0.75

1 AEA used the lab. pH (12.83).
2 CU used a ‘calculated pH’ of 12.60.

Table 12.6a Predicted Ra solution speciation and selected solid phase saturation indices for an assumed concentration of 1μgl^{-1}

Radium M1 pH=12.74, pe=4.7

	AEA[1]	CU[2]	MBT	NAGRA	SKB
Aqueous species(%)					
Ra^{2+}	75	97	93		100
$RaOH^{+}$	6	3	7		
$RaSO_4$	18				
$RaCO_3$	1				
Solubility control (saturation index)					
$RaSO_4$	-1.57	-1.30	-1.34		-1.27
$RaCO_3$	-4.85	-5.68	-5.85		

1 AEA used the lab. pH (12.67).
2 CU charge balanced with pH, giving pH=12.27.

Table 12.6b Calculated Ra solubility and speciation selected solid phase saturation indices for an observed Ra concentration of 0.01μgl-1

Radium M1 pH=12.74, pe=4.7

	AEA[1]	CU[2]	MBT	NAGRA	SKB
Aqueous species(%)					
Ra^{2+}	75	97	93		100
$RaOH^{+}$	7	3	7		
$RaSO_4$	18				
$RaCO_3$					
Solubility control (saturation index)					
$RaSO_4$	-3.59	-3.31	-3.35		-3.27
$RaCO_3$	-8.53		-9.03		

1 AEA used the lab. pH (12.67).
2 CU used a ‘calculated pH’ of 12.39.

Table 12.6c Predicted Ra solution speciation and selected solid phase saturation indices for an assumed concentration of 1μgl^{-1}

Radium M3 pH=12.66, pe=2.54

	AEA[1]	CU[2]	MBT	NAGRA	SKB
Aqueous species(%)					
Ra^{2+}	76	96	94		100
$RaOH^{+}$	7	4	6		
$RaSO_4$	16				
$RaCO_3$	1				
Solubility control (saturation index)					
$RaSO_4$	-1.64 (-1.63)	-1.37	-1.36		-1.30
$RaCO_3$	-4.83 (-6.60)	-5.77	-6.03		

1 AEA used the lab. pH (12.76).
2 CU charge balanced with pH, giving pH=12.43.

Table 12.6d Calculated Ra solution speciation and selected solid phase saturation indices for an observed Ra concentration of 0.01μgl^{-1}

Radium M3 pH=12.66, pe=2.54

	AEA[1]	CU[2]	MBT	NAGRA	SKB
Aqueous species(%)					
Ra^{2+}	78	96	94		100
$RaOH^{+}$	6	4	6		
$RaSO_4$	16				
$RaCO_3$					
Solubility control (saturation index)					
$RaSO_4$	-3.63	-3.38	-3.36		-3.30
$RaCO_3$	-8.60		-9.10		

1 AEA used the lab. pH (12.76).
2 CU used a 'calculated pH' of 12.49.

Table 12.6e Predicted Ra solution speciation and selected solid phase saturation indices for an assumed concentration of 1μgl^{-1}

Radium M5 pH=12.92, pe=4.1

	AEA[1]	CU[2]	MBT	NAGRA	SKB
Aqueous species(%)					
Ra^{2+}	51	97	91		100
$RaOH^{+}$	5	3	9		
$RaSO_4$	44				
$RaCO_3$					
Solubility control (saturation index)					
$RaSO_4$	-1.19	-0.76	-0.86		-0.77
$RaCO_3$	-5.06	-5.80	-6.0		

1 AEA used the lab. pH (12.83).
2 CU charge balanced with pH, giving pH=12.42.

Table 12.6f Calculated Ra solution speciation and selected solid phase saturation indices for an observed Ra concentration of 0.01μgl^{-1}

Radium M5 pH=12.92, pe=4.1

	AEA[1]	CU[2]	MBT	NAGRA	SKB
Aqueous species(%)					
Ra^{2+}	51	95	91		100
$RaOH^{+}$	6	5	9		
$RaSO_4$	43				
$RaCO_3$					
Solubility control (saturation index)					
$RaSO_4$	-3.20	-2.78	-2.81		-2.77
$RaCO_3$	-8.83		-9.18		

1 AEA used the lab. pH (12.83).
2 CU used a ‘calculated pH’ of 12.60.

Table 12.7a Predicted Se solution speciation and selected solid phase saturation indices for an assumed concentration of 1μgl^{-1}

Selenium M1 pH=12.74, pe=4.7

	AEA[1]	CU[2]	MBT	NAGRA	SKB
Aqueous species(%)					
SeO_4^{2-}	100	100	100	100	100
SeO_3^{2-}					
Solubility control (saturation index)					
$CaSeO_4$	-7.69	-7.26	-7.74		-7.55
$CaSeO_3$	-11.05	-9.82			
$CaSeO_3.H_2O$	-12.04				
$CaSeO_3.2H_2O$					-11.81
Se				-48.5	

1 AEA used the lab. pH (12.67).
2 CU charge balanced with pH, giving pH=12.27.

Table 12.7b Calculated Se solution speciation and selected solid phase saturation indices for an observed Se concentration of 50ngl^{-1}

Selenium M1 pH=12.74, pe=4.7

	AEA[1]	CU[2]	MBT	NAGRA	SKB
Aqueous species(%)					
SeO_4^{2-}	100	100	100	100	100
Solubility control (saturation index)					
$CaSeO_4$	-5.63	-4.91	-5.67		**?**
$CaSeO_3$	-8.99	-7.68	-9.13		
$CaSeO_3.H_2O$	-9.98				
$CaSeO_3.2H_2O$					**?**
Se				-46.4	

1 AEA used the lab. pH (12.67).
2 CU used a ‘calculated pH’ of 12.39.

Table 12.7c Predicted Se solution speciation and selected solid phase saturation indices for an assumed concentration of 1μgl^{-1}

Selenium M3 pH=12.66, pe=2.54

	AEA[1]	CU[2]	MBT	NAGRA	SKB
Aqueous species(%)					
SeO_4^{2-}	98	87	94		93
SeO_3^{2-}	2	13	6		7
Solubility control (saturation index)					
$CaSeO_4$	-7.69	-7.29	-7.63		-7.47
$CaSeO_3$	-6.89	-5.83	-6.41		
$CaSeO_3.H_2O$	-7.88				
$CaSeO_3.2H_2O$					-7.15

1 AEA used the lab. pH (12.76).
2 CU charge balanced with pH, giving pH=12.43.

Table 12.7d Calculated Se solution speciation and selected solid phase saturation indices for an observed Se concentration of 206ngl^{-1}

Selenium M3 pH=12.66, pe=2.54

	AEA[1]	CU[2]	MBT	NAGRA	SKB
Aqueous species(%)					
SeO_4^{2-}	98	90	94		93
SeO_3^{2-}	2	10	6		7
Solubility control (saturation index)					
$CaSeO_4$	-5.37	-4.85	-5.31		-4.84
$CaSeO_3$	-4.57	-3.31	-4.09		
$CaSeO_3.H_2O$	-5.56				
$CaSeO_3.2H_2O$					-4.52

1 AEA used the lab. pH (12.76).
2 CU used a ‘calculated pH’ of 12.49.

Table 12.7e Predicted Se solution speciation and selected solid phase saturation indices for an assumed concentration of 1μgl^{-1}

Selenium M5 pH=12.92, pe=4.1

	AEA[1]	CU[2]	MBT	NAGRA	SKB
Aqueous species(%)					
SeO_4^{2-}	100	100	100	100	100
Solubility control (saturation index)					
$CaSeO_4$	-7.72	-7.29	-7.78		-7.6
$CaSeO_3$	-10.18	-8.91			
$CaSeO_3.H_2O$	-11.17				
Se				-47.4	

1 AEA used the lab. pH (12.83).
2 CU charge balanced with pH, giving pH=12.42.

Table 12.7f Calculated Se solution speciation and selected solid phase saturation indices for an observed SE concentration of 1315ngl^{-1}

Selenium M5 pH=12.92, pe=4.1

	AEA[1]	CU[2]	MBT	NAGRA	SKB
Aqueous species(%)					
SeO_4^{2-}	100	100	100	100	100
Solubility control (saturation index)					
$CaSeO_4$	-4.59	-4.16	-4.65		-4.64
$CaSeO_3$	-7.05	-6.14			
$CaSeO_3.H_2O$	-8.04				
$CaSeO_3.2H_2O$					**?**
Se				-44.6	

1 AEA used the lab. pH (12.83).
2 CU used a 'calculated pH' of 12.60.

Table 12.8a Predicted Ni solution speciation and selected solid phase saturation indices for an assumed concentration of 1μgl^{-1}

Nickel M1 pH=12.74, pe=4.7

	AEA[1]	CU[2]	MBT	NAGRA	SKB
Aqueous species(%)					
$Ni(OH)_2$	16	4	1		2
$Ni(OH)_3^-$	5	93	90	91	50
$Ni(OH)_4^{2-}$	79	3	9	9	48
Solubility control (saturation index)					
$Ni(OH)_2$	-1.07	-0.96	-1.46	-3.4	-2.78
NiO	-1.77		-3.1	-3.1	-2.44
$NiFe_2O_4$	4.84		3.68		

1 AEA used the lab. pH (12.67).
2 CU charge balanced with pH, giving pH=12.27.

Table 12.8b Calculated Ni solution speciation and selected solid phase saturation indices for an observed Ni concentration of 2.3μgl^{-1}

Nickel M1 pH=12.74, pe=4.7

	AEA[1]	CU[2]	MBT	NAGRA	SKB
Aqueous species(%)					
$Ni(OH)_2$	16	4	1		2
$Ni(OH)_3^-$	4	93	90	91	54
$Ni(OH)_4^{2-}$	80	3	9	9	44
Solubility control (saturation index)					
$Ni(OH)_2$	-0.71	-0.37	-1.10	-2.7	-2.01
NiO	-1.41		-2.74	-3.0	-1.69
$NiFe_2O_4$	5.20		4.04		

1 AEA used the lab. pH (12.67).
2 CU used a ‘calculated pH’ of 12.39.

Table 12.8c Predicted Ni solution speciation and selected solid phase saturation indices for an assumed concentration of 1μgl^{-1}

Nickel M3 pH=12.66, pe=2.54

	AEA[1]	CU[2]	MBT	NAGRA	SKB
Aqueous species(%)					
$Ni(OH)_2$	11	4	1		2
$Ni(OH)_3^-$	4	93	90		54
$Ni(OH)_4^{2-}$	85	3	9		44
Solubility control (saturation index)					
$Ni(OH)_2$	-1.24	-1.12	-1.46		-2.71
NiO	-1.94		-3.01		
$NiFe_2O_4$	4.48		3.93		

1 AEA used the lab. pH (12.76).
2 CU charge balanced with pH, giving pH=12.43.

Table 12.8d Calculated Ni solution speciation and selected solid phase saturation indices for an observed Ni concentration of 4.0μgl^{-1}

Nickel M3 pH=12.66, pe=2.54

	AEA[1]	CU[2]	MBT	NAGRA	SKB
Aqueous species(%)					
$Ni(OH)_2$	11	2.4	1		2
$Ni(OH)_3^-$	4	92.4	91		54
$Ni(OH)_4^{2-}$	85	5.2	8		44
Solubility control (saturation index)					
$Ni(OH)_2$	-0.64	-0.38	-0.86		-1.91
NiO	-1.33		-2.41		-1.59
$NiFe_2O_4$	5.09		4.53		

1 AEA used the lab. pH (12.76)
2 CU used a ‘calculated pH’ of 12.49.

Table 12.8e Predicted Ni solution speciation and selected solid phase saturation indices for an assumed concentration of 1μgl^{-1}

Nickel M5 pH=12.92, pe=4.1

	AEA[1]	CU[2]	MBT	NAGRA	SKB
Aqueous species(%)					
$Ni(OH)_2$	7	3			
$Ni(OH)_3^-$	3	92	84	85	36
$Ni(OH)_4^{2-}$	90	5	15	15	63
Solubility control, (saturation index)					
$Ni(OH)_2$	-1.41	-1.13	-1.66	-3.6	-3.06
NiO	-2.11		-3.32	-3.3	-2.47
$NiFe_2O_4$	4.14		3.6		
$NiSiO_3$				2.0	

1 AEA used the lab. pH (12.83).
2 CU charge balanced with pH, giving pH=12.42.

Table 12.8f Calculated Ni solution speciation and selected solid phase saturation indices for an observed Ni concentration of 5.8μgl^{-1}

Nickel M5 pH=12.92, pe=4.1

	AEA[1]	CU[2]	MBT	NAGRA	SKB
Aqueous species(%)					
$Ni(OH)_2$	7	2			
$Ni(OH)_3^-$	3	91	84	85	36
$Ni(OH)_4^{2-}$	90	7	15	15	63
Solubility control (saturation index)					
$Ni(OH)_2$	-0.65	-0.49	-0.90	-2.8	-2.25
NiO	-1.35		-2.56	-2.6	-1.93
$NiFe_2O_4$	4.91		3.82		
$NiSiO_3$				2.8	

1 AEA used the lab. pH (12.83).
2 CU used a ‘calculated pH’ of 12.49.

Table 12.9a Predicted Sn solution speciation and selected solid phase saturation indices for an assumed concentration of 1μgl^{-1}

Tin M1 pH=12.74, pe=4.7

	AEA[1]	CU[2]	MBT	NAGRA	SKB
Aqueous species(%)					
$Sn(OH)_3^-$		100			
$Sn(OH)_4$					100
$Sn(OH)_5^-$	95		10	9	
$Sn(OH)_6^{2-}$	5		90	91	
Solubility control (saturation index)					
SnO_2 (?)		33.71	-4.24	-4.2	-0.46
SnO_2 (c)	-1.82				
SnO_2 (am)	-3.26				
SnO_2 (ppt)	-5.31				

1 AEA used the lab. pH (12.67).
2 CU charge balanced with pH, giving pH=12.27.

Table 12.9b Calculated Sn solution speciation and selected solid phase saturation indices for an observed Sn concentration of 50ngl^{-1}

Tin M1 pH=12.74, pe=4.7

	AEA[1]	CU[2]	MBT	NAGRA	SKB
Aqueous species(%)					
$Sn(OH)_3^-$		100			
$Sn(OH)_4$					100
$Sn(OH)_5^-$	95		10	9	
$Sn(OH)_6^{2-}$	5		90	91	
Solubility control (saturation index)					
SnO_2 (?)		33.84	-5.55	-5.5	-0.46
SnO_2 (c)	-3.15				
SnO_2 (am)	-4.56				
SnO_2 (ppt)	-6.61				

1 AEA used the lab. pH (12.67).
2 CU used a ‘calculated pH’ of 12.39.

Table 12.9c Predicted Sn solution speciation and selected solid phase saturation indices for an assumed concentration of 1μgl^{-1}

Tin M3 pH=12.66, pe=2.54

	AEA[1]	CU[2]	MBT	NAGRA	SKB
Aqueous species(%)					
$Sn(OH)_3^-$		100			
$Sn(OH)_4$					100
$Sn(OH)_5^-$	93		11		
$Sn(OH)_6^{2-}$	7		89		
Solubility control (saturation index)					
SnO_2 (?)		29.53	-4.09		-0.44
SnO_2 (c)	-1.95				
SnO_2 (am)	-3.36				
SnO_2 (ppt)	-5.41				

1 AEA used the lab. pH (12.76).
2 CU charge balanced with pH, giving pH=12.43.

Table 12.9d Calculated Sn solution speciation and selected solid phase saturation indices for an observed sn concentration of 100ngl^{-1}

Tin M3 pH=12.66, pe=2.54

	AEA[1]	CU[2]	MBT	NAGRA	SKB
Aqueous species(%)					
$Sn(OH)_3^-$		100			
$Sn(OH)_4$					100
$Sn(OH)_5^-$	93		11		
$Sn(OH)_6^{2-}$	7		89		
Solubility control (saturation index)					
SnO_2 (?)		29.64	-5.09		-0.44
SnO_2 (c)	-2.95				
SnO_2 (am)	-4.36				
SnO_2 (ppt)	-6.41				

1 AEA used the lab. pH (12.76).
2 CU used a ‘calculated pH’ of 12.49.

Table 12.9e Predicted Sn solution speciation and selected solid phase saturation indices for an assumed concentration of 1μgl^{-1}

Tin M5 pH=12.92, pe=4.1

	AEA[1]	CU[2]	MBT	NAGRA	SKB
Aqueous species(%)					
$Sn(OH)_3^-$		100			
$Sn(OH)_4$					100
$Sn(OH)_5^-$	92		6	5	
$Sn(OH)_6^{2-}$	8		94	94	
Solubility control (saturation index)					
SnO_2 (?)		32.61	-4.67	-4.7	-0.48
SnO_2 (c)	-2.04				
SnO_2 (am)	-3.45				
SnO_2 (ppt)	-5.50				

1 AEA used the lab. pH (12.83).
2 CU charge balanced with pH, giving pH=12.42.

Table 12.9f Calculated Sn solution speciation and selected solid phase saturation indices for an observed Sn concentration of 270ngl^{-1}

Tin M5 pH=12.92, pe=4.1

	AEA[1]	CU[2]	MBT	NAGRA	SKB
Aqueous species(%)					
$Sn(OH)_3^-$		100			
$Sn(OH)_4$					100
$Sn(OH)_5^-$	92		6	6	
$Sn(OH)_6^{2-}$	8		94	94	
Solubility control (saturation index)					
SnO_2 (?)		32.81	-5.24	-5.2	-0.48
SnO_2 (c)	-2.61				
SnO_2 (am)	-4.02				
SnO_2 (ppt)	-6.07				

1 AEA used the lab. pH (12.67).
2 CU used a ‘calculated pH’ of 12.39.

Table 12.10a Predicted Pb solution speciation and selected solid phase saturation indices for an assumed concentration of 1μgl^{-1}

Lead M1 pH=12.74, pe=4.7

	AEA[1]	CU[2]	MBT	NAGRA	SKB
Aqueous species(%)					
$PbCO_3$					100
$Pb(OH)_3^-$	100	100	100		
Solubility control (saturation index)					
$PbCO_3$					-4.75
$Pb(OH)_2$	-5.68	-5.28	-5.75		
PbO	-6.50	-6.10	-6.58		

1 AEA used the lab. pH (12.67).
2 CU charge balanced with pH, giving pH=12.27.

Table 12.10b Calculated Pb solution speciation and selected solid phase saturation indices for an observed Pb concentration of 0.7μgl^{-1}

Lead M1 pH=12.74, pe=4.7

	AEA[1]	CU[2]	MBT	NAGRA	SKB
Aqueous species(%)					
$PbCO_3$					100
$Pb(OH)_3^-$	100	100	100		
Solubility control (saturation index)					
$PbCO_3$					-4.75
$Pb(OH)_2$	-5.83	-5.39	-5.90		
PbO	-6.65	-6.21	-6.73		

1 AEA used the lab. pH (12.67).
2 CU used a ‘calculated pH’ of 12.39.

Table 12.10c Predicted Pb solution speciation and selected solid phase saturation indices for an assumed concentration of 1μgl^{-1}

Lead M3 pH=12.66, pe=2.54

	AEA[1]	CU[2]	MBT	NAGRA	SKB
Aqueous species(%)					
$PbCO_3$					100
$Pb(OH)_3^-$	100	100	100		
Solubility control (saturation index)					
$PbCO_3$					-4.74
$Pb(OH)_2$	-5.77	-5.44	-5.67		
PbO	-6.59	-6.26	-6.56		

1 AEA used the lab. pH (12.76).
2 CU charge balanced with pH, giving pH=12.43.

Table 12.10d Calculated Pb solution speciation and selected solid phase saturation indices for an observed Pb concentration of 0.8μgl^{-1}

Lead M3 pH=12.66, pe=2.54

	AEA[1]	CU[2]	MBT	NAGRA	SKB
Aqueous species(%)					
$PbCO_3$					100
$Pb(OH)_3^-$	100	100	100		
Solubility control (saturation index)					
$PbCO_3$					-2476
$Pb(OH)_2$	-5.87	-5.49	-5.76		
PbO	-6.69	-6.31	-6.66		

1 AEA used the lab. pH (12.76).
2 CU used a ‘calculated pH’ of 12.49.

Table 12.10e Predicted Pb solution speciation and selected solid phase saturation indices for an assumed concentration of 1μgl^{-1}

Lead M5 pH=12.92, pe=4.1

	AEA[1]	CU[2]	MBT	NAGRA	SKB
Aqueous species(%)					
$PbCO_3$					100
$Pb(OH)_3^-$	100	100	100		
Solubility control (saturation index)					
$PbCO_3$					-4.76
$Pb(OH)_2$	-5.85	-5.44	-5.95		
PbO	-6.01	-6.26	-6.76		

1 AEA used the lab. pH (12.83).
2 CU charge balanced with pH, giving pH=12.42.

Table 12.10f Calculated Pb solution speciation and selected solid phase saturation indices for an observed Pb concentration of 0.7μgl^{-1}

Lead M5 pH=12.92, pe=4.1

	AEA[1]	CU[2]	MBT	NAGRA	SKB
Aqueous species(%)					
$PbCO_3$					100
$Pb(OH)_3^-$	100	100	100		
Solubility control (saturation index)					
$PbCO_3$					-4.74
$Pb(OH)_2$	-6.01	-5.62	-6.10		
PbO	-6.83	-6.44	-6.91		

1 AEA used the lab. pH (12.83).
2 CU used a 'calculated pH' of 12.60.

13. COUPLED MODELLING FOR THE JORDAN NATURAL ANALOGUE PROJECT

A.V. Chambers and A. Haworth

13.1 Introduction

The modelling of coupled chemical and transport processes is important in understanding the long-term evolution of a repository and its surroundings. A number of different approaches have been adopted in the programs developed to model these coupled processes [1, 2]. The approach adopted is largely dependent on the type of systems to which the program is to be applied. In this study, two programs have been used: CHEQMATE [1], which is a general geochemical program applied to a wide range of systems; and MARQUISS [2], which was developed specifically to consider the development and movement of mineral reaction fronts. CHEQMATE has been used previously to examine the effect of alkaline fluids on geological materials [3, 4] but there has been only limited comparison against experimental or field data.

The Jordan Natural Analogue Project is a good opportunity to test the applicability of the coupled programs and thermodynamic databases for modelling the interaction between alkaline porewater and rock. In particular, it allows testing of the models over a longer timescale than is available in laboratory experiments. In addition, there has been close collaboration between the modellers and the analytical teams so that the information required to parameterise and test the models has been obtained, wherever possible. Particular attention has been paid to characterising the solid as well as the aqueous phase. The predictions of the model for the solid phase development can also be compared with field data. A secondary aim of the modelling was to try and gain an understanding of the timescales of the interactions at Jordan.

The use of the two programs, as well as testing the predictions against field data, allowed comparison of the effects of the different assumptions in each program. Each of the programs has different limitations and different data requirements. The MARQUISS calculations were based on preliminary calculations using CHEQMATE to identify key minerals. The initial calculations with CHEQMATE were carried out with parameters based on knowledge of the site, but without fitting to the experimental data. Later refinements were made, for example to include product minerals that had been identified from the rock samples.

13.2 Background to the Modelling

13.2.1 Computer programs

CHEQMATE is a coupled chemistry and transport program that simulates ionic transport with chemical equilibrium being provided by HARPHRQ [5]. It has been used for a number of different problems associated with radioactive waste disposal as part of the Nirex Safety Assessment Research Programme (NSARP). It employs a two-step solution to simulate coupled ionic transport and chemical equilibrium. The simulations are carried out for a one-dimensional section of the material of interest divided into a number of different cells. The flux of each species over the cell boundaries is calculated using a finite difference representation of the transport equations. The change in concentration in each cell is then calculated and passed to the program HARPHRQ to calculate the

equilibrium chemistry. The use of the two-step solution allows complex chemistry to be considered. However, there may be numerical problems associated with solving the transport equations where sharp reaction fronts occur (such as in the case of mineral precipitation/dissolution). MARQUISS has, therefore, been developed to complement the use of CHEQMATE for these types of problems.

MARQUISS applies the quasi-stationary state approximation to the coupled chemistry-transport equations i.e. it approximates the time evolution of geochemical processes using a sequence of 'stationary states'. Each 'stationary state' represents a solution composition and set of mineral reaction rates for a particular spatial configuration of the host rock. The spatial configuration can be expressed in terms of the mineral composition, porosity, the mineral-surface area, permeability and the position of reaction zone boundaries. The reaction zone boundaries represent chemical fronts; they are boundaries between regions with different mineral and aqueous chemical compositions. MARQUISS can simulate advection and diffusion in a one-dimensional homogeneous porous medium. and uses a finite difference scheme similar to that employed by CHEQMATE. The precipitation and dissolution reactions of minerals are described using pseudo-kinetic rate laws.

13.2.2 Modelling scenarios

At Maqarin, samples of porewater and rock have been taken from a fracture that runs from the metamorphosed zone through marl to Adit 6. The high pH fluid from the metamorphosed zone will flow along the fracture and diffuse into the marl. This will cause chemical changes in the porewater in the fracture and in the solid adjacent to the fracture. Two modelling scenarios can be identified:

(i) Diffusive transport perpendicular to the fracture into the marl - the aim of the modelling would be to predict the type and scale of mineralogical changes. The predictions can be compared with the information from the solid samples;

(ii) Advective transport along the fracture with diffusion into the rock matrix - the aim here would be to predict the changes in the water composition in the fracture. These predictions could be compared with the water samples from the adit.

The second calculation is computationally difficult and requires simplifications to be made, particularly for diffusion into the rock matrix. In order to make these simplifications, it is first necessary to understand the rock-matrix interactions in more detail. Therefore, at this stage, effort was concentrated on modelling the diffusive transport perpendicular to the fracture. However, preliminary calculations for the advective transport are also presented in Section 13.4.

13.3 Modelling of Diffusive Transport and Alteration of Marl

13.3.1 Model parameters

13.3.1.1 Selection of minerals database

Thermodynamic data for a large number of minerals exist and selection of a subset of these data is usually necessary for a particular problem. For purely predictive calculations this selection is based only on knowledge of the formation conditions of the mineral. This selection may be refined by data from the system being modelled and using scoping calculations. In this study, initial calculations were performed using a database including

minerals which could form under the field conditions and was refined using information on minerals found at the site (Chapter 6).

HARPHRQ calculations were performed to select the minerals used to represent the unaltered marl. The mineralogy of the marl is discussed in detail in Chapter 6. In this study, the unaltered marl is simulated as calcite, illite, kaolinite and opal in equilibrium with M6 water. The pyrite and apatite content of the marl has not been included at this stage in order to limit the complexity of the problem and concentrate on the main processes occurring. At the time of this modelling, the best available groundwater analyses suggested slight supersaturation of calcite. The equilibration with the calcite for both porewaters was therefore carried out so that a saturation index of 0.3 was maintained. The composition of these waters is given in Table 13.1. It is now thought that this apparent supersaturation was due to contamination of the groundwaters by adsorption of atmospheric CO_2 during sampling (Chapter 4). Ideally, the measured groundwater should have been corrected to allow for this contamination. However, it was not thought that such a correction would significantly affect the calculations presented in this chapter, and therefore the calculations were not repeated.

13.3.1.2 CHEQMATE diffusive modelling

CHEQMATE is a program that models one-dimensional transport in a porous medium. The program was used to simulate diffusive transport into the marl. The direction of this diffusive transport was perpendicular to the direction of groundwater flow in the fracture. The calculations simulate alkaline water-rock interaction with the marl close to the metamorphic zone and assume constant composition of solution in the fracture. For these calculations a computational grid is set up with one cell representing the fracture and the rest representing the marl. The CHEQMATE grid is assumed to extend into the unaltered marl and the transport over the last cell boundary is therefore calculated using an unaltered marl solution composition. The porewater in the fracture is assumed to discharge from the metamorphosed zone and is based on the M1 water composition (Chapter 3). This porewater is predicted to be supersaturated with respect to calcite and portlandite. In the base case calculation the solution was equilibrated with these minerals. Sensitivity to this was tested and the predictions were essentially the same.

The thermodynamic data for these calculations were obtained from the HATCHES database [6], with the exception of the mineral, jennite. Data for jennite were obtained from an unpublished experimental study [7]. Several scoping studies were also performed to identify important minerals and collaboration with BGS further helped in this identification. The early scoping studies predicted essentially the same trends as the base case calculations presented in this report. In particular, the major minerals predicted to precipitate were the same. The base case calculations were performed with a database of minerals selected to include those which are known to form at Maqarin. All the mineral reactions were assumed to reach equilibrium.

The mineralogical studies show that most of the changes in the marl are very close (μm - mm) to the edge of the fracture. The spatial grid in CHEQMATE must be fine enough to predict the details of these changes. The calculations were first performed with a linear grid but this was later refined to include variable cell sizes, with smaller cells near the fracture. The variable grid was selected to ensure that the section extended into unaltered marl without including a very large number of computational cells. Because of the small size of the cells closest to the fracture the size of the timestep was limited. The

physical properties for the marl are based on measurements made by AEA Technology (Chapter 9). The model parameters are summarised in Table 13.2.

13.3.1.3 MARQUISS diffusive modelling

The parameters for the MARQUISS modelling of the diffusive transport into the marl were taken from the CHEQMATE calculations. MARQUISS uses a reduced set of aqueous species and mineral reactions. The data for the minerals and the aqueous species are shown in Tables 13.3 and 13.4. The transport parameters are the same as in the CHEQMATE calculation. However, in using the quasi-stationary state approximation, a finer spatial grid can be used than employed by CHEQMATE. This is because restrictions on the choice of time step employed by MARQUISS are different. A timestep of 10^4 seconds was used in the MARQUISS calculations, with a spatial grid employing 400 cells of size 10^{-5}m. As no experimentally-derived data were available for the minerals included in the MARQUISS calculations, illustrative rate coefficients† of 10^{-6} mol $m^{-3}s^{-1}$ were used.

13.3.2 Results of the diffusive modelling

13.3.2.1 CHEQMATE results

The CHEQMATE model predictions are presented in Figures 13.1 to 13.6 for times up to 5 years. The short timescales presented are due to the limitations imposed by the small cell size and therefore timestep. CHEQMATE predicts precipitation of CSH phases (jennite and tobermorite), ettringite and minor amounts of brucite and talc. The predicted evolution of the CSH minerals is shown in Figure 13.1. Jennite precipitates close to the fracture, with tobermorite precipitation starting at 0.8mm. The peak in the jennite remains at 5 mol dm^{-3} but begins to broaden while the tobermorite peak increases in time.

The predicted brucite, ettringite and talc profiles are shown in Figures 13.2 and 13.3. Both brucite and ettringite are predicted to precipitate in the first millimetre of the marl, with significant quantities of the ettringite forming. The talc shows a broader precipitation band but the amounts are insignificant.

The predicted changes in calcite amounts are shown in Figure 13.4. Close to the fracture calcite is predicted to precipitate and then deplete next to the unaltered marl. A dissolution front for the minor marl minerals (Figure 13.5) moves away from the fracture. The pH is predicted to rise to 11 up to 7cm from the fracture (Figure 13.6). The zeolite waikairite observed at Maqarin is not predicted to precipitate.

The change in volume of the solid can be calculated from the amounts predicted to be precipitated and dissolved and the molar volumes (Table 13.3). By 5 years, the precipitation of ettringite close to the fracture is predicted to be sufficient to close the pore volume. Only where the calcite is depleted next to the marl is there predicted to be any opening of the pores.

13.3.2.2 MARQUISS results

MARQUISS calculations for diffusive transport into the marl produce results largely in qualitative agreement with those of CHEQMATE. MARQUISS predicts the precipitation

† Rate constants are more usually given in units of mol m^{-2} s^{-1}, i.e. moles reaction per unit surface area per second. In MARQUISS, this rate constant is used in combination with the surface area per unit volume solution (m^2 m^{-3}) giving a 'rate coefficient' (mol $m^{-3}s^{-1}$).

of CSH phases tobermorite and foshagite (jennite is not included in the MARQUISS database), ettringite, and minor quantities of brucite and talc (Figures 13.7 to 13.10). Kaolinite, illite and opal are seen to slowly dissolve.

Tobermorite precipitation is predicted at 0.72mm, and foshagite precipitation at 0.16mm, from the source of high pH groundwater. The scale of the alteration is smaller than that predicted by CHEQMATE, possibly due to the better spatial resolution that could be employed in the MARQUISS calculations, or possibly because MARQUISS can simulate only steady-state diffusion and ignores any effects resulting from the transient behaviour of the system. The calcite is predicted to precipitate close to the fracture, which is in agreement with the CHEQMATE predictions. However calcite depletion is not observed next to the unaltered marl.

The expansion of the mineral alteration zone through the unaltered marl appears to be slow, covering less than 4mm after 3 years. However, as mentioned above, such a low expansion rate may be an underestimate given that MARQUISS simulates only steady-state diffusive transport, and so ignores any initial transient behaviour.

13.4 Advective Modelling

13.4.1 Model parameters

Preliminary modelling of the advective front along the fracture has been carried out using MARQUISS. The hydrogeological data for the Maqarin area have not been analysed as part of this project, so the water flow velocity has been estimated from the observed rate of flow during collection of the water samples. A Darcy velocity of $1.12\ 10^{-5}$ $m^3m^{-2}s^{-1}$† was selected. Diffusion and dispersion within the fracture was ignored and the exchange of solute species between the fracture and the wall rock was not included.

The length of the fracture has been calculated from information collected in the adit (Chapter 2 gives details of these calculations). The porosity of the fracture infill was taken as 0.17 and held fixed. Porosity changes arising from mineral alteration processes within the fracture were ignored. The advective modelling uses the same mineral and aqueous species dataset as for the diffusive modelling.

13.4.2 Results of the advective modelling

Preliminary calculations using MARQUISS suggest rapid migration of CSH phase, ettringite, brucite and talc precipitation fronts along the fracture, with the fracture sealing largely due to ettringite precipitation, around 0.6m from the source of the high pH groundwater. Ettringite, brucite and foshagite are seen to precipitate along the full length of the fracture, but tobermorite only starts to appear around 0.3m, and talc, around 0.5m from the source. All these minerals, except ettringite, are transient and subsequently dissolve, with dissolution fronts slowly migrating along the fracture. Kaolinite, illite and opal also slowly dissolve, and calcite levels remain unaltered. Some calculated mineral precipitation and dissolution front velocities are given in Table 13.5.

† this value corresponds to an average of the estimated fluxes for the two fractures described in Chapter 3 (before correction following consideration of the effect of the adit on flow patterns).

13.5 Sensitivity Calculations

13.5.1 CHEQMATE diffusive modelling

The timestep used in the calculations is restricted by the small cell size required to look at the spatial changes in detail. The simulations were repeated using larger cells (Table 13.2) to examine the evolution over longer time scales. The overall trends predicted were very similar to those obtained from the base case calculations. Figure 13.11 shows the predicted CSH phase precipitation up to 30 years. The peak in the jennite precipitation is lower but it is spread over 5 - 10mm instead of less than 1mm. The tobermorite precipitation band is also extended. By 30 years it can be seen that the jennite close to the fracture has started to re-dissolve. The calcite profile (Figure 13.12) is similar to that predicted for the smaller cells. However, by 30 years the calcite next to the fracture has begun to deplete and re-precipitate further into the marl. The ettringite is also beginning to dissolve next to the fracture which could result in an opening of porosity.

In the field, precipitation was also observed within the fracture. To test sensitivity to this, a simulation was undertaken with two cells within the fracture. This simulation was not intended to be a realistic representation of the situation in the fracture, as no transport along the fracture was included. However, it should scope the effect of precipitation in the fracture. The total length of the two fracture cells was taken to be half the fracture width. The concentrations in the first cell were kept constant to represent the centre of the fracture. Ettringite, jennite and calcite were predicted to precipitate in the fracture, but the profiles within the marl were substantially unaltered.

The zeolites waikairite and mordenite have been observed at Maqarin. There is no thermodynamic data for calcium mordenite in the HATCHES database. A sensitivity calculation was carried out using data from the EQ3/6 database [8]. Mordenite was predicted to precipitate early in the simulation, but the amounts were small. It was then predicted to re-dissolve. The profiles of the other minerals were not significantly altered by the mordenite precipitation.

13.6 Discussion

For diffusive transport into the marl (i.e. considering a section perpendicular to the fracture), the general trends in terms of the types of mineral precipitated were in agreement with those observed. The main difference was in the calcite profiles. In the model calcium diffuses into the marl from the high calcium porewater in the fracture. This precipitates as calcite, CSH phases and ettringite giving an initial enrichment of calcium in the solid. In the simulation over a longer time, the calcium phases next to the fracture begin to re-dissolve. This is consistent with observations in the samples from Maqarin, which show depletion of calcium (Chapter 7). However, in the calculations over longer time scales there is alteration of the marl minerals in the whole of the grid. The far boundary condition for the calculation (Section 13.3.1.2) assumes that the CHEQMATE grid is of sufficient length that the far end of the grid extends into unaltered marl. The calculations have shown this not to be the case. The model also predicts the more calcium rich CSH phase, jennite, being precipitated closest to the fracture i.e. closest to the high pH source. The observation is that tobermorite should precede jennite and this is not predicted in the calculations.

In the CHEQMATE modelling the mineral alteration occurred over longer distances than was observed in the solid samples. However, some of the uranium data (Chapter 6) suggest that there may be alteration over much longer distances than can be observed by

examining the minerals. The predicted pH changes occur over much longer distances than the mineral alteration. The limitations on the grid size in the CHEQMATE calculations may also explain the length scales. The predicted timescales for the alteration were short, making interpretation of the Maqarin timescales difficult. Reliable kinetic data are not available for the dissolution and precipitation rates of the minerals under these conditions. None of the programs, therefore, included any kinetic limitations which would have implications for the predicted length and timescales. Thermodynamic data for some of the key minerals were also missing or sparse.

Despite the different assumptions in the programs described in this chapter, there was broad agreement between the predictions. The order of the mineral precipitation and the types of profiles were in good agreement. The width of the mineral profiles appear greater in the CHEQMATE calculations than in MARQUISS, partly because MARQUISS can achieve a greater spatial resolution in its calculations, and partly because MARQUISS can examine only steady-state diffusive transport, and so ignores any mineral profile broadening resulting from the transient behaviour of the system..

Advective calculations using MARQUISS give predictions consistent with the observed distribution of ettringite and tobermorite along the fracture. Reaction fronts are predicted to move rapidly along the fracture. Many of the phases are predicted to be transient. This is also consistent with the field observation of zoned alteration fronts.

13.7 Conclusions

The development of the coupled models of the interaction of porewater from a cementitious repository with geological materials is in its early stages. The agreement for the types of minerals precipitated at Maqarin is, therefore, encouraging. The differences between the predictions and the field data may be partly due to a lack of kinetic data and partly due to the short timescales of the simulations. In addition, there was good agreement between the predictions of programs using different assumptions in the model formulation which suggests they may be used in a complementary manner. However, the modelling also highlighted some of the problems with these types of calculations. With CHEQMATE there are computational difficulties in solving transport and chemical processes over such short distances and a compromise has to be made between using a small computational grid and using a reasonable timestep. The use of programs such as MARQUISS helps overcome this problem but there are also limitations in this approach. The lack of thermodynamic and kinetic data for key minerals was also apparent. In future, it will be important to focus on those data required for particular disposal scenarios.

13.8 References

[1] A Haworth, S.M. Sharland, P.W. Tasker and C.J. Tweed, *A Guide to the Coupled Chemical and Equilibria Code CHEQMATE*, Nirex Report NSS/R113, 1988.

[2] A.V. Chambers, *Use of the Quasi-Stationary State Approximation to Determine the Migration of Mineral Alteration Zones at a Natural Analogue for the Disturbed Zone of a Cementitious Radioactive Waste Repository.* Sci. Basis Nucl. Waste Manag. XVII (Eds. A. Barkatt and R.A. van Konynenburg), 639-644, Materials Research Society, Pittsburgh (1994).

[3] A Haworth, S.M. Sharland, P.W. Tasker and C.J. Tweed, *Evolution of the Groundwater Chemistry around a Nuclear Waste Repository*, Nirex Report NSS/R111, 1987.

[4] M.C. Braney, A Haworth, N.L. Jefferies and A.C. Smith, *A Study of the Effects of an Alkali Plume from a Cementitious Repository on Geological Materials*, J. Contaminant Hydrology, **13**, 379-402, 1993.

[5] P.L. Brown, A Haworth, S.M. Sharland and C J Tweed, *HARPHRQ: A Geochemical Speciation Program based on PHREEQE*, Nirex Report NSS/R188, 1991.

[6] J.E. Cross and F.T. Ewart, *HATCHES - A Thermodynamic Database and Management System*, Nirex Report NSS/R212, 1990.

[7] A. Kindness (University of Aberdeen), Personal communication, 1992.

[8] EQ3/6 database, version r3245R54, Lawrence Livermore National Laboratory, 1990.

Table 13.1 Starting solutions for the diffusive CHEQMATE calculations

	Fracture Porewater, M	Marl Porewater, M
pH	12.67	7.59
Ca	$1.14\ 10^{-2}$	$1.8\ 10^{-3}$
Mg	-	$2.02\ 10^{-4}$
Na	$2.05\ 10^{-3}$	$5.40\ 10^{-4}$
K	$2.53\ 10^{-4}$	$4.09\ 10^{-5}$
Al	-	$1.18\ 10^{-7}$
Si	-	$1.26\ 10^{-4}$
Cl	$1.48\ 10^{-3}$	$5.90\ 10^{-4}$
C	$1.46\ 10^{-5}$	$3.54\ 10^{-3}$
S	$3.18\ 10^{-3}$	$1.02\ 10^{-4}$
N	$5.30\ 10^{-5}$	$4.07\ 10^{-4}$

Table 13.2 Model parameters for the CHEQMATE diffusive case

Diffusion coefficient marl /m^2s^{-1}	$3\ 10^{-11}$
Porosity marl	0.3
Section length /m	0.07
Smallest cell size /m	$1.45\ 10^{-4}$, $5.45\ 10^{-4}$

Table 13.3 Mineral Data Used in MARQUISS Simulation of Mineral Alteration Reactions at the Jordan Natural Analogue Site.

Mineral	Solubility Log_{10} K	Molar density, mol m^{-3}	[a]Rate coefficient, mol m^{-3} s^{-1}
Opal	+2.48	$4.41\ 10^4$	10^{-6}
Calcite	-8.17	$2.72\ 10^4$	10^{-6}
Illite	-2.73	$7.17\ 10^3$	10^{-6}
Kaolinite	+3.84	$7.17\ 10^3$	10^{-6}
Foshagite	-28.0	$6.49\ 10^3$	10^{-6}
Tobermorite	-37.6	$3.49\ 10^3$	10^{-6}
Ettringite	-40.6	$1.44\ 10^3$	10^{-6}
Brucite	-8.91	[b]10^4	10^{-6}
Talc	-30.3	[b]10^4	10^{-6}
Dolomite	-14.0	[c]$2.72\ 10^4$	10^{-6}

a The product of the active mineral surface area and rate constant is not known, but for the purposes of this calculation is assumed constant and assigned the values given here.

b These molar densities were estimated.

c The molar density of dolomite was assumed to be the same as that of calcite.

Table 13.4 Initial Rock and Solution Compositions Used in MARQUISS Simulations.

Concentration	At upstream boundary (high pH)	Initially within unaltered rock
Ca^{2+} / M	$9.4246\ 10^{-3}$	$1.7282\ 10^{-3}$
$MgOH^{+}$ / M	$1.0435\ 10^{-8}$	$9.5049\ 10^{-9}$
K^{+} / M	$2.512\ 10^{-4}$	$2.911\ 10^{-5}$
$Al(OH)_4^{-}$ / M	$3.5894\ 10^{-8}$	$1.2398\ 10^{-7}$
$H_2SiO_4^{2-}$ / M	$4.5859\ 10^{-11}$	$6.1107\ 10^{-11}$
Cl^{-} / M	$1.48\ 10^{-3}$	$5.897\ 10^{-4}$
SO_4^{2-} / M	$2.3228\ 10^{-3}$	$8.538\ 10^{-5}$
CO_3^{2-} / M	$7.1736\ 10^{-7}$	$3.9121\ 10^{-6}$
OH^{-} / M	$3.86\ 10^{-2}$	$4.4983\ 10^{-7}$
NO_3^{-} / M	$5.296\ 10^{-5}$	$4.06\ 10^{-4}$
Chalcedony / [a] $m^3\ m^{-3}$	0.0	$4.499\ 10^{-2}$
Calcite / $m^3\ m^{-3}$	0.0	0.5698
Illite / $m^3\ m^{-3}$	0.0	$1.701\ 10^{-2}$
Kaolinite / $m^3\ m^{-3}$	0.0	$6.797\ 10^{-2}$
Foshagite/ $m^3\ m^{-3}$	0.0	0.0
Tobermorite/ $m^3\ m^{-3}$	0.0	0.0
Ettringite/ $m^3\ m^{-3}$	0.0	0.0
Brucite / $m^3\ m^{-3}$	0.0	0.0
Talc / $m^3\ m^{-3}$	0.0	0.0
Dolomite / $m^3\ m^{-3}$	0.0	0.0

[a] units are m^3 of mineral per m^3 of rock + pore space, i.e. the volume fraction.

Table 13.5 Mineral Precipitation and Dissolution Front Velocities Determined by MARQUISS for Advection along a Fracture at Maqarin

Mineral	Precip. front vel., ms^{-1}	Dissol. front vel., ms^{-1}
Tobermorite	$7\ 10^{-5}$	10^{-9}
Talc	$7\ 10^{-5}$	$7\ 10^{-10}$
Ettringite	$7\ 10^{-5}$	-
Foshagite	$7\ 10^{-5}$	10^{-11}
Brucite	$7\ 10^{-5}$	$3\ 10^{-12}$
Illite	-	$9\ 10^{-13}$

Figure 13.1: Predicted Precipitation of CSH Phases

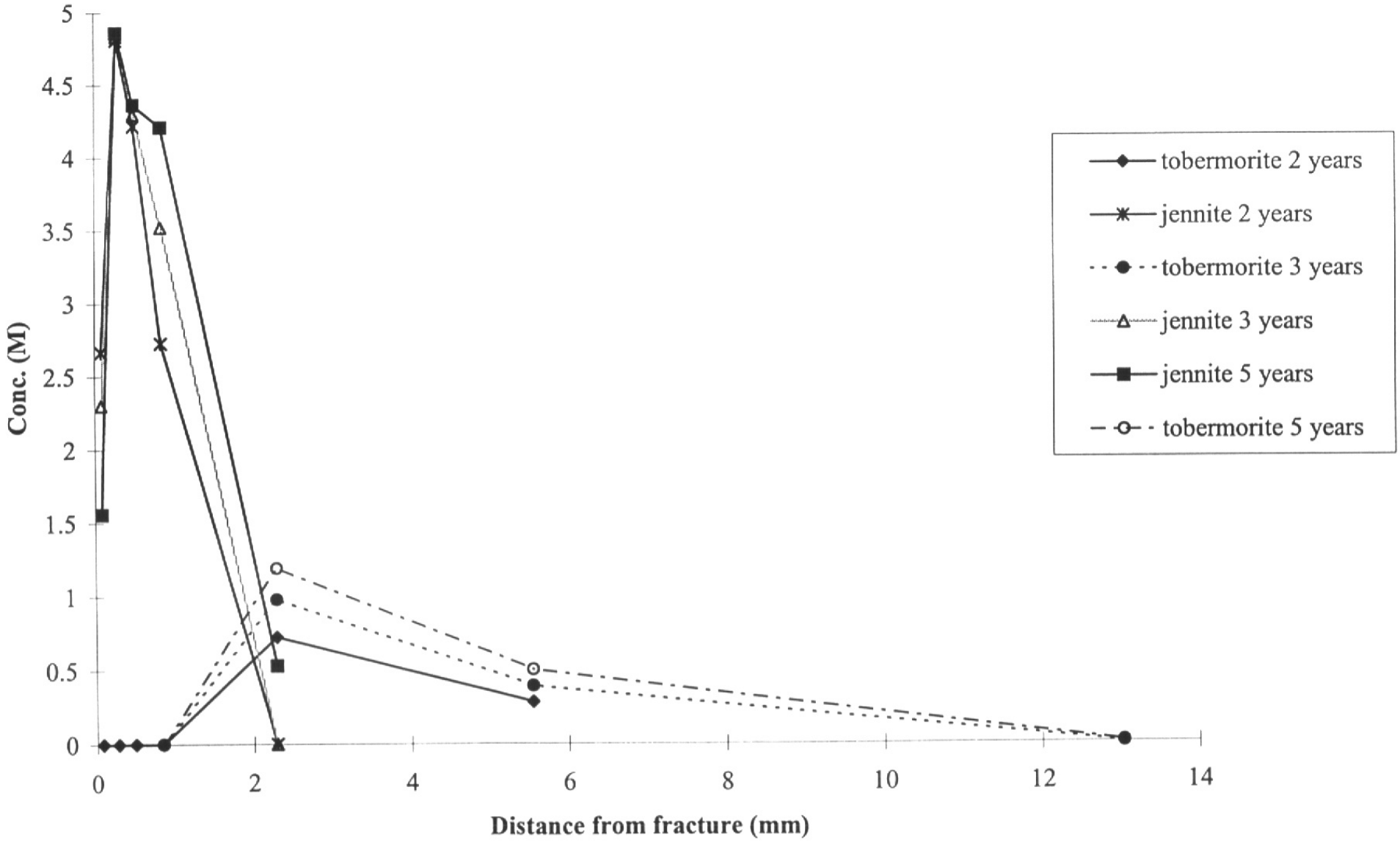

Figure 13.2: Predicted Precipitation of Ettringite and Brucite

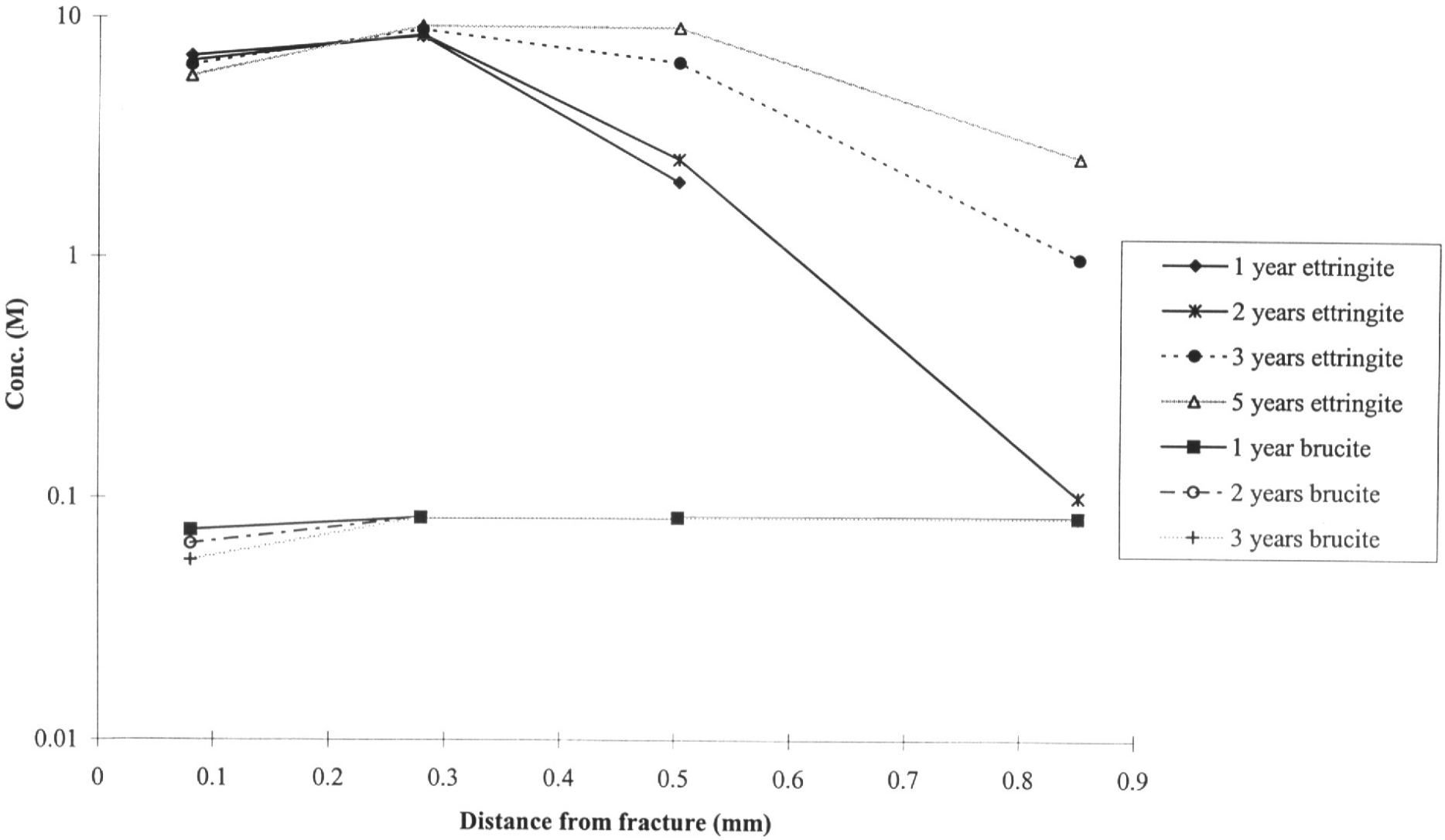

Figure 13.3: Predicted Precipitation of Tale

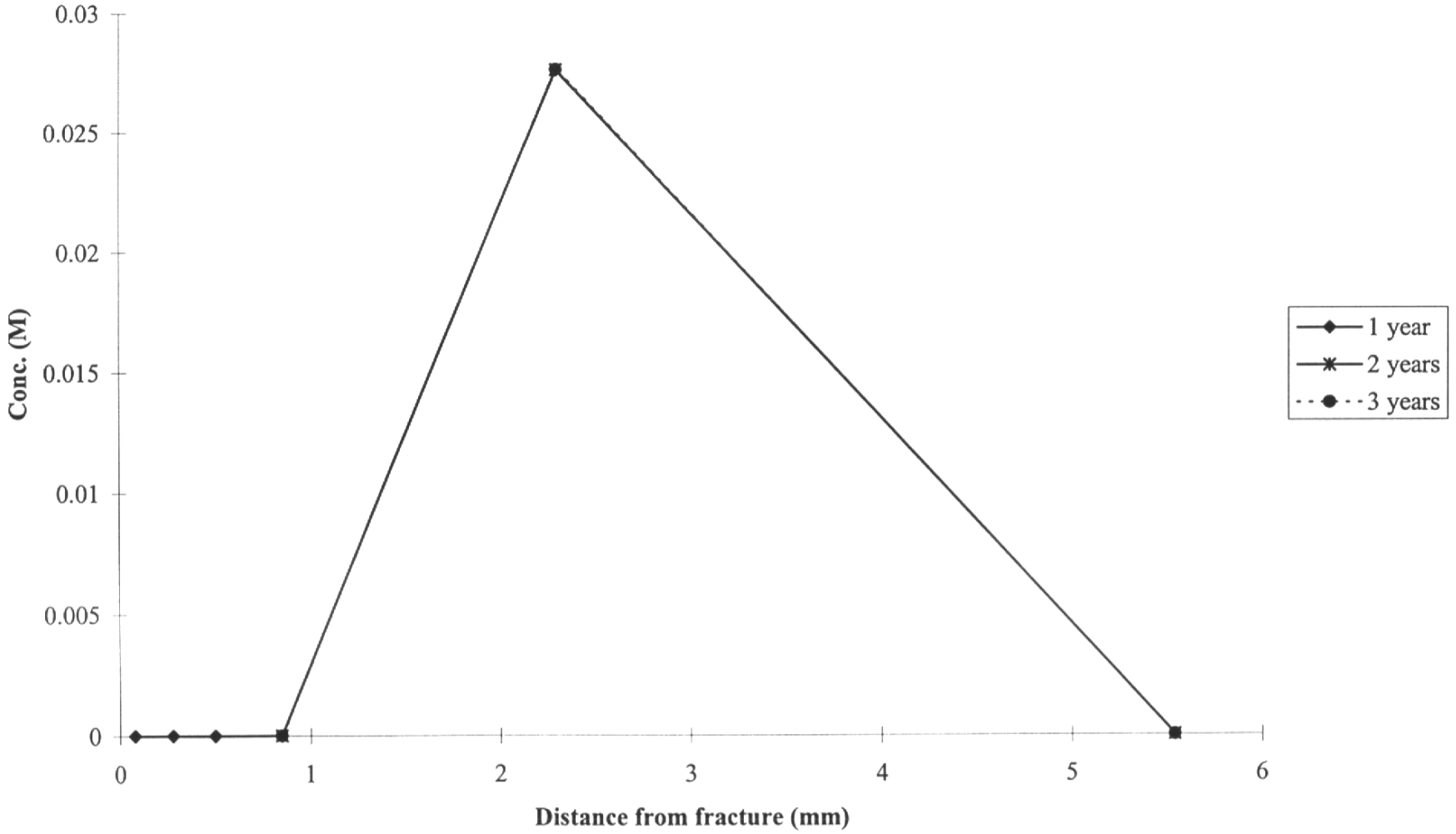

Figure 13.4: Predicted Evolution of Calcite

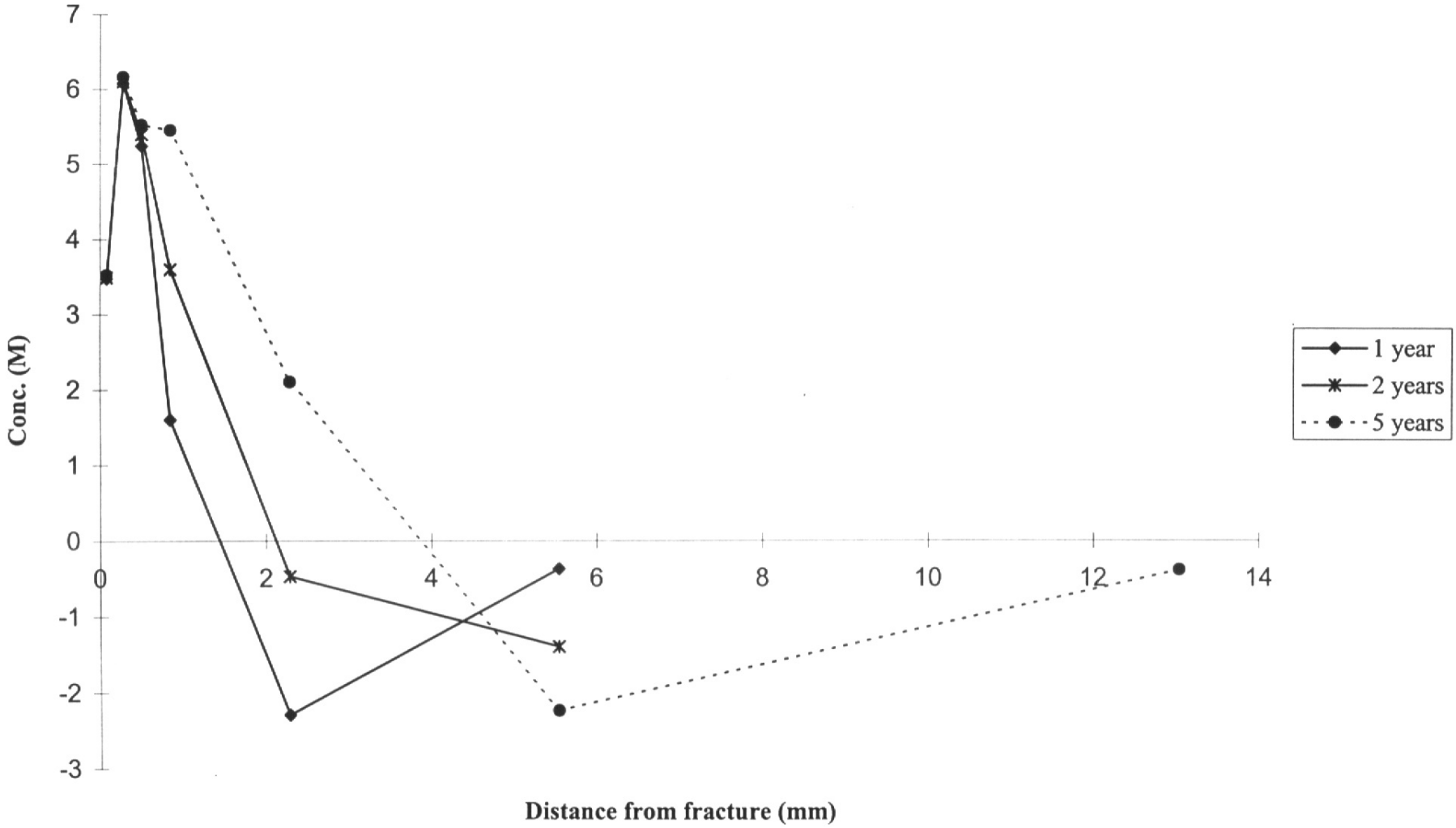

Figure 13.5: Evolution of the Minor Marl Minerals

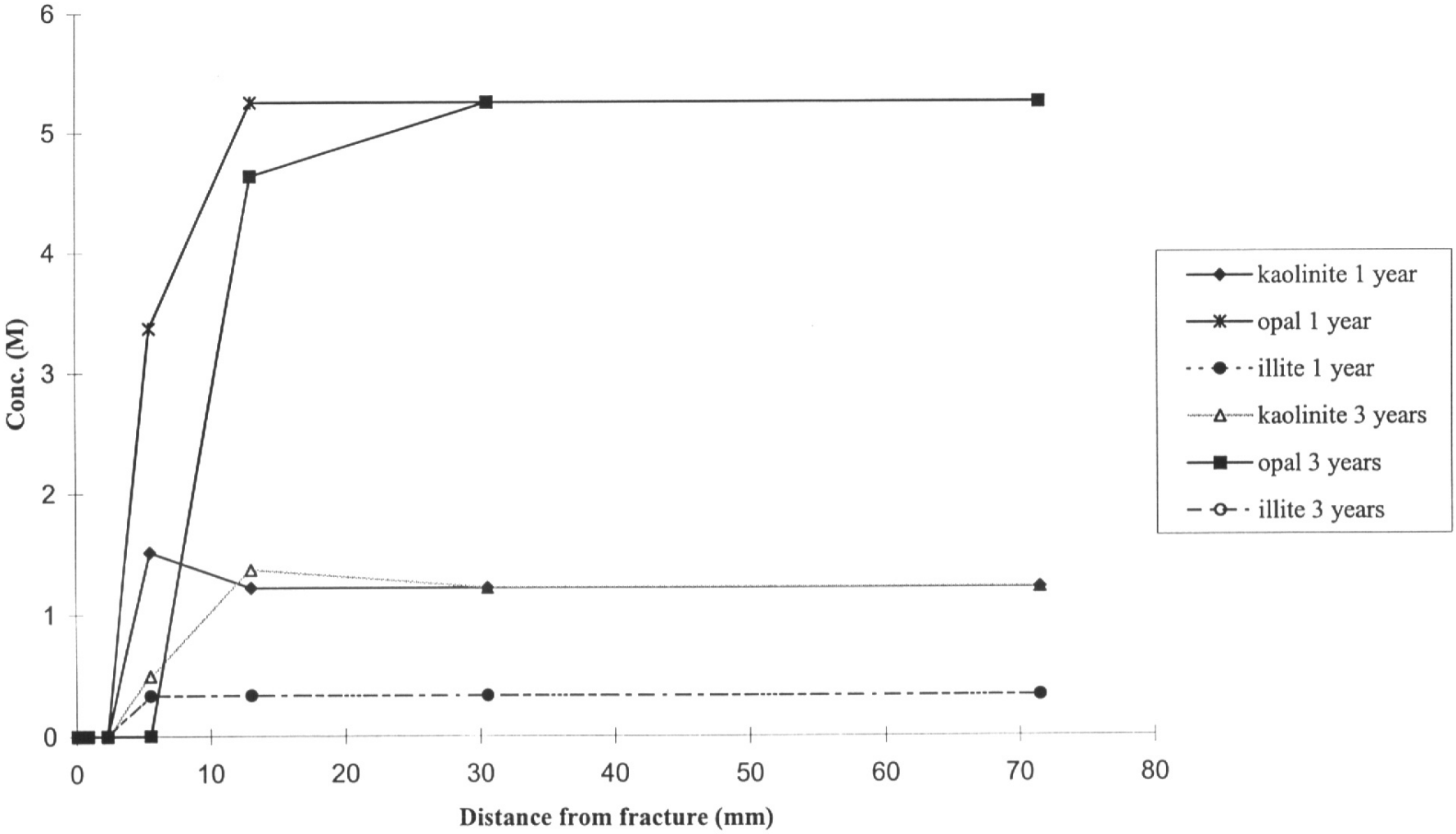

Figure 13.6: Predicted pH in the Marl

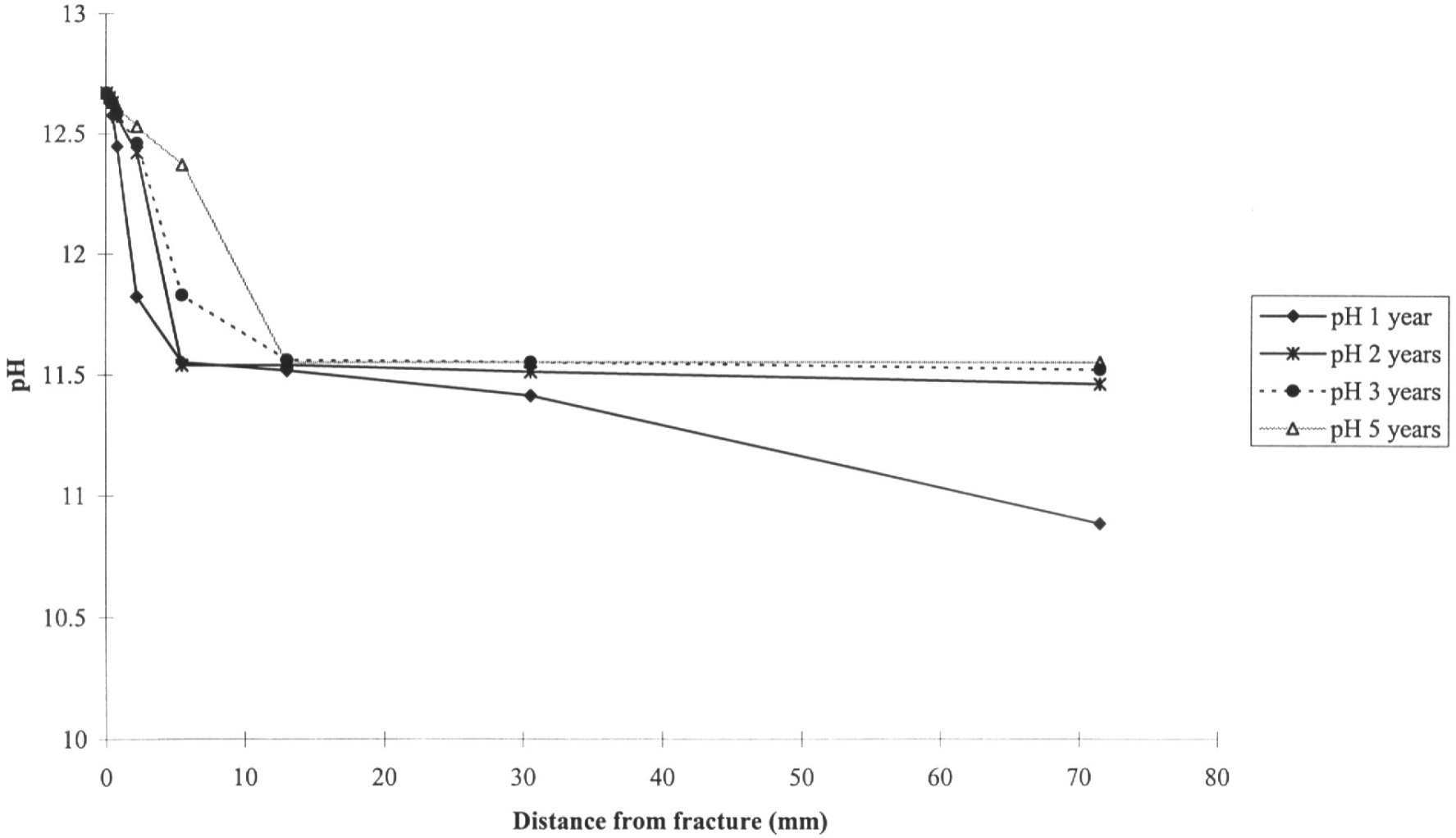

Figure 13.7:Mineral Profiles for High pH Plume Migration into Fracture Wall Rock Simulation of Mineral Alteration Reactions at the Jordan Natural Analogue

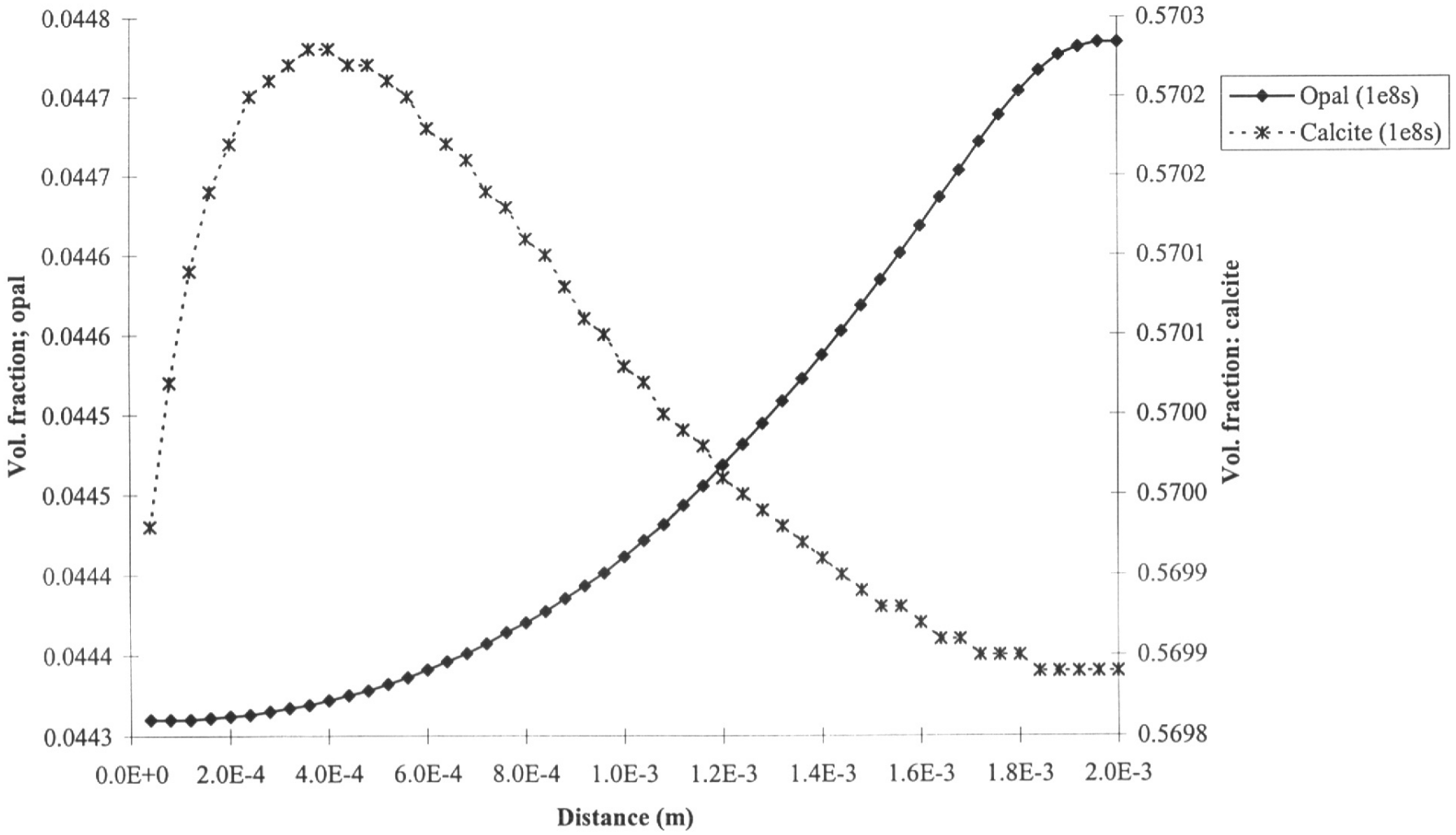

Figure 13.8: Mineral Profiles for High pH Plume Migration into Fracture Wall Rock
Simulation of Mineral Alteration Reactions at the Jordan Natural Analogue

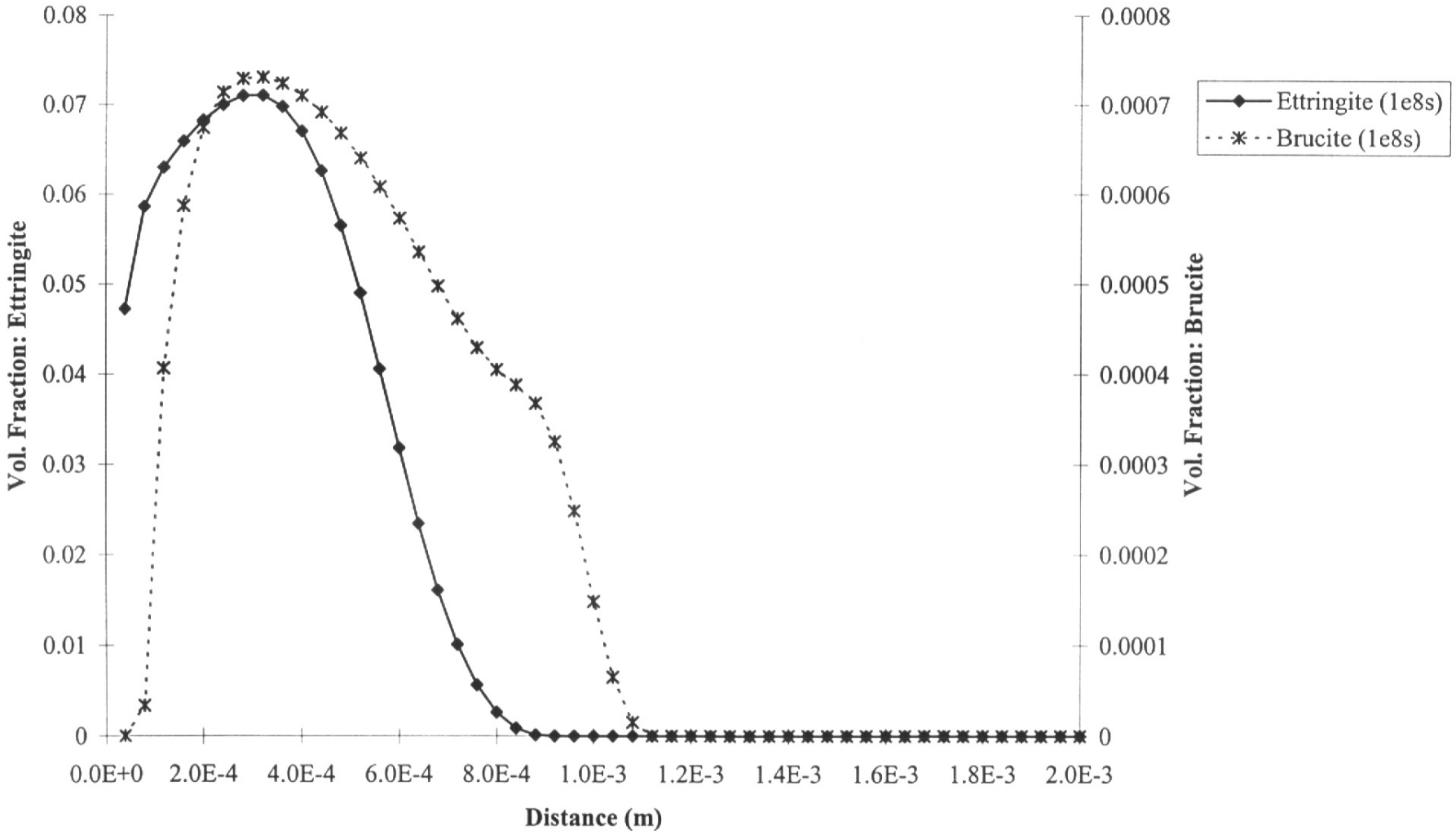

Figure 13.9: Mineral Profiles for High pH Plume Migration into Fracture Wall Rock Simulation of Mineral Alteration Reactions at the Jordan Natural Analogue

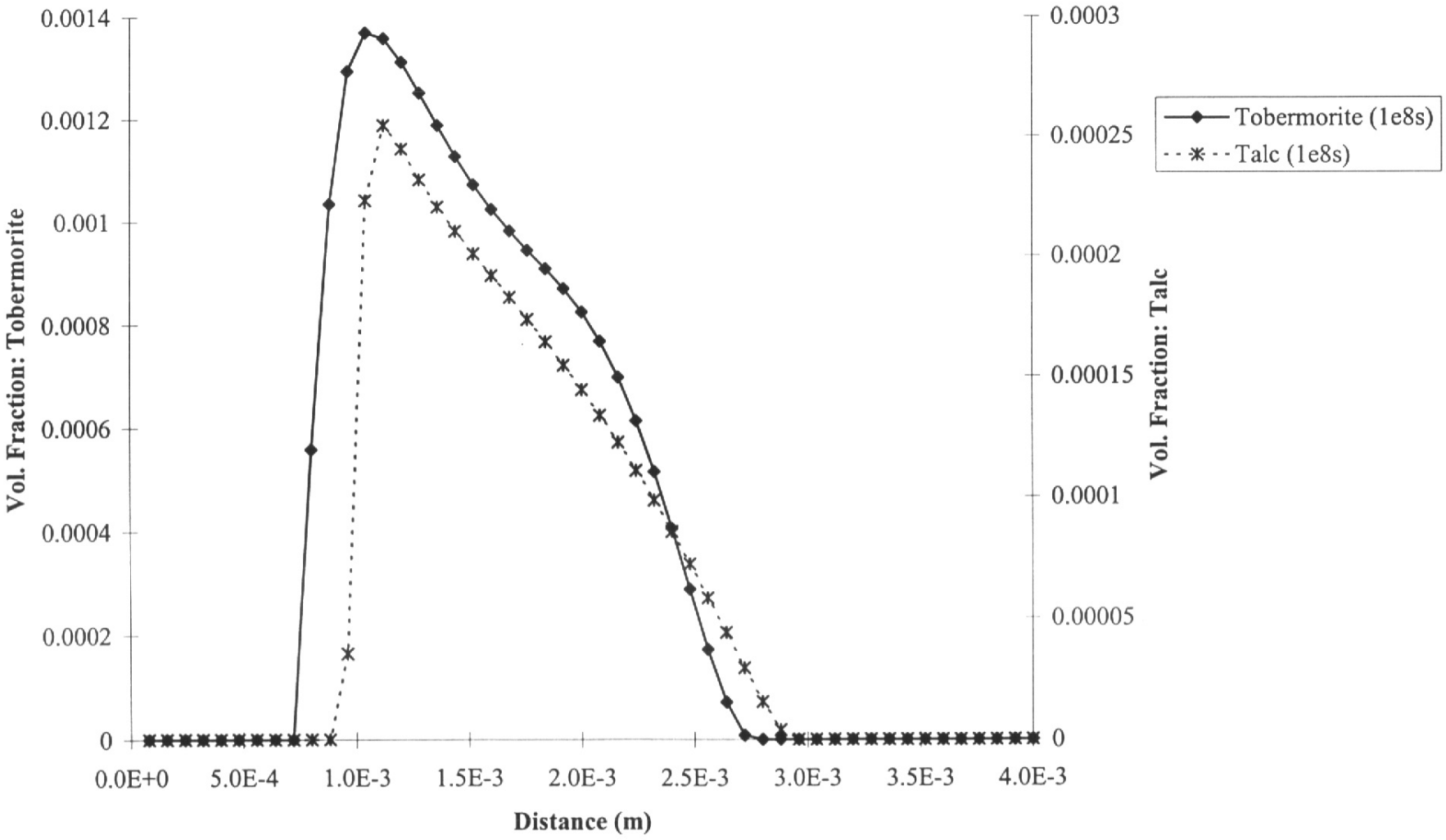

Figure 13.10: Mineral Profiles for High pH Plume Migration into Fracture Wall Rock
Simulation of Mineral Alteration Reactions at the Jordan Natural Analogue

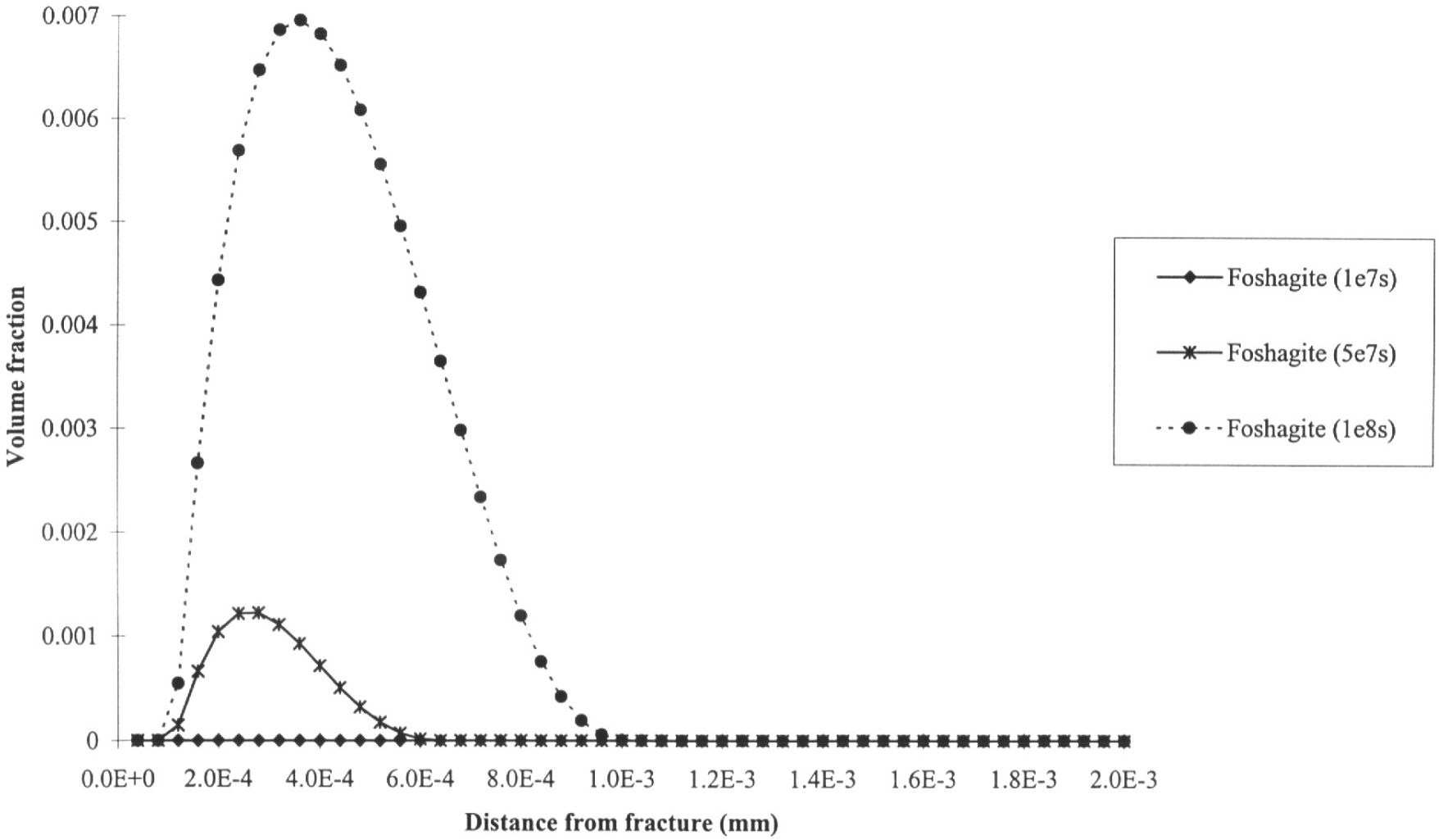

Figure 13.11: Predicted CSH Phase Precipitation for Simulation with larger Calculation Grid

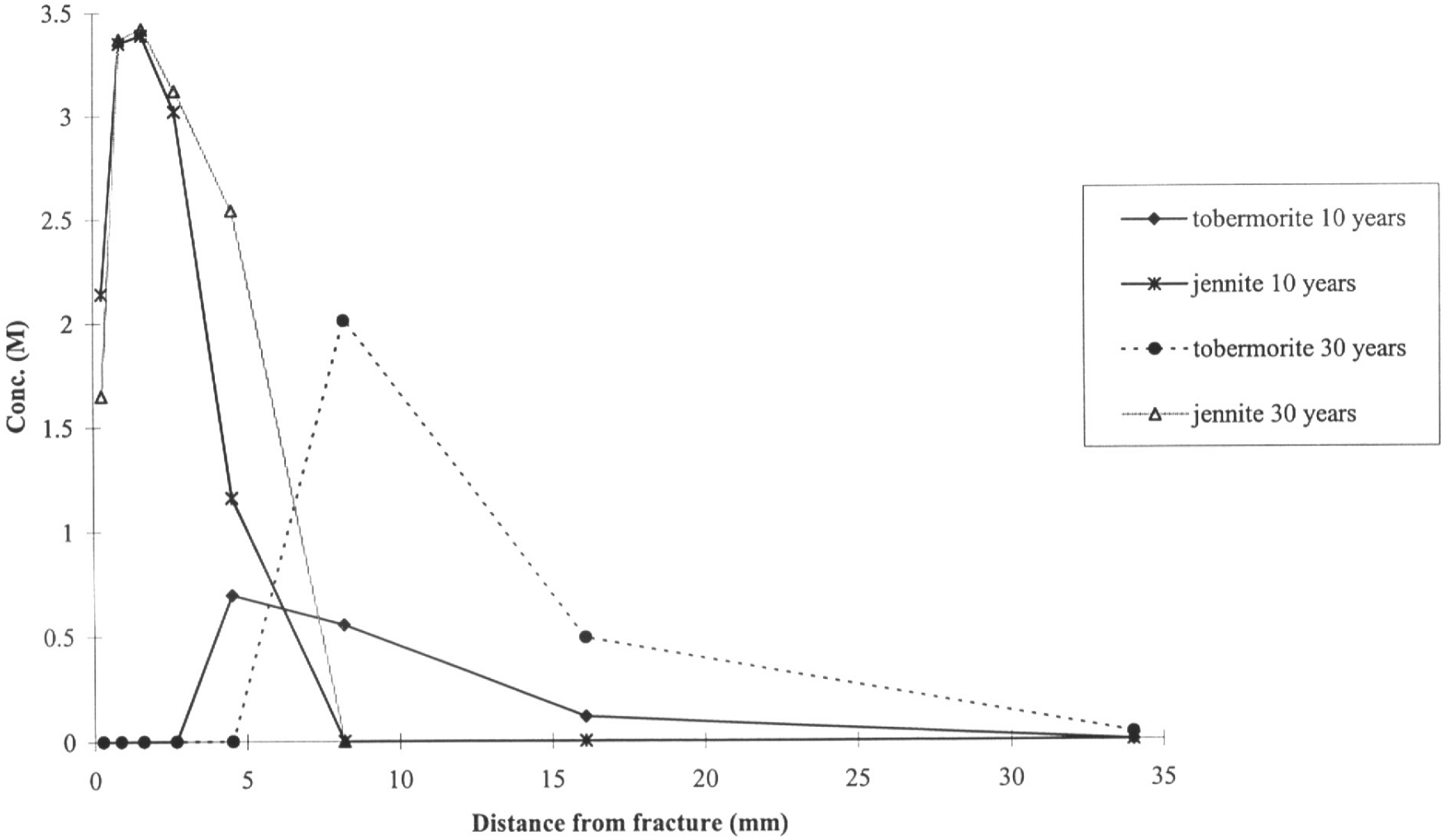

Figure 13.12: Predicted Evolution of Calcite for Simulation with larger Calculation Grid

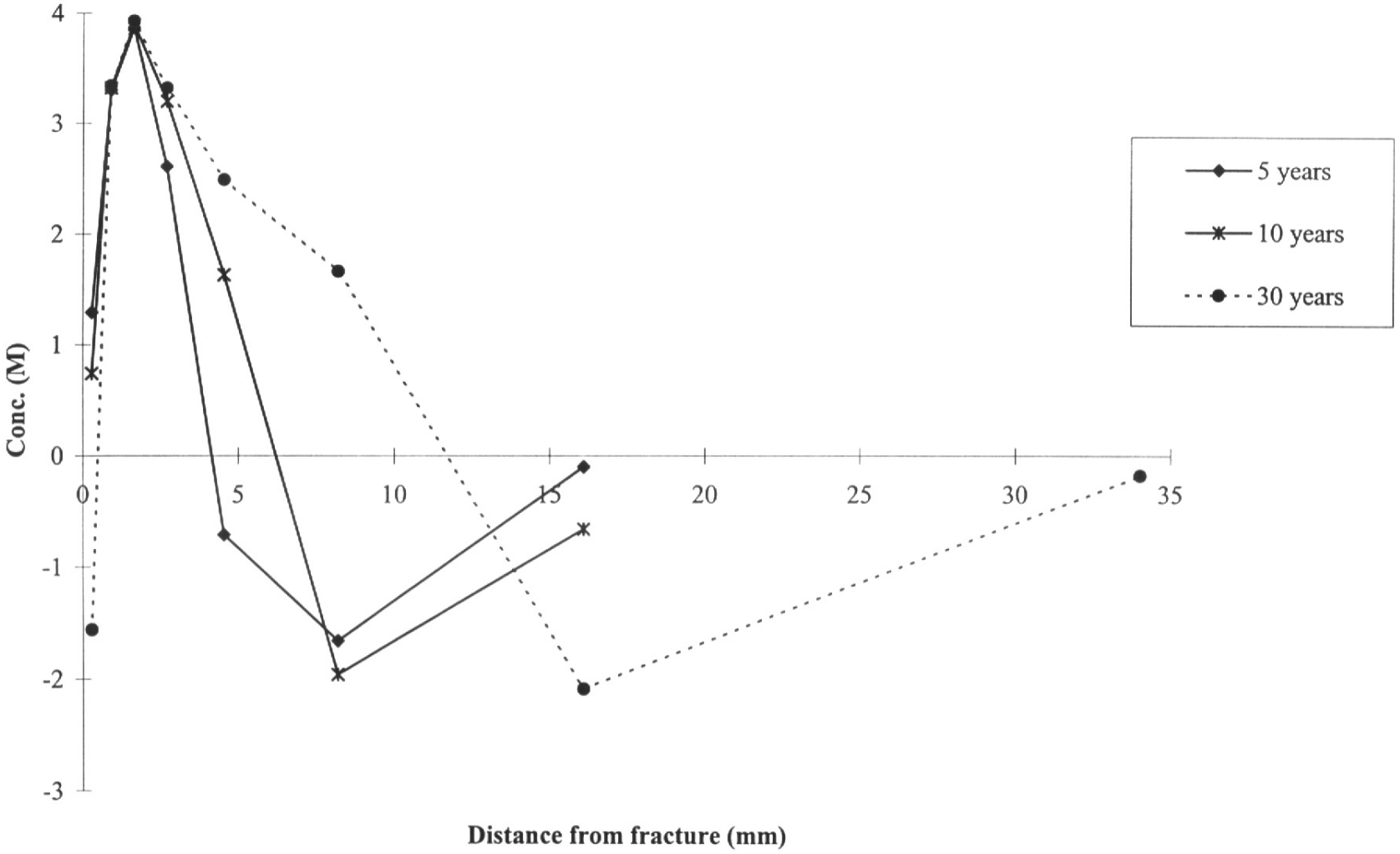

14. CONCLUSIONS

C.J. Tweed and C.M. Linklater

The Maqarin site, Northern Jordan, has been used as a field-scale analogue of the water/rock interaction expected downstream from an underground cementitious repository for radioactive waste. Detailed interpretation of data from the Maqarin project has provided much insight into the reaction of high pH water with carbonate rock in a system that has evolved over a geological timescale. An understanding of the long-term effect of a cementitious repository on the surrounding host rock, particularly the scale of the interaction and the nature of the reaction products, is an important contributor to the assessment of the performance of a cementitious repository.

14.1 Nature of Water/Rock Interaction

Secondary alteration products

The Maqarin study has given important insight as to the types of secondary alteration products that might be expected as a consequence of such interaction; the most important alteration products are CSH(I) and CSH(II) hydrogels and related minerals such as tobermorite, tacharanite and jennite, and zeolites. In more calcareous environments it would appear that the dominant zeolite species will be similar to laumontite whereas in more silicate-dominated host rocks more siliceous zeolites such as mordenite sub-group zeolites will be more important.

Extent of 'alkaline disturbed zone'

A key issue in relation to performance assessment is providing an estimate of the extent of an 'alkaline disturbed zone' around an underground repository. Due to lack of outcrop at Maqarin, it was not possible to detect the maximum distance over which there was evidence of hyperalkaline water/rock interaction. The influence of zeolite alteration decreased rapidly away from the metamorphic zone; 'Stage 4' zeolite precipitation was not observed at distances greater than a few metres. It was, however, noted that ettringite and thaumasite ('Stage 2') were precipitating in fractures at distances of at least 140m from the metamorphic zone. At Maqarin, therefore, it appears that an extensive disturbed zone has formed. This may to some extent be a function of the very rapid groundwater flow rates in Maqarin system. Groundwater flow rates around a repository are likely to be considerably lower, and the extent of an associated alkaline disturbed zone much reduced.

At Maqarin, fractures become sealed with secondary precipitates. Such sealing might also be expected in the alkaline disturbed zone around a cementitious repository.

Rock-matrix diffusion

Diffusion into rock-matrix adjacent to fractures has been identified as a potentially important radionuclide retardation mechanism in performance assessment. Study of the Maqarin analogue has therefore included consideration of wallrock alteration, and whether the diffusion properties of the clay biomicrite were affected by the alkaline water/rock reaction. It was noted that significant wallrock alteration extended for only very small distances into the wallrock (μm to mm). This was possibly due to blocking of available porosity by secondary products, which would tend to inhibit matrix diffusion perpendicular to the fracture. Attempts to measure directly the diffusion properties as a function of distance from the fracture wall failed due to the very narrow scale of the alteration zone. At distances of greater than 20m from the metamorphic zone, no significant wallrock alteration was observed and there is no

evidence that blocking of porosity occurs. This suggests that if inhibition of matrix diffusion in the wallrock occurs within the alkaline disturbed zone it is restricted to a narrow zone close to the high pH source.

14.2 Behaviour of Trace Elements

The Maqarin study has demonstrated that zeolite, jennite, tobermorite or CSH take up significant amounts of U, Pb, Sr and Ba. Incorporation into secondary minerals forming within fractures will tend to retard trace element movement along the fracture systems. Diffusion laterally into wallrock, and incorporation within secondary phases forming there, will further retard trace element movement along fractures. Evidence for this latter process has been provided by profiles of whole rock uranium concentration within the fracture wallrock at Maqarin.

For performance assessment, it is noteworthy that some phases forming within the alkaline disturbed zone can act as sinks for certain radioelements. It was observed, however, that the volumetrically more important alteration products, ettringite and thaumasite, incorporated considerably lower amounts of trace elements (except for Cr and Zn).

Not enough data are available at present to quantify trace element incorporation processes. For example, in order to define partition coefficients, data are required for both the mineral phases and the groundwater associated with their formation. At Maqarin the vein mineralisation is polycyclic and extremely complex, and it was not possible to unequivocally correlate groundwater samples with particular stages of secondary mineralisation.

14.3 Age of the Hyperalkaline System

The maximum age of hyperalkaline groundwaters at Maqarin has not yet been established. The lack of ^{36}Cl from nuclear weapons testing in these groundwaters supports evidence from ^{3}H that these waters are older than 40 years.

The age of the combustion event has not yet been determined at Maqarin. ^{14}C concentrations in the secondary carbonates formed by recarbonation of portlandite and CSH-like phases suggest that some alteration may be less than a few hundred years old. $^{230}Th/U$ dating of secondary hyperalkaline vein mineralisation has suggested that the hyperalkaline groundwater fracture-flow system may have been operative for the order of 80 000 to 100 000 years. These apparently conflicting estimates of age have been rationalised in terms of several episodes of water-rock reaction, including reaction ongoing at the present day. Indeed, the persistence of secondary fracture materials of differing ages suggests that, once sealed, the secondary fracture-filling mineralogy in the hyperalkaline disturbed zone can remain stable for long timescales - with the implication that radionuclides associated with these secondary phases also can be isolated from the evolving groundwaters.

14.4 Microbial Activity

Diverse populations of alkaline tolerant microbes were found at all sites sampled at Maqarin. Tolerance was demonstrated up to pH 11 and appeared particularly associated with sulphate-reducing bacteria. The Maqarin microbial populations observed were grown in the laboratory under nutrient-rich conditions, implying that a steady supply of nutrients and energy was present at all sites. However, the actual activity of microbes in-situ was not determined and this remains an area of uncertainty.

These observations suggest that significant microbial activity could occur under the hyperalkaline conditions of a cementitious repository, but that a steady supply of nutrients would be required to maintain the population.

14.5 Use of Modelling Techniques

Modelling using both an equilibrium and a kinetic approach was used to simulate the nature of alkaline water/rock interaction at Maqarin. In terms of general trends with regard to the types of secondary minerals precipitated, both approaches gave results that were in agreement with observation. However, the calculated widths of reaction zones were typically greater than those observed. This may be due to limitations in the representations of chemical kinetics due to insufficient data, or modification of the transport processes as reaction proceeds and porosity decreases. Overall, the modelling has given confidence in the use of coupled codes to represent this type of water/rock reaction.

Geochemical modelling of trace element solubility and speciation reinforced the conclusions of Maqarin Phase I: in most cases, the observed solution concentration for the elements of interest is several orders of magnitude less than would have been predicted assuming that the elemental concentrations were fixed by the simple stoichiometric oxides, hydroxides, carbonates and sulphates contained in the thermodynamic databases. There are two main limitations to the prediction of elemental solubilities by the method used here. First, the minerals included in the databases are pure end-members and are rarely observed in nature. Second, it is very difficult to test effectively how realistic is the predicted elemental speciation. Attempts to measure speciation in the groundwater samples were inconclusive.

Microbiological modelling techniques could not be tested fully due to restrictions in available data, e.g. a detailed breakdown of the organic phases present is required to parameterise the model.

APPENDICES

APPENDIX A GROUNDWATER ANALYSIS METHODS

M.R. Cave, S. Reeder, B. Smith, K. Harmon, N. Mitchell, J. Trick, P. Blackwell, S.R.N Chenery and J.M. Cook

A1 Field Measurements

Temperature, Eh, pH, conductivity and dissolved oxygen were determined in the field and the methods used are described in Chapter 3.

A2 Determination of pH and Total Alkalinity by Titration

A2.1 Instrumentation

The instrumentation used is a Radiometer VIT90 Video Titrator Controller module with an ABU93 autoburette and a SAM90 sample station. Sample pH is determined using Radiometer G2040B glass pH and K4040 calomel reference electrodes.

A2.2 Theory

'Total Alkalinity' may be defined as the amount of sulphuric acid required to titrate to the equivalence point of bicarbonate at approximately pH 4.5, expressed as the equivalent mg/l of bicarbonate. It is actually a measure of the acid neutralising capacity of the sample, but as groundwaters are dominated by the carbonic acid equilibria system, the expression of total alkalinity in terms of bicarbonate is common practice.

Theoretically, total alkalinity is a measure of the hydroxide, carbonate (x2) and bicarbonate contents, as well as any contribution from other anions that take part in hydrolysis, e.g. organic bases, silicates, borates, sulphides and phosphates. For these solutions, samples which were > pH 12.0 have been characterised in terms of hydroxide and carbonate concentration. The concentration of bicarbonate in these solutions is assumed to be negligble (aqueous speciation < 5% [HCO_3^-]) for the purposes of this calculation. For samples with pH < 9.0 the concentration of hydroxide is assumed to be negligible (<10mg/l [OH^-]) and the results calculated as carbonate and bicarbonate concentration.

A2.3 Analytical Method

Total alkalinity and pH are determined on all samples as soon as possible after delivery to the laboratory with minimal contact with the atmosphere. The pH electrode is calibrated using pH 7 and 9.2 or 7 and 13 buffers, depending on the sample pH. 2ml of sample is titrated to pH 2.5 with 0.01M sulphuric acid, and the amount of acid added to the bicarbonate equivalence point at approximately pH 4.5 automatically calculated and used to determine the bicarbonate concentration. An independent standard is analysed after at least every 10 samples and at the end of the run to check for any drift.

To check the accuracy of the field measurement, the pH 12 buffer solution used in the field was measured against the laboratory pH 13 standard and gave a value of 11.92 at 22•C.

A2.4 Data quality

Because of the highly alkaline nature of the sample, absorption of atmospheric CO_2 is the major problem in contamination. Every effort was made to fill bottles to the brim so that no air space existed on sampling and that the samples were analysed quickly when returned to the laboratory. Nevertheless, some CO_2 absorption will have occurred and the results must be regarded as maximum values.

A3 Determination of Major Cations and Trace Elements by Inductively Coupled Plasma-Atomic Emission Spectrometry (ICP-AES)

A3.1 Instrumentation

The ICP-OES used in this work is a Perkin-Elmer Plasma II sequential scanning system with twin 1m vacuum monochromators. Monochromator A has a 3600 line/mm grating and wavelength range of 160-400nm and the second (B) has a 1800 line/mm grating and wavelength range of 160-800nm. The monochromator gratings, plasma power, plasma gas flows, plasma viewing height, 50-position autosampler and nebuliser peristaltic pump are all under computer control.

A3.2 Theory

The sample is swept into the central channel of the inductively coupled plasma in a stream of argon carrier gas. Introduction is achieved by direct nebulisation of the aqueous sample to form a fine mist. On introduction to the plasma, the sample undergoes desolvation, evaporation and atomisation/ ionisation. The atoms or ions decay from the excited state through radiative energy transitions emitting light of specific energies (or wavelengths). The light emission from the plasma is separated into its component wavelengths by a monochromator, and a photomultiplier tube at the exit slit of the monochromator quantifies the light intensity at specific wavelengths. The intensity of the light emitted at the characteristic wavelength for a particular element is proportional to the amount of the element in the sample being sprayed into the plasma. The instrument is calibrated against standards containing known amounts of the elements to be analysed.

A3.3 Analytical method

Major cations (Ca, Mg, Na, K), trace cations (Si, Ba, Sr, Mn, Fe, Al, Co, Ni, Cu, Zn, Cr, Zr, Mo, Cd, Pb, V, Li,), total S and Si are determined directly by ICP-AES. Analysis is carried out on samples acidified 1% with respect to Aristar HNO_3. The instrument is standardised after at least every 10 samples and quality control checks are run every 20 samples. The control standards are always analysed at the end of the run to check for drift. Reported measurements are based on the average of three replicates.

A3.4 Data quality

All species preserved by acidification are considered to be stable over an appreciable length of time and certainly within the delay between sampling and analysis.

Wavelengths and conditions of analysis are optimised to ensure that interference effects are minimised for all elements; in complex matrices the sample is diluted prior to analysis. The accuracy of the major cation (and anionic) determinations can be determined by considering the ionic charge balances. A discussion on the precision and accuracy for this method on these highly alkaline solutions is presented later.

A4 Determination of Major and Trace Anions by Ion Chromatography

A4.1 Instrumentation

The ion chromatography system used for the anion analysis is a Dionex 2000i with an AutoIon 100 control unit and auto sampler. The data is processed using a Spectra Physics 4270 computing integrator and WINNER data capture and manipulation software.

A4.2 Theory

When a solvent containing dissolved anions is passed through a column of anion exchange resin, the progress of the anions through the column is retarded with respect to the solvent. Different anions are retained to different degrees according to their size and charge and this is used to separate anions in solution. The conductivities of the separated anions eluted from the column are detected as transient peaks and quantification may be achieved by comparing the peak area or peak height of the samples with those of known standards. For measurements to be accurate, the high background conductivity of the eluent is removed using chemical suppression. This relies on the exchange of sodium and hydrogen ions across a membrane to convert the sodium carbonate and sodium bicarbonate eluent to weakly conducting carbonic acid, and the weakly conducting anionic salts of the sample to more conductive anionic acids.

A4.3 Analytical method

Major and trace anions (Cl, SO_4, NO_3, NO_2 and Br) are determined by ion chromatography. The instrument is standardised after at least every 11 samples and quality control check samples are also run at the same interval. The analysis follows an automatic programme and the data are collected by an integrator which is pre-programmed to identify peaks by retention time and calculate peak areas. Calibration against the standards is also pre-programmed and is based on a quadratic curve over the range covered by the standards. All raw data are downloaded to floppy disk and can, if required, be re-integrated, for example using different standards.

The method is limited by the number of exchange sites available within the column. With the injection loop and column in use, solutions with total anion concentrations of up to 500mg/l can be analysed; above this the column becomes overloaded, causing poor peak shapes, variable retention times and thus unreliable results. To overcome this problem, more concentrated solutions are diluted. Dilution is also used to bring the analyte concentration within the concentration range covered by the standards and to reduce sample viscosity.

A4.4 Data quality

Most anions are stable in solution for an appreciable length of time and certainly within the delay between sampling and analysis. Nitrate and nitrite may, however, be modified by microbial activity and for this reason ion chromatography analysis is carried out as soon as possible after collection of the samples. The alkaline nature of the samples altered the column retention charateristics to shorter retention times compared to the standards. Consequently, the results for each sample had to be calculated manually as the integrator did not correctly identify each peak. This had no effect on the peak area and hence did not effect the accuracy of the measurement.

A5 Determination of Total Organic and Inorganic Carbon

A5.1 Instrumentation

The measurements are made on a Shimadzu TOC-5000 total organic carbon analyser with a ASI-5000 autosampler.

A5.2 Theory

In the measurement of total carbon content, pure air carrier gas flows at 150ml/minute through the Total Carbon (TC) combustion tube, which is packed with Pt-coated alumina

catalyst maintained by an electrically heated furnace at 680°C. When the sample enters the TC combustion tube, all of the carbon is oxidised to carbon dioxide and swept out of the tube by the carrier gas into a non-dispersive infrared (NDIR) detector which measures the carbon dioxide concentration by energy absorption. The output signal (analogue) of the NDIR detector is displayed as a response peak, the area of which is proportional to the total carbon concentration. The total carbon in a sample can be determined from the calibration curve prepared using standard solutions of known content. The total carbon is the sum of the total organic carbon and the total inorganic carbon.

In the measurement of total inorganic carbon, the sample is injected into the Inorganic Carbon (IC) reaction vessel which has carrier gas bubbling through a phosphoric acid reaction solution. The IC reacts with the acid to form carbon dioxide which is then detected by the NDIR detector. The inorganic carbon content is the sum of the carbonate and bicarbonate present in solution.

A5.3 Analytical method

The instrument is calibrated using separate 100mg/l organic and inorganic carbon standards, fitting a regression through zero. The quality control check standards, a mixed 50ppm and a mixed 10ppm solution, are analysed throughout the run.

Samples are analysed in triplicate and if the precision is better than 2% then, assuming that the check standards are within specification, the data is approved. If outside the initial 2% limit, further replicates may be analysed and outliers discarded. A precision of better than 5% must be maintained.

A5.4 Data quality

The method is essentially interference-free as long as the IC or TOC is totally converted to CO2 during the two different oxidation procedures, which is verified by the external check standards. The error in the analysis of the organic carbon is slightly greater than that for the inorganic carbon as it is calculated by difference. The inorganic carbon values must be regarded as maximum values as small amounts of atmospheric carbon have probably been absobed by the alkaline samples

A6 The Determination of Reduced Sulphur by Hydride Generation ICP-AES

A6.1 Instrumentation

The ICP-AES used in this work is that described in Appendix A3. A gas-liquid separator, specifically designed and built in-house, is coupled to the sample introduction assembly, replacing the nebuliser.

A6.2 Theory

The theory of the analytical technique is as described in Appendix A3, with the exception that sample is introduced as hydrogen sulphide gas. The H_2S is liberated by reaction of the sample with HCl and is separated from the solution by diffusion through a silicon rubber gas permeable membrane [1].

A6.3 Analytical methods

Reduced sulphur is determined on a sample preserved using NaOH (made up to 1% by weight NaOH). Hydrogen sulphide gas (H_2S) is liberated by reaction with 10% HCl and measured as elemental sulphur. The instrument is standardised after at least every 5

samples using a sodium sulphide standard, the concentration of which is accurately determined immediately prior to analysis by titration against standard silver nitrate.

A6.4 Data quality

Sulphide is stabilised under alkaline conditions but it is still likely that some loss will be incurred within a relatively short timescale. For this reason, reduced sulphur content is determined as soon as possible after collection of the samples.

The reduced sulphur content is determined on an unfiltered sample, as it is likely that degassing of H_2S would occur on filtration. Particulate sulphide may therefore contribute to the reported total. The reported value may also include a contribution from any organic sulphur released from solution as gaseous organic sulphur species or sulphide gas on acidification.

A7 The Determination of As and Se by Hydride Generation ICP-AES

A7.1 Instrumentation

This method ues the same instrumentation used for reduced sulphur determination (Appendix A6).

A7.2 Theory

The theory of the analytical technique is as described in Appendix A6.2, with the exception that sample is introduced as As or Se hydrides. The hydrides are liberated by reaction of the sample with $NaBH_4$ and separated from the solution by diffusion through a silicone rubber gas permeable membrane [2].

A7.3 Analytical methods

As and Se determined on a sample preserved 1% v/v with respect to HCl. Hydrides are liberated by reaction with 0.4% w/v NaBH4 and measured as elemental As and Se at emission wavelenghts of 189.042 nm and 196.090 nm respectively The instrument is standardised after at least every 10 samples. As the hydride generation is dependant on the oxidation state of the element, pretreatment of the sample to ensure that As is in its +3 and Se in its +4 oxidation state prior to analysis. For As this is achieved by pipetting 10 ml of sample + 3ml of concentrated Aristar HCl and 1 ml of 10% KI into a test tube which is left one hour before analysis. For Se the sample preparation consists of pipetting 5 ml of sample + 3ml of concentrated Aristar HCl into a test tube which is heated to 50°C in a water bath overnight. Standards samples and blanks are all prepared in the same manner.

A7.4 Data quality

The formation of the hydride can be suppressed by the presence of Ni or Cu at levels >1 mg/l. Analysis shows that these elements do not occur at such levels and the analysis should, therefore, be accurate.

A8 Determination of Reduced Iron by Colorimetry

A8.1 Instrumentation

Colorimetric measurements are made on a Phillips PU 8740 scanning UV/visible spectrophotometer.

A8.2 Theory

Iron exists in two oxidation states forming the simple ferrous-ferric redox equilibrium:

$$Fe^{3+} + e^{-} \bullet Fe^{2+}$$

The distinction and accurate determination of ferrous and ferric ions enable the redox couple and hence the redox conditions of the groundwaters to be calculated. Ferrous iron is determined colorimetrically using the chromogenic reagent 2,2-bipyridyl. Ferrous iron forms a red colour complex almost instantaneously with 2,2-bipyridyl throughout the pH range of most natural waters. The absorbance of the complex, measured at a wavelength of 520nm, is directly proportional to the concentration of Fe^{2+} in solution. The Beer-Lambert law is obeyed for all Fe^{2+} concentrations up to 250 mg/l.

A8.3 Analytical method

The samples and standards are prepared 0.1% with respect to 2,2-bipyridyl. The solution is shaken and the complex formed immediately. The colour of the complexed sample is checked visually against the prepared standards and those samples more intensely coloured than the top standard are diluted to within the calibration range (0.05mg/l to 10mg/l).

The complexed standards and samples are poured into 1cm cells and their absorbances at 520nm are recorded, running an independent 1mg/l QC standard at regular intervals. A calibration curve of the standards is plotted and the regression equation from this calibration used to calculate the ferrous iron content of the samples.

For coloured samples, eg. those with high organic contents, etc., there is the possibility of an inherent absorbance due to turbidity and the absorption of the matrix. To correct for this samples with no reagent added are measured at the same dilution as the corresponding complexed sample. The absorbance of the sample blank is subtracted from that with reagent before the result is calculated from the calibration curve.

A8.4 Data quality

Ferrous iron is rapidly oxidised in air to ferric iron, so the sampling methods used must ensure that air is excluded during sampling and filtration. Where possible 2, 2-bipyridyl colorimetric reagent is pipetted into the sample tube and the sample filtered directly into the tube so that the reduced iron is stabilised immediately. The complex stabilises the ferrous iron in solution and deterioration is considered negligible over the timescale between collection and analysis.

The validity of the data can also be checked by comparing the results for the colorimetric method with the ICP-AES results for total Fe. The value for the reduced iron should never be higher than the total Fe (within the error of the analytical measurements).

A9 Determination of Ammonium by Flow-Injection Analysis

A9.1 Instrumentation

The instrumentation used is a Tecator FIAstar 5010 analyser unit (SN 1261) with two 4-channel peristaltic pumps and injection valve controlled by a microprocessor. The unit has interchangeable Chemifold trays for different sample chemistries. The samples are fed in automatically using a 5017 Sampler (SN 3810) with 40 sampling positions and a wash station to prevent carry over from sample to sample. The absorbance of the coloured complex is measured using the 5023 Spectrophotometer (SN 1799) which is a dual beam continuous interference filter monochromator and covers a wavelength range of 400 to 700nm. The whole system is controlled by the FIAstar SuperFlow software package run on an IBM PS2 Model 30 computer.

A9.2 Theory

The sample (250 •l) is injected into a KCl carrier stream which is mixed with an EDTA/sodium hydroxide solution. This reagent has a twofold function: the high pH ensures that the ammonium in solution exists entirely as ammonia gas, and also acts as an ionic strength buffer to keep the concentration of dissolved species in samples and standards high and constant. The EDTA complexes metals to prevent precipitation of metal hydroxides which could cause blockages of the flow through system.

The joint stream passes along a PTFE semi-permeable membrane in a gas diffusion cell and the ammonia gas formed diffuses through the membrane into an indicator stream (Tectator proprietary indicator). The change in absorbance of the indicator solution, measured at 590nm, is proportional to the ammonium concentration.

A9.3 Analytical method

For each determinand an aqueous calibration of 0, 0.5 and 1mg/l is used.

The nitric acid preserved samples are run directly against aqueous standards preserved in the same manner. Matrix and inherent absorbance effects are not relevant to the determination, as it is the ammonia gas produced from the reaction which causes the change in indicator colouration. Samples are diluted only if they are outside of the calibration range.

A9.4 Data quality

The sample type and method of sampling are important in this determination. The amount of free ammonia present varies with pH. Above pH 12, the ammonium/ammonia equilibrium in solution is such that over 99% exists as free ammonia. For the samples with high pH (M1, M2, M3, and M5) there would, undoubtedly, have been losses of ammonia during the sampling although they were acidified in the field. It is not possible to give an accurate estimate of these losses and this should be taken into consideration when interpreting and presenting the data.

The technique is virtually free from interference. As the gas permeable membrane is hydrophobic, neither dissolved anions or cations can interfere with the response. However, interferences do result from volatile or filming amines in the solution, such as hydrazine, cyclohexylamine or octadecylamine; these produce an apparent increase in the ammonia concentration in the samples. It unlikely that such compounds would be found in these groundwaters.

A10 Determination of Orthophosphate by Flow-Injection Analysis

A10.1 Instrumentation

The instrumentation used is the same as that described in Section A9.1

A10.2 Theory of orthophosphate determination

The sample (250 •l) containing orthophosphate is injected into a deionised water carrier stream, and merged with a second deionised water carrier stream, which helps to minimise matrix effects. The combined stream is then mixed with an acidic ammonium molybdate solution to form a heteropoly acid, which is reduced to molybdenum blue by the addition of acidic stannous chloride in a second stream [3]. The absorbance of the reduced heteropoly blue complex is proportional to the orthophosphate concentration and measured at 690nm.

A10.3 Analytical method

The groundwater samples are run directly against aqueous standards, unless they are observed to be visibly coloured, in which case the inherent absorbance of the sample is measured and a correction for the false positive reading is made.

A10.4 Data quality

The method is relatively free from interference. Silica and As can form blue complexes which interfere but these form at a much slower rate than the orthophosphate complex and are not measured during the period that the sample is reacted and passed into the spectrophotometer of the flowing stream of the FIA technique. In this respect it should be noted that Si is very low in the groundwaters from Maqarin and therefore interference from silica is unlikely.

A11 Determination Of REE's, Th and U by Inductively Coupled Plasma Mass Spectrometry (ICP-MS)

A11.1 Instrumentation

The ICP-MS used in this work was a VG Plasmaquad 2+ in conjunction with a Gilson 222 autosampler. The system is controlled by a Compaq 386 computer through dedicated ICP-MS software. The ICP-MS operating conditions are given in the following table.

ICP-MS Operating Conditions

ICP RF forward power:	1350 W
ICP gas flow rates:	
Coolant:	13 l min^{-1}
Auxillary	1.0 l min^{-1}
Injector:	0.98 l min^{-1}
Data acquisition mode:	Scanning
Wash between samples:	120 s
Sample preflush:	120 s
Number of sweeps:	50
Collector type:	Pulse counting

A11.2 Theory

An ICP-MS consists of an ICP, which provides a source of positively charged ions, and a quadrupole mass spectrometer, which detects these ions, linked by an interface. Apart from its horizontal orientation, the ICP is essentially the same as those used in ICP-OES. Liquid samples are pumped through a nebuliser, and the resulting sample aerosol/argon mixture passes through a water-cooled spray chamber, to remove the larger droplets, before injection into the central channel of the ICP torch. At the high temperatures of the ICP (in excess of 6000•C) the sample is desolvated and substantially ionised.

The positively charged elemental ions are then extracted from the plasma into the vacuum system of the mass spectrometer. The ions first flow through a sampling orifice of 1mm diameter into a mechanically pumped vacuum system, where a supersonic jet forms. The central section of this jet flows through the skimmer orifice of 0.7 mm diameter; a series of electrostatic ion lenses transmit and focus the ions into the quadrupole mass analyser. DC and RF voltages are applied to opposite pairs of the four rods of the quadrupole. These voltages are varied such that only ions of a given mass:charge ratio will have stable paths through the rods and will emerge from the other end. By varying the DC and RF

voltages rapidly, the mass spectrometer is able to sweep across the mass range from 0 to 300 mass units in less than a second.

The ions transmitted by the quadrupole are detected using a Channeltron electron multiplier. Counts for a particular mass are accumulated for a number of sweeps across the mass range and are proportional to the concentration of that element in the sample being aspirated. The response at any mass is calibrated against standards containing a known concentration of the element of interest.

A11.3 Analytical method

The isotope channels monitored for the ICP-MS analysis are summarised in the table below.

Element	Mass
La	139
Ce	140
Pr	141
Nd	146
Sm	152
Eu	153
Gd	155
Tb	159
Dy	162
Ho	165
Er	166
Tm	169
Lu	175
Th	232
U	238

The instrument was standardised on 0 and 10 g/l of each each element. The 10 g/l standard was run as a check in the middle and at the end of the analytical run. As all the values for the 10 g/l standards were within 5%, no correction for calibration drift was considered necessary. Samples M2, M1, M3 and M5 were diluted by factors of 2, 3, 3, and 5 respectively to minimise inerferences due to matrix effects. The REE elements were re-run after passing the samples through an ion exchange procedure which gave a ten fold sample preconcentration.

A11.4 Data quality

All species preserved by acidification are considered to be stable over an appreciable length of time and certainly within the delay between sampling and analysis.

Conditions of analysis are optimised to ensure that isotope interference effects are minimised for all elements; in complex matrices the sample is diluted prior to analysis.

A12 Extraction, Reconcentration and Matrix Cleanup of Aqueous Samples for U and Th Determination by ICP-MS

A12.1 Theory

High concentrations of dissolved salts present a special challenge to the analyst determining total uranium, thorium and the rare earth elements (REE's) by ICP-MS. In order to overcome these difficulties we have attempted to use a chromatographic material

based on a supported bi-functional organophosphorus extractant (TRU-Spec; EIChroM Industries Inc. Darien, IL 60559) to preferentially extract U and Th from hyperalkaline water samples.

The five-fold dilution of these samples required to reduce matrix effects for ICP-MS effectively reduces the detection limit by a factor of 5 (to approximately <0.03 ppb from <0.006 ppb). Therefore, in an attempt to increase the practical detection limit it was decided to investigate the use of TRU-Spec resin to preferentially absorb actinides from solution prior to elution by HCl and analysis by ICP-MS. If successful this method offers the opportunity to increase the sensitivity of ICP-MS detection by a factor of 50 while considerably reducing interferences due to the presence of mono and divalent species, which have been demonstrated not to be retained by the resin.

A12.2 Method

The samples were acidified with concentrated AristaR nitric acid to a concentration of 2M and the resultant dilution factor recorded. 100 ml of each sample was then passed in parallel through 5 previously conditioned columns of TRU-Spec resin (of 1 ml bed volume; conditioned with 10 ml 0.001M HCl followed by 20 ml 2M HNO_3) at a flow rate of 4 ml/minute. The majority of interfering matrix elements and dissolved salts are unretained by the ion-exchange columns under these conditions and are eluted. After passing the sample through the column, any remaining mono and divalent cations were removed by washing with 10 ml of 2M HNO3 before elution of the retained actinides in 10 ml 0.01M HCl. The weights of collected eluate were recorded (Appendix Table A12.1) in order to allow concentration factors to be calculated. After concentration and weighing, the eluents were assayed undiluted for U and Th, by ICP-MS.

A12.3 Data quality

Results for the extraction and preconcentration of samples are shown in Appendix Table A12.1 along with appropriate factors. From these results it is evident that Standards 1 and 2 gave vastly higher concentrations of Th than expected. In the case of the spiked Th sample (Standard 2), an unrealistic recovery of >22 000% was calculated. Both this and the variable % recovery for U place considerable doubt on the methodology employed and suggest that an error had been made in the preparation of this particular standard solution. Whilst high concentrations of Th observed in the following two samples (Standard 2 and the Blank) are most probably due to sample carry over during the ICP-MS. A recovery factor for U of 52% for the sample standard (Standard 2, 0.5 ppb U, appears more reasonable.

Sample M4, previously determined to contain c.12 ppb U, deposited a significant quantity of light brown material onto the column. It is likely that this material was organic matter sorbed to the support phase through hydrophobic interaction. This brown colouration was not eluted from the column, and any associated U or Th may have remained with it, explaining the low concentration of U in the eluate (<0.002 ppb).

Initial investigations into the preconcentration of U and Th using TRU-spec resins appear hopeful. However, marked inconsistencies indicate that considerably more work needs to be done on the assessment of recoveries using both artificial and spiked natural standards, before any validity can be placed on the results produced by this study. However, the results (with the exception of that for M4) are broadly similar to those obtained by dilution of the original samples (i.e. U and Th are below 0.05 ppb in most samples. The

effect of dissolved organic carbon on these columns (e.g. M4) may be reduced by oxidising the samples by H_2O_2/HNO_3 attack prior to preconcentration.

A13 References

[1] M.R. Cave and K.A. Green, *Determination of Reduced Sulphur Content of Groundwaters by Hydrogen Sulphide Generation-inductively Coupled Plasma Optical Emission Spectroscopy,* Atomic Spectroscopy, **9**, 149-152, 1988.

[2] M.R. Cave and K.A. Green, Feasibility Study of the Determination of Iodide, Tin, Arsenic, Selenium and Hydrogen Carbonate in Groundwaters by Inductively Coupled Plasma Atomic Emission Spectroscopy Using aMembrane Gas-liquid Separator, Journal of Analytical Spectroscopy, **4**, 223-225, 1989.

[3] Q.W. Osburn, D.E. Lemmel and R.L. Downey, *Automated Method for Ortho, Ortho plus Hydrolysable and Total Phosphate in Surface and Waste Waters,* Environmental Science and Technology, **8**, 363-366, 1974.

Table A12.1 Sample preparation details and results of U and Th ICP-MS analyses

BGS No.	Column Number	Site Location	Dilution Factor to 2M HNO3	Volume Sample	Volume Collected	Concentration Factor	Measured Th Conc. (ppb)	Measured U Conc. (ppb)	Dil. Corr. Th Conc. (ppb)	Dil. Corr. U Conc. (ppb)	% Recovery Th	% Recovery U
5155	1	M1	1.144	100	10.37	8.43	0.02	0.01	0.0024	0.0012	na	na
5156	2	M2	1.144	100	12.12	7.21	0.01	0.01	0.0014	0.0014	na	na
5157	3	M3	1.144	100	10.32	8.47	-0.005	0.01	-0.0006	0.0012	na	na
5158	4	M4	1.144	70	10.26	5.96	-0.005	0.01	-0.0008	0.0017	na	na
5159	5	M5	1.144	100	10.35	8.45	-0.005	0.02	-0.0006	0.0024	na	na
5160	1	M6	1.144	100	10.29	8.49	0.01	0.02	0.0012	0.0024	na	na
5161	2	M7	1.144	100	10.34	8.45	-0.005	0.01	-0.0006	0.0012	na	na
Std 1	3	0.5 ppb Spike M3	na	100	10.41	9.61	1100	26.7	114.51	2.7795	22902%	556%
Std 2	4	0.5 ppb	na	100	10.28	9.73	126	2.53		0.2601		52%
Blank	5	na	na	100	10.35	9.66	6.08	0.05			na	na

Possible error due to high TOC
Possible contamination due to carryover during ICP-MS analysis

APPENDIX B MINERALOGICAL AND PETROLOGICAL METHODS

A.E. Milodowski, C.R. Hughes, S.D.J. Inglethorpe, A.B. McKenzie, J.M. Pearce, S.R.N. Chenery, G.E. Strong and N. Wheal.

B1 X-Ray Diffraction Analysis (XRD)

B1.1 Sample preparation

For fracture-mineralised/fracture alteration samples, a hand-held laboratory saw was used to extract a series of rectangular slices of clay biomicrite oriented parallel to external fractures. Where no fractures were apparant a representative split (cut perpendicular to bedding) of the sample was taken for analysis. The sub-samples obtained were ground to pass through a <125 •m aperture metal sieve using an automatic agate mortar and pestel and 'coned-and-quartered' and then re-combined to obtain two portions. One portion was used for bulk rock X-ray diffraction analysis (XRD), thermogravimetric analysis (TG) and evolved gas analysis (EGA). The other portion was used for the carbonate dissolution procedure (Section B1.2) and subsequent extraction and XRD analysis of a nominal <2 •m fraction.

Fracture-fill material was removed by gentle scraping of the fracture coatings on the external surfaces of samples and the extracted material was then hand-ground to a powder using a small agate mortar and pestel.

B1.2 Carbonate removal and separation of <2 •m 'clay' fraction

Carbonate removal

To enable the liberation and subsequent extraction of clay minerals an acid digestion method was used to remove the dominant carbonate matrix present in the samples.

5 g of the <125 •m sub-sample were added to 200 ml of 1M sodium acetate solution buffered with acetic acid at pH5.3; carbonates enter solution at this pH but clay minerals remain unaltered. The resulting suspensions were agitated for 6-8 hours at 60•C using a heated ultrasonic bath and then left overnight. The suspensions were then centrifuged and the supernatant liquid removed by decantation. Further 200 ml additions of buffered sodium acetate/acetic acid were added and the procedure repeated until no further reaction was evident. When carbonate dissolution was complete, the residues were shaken for 5 minutes with 200 ml deionised water, centrifuged and the supernatant liquid removed by decantation. This was repeated several times to thoroughly wash the residues.

Clay separation

When dispersed in water, the clay component of a sample is generally present in the particle size range below 2 •m, and so clay minerals can usually be concentrated and extracted by separation of the < 2•m fraction. This was carried out using a conventional sedimentation method. The washed residue after carbonate removal was dispersed thoroughly in 250 ml of deionised water in a measuring cylinder. The resulting suspension was then left undisturbed to allow the sedimentation of particles in accordance with Stokes' Law, which states that the sedimentation or settling rate of a particle is proportional to the square of its 'equivalent diameter'. This principle was thus used to determine a suitable settling time and the corresponding sedimentation depth for a particle of 2 •m diameter. The < 2•m fractions were then obtained by decantation of part of the suspension above a fixed level in the measuring cylinder, after allowing the suspensions to sediment for the appropriate period of time. This operation was repeated until no

further <2 •m material was recovered from the suspensions. The total quantity of <2 •m material recovered from each residue was dried at 55°C and weighed. The mass proportion of <2 •m fraction was then calculated as a percentage of the mass of starting material prior to carbonate removal (Chapter 5, Table 5.5).

B1.3 Bulk rock, fracture-fill and <2 •m fraction X-ray diffraction analysis (XRD)

X-ray diffraction (XRD) analyses were carried out on a Philips 1700 series automatic diffractometer using Co-K radiation and operating at 45kV and 40mA. Diffraction traces were analysed using Philips APD1700 software coupled to a Joint Committee on Powder Diffraction Standards (JCPDS) database running on a DEC MicroVax 2000 computer system.

Larger bulk rock samples were examined after first reducing 5 g of the <125 •m sub-samples to a uniform particle size by micronising under acetone. The micronised powders were back-loaded into aluminium holders. Samples were examined over an angular scanning range of 3-50° 2• at a scan speed of 0.9° 2•/minute. Fracture-fill samples were first prepared by mounting a small amount of material onto a silicon wafer substrate and then analysed under identical conditions to the bulk rock samples. Qualitative mineral compositions of bulk and fracture-fill samples were obtained using JCPDS search procedures. Additionally, to aid the identification of clay minerals in bulk rock samples, orientated mounts (prepared by sedimentation of a suspension onto silicon wafers) of prepared <2 •m fractions (Section B1.2) were analysed by XRD over an angular scanning range of 2-35° 2• at a scanning speed of 0.75° 2•/minute.

B2 Thermogravimetric Analysis (TG)

Thermogravimetric analysis (TG) were carried out using a Stanton Redcroft TG770 microthermobalance. Weight loss curves were produced by heating c.10 mg samples at 50°C/minute in a flowing CO_2 atmosphere. Calcite ($CaCO_3$) contents were calculated from the weight loss obtained between 800-1050°C associated with the decomposition of calcite and evolution of CO_2.

$$CaCO_3 \bullet CaO + CO_2 \quad \text{(equivalent to 44\% weight loss)}$$

B3 Evolved Gas Analysis (EGA)

Evolved gas analysis was used to attempt to quantify those minerals that released or generated volatiles on heating as a result of desorption, decomposition or oxidation reactions. The identification and quantification of minerals in natural mixtures by this method requires that the volatile evolution occurs in a well-defined manner over a distinct temperature range. These criteria are normally met for the thermal decomposition of common simple carbonate minerals, and sulphide minerals such as pyrite, enabling detection down to very low levels of 50 ppm [1]. Unfortunately, for CSH minerals the volatile evolution profiles (H_2O) are less distinct and are not unique, because of their similarities in chemical properties and their often poor crystallinities - which means that the evolution of adsorbed water, water of crystallisation and structurally-bound water is ill-defined. Therefore quantification of the CSH minerals by EGA proved impossible.

The EGA system used was a modified version of that described by Morgan [2], using a tube furnace rather than DTA furnace and with the addition of NH_3 and CO detectors. A 25-100 mg sample was heated in a Stanton Redcroft tube furnace controlled by a Cambridge Process Controls temperature programmer. The samples were continuously heated at 20°C/minute from 20° to 1050°C. Volatiles generated by the sample were

swept from the furnace by a 2:1 N_2:O_2 carrier gas at a flow-rate of 300 ml/minute, regulated by a Brooks Instruments mass flow controller unit. The concentrations of five volatiles in the carrier stream were continuously monitored by passing the carrier gas through five in-series non-dispersive infrared (NDIR) analysers capable of specifically detecting H_2O vapour, CO_2, CO, SO_2 and NH_3, and recording the output from the NDIR detectors using an external chart recorder. The mass of evolved gas was determined by measurement of peak areas for each volatile evolution profile.

Percentage mineral proportions were calculated as follows:

(i) Calcite content was calculated from the mass of CO_2 evolved between 650-900°C (Equation 1).

(ii) Organic carbon content was calculated from the mass of CO_2 and CO evolved in two stages between 250-600°C (Equation 2).

(iii) Organic sulphur content was calculated from the mass of SO_2 evolved at 300-400°C (Equation 3).

(iv) Pyrite content was calculated from the SO_2 evolved between 400-500°C (Equation 4).

Equation 1:

Calcite decomposition: $CaCO_3$ • CO_2 + CaO

Molar proportions: 1M 1M

Molecular weight: 100.08 44.01

Mass of calcite = mass evolved CO_2 x (100.08/44.01)

Equation 2:

Molecular weight CO_2 = 44.01

Molecular weight CO = 28.01

Atomic weight C = 12.01

Mass of organic carbon = [mass evolved CO_2 x (12.01/44.01) + mass evolved CO x (12.01/28.01)]

Equation 3:

Molecular weight SO_2 = 64.06

Atomic weight S = 32.06

Mass of organic sulphur = mass of evolved SO_2 x (32.06/64.06)

Equation 4:

Pyrite oxidation: $4FeS_2 + 11O_2$ • $8SO_2$ + $2Fe_2O_3$

Molecular proportions: 1M 2M

Molecular weight: 119.98 128.12

Equivalent pyrite = mass evolved SO_2 x (119.98/128.12)

B4. Optical Petrography

Optical petrographic analysis was carried out by examination of polished thin-sections of rock in transmitted light using a Zeiss Universal petrological microscope. Polished sections, rather than standard covered thin sections, were used so as to facilitate their subsequent study by backscattered scanning electron microscopy (Section B5), electron microprobe (Section B6) and fission track analysis (Appendix C). The sections were prepared after impregnation of the rocks and fracture mineralisation with an epoxy-resin to consolidate the friable materials. A blue dye was added to the epoxy-resin to enable the presence of porosity within the sample to be more easily distinguished when examined optically.

B5 Backscattered Scanning Electron Microscopy (BSEM)

After optical examination, the polished thin sections were studied by backscattered scanning electron microscopy (BSEM). BSEM observations were made using a Cambridge Instruments Stereoscan S250 Mark I SEM instrument equipped with a KE Developments 4-element solid-state backscattered electron detector. Mineral identification was made by qualitative examination of the characteristic energy-dispersive X-ray spectra (EDXA) recorded during observation of a given phase, with a Link Systems 860 Mark I energy-dispersive X-ray spectrometer fitted to the electron microscope. Observations were made at 20kV electron beam excitation. The EDXA system has a detection limit of approximately 0.2% (weight) for most common elements but this is probably of the order of 0.5% (weight) for uranium, thorium and lanthanides. The polished sections were coated with a thin layer of carbon (c.250Å thick) prior to examination in the SEM in order to make the surface electrically conductive.

The theoretical aspects of SEM techniques and their interpretation are discussed in detail by Goldstein et al. [3] and the salient points of BSEM are outlined below. In BSEM mode the image obtained from polished sections is related to the composition of the material being examined. Image brightness is proportional to a combination of the average atomic number of the material and its density, thus allowing the distribution of different minerals or phases to be determined on the basis of their chemical composition. BSEM has much finer resolution than conventional optical petrographic techniques and, coupled with semi-quantitative/qualitative EDXA (which allows chemical discrimination), is particularly useful in the study of fine-grained rocks [4],[5],[6]. It proved to be an extremely useful technique during the initial Phase I natural analogue study, for examining the fine-grained alteration characteristic of rocks from the Maqarin site [7].

B6 Electron Microprobe Analysis (EMPA)

Electron microprobe analyses (EMPA) were undertaken to determine the major element (and some trace element) compositions of individual mineral phases in polished thin sections. Also by using a defocussed beam, the variation in the approximate, ‘average (areal) fine-grained rock matrix composition’ was obtained by EMPA for a series of profiles across polished thin sections; from fracture surfaces, across the wallrock alteration zone, and into the unaltered wallrock.

Most EMPA was performed on a Cameca SX50 electron microprobe using wavelength dispersive spectrometers. The electron microprobe was calibrated using mineral, synthetic oxides, and metal standards. The spectrometers and data aquisition were computer controlled, and the data obtained were processed using Cameca software.

Quantitative weight percent concentrations of the elements Ca, Al, Si S, P, Mg, Fe and Cl were determined with spectrometer peak counting times for each element chosen based upon the anticipated concentrations in the samples. For example, Ca concentrations are high in the wallrock and the peak counting time for Ca was 10 seconds. Iron concentrations are low and hence the peak counting time for Fe was 60 seconds to improve the accuracy of results. Analyses were made with a 20 kV electron beam with a beam diameter of 40 •m. A large beam diameter was chosen to obtain an average composition of the wallrock at a given distance from the fracture wall. This beam diameter also minimised damage to heat-sensitive phases that may be present. Analysis positions were recorded on BSEM photomosaics to facilitate analysis of the same areas by LA-ICP-MS (Section B8) and the distance from the fracture wall determined by direct measurement from the BSEM images. Mineral phases infilling fractures were also analysed under the same conditions.

Additional EMPA of mineral phases in thin section were also determined by energy-dispersive EMPA using a Cambridge Instruments Microscan V instrument fitted with a Link Systems AN10000 energy-dispersive X-ray microanalysis system. Analyses were made using a 15 kV electron beam focussed to approximately 2 •m diameter and 60-100 second livetime counting times (with beam currents adjusted to give less than 30% deadtime). Data were processed using Link Systems ZAF software. The instrument was calibrated using mineral, synthetic oxides, and metal standards, and internally standardised using a cobalt metal reference.

B7 Analytical Transmission Electron Microscopy (ATEM)

B7.1 Background to Analytical Transmission Electron Microscopy (ATEM)

Previous work [8] has demonstrated that the only way to obtain quantitative analytical data from individual phases in mixtures of ultra-fine material is by ATEM. With this technique, quantitative compositional, crystallographic and morphological data can be obtained from individual crystal fractions less than a micron in size.

The development and limitations of quantitative ATEM are described by Lorimer and Cliff [9] and Lorimer [10]. More detailed accounts of the limitations are available in the following texts: Lorrimer et al. [11], Scott and Love [12], Loretto [13] and Joy et al. [14]. A thorough examination of sources of experimental error which are particularly appropriate in the ATEM examination of phyllosilicates is given by Hughes et al. [15]. The method assumes that in sufficiently thin mineral sections, incident beam electrons lose little energy. Consequently, X-ray absorption and fluorescence matrix effects can be assumed to be negligible. When this ‘thin film’ criterion is satisfied, the ratio of any two characteristic X-ray peak intensities I_A/I_B is related to the corresponding weight fraction ratio C_A/C_B by the equation:

$$C_A/C_B=k_{AB}(I_A/I_B)$$

where k_{AB} is a value (‘k’ value) which accounts for the relative efficency of the system in terms of X-ray production and detection. In a sample containing detectable elements, a normalisation procedure (eg CN = 1) can be used to convert element ratios to conventional weight percentages. To calculate mineral formulae, assumptions must be made for elements not detected. Mineral formulae presented here are calculated only as empirical formulae, re-calculated to a fixed number of ions of one of the components (e.g. Si or Ca) based on the identity of the phase and assuming an ideal stoichiometry.

ATEM analyses were carried out using a Philips 400T transmission electron microscope (TEM) with EDAX energy-dispersive X-ray microanalysis. X-ray emission spectra were processed according to the thin-film method of Cliff and Lorimer [16]. The ATEM system at Manchester University has been calibrated for the analysis of phylosilicates by determining proportionality constants relative to silicon from ultra-thin sections of standard micas.

Ultra-thin sections of the samples were prepared following the ion-etching technique of Phakey et al. (1972). This method of analysis does not facilitate the rapid aquisition of representative chemical data as readily as from dispersed mounts but does allow the crystallographic, ultra-micropetrographic and textural relationships of different phases to be examined (cf. Hughes et al., [17])

B7.2 Limitations of ATEM

X-ray counting statistics impose a fundamental limit in ATEM. The excitation volume is very small, often <0.05 •m^3, hence sensitivity is low. The procedure used in Manchester usually gives a precision of better than 5% for major detectable elements, falling to about 11% for minor components. Data for elements present in concentrations <5% by weight are of qualitative value only and values <0.5% are considered ambiguous. Thermolabile elements, specially Na and K, are not readily quantified in ATEM unless some account is made of the mobility under the operating conditions used (a cryogenic stage offers currently the best solution to this problem, for discussion see references above). During the analysis of clay phases, especially smectites, additional problems with the quantification of Na and K occur because of the common presence of ultra-fine salts admixed with clay laths. Indeed, even in the TEM smectite laths cannot always be sufficiently isolated to negate this sort of contamination. As a consequence, concentrations of Na and K in smectites are rarely given with confidence.

B8 Laser Ablation Microprobe Inductively-Coupled Plasma - Mass Spectrometry (LAMP-ICP-MS)

B8.1 Instrumentation and methodology

Laser ablation microprobe - inductively coupled plasma - mass spectrometry (LAMP-ICP-MS) analyses were carried out on three selected polished thin sections of samples of clay biomicrite showing wallrock alteration adjacent to fractures, and of a selected suite of major secondary minerals from the Maqarin site, in order to determine their trace element composition at lower levels than is possible by conventional EMPA techniques. The method works on the principle that the test material is placed in an ablation cell and a small amount of sample is removed by ablation with a laser. The ablated material is then introduced into the ICP-MS and elemental ratios determined.

LAMP-ICP-MS analysis was undertaken by BGS using a purpose-built laser ablation microprobe system designed and built for BGS by the Department of Chemistry, Birkbeck College, University of London. The system is based on a Spectron Nd YAG ultra-violet laser system operating linked to a high-quality Leitz optical microscope. The laser-microscope system utilises a custom-designed laser ablation chamber, with an optical quartz window, which is flushed by an Ar carrier gas stream. The argon stream transfers ablated material to a ICP-MS, via a polythene tube that connects the ablation cell to the ICP torch in a VG Plasmaquad 2+ spectrometer, using a modified dual-flow sample introduction system described in Chenery & Cook [18]. The LAMP-ICP-MS used by BGS achieves both very small beam diameters (down to 4 •m craters) and very good

detection limits (sub-ppm levels detectable using 40 •m craters). The design and basic operation of the LAMP are described in UK Patent No. 91066337.0, Serial 2254444, and by Chenery & Cook [18]. The VG Plasmaquad 2+ ICP-MS spectrometer instrument is described in Appendix A11, and is capable of detecting ions in the mass range 6-250 amu. The instrumentation is controlled by a Compaq 386 Model 20e computer through dedicated ICP-MS software, with analytical results being stored automatically on the hard disc.

Aqueous LAMP-ICP-MS standards for calculating elemental/isotopic sensitivities are usually made up from commercial multi-element ICP-standards that are certified and traceable to international standards. Individual element solutions of appropriate quality may be used if chemical compatibility or calibration ranges require this. Background data are aquired for each sample analysis, and standard and LAMP-ICP-MS spectra are processed using Time Resolved Analysis (TRA) software (version 3.2.1A). Using TRA software, each spectrum is plotted as response versus time. The spectrum is divided into two or more parts of equal time. These parts represent peaks and background and are then integrated and saved as separate files.From the background signal a detection limit (d.l.) and a quantification limit (q.l.) are calculated. If the background counts are less than 10000 the d.l. is 3 standard deviations calculated from Poissonian statistics, but if the background counts are greater than 10000 then the d.l. is taken to be 9% of the background. The q.l. is taken to be 10 standard deviations for a background signal of less than 10000 counts and 30% of the background signal of greater than 10000 counts.

LAMP-ICP-MS data are determined in terms of elemental ratios. Data from EMPA from the same areas of the sample were used to convert these values to absolute concentrations. For this purpose Ca was chosen as the internal standard since it could be measured appropriately by both LAMP-ICP-MS and EMPA.

LAMP-ICP-MS is a relatively ‘young’ analytical tool and its application in this project, for estimating gross trace element variations in areas of rock matrix along profiles away from fracture surfaces, is an unique trial. Therefore, potential problems with the quality of the data are discussed in more detail below.

B8.2 Evaluation of data quality

General observations

When evaluating the accuracy and precision of the LAMP-ICP-MS data from the Maqarin natural analogue site materials, the degree of homogeneity of the test material is of crucial importance. To minimise any `nugget effects' associated with minor phases, the laser beam was rastered over a 50 •m x 50 •m area, with a typical ablation depth of 5-10 •m. However, this will not completely solve the problem of representative sampling. Assuming that the test material has a relative density of 3, the typical mass of material ablated was 10^{-7} g, while the usual minimum mass analysed after conventional acid decomposition is 0.1 g. Obviously the sampling effect will be least for major elements such as Mg, Al and Fe, and is also likely to be at a minimum for trace elements isomorphic with major elements (e.g. Sr and Ba for Ca in calcite). The problem is likely to be greatest for elements such as the high field strength elements, rare earth elements, uranium and thorium, which are often associated with discrete minor microphases.

A specific problem was found with the calibration for sample A965. Unfortunately, the concentration of Ca in the standard solution was not high enough to give a sensible calibration point above the background. This was a potentially serious problem as Ca was

the internal standard element. However, it was possible to use the glass reference material, normaly run as an accuracy check, to determine the Ca sensitivity.

Element specific comments

Si Not reported due to excessively high detection limits.

Mg/Al/Fe All at major element levels and well above their detection limits. Should provide good data despite being in regions of the mass spectrum with various polyatomic background interferences.

Mn Although at relatively low levels, tens of ppm, in most cases, it is well above detection limits and should provide reasonable data.

Cr Normally a relatively poor element because of polyatomic backgrounds. This is reflected in detection limits often in the 100+ ppm level. However, in most cases the concentrations determined were in the hundreds of ppm and gave significant results, although precision might be a problem.

Co The levels are very low in the majority of caes and this is reflected in the number of values below the quantification limit. Numbers below the quantification limit must be treated as a guide only.

Cu/Zn Poorer detection limits due to polyatomic backgrounds. The typical concentrations of tens of hundreds of ppm should provide reliable data. A potential complication in the determination of Cu is the polyatomic interference from $^{40}Ar^{23}Na^{+}$; assuming there are no sodium rich minerals this should not be a problem.

Sr/Ba These elements should give excellent determinations. The only problem is that of representative sampling if small grains of barite, strontianite, celestite or hashemite are present.

Pb/U These elements have very good detection limits, although their concentrations in the samples are not particularly high (i.e. 1-20 ppm), but this should not be a major problem, except when ablating small masses of material. An additional potential problem with U might be its association with an organic phase (such as is present in the bituminous marls and limestones at Maqarin - cf. organic extraction experiments from Phase I [7], which might result in preferential ablation of the U (and any other trace elements associated with the more volatile organic components).

Th Very low abundance in the samples (i.e. <3 ppm), but very good detection limits are possible. The mass of material available from the ablation will be the limiting factor.

Specific comments on accuracy and precision of data

Two specific methods were available for determining accuracy and precision of the data, although neither was ideal. The first was a comparison of LAMP-ICP-MS trace elemental determinations of concentrations in the bulk wall rock from broad areal analyses from thin sections, with bulk determinations on solutions of whole rock powders. This comparison is shown in Appendix Table B1. The agreement for sample A960 was good except for: Ba - which might have been held in discrete grains of barite (confirmed by BSEM-EDXA petrography); Zn - for which there is currently no explanation for the lower results obtaned by LAMP-ICP-MS (although traces of discrete

Zn-rich clays were identified); and U, which was thought to be associated at least in part with organic matter (confirmed by fission track analyses - Chapter 8) and would therefore have undergone preferential ablation. For sample A965, a comparison of LAMP-ICP-MS data with three sub-samples of this wall rock shows good general agreement except for Al, Mg, Cu and Zn. In this case the LAMP-ICP-MS data were lower for Al and higher for Mg, Cu and Zn. The most reasonable explanation for the difference between the two data sets may be sampling error. Mg, Cu, and Zn are enriched near to fracture walls in A960 and LAMP-ICP-MS analayses will be biased towards this material in the thin sections. In contrast the bulk rock solution data set will have sampled a much larger sample away from the main wallrock alteration.

Comparison of the data obtained from the bulk and thin section wall rock was a suitable measure of accuracy because the matrix was similar in each case. However, LAMP-ICP-MS data from the thin section would be a poor measure of instrumental precision because of the problem of sampling polymineralic mixture systems. To overcome this problem a certified glass reference material SRM611 from the National Institute of Standards and Testing (NIST) was ablated a number of times, at very different laser powers, thus removing different amounts of test material each time, and simulating a realistic analysis session. The data were processed in exactly the same way as the samples. The data were inspected and those either below quantification or producing non-linear responses due to excessive masses of ablated material were discarded. The remaining 12 ablations were used to construct Appendix Table B2. Table B2 presents the expected concentration and the mean of the results, together with the precentage error of the mean compared to expected, and the relative standard deviation (RSD). The RSD for most elements is between 10% and 20% of the determined concentration, with the exception of Zn, for reasons unknown. Iron is not reported because the concentrations are below the detection limit. The accuracy, as defined by the percentage error, varied widely between ±60%. The error also appeared to be mass dependent, with light elements being low and heavy elements high. Again, as yet, we have no explanation for this observation. The results for precision were as expected, but those for accuracy were disappointing. Whether the accuracy depends on the matrix requires further investigation.

B9 Natural Decay Series Radionuclide Analysis

Natural decay-series radionuclides (NDS) analysis was undertaken on a limited selection of 9 samples from Maqarin and central Jordan. The aim was both to examine the uranium mobility and disequilibrium associated with the hyperalkaline groundwater interaction with the marl , and to attempt to date well characterised secondary fracture minerals in order to try to place constraints on the timescale over which the Maqarin and central Jordan analogue systems have been active. The samples analysed included:

(i) Hand-picked mineral separate essentially comprising vein fillling ettringite-thaumasite (containing other vein minerals - calcite, wairakite/mordenite and gypsum, as contaminants) from sample A960 (Adit A6, Maqarin).

(ii) Altered wallrock from A960 (Adit A6, Maqarin).

(iii) Hand-picked single mineral separate of vein-filling tobermorite from sample A962 (Adit A6, Maqarin).

(iv) Wallrock adjacent to tobermorite vein in A962 (Adit A6, Maqarin).

(v) Wallrock 3 cm distant from tobermorite vein in A962 (Adit A6, Maqarin).

(vi) Hand-picked mineral separate essentially comprising vein-fillling jennite (with minor amounts of vein ettringite-thaumasite and chrome-smectite mineralisation) from sample A965 (Adit A6, Maqarin).

(vii) Wallrock adjacent to jennite vein in sample A960 (Adit A6, Maqarin).

(viii) Whole rock sample of lower silicified travertine essentially composed of secondary silica and later secondary calcite and chrome clay and little or no obvious detrital components. Sample A974 (Khan-ez-Zabib, central Jordan).

(ix) Whole rock sample of upper silicified travertine essentially composed of secondary silica and later secondary calcite and chrome clay and no obvious detrital components. Sample A9746 (Khan-ez-Zabib, central Jordan).

NDS analyses were carried out at the Scottish Universities Research and Reactor Centre (SURRC), East Kilbride, Scotland. The analysis of the natural decay series radionuclides was performed by alpha spectroscopy based on the method described by Bacon and Rosholt [19]. Powdered samples were divided into two sub-samples, one of which was spiked with $^{232}U/^{228}Th$ yield tracer (Harwell certified standard) and the other was left unspiked for determination of the natural $^{228}Th/^{232}Th$ activity ratio. The samples were dissolved in teflon beakers using HCl, HNO_3 and HF. After dissolution, the samples were taken up in 8M HCl and Fe extracted using di-isopropyl ether. Thereafter, uranium was extracted using Bio-Rad AG1x8 anion exchange resin in the chloride form and thorium using AG1x8 resin in the nitrate form. Thin sources were prepared by electrodeposition of the uranium and thorium onto stainless steel planchettes. Alpha spectroscopy was performed using a Canberra Quad Alpha Spectroscopy System. Correction was made for the natural ^{228}Th contribution to the spiked sample spectrum on the basis of the $^{228}Th/^{232}Th$ ratio of the unspiked sample.

Estimation of the ages was based upon the ingrowth of ^{230}Th as described by Ivanovich et al. [20].

B10 Quantitative Image Analysis

Quantitative analysis of mineral phases in rock specimens was undertaken using image analysis techniques on BSEM photomicrograph images. This study was carried out in order to determine variations (if any) of mineral species with distance from a mineralised vein.

Each grey-scale backscattered image was scanned using a Logitech 256 grey-level hand scanner, and transferred to a Kontron Image Analysis System for grey-level segmentation and analysis [21]. An image analysis procedure (macro programme) was custom-designed for this study, and allowed semi-automated generation of data for each image analysed. The data were stored in free-text format for processing using commercial spreadsheet software on an IBM-compatible PC, and presented as line charts.

B11 References

[1] A.E. Milodowski and D.J. Morgan, *Identification and Estimation of Carbonate Minerals at Low Levels by Evolved CO_2 Analysis*, Nature, **286**, 248-249, 1980.

[2] D.J. Morgan, *Simultaneous DTA-EGA of Minerals and Natural Mineral Mixtures,* Journal of Thermal Analysis, **12**, 245-263, 1977.

[3] J.I. Goldstein, D.E. Newbury, P. Echlin, D.C. Joy, C. Fiori and E. Lifshin, *Scanning Electron Microscopy and X-ray Microanalysis: A Text for Biologists, Materials Scientists and Geologists*, Plenum Press, 1981.

[4] D.H. Krinsley, K. Pye and A.T. Kearsley, *Application of Backscattered Electron Microcopy in Shale Petrology,* Geological Magazine, **120**, 109-118, 1983.

[5] J.M. Huggett, *An SEM Study of Phyllosilicates in a Westphalian Coal Measures Sandstone using Backscattered Electron Imaging and Wavelength-dispersive Spectral Analysis,* Sedimentary Geology, **40**, 233-247, 1984.

[6] K. Pye and D.H. Krinsley, *Petrographic Examination of Sedimentary Rocks in the SEM using Backscattered Electron Detectors,* Journal of Sedimentary Petrology, **54**, 877-888, 1984.

[7] W.R. Alexander, *A Natural Analogue Study of the Maqarin Hyperalkaline Groundwaters. I. Source Term Description and Thermodynamic Database Testing*, NAGRA Technical Report, NTB 91-10, 1992.

[8] C.R. Hughes, *The Application of Analytical Transmission Electron Microscopy to the study of Ozolitic Ironstones: A Preliminary Study*,in Phanerozoic Special Publication of the Geographical Society, **46**, 121-131, 1989.

[9] G.W. Lorimer and G. Cliff, *Quantitative X-ray Microanalysis of Thin Sections,* Proceedings 25th Scottish School in Physics, University of Edinburgh, 1984.

[10] G.W. Lorimer, *Quantitative X-ray Microanalysis of Thin Sections in the Transmission Electron Microscope: A Review*, Mineralogical Magazine, **51**, 49-69, 1987.

[11] G.W. Lorimer, M.H. Jacobs and P.Doig, *Quantitative Microanalysis with High Spatial Resolution*, The Metals Society, 1981.

[12] V.D. Scott and G. Love, *Quantitative Electron-Probe Microanalysis,* Ellis Horwood, 1983.

[13] M.H. Loretto, *Electron Beam Analysis of Materials*, Chapman and Hall, 1984.

[14] D.C. Joy, A.D. Romig and J.I. Goldstein, *Principles of Analytical Electron Microscopy,* Plenum Press, 1986.

[15] C.R. Hughes, C.D. Curtis, J.A. Whiteman, Sun Heping, C.K. Whittle and B.J. Ireland, *Selected Applications of Analytical Electron Microscopy in Clay Mineralogy,* Clay Mineral Society Workshop Lectures, **2**, 69-88, 1990.

[16] G. Cliff and G.W. Lorimer, *The Quantitative analysis of Thin Specimens*, Journal of Microscopy, **103**, 203-207, 1975.

[17] C.R. Hughes, R.C. Davey and C.D. Curtis, *Chemical Reactivity of some Reservoir Illites: Implications for Petroleum Production,* Clay Minerals, **24**, 445-458,1989.

[18] S. Chenery and J.M. Cook, *Determination of Rare Earth Elements in Single Mineral Grains by Laser Ablation Microprobe-inductively Coupled Plasma Mass Spectrometry,* Journal of Analytical Atomic Spectroscopy, **8**, 299-303, 1993.

[19] M.P. Bacon and J.N. Rosholt, *Accumulation Rates of Th-230, Pa-231 and Some Transition Metals on the Bermuda Rise,* Geochimica and Cosmochimica Acta, **46**, 651-666, 1982.

[20] M. Ivanovich, A.G. Latham and T.L. Ku, *Uranium Series Disequilibrium Applications in Geochronology,* in *Uranium Series Disequilibrium: Applications to Environmental Problems,* Oxford University Press, 1982.

[21] G.E. Strong, *SEM to KONTRON Image Transfer Using a Logitech Hand Scanner and Conversion Software*, British Geological Survey, Mineralogy and Petrology Group Short Report, MPSR/92/91, 1992.

Table B1 Comparison of ICP-AES and ICP-MS solution data with LAMP-ICP-MS

Sample/Method:	A960/soln.	A960/LAMP	A965/soln.	A965/1 soln.	A965/2 soln.	A965/LAMP
Al (%)	1.21	1.10	1.08	0.27	0.84	0.17
Fe (ppm)	8970	8200	5770	4670	4340	4640
Mg (ppm)	1230	1662	930	1910	1100	2695
Sr (ppm)	870	883	1050	1180	987	1100
Ba (ppm)	174	8	88	124	51	77
Mn (ppm)	30	33	35	34	26	27
Cr (ppm)	445	693	123	198	266	360
Co (ppm)	<20	3	<20	<20	<20	14
Cu (ppm)	58	63	57	27	<20	92
Zn (ppm)	446	148	166	203	142	497
Pb (ppm)	<60	8	<60	<60	<60	2
Th (ppm)	1.8	1.3	0.79	1.07	0.9	0.72
U (ppm)	32	60	12	13	12	14

Notes:

'soln.' refers to data derived by ICP-AES and ICP-MS from conventional rock-dissolution method

'LAMP' refers to data derived by laser-ablation microprobe ICP-MS.

A965/soln. = analysis of whole rock sample of background bituminous biomicrite. A965/1 soln. and A965/2 soln represent analyses of thin slices of wallrock taken immediately adjacent (0-2cm) to fracture surface and will correspond most closely with the region of the sample from which A965/LAMP data have been obtained.

Table B2 Accuracy and precision data for replicate LAMP-ICP-MS analyses of SRM611

	SRM Value	Mean	% Error	Std. Dev.	% RSD
Mg-24	500	355	-29	45	12.8
Al-27	10588	7189	-32	565	7.9
Si-28	336000	134449	-60	13686	10.2
Ca-42	85717	68563	-20	83752	122.2
Ca-44	85714	85714	0	0	0.0
Cr-52	500	605	21	69	11.4
Mn-55	485	649	34	98	15.1
Fe-57	459	1756	283	2897	165.0
Co-59	390	596	53	108	18.1
Cu-63	444	714	61	94	13.2
Zn-66	433	698	61	298	42.7
Sr-88	516	615	19	70	11.3
Ba-138	500	535	7	58	10.9
Pb-208	426	611	43	61	10.1
Th-232	457	663	45	58	8.7
U-238	462	632	37	104	16.5

Note:

Assumes Ca-44 = 85714 ppm in SRM611

Table B3 EMPA and LA-ICP-MS data for selected fracture infilling minerals From Maqarin.

PHASE	Jennite	Jennite	Jennite	Jennite	Jennite	Jennite	Jennite	Jennite	Jennite	Jennite	Jennite	Ettringite	Ettringite	Ettringite	Ettringite
Point	LA965/1	LA965/2	LA965/3	LA965/4	LA965/6	LA965/8	LA965/21	LA965/22	LA965/24	LA965/25	LA965/27	LAM91/1	LAM91/2	LAM91/3	LAM91/4
EPMA Data															
Mg	n/a	n/a	0.06	0.01	0.04	0.05	0.07	0.04	0.05	0.03	0.03	0.00	0.00	0.00	0.00
Al	n/a	n/a	0.05	0.06	0.09	0.08	0.37	0.09	0.10	0.10	0.12	1.19	1.19	1.19	1.19
Si	n/a	n/a	16.68	16.27	16.26	16.41	15.97	16.28	16.38	15.93	15.76	0.14	0.14	0.14	0.14
Ca	n/a	n/a	33.88	34.34	34.27	34.76	33.51	34.82	35.26	34.65	33.68	18.97	18.97	18.97	18.97
Fe	n/a	n/a	0.00	0.00	0.00	0.00	0.09	0.00	0.02	0.00	0.00	0.00	0.00	0.00	0.00
P	n/a	n/a	0.35	0.38	0.39	0.37	0.39	0.40	0.40	0.37	0.40	0.02	0.02	0.02	0.02
S	n/a	n/a	0.06	0.07	0.12	0.06	0.32	0.05	0.04	0.08	0.28	10.22	10.22	10.22	10.22
Cl	n/a	n/a	0.04	0.03	0.04	0.04	0.04	0.02	0.02	0.02	0.09	0.73	0.73	0.73	0.73
LA-ICP-MS Data															
Mg	298	264	248	172	301	163	582	177	206	205	226	192	111	130	506
Al	6949	46952	538	632	640	410	1346	1511	341	2139	439	66000	64000	49000	38000
Si	109353	31669	133279	148041	155541	130433	132014	138063	137100	127817	132520	<0.6%	<0.6%	<0.4%	*0.60%*
Ca	330000	330000	338800	343400	342700	347600	335100	34200	352600	346500	336800	190000	190000	190000	190000
Cr	N/A	*80*	408	193	310	29	324	60	233	135	31	*27*	*13*	<7	*9*
Mn	15	*9*	*9*	8	8	8	12	11	9	8	7	<2	<1.2	<0.8	4
Fe	883	2380	316	464	143	339	929	709	504	482	*28*	516	128	462	555
Co	N/A	*1*	*2*	*1*	*1*	*0.50*	*0.22*	*0.31*	*0.35*	0.40	*0.36*	<0.6	*0.7*	*0.7*	<0.5
Cu	21	42	14	19	5	13	13	11	10	12	12	8	<1.7	4	6
Zn	1526	60	158	29	432	38	240	1095	203	16	42	*10*	n.d.	*2*	12
Sr	156	786	137	73	326	80	293	31	256	110	180	744	617	474	313
Ba	8	5	11	4	12	3	16	4	8	4	8	29	19	17	4
Pb	4	6	5	2	3	*1*	2	4	2	1	2	15	5	9	21
Th	*0.46*	*2*	*2*	*1*	*1*	*0.37*	*0.18*	*0.02*	0.28	*0.19*	*0.27*	n.d.	n.d.	n.d.	n.d.
U	9	*2*	14	13	19	15	29	14	18	23	22	9	8	5	0.48
Ionic Proportions															
Ca^{2+}	n/a	n/a	8.54	8.87	8.86	8.90	8.82	8.99	9.05	9.15	8.99	6.00	6.00	6.00	6.00
Al^{3+}	n/a	n/a	0.02	0.02	0.03	0.03	0.14	0.03	0.04	0.04	0.05	0.56	0.56	0.56	0.56
SO_4^{2-}	n/a	n/a	0.02	0.02	0.04	0.02	0.11	0.02	0.01	0.03	0.09	4.04	4.04	4.04	4.04
Si^{4+}	n/a	n/a	6.00	6.00	6.00	6.00	6.00	6.00	6.00	6.00	6.00	0.06	0.06	0.06	0.06
Molar Ratio															
Ca:Si	n/a	n/a	1.42	1.48	1.48	1.48	1.47	1.50	1.51	1.52	1.50	94.95	94.95	94.95	94.95
Al:Si	n/a	n/a	0.00	0.00	0.01	0.01	0.02	0.01	0.01	0.01	0.01	8.85	8.85	8.85	8.85

Table B3 continued.

PHASE	Ettringite	Ettringite	Ettringite	Ettringite	Ettringite	Ettringite	Ettringite	Ettringite	Ettringite	Wairakite	Wairakite	Wairakite	Wairakite	Wairakite
Point	**LAM91/5**	**LAM91/6**	**LA965/5**	**LA965/7**	**LA965/10**	**LA965/11**	**LA965/23**	**LA965/26**	**LA965/30**	**LA960/4**	**LA960/5**	**LA960/6**	**LA960/17**	**LA960/18**
EPMA Data														
Mg	0.00	0.00	0.17	0.02	0.02	0.02	0.41	0.02	0.02	0.00	0.00	0.00	0.00	0.00
Al	1.19	1.19	3.94	5.09	5.33	4.84	3.97	4.46	4.66	1.19	1.19	1.19	1.19	1.19
Si	0.14	0.14	1.43	0.26	0.35	0.40	0.99	0.46	0.93	0.14	0.14	0.14	0.14	0.14
Ca	18.97	18.97	22.79	20.18	25.19	23.41	21.15	21.91	24.73	18.97	18.97	18.97	18.97	18.97
Fe	0.00	0.00	0.10	0.03	0.03	0.00	0.09	0.02	0.02	0.00	0.00	0.00	0.00	0.00
P	0.02	0.02	0.25	0.24	0.24	0.23	0.20	0.24	0.29	0.02	0.02	0.02	0.02	0.02
S	10.22	10.22	6.31	6.50	7.86	7.11	5.97	6.57	7.43	10.22	10.22	10.22	10.22	10.22
Cl	0.73	0.73	0.27	0.41	0.12	0.25	0.33	0.36	0.17	0.73	0.73	0.73	0.73	0.73
LA-ICP-MS Data														
Mg	328	380	3470	138	1741	3127	729	762	2047	12000	2300	5020	3280	4410
Al	29000	37000	34557	35556	32161	33862	11653	28448	31174	190000	78000	680000	131000	133000
Si	<0.3%	<0.4%	22905	80976	6314	44589	53105	*73475*	30418					
Ca	190000	190000	227900	201800	251900	234100	211500	219100	247300	190000	190000	190000	190000	190000
Cr	*8*	*9*	7455	30	700	428	126	43	25	<236	*133*	<129	1610	239
Mn	4	3	7	3	8	16	8	3	10	102	26	*13*	44	36
Fe	337	373	1599	909	826	1620	1038	884	1383	17000	1500	5230	3550	1910
Co	*0.6*	3	2	*1*	*1*	1	0.47	1	0.38	36	<2	*5*	<1	2
Cu	5	*2*	18	12	14	9	10	10	9	636	206	1030	296	154
Zn	9	n.d.	1011	9	119	160	2838	14	49	110	248	139	332	55
Sr	301	331	197	288	360	265	88	334	829	1900	546	3680	3280	2980
Ba	4	6	4	2	7	10	6	8	8	807	918	768	703	715
Pb	11	12	4	3	3	3	5	1	3	94	31	30	50	25
Th	n.d.	n.d.	*0.41*	*1*	*0.44*	*0.34*	*0.09*	*0.16*	*0.31*	*2.4*	n.d.	n.d.	2	<0.61
U	*0.25*	1.9	3	*1*	*1*	1	6	*0.22*	*0.26*	20	8	75	100	29
Ionic Proportions														
Ca^{2+}	6.00	6.00	6.00	6.00	6.00	6.00	6.00	6.00	6.00	379.81	379.81	379.81	379.81	379.81
Al^{3+}	0.56	0.56	1.54	2.25	1.89	1.84	1.67	1.81	1.68	35.39	35.39	35.39	35.39	35.39
SO_4^{2-}	4.04	4.04	2.08	2.42	2.34	2.28	2.12	2.25	2.25	255.81	255.81	255.81	255.81	255.81
Si^{4+}	0.06	0.06	0.54	0.11	0.12	0.15	0.40	0.18	0.32	4.00	4.00	4.00	4.00	4.00
Molar Ratio														
Ca:Si	94.95	94.95	11.20	53.55	50.75	40.99	14.98	33.25	18.69	94.95	94.95	94.95	94.95	94.95
Al:Si	8.85	8.85	2.87	20.05	15.95	12.59	4.17	10.05	5.24	8.85	8.85	8.85	8.85	8.85

Table B3 continued.

PHASE	Ettringite	Ettringite	Thaumasite	Thaumasite	Thaumasite	Calcite	Calcite	Calcite	Calcite	Calcite	Calcite	Calcite	Aragonite	Aragonite
Point	LA967/8	LA967/9	LA965/28	LA965/29	LA965/9	LA960/1	LA960/2	LA960/3	LA960/15	LA960/16	LAM81/8	LAM81/9	LA967/1	LA967/3
EPMA Data														
Mg	0.00	0.00	0.02	0.02	0.00	0.14	0.14	0.14	0.14	0.14	0.14	0.14	0.64	0.64
Al	1.19	1.19	2.14	2.14	1.30	0.79	0.79	0.79	0.79	0.79	0.79	0.79	0.26	0.26
Si	0.14	0.14	2.47	2.47	3.91	0.30	0.30	0.30	0.30	0.30	0.30	0.30	0.30	0.30
Ca	18.97	18.97	20.26	20.26	22.90	39.82	39.82	39.82	39.82	39.82	39.82	39.82	40.18	40.18
Fe	0.00	0.00	0.02	0.02	0.00	0.03	0.03	0.03	0.03	0.03	0.03	0.03	0.16	0.16
P	0.02	0.02	0.26	0.26	0.23	0.18	0.18	0.18	0.18	0.18	0.18	0.18	0.19	0.19
S	10.22	10.22	5.04	5.04	5.14	0.05	0.05	0.05	0.05	0.05	0.05	0.05	0.09	0.09
Cl	0.73	0.73	0.55	0.55	0.45	0.02	0.02	0.02	0.02	0.02	0.02	0.02	0.02	0.02
LA-ICP-MS Data														
Mg	514	561	240	421	1041	1990	2610	2270	3280	3340	540	234	3620	5840
Al	300	400	9418	8773	7889	1.10%	0.76%	0.62%	0.90%	1.20%	6.20%	0.60%	0.24%	0.21%
Si	<0.36	<0.04	28252	35815	57946						*1.60%*	*2.30%*	*3.40%*	*3.00%*
Ca	190000	190000	202600	202600	229000	39.80%	39.80%	39.80%	39.80%	39.80%	39.80%	39.80%	40.20%	40.20%
Cr	<5	<6	*11*	286	38	553	483	350	500	1050	*79*	57	*62*	<18
Mn	n.d.	*0.5*	2	3	7	60	80	56	84	77	31	*5*	43	15
Fe	332	358	421	580	576	*60*	1480	2200	1900	1690	8610	1790	1050	711
Co	n.d.	n.d.	0	0	*0.33*	*3*	*4*	*4*	3	4	<1.3	<0.7	*2*	<0.6
Cu	4	5	8	10	11	58	84	51	81	154	48	38	25	8
Zn	10	12	33	249	16	*11*	177	*14*	64	76	54	20	n.d.	47
Sr	941	802	216	151	175	846	835	1000	758	1600	690	859	1210	1180
Ba	11	13	2	3	4	31	30	49	33	99	27	11	26	25
Pb	n.d.	1.9	0.26	1	2	16	22	14	7	26	26	18	11	10
Th	n.d.	n.d.	*0.09*	*0.10*	0.39	<0.7	*1.4*	<0.7	*0.5*	n.d.	<0.5	*0.2*	<0.8	*0.71*
U	n.d.	n.d.	*0.19*	2	*0.35*	11	11	6	16	16	*0.74*	<0.3	<0.45	*0.63*
Ionic Proportions														
Ca^{2+}	6.00	6.00	6.00	6.00	6.00									
Al^{3+}	0.56	0.56	0.94	0.94	0.50									
SO_4^{2-}	4.04	4.04	1.87	1.87	1.68									
Si^{4+}	0.06	0.06	1.04	1.04	1.46									
Molar Ratio														
Ca:Si	94.95	94.95	5.75	5.75	4.11									
Al:Si	8.85	8.85	0.90	0.90	0.35									

Table B3 continued.

PHASE	Aragonite	Aragonite	Aragonite	Aragonite	Aragonite	Aragonite	Strontianite	CSH	CSH	CSH	CSH	CSH	Brucite
Point	LA967/4	LA967/5	LA967/6	LA967/7	LAM81/5	LAM81/6	LAM81/7	LAM86/1	LAM86/2	LAM86/3	LAM86/4	LAM86/5	LAM86/6
EPMA Data													
Mg	0.64	0.64	0.64	0.64	0.64	0.64	n/a	0.01	0.01	0.01	0.01	0.01	42.41
Al	0.26	0.26	0.26	0.26	0.26	0.26	n/a	0.06	0.06	0.06	0.06	0.06	0.00
Si	0.30	0.30	0.30	0.30	0.30	0.30	n/a	44.13	44.13	44.13	44.13	44.13	0.00
Ca	40.18	40.18	40.18	40.18	40.18	40.18	n/a	40.45	40.45	40.45	40.45	40.45	0.00
Fe	0.16	0.16	0.16	0.16	0.16	0.16	n/a	0.02	0.02	0.02	0.02	0.02	0.00
P	0.19	0.19	0.19	0.19	0.19	0.19	n/a	0.06	0.06	0.06	0.06	0.06	0.00
S	0.09	0.09	0.09	0.09	0.09	0.09	n/a	0.12	0.12	0.12	0.12	0.12	0.00
Cl	0.02	0.02	0.02	0.02	0.02	0.02	n/a	0.05	0.05	0.05	0.05	0.05	0.00
LA-ICP-MS Data													
Mg	25000	2200	2500	585	*217*	*178*	<45	2600	2190	2380	778	7210	42.40%
Al	0.13%	0.09%	0.10%	0.04%	<0.04%	0.10%	<0.01%	0.62%	0.11%	0.59%	0.65%	0.47%	833
Si	*1.10%*	*1.90%*	*1.50%*	1.90%	<13%	<8%	<5%	12%	5.50%	6.30%	6.00%	18%	<0.8%
Ca	40.20%	40.20%	40.20%	19%	40.20%	40.20%	40.20%	40.50%	19.60%	19.60%	19.60%	40.50%	0.21%
Cr	<16	<14	<18	24	<242	<171	*149*	92	<18	*24*	*27*	<50	n.d.
Mn	6	8	15	2	n.d.	26	n.d.	60	12	8	7	100	n.d.
Fe	741	637	2520	659	n.d.	8710	1970	4600	836	894	4630	6040	88
Co	<0.5	1	n.d.	<0.2	*18*	n.d.	<5	n.d.	n.d.	<1	<0.54	<3	n.d.
Cu	15	9	14	5	n.d.	*43*	<16	*19*	*8*	<4	9	39	<6
Zn	94	10	18	11	n.d.	n.d.	<27	415	115	108	167	693	*9*
Sr	1270	1210	1480	412	2370	5555	1370	1290	931	775	978	1540	40
Ba	16	20	31	74	241	174	76	310	113	151	166	283	15
Pb	7	9	12	1.5	*56*	58	36	620	200	288	325	10600	n.d.
Th	<0.29	*0.31*	*0.48*	n.d.	<4	<3	*1.9*	n.d.	*0.63*	n.d.	*0.2*	1	<0.7
U	<0.22	<0.28	<0.31	n.d.	<6	<4	*2*	10	6	7	8	7	n.d.
Ionic Proportions													
Ca^{2+}								3.85	3.85	3.85	3.85	3.85	
Al^{3+}								0.01	0.01	0.01	0.01	0.01	
SO_4^{2-}								0.01	0.01	0.01	0.01	0.01	
Si^{4+}								6.00	6.00	6.00	6.00	6.00	
Molar Ratio													
Ca:Si								0.64	0.64	0.64	0.64	0.64	
Al:Si								0.00	0.00	0.00	0.00	0.00	

Table B3 continued.

PHASE	Brucite	Brucite	Portlandite	Portlandite	Portlandite	Average		Average		Average		Average	
Point	LAM86/7	LAM86/8	LAM81/2	LAM81/3	LAM81/4	Jennite	±s.d	Wairakite	±s.d	Ettringite	±s.d.	Thaumasite	±s.d.
EPMA Data													
Mg	42.41	42.41	0.00	0.00	0.00	0.04	0.02	0.00	0.00	0.05	0.11	0.02	0.01
Al	0.00	0.00	0.00	0.00	0.00	0.12	0.10	1.19	0.00	2.79	1.80	1.86	0.48
Si	0.00	0.00	0.00	0.00	0.00	16.22	0.28	0.14	0.00	0.40	0.40	2.95	0.83
Ca	0.00	0.00	54.09	54.09	54.09	34.35	0.58	18.97	0.00	20.74	2.30	21.14	1.52
Fe	0.00	0.00	0.00	0.00	0.00	0.01	0.03	0.00	0.00	0.02	0.03	0.01	0.01
P	0.00	0.00	0.00	0.00	0.00	0.38	0.02	0.02	0.00	0.12	0.12	0.25	0.02
S	0.00	0.00	0.00	0.00	0.00	0.12	0.11	10.22	0.00	8.63	1.81	5.07	0.06
Cl	0.00	0.00	0.00	0.00	0.00	0.04	0.02	0.73	0.00	0.52	0.25	0.52	0.06
LA-ICP-MS Data													
Mg	42.40%	42.40%	684	3380	2760	253	131	5650.00	4380.21	982.40	1097.00	567	420
Al	302	340	0.09%	0.21%	0.22%	888	627	269750.00	277299.33	32740.73	18868.33	8693	768
Si	6%	<2%	<7%	<2.7%	<13%	137201	9032	n/a	n/a	38972.75	29526.66	40671	15431
Ca	0.95%	0.42%	54.10%	54.10%	54.10%	308633	103061	190000.00	0.00	207573.33	22853.71	211400	15242
Cr	183	*69*	*162*	*100*	<257	191	138	871.50	1044.40	739.42	2125.81	112	152
Mn	23	<6	<20	<9	<38	9	2	46.25	39.28	6.05	4.36	4	3
Fe	5620	933	430	1080	11700	435	274	6820.00	6955.95	754.67	479.11	526	91
Co	*9*	n.d.	n.d.	<4	*19*	1	1	20.50	21.92	1.08	0.77	0	0
Cu	*16*	*17*	86	99	206	12	4	542.00	374.34	8.29	4.39	10	2
Zn	114	41	*83*	524	496	250	345	207.25	102.21	327.31	802.43	99	130
Sr	36	19	3710	3950	5600	165	105	2351.50	1424.86	458.93	261.12	181	33
Ba	23	*13*	286	361	467	8	4	799.00	90.19	9.87	7.18	3	1
Pb	50	805	86	41	113	2	1	51.25	29.95	6.92	5.87	1	1
Th	n.d.	n.d.	<2	*0.7*	<6	1	1	2.20	0.28	0.39	0.30	0	0
U	26	n.d.	<3	7	22	19	5	50.75	43.92	2.85	3.11	1	1
Ionic Proportions													
Ca^{2+}						8.91	0.17			6.00			
Al^{3+}						0.05	0.04			1.81			
SO_4^{2-}						0.04	0.04			2.25			
Si^{4+}						6.00	0.00			0.26			
Molar Ratio													
Ca:Si						1.48	0.03			31.92			
Al:Si						0.01	0.01			10.13			

Table B3 continued.

PHASE		Average		Hydrated		Average		Average	
Point	±s.d.	Aragonite	±s.d.	CSH	±s.d.	Brucite	±s.d.	Portlandite	±s.d.
EPMA Data									
Mg	0.00	0.64	0.00	0.01	0.00	42.41	0.00	0.00	0.00
Al	0.00	0.26	0.00	0.06	0.00	0.00	0.00	0.00	0.00
Si	0.00	0.30	0.00	44.13	0.00	0.00	0.00	0.00	0.00
Ca	0.00	40.18	0.00	40.45	0.00	0.00	0.00	54.09	0.00
Fe	0.00	0.16	0.00	0.02	0.00	0.00	0.00	0.00	0.00
P	0.00	0.19	0.00	0.06	0.00	0.00	0.00	0.00	0.00
S	0.00	0.09	0.00	0.12	0.00	0.00	0.00	0.00	0.00
Cl	0.00	0.02	0.00	0.05	0.00	0.00	0.00	0.00	0.00
LA-ICP-MS Data									
Mg	1233	5018	8301	3032	2442	0	0	2275	1412
Al	0	0	0	0	0	321	27	0	0
Si	0	0	0	0	0	0	n.d.	n.d.	n.d.
Ca	0	0	0	0	0	0	0	1	0
Cr	336	43	27	48	38	126	81	131	44
Mn	29	16	14	37	41	23	n.d.	n.d.	n.d.
Fe	2767	2147	2971	3400	2386	3277	3314	4403	6327
Co	1	7	10	n.d.	n.d.	9	n.d.	19	n.d.
Cu	39	17	13	19	14	17	1	130	66
Zn	58	36	36	300	253	78	52	368	247
Sr	306	1836	1595	1103	308	28	12	4420	1029
Ba	28	76	85	205	87	18	7	371	91
Pb	7	21	23	2407	4583	428	534	80	36
Th	1	1	0	1	0	n.d.	n.d.	1	n.d.
U	6	1	n.d.	8	2	26	n.d.	15	11
Ionic Proportions									
Ca^{2+}				6.00					
Al^{3+}				1.00					
SO_4^{2-}				3.45					
Si^{4+}				0.13					
Molar Ratio									
Ca:Si				76.13					
Al:Si				10.22					

APPENDIX C URANIUM DISTRIBUTION AND WHOLE ROCK GEOCHEMISTRY

E.K. Hyslop

C1 Fission Track Analysis Technique

Examination of individual uranium-bearing phases by optical and backscattered scanning electron microscopy was facilitated by prior precise location of all uranium sites in polished thin sections by the technique of recording fission fragments derived from uranium under neutron irradiation in a reactor [(n,f) reaction]. Interference from thorium was avoided by selecting a highly thermalised neutron flux in which only ^{235}U undergoes appreciable fission. Irradiations were carried out at the Scottish Universities Research and Reactor Centre, East Kilbride.

The method employed was based on that of Kleeman & Lovering [1]. 'Lexan' polycarbonate plastic was used as a detector and tracks of the induced fission fragments revealed by etching for 5-10 minutes at 60•C in 6M NaOH solution. The technique yields accurate spatial information on the location of uranium in the sample in the form of micromaps. Quantitative estimation of the uranium content of different host mineral phases was achieved by the irradiation of uranium-doped standard glasses along with the sample batches and consequent track counting on an equal area basis using an optical microscope. Neutron fluence was chosen to yield discrete tracks with minimum overlap to ensure reasonable counting accuracy (typically 2 10^{15} t.n.cm^{-2} is used).

Backscattered scanning electron microscope (BSEM) analysis was undertaken using a Cambridge Instruments Stereoscan S250 scanning electron microscope fitted with a 4-element solid-state (diode) backscattered electron detector (KE Developments Ltd). Mineralogical and chemical characterisation of phases imaged under BSEM was facilitated by qualitative observation of their energy-dispersive X-ray spectra. These were recorded using a Link Systems 860 energy-dispersive X-ray microanalyser (EDXA). The EDXA system has a detection limit of approximately 0.2% (weight) for most common elements but this is probably of the order of 0.5% (weight) for uranium, thorium and other heavy elements at typical count-times of 100 seconds using a 20kV beam voltage. BSEM analysis of the polished thin sections was carried out after coating the sections with a thin film of carbon (approximately 200Å thick). This was done by evaporation and redeposition of carbon under vacuum onto the surface of the thin section.

Images obtained by BSEM are related to the composition of the material being examined. Image brightness is proportional to the average atomic number of the material, thus allowing the distribution of different minerals or phases to be determined on the basis of their chemical composition [3]. In order to identify the uranium-bearing phases systematically, comparison of the BSEM images was made with fission-track registration prints. Enlargements of these were made by microfiche photocopier in order to produce a large-scale 'map' of the uranium distribution for each polished section. From such maps it is possible to locate the uranium-bearing phases accurately and rapidly under BSEM in order to identify them by EDXA and determine their petrogenetic relationships [2],[3],[4].

C2 Detailed Petrology and U Distribution Studies of Samples

C2.1 Maqarin samples

A960AP2/MQN2a

2.5m north of the metamorphic contact zone on the west wall 107.5m into Adit 6. Unmetamorphosed, rather clay-rich clay biomicrite containing fractures with intense alkali interaction.

Very fine grained rock almost opaque in thin section, containing common foraminifera and elongate microfossil fragments. The latter are aligned and define bedding. Rock contains thin veins perpendicular to bedding, and a major vein several millimetres thick. Alteration of the rock matrix around the main vein is intense with a broad zone of calcification up to 15mm wide. Immediately adjacent to the vein the rock matrix is porous forming a zone typically 5mm thick. In the less altered material further from the vein are preserved patches of relatively unaltered brown-grey coloured matrix.

Fine grained framboidal pyrite is present throughout the matrix. It commonly replaces microfossils. The pyrite is typically highly altered to Fe oxide, particularly strongly in the calcified zone. However the secondary Fe oxide does not appear to have been mobilised from these sites. A pyrite rich band can be traced along the bedding into the highly altered veined zone. Oxidation is highest in the calcified zone but less oxidised in the porous wallrock zone.

Uranium in the relatively unaltered rock away from the vein is present at levels of c.16ppmU, with small areas of higher concentrations, typically c.44ppmU. Such concentrations are related to small particles of (typically ragged) collophane (hydrous phosphatic material). The calcified zone has much more uniformly distributed U, with levels of c.23ppmU and no discrete concentrations. This material contains common fine grained apatite throughout which is probably responsible for the more uniform U distribution.

The pyrite band contains slightly enhanced levels of U, typically 36ppmU, and similar levels are present in both oxidised and less altered parts of the band. Where this band is cut by an offshoot of the main vein, high U concentrations of 100-150ppmU are present along the vein margins in the area around the pyrite band (Plate 2). This material appears to be a CSH gel containing detectable Fe, P, Ni, Cr, Zn, V and Ti.

The porous wallrock zone contains a relatively large elongate fragment of collophane (Plate 1) which contains high levels of U (50-150ppmU). It has a thin outer margin of apatite-like material, with an interior composed of less phosphatic (probably hydrated) material. Towards the vein the outer apatite shell becomes degraded.

At the vein margins the thoroughly altered wallrock is a mixture of calcite, ettringite and thaumasite (or a CASH phase) with highly corroded fossils replaced by calcite and gypsum. It has uniform diffuse U of c.27ppm, probably contained in fine grained phosphatic material. Gypsum becomes more common towards the immediate vein margins. In the vein relatively coarse patches of a Si-Al-Ca hydrous phase, gypsum and calcite are present. None of these phases contain U. Several generations of gypsum are present and it also occurs in thin perpendicular veins which cut the main vein. Calcite is a major vein fill phase and forms large masses with voids containing ettringite. Common needle-like crystal terminations suggest aragonite.

Late thin veins in the wallrock parallel to the main vein also contain a CASH phase. In the main vein the CASH is zoned, and where it forms large masses it contains U levels similar to the host rock (25-30ppmU). EMPA examination indicates that this material is possibly a zeolite, similar in composition to laumontite.

A961AP2/MQN10

Organic-rich clay biomicrite from near the entrance to Adit 6, where no or little alkali alteration appears to have occurred (c.7m into adit). The rock is very fine grained and optically dark brown and semi-opaque. It is relatively uniform with little banding in the sample. It contains common sub-spherical microfossils (dominantly foraminifera) which have been replaced by clear calcite. Small thin shell fragments are also scattered throughout. Framboidal pyrite is present in some of the microfossils and also occurs as very small grains scattered throughout the matrix.

Uranium is dispersed in a relatively uniform fashion throughout the matrix with no discrete concentrations, though patches of higher U are present. Levels are generally c.12ppmU, with 13-16ppmU in the higher patches. Rare small radial clusters of c.35ppm U are present Uranium is not associated with forams or pyrite.

The distribution of U shows no evidence of secondary remobilisation. It is present in a diffuse form associated with fine organic material throughout the rock matrix.

A962AP2/MQN3

Very organic-rich clay biomicrite with pink coloured veins from 99m into Adit 6. The sample has light staining by alkali fluids on joint faces, though no active drips were observed. The rock is very fine grained, and opaque to semi-opaque in thin section. Microfossils are common and replaced by calcite, and shelly fragments and elongate pellets of very fine grained carbonate are also present. The shelly material is aligned, defining bedding. Abundant thin veins parallel to bedding contain a clear-light brown phase overgrown by brown fibres aligned across the fracture. Both phases are optically isotropic. Larger veins are typically c.4mm across.

Uranium is present in a uniform diffuse form throughout the matrix at levels of c.14ppm. It appears to be slightly enhanced nearer the larger veins, where in calcified wallrock it reaches 16ppmU.

The matrix contains discrete grains of Fe oxide and barite in a fine grained calcite-rich matrix, also with patches of Si-Al-Ca phases. The altered matrix has small irregular grains of apatite throughout the matrix.

The main vein has variable U at its margins. The immediate edge has 6-7ppmU associated with a spongy-looking Ca-Si-Al phase (minor K) with small poorly formed calcite. Further into the vein a zone of dense brown fibrous material contains c.11ppm. It consists of Ca-Si-Al fibres which are less porous than the marginal zone. The central vein material has <1ppmU, composed of fibres aligned perpendicular to the vein margins with high Ca/Si and minor Al. The vein fill has abundant shrinkage cracks, contains detectable Cr and minor S, and is very hydrous. It is probably tobermorite. Selinides containing Zn, Fe, Ni, Cu and As are also present.

A963AP2/MQN5

Dark organic-rich clay biomicrite from c.60m into Adit 6. Active alkaline interaction reactions present on fracture surfaces. Fine grained, optically semi opaque with common

microfossils, most replaced by calcite and some filled by pyrite. Veins are common, generally <1mm thick and subparallel to bedding, though many are <0.25mm wide. Wallrock alteration zones are typically up to 0.3mm wide (though highly variable). The veins contain a clear though optically isotropic phase.

Diffuse U is present in the matrix at levels of c.13ppm, and in altered wallrock at consistently lower levels (c.11-13ppmU). Vein fillings have <2ppmU, but some enhancement occurs along the vein edges in the thickest veins (4-7ppmU).

A965AP2/MQN23

Unmetamorphosed clay biomicrite from 45-50m into Adit 6 at Fracture Zone FZ2 (water drip site M2). Active alkali water interaction along fractures. Sample represents fractures from where waters were sampled. Rock is fine grained and highly fossiliferous with abundant forams and shelly fragments. Veins are very common, forming a subparallel anastomosing series. Most <1mm wide, though some are >3mm. Most veins contain a single generation of cross fibre ettringite fill, though some contain fibrous jennite lining central voids. Early calcite lines the wallrock and is corroded and coated by a thin layer of Cr- and Zn-rich clay. The rock matrix is extensively altered to a grey-brown colour. Irregular lensoid zones of preserved original host rock of light brown colour are present. The interface between the zones is a thin front of opaque ?organic material.

The rock contains uniform U at levels of c.10ppm. Uranium levels are similar in altered and unaltered rock. The interface between zones has no U enhancement. The main ettringite vein fill contains no U, though the more complex veins contain U associated with dark semi-opaque fibrous jennite which forms irregular clusters (some radial) lining voids in the centre of veins. It contains 10-15ppmU (Plate 48). The veins contain a complex paragenesis with early ettringite replaced by calcite and clays, then a period of corrosion followed by formation of ettringite-thaumasite which are in turn replaced by jennite and ettringite filling central voids. An earlier generation of jennite forms botryoidal masses near wallrock, yet has no U. The lack of U in the marginal phases, and its presence in the vein centres suggests that U may have migrated relatively late in the vein system.

A966AP2/MQN20

Bituminous clay biomicrite from Maqarin railway cutting showing active alkali water flow and precipitation in fractures. Very fine grained organic rich rock, semi-opaque in thin section, matrix appears altered. Microfossils have been replaced by coarse calcite and framboidal pyrite. Contains common microfractures typically <0.1mm thick, related to larger fractures several millimetres thick, subparallel to bedding. The microfractures have a cross fibre ettringite fill, whilst the thicker veins have a more massive ettringite fill with fine radial fibrous growth of semi-opaque needles. Some veins are composite with a further later input of ettringite along the vein margins. None of the vein fills contain U.

Larger veins have thaumasite coatings on wallrock with a later ettringite vein centre fill. The veins contain considerable open pore space. Fine grained pyrite is present in the veins and wallrock, where it forms irregular masses unlike the pyrite framboids in the host rock.

The host rock matrix contains uniform dispersed U at levels of 10-17ppm U, averaging 13ppmU. Small concentrations of c.30-50ppmU are present throughout the matrix, related to degraded collophane. Larger elongate lenses of collophane contain

c.20-30ppmU. In places these are cut by thin ettringite veins, though no U appears to have been mobilised. The altered wallrock of larger veins contains reduced levels of U. The immediate wallrock at a distance of 0-0.3mm from the vein edge has 9-10ppmU. From 0.3-0.6mm it is 10.5ppmU, and 0.6-0.9mm from the vein 12ppmU.

C2.2 Central Jordan samples

A972AP1/CJ6

Highly fractured, altered and veined metamorphosed marble from anticline crest exposed in Daba roadcutting, which in thin section is observed to be a highly veined fine grained brown organic rich clay biomicrite containing abundant microfossils.

Uranium is present in low levels in the matrix in an inhomogeneous distribution (Plate 51). Most of the matrix has very low levels of <1ppm U, whilst most of the U is concentrated into moderate sized patches that appear to relate to the presence of fine organic material. These patches typically contain 30-50ppmU, though a small opaque phase (possible bitumen) contains 70-90ppmU. The major vein filling is clear fibrous ?ettringite, and has very low levels of U (<1ppmU). Other vein minerals have no detectable U. There is no detectable difference in U concentrations in the vein wallrock to those in the less altered rock away from veins. Uranium is present throughout the rock apparently associated with fine grained organic matter. No remobilisation of U appears to have occurred as a result of alteration or veining.

A974AP1/CJ13

Green-stained in hand specimen, earthy siliceous travertine underlying breccia deposit on Khan-ez-Zabib Hills.

The rock has a complex fabric comprising banded brown and semi-opaque, micritic carbonate with voids filled by transparent, isotropic material. Masses of coarser, bladed calcite are also present disseminated throughout the rock. The void filling is opaline silica which forms botryoidal masses in vugs. EMPA shows this silica to have c.10% H_2O. The botryoidal material shows very fine layering. Patches of highly porus carbonate containing Cr-smectite (also with Fe, Mg, Zn and possible Cu) are present within the silica gel. Barite is associated with the smectite in the carbonate, and is coated by the botryoidal silica.

The botryoidal silica gel contains relatively uniform diffuse U at levels of c.60-70ppmU, though this varies in concentration at void margins (Plate 49). Outer edges of botryoidal masses are commonly enhanced with 60-80ppmU whilst areas just before the edges have lower contents typically 40-50ppmU. Some voids have silica with 90-160ppmU. The carbonate-clay patches contain c.30ppmU. Dark elongate patches composed of granular fine grained carbonate with apatite and silica contain high U, typically 100-130ppmU. The overall shape suggests these may be organic plant fragments and relict cellular structures are present (Plate 50). The fission tracks are distributed in a relatively uniform fashion, suggesting that U is dispersed throughout the silica, rather than present as discrete concentrations in apatite. Secondary euhedral calcite containing Fe-Cr smectite is also present.

The paragenesis of the travertine deposits suggests a primary stage of granular dark carbonate containing clay, followed by a later stage clear well-formed calcite. The later calcite has corroded margins which have been coated by silica. The early carbonate has c.50-60ppmU, whilst the later well formed calcite has only a few ppm.

A975AP1/CJ15

Breccia overlying the lower travertine on Khan-ez-Zabib Hills. Colluvium deposit containing chert, marble and clay biomicrite showing reaction zones. Cemented by carbonate tufa. Contains clasts of underlying green-coloured Cr-rich deposit. Clasts of clay biomicrite and possible chert are contained within a matrix of carbonate and opaline silica. The clay biomicrite is dark and organic rich and contains abundant microfossils. It is highly altered with prominent alteration zones. The breccia matrix consists of fine grained carbonate and banded transparent (though optically isotropic) silica gel which coats the clasts and fills cavities. Radial fibrous silica is also present coating the clasts.

The rock has low U, with some rare concentrations. Uranium is variable in the marls. The relatively unaltered central parts of clasts contain 6-9ppmU, whilst the lighter coloured altered margins have 1-3ppmU. In the breccia matrix the fine granular carbonate at the margins has no U, whilst the central silica void filling contains 7-15ppmU. Phosphatic material in the clay biomicrite clasts has U levels typically 50-100ppmU. These probably represent original fossil material or possible fecal pellets. Many of these are degraded with an irregular spongy morphology and are coated by opaline silica. Uranium may have been released into the silica. Some have a composition similar to ellastadite, also containing detectable REE (Sm, Pm, ?Eu).

Opaline silica in the voids shows varying degrees of crystallisation. In many places it consists of a very fine grained mixture of poorly crystalline silica and clay, which displays a transformation to a purer crystalline silica (quartz). Uranium is higher in the more crystalline silica. Such voids are commonly lined by an early coating of calcite, and the silica is also overprinted by a later generation of calcite.

A976AP1/CJ17

Upper green-coloured travertine overlying breccia on Khan-ez-Zabib Hills. Contains abundant rootlets.

Complex rock with large areas of brown granular carbonate surrounded by fringes of opaline silica lining open voids. Much of the carbonate material appears to be large roots and cellular material which has been cemented by carbonate then coated by silica. Open areas within roots and in matrix voids are lined by silica. BSEM indicates a single generation of granular carbonate (with minor barite) coated by silica. Some cavities are also filled by late ettringite, and barite also occurs in late veins associated with hashamite (Cr-barite).

The large areas of granular carbonate typically contain c.20-40ppmU, though some parts have negligible U. Concentric brown carbonate precipitates contain only c.1ppmU. Silica void linings contain 25-50ppmU, typically c.40ppm though up to 75ppm in places.

A977AP1/CJ18

Layer of chert nodules showing intense alteration associated with breccia colluvium deposit on Khan-ez-Zabib Hills.

Very fine grained highly brecciated siliceous rock with intense alteration zones forming broad fringes typically 2-3mm wide around clast edges. The altered zone is whitened (calcified) and contains just over 5ppmU, whilst the relatively unaltered material has less than 5ppmU. Thus there appears to be a very slight enhancement of U in altered wallrock.

At between 0.2-0.3mm from clast margins the wallrock has enhanced U levels of 9-12ppm. At the margins of open voids 16-18ppmU is present along the immediate margins. The remainder of the calcified zone has similar U contents to the host rock of 5-6ppmU. The rock contains common veins, though no U is present in the vein fill. Elongate cellular material and organic detritus contains c.50-100ppmU. These are cut by veins, although no mobilisation of U is apparent.

A978AP1/CJ20

Apatite-rich marble from marble quarries in Central Jordan. Fine grained uniform, brown coloured granular carbonate.

The sample is enriched in U which is unevenly distributed. Large areas of the sample contain many small clusters of high U of several hundred ppm or more. Although difficult to resolve optically, these probably represent clusters of small individual U-bearing apatite grains. The matrix of the rock is also relatively enriched in U, though with a patchy distribution at levels typically c.6ppmU.

A980AP1/CJ24

Unmetamorphosed chalky clay biomicrite, unaffected by alkaline fluids. Roadcutting c.3km north of Daba.

Dark brown coloured foram-rich clay biomicrite, semi-opaque in thin section, containing rare fractures filled by carbonate. Fossil debris is present throughout and is replaced by hydrous collophane with c.40-50ppmU, and brown stained organic detritus like bone (also collophanic but possibly containing hydrocarbon) has higher U of c.50-70ppm.

Uranium is distributed in an inhomogeneous manner throughout the rock. It is concentrated in irregular patches typically 0.2mm in size which contain c.26-41ppmU, amongst a general background of typically <3ppmU.

Large voids are filled by clear ?carbonate which contains negligible U, though a clear granular high relief phase lining void margins (and completely filling smaller voids) contains U at levels of c.20-30ppm.

A981AP1/CJ25

Lateral equivalent of A980; unmetamorphosed clay biomicrite affected by alkaline fluids. Roadcutting c.3km north of Daba.

Brown organic-rich fossiliferous clay biomicrite, similar to sample A980. Contains common veins mostly subparallel to bedding though some perpendicular to bedding forming an interconnecting network. Alteration zones around fractures are typically 2 mm wide on either side of a fracture.

Many veins are open, and the rock itself appears highly porous, though altered wallrock adjacent to fractures is impervious to the thin section resin.

Uranium is distributed in a similar way to A980 in inhomogeneous patches throughout the rock matrix. The normal matrix has c.1.5ppmU. Possible collophane fossil debris present throughout has small concentrations of c.20-40ppmU. Altered wallrock contains slightly enhanced levels of U (c.2.5ppmU). The vein-filling phase contains negligible U.

A982AP1/CJ26

Highly altered lateral equivalent of A980; unmetamorphosed clay biomicrite severely affected by alkaline fluids. Roadcutting c.3km north of Daba.

Highly altered and veined fossiliferous organic-rich clay biomicrite. Veins contain brecciated fragments of wallrock within a vuggy vein fill containing open voids. The vein fill appears optically to be a relatively simple one-stage calcite fill.

The rock has an inhomogeneous U distribution similar to samples A980 & A981, with low U of <3ppm in the matrix and abundant small patches of fossil debris containing high-moderate U of c.20-45ppmU. This appears to be spongy collophane replacing microfossil tests. Certain bands have slightly higher U matrix contents which is related to original bedding and does not appear to be affected by vein-related alteration.

The altered wallrock contains slightly enhanced matrix U levels of 3-4ppmU. Granular brown material forming linings on breccia clasts and void margins contains 10-20ppmU. This is a mixture of a hydrous Ca-Al-Si zeolite with fine grained Fe- and Cr-bearing smectite clay. The zeolite has a rather blocky morphology. The vein fill material is calcite which contains negligible U.

References

[1] J.D. Kleeman and J.F. Lovering, *Uranium Distribution in Rocks by Fission Track Registration in Lexan Plastic Prints,* Atomic Energy Australia, 10 (4), 3-8, 1967.

[2] I.R. Basham, A.E. Milodowski, E.K. Hyslop and J.M. Pearce, *The Location of Uranium in Source Rocks and Sites of Secondary Deposition at the Needles Eye Natural Analogue Site, Dumfries and Galloway,* Report British Geological Survey, WE/89/56, 1989.

[3] A.E. Milodowski, D. Savage, A.H. Bath, N.J. Fortey, P.H.A. Nancarrow and T.J. Shepherd, *Hydrothermal mineralogy in geothermal Assessment: Studies of Miravalles Field, Costa Rica and Experimental simulations of Hydrothermal Alteration,* British Geological Survey, Technical Report, WE/89/63, 1989.

[4] A.E. Milodowski, J.M. Pearce, C.R. Hughes and H.N. Khoury, *A Preliminary Mineralogical Investigation of a Natural Analogue of a Cement-buffered Hyperalkaline Groundwater Interaction with Marl, Maqarin, Northern Jordan, Nagra Unpublished Internal Report, 1992.*

C3.1 Major and trace element analysis

		A960	A961	A962	A963	A965	A965(i)	A965(ii)	A966	A966(i)	A966(ii)	A970	A971	A972	A976	A980	A981	A982
SiO_2	wt.%	9.7	5.0	9.0	7.8	4.9	4.3	5.3	8.9	8.8	9.2	9.3	6.8	38.9	85.2	7.1	5.1	5.5
Na	ppm	392	848	589	480	241	292	254	329	381	394	724	1160	2450	510	562	510	1050
Mg	ppm	1230	1420	1350	1480	923	1910	1100	5550	2350	3470	1590	1880	9670	2830	3310	2780	1940
Al	ppm	12100	7320	22100	16200	10900	2720	8410	18100	18500	20000	18700	13400	5770	856	9880	7940	5720
S	wt.%	0.29	1.42	0.24	2.04	1.90	1.26	1.81	2.62	2.96	2.76	0.64	0.01	0.06	0.02	<0.01	<0.01	<0.01
P	ppm	6800	6390	8500	7800	6560	7460	6340	6200	6320	6740	7100	8450	3210	<90	12700	16600	4510
K	ppm	<200	1100	2060	2770	<200	<200	<200	1760	2070	2430	1920	2940	1930	477	1500	414	484
Ca	wt.%	30.6	31.4	32.0	27.7	32.2	34.4	32.4	29.3	29.7	29.1	31.4	35.4	20.4	5.53	36.8	37.3	36.4
Ti	ppm	546	252	733	634	241	348	298	806	788	899	753	663	388	27	570	398	184
V	ppm	84	70	131	114	84	83	91	143	153	158	115	118	66	87	303	52	119
Cr	ppm	443	110	306	370	121	198	266	298	310	275	597	557	33	4750	601	236	1440
Mn	ppm	31	28	37	33	36	34	26	74	83	86	44	62	20	41	33	18	17
Fe	ppm	8980	4370	14400	8350	5780	4670	4340	16400	20300	21900	10800	9620	4150	390	3660	1920	5140
Co	ppm	<20	<20	<20	<20	<20	<20	<20	<20	<20	<20	<20	<20	<20	<20	<20	<20	<20
Ni	ppm	192	133	167	152	110	101	71	112	125	129	155	174	92	32	155	118	127
Cu	ppm	56	46	59	54	55	27	<20	57	62	61	69	61	29	<20	52	51	33
Zn	ppm	444	276	275	284	164	203	142	174	151	155	316	284	303	277	347	292	291
Sr	ppm	869	1500	2330	1510	1050	1180	987	1090	1140	1200	2420	3700	1270	61	594	583	493
Zr	ppm	19	<15	<15	20	<15	<15	<15	24	25	31	33	<15	<15	<15	<15	<15	21
Cd	ppm	<15	<15	<15	<15	<15	<15	<15	<15	<15	<15	<15	<15	<15	<15	<15	<15	<15
Ba	ppm	174	139	96	182	88	124	51	93	112	130	112	75	1210	123	153	80	151
Pb	ppm	<60	<60	<60	<60	<60	<60	<60	<60	<60	<60	<60	<60	<60	<60	<60	<60	<60
Se	ppm	25.6	34.3	50.9	36.3	49.5	46.0	50.8	17.2	20.0	22.8	15.2	56.9	0.136	1.488	0.223	0.152	0.058
As	ppm	9.66	4.56	16.19	6.65	9.38	7.07	13.78	5.76	6.26	6.62	16.99	15.10	1.84	2.61	1.90	2.11	4.89
Th	ppm	1.84	1.14	2.45	1.75	0.79	1.07	0.90	1.91	1.63	2.09	2.05	2.67	1.13	0.03	1.69	1.07	0.53
U	ppm	31.81	15.71	19.48	18.31	12.24	13.33	11.82	13.37	13.05	14.72	19.75	21.99	2.28	30.11	10.79	11.14	4.38
%LOI 110°C		6.3	0.4	0.8	4.3	4.6	1.6	4.7	3.5	2.4	0.8	6.4	0.3	3.3	0.4	0.7	0.4	0.2
%LOI 450°C		6.7	14.7	10.6	18.7	12.5	13.4	12.7	10.9	11.2	11.6	6.8	5.6	8.1	2.1	4.0	3.3	2.6
%LOI 1050°C		32.2	29.2	27.6	25.6	30.3	30.5	29.9	27.0	25.3	24.3	32.5	32.2	19.8	6.0	33.9	34.6	37.7

Sample		A960	A961	A962	A963	A965	A965(i)	A965(ii)	A966
Y	ppm	26.27	21.15	27.02	22.88	17.82	20.49	17.56	22.02
La	ppm	17.72	12.65	19.25	15.35	11.50	12.94	11.39	14.89
Ce	ppm	17.42	10.35	20.99	15.67	9.58	11.44	9.53	16.14
Pr	ppm	4.22	2.97	4.70	3.56	2.43	2.91	2.50	3.27
Nd	ppm	12.44	9.06	14.47	10.91	7.43	8.81	7.32	9.60
Sm	ppm	2.86	2.37	3.92	2.70	1.76	2.07	1.62	2.26
Eu	ppm	0.80	0.72	1.26	0.76	0.47	0.57	0.45	0.60
Gd	ppm	2.84	2.22	3.66	2.49	1.75	1.95	1.71	2.35
Tb	ppm	0.60	0.51	0.81	0.58	0.38	0.42	0.36	0.51
Dy	ppm	2.99	2.42	3.55	2.63	1.87	2.21	1.83	2.61
Er	ppm	2.10	1.79	2.79	1.94	1.26	1.62	1.30	1.77
Tm	ppm	0.37	0.37	0.53	0.34	0.23	0.26	0.22	0.31
Yb	ppm	1.92	1.66	2.44	1.82	1.24	1.44	1.22	1.74
Lu	ppm	0.37	0.36	0.58	0.38	0.25	0.30	0.23	0.31

Sample		A966(i)	A966(ii)	A970	A971	A972	A976	A980	A981	A982
Y	ppm	20.56	23.81	24.24	28.08	7.27	0.17	13.80	14.48	5.78
La	ppm	13.60	16.04	15.12	16.48	5.81	0.32	10.40	10.26	5.11
Ce	ppm	14.63	17.55	16.33	15.02	5.53	0.33	9.56	7.00	3.55
Pr	ppm	2.99	3.66	3.65	4.25	1.45	0.09	2.15	1.94	1.21
Nd	ppm	9.08	10.92	11.75	14.73	4.47	0.08	6.09	5.35	2.22
Sm	ppm	2.08	2.57	3.15	5.64	1.89	0.09	1.36	1.15	0.55
Eu	ppm	0.59	0.68	0.96	1.92	0.83	-0.01	0.32	0.29	0.09
Gd	ppm	2.12	2.30	2.94	4.14	1.14	0.01	1.29	1.26	0.43
Tb	ppm	0.47	0.54	0.66	1.12	0.26	0.00	0.29	0.26	0.11
Dy	ppm	2.40	2.84	3.00	4.63	1.17	0.03	1.56	1.42	0.57
Er	ppm	1.65	1.98	2.33	3.92	0.96	0.03	1.22	1.13	0.43
Tm	ppm	0.29	0.36	0.46	0.85	0.20	0.00	0.18	0.19	0.07
Yb	ppm	1.64	1.93	2.13	3.48	0.86	0.03	1.12	1.10	0.46
Lu	ppm	0.32	0.37	0.46	0.91	0.22	0.01	0.23	0.23	0.10

Table D1 A960 ATEM Data

	Analysis 1 Zeolite	Analysis 2 CASH	Analysis 3 CASH	Analysis 4 CASH	Analysis 5 CASH	Analysis 6 CASH	Analysis 7 CASH	Analysis 8 CASH	Analysis 9 CASH	Analysis 10 CASH	Analysis 11 CASH
Na	6.11	2.50	2.33	2.20	3.71	1.90	2.29	2.00	1.58	1.46	1.91
Mg	0.00	0.33	0.00	0.00	0.00	0.00	0.00	0.00	0.00	0.00	0.00
Al	8.84	7.43	3.79	4.24	4.22	4.29	4.39	4.12	4.24	5.23	5.75
Si	34.83	20.43	11.71	19.01	19.84	20.75	18.14	19.77	20.53	19.95	18.81
P	0.00	0.00	0.00	0.00	0.00	0.00	0.00	0.00	0.00	0.00	0.00
S	N/A	N/A	N/A	2.27	2.00	2.31	1.79	1.90	1.82	1.84	1.83
K	0.00	0.00	0.00	0.00	0.00	0.23	0.00	0.00	0.00	0.00	0.00
Ca	0.40	25.16	45.42	30.50	28.30	27.82	32.41	30.36	29.60	28.42	28.86
Cr	0.00	0.00	0.00	0.00	0.00	0.00	0.00	0.00	0.00	0.00	0.00
Mn	0.00	0.00	0.00	0.00	0.00	0.00	0.00	0.00	0.00	0.00	0.00
Fe^{2+}	0.00	2.45	0.86	0.00	0.00	0.00	0.00	0.00	0.00	0.87	1.08
Fe^{3+}	0.00	0.00	0.00	0.00	0.00	0.00	0.00	0.00	0.00	0.00	0.00
Na^{+}	0.43	0.90	1.46	0.85	1.37	0.67	0.93	0.74	0.56	0.54	0.75
K^{+}	0.00	0.00	0.00	0.00	0.00	0.05	0.00	0.00	0.00	0.00	0.00
Ca^{2+}	0.83	5.18	16.31	6.75	6.00	5.64	7.51	6.46	6.06	5.99	6.45
Al^{3+}	0.79	2.27	2.02	1.39	1.33	1.29	1.51	1.30	1.29	1.64	1.91
SO_4^{2+}	N/A	N/A	N/A	0.63	0.53	0.59	0.52	0.51	0.47	0.49	0.51
Si^{4+}	3.00	6.00	6.00	6.00	6.00	6.00	6.00	6.00	6.00	6.00	6.00
P^{5+}	0.00	0.00	0.00	0.00	0.00	0.00	0.00	0.00	0.00	0.00	0.00
(Ca+Na+K):Si	0.42	1.01	2.96	1.27	1.23	1.06	1.41	1.20	1.10	1.09	1.20
Ca:Si	0.01	0.86	2.72	1.12	1.00	0.94	1.25	1.08	1.01	1.00	1.08
Al:Si	0.26	0.38	0.34	0.23	0.22	0.22	0.25	0.22	0.22	0.27	0.32

	Analysis 12 Thaum.-Ettr.	Analysis 13 Thaum.-Ettr.	Analysis 14 CASH	Analysis 15 CASH	Analysis 16 CASH	Analysis 17 CASH	Analysis 18 CASH	Analysis 19 Calcite/CASH	Analysis 20 Calcite/CASH
Na	1.71	1.60	0.00	0.00	0.00	0.00	0.00	0.00	0.00
Mg	0.00	0.00	0.63	0.61	0.00	0.42	0.36	0.00	0.00
Al	2.24	3.05	7.28	5.80	3.65	4.17	4.89	0.78	0.00
Si	11.38	17.55	15.31	19.08	14.71	22.60	22.27	6.03	1.89
P	0.00	0.00	0.00	0.00	0.00	0.00	0.00	10.00	14.92
S	10.72	5.49	1.87	2.04	2.01	1.85	1.95	1.66	1.69
K	0.00	0.00	0.00	0.00	0.00	0.00	0.00	0.00	0.00
Ca	30.26	29.19	32.31	29.35	40.46	27.50	26.92	41.86	41.13
Cr	0.00	0.00	0.00	0.00	0.00	0.00	0.00	0.00	0.00
Mn	0.00	0.00	0.00	0.83	0.00	0.00	0.00	0.00	0.00
Fe^{2+}	0.00	0.00	2.02	0.00	0.00	0.00	0.00	0.00	0.00
Fe^{3+}	0.00	0.00	0.00	0.00	0.00	0.00	0.00	0.00	0.00
Na^{+}	0.59	0.57	0.00	0.00	0.00	0.00	0.00	0.00	0.00
K^{+}	0.00	0.00	0.00	0.00	0.00	0.00	0.00	0.00	0.00
Ca^{2+}	6.00	6.00	8.87	6.47	11.56	5.12	5.08	29.20	91.58
Al^{3+}	0.66	0.93	2.97	1.90	1.55	1.15	1.37	0.81	0.00
SO_4^{2+}	2.66	1.41	0.64	0.56	0.72	0.43	0.46	1.45	4.71
Si^{4+}	3.22	5.15	6.00	6.00	6.00	6.00	6.00	6.00	6.00
P^{5+}	0.00	0.00	0.00	0.00	0.00	0.00	0.00	9.03	42.99
(Ca+Na+K):Si	2.05	1.28	1.48	1.08	1.93	0.85	0.85	4.87	15.26
Ca:Si	1.86	1.17	1.48	1.08	1.93	0.85	0.85	4.87	15.26
Al:Si	0.21	0.18	0.49	0.32	0.26	0.19	0.23	0.14	0.00

	A960AP2/1A	A960AP2/1	A960AP2/2A	A960AP2/3	A960AP2/4	A960AP2/5	A960AP2/6	A960AP2/7	A960AP2/8
Si	2.10	23.00	24.90	20.40	20.10	21.30	14.80	13.60	7.90
P	n.d.	0.00	n.d.	n.d.	n.d.	n.d.	n.d.	n.d.	n.d.
Cr	0.00	0.00	0.00	0.00	0.00	0.00	0.00	0.00	0.00
Al	0.70	5.40	5.80	4.60	4.20	4.40	5.50	4.60	2.70
Ca	0.60	4.30	4.40	3.90	3.70	3.80	4.00	3.30	3.00
Mg	0.00	0.00	0.00	0.00	0.00	0.00	0.10	0.00	0.00
Fe	0.00	0.00	0.00	0.00	0.00	0.00	0.00	0.00	0.00
Mn	0.00	0.00	0.00	0.00	0.00	0.00	0.00	0.00	0.00
K	0.00	0.10	0.10	0.00	0.00	0.00	0.20	0.10	0.00
Na	0.00	0.00	0.20	0.00	0.20	0.00	0.20	0.00	0.00
S	0.00	0.10	0.10	0.10	0.00	0.00	0.10	0.00	0.00
Cl	1.90	0.50	0.40	0.70	0.70	0.60	0.90	1.20	1.40
Sr	0.00	0.00	0.00	0.50	0.00	0.00	0.00	0.00	0.00
Ba	0.00	0.00	0.00	0.00	0.00	0.00	0.00	0.00	0.00
O	3.90	33.10	35.70	29.50	28.50	30.00	24.00	21.40	13.10
Ca^{2+}	0.80	0.52	0.50	0.54	0.52	0.50	0.76	0.68	1.06
Al^{3+}	1.39	0.98	0.97	0.94	0.87	0.86	1.55	1.41	1.42
SO_4^{2-}	N/A	0.02	0.01	0.02	N/A	N/A	0.02	N/A	N/A
Si^{4+}	4.00	4.00	4.00	4.00	4.00	4.00	4.00	4.00	4.00
Ca:Si	0.20	0.13	0.12	0.13	0.13	0.13	0.19	0.17	0.27

	A960AP2/9	A960AP2/10	A960AP2/11	A960AP2/12	A960AP2/13	A960AP2/14	A960AP2/15	A960AP2/16
Si	14.50	7.10	6.30	11.80	11.10	10.80	7.20	5.90
P	n.d.	n.d.	n.d.	n.d.	n.d.	n.d.	n.d.	n.d.
Cr	0.00	0.00	0.00	0.00	0.00	0.00	0.00	0.00
Al	5.50	3.10	2.50	5.20	11.60	4.80	3.20	2.80
Ca	3.80	2.30	1.90	4.10	2.80	3.50	2.40	1.90
Mg	0.00	0.00	0.00	0.00	0.00	0.00	0.00	0.00
Fe	0.00	0.00	0.00	0.00	0.00	0.00	0.00	0.00
Mn	0.00	0.00	0.00	0.00	0.00	0.00	0.00	0.00
K	0.10	0.00	0.00	0.10	0.00	0.10	0.10	0.00
Na	0.00	0.00	0.00	0.20	0.00	0.00	0.00	0.00
S	0.00	0.00	0.00	0.10	0.20	0.10	0.00	0.10
Cl	0.90	1.70	1.70	1.00	0.80	1.30	1.30	1.50
Sr	0.60	0.00	0.00	0.00	0.00	0.00	0.00	0.00
Ba	0.00	0.00	0.00	0.00	0.00	0.00	0.00	0.00
O	23.40	12.30	10.70	20.30	24.60	18.70	12.50	10.50
Ca^{2+}	0.73	0.91	0.85	0.97	0.71	0.91	0.93	0.90
Al^{3+}	1.58	1.82	1.65	1.83	4.35	1.85	1.85	1.98
SO_4^{2-}	N/A	N/A	N/A	0.03	0.06	0.03	N/A	0.06
Si^{4+}	4.00	4.00	4.00	4.00	4.00	4.00	4.00	4.00
Ca:Si	0.18	0.23	0.21	0.24	0.18	0.23	0.23	0.23

	A962AP1/2 Tobermorite	A962AP1/3 Tobermorite	A962AP1/4 Tobermorite	A962AP1/5 Tobermorite	A962AP1/6 Tobermorite	A962AP1/7 Tobermorite	A962AP1/8 Tobermorite	A962AP1/9 Tobermorite	A962AP1/10 Tobermorite	A962AP1/11 Tobermorite
Si	8.00	8.90	8.40	9.60	8.10	8.50	13.20	8.60	10.30	10.50
P	0.00	0.00	0.00	0.00	0.00	0.00	0.00	0.00	0.00	0.00
Cr	0.00	0.00	0.00	0.00	0.00	0.00	0.00	0.00	0.00	0.00
Al	1.60	1.70	1.80	1.90	1.60	1.60	2.50	1.90	2.10	2.10
Ca	7.00	8.40	7.80	9.10	7.30	7.30	11.00	7.80	10.10	9.70
Mg	0.00	0.00	0.00	0.00	0.00	0.00	0.00	0.00	0.00	0.00
Fe	0.00	0.00	0.00	0.00	0.00	0.00	0.00	0.00	0.00	0.00
Mn	0.00	0.00	0.00	0.00	0.00	0.00	0.00	0.00	0.00	0.00
K	0.20	0.30	0.20	0.20	0.20	0.20	0.40	0.30	0.20	0.30
Na	0.20	0.20	0.00	0.20	0.10	0.20	0.30	0.20	0.10	0.10
S	0.00	0.10	0.10	0.00	0.00	0.00	0.10	0.20	0.00	0.00
Cl	1.00	0.90	0.90	0.90	1.00	1.00	0.70	1.00	0.80	0.90
Sr	0.40	0.00	0.00	0.00	0.40	0.00	0.00	0.00	0.00	0.00
Ba	0.00	0.00	0.00	0.00	0.00	0.00	0.00	0.00	0.00	0.00
Zn	0.00	0.00	0.00	0.00	0.00	0.00	0.00	0.00	0.00	0.00
Ti	0.00	0.00	0.00	0.00	0.00	0.00	0.00	0.00	0.00	0.00
O	13.90	15.70	14.90	16.90	14.00	14.40	22.30	15.40	18.00	18.10
Ca^{2+}	3.68	3.97	3.90	3.99	3.79	3.61	3.50	3.81	4.12	3.88
Al^{3+}	1.25	1.19	1.34	1.24	1.23	1.18	1.18	1.38	1.27	1.25
SO_4^{2-}	0.26	0.00	N/A	N/A	0.26	0.00	N/A	N/A	N/A	0.00
Si^{4+}	6.00	6.00	6.00	6.00	6.00	6.00	6.00	6.00	6.00	6.00

	A962AP1/12 Tobermorite	A962AP1/13 Tobermorite	A962AP1/14 Tobermorite	A962AP1/15 Tobermorite	A962AP1/16 Tobermorite	A962AP1/17 Tobermorite	A962AP1/18 Tobermorite	A962AP1/19 Tobermorite	A962AP1/20 Tobermorite
Si	13.00	15.60	17.80	18.20	19.80	17.30	17.10	16.00	15.10
P	0.00	0.00	0.00	0.00	0.00	0.00	0.00	0.00	0.00
Cr	0.00	0.00	0.00	0.00	0.00	0.00	0.00	0.00	0.20
Al	2.60	4.70	3.60	3.50	3.50	3.50	3.60	3.30	4.00
Ca	13.50	16.40	19.90	20.40	23.20	21.00	20.90	20.00	18.30
Mg	0.00	0.00	0.00	0.00	0.00	0.00	0.00	0.00	0.10
Fe	0.00	0.00	0.00	0.00	0.00	0.00	0.00	0.20	0.20
Mn	0.00	0.00	0.00	0.00	0.00	0.00	0.00	0.00	0.00
K	0.40	0.30	0.30	0.30	0.20	0.20	0.20	0.10	0.20
Na	0.30	0.30	0.30	0.50	0.00	0.40	0.40	0.50	1.50
S	0.10	0.40	0.30	0.40	0.10	0.30	0.30	0.50	0.80
Cl	0.70	0.50	0.10	0.10	0.00	0.20	0.10	0.20	0.30
Sr	0.50	0.50	0.80	0.50	0.00	0.00	0.00	0.50	0.00
Ba	0.00	0.40	0.00	0.00	0.50	0.00	0.00	0.00	0.00
Zn	0.00	0.00	0.00	0.00	0.00	0.00	0.00	0.00	1.80
Ti	0.00	0.00	0.00	0.00	0.00	0.00	0.00	0.00	0.00
O	23.30	29.60	32.40	33.10	35.40	32.00	32.00	30.40	30.70
Ca^{2+}	4.37	4.42	4.70	4.71	4.93	5.10	5.14	5.26	5.10
Al^{3+}	1.25	1.88	1.26	1.20	1.10	1.26	1.31	1.29	1.65
SO_4^{2-}	0.20	0.17	0.24	0.14	N/A	0.00	N/A	0.16	N/A
Si^{4+}	6.00	6.00	6.00	6.00	6.00	6.00	6.00	6.00	6.00

	Analysis 1	Analysis 2	Analysis 3	Analysis 4	Analysis 5	Analysis 6	Analysis 7	Analysis 8	Analysis 9	Analysis 10	Analysis 11
Na^{+}	5.32	4.89	0.69	0.42	0.00	0.00	0.00	0.00	0.00	0.00	0.00
K^{+}	0.00	0.28	0.24	0.33	0.39	0.38	0.40	0.30	0.25	0.35	0.26
Ca^{2+}	69.89	77.28	0.93	0.57	6.58	5.77	6.73	3.91	3.79	5.87	5.34
Al^{3+}	0.00	0.00	2.51	3.02	1.01	0.99	1.01	0.94	1.02	0.96	0.99
Si^{4+}	6.00	6.00	6.00	6.00	6.00	6.00	6.00	6.00	6.00	6.00	6.00
P^{5+}	35.24	36.95	0.00	0.00	0.00	0.00	0.00	0.00	0.00	0.00	0.00
$Ca + Na_2 + K_2$	72.55	79.86	1.40	0.95	6.77	5.96	6.93	4.05	3.92	6.04	5.47
S^{6+}	0.00	0.00	1.45	0.81	0.00	0.00	0.00	0.00	0.00	0.00	0.00

	Analysis 1	Analysis 6	Analysis 7	Analysis 2	Analysis 8	Analysis 9	Analysis 3	Analysis 4	Analysis 5	Analysis 10	Analysis 11
Na^{+}	1.58	0.00	0.00	0.00	0.00	0.00	0.00	0.00	0.00	0.00	0.00
K^{+}	0.00	0.06	0.00	0.25	0.24	0.22	0.22	0.06	0.10	0.51	0.63
Ca^{2+}	5.90	5.03	4.39	1.70	1.36	1.77	3.66	0.36	0.24	3.38	30.67
Al^{3+}	0.17	0.73	1.00	5.36	4.09	3.63	4.85	5.61	5.70	0.81	0.77
Si^{4+}	6.00	6.00	6.00	6.00	6.00	6.00	6.00	6.00	6.00	6.00	6.00
P^{5+}	0.00	0.00	0.00	0.00	0.00	0.00	0.00	0.00	0.00	0.00	0.00
$Ca + Na_2 + K_2$	6.69	5.06	4.39	1.82	1.48	1.88	3.77	0.38	0.29	3.63	30.98
S^{6+}	N/A	N/A	N/A	N/A	N/A	N/A	N/A	N/A	N/A	N/A	N/A

	Acicular CASH	Acicular CASH	Acicular CASH	Acicular CASH	Acicular CASH	Acicular CASH	Acicular CASH	Acicular CASH	Acicular CASH	Acicular CASH	Acicular CASH	Acicular CASH	Acicular CASH	Acicular CASH	Acicular CASH	Acicular CASH
F	0.42	0.37	0.02	0.31	0.48	0.58	0.55	0.18	0.36	0.26	0.07	0.62	0.76	0.48	0.47	0.80
Cl	0.40	0.35	0.67	0.49	0.66	0.19	0.34	0.24	0.92	0.66	0.93	1.38	0.59	0.26	0.29	0.14
Fe	0.04	0.04	0.00	0.00	0.00	0.00	0.02	0.03	0.03	0.04	0.00	0.03	0.03	0.02	0.02	0.03
Na	0.15	0.10	0.12	0.19	0.19	0.16	0.13	0.22	0.25	0.22	0.36	0.20	0.25	0.15	0.17	0.22
K	0.02	0.00	0.01	0.00	0.01	0.00	0.00	0.01	0.07	0.01	0.03	0.00	0.00	0.00	0.00	0.01
Mn	0.00	0.00	0.01	0.00	0.00	0.00	0.00	0.00	0.01	0.01	0.00	0.02	0.00	0.00	0.00	0.01
Mg	0.22	0.09	0.15	0.29	0.25	0.30	0.23	0.33	0.26	0.35	0.19	0.46	0.45	0.16	0.27	0.17
Ca	24.21	25.03	23.58	23.66	22.37	24.68	23.21	23.47	19.18	22.28	21.25	23.08	23.62	24.75	24.31	24.17
Cr	0.00	0.00	0.00	0.00	0.01	0.00	0.01	0.02	0.00	0.00	0.00	0.01	0.02	0.00	0.02	0.00
Al	8.95	7.59	7.68	8.86	9.29	8.98	9.45	8.74	6.59	9.33	5.91	10.45	9.40	7.70	9.59	7.64
S	9.05	8.90	8.73	8.25	7.49	8.84	9.41	7.18	3.91	7.37	4.67	8.48	8.09	8.34	8.94	7.81
Si	3.00	3.85	4.83	3.95	4.80	2.81	2.98	5.02	11.36	4.92	10.23	2.12	3.18	4.25	2.44	4.81
P	0.03	0.04	0.04	0.04	0.03	0.02	0.04	0.03	0.07	0.03	0.06	0.01	0.03	0.04	0.04	0.10
Ti	0.00	0.00	0.00	0.01	0.00	0.01	0.00	0.00	0.00	0.00	0.00	0.00	0.01	0.00	0.01	0.00
Ionic Proportions																
Ca^{2+}	6.00	6.00	6.00	6.00	6.00	6.00	6.00	6.00	6.00	6.00	6.00	6.00	6.00	6.00	6.00	6.00
Al^{3+}	3.30	2.70	2.90	3.34	3.70	3.24	3.63	3.32	3.06	3.73	2.48	4.04	3.55	2.77	3.52	2.82
SO_4^{2-}	2.80	2.67	2.78	2.62	2.51	2.69	3.04	2.30	1.53	2.48	1.65	2.76	2.57	2.53	2.76	2.42
Si^{4+}	1.06	1.32	1.75	1.43	1.84	0.97	1.10	1.83	5.07	1.89	4.12	0.78	1.15	1.47	0.86	1.70
Molar Ratio																
Ca:Si	5.65	4.56	3.42	4.20	3.27	6.16	5.45	3.28	1.18	3.17	1.46	7.64	5.20	4.08	6.98	3.52
Al:Si	3.10	2.05	1.65	2.33	2.01	3.33	3.30	1.81	0.60	1.97	0.60	5.14	3.07	1.89	4.09	1.66

	Acicular CASH	Acicular CASH	Acicular CASH	s.d.	Massive CASH	Massive CASH	Massive CASH	Massive CASH	Massive CASH	Massive CASH	Massive CASH	Massive CASH	Massive CASH	Massive CASH	Massive CASH	Massive CASH	Massive CASH	Massive CASH
F	0.20	0.00	**0.38**	**±0.23**	0.18	0.12	0.19	0.07	0.17	0.00	0.03	0.04	0.09	0.00	0.00	0.07	0.00	0.11
Cl	1.26	0.64	**0.58**	**±0.36**	0.01	0.02	0.00	0.01	0.05	0.00	0.01	0.01	0.06	0.02	0.04	0.01	0.00	0.01
Fe	0.07	0.02	**0.02**	**±0.02**	0.01	0.02	0.01	0.00	0.00	0.00	0.00	0.00	0.00	0.01	0.00	0.00	0.00	0.02
Na	0.41	0.25	**0.21**	**±0.08**	0.07	0.04	0.04	0.03	0.13	0.02	0.01	0.01	0.36	0.10	0.16	0.09	0.07	0.06
K	0.03	0.02	**0.01**	**±0.02**	0.21	0.18	0.20	0.17	0.17	0.13	0.18	0.20	0.25	0.21	0.22	0.22	0.22	0.24
Mn	0.00	0.00	**0.00**	**±0.01**	0.01	0.00	0.00	0.00	0.01	0.01	0.00	0.00	0.00	0.01	0.01	0.01	0.00	0.00
Mg	0.20	0.11	**0.25**	**±0.10**	0.00	0.00	0.00	0.00	0.00	0.00	0.00	0.00	0.13	0.01	0.00	0.00	0.00	0.01
Ca	21.64	23.56	**23.22**	**±1.45**	17.46	17.28	17.51	18.04	17.96	18.29	17.59	18.05	17.35	17.48	17.58	17.44	17.75	17.73
Cr	0.00	0.03	**0.01**	**±0.01**	0.00	0.00	0.00	0.00	0.00	0.02	0.00	0.00	0.00	0.00	0.02	0.01	0.00	0.00
Al	8.65	7.14	**8.44**	**±1.18**	3.67	3.69	3.65	3.62	3.65	3.62	3.77	3.75	4.06	3.75	3.70	3.65	3.62	3.73
S	7.08	8.09	**7.81**	**±1.45**	0.02	0.01	0.01	0.01	0.03	0.02	0.03	0.02	0.02	0.03	0.05	0.02	0.00	0.03
Si	5.79	5.65	**4.78**	**±2.45**	18.37	18.52	18.36	18.11	18.01	18.09	18.33	18.02	17.96	18.33	18.23	18.43	18.32	18.12
P	0.03	0.04	**0.04**	**±0.02**	0.01	0.02	0.03	0.02	0.01	0.03	0.01	0.01	0.02	0.02	0.03	0.02	0.01	0.03
Ti	0.03	0.01	**0.00**	**±0.01**	0.00	0.00	0.00	0.01	0.00	0.00	0.00	0.00	0.00	0.00	0.00	0.00	0.00	0.01
Ionic Proportions																		
Ca^{2+}	6.00	6.00	**6.00**		4.00	3.92	4.01	4.19	4.19	4.25	4.03	4.21	4.06	4.01	4.05	3.98	4.07	4.11
Al^{3+}	3.56	2.70	**3.24**		1.25	1.25	1.24	1.25	1.27	1.25	1.29	1.30	1.41	1.28	1.27	1.24	1.23	1.29
SO_4^{2-}	2.45	2.58	**2.52**		0.00	0.00	0.00	0.00	0.01	0.00	0.01	0.01	0.01	0.01	0.01	0.00	0.00	0.01
Si^{4+}	2.29	2.05	**1.76**		6.00	6.00	6.00	6.00	6.00	6.00	6.00	6.00	6.00	6.00	6.00	6.00	6.00	6.00
Molar Ratio																		
Ca:Si	2.62	2.92	**3.41**		0.67	0.65	0.67	0.70	0.70	0.71	0.67	0.70	0.68	0.67	0.68	0.66	0.68	0.69
Al:Si	1.55	1.32	**1.84**		0.21	0.21	0.21	0.21	0.21	0.21	0.21	0.22	0.24	0.21	0.21	0.21	0.21	0.21

	Massive CASH	Massive CASH	Massive CASH	Massive CASH	Massive CASH	Massive CASH	Massive CASH	Massive CASH	Massive CASH	Massive CASH	Massive CASH		sample ref.	M93001	M93002	M93003	M93004
F	0.10	0.22	0.15	0.12	0.18	0.06	0.15	0.06	0.21	0.06	**0.10**	**±0.07**	No data	No data	No data	No data	No data
Cl	0.01	0.02	0.04	0.01	0.00	0.03	0.04	0.01	0.02	0.01	**0.02**	**±0.02**	No data	No data	No data	No data	No data
Fe	0.00	0.00	0.00	0.00	0.00	0.00	0.01	0.01	0.02	0.00	**0.00**	**±0.01**	Fe	3.59	0.94	4.73	0.50
Na	0.08	0.18	0.10	0.04	0.10	0.05	0.04	0.05	0.07	0.01	**0.08**	**±0.08**	Na	0.00	0.00	0.96	0.00
K	0.24	0.28	0.21	0.14	0.38	0.17	0.13	0.20	0.23	0.15	**0.20**	**±0.05**	K	0.83	0.83	0.83	0.83
Mn	0.00	0.00	0.00	0.01	0.01	0.00	0.00	0.01	0.00	0.00	**0.00**	**±0.00**	No data	No data	No data	No data	No data
Mg	0.00	0.00	0.00	0.00	0.00	0.00	0.01	0.00	0.00	0.00	**0.01**	**±0.03**	Mg	0.00	0.00	0.60	0.00
Ca	17.27	17.21	17.69	17.77	17.81	17.77	17.75	18.37	17.58	17.78	**17.69**	**±0.30**	CA	44.49	52.52	5.56	64.06
Cr	0.00	0.00	0.00	0.00	0.01	0.00	0.01	0.01	0.00	0.00	**0.00**	**±0.01**	No data	No data	No data	No data	No data
Al	3.68	4.40	3.67	3.74	2.30	3.76	3.72	3.81	3.63	3.73	**3.68**	**±0.34**	Al	4.64	2.59	18.16	0.40
S	0.03	0.03	0.02	0.01	0.03	0.02	0.01	0.03	0.03	0.01	**0.02**	**±0.01**	S	0.00	0.00	0.00	0.00
Si	18.51	17.80	18.19	18.18	19.16	18.17	18.17	17.69	18.28	18.24	**18.23**	**±0.28**	Si	9.07	7.85	18.43	3.44
P	0.01	0.03	0.02	0.01	0.02	0.02	0.02	0.01	0.02	0.01	**0.02**	**±0.01**					
Ti	0.00	0.00	0.00	0.00	0.00	0.00	0.00	0.00	0.00	0.00	**0.00**	**±0.00**					
Ionic Proportions																	
Ca^{2+}	3.92	4.07	4.09	4.11	3.91	4.11	4.11	4.37	4.04	4.10	**4.08**			20.61	28.13	1.27	78.28
Al^{3+}	1.24	1.54	1.26	1.29	0.75	1.29	1.28	1.34	1.24	1.28	**1.26**			3.20	2.06	6.15	0.72
SO_4^{2-}	0.01	0.01	0.01	0.00	0.01	0.01	0.00	0.01	0.01	0.00	**0.01**			0.00	0.00	0.00	0.00
Si^{4+}	6.00	6.00	6.00	6.00	6.00	6.00	6.00	6.00	6.00	6.00	**6.00**			6.00	6.00	6.00	6.00
Molar Ratio																	
Ca:Si	0.65	0.68	0.68	0.68	0.65	0.69	0.68	0.73	0.67	0.68	**0.68**			3.44	4.69	0.21	13.05
Al:Si	0.21	0.26	0.21	0.21	0.12	0.22	0.21	0.22	0.21	0.21	**0.21**			0.53	0.34	1.03	0.12

	M93005	M93006	M93007	M93008	M93009	M93010	M93011	M93012	M93013	M93014	M93015	M93016	M93017	M93018	M93019	M93020
F	No data	No data	No data	No data	No data	No data	No data	No data	No data	No data	No data	No data	No data	No data	No data	No data
Cl	No data	No data	No data	No data	No data	No data	No data	No data	No data	No data	No data	No data	No data	No data	No data	No data
Fe	0.70	1.87	5.53	6.86	0.65	0.89	0.72	2.74	1.38	17.87	28.39	0.00	3.26	4.24	4.78	0.26
Na	0.00	0.00	1.56	0.69	0.00	0.00	0.00	0.56	0.85	0.00	0.00	0.00	0.00	0.00	0.00	0.00
K	0.83	0.83	0.83	0.83	0.83	0.83	0.83	0.83	0.83	0.83	0.83	0.83	0.83	0.83	0.83	0.83
Mn	No data	No data	No data	No data	No data	No data	No data	No data	No data	No data	No data	No data	No data	No data	No data	No data
Mg	0.00	0.00	1.71	1.43	0.00	0.19	0.00	1.06	0.65	0.00	0.00	0.00	0.00	0.49	0.00	0.42
Ca	62.71	30.96	7.06	5.77	23.70	22.18	22.52	3.86	2.27	21.89	8.17	66.22	14.70	5.45	13.64	1.34
Cr	No data	No data	No data	No data	No data	No data	No data	No data	No data	No data	No data	No data	No data	No data	No data	No data
Al	0.81	5.72	13.41	11.61	6.19	7.34	6.15	17.86	20.65	5.60	7.00	0.34	9.41	18.05	11.31	24.19
S	0.00	0.00	0.00	0.00	0.00	0.00	0.00	0.00	0.00	0.00	0.00	0.00	0.24	0.00	0.00	0.00
Si	3.58	16.94	18.63	20.56	21.27	20.74	21.86	19.34	18.83	12.01	11.97	2.70	21.28	20.00	20.04	20.53
P																
Ti																
Ionic Proportions																
Ca^{2+}	73.71	7.68	1.59	1.18	4.68	4.50	4.33	0.84	0.51	7.66	2.87	103.17	2.90	1.15	2.86	0.28
Al^{3+}	1.41	2.11	4.50	3.53	1.82	2.21	1.76	5.77	6.85	2.91	3.65	0.80	2.76	5.64	3.52	7.36
SO_4^{2-}	0.00	0.00	0.00	0.00	0.00	0.00	0.00	0.00	0.00	0.00	0.00	0.00	0.06	0.00	0.00	0.00
Si^{4+}	6.00	6.00	6.00	6.00	6.00	6.00	6.00	6.00	6.00	6.00	6.00	6.00	6.00	6.00	6.00	6.00
Molar Ratio																
Ca:Si	12.28	1.28	0.27	0.20	0.78	0.75	0.72	0.14	0.08	1.28	0.48	17.20	0.48	0.19	0.48	0.05
Al:Si	0.24	0.35	0.75	0.59	0.30	0.37	0.29	0.96	1.14	0.49	0.61	0.13	0.46	0.94	0.59	1.23

	1 Wallrock alteration	2 Wallrock alteration	3 Wallrock alteration	7 Wallrock alteration	8 Wallrock alteration	9 Wallrock alteration	10 Wallrock alteration	11 Wallrock alteration	12 Wallrock alteration	13 Wallrock alteration	Average wallrock alteration	s.d.	4 Cross-cutting late vein	5 Cross-cutting late vein	6 Cross-cutting late vein	vein	18 Amorphous CSH in wallrock	19 Amorphous CSH in wallrock	20 Amorphous CSH in wallrock	Average Amorphous CSH in wallrock
F	0.14	0.00	0.19	0.11	0.05	0.01	0.26	0.00	0.24	0.40	**0.14**	**± 0.13**	0.12	0.02	0.20	**0.07**	0.00	0.02	0.43	**0.15**
Cl	0.71	0.57	0.58	0.60	0.50	0.54	0.38	0.42	0.36	0.35	**0.50**	**± 0.11**	0.86	0.88	0.87	**0.87**	0.62	0.51	0.46	**0.53**
Fe	0.21	0.51	0.35	0.80	0.29	0.64	0.06	0.88	0.29	0.54	**0.46**	**± 0.25**	0.43	0.23	0.43	**0.33**	0.40	0.40	0.14	**0.31**
Na	0.12	0.02	0.05	0.07	0.07	0.06	0.07	0.07	0.07	0.08	**0.07**	**± 0.02**	0.02	0.05	0.05	**0.04**	0.05	0.05	0.09	**0.06**
K	0.05	0.02	0.02	0.03	0.02	0.03	0.01	0.01	0.01	0.00	**0.02**	**± 0.01**	0.01	0.01	0.04	**0.01**	0.02	0.02	0.05	**0.03**
Mn	0.00	0.00	0.01	0.03	0.01	0.00	0.00	0.00	0.02	0.01	**0.01**	**± 0.01**	0.00	0.02	0.00	**0.01**	0.00	0.00	0.00	**0.00**
Mg	0.47	0.15	0.18	0.45	0.21	0.36	0.25	0.21	0.26	0.10	**0.26**	**± 0.12**	0.25	0.18	0.37	**0.21**	0.40	0.30	0.28	**0.32**
Ca	16.51	20.51	22.32	21.16	22.91	22.70	25.51	23.98	25.04	28.78	**22.94**	**± 3.12**	14.84	14.97	5.59	**14.90**	20.33	21.41	23.38	**21.70**
Cr	0.14	0.08	0.08	0.14	0.06	0.08	0.06	0.09	0.07	0.10	**0.09**	**± 0.03**	0.06	0.06	0.05	**0.06**	0.09	0.11	0.14	**0.11**
Al	3.17	0.77	0.79	2.01	1.20	1.45	2.19	1.80	2.50	1.21	**1.71**	**± 0.73**	0.69	0.50	0.76	**0.60**	0.99	0.98	0.76	**0.91**
S	0.89	0.44	0.63	0.72	0.55	0.52	3.43	0.55	0.90	1.82	**1.04**	**± 0.88**	0.20	0.24	0.32	**0.22**	0.33	0.46	1.23	**0.68**
Si	6.73	5.28	4.22	6.04	6.11	5.24	5.83	5.39	3.66	2.50	**5.10**	**± 1.22**	3.93	5.20	4.45	**4.56**	5.36	6.11	6.63	**6.03**
P	0.67	0.60	0.48	0.54	0.11	0.38	0.19	0.44	0.47	1.03	**0.49**	**± 0.24**	0.05	0.07	0.14	**0.06**	0.09	0.15	1.14	**0.46**
Ti	0.03	0.09	0.09	0.13	0.06	0.12	0.03	0.19	0.07	0.09	**0.09**	**± 0.04**	0.06	0.04	0.08	**0.06**	0.07	0.07	0.04	**0.06**
Ionic Proportions																				
Ca^{2+}	10.32	16.33	22.24	14.73	15.77	18.22	18.42	18.70	28.74	48.37	**18.92**		15.89	12.10	5.28	**13.73**	15.96	14.73	14.82	**15.13**
Al^{3+}	2.94	0.92	1.17	2.08	1.23	1.73	2.34	2.08	4.25	3.03	**2.09**		1.09	0.60	1.07	**0.81**	1.16	1.01	0.71	**0.94**
SO_4^{2-}	0.69	0.44	0.79	0.63	0.47	0.52	3.09	0.54	1.29	3.82	**1.08**		0.27	0.24	0.37	**0.25**	0.33	0.40	0.97	**0.59**
Si^{4+}	6.00	6.00	6.00	6.00	6.00	6.00	6.00	6.00	6.00	6.00	**6.00**		6.00	6.00	6.00	**6.00**	6.00	6.00	6.00	**6.00**
Molar Ratio																				
Ca:Si	1.72	2.72	3.71	2.46	2.63	3.04	3.07	3.12	4.79	8.06	**3.15**		2.65	2.02	0.88	**2.29**	2.66	2.46	2.47	**2.52**
Al:Si	0.49	0.15	0.19	0.35	0.20	0.29	0.39	0.35	0.71	0.51	**0.35**		0.18	0.10	0.18	**0.14**	0.19	0.17	0.12	**0.16**

	s.d.	14 Ettringite	15 Gibbsite in wallrock	16 Gibbsite in wallrock	17 Gibbsite in wallrock	21 Ellestadite	22 Ellestadite	23 Ellestadite	24 Ellestadite	25 Ellestadite	26 Ellestadite	27 Ellestadite	28 Ellestadite	29 Ellestadite	30 Ellestadite	Average ellestadite	s.d.	31 Dull amorphous CSH lining fracture	32 Dull amorphous CSH lining fracture	33 Dull amorphous CSH lining fracture
F	**± 0.20**	0.40	0.84	1.09	1.09	1.21	0.68	0.41	0.55	0.76	0.88	0.39	0.98	0.27	0.58	**0.67**	**0.28**	0.00	0.05	0.00
Cl	**± 0.06**	0.26	0.11	0.16	0.18	0.20	0.34	0.45	0.24	0.02	0.26	0.48	0.16	0.54	0.08	**0.28**	**0.16**	0.50	0.47	0.53
Fe	**± 0.12**	0.49	0.06	0.10	0.02	0.47	0.44	0.13	0.30	0.20	0.34	0.55	0.33	0.14	0.31	**0.32**	**0.13**	0.00	0.02	0.00
Na	**± 0.02**	0.04	0.11	0.08	0.08	0.14	0.14	0.07	0.12	0.12	0.14	0.08	0.11	0.06	0.15	**0.11**	**0.03**	0.04	0.02	0.04
K	**± 0.02**	0.01	0.00	0.03	0.02	0.32	0.01	0.03	0.02	0.02	0.02	0.01	0.01	0.02	0.02	**0.05**	**0.09**	0.02	0.01	0.04
Mn	**± 0.00**	0.01	0.00	0.00	0.02	0.00	0.01	0.00	0.00	0.00	0.00	0.00	0.01	0.03	0.00	**0.01**	**0.01**	0.00	0.10	0.04
Mg	**± 0.05**	0.24	0.21	0.19	0.17	0.22	0.14	0.60	0.22	0.05	0.18	0.37	0.18	0.14	0.03	**0.21**	**0.16**	0.05	0.04	0.06
Ca	**± 1.26**	26.04	6.33	3.13	3.68	33.86	28.93	23.89	30.66	39.24	31.24	24.04	32.37	23.13	36.34	**30.37**	**5.18**	20.22	19.92	20.20
Cr	**± 0.02**	0.11	0.00	0.02	0.00	0.35	0.30	0.19	0.30	0.21	0.32	0.12	0.28	0.11	0.26	**0.24**	**0.08**	0.01	0.00	0.01
Al	**± 0.11**	3.62	39.20	41.14	40.81	0.43	0.48	0.80	0.49	0.22	0.37	1.01	1.39	0.73	0.44	**0.64**	**0.33**	0.81	0.86	0.77
S	**± 0.39**	5.32	0.29	0.24	0.24	3.77	2.64	1.34	2.70	2.28	3.21	1.36	3.15	0.92	2.36	**2.37**	**0.87**	0.03	0.05	0.06
Si	**± 0.52**	5.52	0.68	0.66	0.58	6.17	6.07	7.09	6.26	3.07	6.18	6.39	7.47	7.96	4.61	**6.13**	**1.33**	10.95	11.87	10.34
P	**± 0.48**	0.46	0.06	0.06	0.06	3.78	2.62	1.46	2.85	1.99	3.04	1.32	3.25	0.91	2.28	**2.35**	**0.88**	0.03	0.03	0.01
Ti	**± 0.02**	0.12	0.00	0.03	0.01	0.11	0.08	0.03	0.06	0.06	0.08	0.12	0.04	0.06	0.07	**0.07**	**0.03**	0.00	0.00	0.00
Ionic Proportions																				
Ca^{2+}		19.83	39.41	20.02	26.86	23.07	20.03	14.18	20.61	53.70	21.24	15.81	18.22	12.22	33.16	**20.84**		7.77	7.05	8.21
Al^{3+}		4.10	362.71	390.47	442.56	0.43	0.49	0.71	0.48	0.45	0.37	0.99	1.16	0.57	0.60	**0.65**		0.46	0.45	0.47
SO_4^{2-}		5.06	2.24	1.93	2.21	3.21	2.28	1.00	2.27	3.90	2.72	1.12	2.22	0.61	2.69	**2.04**		0.01	0.02	0.03
Si^{4+}		6.00	6.00	6.00	6.00	6.00	6.00	6.00	6.00	6.00	6.00	6.00	6.00	6.00	6.00	**6.00**		6.00	6.00	6.00
Molar Ratio																				
Ca:Si		3.31	6.57	3.34	4.48	3.84	3.34	2.36	3.43	8.95	3.54	2.64	3.04	2.04	5.53	**3.47**		1.29	1.18	1.37
Al:Si		0.68	60.45	65.08	73.76	0.07	0.08	0.12	0.08	0.08	0.06	0.16	0.19	0.10	0.10	**0.11**		0.08	0.08	0.08

	34 Dull amorphous CSH lining fracture	35 Dull amorphous CSH lining fracture	36 Dull amorphous CSH lining fracture	37 Dull amorphous CSH lining fracture	38 Dull amorphous CSH lining fracture	39 Dull amorphous CSH lining fracture	40 Dull amorphous CSH lining fracture	41 Dull amorphous CSH lining fracture	42 Dull amorphous CSH lining fracture	43 Dull amorphous CSH lining fracture	44 Dull amorphous CSH lining fracture	45 Dull amorphous CSH lining fracture
F	0.00	0.01	0.02	0.00	0.03	0.00	0.04	0.00	0.04	0.00	0.01	0.00
Cl	0.48	0.33	0.57	0.55	0.42	0.56	0.59	0.63	0.57	0.62	0.57	0.58
Fe	0.01	0.01	0.03	0.00	0.08	0.06	0.00	0.01	0.00	0.02	0.02	0.00
Na	0.30	0.01	0.03	0.02	0.03	0.02	0.02	0.02	0.01	0.03	0.00	0.01
K	0.00	0.03	0.01	0.01	0.02	0.01	0.02	0.00	0.01	0.01	0.01	0.01
Mn	0.01	0.01	0.01	0.00	0.00	0.03	0.00	0.00	0.01	0.00	0.03	0.00
Mg	0.04	0.06	0.05	0.05	0.03	0.04	0.03	0.04	0.03	0.03	0.03	0.05
Ca	19.37	22.15	18.24	17.31	20.46	18.86	16.68	17.60	17.79	17.52	15.64	17.65
Cr	0.05	0.00	0.03	0.03	0.01	0.04	0.01	0.00	0.03	0.05	0.01	0.04
Al	0.82	0.97	0.72	0.76	0.80	0.77	0.81	0.69	0.78	0.68	0.64	0.70
S	0.03	0.07	0.04	0.02	0.14	0.03	0.18	0.12	0.14	0.06	0.02	0.09
Si	10.90	13.35	9.82	10.22	11.31	10.81	9.58	8.65	9.26	9.64	9.27	9.38
P	0.01	0.03	0.02	0.03	0.05	0.03	0.03	0.02	0.03	0.01	0.02	0.03
Ti	0.00	0.00	0.00	0.00	0.00	0.00	0.00	0.00	0.00	0.00	0.01	0.01
Ionic Proportions												
Ca^{2+}	7.47	6.98	7.81	7.12	7.60	7.34	7.32	8.56	8.08	7.65	7.10	7.91
Al^{3+}	0.47	0.46	0.46	0.47	0.44	0.45	0.53	0.50	0.52	0.44	0.43	0.46
SO_4^{2-}	0.01	0.03	0.02	0.01	0.06	0.01	0.10	0.07	0.08	0.03	0.01	0.05
Si^{4+}	6.00	6.00	6.00	6.00	6.00	6.00	6.00	6.00	6.00	6.00	6.00	6.00
Molar Ratio												
Ca:Si	1.24	1.16	1.30	1.19	1.27	1.22	1.22	1.43	1.35	1.27	1.18	1.32
Al:Si	0.08	0.08	0.08	0.08	0.07	0.07	0.09	0.08	0.09	0.07	0.07	0.08

	46 Dull amorphous CSH lining fracture	47 Dull amorphous CSH lining fracture	48 Dull amorphous CSH lining fracture	49 Dull amorphous CSH lining fracture	50 Dull amorphous CSH lining fracture	Average Dull amorphous CSH lining fracture	s.d.	51 Jennite	52 Jennite	53 Jennite	54 Jennite	55 Jennite	56 Jennite	57 Jennite	58 Jennite	59 Jennite	60 Jennite	61 Jennite	62 Jennite	63 Jennite
F	0.08	0.00	0.00	0.03	0.03	**0.02**	**± 0.02**	0.00	0.02	0.00	0.07	0.00	0.03	0.01	0.02	0.13	0.00	0.00	0.05	0.02
Cl	0.55	0.87	0.82	0.77	0.63	**0.58**	**± 0.12**	0.11	0.13	0.16	0.23	0.12	0.21	0.15	0.17	0.19	0.13	0.18	0.15	0.13
Fe	0.07	0.00	0.00	0.00	0.00	**0.02**	**± 0.02**	0.01	0.00	0.03	0.00	0.04	0.00	0.00	0.00	\0	0.00	0.01	0.01	0.00
Na	0.03	0.10	0.10	0.09	0.02	**0.05**	**± 0.06**	0.01	0.00	0.01	0.00	0.01	0.03	0.01	0.00	0.01	0.03	0.02	0.03	0.00
K	0.00	0.08	0.11	0.11	0.00	**0.03**	**± 0.03**	0.01	0.00	0.01	0.02	0.00	0.01	0.00	0.00	0.00	0.00	0.00	0.00	0.00
Mn	0.00	0.00	0.00	0.01	0.00	**0.01**	**± 0.02**	0.00	0.00	0.04	0.04	0.00	0.00	0.00	0.02	0.00	0.00	0.02	0.00	0.00
Mg	0.05	0.07	0.07	0.05	0.04	**0.05**	**± 0.01**	0.00	0.04	0.03	0.03	0.01	0.06	0.02	0.02	0.04	0.03	0.02	0.03	0.02
Ca	17.96	13.84	14.22	15.23	16.13	**17.85**	**± 2.12**	32.78	32.01	31.61	30.82	34.93	31.56	32.69	32.26	31.47	33.67	31.64	32.67	33.21
Cr	0.01	0.01	0.00	0.02	0.01	**0.02**	**± 0.01**	0.06	0.05	0.07	0.06	0.07	0.08	0.04	0.05	0.07	0.08	0.11	0.11	0.08
Al	0.92	0.73	0.73	0.62	0.64	**0.76**	**± 0.09**	0.68	0.40	0.54	0.78	0.16	0.60	0.20	0.24	0.37	0.16	0.30	0.40	0.26
S	0.24	0.18	0.19	0.14	0.07	**0.09**	**± 0.07**	0.68	0.14	0.16	0.70	0.10	0.28	0.14	0.14	0.32	0.03	0.28	0.29	0.08
Si	8.93	8.65	8.88	8.54	9.45	**9.99**	**± 1.21**	14.33	15.24	14.80	13.03	11.80	14.39	15.09	14.89	14.59	15.10	14.66	14.36	14.73
P	0.02	0.02	0.02	0.02	0.04	**0.03**	**± 0.01**	0.05	0.03	0.03	0.04	0.06	0.04	0.05	0.05	0.04	0.03	0.06	0.05	0.04
Ti	0.00	0.00	0.00	0.01	0.01	**0.00**	**± 0.00**	0.00	0.00	0.01	0.00	0.01	0.01	0.00	0.00	0.03	0.00	0.00	0.00	0.01
Ionic Proportions																				
Ca^{2+}	8.45	6.72	6.74	7.49	7.18	**7.51**		9.62	8.83	8.98	9.95	12.45	9.22	9.11	9.11	9.07	9.37	9.07	9.56	9.48
Al^{3+}	0.65	0.53	0.52	0.45	0.42	**0.48**		0.30	0.16	0.23	0.37	0.09	0.26	0.08	0.10	0.16	0.07	0.13	0.17	0.11
SO_4^{2-}	0.14	0.11	0.11	0.09	0.04	**0.05**		0.25	0.05	0.06	0.28	0.04	0.10	0.05	0.05	0.11	0.01	0.10	0.11	0.03
Si^{4+}	6.00	6.00	6.00	6.00	6.00	**6.00**		6.00	6.00	6.00	6.00	6.00	6.00	6.00	6.00	6.00	6.00	6.00	6.00	6.00
Molar Ratio																				
Ca:Si	1.41	1.12	1.12	1.25	1.20	**1.25**		1.60	1.47	1.50	1.66	2.08	1.54	1.52	1.52	1.51	1.56	1.51	1.59	1.58
Al:Si	0.11	0.09	0.09	0.08	0.07	**0.08**		0.05	0.03	0.04	0.06	0.01	0.04	0.01	0.02	0.03	0.01	0.02	0.03	0.02

	64 Jennite	65 Jennite	66 Jennite	67 Jennite	68 Jennite	69 Jennite	70 Jennite	Average Jennite	s.d.	71 Ettringite	72 Ettringite	73 Ettringite	74 Ettringite	75 Ettringite	76 Ettringite	77 Ettringite	78 Ettringite	79 Ettringite	80 Ettringite	81 Ettringite	82 Ettringite	83 Ettringite	84 Ettringite	85 Ettringite	86 Ettringite
F	0.08	0.13	0.00	0.12	0.00	0.01	0.00	**0.03**	**± 0.04**	0.33	0.43	0.37	0.11	0.14	0.08	0.85	0.98	0.08	0.10	0.14	0.25	0.62	0.36	0.61	0.70
Cl	0.12	0.18	0.18	0.19	0.13	0.17	0.13	**0.16**	**± 0.03**	0.97	0.79	0.70	0.65	0.73	0.86	0.71	0.81	0.65	1.02	0.84	1.02	0.59	0.63	0.64	0.28
Fe	0.00	0.00	0.02	0.00	0.00	0.19	0.00	**0.02**	**± 0.04**	0.02	0.05	0.00	0.05	0.02	0.00	0.02	0.00	0.00	0.00	0.00	0.08	0.03	0.03	0.01	0.00
Na	0.02	0.00	0.03	0.03	0.00	0.02	0.03	**0.01**	**± 0.01**	0.08	0.08	0.10	0.07	0.06	0.06	0.05	0.06	0.09	0.03	0.03	0.04	0.06	0.03	0.07	0.08
K	0.00	0.01	0.00	0.00	0.00	0.01	0.00	**0.00**	**± 0.01**	0.01	0.00	0.05	0.00	0.00	0.00	0.00	0.00	0.07	0.02	0.00	0.01	0.00	0.00	0.01	0.01
Mn	0.00	0.01	0.00	0.03	0.00	0.00	0.05	**0.01**	**± 0.02**	0.03	0.00	0.04	0.03	0.01	0.01	0.01	0.00	0.01	0.00	0.00	0.00	0.01	0.00	0.00	0.03
Mg	0.00	0.01	0.03	0.02	0.03	0.01	0.02	**0.02**	**± 0.01**	0.37	0.42	0.31	0.24	0.29	0.10	0.26	0.32	0.05	0.13	0.20	0.21	0.18	0.03	0.05	0.07
Ca	33.63	32.41	32.05	32.14	33.18	32.55	33.01	**32.51**	**± 0.92**	12.68	14.78	16.41	20.09	14.85	12.83	15.82	14.10	15.85	10.28	11.61	8.37	17.71	18.98	17.64	24.27
Cr	0.02	0.08	0.06	0.09	0.08	0.04	0.06	**0.07**	**± 0.02**	0.06	0.06	0.10	0.08	0.06	0.08	0.09	0.10	0.02	0.48	0.07	0.07	0.07	0.26	0.19	0.25
Al	0.15	0.37	0.43	0.39	0.23	0.15	0.31	**0.35**	**± 0.17**	3.94	4.57	4.19	2.28	3.38	1.97	4.25	4.32	0.70	3.40	3.50	3.19	4.81	3.87	4.09	5.08
S	0.10	0.24	0.41	0.08	0.11	0.03	0.09	**0.22**	**± 0.19**	3.49	4.66	4.87	2.29	3.60	2.18	4.85	4.83	0.17	4.08	4.35	3.16	6.03	6.14	6.00	7.82
Si	13.56	14.83	14.11	15.91	14.87	15.04	15.17	**14.52**	**± 0.87**	1.53	1.65	2.07	6.49	2.72	5.69	2.08	0.69	9.57	0.54	0.43	0.56	1.22	1.83	0.86	1.18
P	0.04	0.04	0.03	0.03	0.04	0.04	0.05	**0.04**	**± 0.01**	0.03	0.02	0.03	0.04	0.04	0.03	0.03	0.03	0.03	0.03	0.01	0.02	0.02	0.02	0.04	0.05
Ti	0.00	0.00	0.00	0.01	0.00	0.00	0.01	**0.00**	**± 0.01**	0.00	0.00	0.00	0.00	0.00	0.01	0.00	0.00	0.01	0.00	0.00	0.00	0.01	0.00	0.00	0.02
Ionic Proportions																									
Ca^{2+}	10.43	9.19	9.55	8.49	9.38	9.10	9.15	**9.41**		6.00	6.00	6.00	6.00	6.00	6.00	6.00	6.00	6.00	6.00	6.00	6.00	6.00	6.00	6.00	6.00
Al^{3+}	0.07	0.16	0.19	0.15	0.10	0.06	0.13	**0.15**		2.77	2.75	2.28	1.01	2.03	1.37	2.39	2.73	0.39	2.95	2.69	3.39	2.42	1.82	2.06	1.87
SO_4^{2-}	0.04	0.09	0.15	0.03	0.04	0.01	0.03	**0.08**		2.07	2.37	2.23	0.86	1.82	1.27	2.30	2.57	0.08	2.98	2.81	2.83	2.55	2.43	2.55	2.42
Si^{4+}	6.00	6.00	6.00	6.00	6.00	6.00	6.00	**6.00**		1.03	0.96	1.08	2.77	1.57	3.80	1.12	0.42	5.17	0.45	0.31	0.57	0.59	0.82	0.42	0.42
Molar Ratio																									
Ca:Si	1.74	1.53	1.59	1.42	1.56	1.52	1.52	**1.57**		5.81	6.28	5.56	2.17	3.83	1.58	5.33	14.32	1.16	13.47	19.06	10.53	10.21	7.28	14.39	14.38
Al:Si	0.01	0.03	0.03	0.03	0.02	0.01	0.02	**0.03**		2.68	2.88	2.11	0.37	1.29	0.36	2.13	6.52	0.08	6.62	8.53	5.95	4.12	2.21	4.95	4.47

	87 Ettringite	88 Ettringite	89 Ettringite	90 Ettringite	Average Ettringite	s.d.	M81001	M81002	M81003	M81004	M81005	M81006	M81007	M81008	M81009	M81010	M81011	M81012	M81013	M81014	M81015
F	0.02	0.53	0.16	0.52	**0.37**	**± 0.27**	No Data	No Data	No Data	No Data	No Data	No Data	No Data	No Data	No Data	No Data	No Data	No Data	No Data	No Data	No Data
Cl	0.64	0.52	0.51	0.36	**0.70**	**± 0.19**	No Data	No Data	No Data	No Data	No Data	No Data	No Data	No Data	No Data	No Data	No Data	No Data	No Data	No Data	No Data
Fe	0.04	0.02	0.09	0.02	**0.02**	**± 0.03**	0.00	0.00	0.00	0.00	0.00	0.00	0.00	0.34	0.45	0.29	0.00	0.00	0.00	0.22	0.00
Na	0.03	0.05	0.02	0.04	**0.06**	**± 0.02**	0.00	0.00	0.00	0.00	0.00	0.00	0.00	0.00	0.00	0.00	0.00	0.00	0.00	0.00	0.00
K	0.00	0.00	0.00	0.00	**0.01**	**± 0.02**	0.00	0.00	0.00	0.00	0.00	0.00	0.22	0.00	0.14	0.17	0.18	0.15	0.12	0.17	0.23
Mn	0.01	0.00	0.02	0.02	**0.01**	**± 0.01**	No Data	No Data	No Data	No Data	No Data	No Data	No Data	No Data	No Data	No Data	No Data	No Data	No Data	No Data	No Data
Mg	0.07	0.05	0.04	0.04	**0.17**	**± 0.12**	0.00	0.00	0.00	0.00	0.00	0.00	0.00	0.00	0.00	0.00	0.00	0.29	0.00	0.18	0.00
Ca	18.96	20.88	20.27	25.72	**16.60**	**± 4.33**	42.53	43.39	45.20	43.21	42.92	42.95	41.76	39.17	38.01	38.00	36.56	36.31	34.19	37.84	43.00
Cr	0.16	0.02	0.16	0.32	**0.13**	**± 0.11**	No Data	No Data	No Data	No Data	No Data	No Data	No Data	No Data	No Data	No Data	No Data	No Data	No Data	No Data	No Data
Al	3.13	3.96	2.62	4.52	**3.59**	**± 1.04**	8.02	10.73	7.82	10.71	10.05	7.94	0.72	1.99	2.56	3.60	7.78	7.41	7.85	2.81	0.51
S	4.05	5.74	3.19	6.87	**4.42**	**± 1.74**	9.32	6.60	3.32	4.70	4.41	3.45	0.60	2.09	3.05	5.67	12.52	12.71	14.08	3.48	0.21
Si	3.06	3.51	5.15	3.42	**2.71**	**± 2.33**	0.99	1.21	6.41	3.55	4.66	7.63	17.97	16.70	15.67	11.80	1.28	1.33	0.97	15.07	17.79
P	0.01	0.32	0.03	0.05	**0.04**	**± 0.06**	No Data	No Data	No Data	No Data	No Data	No Data	No Data	No Data	No Data	No Data	No Data	No Data	No Data	No Data	No Data
Ti	0.00	0.01	0.02	0.00	**0.00**	**± 0.01**	No Data	No Data	No Data	No Data	No Data	No Data	No Data	No Data	No Data	No Data	No Data	No Data	No Data	No Data	No Data
Ionic Proportions																					
Ca^{2+}	6.00	6.00	6.00	6.00	**6.00**		179.76	150.82	29.66	51.18	38.72	23.68	9.77	9.86	10.20	13.54	120.12	115.10	148.00	10.56	10.16
Al^{3+}	1.47	1.69	1.15	1.57	**1.93**		50.39	55.40	7.62	18.84	13.46	6.50	0.25	0.74	1.02	1.91	37.96	34.90	50.48	1.16	0.18
SO_4^{2-}	1.60	2.06	1.18	2.00	**2.00**		49.22	28.68	2.73	6.96	4.97	2.38	0.17	0.66	1.02	2.53	51.41	50.38	76.21	1.21	0.06
Si^{4+}	1.38	1.44	2.18	1.14	**1.40**		6.00	6.00	6.00	6.00	6.00	6.00	6.00	6.00	6.00	6.00	6.00	6.00	6.00	6.00	6.00
Molar Ratio																					
Ca:Si	4.35	4.17	2.76	5.27	**4.29**		29.96	25.14	4.94	8.53	6.45	3.95	1.63	1.64	1.70	2.26	20.02	19.18	24.67	1.76	1.69
Al:Si	1.07	1.18	0.53	1.37	**1.38**		8.40	9.23	1.27	3.14	2.24	1.08	0.04	0.12	0.17	0.32	6.33	5.82	8.41	0.19	0.03

	1 Fracture wall lining	2 Fracture wall lining	3 Fracture wall lining	4 Fracture wall lining	5 Fracture wall lining	6 Fracture wall lining	7 Fracture wall lining	8 Fracture wall lining	9 Fracture wall lining	10 Fracture wall lining	11 Fracture wall lining	12 Fracture wall lining	13 Fracture wall lining	1 to 13 Average Fracture wall lining	s.d	14 Amorphous CSH	15 Amorphous CSH
F	0.14	0.17	0.17	0.23	0.20	0.15	0.23	0.19	0.13	0.26	0.27	0.19	0.22	**0.19**	**±0.04**	0.10	0.13
Cl	0.67	0.76	0.79	0.42	0.87	0.88	0.83	0.71	0.95	0.62	0.66	0.66	0.54	**0.72**	**±0.14**	0.95	1.14
Fe	0.29	0.22	0.43	0.45	0.18	0.14	0.17	0.18	0.09	0.34	0.15	0.29	0.25	**0.24**	**±0.11**	0.02	0.05
Na	0.02	0.04	0.04	0.04	0.03	0.04	0.02	0.04	0.01	0.05	0.05	0.04	0.04	**0.04**	**±0.01**	0.05	0.02
K	0.12	0.11	0.41	0.07	0.09	0.09	0.15	0.10	0.04	0.10	0.16	0.15	0.16	**0.13**	**±0.09**	0.13	0.05
Mn	0.00	0.00	0.00	0.00	0.00	0.01	0.00	0.01	0.00	0.01	0.00	0.01	0.02	**0.00**	**±0.01**	0.00	0.01
Mg	4.08	4.14	3.85	2.93	2.44	3.31	3.35	4.39	2.98	3.22	3.93	3.36	3.87	**3.53**	**±0.54**	0.03	0.02
Ca	3.95	6.76	5.26	14.73	4.69	2.76	3.09	3.69	6.01	7.91	3.58	5.07	4.40	**5.53**	**±3.01**	4.66	3.31
Cr	0.26	0.24	0.50	0.33	0.47	0.19	0.23	0.26	0.13	0.13	0.12	0.20	0.18	**0.25**	**±0.12**	0.01	0.00
Al	3.98	3.22	4.19	3.29	3.54	2.92	2.93	3.79	2.74	2.58	3.60	4.42	4.67	**3.53**	**±0.63**	7.01	7.97
S	1.49	1.26	0.71	1.25	0.92	1.88	1.79	1.88	0.78	2.18	2.23	1.42	1.40	**1.48**	**±0.48**	0.20	0.16
Si	8.61	7.50	9.10	6.49	6.44	6.69	6.81	8.80	6.13	5.84	8.02	8.60	8.89	**7.53**	**±1.14**	8.90	6.02
P	0.68	0.50	0.62	0.67	0.31	0.26	0.23	0.68	0.26	0.46	0.80	0.82	0.80	**0.54**	**±0.21**	0.01	0.00
Ti	0.04	0.06	0.50	0.05	0.01	0.03	0.04	0.06	0.00	0.02	0.03	0.06	0.04	**0.07**	**±0.12**	0.00	0.00
Ionic Proportions																	
Ca^{2+}	1.93	3.79	2.43	9.54	3.06	1.73	1.91	1.76	4.12	5.69	1.88	2.48	2.08	**3.09**		2.20	2.31
Al^{3+}	2.89	2.68	2.87	3.16	3.43	2.72	2.68	2.69	2.79	2.76	2.80	3.21	3.28	**2.92**		4.92	8.28
SO_4^{2-}	0.91	0.89	0.41	1.01	0.75	1.47	1.38	1.13	0.66	1.96	1.46	0.87	0.83	**1.03**		0.12	0.14
Si^{4+}	6.00	6.00	6.00	6.00	6.00	6.00	6.00	6.00	6.00	6.00	6.00	6.00	6.00	**6.00**		6.00	6.00
Molar Ratio																	
Ca:Si	0.32	0.63	0.41	1.59	0.51	0.29	0.32	0.29	0.69	0.95	0.31	0.41	0.35	**0.51**		0.37	0.39
Al:Si	0.48	0.45	0.48	0.53	0.57	0.45	0.45	0.45	0.47	0.46	0.47	0.54	0.55	**0.49**		0.82	1.38

	16 Amorphous CSH	17 Amorphous CSH	18 Amorphous CSH	19 Amorphous CSH	20 Amorphous CSH	21 Amorphous CSH	22 Amorphous CSH	23 Amorphous CSH	14 to 23 Average amorphous CSH	s.d	31 Amorphous CSH	32 Amorphous CSH	33 Amorphous CSH	34 Amorphous CSH	35 Amorphous CSH	31 to 35 Average Amorphous CSH
F	0.11	0.02	0.08	0.13	0.13	0.23	0.17	0.08	**0.12**	**±0.05**	0.15	0.16	0.04	0.19	0.20	**0.15**
Cl	1.61	1.34	1.28	1.33	1.40	0.82	1.17	1.01	**1.21**	**±0.22**	0.26	0.46	0.38	0.16	0.12	**0.28**
Fe	0.00	0.00	0.00	0.02	0.01	0.00	0.00	0.03	**0.01**	**±0.01**	0.07	0.03	0.06	0.05	0.02	**0.04**
Na	0.00	0.03	0.04	0.05	0.02	0.05	0.01	0.04	**0.03**	**±0.02**	0.06	0.04	0.09	0.05	0.10	**0.07**
K	0.01	0.05	0.08	0.08	0.06	0.08	0.01	0.15	**0.07**	**±0.04**	0.32	0.22	0.36	0.41	0.55	**0.37**
Mn	0.01	0.01	0.02	0.00	0.00	0.01	0.01	0.00	**0.01**	**±0.01**	0.00	0.01	0.01	0.02	0.02	**0.01**
Mg	0.00	0.02	0.02	0.02	0.01	0.03	0.01	0.51	**0.07**	**±0.15**	0.04	0.03	0.03	0.03	0.03	**0.03**
Ca	1.06	2.29	2.41	2.55	2.02	4.54	3.15	5.34	**3.13**	**±1.28**	8.50	5.97	9.89	7.86	13.47	**9.14**
Cr	0.00	0.00	0.01	0.00	0.01	0.03	0.00	0.11	**0.02**	**±0.03**	0.04	0.03	0.03	0.01	0.02	**0.02**
Al	1.62	3.78	4.19	4.47	3.52	8.54	5.94	2.78	**4.98**	**±2.17**	7.86	7.94	6.08	5.46	6.69	**6.80**
S	0.04	0.15	0.12	0.15	0.12	0.31	0.23	0.12	**0.16**	**±0.07**	0.22	0.11	0.23	0.12	0.60	**0.26**
Si	1.85	4.11	4.57	4.85	3.71	8.32	5.29	9.58	**5.72**	**±2.36**	18.80	18.28	15.95	23.34	16.58	**18.59**
P	0.00	0.00	0.01	0.00	0.00	0.00	0.02	0.02	**0.01**	**±0.01**	0.22	0.01	0.01	0.01	0.03	**0.06**
Ti	0.00	0.00	0.01	0.00	0.00	0.00	0.00	0.00	**0.00**	**±0.00**	0.00	0.00	0.00	0.02	0.00	**0.00**
Ionic Proportions																
Ca^{2+}	2.40	2.34	2.22	2.21	2.29	2.29	2.50	2.34	**2.30**		1.90	1.37	2.61	1.42	3.42	2.07
Al^{3+}	5.47	5.74	5.73	5.75	5.94	6.41	7.00	1.81	**5.44**		2.61	2.71	2.38	1.46	2.52	2.29
SO_4^{2-}	0.12	0.19	0.14	0.16	0.16	0.20	0.23	0.07	**0.15**		0.06	0.03	0.08	0.03	0.19	0.07
Si^{4+}	6.00	6.00	6.00	6.00	6.00	6.00	6.00	6.00	**6.00**		6.00	6.00	6.00	6.00	6.00	6.00
Molar Ratio																
Ca:Si	0.40	0.39	0.37	0.37	0.38	0.38	0.42	0.39	**0.38**		0.32	0.23	0.43	0.24	0.57	0.34
Al:Si	0.91	0.96	0.96	0.96	0.99	1.07	1.17	0.30	**0.91**		0.43	0.45	0.40	0.24	0.42	0.38

		24	25	26	27	28	29	30	24 to 30		36	37	38	39	40
	s.d	CSH replacing calcite	CSH replacing calcite	CSH replacing calcite	CSH replacing calcite	CSH replacing calcite	CSH replacing calcite	CSH replacing calcite	CSH replacing calcite	s.d.	Ettringite & gypsum	Ettringite & gypsum	Ettringite & gypsum	Ettringite & gypsum	Ettringite & gypsum
F	**±0.06**	0.00	0.12	0.08	0.12	0.08	0.07	0.10	**0.08**	**±0.04**	0.70	1.06	0.41	0.37	0.51
Cl	**±0.13**	0.94	0.87	0.79	0.51	0.69	0.61	0.43	**0.72**	**±0.17**	0.40	0.40	0.41	0.31	0.30
Fe	**±0.02**	0.03	0.05	0.04	0.04	0.01	0.02	0.05	**0.03**	**±0.01**	0.00	0.00	0.00	0.00	0.00
Na	**±0.02**	0.03	0.05	0.04	0.03	0.06	0.12	0.10	**0.07**	**±0.03**	0.03	0.01	0.02	0.02	0.03
K	**±0.11**	0.14	0.13	0.15	0.10	0.19	0.28	0.32	**0.20**	**±0.07**	0.00	0.00	0.00	0.01	0.02
Mn	**±0.01**	0.02	0.00	0.01	0.01	0.01	0.00	0.01	**0.01**	**±0.01**	0.00	0.00	..016	0.00	0.00
Mg	**±0.00**	0.33	0.11	0.04	0.01	0.39	0.61	0.43	**0.32**	**±0.19**	0.00	0.03	0.00	0.00	0.01
Ca	**±2.51**	5.52	6.59	6.46	17.76	7.64	8.30	9.90	**7.40**	**±1.43**	19.90	17.32	19.93	21.30	20.17
Cr	**±0.01**	0.17	0.15	0.14	0.11	0.08	0.08	0.24	**0.14**	**±0.06**	0.00	0.00	0.01	0.00	0.00
Al	**±0.97**	3.01	3.14	3.21	1.92	3.62	4.04	5.06	**3.68**	**±0.71**	6.83	9.10	4.35	5.32	7.93
S	**±0.18**	0.09	0.09	0.11	0.22	0.10	0.17	0.17	**0.12**	**±0.03**	10.83	12.05	14.37	14.99	14.58
Si	**±2.59**	9.97	10.51	10.24	6.09	13.30	14.84	17.59	**12.74**	**±2.80**	0.11	0.13	0.08	0.11	0.11
P	**±0.08**	0.01	0.02	0.00	0.21	0.00	0.01	0.03	**0.01**	**±0.01**	0.03	0.02	0.02	0.04	0.03
Ti	**±0.01**	0.00	0.00	0.00	0.01	0.00	0.00	0.00	**0.00**	**±0.00**	0.00	0.01	0.00	0.02	0.02
Ionic Proportions															
Ca^{2+}		2.33	2.64	2.65	12.26	2.41	2.35	2.37	**2.44**		6.00	6.00	6.00	6.00	6.00
Al^{3+}		1.89	1.87	1.96	1.97	1.70	1.70	1.80	**1.80**		3.06	4.68	1.95	2.22	3.50
SO_4^{2-}		0.05	0.04	0.05	0.19	0.04	0.06	0.05	**0.05**		4.08	5.22	5.41	5.28	5.42
Si^{4+}		6.00	6.00	6.00	6.00	6.00	6.00	6.00	**6.00**		0.05	0.06	0.03	0.05	0.05
Molar Ratio															
Ca:Si		0.39	0.44	0.44	2.04	0.40	0.39	0.39	**0.41**						
Al:Si		0.31	0.31	0.33	0.33	0.28	0.28	0.30	**0.30**						

	41 Ettringite & gypsum	42 Ettringite & gypsum	43 Ettringite & gypsum	44 Ettringite & gypsum	36-44 Ettringite & gypsum	s.d.	45 Ettringite & gypsum	48 Ettringite & gypsum	49 Ettringite & gypsum	50 Ettringite & gypsum	45-50 Ettringite & gypsum	s.d.
F	0.55	0.42	0.74	0.86	**0.62**	**±0.22**	1.84	0.55	1.65	1.31	**1.34**	**±0.49**
Cl	0.30	0.50	0.31	0.37	**0.36**	**±0.06**	0.07	0.15	0.19	0.26	**0.17**	**±0.07**
Fe	0.00	0.00	0.02	0.00	**0.00**	**±0.01**	0.04	0.04	0.03	0.01	**0.03**	**±0.01**
Na	0.04	0.02	0.03	0.02	**0.02**	**±0.01**	0.01	0.00	0.03	0.03	**0.02**	**±0.01**
K	0.01	0.01	0.00	0.01	**0.01**	**±0.01**	0.01	0.01	0.00	0.01	**0.01**	**±0.01**
Mn	0.00	0.00	0.00	0.00	**0.00**	**±0.00**	0.01	0.01	0.00	0.30	**0.08**	**±0.13**
Mg	0.00	0.00	0.01	0.00	**0.01**	**±0.01**	0.05	0.00	0.09	0.11	**0.06**	**±0.04**
Ca	18.91	21.67	19.55	20.31	**19.90**	**±1.21**	26.90	34.93	24.97	23.83	**27.66**	**±4.34**
Cr	0.03	0.00	0.00	0.00	**0.00**	**±0.01**	0.00	0.02	0.00	0.00	**0.00**	**±0.01**
Al	7.56	1.72	5.76	4.20	**5.86**	**±2.14**	6.46	3.33	6.32	5.54	**5.41**	**±1.25**
S	13.76	14.62	13.82	14.46	**13.72**	**±1.30**	9.19	1.12	8.35	8.45	**6.78**	**±3.28**
Si	0.11	0.06	0.11	0.11	**0.10**	**±0.02**	0.19	0.09	0.29	0.24	**0.20**	**±0.07**
P	0.03	0.02	0.01	0.02	**0.02**	**±0.01**	0.04	0.03	0.05	0.03	**0.04**	**±0.01**
Ti	0.00	0.00	0.00	0.00	**0.00**	**±0.01**	0.00	0.01	0.00	0.02	**0.01**	**±0.01**
Ionic Proportions												
Ca^{2+}	6.00	6.00	6.00	6.00	**6.00**		6.00	6.00	6.00	6.00	**6.00**	
Al^{3+}	3.56	0.71	2.63	1.84	**2.63**		2.14	0.85	2.26	2.07	**1.74**	
SO_4^{2-}	5.46	5.06	5.30	5.34	**5.17**		2.56	0.24	2.51	2.66	**1.84**	
Si^{4+}	0.05	0.02	0.05	0.05	**0.04**		0.06	0.02	0.10	0.09	**0.06**	
Molar Ratio												
Ca:Si												
Al:Si												

Table D8 A968 Data

	Amorphous gel A968AP1/1	Crystalline zeolite A968AP1/2	Crystalline zeolite A968AP1/3	Crystalline zeolite A968AP1/4	Crystalline zeolite A968AP1/5	Crystalline zeolite A968AP1/6	Crystalline zeolite A968AP1/7	Amorphous gel A968AP1/8	Amorphous gel A968AP1/9	Amorphous gel A968AP1/10	Amorphous gel A968AP1/11	Amorphous gel A968AP1/12	Amorphous gel A968AP1/13
Si	8.60	19.10	17.50	18.60	19.00	20.60	20.20	22.50	18.20	20.60	14.90	18.20	18.40
Ti	0.30	0.00	0.00	0.00	0.00	0.00	0.00	0.00	0.00	0.00	0.00	0.00	0.00
Al	3.20	4.20	3.90	4.10	4.10	4.60	4.60	4.80	3.80	4.40	3.20	4.00	4.10
Cr	0.00	0.00	0.00	0.00	0.00	0.00	0.00	0.00	0.00	0.00	0.00	0.00	0.00
Fe	4.60	0.00	0.00	0.00	0.00	0.00	0.00	0.00	0.00	0.00	0.00	0.00	0.00
Mn	0.00	0.00	0.00	0.00	0.00	0.00	0.00	0.00	0.00	0.00	0.00	0.00	0.00
Mg	0.50	0.00	0.00	0.00	0.00	0.00	0.00	0.00	0.00	0.00	0.00	0.00	0.00
Ca	17.60	0.50	0.50	0.50	0.40	0.40	0.40	0.80	0.70	0.80	0.30	0.40	0.40
Na	0.40	1.70	1.50	1.60	1.60	1.80	1.80	1.50	1.10	1.20	1.40	1.50	1.90
K	1.80	4.60	4.10	4.40	4.30	4.70	4.70	4.20	3.40	3.40	3.20	3.60	4.40
Sr	0.00	0.00	0.00	0.00	0.00	0.00	0.00	0.00	0.00	0.00	0.00	0.00	0.00
O	22.10	27.40	25.10	20.00	27.00	29.30	29.30	31.60	25.50	28.80	21.00	25.70	26.40
Ca+(K+Na)/2		2.82	2.73	2.75	2.65	2.71	2.71	2.16	2.08	1.90	2.69	2.43	2.98
Al^{3+}		4.58	4.64	4.59	4.49	4.65	4.65	4.44	4.35	4.45	4.47	4.58	4.64
Si^{4+}		20.00	20.00	20.00	20.00	20.00	20.00	20.00	20.00	20.00	20.00	20.00	20.00
Ca+K+Na:Si		0.14	0.14	0.14	0.13	0.14	0.14	0.11	0.10	0.09	0.13	0.12	0.15

APPENDIX E MEDIA COMPOSITIONS

The following were used for enrichment of the groups of microorganisms under study. They are all at ten times normal concentration, for samples where solid material were to be added they were made up to normal strength with the addition of 900 mls of distilled water for dilution. All media were sterilised by autoclaving at 15 psi, 121°C for 15 mins.

E1 Aerobic and Anaerobic Heterotrophic Bacteria (CPS Medium)

peptone	0.5 g
casein hydrolysate	0.5 g
soluble starch	0.5 g
K_2HPO_4	0.02 g
$MgSO_4.7H_2O$	0.05 g
Glycerol	1 ml
$FeCl_3.6H_2O$ (0.01%w/v)	4 drops
distilled water	to 100 ml

(Agar 1.5% when required.)

E2 Oligotrophic Bacteria

1% CPS medium (1 ml of the above in 100 mls distilled water)

E3 Sulphur-Oxidising Bacteria

E3.1 Obligate chemolithotrophs

$(NH_4)2SO_4$	0.1 g
K_2HPO_4	0.4 g
KH_2PO_4	0.4 g
$MgSO_4.7H_2O$	0.1 g
$CaCl_2$	0.1 g
$FeCl_3.6H_2O$	0.02 g
$MnSO_4.4H_2O$	0.02 g
$Na_2S_2O_3.5H_2O$	10.0 g
Distilled water	to 100 ml

E3.2 Facultative chemolithotrophs [1]

K_2HPO_4	0.4 g
KH_2PO_4	0.15 g
$(NH_4)2SO_4$	0.3 g
$MgSO_4.7H_2O$	0.5 g
Yeast extract	0.3 g
$Na_2SO_3.5H_2O$	10 g
Trace mineral solution	*10 ml
Distilled water	to 100ml

* Trace mineral solution

$FeCl_2.4H_2O$	1.5 g
H_3BO_3	60 mg
$MnCl_2.4H_2O$	100 mg
$CoCl_2.6H_2O$	120 mg
$ZnCl_2$	70 mg
$NiCl_2.6H_2O$	25 mg
$CuCl_2.2H_2O$	15 mg
$Na_2MoO_4.2H_2O$	25 mg
HCl (25%)	6.5 ml
Distilled water	993 ml

E4 Sulphate Reducing Bacteria

E4.1 Postgate medium B [2]

This medium was used for the enrichment of lactate-utilising SRB

KH_2PO4	0.5 g
NH_4Cl	1.0 g
$CaSO_4$	1.0 g
$MgSO_4.7H_2O$	2.0 g
Sodium Lactate	3.45 mls
Yeast extract	1.0 g
Ascorbic acid	0.1 g
Thioglycollic acid	0.1 ml
$FeSO_4.7H_2O$	0.5 g
Distilled water	to 100 ml

N.B.The media is adjusted to pH7-7.5 with NaOH prior to autoclaving. This medium contains a precipitate

E4.2 Postgate medium E [2]

This medium was used for isolation

H_2PO_4	0.5 g
NH_4Cl	1.0 g
Na_2SO_4	1.0 g
$CaCl_2.6H_2O$	1.0 g
$MgCl_2.7H_2O$	2.0 g
Sodium lactate	3.45 ml
Yeast extract	1.0 g
$FeSO_4.7H_2O$	0.5 g
Ascorbic acid	0.1 g
Thioglycollic acid or Mercaptoacetic acid	0.1 ml
Agar	15 g
Distilled water	to 1 litre

This media is adjusted to pH7-7.5 with NaOH prior to autoclaving

E5 Artificial Medium for Algal Growth (Chu No.10)

$Ca(NO_3)_2$	0.04 g
K_2HPO_4	0.01 g
$MgSO_4.7H_2O$	0.025 g
Na_2CO_3	0.02 g
$Na_2S_2O_3$	0.025 g
$FeSO_4.7H_2O$	13.6 mg
Distilled water	to 100 ml

E6 Fungi (Sabourauds' Dextrose Agar)

Mycological peptone	10 g
Dextrose	10 g
Agar No.1(Oxoid)	15 g
Distilled water	to 1 litre

E7 References

[1] R.H. Starkey, *Isolation of some bacteria which oxidise thiosulphate*, Soil Science, **39**, p197-219, 1935.

[2] J.R. Postgates, *The sulphate-reducing bacteria*. Second edition. Cambridge University Press, 1984.

The following Appendix is a thesis submitted in partial fulfilment of the requirements for the degree of BSc Hons Biological Sciences (Part-time) for the Council for National Academic Awards (CNAA).

This work formed a component of the microbiological work carried out during Phase II of the Jordan Natural Analogue Project and, for completeness, has been included here without modification (except for numbering of sections, tables and figures).

Therefore this Appendix has not been subject to the same verification and approval process as the remainder of the report contents.

APPENDIX F ASPECTS OF GEOMICROBIOLOGY: INVESTIGATING THE MICROBIAL POTENTIAL OF A HIGHLY ALKALINE SUBSURFACE ENVIRONMENT

S.J. Gardner

Abstract

Geomicrobiology has been defined as the study of the role that microorganisms have played and are playing in a number of fundamental geological processes: for example, in the weathering of rocks, in soil and sediment formation and transformation, in the genesis and degradation of minerals, and in the genesis and degradation of fossil fuels [1]. So, it could be said that geomicrobiology is concerned with the study of natural environments. These environments, by their very nature, are extremely diverse and the majority contain a wide range of microorganisms which reflect the nature of the habitat and the ability of individual members to compete successfully and coexist within that given ecosystem. The aim of this investigation was to assess the microbial potential of one such diverse subsurface environment.

As part of a multidisciplinary project, microbiological studies were carried out on soil and water samples collected from a naturally occurring highly alkaline (pH 12.6-12.8) site near Amman in northern Jordan to determine the pH tolerance of the microbial population. Earlier investigations [2] had detected the presence of Sulphate Reducing Bacteria (SRB). Therefore, the presence and viability of the SRB and heterotrophic bacteria was determined and the pH tolerance of the microbial population assessed. In addition, observation of morphological characteristics on agar plates, by Gram staining and Scanning Electron Microscopy (SEM) were performed. The results demonstrated the presence of viable SRB and heterotrophic bacteria, showed that the heterotrophic population has a pH tolerance of pH 6-11, and identified a mixed microbial population.

F1 Introduction

F1.1 Geomicrobiology

Geomicrobiology is derived from the term ‘geological microbiology’ and Ehrlich [1] defined it as ‘the role that microbes have played and are playing in a number of fundamental geological processes.’ Kutznetsov et al [3] defined geomicrobiology as ‘the study of microbiological processes currently taking place in the modern sediments of various bodies of water, in groundwater circulating through sediments and igneous rocks and in weathered earth crust’ and ‘the physiology of specific microorganisms taking part in presently occurring geochemical processes.’ The areas of study known as microbial ecology and microbial biogeochemistry can be partially included in geomicrobiology although they are distinct areas of research. Microbial ecology is the study of interrelationships between different organisms and the environment. Microbial biogeochemistry is the study of microbially catalysed reactions and their kinetics, often in the context of mineral cycles, with emphasis on energy transfer. Figure F1 illustrates the interrelationship of these subjects, after [1].

Historical

Geomicrobiology is not a new field of study indeed, pioneers in the subject date back to the nineteenth century. One important early contributor to geomicrobiology was Winogradsky, who in 1888 discovered that *Beggiatoa* could oxidise H_2S to elemental sulphur and, a year later, that *Leptothrix ochracea* could oxidise $FeCO_3$ to ferric oxide.

He believed that both organisms gained energy from these processes. Other early contributors included Harder [4], a researcher trained as a geologist and microbiologist, who studied the significance of microbial iron oxidation and precipitation in relation to sedimentary iron deposits, and Stutzer [5], Vernadsky [6] and others, whose studies led to recognition of the significance of microbial oxidation of H_2S and elemental sulphur in the formation of sedimentary sulphur deposits. The understanding of the role of bacteria in sulphur deposition in nature was further increased by the discovery of bacterial sulphate reduction [7, 8].

The role of microorganisms in methane formation became apparent through the observations and studies of Béchamp [9], Tappeiner [10], Popoff [11] and others. Later, the involvement of acid producing microbes such as nitrifiers and of crustose lichens and fungi was suggested [12]. So, by the beginning of the twentieth century, many of the important areas of geomicrobiology had started to receive attention from microbiologists. In general, it could be said that many of the geomicrobiologically important discoveries of the nineteenth century, made through physiological studies in the laboratory which revealed the capacity of specific organisms for geomicrobiologically important transformations, caused later workers to study the extent of the microbial activities in the field.

Fundamental discoveries in geomicrobiology continue to be made, with some being comparatively recent. For instance, the concept of environmental limits of pH and Eh for microorganisms in their natural habitats was first introduced by Baas Becking et al. in 1960 [13]. The discovery of acidophilic, iron-oxidising bacteria and their identification as the primary cause of acid coal-mine drainage came in 1950 [14]. Subsequent demonstration of the presence of these same organisms in acid mine drainage from a copper sulphide ore body in Utah and the experimental demonstration that these organisms can promote the leaching of metals from various metal sulphides ore [15] led to the first industrial application of geomicrobiologically active organisms [16]. Currently, many areas of geomicrobiology remain to be explored and developed.

An assessment of the potential for microbial activity is now seen as an important component in the management of a number of environmental concerns including groundwater resources, contaminated land, bioremediation and radioactive waste disposal to name but a few. The microbial population in aquifer sediments for example, has the potential for improving groundwater quality through the removal of nitrate and industrial pollutants, or for lowering quality through the production of noxious metabolic products. Very little is known about the ecology of subsurface microbes, their source of organic substrates, growth rates, and interspecies interactions, or other factors influencing their distribution.

F1.2 Scope of the investigation

This study forms part of a large project which included petrochemical and geochemical analyses of both water and soil samples from a hyperalkaline (pH 12.6-12.8), site near Amman, in northern Jordan. It focuses on investigating the pH tolerance of the microbial population, particularly the bacteria involved in the reduction of sulphate and the heterotrophic organisms. Prolonged sample storage, prior to starting this investigation, gave cause for concern thus a series of preliminary experiments were performed to determine the viability of the microbial population. An overview of the scope of this investigation is shown in Figure F2.

F1.3 Hyperalkaline site near Amman, Jordan.

The site in northern Jordan is an unusual area containing highly alkaline (pH 12-13) groundwater occurring naturally within a limestone/marl environment. The high pH waters are produced by the interaction of background bicarbonate rock groundwater with zones of high temperature metamorphosed rock hosted between Cretaceous and Tertiary pyritic organic-rich marls and limestones. Hydration of the calcined rock, buffers the groundwater and has produced secondary mineralogy similar to that found in hydrated portland cements and thus provides an analogue of a cementitious radioactive waste repository. The hyperalkaline environment of a cementitious repository has been the focus of extensive modelling and laboratory research in speciation, radionuclide transport and host rock interaction with high pH porewaters. Thus, the site near Amman in northern Jordan provides a unique field-scale analogue to a radioactive waste repository.

Background on Jordanian samples

Microbiological assessment of soil and groundwater samples from four sites near Amman, Jordan were performed. Samples were collected from four sites; M1, M2, M3 and M5 into a suite of enrichment media, which included enrichments for heterotrophs and SRBs. Further information on the location and description of the sites can be found in Khoury et al [17]. In addition unpreserved soil and groundwater samples were collected. Initial investigations [2] assessed the occurrence of a number of microbial groups which included heterotrophic and oligotrophic bacteria, sulphur oxidisers, sulphate reducers, algae and fungi. Sulphate reducers were identified in samples from all sites and these SRBs were stored under anaerobic conditions prior to this study. Heterotrophic organisms were also detected and distribution studies revealed that more microbes were associated with solid material than with the liquid. This study began after a period of 9 months had elapsed from the initial investigation.

F2 Preliminary Investigation

F2.1 Introduction

In order to perform pH tolerance investigations viable bacteria were required. Thus a range of samples from each site; M1, M2, M3 and M5, were assess for viability of the heterotrophic and sulphate reducing bacteria. The samples assessed included :

A. SRB cultures identified in the initial investigation.

B. Heterotrophic field enrichments.

C. SRB field enrichments.

D. Unpreserved soil material.

E. Unpreserved groundwater.

A summary of the origin, history and coding of the samples used in both the preliminary and main investigations is given in Table F1.

F2.2 Viability of SRBs

Materials and Methods

The viability of samples A, C and D (Table F1) from each site was assessed for the presence of viable SRB using Postgates B enrichment broth [18]

Media preparation

Postgates B broth medium was prepared according to the recipe given in Table F2 and dispensed in 25ml aliquots into glass universals. Following autoclave sterilisation at 121°C for 20 minutes at 15 psig, the media was transferred to an anaerobic chamber (Don Whitley Scientific) to equilibrate for a minimum of 24 hours. All subsequent inoculations, observations and transfers were performed in the anaerobic chamber.

Inoculating media

Postgates B broth, 25ml volumes, were inoculated with 5ml volumes of samples A and C and a weight of approximately 5g of sample D from each site. Duplicate sample inoculations were performed and suitable controls were prepared in triplicate for all broth cultures. Controls included autoclave sterilised samples, and uninoculated Postgates B broth (blanks). All inoculations were performed in the anaerobic chamber using aseptic technique. Local safety regulations prevented the use of a flame in the anaerobic chamber so disposable sterile tips, pipettes and spatulas were used once and discarded. All surfaces were swabbed with an alcohol based cleaner prior to commencement of work. To avoid possible contamination from air borne organisms bottles were held at an angle and petri dish lids were tilted over the dish during inoculation. Care was taken to avoid touching bottle lips, surfaces of media etc.

Inoculations were incubated at 25°C in the dark and observed at regular intervals for the presence of SRB indicated by the formation of a black precipitate. Broths inoculated with A were observed after 20 days and 6 weeks incubation. Inoculations of C and D were observed and recorded after 48 hours, 7 days and 30 days incubation.

F2.3 Viability of heterotrophic bacteria

Materials and Methods

Heterotrophic viability in B samples from each site was assessed using CPS agar plates [19].

Media preparation

CPS medium was prepared according to the recipe given in Table F3. Following autoclave sterilisation at 121°C for 20 minutes at 15 psig, a volume of 15-20mls was dispensed into sterile disposable 90mm triple vent petri dishes and allowed to cool. Prior to inoculation, plates were dried in a drying oven to remove surface moisture.

Inoculating plates

A 0.1ml volume of sample B from each site was used to inoculate CPS plates using the spread plate technique. Triplicate inoculations were performed for incubation under aerobic and anaerobic conditions at 25°C. Suitable controls were prepared as described previously and observations of colony growth recorded.

F2.4 Results

Presence and viability of SRBs

The results for Sample A from the four sites are summarised in Table F4. Briefly, poor viability was observed in samples from sites M2, M3, and M5 where growth was detected as slight blackening of the Postgates B broth after 6 weeks incubation. No growth was detected in cultures from site M1.

Viable SRBs were detected in sample C from the four sites. A black precipitate was detected in samples from sites M1 and M3 within 48 hours of inoculation. Whilst blackening was recorded in M2 and M5 samples after 7 days incubation, although M2 produced only slight blackening. These results (duplicate observations) are shown in Table F5.

No growth was detected in sample D inoculations after 48 hours. M3 sample D indicated the presence of viable SRB after 7 days incubation, detected as blackening of the Postgates B broth. An indication of growth was observed with M5 sample D after a period of 7 days incubation, however this was noted as only slight blackening on the surface of the media. After 30 days incubation, inoculations from M5 demonstrated the presence of viable SRB. Sample D from both M1 and M2 appeared poorly viable after 30 days incubation. A summary of duplicate observations is shown in Table F6.

Viability of heterotrophic bacteria

Assessment of sample B indicated the presence of viable heterotrophic bacteria in samples from all sites. The results of colony counts (Figure F3) reveal that more microbes are present in sample B(ii) than sample B(i) with the number being ten times greater in (ii) than (i).

F2.5 Conclusion

Preliminary investigations assessing the viability of samples A, B, C and D from the four sites; M1, M2, M3, and M5, demonstrated that samples B and C were more viable than samples A and D. Therefore, samples B(i), B(ii) and C from each site were used for further investigation into pH tolerance. It was also noted that the viability of sample B(ii) was greater than sample B(i).

F3 Investigating pH Tolerance

F3.1 Introduction

Preliminary viability assessment indicated that the microbial population in samples B and C were still active despite prolonged storage at 4°C. Therefore, these samples were used for assessment of pH tolerance. Firstly, the pH tolerance of sample B and C (enrichments for heterotrophic bacteria and SRBs respectively, Table F1) was assessed using CPS medium. CPS agar plates at pH 7, 9 and 11 and broths at pH 4, 5, 6, 7, 9 and 11 were used adjusting pH with NaOH. It proved impossible to assess the pH tolerance using Postgates B media (recognised SRB enrichment media) due to precipitation of the reducing agent, thioglycollic acid, on altering the pH. Secondly, cultures selected randomly from the above inoculations were subcultured from the initial pH media to medium of a different pH to assess growth over a pH range. In addition, observations of morphological characteristics of the heterotrophic organisms on the CPS agar plates and by Gram staining were made.

F3.2 Materials and Methods

F3.2.1 Growth on pH media

Media preparation

CPS medium was prepared for agar plates according to the recipe given in Table F3. The agar was dissolved by heating to approximately 30°C prior to pH adjustment. Following autoclave sterilisation at 121°C for 20 minutes at 15 psig, a volume of 15-20mls was dispensed into sterile disposable 90mm triple vent petri dishes and allowed to cool. It

was not possible to ascertain the actual pH of the CPS agar plates once they had been autoclaved however, a colour difference was noted which indicated the more alkaline the medium the darker the colour. This colour difference ranged from creamy opaque (pH 7) to transparent caramel (pH 11). CPS broth was prepared according to the recipe for CPS medium (Table F3) without the addition of agar. The pH was adjusted using NaOH and aliquots of 15mls were dispensed into glass universals and labelled with the relevant pH, prior to autoclave sterilisation. Several universal bottles of each pH were sacrificed after autoclaving to determine the actual pH. The findings are given in Table F7.

Sample inoculations

Sample B(ii) from each site was inoculated on to CPS agar plates of pH 7, 9 and 11. Dilutions were prepared using sterile distilled water to achieve 1:10 and 1:100 dilutions. Triplicate 0.1ml inoculations of the neat and diluted samples were prepared, using the spread plate technique, for incubation in an aerobic and anaerobic environment at 25°C. Plates were assessed for growth at regular intervals and observations of colony characteristics and number of colony forming units (CFUs) noted after 3, 6, 9 and 14 days. In addition, samples B(i) and C from each site were inoculated into CPS broth of pH 4, 5, 6, 7, 9 and 11 and incubated for a period of 48 hours. Growth was assessed by turbidity of the media.

F3.2.2 Subculturing pH colonies

Selection of colonies

Six colonies, randomly selected from the CPS pH plates, were used to inoculate CPS broth of pH 4, 5, 6, 7, 9, and 11. These subcultures were numbered 1-6 for reference purposes and a brief summary of the incubation history is given in Table F8. In addition, these colonies were prepared for Gram staining.

Inoculation of CPS pH broth

A loopful of the subculture suspensions was transferred to universals containing 10mls of CPS pH broths. A description of the colony characteristics of the colonies selected for subculturing are shown in Table F9.

All pH broth cultures (Sample B(i) and C inoculations) were incubated in an anaerobic atmosphere at 25°C and observed for growth, indicated by a cloudy precipitate (turbid), after 2 days. Observations were noted as (-) indicating no growth or, (+) indicating growth. In addition, a score of one (+) to four (+)'s were used as an indication of the amount of precipitation, this was an arbitrary assessment, based on interpretation by eye, of the degree of turbidity. The greater the turbidity of the culture the greater the score of (+)'s. In addition, an assessment of bacterial numbers was performed on the subcultured samples by determining turbidity by spectrophotometric analysis.

Turbidity assessment

Determination of turbidity was used for an assessment of the number of viable bacteria in the subcultured samples, 1-6. Turbidity of the pH broth cultures was measured by absorbance at 650nm using a single beam spectrophotometer (Pye Unicam PU 8600 UV/VIS Spectrophotometer). A standard curve was prepared for calculation of numbers of viable bacteria using samples from broth the cultures. Samples of different turbidity values, were selected to provide a range of absorbance readings for the standard curve. CPS agar plates of the relevant pH were inoculated with 0.1ml of neat, 1:10 and 1:100 dilutions of the broth cultures using the streak plate technique. Resultant bacterial

colonies were counted after 3 days incubation. Results are expressed as absorbance @ 650nm against number of CFUs (logarithmic values) per ml. Turbidity of the samples was determined after 2, 3 and 6 days incubation and the number of bacteria calculated. The spectrophotometer was zeroed using CPS broth before and between sample readings to eliminate the possibility of errors due to 'drift'. For zeroing purposes it was found that the pH of the CPS broth had no significant effect on the absorbance reading.

F3.2.3 Morphological characteristics

Colony Characteristics

Colony characteristics were observed on the CPS pH plates, and described according to Collins et al [20]. Briefly, approximate size and colour were noted, and appearance from above described as round (entire), or irregular. The appearance from the side was noted according to whether colonies appeared flat, raised, domed or umbonate. In addition, the texture was described as shiny or dull.

Gram staining

The method used for gram staining was according to Jensen (Table F10) as described by Collins et al [20].

Colonies 1-6 selected for subculturing were prepared using the Gram stain technique. Colonies were removed using an alcohol sterilised wire loop and resuspended in 1.0ml of filter sterilised (0.2µm Acrodisc, Gelman) distilled water. A loopful of the bacterial suspension was smeared on to a clean, alcohol sterilised microscope slide (76 x 26mm, 0.8-1.0mm, Analytical Supplies Ltd.) and heat fixed over a bunsen flame prior to gram staining as described in Table F10. Decolourisation was achieved using 95% ethanol and safranin was used for counterstaining. Oil immersion observations (X100 magnification) were made using a Zeiss microscope fitted with a transmitted light source. The organisms were described according to their shape, cocci or rods, their approximate size and whether they were Gram positive or Gram negative indicated by violet or red stained organisms respectively. Samples were prepared and observed in triplicate.

Scanning Electron Microscopy (SEM)

Using samples D and E (Table F1) from each site, preparations were made for SEM examination. These were prepared according to a modified version of the method described by Jass and Lappin-Scott [21]. Briefly, slurries of sample D were prepared with 0.1M cacodylate buffer pH 7.4 and filtered through 0.2µ filter (nucleopore), to obtain a fine even layer of sample on the surface of the filter. Filters of sample E were prepared using a 15ml volume. Samples were fixed in 3-5% gluteraldehyde in cacodylate buffer for 2 hours at room temperature, surface washed to remove residual gluteraldehyde, and dehydrated with an ethanol/distilled water series of 30, 50, 70 and 100%. Samples were allowed to air dry prior to mounting on aluminium stubs with colloidal carbon conducting cement (Leit-C). Once mounted samples were coated with approximately 25nm of carbon in an evaporation coater (Edwards 306A carbon evaporation coater) and archived prior to SEM examination. Coated samples can be stored in the archives for an extended period, 2 to 4 months, provided they are stable and not subjected to mechanical damage although further coating may be required. Use of the SEM is both time consuming and expensive therefore, observations were made of samples prepared from site M1 only. Samples prepared from the other sites remained in the archives for future examination. An excel voltage of 20 KV was used for SEM examination.

F3.3 Results

F3.3.1 Observations of growth

CPS pH plates

The results for pH tolerance assessment of Sample B(ii) from each site, using CPS medium pH 7, 9 and 11 are shown in Tables F11A and F11B. Table F11A summarises growth observations where (-) indicates no growth and (+) indicates growth. Each (+) represents a 10 fold increase in growth for example, (+) indicates an observation of 1 to 10 CFUs and (++) indicates 11 to 100 CFUs etc. Rate of growth is also indicated in this table as observations are recorded at 3, 6, 9 and 14 days. Table F11B gives a summary of the colony characteristics and observations indicate that the morphology is predominantly of one type. The information in Table F11A is further illustrated in Figure F4 where bacterial numbers determined by counting colonies, are shown. The results show the microbial population to be greatest in site M1 and M2, with the numbers being significantly higher than for sites M3 and M5. The pH yielding the highest number of bacteria in both M1 and M2 is pH 9 where the microorganisms appear to favour an anoxic environment to aerobic conditions. Growth at pH 11 was observed in samples from sites M1 and M2 only, with numbers being significantly less in M1 than in M2. Again the anaerobic population predominates in M2 pH 11 samples. Table F11B gives a summary of the colony characteristics.

CPS pH broth

The results for pH tolerance assessment of samples B(i) and C, using CPS broths of pH 4, 5, 6, 7, 9 and 11 are shown in Table F12. To summarise, no growth was observed in broth cultures inoculated with samples B(i) from any of the four sites. Growth was observed for sample C inoculations, from sites M1 and M2. The pH tolerance of the M1 samples ranged from pH 5 to pH 11 with pH 6 and pH 11 broth cultures showing the most growth, indicated by higher turbidity of the media. The pH tolerance of M2 samples ranged from pH 7 to pH 11, where an increase in turbidity was observed with increasing alkalinity of the media.

F3.3.2 Assessment of subcultured colonies

Growth

Results for pH tolerance of selected colonies subcultured from CPS pH plates, indicate poor tolerance to the pH range (Table F13). Growth was observed in broths inoculated with samples from site M2 only, subcultures 2 and 3. Subculture 2 demonstrated a tolerance to pH ranging from pH 6 to pH 11 with growth being greatest at pH 6 and 7. Growth was noted at pH 6 and pH 9 for subculture 3 although the degree of cloudiness of the media was low, noted by (+).

Turbidity

The turbidity standard curve is shown in Figure F5. The lower portion of the curve has been extrapolated to zero for calculation of bacterial numbers below the lowest value used in preparation of the standard curve. Calculated bacterial numbers are given in Figure F6(a - f). The enumeration results reveal that subcultures 2 and 3 (Figure F6b and c), which are both from site M2, are the most microbiologically active although a difference in pH tolerance, between the two subcultures, is apparent. Subculture 2 demonstrates tolerance to a wide pH range, from pH 6 to pH 11, whereas the microbial population in subculture 3 favours pH 6 and pH 9. The findings for the other subcultures

should be treated with caution due to the low numbers of bacteria recorded, with the exception of subculture 5 (Figure F6e) which indicates pH 9 to be the preferred pH. The results for subculture 1, Figure F6a, show that microorganisms preferring pH 7 predominate initially. However, this population appears to decline after 3 days incubation when the numbers in pH 5 media increase. The noticeable effect of pH on subculture 6 (Figure F6f) is the growth of organisms favouring acidic conditions. This is demonstrated by growth in pH 4 and pH 5 media after 3 days incubation then, significantly after 6 days incubation when increased growth in pH 4 media is evident.

F3.3.3 Morphology

Gram stain

The results in Table F14 indicate the presence of a mixed microbial population as Gram positive and Gram negative rods and cocci were observed although, Gram negative cocci were observed most frequently. It should be noted that in some instances it was difficult to define whether bacteria were red or violet and, depending on the depth of focus used, whether rods or cocci were present, again indicating a mixed population. Characteristics could not be defined for samples prepared from subcultures 1 and 6.

SEM examination

M1 soil preparations revealed the presence of clusters of rod shaped bacteria which appeared to be adhered to the solid material. The size of these organisms was determined as approximately 0.5µ x 4.5-5.0µ. Microorganisms were not seen in samples prepared from M1 groundwater. Photographs showing the microbial clusters from M1 soil preparations are shown in Plate 1.

F4 Discussion

F4.1 General

This project has attempted to establish the pH tolerance of the microbial population, particularly the heterotrophic and sulphate reducing bacteria, indigenous to a naturally occurring highly alkaline (pH 12.6-12.8) site. The relevance of this study can be explained by appreciating that the secondary mineralogy of this site is similar to that found in hydrated portland cements and thus provides an unique field-scale analogue to a cementitious radioactive waste repository.

The first part of this report gives a brief introduction to geomicrobiology, defining the terminology and introducing interrelationships with other fundamental geological processes. A synopsis of notable discoveries and developments has been attempted and an assessment of the importance of future geomicrobiological investigations, with particular reference to the management of a number of environmental concerns, addressed. The material used in this study was obtained from an unusual area containing highly alkaline (pH 12-13) groundwaters occurring naturally in the environment, thus a short section has been included describing the basic geology of the area. In addition, a brief history of the samples has been included.

F4.2 Interpretation of results

F4.2.1 Preliminary experiments

A series of preliminary experiments were performed in order to determine whether the microbial population in the samples had remained viable despite prolonged storage. Of particular interest were the heterotrophic bacteria, those requiring a supply of organic

material from the environment, and the sulphate reducing bacteria. The outcome of this set of experiments was crucial for the continuation of the study to investigate the pH tolerance. Five groups of samples were assessed, each having undergone slightly different procedures during or after collection thus providing a wide scope for obtaining viable bacteria. The results demonstrated that the viability of the heterotrophic and sulphate reducing microbial populations was highest in samples which had been collected into enrichment media, enriched for the specific microbial groups, then stored at 4°C without further attention. Interestingly, SRBs which had been identified by the initial investigation [2] and maintained in nutrient rich media, in an anoxic environment at 25°C, were poorly viable. This can be explained by the use of the batch culture technique which provides a limited supply of nutrients. Thus, whilst the conditions for growth may have been ideal initially, over the extended storage period the nutrient supply had expired. In essence the population had outgrown its environment and had declined progressively through the death phase. It should be noted however, that an indication of growth in these SRB cultures was observed in samples from sites M2, M3, and M5. This can be explained in two ways firstly, a few residual members of the original population could have remained viable or alternatively, growth could be due to the recovery of bacteria from the starvation survival state (analogous to dormancy in plants). This will be discussed later. This preliminary investigation provided the additional information that the microbial activity was greater in the solid material than in that of the liquid. This confirmed the findings of the initial investigation [2]. From these results it was concluded that samples containing viable populations of both heterotrophic bacteria and sulphate reducers were available for further investigation into the pH tolerance of the two microbial groups of interest.

F4.2.2 pH tolerance

The main content of this investigation focuses on assessing the pH tolerance of the heterotrophs and SRBs. Basically this was attempted in two stages firstly, assessment of growth using media of a pH ranging from 4 to 11 and secondly, subculturing colonies observed from the first stage onto media of a different pH. Attempts were made to assess the growth of SRBs in Postgates B medium, however it was only possible to achieve a pH of approximately 7 due to precipitation of the reducing agent when pH was altered. It may have been possible to use a different reducing agent or use a different method of reducing the media. This in itself, could have presented a large area of investigation and will be discussed further in Section F4.3. Thus, pH tolerance was assessed using CPS media which is a general purpose nutrient rich media recognised as an ideal media for growth of heterotrophs although, that does not necessarily mean that it would inhibit growth of SRBs. The heterotrophic population were assessed under aerobic and anaerobic conditions whereas SRB inoculum were assessed under anoxic conditions only, due to their requirement for reduced conditions. It should be noted that cultivation of SRBs in pure culture requires an element of art, as well as science, as they are notoriously temperamental [18, 22, 23]. One of the major prerequisites for growth of SRBs is the redox potential (Eh) of the environment which must start around -100mV. To achieve these conditions providing anoxic atmosphere does help but generally, use of a reducing agent is required which, once a vigorously growing culture is established, can be omitted.

The growth assessment results of both heterotrophs and SRBs revealed that a pH tolerant microbial population was present in samples from sites M1 and M2. The heterotrophic organisms from site M1 (Table F11A and Figure F4) appear to favour anoxic conditions at pH 7 and 9 whereas the heterotrophs from site M2 show maximal growth regardless of

the incubation atmosphere or pH. It should be noted that these results are for the alkaline pH range only thus growth of the indigenous population would be expected as pH conditions simulate those of the natural environment. The SRBs from site M2 (Table F12) when assessed over a pH range from 4 to 11, were found to tolerate alkaline conditions only, ranging from pH 7 to 11. Notably, pH tolerance increased as alkalinity increased, this result was not surprising considering the pH of their native environment. The results of the pH tolerance of SRBs from site M1 however, were surprising as growth was recorded from pH 5 to pH 11 with most growth observed at pH 6 and pH 11. This demonstrates a mixed microbial population but it also indicates the presence of a subset of the native population which are surviving in an environment presenting growth conditions alien to their requirements. This could be explained by the starvation survival response. Alternatively, another consideration is that the microorganisms may have different origins, firstly, they were already resident in the geological formation (autochthonous microorganisms) or secondly, they were introduced as contaminants during collection and operational procedures (allochthonous microorganisms). The problem of the origin of the microbes is beyond the scope of this investigation as it would involve the study of in-situ microorganisms although, repeating the experiment and increasing the number of replicates would assist in detecting whether observations are due to contaminants introduced in the experimental procedure thus validating the significance of the results.

Colony characteristics observations of the heterotrophs (Table F11B) revealed the presence of a predominant type which are described as 1-2mm, cream, round, shiny, domed. These colonies tended to grow quickly, within 24 -48 hours incubation, and rapidly. In addition, pigmented colonies were observed which were generally detected after 9 to 14 days incubation and were noted in low numbers indicating a slower rate of growth. Interestingly, the pigmented colonies were observed in cultures grown under anoxic conditions and generally on media of a higher pH (9 and 11). These results further indicate the presence of a mixed microbial population they also comply with the expectations of growth of organisms from extreme environments [18, 24, 25], that is, that they are slow growing and tend to be outnumbered by other organisms.

Generally, the pH tolerance of the colonies selected for subculturing, into CPS broth of pH ranging from 4 to 11, was poor. Indeed when cultures were observed by eye, growth was detected for subcultures 2 and 3 only (Table F13). No growth was detected below pH 6 for either subculture. Subculture 2 demonstrated highest growth at pH 6 and 7 although growth was detected up to pH 9 whereas growth of subculture 3 was limited to pH 6 and 9. It is interesting that both of these subcultures originated from site M2, indicating a greater pH tolerance of the microbial population from site M2 than the other three sites. It should be noted that these findings reinforce the observations of the initial pH tolerance growth assessments. Use of a spectrophotometer to determine turbidity achieved similar results to those obtained for observations by eye. The advantage in using the spectrophotometer was that it provided a method for enumeration. It should be stated however, that the enumeration results are not quantitative as the limitation of this assessment is, in fact, the parameter it is measuring. This method measures turbidity, and in the assessment an assumption is made that turbidity is proportional to growth. However, this will only be the case up to a point as once maximal growth is achieved the population will begin to die and enter a decline. The processes involved with death generate toxins which themselves can and do cause precipitates which would be detected as increased turbidity. In essence, the turbidity results serve as a indication of the

potential of the microorganisms to grow. The validity of the turbidity results could be enhanced using a number of methods, for example; taking samples for growth on agar plates (viability assessment), measuring biomass by ATP analysis, performing direct bacterial counts using acridine orange staining (epifluorescence technique) and measuring metabolic activity by INT-Formazan formation, to name but a few. These are all ideas which could be proposed as areas for future work.

F4.3 Comments

This investigation has provided a useful insight into the potential of microorganisms to tolerant a wide pH range as it has demonstrated the presence of a microbial population able to tolerate a pH range from pH 6 to pH 11. Of particular relevance is the detection of organisms tolerating highly alkaline conditions analogous to a cementitious radioactive waste repository. These organisms were found to be diverse in nature demonstrated by their morphological characteristics observed on agar plates, by gram staining and SEM examination. Limitations on time and resources resulted in the assessment, primarily of the heterotrophic population and further work is recommended on developing a method for monitoring the pH tolerance of SRBs. This would initially involve manipulation of media to achieve the required pH range in addition to providing conditions required for growth of sulphate reducers.

As mentioned earlier SRBs have a specific requirement for Eh to start around -100mV. This phenomena has been known and widely accepted since 1953 and numerous studies have been undertaken to achieve the required redox conditions. Methods include the use of reductants; for example, sodium sulphide, a thiol compound such as cysteine or sodium thioglycollate, or sodium dithionate. It should be noted however that different agents are recommended for different genera of sulphate reducers. In addition media are incubated in the absence of air using procedures customary in handling anaerobes: completely filled and stoppered containers, vessels with plugs containing alkaline pyrogallol to remove traces of oxygen, or in anaerobic jars or cabinets filled with an inert gas such as nitrogen. I feel it is worth mentioning that I am not alone in the search for a suitable media to assess the pH tolerance of SRBs, others [26, 27] have also experienced difficulties. A comment made by Postgates [18] lurks menacingly in the back of my mind ‘the most remarkable fact that even nowadays, 45 years after Beijerinck’s pioneering work, the number of laboratories in which pure cultures of sulphate-reducing bacteria have been obtained can probably be counted on the fingers of one hand’.

F4.3.1 General review

Literature on research into the microbial potential in extreme environments is continually increasing [e.g. 24, 25, 28, 29]. Bååth et al [29] reviewed the idea of a starvation response of bacteria. The classical growth pattern defined as lag, exponential, stationary and decline (death) is universally accepted. However, studies dating back to the 1920’s reported the survival and persistence of bacteria in the absence of carbon, energy or other essential growth nutrients. During this starvation survival, bacteria survive for indefinite periods and adopt specific starvation responses. These responses indicated that when growth ceased, due to nutrient depletion, a proportion of the bacterial population entered a dormant, viable, starved state and remained in that state until favourable growth conditions were restored. Many natural environments, including soil and rocks, have poor and unevenly distributed areas of nutrients and are considered to be oligotrophic so that starvation is the normal state of their microinhabitants. These microhabitats may differ in nutrient status to adjacent habitats. Therefore, some specific responses must

occur that allow bacteria to survive in such areas of differing nutrient status for long periods. It is readily appreciated therefore, that an understanding of how bacteria change in response to nutrient limitations will improve our knowledge of how they behave in nature.

Of particular relevance to this study are the observations of West [24], who describes how sampling of relevant geological formations has shown the presence of microbes known to be important in biodeterioration and geological processes. In addition a review of the microbial presence in extreme environments demonstrated that certain microbes can tolerate individual repository conditions. Within such a situation microbial activity could produce both direct and indirect effects . Biodeterioration can affect waste forms and engineered barriers in the form of deterioration of repository materials, for example cement. Also, radionuclide mobilisation and transport could be influenced both directly or indirectly as microbes may directly take up nuclides or compete for sites on rock material, or they may alter the geochemical environment by changing, for example, the pH thus rendering radionuclides more mobile. Conversely, microbes may have positive effects such as inhibition of movement by blocking fissures and pores by biofilm production. Until relatively recently, literature was sparse on the effects of microorganisms on repository containment but as advances are made in microbial techniques more information becomes available and already indicates that microbial presence will have some influence on corrosion and biodeterioration and thus on release and transport of radionuclides.

F5 Acknowledgements

I would like to thank my employer and sponsor the British Geological Survey for enabling me to undertake this part-time degree and Dr. Julia West for her initial support and encouragement to embark on the course. Thanks also to NAGRA (Nationale Genossenschaft für die Langerung radioaktiver Abfälle - the Swiss National Cooperative for the Disposal of Radioactive Waste), for supplying material for this project and allowing the publication of results.

Special thanks are due to Pat Coombs, a friend and colleague, whose patience, understanding and assistance have helped me retain my sanity throughout the preparation of this thesis.

F6 References

[1] H.L. Ehrlich, *Geomicrobiology*. Second edition (revised). Marcel Dekker, Inc, 1990.

[2] P. Coombs, S. Gardner and J. West, *Natural Analogue for Geochemistry and Microbiology of Cement Porewaters and Cement Porewater Host Rock/Near Field Interactions.* Progress Report: April - September 1992. British Geological Survey, Fluid Processes series Technical Report Number WE/92/31C, 1992.

[3] S.I. Kuznetsov, M.V. Ivanov and N.N. Lyalikova, *Introduction to Geological Microbiology.* English Translation. McGraw-Hill, 1963.

[4] E.C. Harder, *Iron depositing bacteria and their geologic relations.* U.S. Geological Survey. Paper 133 (89pp), 1919.

[5] O. Stutzer, *Origin of Sulfur deposits.* Econ Geol, **7**, 733-743, 1912.

[6] V.I. Vernadsky, *An attempt at descriptive mineralogy.* Izbrannye Trudy, Volume 2, 1908-1922.

[7] M.W. Beijerinck, 1895 (as cited by Ehrlich, 1990)
[8] A. van Delden, 1903 (as cited by Ehrlich, 1990).
[9] E. Béchamp, Ann. Chem. Phys. **13**, 103, 1868 (as cited by Ehrlich, 1990).
[10] W. Tappeiner, 1882 (as cited by Ehrlich, 1990).
[11] L. Popoff, Arch. Ges. Physiol. **10**, 142, 1875 (as cited by Ehrlich, 1990).
[12] S.A. Waksman, *Principles of Soil Microbiology.* Second edition, revised. Williams & Wilkins, 1932.
[13] baas becking et al 1960
[14] colmer, temple and hinkle, 1950
[15] L.C. Bryner, J.V. Beck, D.B. Davis and D.G. Wilson, *Microorganisms in leaching sulfide minerals.* Industrial Engineering Chemistry. **46**, 2587-2592, 1954.
[16] S.R. Zimmerley, D.G. Wilson and J.D. Prater, *Cyclic leaching process employing iron oxidizing bacteria.* U.S. patent US 2, 829, 964, 1958.
[17] H.M. Khoury, E. Salameh, I.D. Clark, P. Fritz, W. Vajjali, A.E. Milodowski, M.R. Cave and W.R. Alexander, *A natural analogue of high pH cement pore waters from the Marqarin area of northern Jordan. 1: Introduction to the site.* J. of Geochemical Exploration. **46**, 117-132, 1992.
[18] J.R. Postgates, *The sulphate-reducing bacteria.* Second edition. Cambridge University Press, 1984.
[19] V.G. Collins, *The distribution and ecology of bacteria in fresh water.* Proc. Soc. Wat Treat. Exam. **12**, 40-67, 1963
[20] C.H. Collins, P.M. Lyne and J.M. Grange, *Microbiological Methods.* Sixth Edition (Revised). Butterworth-Heinemann, 1991.
[21] J. Jass and H.M. Lappin-Scott, *Practical Course on Biofilm Formation Using the Modified Robbins Device.* Biofilm Technologies Research Group. University of Exeter, 1992.
[22] F. Widdel and N. Pfennig, *A new, anaerobic, sporing,acetate-oxidizing sulfate-reducing bacterium.* Arch. Microbiol., **112**, 119-22, 1977.
[23] N. Pfennig and H. Biebl, *The dissimilatory sulfur reducing bacteria. In The Prokaryotes. A handbook on the habitats, isolation, and identification of bacteria,* Ed. Starr, M.P., Stolp, H., Trüper, H.G., Balows, A. and Schlegel, H.G. **1**, 926-40, 1981.
[24] J.M. West, *Geomicrobiological aspects of the deep disposal of radioactive waste.* Council for National Academic Awards PhD Thesis, 1987.
[25] H.M. Lappin-Scott and J.W. Costerton, *Starvation and penetration of bacteria in soils and rocks.* Experimentia. **46**, 807-812, 1990.
[26] Grant et al, Personal Communication
[27] Jass et al, Personal Communication
[28] A.H. Bath, N. Christofi, C. Neal, J.C. Philp, M.R. Cave, I.G. McKinley and U. Berner, *Trace element and microbiological studies of alkaline groundwaters in Oman, Arabian Gulf: A natural analogue for cement pore-waters.* British Geological Survey Report FPLU 87-2, 1987.
[29] E. Bååth, Å. Frostegård and H. Fritze, *Soil Bacterial Biomass, Activity, Phospholipid Fatty Acid Pattern, and pH Tolerance in an Area Polluted with Alkaline Dust Deposition.* Applied and Environmental Microbiology. **58(12)**, 4026-4031, 1992.

Bibliography

Baas Becking, L.G.M., Kaplan, I.R. and Moore, D. 1960. Limits of the environment in terms of pH and oxidation and reduction potentials. Journal of Geology. **68:** 243-284.

Beller, H.R., Reinhard, M. and Grbic-Galic, D. 1992. Metabolic By Products of Anaerobic Toluene Degradation by Sulfate-Reducing Enrichment Cultures. Applied and Environmental Microbiology. **58**(9), 3192-3195.

Bull, A.T., Ellwood, D.C. and Ratledge, C. 1979. Microbial Technology: Current State, Future Prospects. (Symposium of the Society for General Microbiology; 29) Cambridge University Press.

Burback, B.L. and Perry, J.J. 1993. Biodegradation and Biotransformation of Groundwater Pollutant Mixtures by *Mycobacterium vaccae*. Applied and Environmental Microbiology. **59**(4), 1025-1029.

Burns, R.G. and Slater, J.H. (Eds) 1982. Experimental Microbial Ecology. Blackwell Scientific Publications.

Colmer, A.R., Temple, K.L. and Kinkle, H.E. 1950. An iron oxidising bacterium from the acid drainage of some bituminous coal mines. J. Bacteriol. **59:** 317-328.

Dowling, N.J.E., Guezennec, J. and White, D.C. 1987. Microbial problems in the offshore oil industry. John Wiley & Sons.

Elliot, J.M. 1983. Some methods for the statistical analysis of samples of Benthic Invertebrates. Freshwater Biological Association Scientific Publications No. 25.

Environmental control and public health: Technology Unit 4 - Statistics and Epidemiology. 1992. The Open University.

Håggblom, M.M., Rivera, M.D. and Young, L.Y. 1993. Influence of Alternative Electron Acceptors on the Anaerobic Biodegradability of Chlorinated Phenols and Benzoic Acids. Applied and Environmental Microbiology. **59**(4), 1162-1167.

Johnson, A.C. and Wood, M. 1992. Microbial Potential of Sandy Aquifer Material in the London Basin. Geomicrobiology Journal. **10**, 1-13.

Mustin, C., Berthelin, J., Marion, P. and De Donato, P. 1992. Corrosion and Electrochemical Oxidation of a Pyrite by *Thiobacillus ferrooxidans*. Applied and Environmental Microbiology. **58**(4), 1175-1182.

Pronk, J.T., De Bruyn, J.C., Bos, J. and Kuenen, J.G. 1992. Anaerobic Growth of *Thiobacillus ferrooxidans*. Applied and Environmental Microbiology. **58**(7), 2227-2230.

Shaw, J.C., Bramhill, B., Wardlaw, N.C. and Costerton, J.W. 1985. Bacterial Fouling in a Model Core System. Applied and Environmental Microbiology. **9(3):** 693-701.

Suzuki, I., Chan, C.W. and Takeuchi, T.L. 1992. Oxidation of Elemental Sulfur to Sulfite by *Thiobacillus thioxidans* Cells. Applied and Environmental Microbiology. **58**(11),3767-3769.

Table F1 Summary of the origin, history and coding of samples

Code	Sample	Historical
A	SRB culture	Cultures of (i) groundwater and (ii) solid material inoculum, identified as SRB positive by the initial investigation [2]. Cultures stored* under anaerobic conditions at 25°C, in media enriched for growth of SRB, without further maintenance[1].
B	Heterotrophic	Selection media enriched for growth of heterotrophic field enrichments bacteria. Media inoculated 'in the field' (in Jordan) with (i) groundwater or (ii) solid material. Samples stored* at 4°C[1,2].
C	SRB field	Selection media enriched for growth of SRB. Media enrichments inoculated with solid material and stored* as described in B above[1,2].
D	Unpreserved	Solid material collected into whirlpak bags and stored* at solid material 4°C[1,3].
E	Unpreserved	Groundwater collected into 500ml nalgene® bottles and groundwater stored* at 4°C[3].

Stored*- refers to a storage period of 9 months from sample collection to initiation of this series of experiments.

1 Samples used in Viability assessment

2 Samples used in pH tolerance investigation.

3 Samples used for SEM examination.

Table F2 Postgates B medium - General purpose enrichment broth for SRB [18]

Compound	g/litre
KH_2PO_4	0.5
NH_4Cl	1.0
$CaSO_4$	1.0
$MgSO_4.7H_2O$	2.0.
Sodium Lactate	3.45mls
Yeast extract	1.0
Ascorbic acid	0.1
Thioglycollic acid	0.1ml
$FeSO_4.7H_2O$	0.5

Tap water 1 litre, adjust media to between pH 7 and 7.5. This media will always contain a precipitate.

Table F3 CPS medium - General medium for heterotrophic bacteria

Compound	g/litre
Glycerol	1m
$FeCl_3.6H_2O$	25µl (0.01% w/v solution)
Peptone	0.5.
Casein hydrolysate	0.5
Starch	0.5
$MgSO_4.7H_2O$	0.05
K_2HPO_4	0.2
Agar	15

Distilled water to 1 litre. This usually gives a medium of pH 7.0 to 7.5. Agar dissolved prior to pH adjustment

Table F4 SRB viability in sample A

SITE	CODE	OBSERVATION	
		20 DAYS	6 WEEKS
M1	A(i)	No Blackening	No Blackening
	A(ii)	No Blackening	No Blackening
M2	A(i)	No Blackening	Slight Blackening
	A(ii)	No Blackening	Slight Blackening
M3	A(i)	No Blackening	Slight Blackening
	A(ii)	No Blackening	Slight Blackening
M5	A(i)	No Blackening	Slight Blackening
	A(ii)	No Blackening	Slight Blackening

Table F5 SRB viability in sample C

SITE	OBSERVATION		
	48 Hours	7 Days	30 Days
M1	Black precipitate	Black precipitate	Black precipitate
	Black precipitate	Black precipitate	Black precipitate
M2	No change	No change	Slight blackening
	No change	Surface precipitate	Black precipitate
M3	Black precipitate	Black precipitate	Black precipitate
	Black precipitate	Black precipitate	Black precipitate
M5	No change	Slight blackening	Black precipitate
	No change	Black precipitate	Black precipitate

Table F6. SRB viability in sample D

SITE	OBSERVATION		
	48 Hours	7 Days	30 Days
M1	No change	No change	Slight blackening
	No change	No change	No change
M2	No change	No change	Surface blackening
	No change	No change	Surface blackening
M3	No change	Black precipitate	Black precipitate
	No change	Black precipitate	Black precipitate
M5	No change	Slight surface blackening	Black precipitate
	No change	No change	Surface blackening

Table F7 The effect of autoclave sterilisation on the pH of CPS broth

Before	After
4	4.15
5	5.18
6	6.07
7	7.09
9	9.1
11	10.45

Table F8 Summary of incubation history of colonies selected for subculturing to assess pH tolerance using CPS pH broths

Site	Subculture Number	INCUBATION HISTORY	
		Atmosphere	Media
M1	1	Anaerobic	CPS pH 11
M2	2	Anaerobic	CPS pH 11
M2	3	Anaerobic	CPS pH 11
M3	4	Anaerobic	CPS pH 7
M3	5	Anaerobic	CPS pH 7
M5	6	Anaerobic	CPS pH 7

Table F9 Colony characteristics of colonies selected for subculturing

Subculture Number	Colony description*
1	4-5mm, pinkish brown, irregular, dull, umbonate.
2	2-3mm, light brown, regular, shiny, domed.
3	1mm, white, irregular, shiny, flat.
4	4-5mm, pink, regular, shiny, domed.
5	3-4mm, white, irregular, dull, umbonate.
6	5mm, pink, regular, shiny, flat.

*Colonies described according to Collins et al [20].

Table F10 Jensen's method for Gram staining [20]

1. Dissolve 0.5g methyl violet in 100mls distilled water.
2. Dissolve 2g potassium iodide in 20mls distilled water. Add 1g of finely ground iodine and stand overnight. Make up to 300mls when dissolved.
3. Dissolve 1g of safranin or 1g of neutral red in 100mls of distilled water.

   Stain with methyl violet solution for 20 seconds. Wash off and replace with iodine solution. Leave for 1 minute. Wash off iodine solution with 95% alcohol or acetone, leaving on for a few seconds. Wash with water. Counter stain with fuchsin or Safranin for 30 seconds.

   Note: Some practice is required with this stain to achieve the correct degree of decolourisation. Acetone decolourises much more rapidly.

Table F11A Assessment of pH tolerance: Summary of growth for sample B(ii) on CPS pH plates.

CPS pH	Incubation Atmosphere	Incubation period 3 days	6 days	9 days	14 days
M1 B(ii)					
7	Aerobic	+++	++++	(d)	
	Anaerobic	++++	(d)		
9	Aerobic	+++	(d)		
	Anaerobic	++++	(d)		
11	Aerobic	++	++	(d)	
	Anaerobic	++	++	(d)	
M2 B(ii)					
7	Aerobic	++++	(d)		
	Anaerobic	++++	(d)		
9	Aerobic	++++	(d)		
	Anaerobic	++++	(d)		
11	Aerobic	++++	(d)		
	Anaerobic	++++	(d)		
M3 B(ii)					
7	Aerobic	-	-	++	++
	Anaerobic	-	-	+	(d)
9	Aerobic	-	-	++	++
	Anaerobic	-	+	+	(d)
11	Aerobic	-	-	-	-
	Anaerobic	-	-	-	-
M5 B(ii)					
7	Aerobic	-	-	-	-
	Anaerobic	-	+++	(d)	
9	Aerobic	-	-	+	+
	Anaerobic	-	+	+	(d)
11	Aerobic	-	-	-	-
	Anaerobic	-	-	+	(d)

Note: (+) indicates growth where each + represents a 10 fold increase in CFU. (-) indicates no growth. (d) means plates discarded. This information is illustrated histographically in Figure 4. Details of sample coding are given in Table 1.

Table F11B Assessment of pH tolerance: Summary of colony characteristics for sample B(ii) on CPS pH plates.

CPS pH	Incubation Atmosphere	OBSERVATION Colony characteristics
M1 B(ii)		
7	Aerobic	Very small (<1mm), cream, round, shiny, domed.
	Anaerobic	Very small (<1mm), cream, round, shiny, domed
9	Aerobic	1-2mm, cream, round, shiny, domed.
	Anaerobic	1-2mm, cream, round, shiny, domed.
11	Aerobic	3-4mm, creamy yellow, regular, smooth, raised.
	Anaerobic	2-3mm, creamy yellow, regular, smooth, raised & 4-5mm, pinkish-brown, irregular, dull, umbonate.
M2 B(ii)		
7	Aerobic	1-2mm, cream, round, shiny, domed.
	Anaerobic	1-2mm, cream, round, shiny, domed
9	Aerobic	1-2mm, cream, round, shiny, domed.
	Anaerobic	1-2mm, cream, round, shiny, domed
11	Aerobic	1-2mm, cream, round, shiny, domed
	Anaerobic	2-3mm, light brown, regular, shiny, domed & 1mm,white, irregular, flat.
M3 B(ii)		
7	Aerobic	2-3mm, cream, round, shiny, domed & 2-3mm, white, regular, shiny, raised.
	Anaerobic	4-5mm, pink, regular, shiny, domed & 3-4mm, white, irregular, dull, umbonate.
9	Aerobic	2-3mm, white, regular, shiny, raised.
	Anaerobic	1-2mm, cream, round, shiny, raised.
11	Aerobic	No growth.
	Anaerobic	No growth.
M5 B(ii)		
7	Aerobic	No growth.
	Anaerobic	1mm, off white, round, shiny, domed and 5mm, pink, regular, shiny, raised.
9	Aerobic	3mm, yellow, round, shiny, raised.
	Anaerobic	1mm, off white, round, shiny, domed.
11	Aerobic	No growth.
	Anaerobic	5mm, pink, regular, shiny, flat.

Table F12 Observations of growth for samples B(i) and C in CPS pH broths after 48 hours incubation.

Sample Code	CPS broth pH	Growth(+,-)	Sample Code	CPS broth pH	Growth (+,-)
M1 B(i)	4	-	M1 C	4	-
	5	-		5	+
	6	-		6	+++
	7	-		7	++
	9	-		9	++
	11	-		11	+++
M2 B(i)	4	-	M2 C	4	-
	5	-		5	-
	6	-		6	-
	7	-		7	++
	9	-		9	+++
	11	-		11	++++
M3 B(i)	4	-	M3 C	4	-
	5	-		5	-
	6	-		6	-
	7	-		7	-
	9	-		9	-
	11	-		11	-
M5 B(i)	4	-	M5 C	4	-
	5	-		5	-
	6	-		6	-
	7	-		7	-
	9	-		9	-
	11	-		11	-

Note: + indicates growth, - indicates no growth.

Table F13 Observations of growth of Subcultures in CPS pH broths after 48 hours incubation

Site	Code	Broth pH	Growth (+,-)	Site	Code	Broth pH	Growth (+,-)
M1	1	4	0	M2	2	4	0
		5	0			5	0
		6	0			6	+++
		7	0			7	+++
		9	0			9	++
		11	0			11	+
M2	3	4	0	M3	4	4	0
		5	0			5	0
		6	+			6	0
		7	0			7	0
		9	+			9	0
		11	0			11	0
M3	5	4	0	M5	6	4	0
		5	0			5	0
		6	0			6	0
		7	0			7	0
		9	0			9	0
		11	0			11	0

Note: See Tables 8 and 9 for background on subcultures.

Table F14 Gram stain observations for subcultures 2 - 5.

Code	Subculture	Gram stain Observation
M2	2	Gram +ve rods, 0.5µ x 1µ
M2	3	Gram -ve cocci, very small <1µ, difficult to define whether rods or cocci.
M3	4	Mixed population: Gram -ve cocci, 1-2µ and Gram -ve rods, 0.5-1.0µ x 4.0-5.0µ.
M3	5	Mixed population: Gram -ve cocci, 1-2µ and Gram -ve rods, 0.5-1.0µ x 4.0-5.0µ.

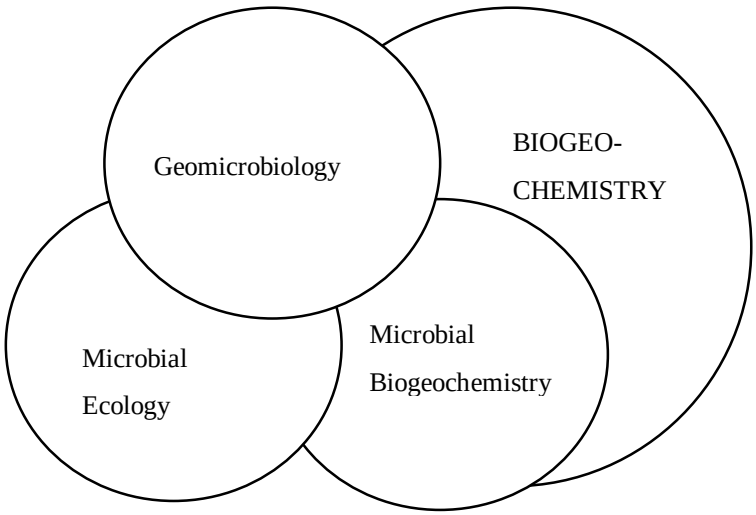

Figure F1 Interrelationships between geomicrobiology, microbial ecology, microbial biogeochemistry and biogeochemistry.

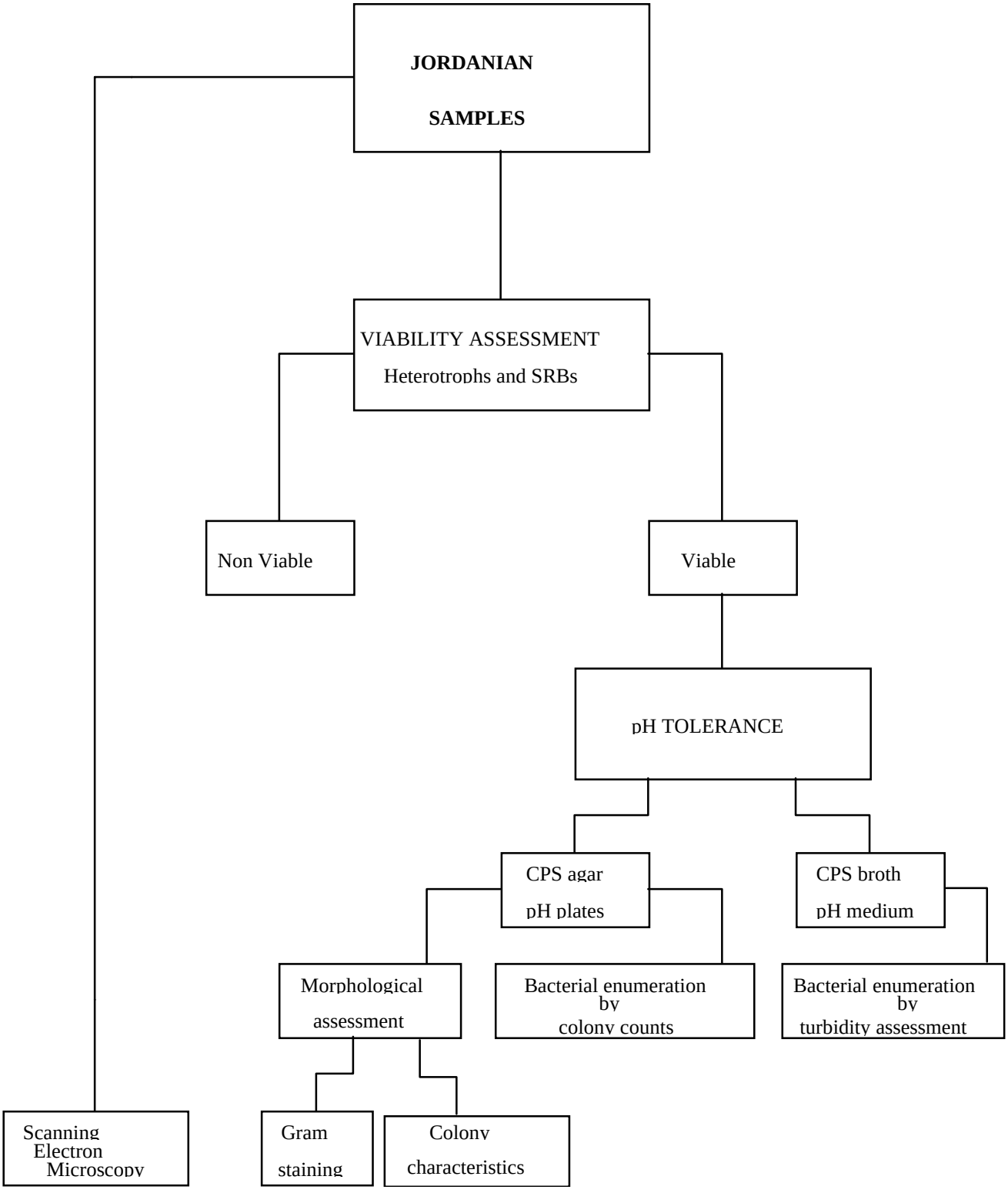

Figure F2 An overview of the scope of the investigation

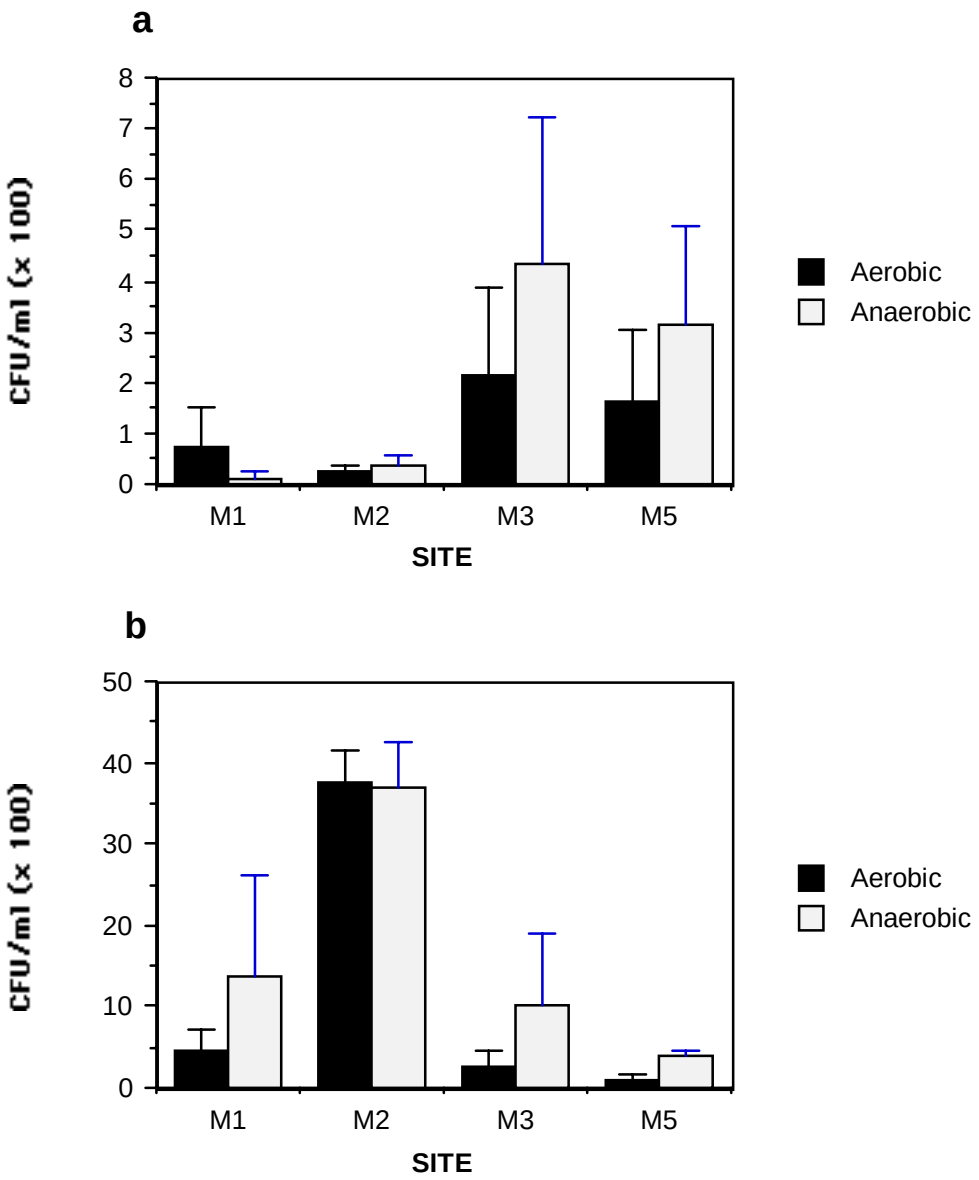

Figure F3 **Growth of the heterotrophic organisms in sample B from each site. The histograms show the number of CFU/ml in (a) sample B(i) and, (b) sample B(ii). Results are mean of triplicate plate inoculations plus standard error bars.**

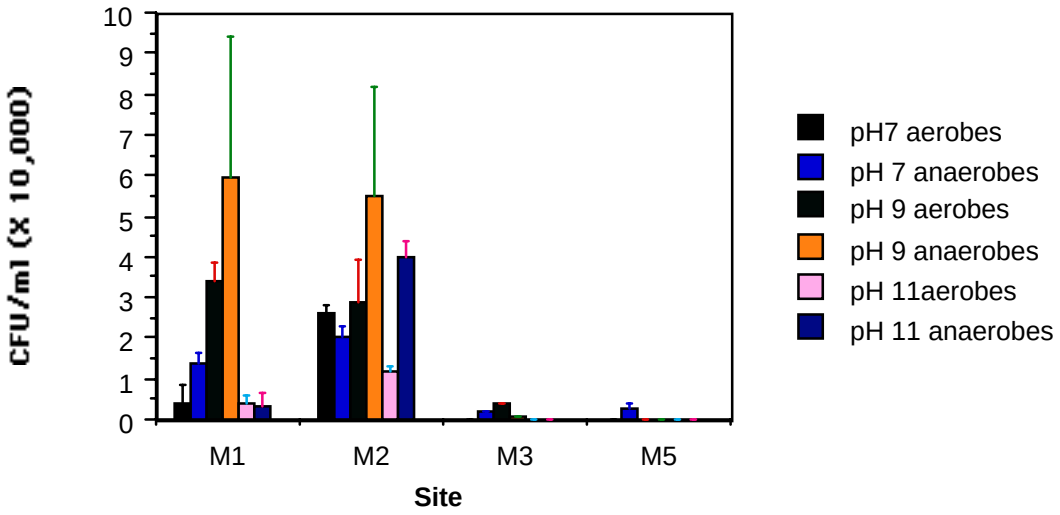

Figure F4 **Histogram showing results of bacterial enumeration for sample B(ii) when grown on CPS agar plates of different pH. Results are mean of triplicate plate inoculations plus standard error bars.**

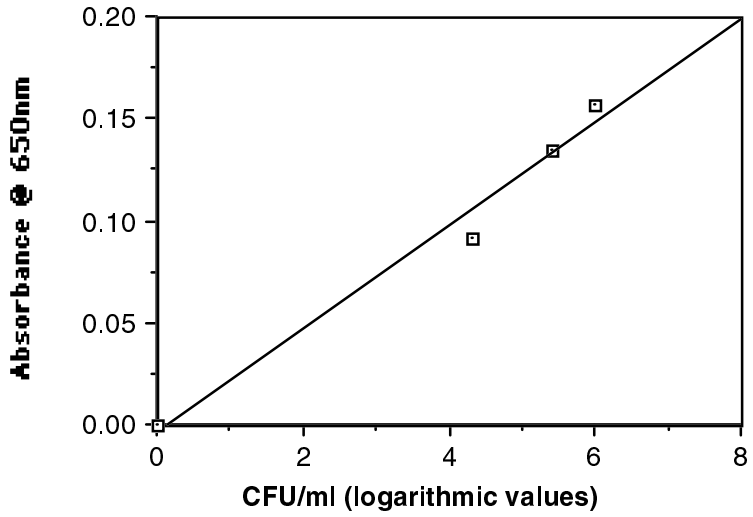

Figure F5 **Turbidity standard curve. Used for bacterial enumeration of subcultures grown in CPS pH broth media.**

6a

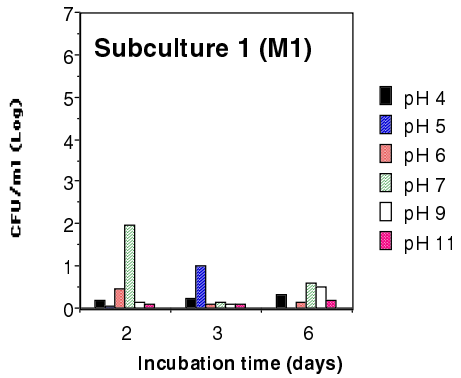

6b

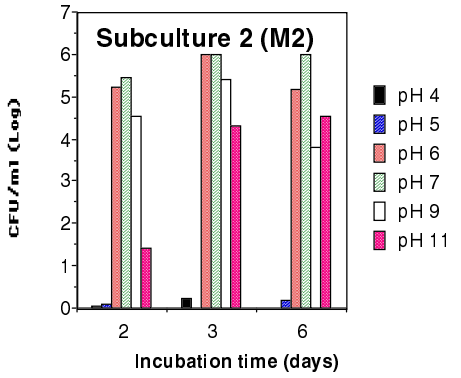

6c

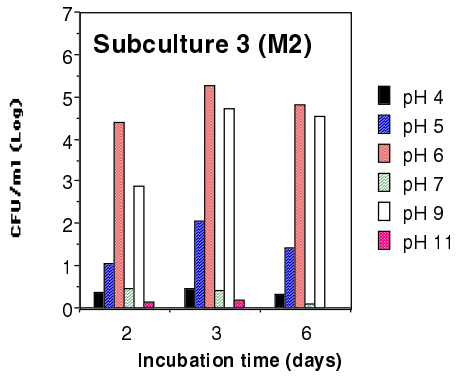

6d

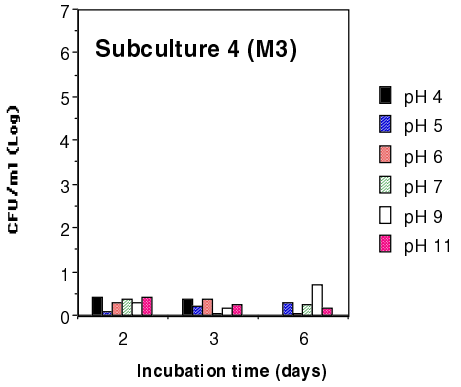

6e

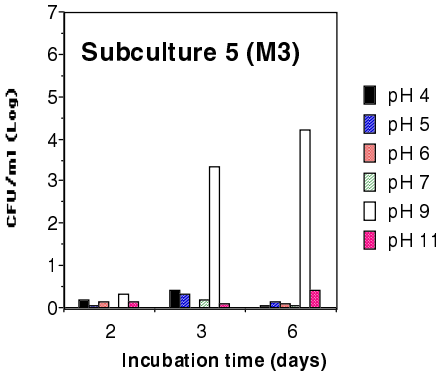

6f

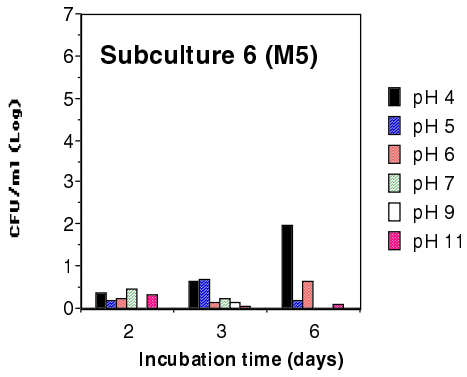

Figure F6 **Bacterial enumeration of selected subcultures calculated by turbidity assessment. Histograms (a)-(f) show the number of CFU/ml in subcultures 1 - 6 respectively.**

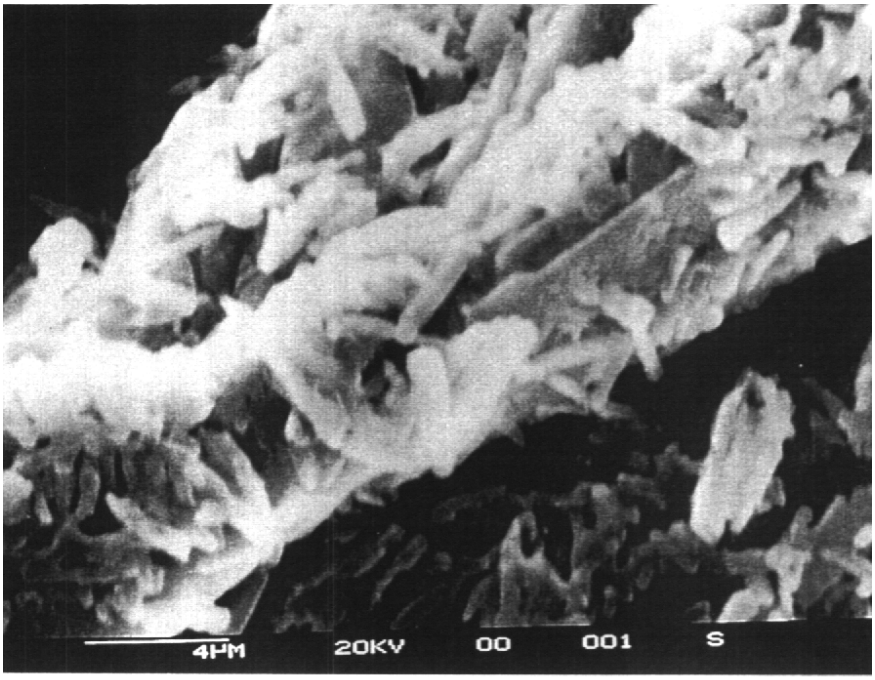

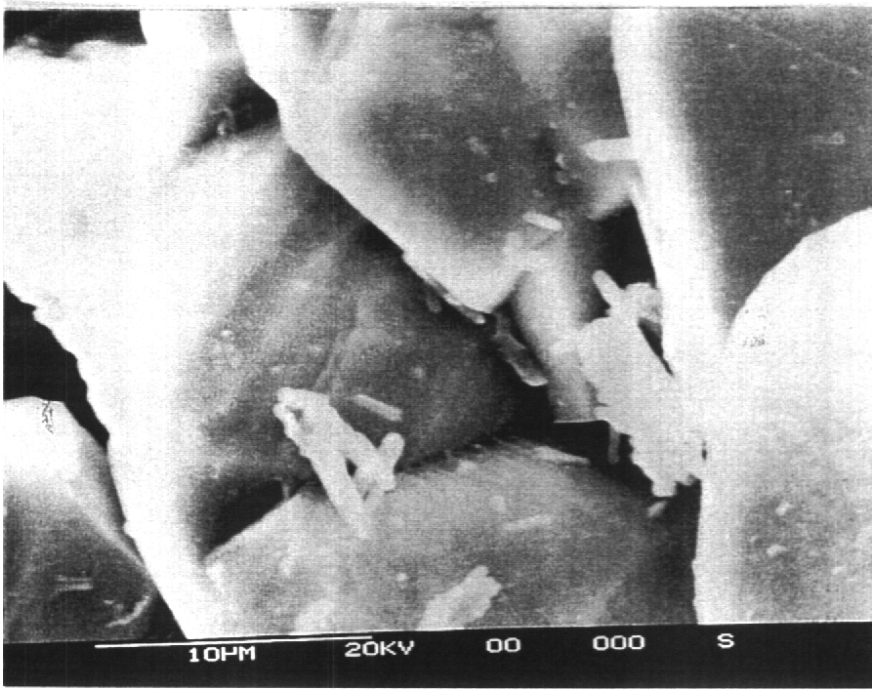

Plate F1 **Scanning electron micrograph showing clusters of rod shaped bacteria detected in solid material from site M1.**
(a) bar, 4µm
(b) bar, 10µm

ISBN 1-84029-211-3

For further information contact
United Kingdom Nirex Limited
Curie Avenue, Harwell, Didcot,
Oxfordshire OX11 0RH

NIREX